Dissertation zur Erlangung des Doktorgrades
der Fakultät für Chemie und Pharmazie
der Ludwig-Maximilians-Universität München

Development of Low-scaling Tensor Hypercontracted Electron Correlation Methods for Energies and Magnetic Properties

Felix Heinz Bangerter

aus

Stuttgart

2024

Erklärung

Diese Dissertation wurde im Sinne von §7 der Promotionsordnung vom 28. November 2011 von Herrn Prof. Dr. Christian Ochsenfeld betreut.

Eidesstattliche Versicherung

Diese Dissertation wurde eigenständig und ohne unerlaubte Hilfe erarbeitet.

München, 15.09.2024

Felix Heinz Bangerter

Dissertation eingereicht am:	18.06.2024
1. Gutachter:	Prof. Dr. Christian Ochsenfeld
2. Gutachter:	Prof. Dr. Benjamin Fingerhut
Mündliche Prüfung am:	22.07.2024

Für meinen Großvater Jörg

Danksagung

An erster Stelle gebührt mein Dank Herrn Prof. Dr. Christian Ochsenfeld für die Betreuung der vorliegenden Arbeit, die Unterstützung auf dem Weg dahin und die Möglichkeit meinen eigenen Forschungsinteressen nachzugehen. Des Weiteren bedanke ich mich bei Herrn Prof. Dr. Benjamin Fingerhut für die Übernahme des Zweitgutachtens.

Den Fonds der chemischen Industrie danke ich für die finanzielle Unterstützung durch das Kekulé-Stipendium und dem daraus entstandenen wissenschaftlichen Austausch.

Mein besonderer Dank gilt Dr. Michael Glasbrenner für die Betreuung und die Unterstützung während der Anfangszeit der Promotion. Bei Dr. Jörg Kußmann bedanke ich mich für die Zuverfügungstellung des `FermiONs++` Programmpaketes, was die effiziente Implementierung der entwickelten Theorien ermöglicht hat. Auch bedanken möchte ich mich in diesem Sinne bei Dr. Michael Glasbrenner, Dr. Henryk Laqua, Dr. Filippo Sacchetta, Viktoria Drontschenko und Jannik Roth für die produktive Zusammenarbeit. Diese wäre ohne die hervorragende Infrastruktur des arbeitskreiseigenen Rechenclusters nicht möglich gewesen. Daher bedanke ich mich herzlich bei Gökçen Savaşçı für die langjährige Instandhaltung unseres Rechenclusters und für die Einführung in die Welt der Systemadministration. Im gleichen Atemzug bedanke ich mich bei Yannick Lemke für die tatkräftige Unterstützung bei der Fortführung dieser Arbeiten, aber auch für alle (nicht)fachlichen Gespräche und witzigen Momente sowie die zahllosen Stunden der IT-Arbeit. Außerdem möchte ich mich bei Lars Urban, Andreas Hulm, Judit Katalin Szántó und Alexandra Stan-Bernhardt sowie letztlich bei allen Mitgliedern des Arbeitskreises Ochsenfeld, die ich während meiner Zeit hier kennenlernen durfte, für die angenehme Arbeitsatmosphäre, die vielen Backwaren und anregenden Gespräche bedanken. Des Weiteren bedanke ich mich bei Helga Senft und Barbara Wutz für administrative und organisatorische Tätigkeiten am Lehrstuhl.

Bei meiner Familie möchte ich mich für den Rückhalt bedanken, die es mir ermöglicht hat mein Studium nach meinen Wünschen zu gestalten. Zuletzt gilt meine tiefempfundene Dankbarkeit meiner Partnerin Julija Reitenbach für ihre Geduld und Verständnis während meiner Promotion sowie für ihre unnachgiebige Unterstützung in dieser Zeit und alles was im Leben noch wichtig ist.

Summary

Ever since the advent of modern day compute architectures, problems that seemed intractable in the past now have become routine operations on consumer grade hardware. To minimize the time to solution, these hardware improvements should be accompanied by algorithmic advancements. In this regard, the numerical solution of the Schrödinger equation underlying the quantum mechanical description of matter is crucial for the understanding of chemical processes, albeit being computationally expensive.

In this context, wave function methods have proven to provide high accuracy for chemically relevant systems, with one of the central limitations being the necessity to store and contract the fourth-order electron repulsion integral (ERI) tensor. To overcome this impediment, this thesis is concerned with the development of efficient algorithms to obtain lower-order approximations to the ERI tensor through least-squares tensor hypercontraction (LS-THC). LS-THC provides the unique opportunity of expressing the ERI tensor entirely in second-order tensors, thereby significantly reducing the storage requirements, while also lowering the computational cost of integral contractions, ubiquitously occurring in electron correlation methods. Due to the aforementioned advantages, LS-THC is used as a versatile tool for significantly improving the performance of a variety of correlation methods. This is demonstrated for ground state energies of perturbative methods, such as second-order Møller–Plesset perturbation theory (MP2) as well as second-order approximate coupled cluster theory (CC2). Furthermore, the resulting LS-THC-CC2 method is extended to excitation energies using the linear-response coupled cluster formalism. Besides for the calculation of energies, LS-THC is particularly attractive for adaptation to methods aiming at calculating molecular properties. From the underlying energy functional of a given method, properties can be obtained by differentiation, which in general results in a multiplication of occurring ERI types. Through the example of hyperfine coupling constants, it is demonstrated how to efficiently perform the resulting integral contractions in the THC format, when applied to MP2. Overall, the developed LS-THC approach enables the calculation of energies and first-order properties of large chemically relevant systems beyond 500 atoms.

In addition to the development of LS-THC based low-scaling correlation methods, the range of methods suitable for the accurate calculation of nuclear magnetic resonance (NMR) chemical shifts is extended. Based on encouraging results for NMR shifts at the random phase approximation (RPA) level of theory obtained by numerical differentiation, the corresponding analytic second-order derivative is derived and implemented. This represents the first formulation of an analytical second-order property for RPA as a post-Kohn–Sham method based on the adiabatic-connection fluctuation-dissipation theorem.

List of Publications

The present work is a cumulative dissertation comprising four articles (labeled I-IV) published in peer-reviewed journals. All articles and the author's contribution to each of them are stated below:

I **F. H. Bangerter**, M. Glasbrenner, C. Ochsenfeld
"Low-Scaling Tensor Hypercontraction in the Cholesky Molecular Orbital Basis Applied to Second-Order Møller–Plesset Perturbation Theory"
J. Chem. Theory Comput. **17**, 211–221 (2021).
Contribution by the author: *All of the theory, most of the implementation, all of the test calculations and all of the writing.*

II **F. H. Bangerter**, M. Glasbrenner, C. Ochsenfeld
"Tensor-Hypercontracted MP2 First Derivatives: Runtime and Memory Efficient Computation of Hyperfine Coupling Constants"
J. Chem. Theory Comput. **18**, 5233–5245 (2022).
Contribution by the author: *All of the theory, all of the implementation, all of the test calculations and all of the writing.*

III V. Drontschenko, **F. H. Bangerter**, C. Ochsenfeld
"Analytical Second-Order Properties for the Random Phase Approximation: Nuclear Magnetic Resonance Shieldings"
J. Chem. Theory Comput. **19**, 7542–7554 (2023).
Contribution by the author: *Shared first authorship. Parts of the theory, most of the implementation, parts of the test calculations and parts of the writing.*

IV F. Sacchetta, **F. H. Bangerter**, H. Laqua, C. Ochsenfeld
"Efficient Low-scaling Calculation of THC-SOS-LR-CC2 and THC-SOS-ADC(2) Excitation Energies Through Density-based Integral-direct Tensor Hypercontraction"
J. Chem. Theory Comput., *in preparation.*
Contribution by the author: *Shared first authorship. Parts of the theory, parts of the implementation, parts of the test calculations and parts of the writing.*

Contents

A. Appendix

1. Introduction

The ever-increasing demand for faster and more accurate theoretical predictions for experimental observables is driven by the need to tackle problems of increasing size and chemical complexity. Since the introduction of the concept of the general-purpose computer by Alan Turing, the ability of theoretically describing chemical systems beyond analytically solvable model systems was established. The description of systems with more than one electron formally requires the solution of an n-body problem, for which an analytical formulation is not possible, unless certain boundary conditions are fulfilled. Therefore the mean-field approximation to the description of the electron-electron interaction was introduced in the seminal work of Douglas Hartree and Vladimir Fock [1, 2]. In Hartree–Fock (HF) theory the underlying wave function, describing the quantum state of the system, is approximated by a single Slater determinant [3]. However, due to the mean-field description of the electron-electron interactions, HF theory lacks so-called correlation effects, originating from the classical electrostatic repulsion between equally signed charged particles. To account for electron correlation a variety of methods have been developed, which describe correlation starting from the HF reference wave function. The arguably conceptually most simple approach is to describe the correlation effects using perturbation theory, which is well-established in classical physics. Partitioning the interacting Hamiltonian into the mean-field Fock operator and the fluctuation operator describing correlation effects results in what is known as Møller–Plesset perturbation theory (MPn) [4]. While the most frequently used second-order MPn (MP2) provides a relatively affordable $\mathcal{O}(N^5)$ scaling description of correlation, it only accounts for $\approx 90\%$ of the correlation energy. To improve upon the MPn description, the coupled cluster (CC) ansatz for the wave function can be used [5]. In CC theory the wave function is given by an expansion of arbitrarily excited HF reference determinants, which leads to a systematically improvable description of electron correlation by taking into account increasingly excited determinants. The so-called *gold standard of quantum chemistry*, CC with singles, doubles (CCSD) [6] and additional perturbative triples excitations (CCSD(T)) [7] improves the accuracy to $\approx 98\%$ of the correlation energy, which is however accompanied by an increased $\mathcal{O}(N^7)$ scaling cost. To lower the computational cost, while retaining the favorable accuracy, perturbation theory can be adapted for CC theory (CCPT) [8, 9]. If linear response (LR) theory is applied to the second-order CCPT (CC2), the resulting LR-CC2 method generalizes the CCPT formalism to excited states [10]. Thereby, not only ground state energies are accessible but also excitation energies. Conceptually related is the perturbative algebraic diagrammatic construction (ADC) approach [11], which yields similar expressions to LR-CC for the excitation energies and can therefore be treated on an equal footing.

Instead of calculating correlation on top of the HF mean-field description, correlation energies can also be obtained from a preceding Kohn–Sham (KS) density function theory (DFT) calculation [12]. In DFT the energy functional is formulated in terms of the electron density, instead of the wave function, for which the foundation is given by the Hohenberg–Kohn theorems [13]. Like HF theory, KS-DFT is an effective mean-field method, in which the interaction is described by fictitious non-interacting particles through a self-consistent effective potential. The analytically exact connection between the real interacting and fictitious non-interacting systems is thereby given by the adiabatic connection approach (AC). In combination with the fluctuation-dissipation theorem (FDT), which relates density fluctuations to external perturbations in the system, the random phase approximation (RPA) can be derived [14–16]. RPA therefore systematically describes correlation in a post-KS fashion and therefore provides systematical improvement of common (empirical) density function approximations (DFAs) at an $\mathcal{O}(N^6)$ scaling cost if no further approximations are applied [17–20].

The aforementioned correlation methods enable the physically sensible calculation of energies for n-electron systems. Their applicability is however limited by their steep polynomially scaling cost, only permitting the computation of systems with a handful of correlated electrons. In general, the bottleneck for these methods is the necessity to compute, contract and store the repulsion integral (ERI) tensor. Formally, the ERI tensor is a fourth-order tensor, for which the elements are given as four-center-two-electron integrals over Gaussian-type atomic orbitals (AOs). The electron integrals can be interpreted as the Coulombic interaction between charge densities formed by the AOs, which – according to the Gaussian product theorem – are Gaussians as well. Therefore, the orbital pair products can be approximated by a single Gaussian function yielding the resolution-of-the-identity (RI) approximation [21–25]. As a consequence of the RI approximation, the formally fourth-order ERI tensor can be represented by at most third-order tensors, thereby lowering computational demand. When applied to RPA, RI lowers the scaling behavior to $\mathcal{O}(N^4)$ [26], while for MP2 only the prefactor is reduced due to the necessity to rebuild the canonical ERI tensor. Reiterating the unpinning of indices in the ERI tensor, also within the orbital pair products, results in the tensor hypercontraction (THC) format, which allows to represent the ERI tensor entirely in second-order tensors [27–30]. While the THC factorization provides means to reduce the scaling of methods it is applied to, obtaining factorization entails a significant $\mathcal{O}(N^5)$ scaling overhead. In the least-squares (LS) flavor of THC (LS-THC) [28], this overhead is due the necessity to compute the canonical ERI tensor once in advance and to then project it onto a DFT-like quadrature grid. To overcome this limitation, this issue was addressed in **Publication I**. By application of the RI approximation with an attenuated Coulomb metric (ω-RI) [31, 32] in conjunction with screening out non-contributing integrals using the integral partition bounds (IPBs) [33] the cost of the initial formation of the integrals is significantly reduced. Furthermore, sparse linear algebra is used to efficiently perform the subsequent grid projection. Overall, a sub-quadratically scaling algorithm with a low prefactor is developed, to obtain the THC factorization with marginal overhead. Furthermore, the developed LS-THC implementation is applied to scaled opposite-spin

(SOS-) MP2 [34] to yield the (sub-)quadratically scaling THC-ω-RI-CDD-SOS-MP2 method. To address the absent exchange-like term in SOS-MP2, in **Publication II** recipes for the efficient formation of Coulomb- and exchange-like contractions in the THC format are presented.

The developed approaches for efficient contractions of THC-decomposed integrals is continued for the CC family of methods in **Publication IV**. On top of the development of a THC-CC2 method for the calculation of ground state energies, the low-scaling THC algorithm from **Publication I** is extended to excited states within the linear response formulation of CC2 as well as to ADC(2). Furthermore, to circumvent the prohibitive necessity to store the three-center RI integral tensor on disk for the LS-THC fitting procedure, a new integral-direct formulation of LS-THC is developed. The proposed algorithm allows to efficiently obtain the THC tensors in arbitrary orbital bases beyond the integral tensor in the occupied-virtual subspace required for MP2. Applied to LR-CC2 and ADC(2), low-scaling implementations for excitation energies are presented.

The accurate calculation of molecular energies is important for the prediction of thermochemistry, interaction energies, and atomization energies. However, to further bridge the gap between theory and experiment, the ability to theoretically calculate experimental observables, like hyperfine coupling constants (HFCCs) or nuclear magnetic resonance (NMR) shifts, is pivotal. In general, this can be achieved by formulating the derivative of the underlying energy functional of a method with respect to the corresponding perturbation. In case of HFCCs, the energy functional is differentiated with respect to the nuclear magnetic moment. Leveraging the methodology from **Publication I**, in **Publication II** it is demonstrated that the calculation of HFCCs at the MP2 level of theory can be significantly accelerated using LS-THC. Depending on the investigated system, the obtained speedups are on the order of $\approx 500\times$ compared to the already efficient RI-CDD-MP2 method by Vogler *et al.* [35, 36]. Furthermore, LS-THC allows to significantly reduce the storage requirements, which enables the calculation of HFCCs of substantially larger systems up to 500 atoms.

In general, the derivation of analytic expressions for the access of molecular properties is challenging due to the necessity to differentiate the underlying energy equations. This is especially important when seeking not only first derivatives, such as for HFCCs, but also second derivatives. An essential property that is accessible through second differentiation are NMR chemical shifts, which are common observables in experimental chemistry. Quantum chemical computations of NMR shifts therefore allow to aid structure elucidation of chemical compounds. In **Publication III**, the analytic second derivative of RPA is derived for the first time. RPA is a particularly suitable method for the calculation of NMR shifts due to the low formal $\mathcal{O}(N^4)$ scaling in the RI formulation and the favorable accuracy, which is competitive with the vastly more expensive CCSD method [37]. Since analytic expression for the derivatives of key intermediates in the RPA method are presented, this represents a suitable starting point for the development of further properties based on second derivatives.

2. Theoretical Background

2.1. Molecular Time-independent Schrödinger Equation

The time-dependent Schrödinger equation (TDSE) [38] is at the heart of quantum chemistry and describes the evolution of a wave function over time. The TDSE therefore allows to describe dynamic processes such as transitions between quantum states, which in turn can be obtained by solving the time-independent Schrödinger equation (TISE). Since all methods developed in Chapter 3 are based on the TISE, the following introduction is limited to the time-independent case.

In the Born–Oppenheimer approximation [39] the molecular electronic Hamilton operator in atomic units $\hat{\mathcal{H}}_{\text{el}}$ in the familiar first quantization picture is given by

$$\hat{\mathcal{H}}_{\text{el}} = \underbrace{-\frac{1}{2}\sum_{i}^{N_{\text{el}}} \hat{\nabla}_i^2}_{\hat{T}_{\text{e}}} \underbrace{- \sum_{A}^{N_{\text{nuc}}} \sum_{i}^{N_{\text{el}}} \frac{Z_A}{|\mathbf{R}_A - \mathbf{r}_i|}}_{\hat{V}_{\text{eN}}} + \underbrace{\sum_{i}^{N_{\text{el}}} \sum_{j>i}^{N_{\text{el}}} \frac{1}{|\mathbf{r}_j - \mathbf{r}_i|}}_{\hat{V}_{\text{ee}}} , \tag{2.1}$$

where indices A, B and i, j denote nuclei and electrons, respectively. Here, Z_A is the nuclear charge of nucleus A, while $\mathbf{R}_A$ and $\mathbf{r}_i$ denote the coordinates of the nuclei and electrons, respectively. In the context of the Born–Oppenheimer approximation the kinetic energy contribution of the nuclei $\hat{T}_{\text{N}}$ is neglected and the nuclear-nuclear potential $\hat{V}_{\text{NN}}$ is added as a constant to the energy eigenvalues obtained by the solution of the associated electronic TISE. Consequently, only the kinetic energy operator $\hat{T}_{\text{e}}$ of the electrons, as well as the electron-nuclear potential $\hat{V}_{\text{eN}}$ and the electron-electron potential $\hat{V}_{\text{ee}}$ are taken into account. The electronic TISE then reads

$$\hat{\mathcal{H}}_{\text{el}}(\mathbf{r}; \mathbf{R})\Psi_{\text{el}}(\mathbf{r}; \mathbf{R}) = E_{\text{el}}\Psi_{\text{el}}(\mathbf{r}; \mathbf{R}) \tag{2.2}$$

and yields the stationary states of the quantum system with the energy E_{el} in addition to allowing to calculate other properties such as probability densities or physical observables from the wave function $\Psi_{\text{el}}(\mathbf{r}; \mathbf{R})$.

2.2. Electron Correlation Methods

Electron correlation[40, 41] is a fundamental concept in quantum chemistry and describes the complex interactions between electrons as a direct consequence of their repulsion, exchange, and quantum mechanical indistinguishability. Based on its physical origin electron correlation can be separated into *Fermi* and *Coulomb* correlation [42]. Fermi correlation is a result of the Pauli exclusion principle[43], according to which two identical fermions (electrons) cannot occupy the same quantum state. The latter then leads to increased electron-electron repulsion and the formation of an *exchange hole*, i.e., a region with reduced probability of finding a second electron at the location of the first electron. Coulomb correlation on the other hand is a classical phenomenon and arises from the classical electrostatic repulsion between equally charged particles. Due to the repulsive nature of this interaction a second type of hole is formed, the *Coulomb hole*. Based on its chemical origin, i.e., the types of systems correlation occurs in, electron correlation can further be separated into *dynamic* and *static* correlation [42]. Dynamic correlation arises as a response of the electrons to rearrangements of the electron density or fluctuations therein and is inherently short-ranged. In contrast, static correlation is long-ranged as well as persistent throughout the whole system and arises whenever multiple electronic configurations contribute significantly to the total electronic wave function. The accurate description of electron correlation beyond the mean-field treatment in Hartree–Fock theory is a central topic of active research and several so-called *electron correlation methods*, which were used in the publications in Chapter 3, will be explained in the following.

2.2.1. Hartree–Fock Theory

In second quantization [44], for which an introduction is given in Appendix A.1, the electronic Hamilton operator from eq. (2.1) is given as

$$\hat{\mathcal{H}} = \sum_{pq} h_{pq} \hat{a}_p^\dagger \hat{a}_q + \frac{1}{2} \sum_{pqrs} g_{pqrs} \hat{a}_p^\dagger \hat{a}_q^\dagger \hat{a}_s \hat{a}_r \,, \tag{2.3}$$

where the subscript ‘el’ is dropped since all following sections are only concerned with solutions to the electronic TISE. In eq. (2.3), h_{pq} and g_{pqrs} are used as short-hand notations for the commonly encountered one- and two-electron integrals given by

$$h_{pq} := \langle p|\hat{h}|q\rangle = \int d\boldsymbol{\tau} \varphi_p^*(\boldsymbol{\tau}) \hat{h}(\boldsymbol{\tau}) \varphi_q(\boldsymbol{\tau}) \,, \tag{2.4}$$

$$g_{pqrs} := \langle pq|rs\rangle = \iint d\boldsymbol{\tau}_1 d\boldsymbol{\tau}_2 \varphi_p^*(\boldsymbol{\tau}_1) \varphi_q^*(\boldsymbol{\tau}_2) \hat{g}(\boldsymbol{\tau}_1, \boldsymbol{\tau}_2) \varphi_r(\boldsymbol{\tau}_1) \varphi_s(\boldsymbol{\tau}_2) \,. \tag{2.5}$$

Here, $\boldsymbol{\tau}$ denotes the electronic coordinate including spin σ and $\{\varphi_p\}$ denotes the one-particle functional basis. $\hat{h}$ contains the kinetic energy operator of the electrons as well as the electron-nuclei interactions, whereas $\hat{g}$ is the Coulomb operator. Commonly, the Hamilton operator is split into these one- and two-electron contributions, to which Wick's theorem [45], see Appendix A.1.3, can be applied to achieve normal ordering, denoted by $\mathcal{N}(...)$, with respect to a reference state. Applying Wick's theorem to the one-electron part of the Hamiltonian $\hat{O}_1$ yields

$$\hat{O}_1 \coloneqq \sum_{pq} h_{pq} \hat{a}_p^\dagger \hat{a}_q \tag{2.6}$$

$$\overset{\text{Wick}}{=} \sum_{pq} h_{pq} \mathcal{N}(\hat{a}_p^\dagger \hat{a}_q) + \sum_i h_{ii} \,, \tag{2.7}$$

with the second sum being restricted to the occupied-occupied contribution h_{ii}, since non-zero contractions only appear when an annihilation operator appears to the left of a creation operator. According to Wick's theorem, the normal ordered two-electron operator will – in addition to un- and singly contracted terms – also contain double contractions giving rise to the following contributions

$$\hat{O}_2 \coloneqq \frac{1}{2} \sum_{pqrs} g_{pqrs} \hat{a}_p^\dagger \hat{a}_q^\dagger \hat{a}_s \hat{a}_r \tag{2.8}$$

$$\overset{\text{Wick}}{=} \frac{1}{2} \sum_{pqrs} g_{pqrs} \mathcal{N}(\hat{a}_p^\dagger \hat{a}_q^\dagger \hat{a}_s \hat{a}_r) + \sum_{pqi} (g_{piqi} - g_{piiq}) \mathcal{N}(\hat{a}_p^\dagger \hat{a}_q) + \frac{1}{2} \sum_{ij} (g_{ijij} - g_{ijji}) \,. \tag{2.9}$$

Summarizing the results from eq. (2.7) and (2.9), the electronic Hamiltonian $\hat{\mathcal{H}}$ can be expressed as

$$\hat{\mathcal{H}} = E_{\text{HF}} + \hat{\mathcal{H}}_N \,, \tag{2.10}$$

where the Hartree–Fock (HF) [1, 2, 46] energy E_{HF} is the expectation value of the Hamilton operator $\hat{\mathcal{H}}$ for the vacuum state $|0\rangle$, given by

$$E_{\text{HF}} \coloneqq \langle 0 | \hat{\mathcal{H}} | 0 \rangle = \sum_i h_{ii} + \frac{1}{2} \sum_{ij} (g_{ijij} - g_{ijji}) \ . \tag{2.11}$$

The remaining parts are cumulated in the normal ordered electronic Hamiltonian $\hat{\mathcal{H}}_N$ defined as

$$\hat{\mathcal{H}}_N \coloneqq \hat{\mathcal{H}} - \langle 0 | \hat{\mathcal{H}} | 0 \rangle = \sum_{pq} f_{pq} \mathcal{N}(\hat{a}_p^\dagger \hat{a}_q) + \frac{1}{2} \sum_{pqrs} g_{pqrs} \mathcal{N}(\hat{a}_p^\dagger \hat{a}_q^\dagger \hat{a}_s \hat{a}_r) = \hat{f}_N + \hat{V}_N \,, \tag{2.12}$$

in which $\hat{f}_N$ is the normal ordered Fock operator given by

$$\hat{f}_N = \sum_{pq} h_{pq} \mathcal{N}(\hat{a}_p^\dagger \hat{a}_q) + \sum_{pqi} (g_{piqi} - g_{piiq}) \ \mathcal{N}(\hat{a}_p^\dagger \hat{a}_q) = \hat{h} + \hat{V}_{\text{HF}} \,, \tag{2.13}$$

which can be separated into the core Hamilton operator $\hat{h}$ and the Hartree–Fock mean field potential $\hat{V}_{\text{HF}}$. The entries f_{pq} of the Fock matrix are therefore given as

$$f_{pq} \coloneqq \langle p|\hat{f}_N|q\rangle = h_{pq} + \sum_i (g_{piqi} - g_{piiq}) \tag{2.14}$$

$$= h_{pq} + \frac{1}{2}(J_{pq} - K_{pq}) \ , \tag{2.15}$$

with J_{pq} and K_{pq} being elements of the Coulomb $\mathbf{J}$ and exchange matrix $\mathbf{K}$, respectively.

According to eq. (2.11), calculating the HF energy of a system requires the minimization of the HF energy functional with respect to the one-particle functions $\{\varphi_i\}$ (molecular orbitals, MOs), due to their unknownness *a priori*. Ensuring orthonormality of the MOs, a set of eigenvalue problems, with the eigenvalues ε_i being the MO energies, is obtained as

$$\hat{f}|\varphi_i\rangle = \varepsilon_i|\varphi_i\rangle \, , \tag{2.16}$$

which are known as the canonical HF equations. These equations have to be solved in a self-consistent fashion, since the Fock operator $\hat{f}$ in eq. (2.13) depends on the MOs, obtained by the solution of the eigenvalue problem. In practice, the MOs are expanded in a fixed and finite set of atom-centered one-particle functions $\{\chi_\mu\}$ (atomic orbitals, AOs) according to the linear combination of atomic orbitals (LCAO) ansatz defined as

$$|\varphi_i(\boldsymbol{\tau})\rangle = \sum_\mu C_{\mu i} \, |\chi_\mu(\boldsymbol{\tau})\rangle \, , \tag{2.17}$$

which leads to the Roothaan-Hall (RH) equation [47], which is a non-orthogonal matrix eigenvalue problem given by

$$\mathbf{FC} = \mathbf{SC}\boldsymbol{\varepsilon} \, , \tag{2.18}$$

where $\mathbf{S}$ is the overlap matrix in the AO basis, $\mathbf{C}$ is the matrix representation of the LCAO expansion coefficients (MO coefficients) from eq. (2.17), $\boldsymbol{\varepsilon}$ is the diagonal matrix of the MO energies and $\mathbf{F}$ is the Fock matrix defined as

$$\mathbf{F} = \mathbf{h} + \mathbf{J}[\mathbf{P}] + \mathbf{K}[\mathbf{P}] \, . \tag{2.19}$$

Here, $P_{\mu\nu} \coloneqq \sum_i^{N_{\mathrm{occ}}} C^*_{\mu i} C_{\nu i}$ is the one-particle density matrix, which provides information about the electron density distribution in the system. Like the canonical HF equations, the RH equation has to be solved iteratively, due to the dependence of the Fock matrix in eq. (2.19) on the density matrix.

2.2.2. Møller–Plesset Perturbation Theory

Including electron correlation effects as a correction to the mean-field Hartree–Fock or Kohn–Sham (KS) solution can be done in various ways, one of which is perturbation theory. Apart from Brillouin–Wigner perturbation theory [48–50], which is particularly useful for the description of degenerate states, Rayleigh–Schrödinger perturbation theory [51] is most used in quantum chemistry. By ansatz, the Hamiltonian is partitioned into an unperturbed part $\hat{\mathcal{H}}_0$ and a perturbation $\hat{\mathcal{H}}'$, also called fluctuation operator, according to

$$\hat{\mathcal{H}} = \hat{\mathcal{H}}_0 + \hat{\mathcal{H}}' \,. \tag{2.20}$$

If seeking a description of electron correlation effects the zeroth-order Hamiltonian $\hat{\mathcal{H}}_0$ can be chosen as the sum of the Fock operators, which leads to the following expression of the perturbation

$$\hat{\mathcal{H}}' = \hat{\mathcal{H}} - \hat{\mathcal{H}}_0 = \hat{\mathcal{H}} - \hat{f}_N = \frac{1}{2}\sum_{pqrs} g_{pqrs}\hat{a}_p^\dagger \hat{a}_q^\dagger \hat{a}_s \hat{a}_r - \hat{V}_{\mathrm{HF}} \,, \tag{2.21}$$

and is known as Møller–Plesset perturbation theory (MPn) [4]. According to eq. (2.21), inserting the perturbation operator $\hat{\mathcal{H}}'$ into the general expression for the first-order energy expression reveals that – in the context of MPn – the sum of the zeroth- and first-order energy correction is simply the HF energy:

$$E^{(1)} = \langle 0|\hat{\mathcal{H}}'|0\rangle = \langle 0|\hat{\mathcal{H}} - \hat{f}_N|0\rangle = E_{\mathrm{HF}} - E^{(0)} \implies E^{(0)} + E^{(1)} = E_{\mathrm{HF}} \tag{2.22}$$

Consequently, to account for electron interaction beyond the mean-field solution, at least the second-order energy correction (MP2) has to be evaluated. By expanding the first-order correction of the wave function in terms of the unperturbed wave functions of varying excitation orders in a configuration interaction (CI)-like fashion [52] and by applying Brillouin's theorem [53] together with the Slater–Condon rules [3, 54], an expression for the second-order energy correction is obtained as

$$\begin{aligned} E^{(2)} &= \frac{1}{4}\sum_{ij}\sum_{ab}\frac{|\langle ij||ab\rangle|^2}{\varepsilon_i + \varepsilon_j - \varepsilon_a - \varepsilon_b} && (2.23)\\ &= \frac{1}{4}\sum_{ij}\sum_{ab}\langle ij||ab\rangle\, t_{ij}^{ab\,(1)} \,. && (2.24) \end{aligned}$$

Here, intermediate $\mathbf{t}^{(1)}$ is the MP2 amplitude, a concept which will reoccur in Section 2.2.3 on coupled cluster (CC) methods. Among the family of electron correlation methods, MP2 provides a good trade-off with accounting for $\approx 80 - 90\%$ of the total correlation energy, while having – without applying further approximations – $\mathcal{O}(N^5)$ scaling, compared to the more expensive CC methods. Without additional extensions, higher-order MPn methods are only scarcely used due to the divergence behavior of the MPn series [55]. In this context, a low-scaling $\mathcal{O}(N^2)$ formulation of the MP2 energy evaluation is presented by means of tensor hypercontraction (*cf.* Section 2.4) in **Publication I**.

2.2.3. Coupled Cluster Theory

Comparable to the CI ansatz of the correlated wave function, which is expressed as an expansion of arbitrarily excited reference determinants, the CC ansatz [5] for the wave function Ψ_{CC} can be expressed as

$$|\Psi_{\mathrm{CC}}\rangle = e^{\hat{T}}|0\rangle = \sum_{n=0}^{\infty} \frac{\hat{T}^n}{n!}|0\rangle \,. \tag{2.25}$$

Here, the cluster operator $\hat{T}$ is given by

$$\hat{T} = \hat{T}_1 + \hat{T}_2 + \hat{T}_3 + \dots \,, \tag{2.26}$$

$$\hat{T}_n = \left(\frac{1}{n!}\right)^2 \sum_{ij\cdots ab\cdots} t_{ij\cdots}^{ab\cdots} \hat{a}_a^\dagger \hat{a}_b^\dagger \hat{a}_j \hat{a}_i \,, \tag{2.27}$$

as an infinite sum of n-fold cluster operators $\hat{T}_n$, which create determinants with an excitation level of n. By inserting the wave function ansatz from eq. (2.25) into the TISE and by projection onto the reference wave function, an expression for the CC correlation energy E_{CC}^c is obtained as

$$\hat{\mathcal{H}}|\Psi_{\mathrm{CC}}\rangle = E|\Psi_{\mathrm{CC}}\rangle \tag{2.28}$$

$$\iff \left(\hat{\mathcal{H}} - E_{\mathrm{HF}}\right) e^{\hat{T}}|0\rangle = \left(E - E_{\mathrm{HF}}\right) e^{\hat{T}}|0\rangle$$

$$\iff \langle 0|e^{-\hat{T}}\hat{\mathcal{H}}_N e^{\hat{T}}|0\rangle = E_{\mathrm{CC}}^c \,, \tag{2.29}$$

where $\bar{\mathcal{H}} := e^{-\hat{T}}\hat{\mathcal{H}}_N e^{\hat{T}}$ is the so-called similarity transformed Hamiltonian. Projecting instead on the excitation manifold $\mu := \Psi_{ij\cdots}^{ab\cdots}$ and solving the resulting non-linear system of equations given by

$$\langle \mu|e^{-\hat{T}}\hat{\mathcal{H}}_N e^{\hat{T}}|0\rangle = 0 \,, \tag{2.30}$$

yields the CC amplitudes of eq. (2.26).

Approximating the cluster operator by truncating after the double excitations, i.e., $\hat{T}_2$, results in the CC with singles and doubles (CCSD) [6] method. The energy and amplitude expressions for CCSD are therefore given by

$$E^c_{\text{CCSD}} = \langle 0 | e^{-(\hat{T}_1+\hat{T}_2)} \hat{\mathcal{H}}_N e^{(\hat{T}_1+\hat{T}_2)} | 0 \rangle \,, \tag{2.31}$$

$$0 = \langle \Psi_i^a | e^{-(\hat{T}_1+\hat{T}_2)} \hat{\mathcal{H}}_N e^{(\hat{T}_1+\hat{T}_2)} | 0 \rangle \,, \tag{2.32}$$

$$0 = \langle \Psi_{ij}^{ab} | e^{-(\hat{T}_1+\hat{T}_2)} \hat{\mathcal{H}}_N e^{(\hat{T}_1+\hat{T}_2)} | 0 \rangle \,. \tag{2.33}$$

To obtain programmable equations, the similarity transformed normal ordered Hamiltonian is expanded in a Baker–Campbell–Hausdorff (BCH) expansion and the resulting terms are evaluated using Wick's theorem [45] (see Appendix A.1).

2.2.3.1. Coupled Cluster Perturbation Theory

Combining the ideas for the treatment of correlation on a perturbational level, see Section 2.2.2, and the exponential parametrization of the wave function, see Section 2.2.3, results in CC perturbation theory (CCPT) [8, 9]. Here, like in MPn, the Hamiltonian is again partitioned into the zeroth-order Fock operator and the first-order fluctuation potential, which describes the difference between the electron-electron repulsion and the mean-field potential from HF. In CCPT the CC energy and amplitudes are expanded in orders of the fluctuation potential, which results in a hierarchy of n^{th}-order approximate CC (CCn) methods. Starting from the CCSD method of Section 2.2.3 and applying CCPT leads to the following simplification: The singles equations are retained but the doubles equations are approximated to be correct at first order of the fluctuation potential only. Therefore the doubles equations become

$$0 = \langle \Psi_{ij}^{ab} | e^{-\hat{T}_1} \hat{\mathcal{H}}_N e^{\hat{T}_1} + e^{-\hat{T}_2} \hat{f} e^{\hat{T}_2} | 0 \rangle \,, \tag{2.34}$$

which together with eqs. (2.31) and (2.32) defines the CC2 model [8]. The simplification in CC2 is therefore that the $\hat{T}_2$ cluster operator only acts on the Fock operator $\hat{f}$ when doubly excited determinants occur in the bra. Consequently, CC2 provides the means to obtain an analytic expression for the doubles amplitudes that is only dependent on the singles amplitudes and the Fock operator. In turn this means that – unlike in CCSD – the only unknown quantities are singles amplitudes, which have to be solved for iteratively. Overall, this results in a reduction of the formal scaling behavior from $\mathcal{O}(N^6)$ for CCSD to $\mathcal{O}(N^5)$ for CC2 [8]. Nonetheless, since the amplitude equations have to be solved iteratively, CC2 is significantly more expensive than MP2, which motivated the development of an efficient implementation of the CC2 ground state energy expression in **Publication IV**. This implementation leverages the tensor hypercontraction (*cf.* Section 2.4) to reduce the computational effort to perform the expensive integral transformations, which results in quadratic scaling CC2 method applicable to larger system with up to 1000 atoms.

2.2.3.2. Linear Response Coupled Cluster Theory

Apart from its attractiveness for accurate ground state energies, CC theory also allows to calculate excitation energies or properties like transition dipole moments, based on response theory [56]. In response theory [57–61] molecular properties are obtained from the system's response to a time-dependent external perturbation $\hat{V}(t)$, given by

$$\hat{V}(t) = \int_{\mathbb{R}} d\omega \, \hat{V}(\omega) e^{(\mathrm{i}\omega + \eta)t} \tag{2.35}$$

where $\hat{V}(\omega)$ is the external perturbation operator in the frequency domain ω and the infinitesimal $\eta \sim 0$ is switching on the perturbation. Inserting an expansion of the time-dependent wave function in terms of the perturbation $\hat{V}(t)$ into the definition of the expectation value of a general operator $\hat{O}$ yields

$$\begin{aligned} \langle \Psi(t) | \hat{O} | \Psi(t) \rangle = {} & \langle \Psi_0 | \hat{O} | \Psi_0 \rangle \\ & + \int_{\mathbb{R}} d\omega_1 \, \underbrace{\langle\langle \hat{O}; \hat{V}(\omega_1) \rangle\rangle_{\omega_1}}_{\text{linear response}} e^{(-\mathrm{i}\omega_1 + \eta)t} \\ & + \frac{1}{2} \iint_{\mathbb{R}^2} d\omega_1 d\omega_2 \, \underbrace{\langle\langle \hat{O}; \hat{V}(\omega_1), \hat{V}(\omega_2) \rangle\rangle_{\omega_1 \omega_2}}_{\text{quadratic response}} e^{(-\mathrm{i}(\omega_1 + \omega_2) + 2\eta)t} \\ & + \dots . \end{aligned} \tag{2.36}$$

Intermediates $\langle\langle \hat{O}; \cdot \rangle\rangle_\omega$ are the so-called response functions, which contain the information of the systems response to an external perturbation. Taking into account only terms that are linear in $\hat{V}(\omega)$ results in linear response (LR) theory, for which an analytical expression for the response function in the frequency domain is known as

$$\langle\langle \hat{O}; \hat{V}(\omega) \rangle\rangle_\omega = \sum_{n \neq 0} \frac{\langle \Psi_0 | \hat{O} | \Psi_n \rangle \langle \Psi_n | \hat{V}(\omega) | \Psi_0 \rangle}{\omega - (E_n - E_0)} - \sum_{n \neq 0} \frac{\langle \Psi_0 | \hat{V}(\omega) | \Psi_n \rangle \langle \Psi_n | \hat{O} | \Psi_0 \rangle}{\omega - (E_n - E_0)} . \tag{2.37}$$

Analyzing the poles of the response function at $\omega_n = E_n - E_0$ gives access to the excitation energy for the n^{th} excited state [8], see also Appendix A.2. It can be shown that finding the poles of the response function is equivalent to solving an eigenvalue problem of the form

$$\mathbf{A}\mathbf{v}_n = \omega_n \mathbf{v}_n \, , \tag{2.38}$$

where $\mathbf{v}_n$ is the eigenvector and ω_n the eigenvalue of the n^{th} excited state. In the context of LR-CC theory [10], matrix $\mathbf{A}$ is the Jacobian matrix, obtained by taking the derivative of the CC equations with respect to the cluster amplitudes. In the case of LR-CC2 this is equivalent to differentiating eqs. (2.32) and (2.34), resulting in

$$\mathbf{A}^{\mathrm{CC2}} = \begin{pmatrix} \langle \Psi_i^a | [\bar{\mathcal{H}}, \hat{\tau}_k^c] + [[\bar{\mathcal{H}}, \hat{\tau}_k^c], \hat{T}_2] | 0 \rangle & \langle \Psi_i^a | [\bar{\mathcal{H}}, \hat{\tau}_{kl}^{cd}] | 0 \rangle \\ \langle \Psi_{ij}^{ab} | [\bar{\mathcal{H}}, \hat{\tau}_k^c] | 0 \rangle & \langle \Psi_{ij}^{ab} | [\hat{f}, \hat{\tau}_{kl}^{cd}] | 0 \rangle \end{pmatrix} , \tag{2.39}$$

where $\hat{\tau}_{ij\cdots}^{ab\cdots}$ are replacement operators defined as $\hat{\tau}_{ij\cdots}^{ab\cdots} = \hat{a}_a^\dagger \hat{a}_i \hat{a}_b^\dagger \hat{a}_j \cdots$ and $[\hat{A}, \hat{B}]$ is the commutator of two operators $\hat{A}$ and $\hat{B}$. As evident from eq. (2.39), the CC2 Jacobian is non-symmetric resulting in a left and right eigenvalue problem, which increases the computational cost if both solutions are required. The latter is not the case for excitation energies, for which only one eigenvalue problem has to be solved, but for excited state properties both left and right eigenvectors are required.

2.2.4. Algebraic Diagrammatic Construction Theory

As outlined for LR-CC theory [10] in Section 2.2.3.2 and in Appendix A.2 on Green's function theory, excitation energies can be obtained from an analysis of the poles of the response function. Eqs. (2.37) and (A.35) formally are expressions for exact excitation energies and need to be approximated for practical applications. In LR-CC theory the CC wave function is used, whereas in the closely related algebraic diagrammatic construction (ADC) theory [11] the polarization propagator is expanded in a perturbative series using the Møller–Plesset partitioning of the Hamiltonian.[1] Since the polarization propagator $\mathbf{\Pi}$ in eq. (A.35) is expressed in its eigenstates, it can be rewritten in its diagonalized form as

$$\mathbf{\Pi}(\omega) = \mathbf{x}^\dagger (\omega - \mathbf{\Omega})^{-1} \mathbf{x}\,, \tag{2.40}$$

where $\mathbf{x}$ is the transition amplitude matrix and $\mathbf{\Omega}$ is the diagonal matrix of excitation energies. Starting point for ADC theory is then the diagrammatic perturbative expansion of the polarization propagator illustrated in Fig. 2.1, which is used to approximate eq. (2.40) as follows: $\mathbf{x}$ and $\mathbf{\Omega}$ are approximated by effective transition moments $\mathbf{f}$ and an effective Hamiltonian $\mathbf{M}$, respectively [64]. Both quantities are expanded with respect to their perturbation-theoretical order in the fluctuation potential and a like-wise analysis of the expansion of the polarization propagator revealing analytic expressions for the n^{th}-order contributions $\mathbf{f}^{(n)}$ and $\mathbf{M}^{(n)}$.

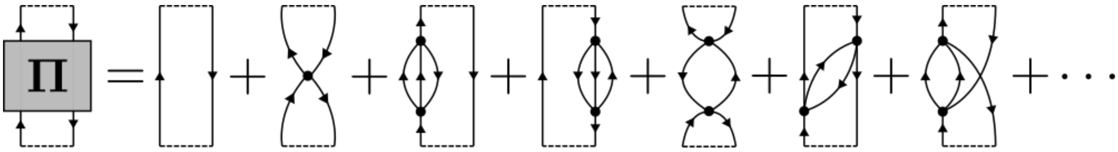

Figure 2.1.: Diagrammatic representation of the perturbative expansion of the polarization propagator in terms of Feynman diagrams in the Abrikosov notation up to second order [11].

As the effective Hamiltonian $\mathbf{M}$ is constructed – hence the name algebraic diagrammatic *construction* theory – to reproduce the exact polarization propagator, the excitation energies can be obtained by diagonalization of $\mathbf{M}$. The perturbative expansion of $\mathbf{f}$ and $\mathbf{M}$ therefore give rise to a hierarchy of ADC(n) methods for excited states, similar to

---

[1] An alternative and nowadays more popular derivation is available in terms of the intermediate state representation [62, 63], which will not be discussed here.

MPn theory for ground states. Contrary to LR-CC, the resulting equations in ADC theory only involve Hermitian eigenvalue problems, circumventing the need to solve a left and right eigenvalue equation for excited state properties. While in (LR-)CC theory ground and excited states are described on an equal footing, in ADC theory the electronic ground state is described at the MPn level of theory with n matching the expansion order in ADC(n), i.e., MP2 in the case of ADC(2). Due to the close relation between LR-CC2 and ADC(2), which differ only slightly in the definition of the corresponding secular matrices, their implementation can be treated equally. Like MP2 and (LR-)CC2, ADC(2) exhibits $\mathcal{O}(N^5)$ scaling, which was addressed in **Publication IV**, where an efficient formulation of the excitation energies is presented. Due to the fact that for the excited state calculations, even more electron integral contractions are required compared to ground state calculations, the favorable application of tensor hypercontraction (*cf.* Section 2.4) is accentuated.

2.2.5. Random Phase Approximation

The random phase approximation (RPA)[2] is intricately linked with all correlation methods presented thus far [20, 66, 67]. For instance, it can be shown that the leading term in the series expansion of the RPA correlation energy in eq. (2.48) is the direct MP2 correlation energy [67] and that RPA is equivalent to CC doubles (CCD) when only including ring diagrams (rCCD) [68]. Here, however, the discussion is restricted to the derivation based on the adiabatic-connection fluctuation-dissipation theorem (ACFDT) [14–16].

In the adiabatic-connection (AC) [14–16] picture, the so-called coupling-strength Hamiltonian $\hat{\mathcal{H}}^\lambda$ is given by

$$\hat{\mathcal{H}}^\lambda = \hat{T}_\mathrm{e} + \lambda \hat{V}_\mathrm{ee} + \hat{V}^\lambda \qquad \text{with} \qquad 0 \leq \lambda \leq 1 \,, \tag{2.41}$$

where $\hat{V}_\mathrm{ee}$ is the exact electron-electron interaction. Here, $\hat{V}^\lambda$ is a local, multiplicative potential, chosen such that the Hamiltonian $\hat{\mathcal{H}}^\lambda$ of the fictitious system at a given coupling strength λ reproduces the exact density n. Applying the Hamiltonian in eq. (2.41) to the TISE with a coupling-strength dependent ground state Ψ_0^λ yields the exact energy for $\lambda = 1$ and the non-interacting KS energy at $\lambda = 0$. Based on this ansatz, a formally exact expression for the correlation energy E^c can be derived form the coupling-strength integration over the difference of the fictitious interacting system Ψ_0^λ and the non-interacting KS system Ψ_0^KS as

---

[2] The term *random phase approximation* is ambiguous in quantum chemistry, as RPA is also synonymously used with time-dependent HF [65]. In this regard RPA is also linked to ADC(n) methods in the sense that RPA – like ADC(n), see Fig. 2.1 – can be viewed as an infinite partial summation of terms in the perturbative expansion of the polarization propagator, which is exact up to first order for the particle-hole excitation energies [11]. Throughout this work, RPA refers to the ACFDT-based post-KS RPA.

$$E^c = \int_0^1 d\lambda \langle \Psi_0^\lambda | \hat{V}_{\mathrm{ee}} | \Psi_0^\lambda \rangle - \langle \Psi_0^{\mathrm{KS}} | \hat{V}_{\mathrm{ee}} | \Psi_0^{\mathrm{KS}} \rangle \,. \tag{2.42}$$

Inserting the definition of the electron-electron Coulomb operator $\hat{V}_{\mathrm{ee}}$ from Appendix A.23 and using the fact that $\langle \Psi_0^\lambda | \hat{n}(\mathbf{r}) | \Psi_0^\lambda \rangle = n(\mathbf{r})$ by construction, yields

$$E^c = \frac{1}{2} \int_0^1 d\lambda \iint_{\mathbb{R}^6} d\mathbf{r}_1 d\mathbf{r}_2 \, \frac{1}{r_{12}} \left[\langle \Psi_0^\lambda | \tilde{n}(\mathbf{r}_1) \tilde{n}(\mathbf{r}_2) | \Psi_0^\lambda \rangle - \langle \Psi_0^{\mathrm{KS}} | \tilde{n}(\mathbf{r}_1) \tilde{n}(\mathbf{r}_2) | \Psi_0^{\mathrm{KS}} \rangle \right] \,, \tag{2.43}$$

with $\tilde{n}(\mathbf{r}) = \hat{n}(\mathbf{r}) - n(\mathbf{r})$ being the density-fluctuation operator. The expectation values of the density-fluctuation operators are simply the density-density response function from eq. (A.34). Consequently, the correlation energy can be written in terms of the density-density response function $\chi(\mathbf{r}_1, \mathbf{r}_2, \omega)$ in the Lehmann representation [69] as

$$E^c = \frac{1}{2} \int_0^1 d\lambda \int_{-\infty}^{\infty} \frac{d\omega}{2\pi} \iint_{\mathbb{R}^6} d\mathbf{r}_1 d\mathbf{r}_2 f_{\mathrm{H}}(\mathbf{r}_1, \mathbf{r}_2) \left[\mathrm{i}\chi_\lambda(\mathbf{r}_1, \mathbf{r}_2, \omega) - \mathrm{i}\chi_0(\mathbf{r}_1, \mathbf{r}_2, \omega) \right] \,, \tag{2.44}$$

where f_{H} denotes the Hartree kernel given as $f_{\mathrm{H}}(\mathbf{r}_1, \mathbf{r}_2) = 1/|\mathbf{r}_1 - \mathbf{r}_2|$. To avoid the fact that the density-density response function given by eq. (A.34) has poles along the real ω axis, contour integration together with the residue theorem is applied to change from a frequency integration over ω to an integration over $\mathrm{i}\omega$. Furthermore, eq. (A.34) reveals that the response function is symmetric with respect to ω, simplifying eq. (2.44) to

$$E^c = -\int_0^1 d\lambda \int_0^{\infty} \frac{d\omega}{2\pi} \iint_{\mathbb{R}^6} d\mathbf{r}_1 d\mathbf{r}_2 f_{\mathrm{H}}(\mathbf{r}_1, \mathbf{r}_2) \left[\chi_\lambda(\mathbf{r}_1, \mathbf{r}_2, \mathrm{i}\omega) - \chi_0(\mathbf{r}_1, \mathbf{r}_2, \mathrm{i}\omega) \right] \,. \tag{2.45}$$

For the non-interacting KS response function χ_0 an exact expression in terms of single-particle functions and energies is known as

$$\begin{aligned} \chi_0(\mathbf{r}_1, \mathbf{r}_2, \mathrm{i}\omega) = \sum_i \sum_a \sum_{\sigma_1 \sigma_2} \Bigg[& \frac{\varphi_i^*(\boldsymbol{\tau}_1) \varphi_a(\boldsymbol{\tau}_1) \varphi_i(\boldsymbol{\tau}_2) \varphi_a^*(\boldsymbol{\tau}_2)}{\mathrm{i}\omega - (\varepsilon_a - \varepsilon_i)} \\ & - \frac{\varphi_i^*(\boldsymbol{\tau}_2) \varphi_a(\boldsymbol{\tau}_2) \varphi_i(\boldsymbol{\tau}_1) \varphi_a^*(\boldsymbol{\tau}_1)}{\mathrm{i}\omega + (\varepsilon_a - \varepsilon_i)} \Bigg] \,. \end{aligned} \tag{2.46}$$

A formally exact expression for the interacting case along the AC path is given by a Dyson-type expression [70] as

$$\begin{aligned} \chi_\lambda(\mathbf{r}_1, \mathbf{r}_2, \mathrm{i}\omega) = \chi_0(\mathbf{r}_1, \mathbf{r}_2, \mathrm{i}\omega) + \iint_{\mathbb{R}^6} & d\mathbf{r}_3 d\mathbf{r}_4 \chi_0(\mathbf{r}_1, \mathbf{r}_3, \mathrm{i}\omega) \Big[\lambda f_{\mathrm{H}}(\mathbf{r}_3, \mathbf{r}_4) \\ & + f_{\mathrm{xc}}^\lambda(\mathbf{r}_3, \mathbf{r}_4, \mathrm{i}\omega) \Big] \chi_\lambda(\mathbf{r}_4, \mathbf{r}_2, \mathrm{i}\omega) \,, \end{aligned} \tag{2.47}$$

where the exchange-correlation kernel f_{xc}^{λ} is the functional derivative of the exchange-correlation potential with respect to the density. Since the exact exchange-correlation kernel f_{xc}^{λ} is unknown, it has to be approximated to solve the above equation. Arguably the simplest approximation is to neglect it entirely, which yields the direct random phase approximation (dRPA) [17–20]. Inserting the RPA response function into eq. (2.45), carrying out the λ-integration analytically and switching from the real space basis to the real MO basis yields the final expression for the dRPA correlation energy as

$$E^c_{\text{dRPA}} = \int_0^\infty \frac{d\omega}{2\pi} \text{Tr}\left[\ln\left(\mathbf{1} - \mathbf{\Pi}_0(\mathrm{i}\omega)\mathbf{V}\right) + \mathbf{\Pi}_0(\mathrm{i}\omega)\mathbf{V}\right] , \tag{2.48}$$

where the matrix representation of the Hartree kernel $\mathbf{V}$ and the non-interacting polarization propagator $\mathbf{\Pi}_0(\mathrm{i}\omega)$[3] are given by

$$V_{iajb} = \iint_{\mathbb{R}^6} d\mathbf{r}_1 d\mathbf{r}_2 \varphi_i(\mathbf{r}_1)\varphi_a(\mathbf{r}_1)\frac{1}{r_{12}}\varphi_j(\mathbf{r}_2)\varphi_b(\mathbf{r}_2) , \tag{2.49}$$

$$\Pi_{0_{iajb}}(\mathrm{i}\omega) = \delta_{ij}\delta_{ab}\frac{-2(\varepsilon_a - \varepsilon_i)}{\omega^2 + (\varepsilon_a - \varepsilon_i)^2} , \tag{2.50}$$

whereby δ is the Kronecker delta.

To extend the applicability of dRPA beyond the calculation of correlation energies, in **Publication III** an analytic expression for the second derivative is developed. The dRPA correlation energy is differentiated with respect to the nuclear magnetic moment and an external magnetic field to compute nuclear magnetic resonance shieldings.

---

[3] As stated in Appendix A.2.2 the distinction between the density-density response function and the polarization propagator is ambiguous. In the context of RPA the polarization propagator is commonly used when working in the MO representation.

2.3. Molecular Properties

2.3.1. Introduction

Bridging the gap between theory and experiment is essential for the validation of theoretical models against real world data. In this regard, methods for the calculation of absolute energies, as presented in Section 2.2, cannot be used directly for the validation as absolute energies are not directly measurable and not the observables relevant to chemistry. Instead, relative energies can be calculated to obtain an experimentally verifiable measure of accuracy. Going beyond energies, molecular properties often offer an experimentally accessible measure through various kinds of spectroscopic methods, like electron paramagnetic resonance (EPR) or nuclear magnetic resonance (NMR) spectroscopy. An array of mathematical methods has been developed to obtain molecular properties from the energy expressions introduced in Section 2.2. Most importantly response (or propagator) theory (*cf.* Section 2.2.3.2 and Appendix A.2), mainly used for describing properties assigned to the transition between electronic states such as ionization or excitation energies, as well as Lagrangian and derivative techniques used for properties specific for a given state [71]. In **Publications II** and **III** the derivative method, for which the energy in the presence of a perturbation ξ is expressed in a Taylor series [72] as

$$E(\xi) = E(0) + \left.\frac{\partial E}{\partial \xi}\right|_{\xi=0} \xi + \frac{1}{2}\left.\frac{\partial^2 E}{\partial \xi^2}\right|_{\xi=0} \xi^2 + \cdots , \tag{2.51}$$

is employed to calculate magnetic properties. Here, the terms $\partial^n E/\partial \xi^n$ containing n^{th} derivative of the energy are referred to as n^{th}-order molecular properties.

2.3.2. Magnetic Properties

In order to obtain an explicit expression for the computation of magnetic properties, the Hamiltonian needs to be reformulated in the presence of an external magnetic field as well as the nuclear magnetic moments. In the approximation of the principle of minimal electromagnetic coupling [73], the canonical momentum operator $\hat{\mathbf{p}}$ is replaced with the kinetic momentum operator $\hat{\boldsymbol{\pi}}$, with

$$\hat{\boldsymbol{\pi}} = \hat{\mathbf{p}} - \mathbf{A} \tag{2.52}$$

in atomic units [73, 74], where $\hat{A}$ is the operator of the vector potential $\mathbf{A}$ of the electromagnetic field. The latter is given by

$$\mathbf{A} = \underbrace{\frac{1}{2}\mathbf{B} \times (\mathbf{r} - \mathbf{R}_0)}_{\text{external magentic field}} + \sum_A \underbrace{\alpha^2 \frac{\mathbf{m}_A \times (\mathbf{r} - \mathbf{R}_A)}{|\mathbf{r} - \mathbf{R}_A|^3}}_{\text{nuclear magnetic moments}} \tag{2.53}$$

with $\mathbf{R}_0$ being the gauge of the magnetic field $\mathbf{B}$, $\mathbf{R}_A$ being the position of nucleus A, α being the fine structure constant (in atomic units: $\alpha = \frac{1}{c}$) and $\mathbf{m}_A$ being the nuclear magnetic moment of nucleus A [73–76]. The first term in eq. (2.53) originates from a static external magnetic field and gives rise to Zeeman interactions, whereas the second contributions stems from the nuclear magnetic dipole of nucleus A and leads to hyperfine interactions. Inserting the definition of the kinetic momentum operator $\hat{\boldsymbol{\pi}}$ from eq. (2.52) into the kinetic energy contribution to the electronic core-Hamilton operator $\hat{h}$ yields additional terms, which – in the non-relativistic case [77, 78] – include the dependence on the vector potential $\mathbf{A}$ as

$$\hat{h}_0 = \sum_i \frac{\hat{\mathbf{p}}_i^2}{2} - \sum_i \sum_A \frac{Z_A}{r_{iA}} \qquad \Longrightarrow \qquad \hat{h} = \hat{h}_0 + \sum_i \hat{\mathbf{p}}_i \cdot \mathbf{A} + \sum_i \frac{\mathbf{A} \cdot \mathbf{A}}{2}\,, \tag{2.54}$$

where $\hat{\mathbf{p}} \cdot \mathbf{A} = \mathbf{A} \cdot \hat{\mathbf{p}}$ due to the application of the Coulomb gauge [73]. Since the first term $\hat{\mathbf{p}} \cdot \mathbf{A}$ has linear dependence on the magnetic field, it constitutes the paramagnetic contribution, whereas the quadratic term $\mathbf{A} \cdot \mathbf{A}$ is the diamagnetic contribution. Following the derivative approach to molecular properties from eq. (2.51), the energy in the presence of an external magnetic field $\mathbf{B}$ and the magnetic moments $\mathbf{m}_A$ associated with the nuclei can be expressed in a multivariable Taylor series as

$$\begin{aligned} E(\mathbf{B}, \mathbf{m}_A) = E(\mathbf{0}, \mathbf{0}) & \\ + \left.\frac{\partial E}{\partial \mathbf{m}_A}\right|_{\mathbf{m}_A = \mathbf{0}} \mathbf{m}_A + \left.\frac{\partial E}{\partial \mathbf{B}}\right|_{\mathbf{B} = \mathbf{0}} \mathbf{B} & \\ + \frac{1}{2} \left.\frac{\partial^2 E}{\partial \mathbf{B} \partial \mathbf{m}_A}\right|_{\mathbf{B} = \mathbf{0}, \mathbf{m}_A = \mathbf{0}} \mathbf{B}\, \mathbf{m}_A + \cdots \,. & \end{aligned} \tag{2.55}$$

According to eq. (2.55), accounting for magnetic effects requires the analytical (mixed) derivatives of the energy expression [72, 79–82]. In consequence, this requires the n^{th} derivatives of the Hamiltonian in eq. (2.54). This leads to an assortment of additional terms that describe various coupling effects, of which only the ones relevant for Sections 2.3.3 and 2.3.4 are discussed here. First differentiation with respect to the magnetic field results in the orbital-Zeeman (OZ) operator $\hat{h}^{\text{OZ}}$ given by

$$\hat{h}^{\text{OZ}} = \frac{1}{2} \sum_i -\mathrm{i}\mathbf{r}_{i0} \times \nabla_i = \frac{1}{2} \sum_i \hat{\mathbf{l}}_{i0}\,, \tag{2.56}$$

which describes the interaction of the external magnetic field with the magnetic moment caused by the movement of the electrons through the angular momentum operator $\hat{\mathbf{l}}$. Here and in the following, the abbreviations $\mathbf{r}_{ij} = \mathbf{r}_i - \mathbf{R}_j$ and $r_{ij} = |\mathbf{r}_i - \mathbf{R}_j|$ are used, where j either belongs to a component of the magnetic field ($\mathbf{R}_0$) or the nucleus position ($\mathbf{R}_A$). Furthermore, first differentiation with respect to the nuclear magnetic moment yields three distinct terms: 1) the paramagnetic spin-orbit (PSO) operator $\hat{h}_A^{\text{PSO}}$ given by eq. (2.57), which couples the nuclear magnetic moments to the orbital motion of the electrons, 2) the spin-dipole (SD) operator $\hat{h}_A^{\text{SD}}$ in eq. (2.58), which describes the classical coupling between two magnetic dipoles, and 3) the Fermi contact (FC) operator $\hat{h}_A^{\mathrm{FC}}$ in eq. (2.59) which couples the nuclear magnetic moments to the spin of the electrons:

$$\hat{h}_A^{\mathrm{PSO}} = \alpha^2 \sum_i \frac{-\mathrm{i}\mathbf{r}_{iA} \times \nabla_i}{r_{iA}^3} \tag{2.57}$$

$$\hat{h}_A^{\mathrm{SD}} = \alpha^2 \sum_i \frac{r_{iA}^2 \mathbf{m}_A - 3(\mathbf{m}_A \cdot \mathbf{r}_{iA})\mathbf{r}_{iA}}{r_{iA}^5} \tag{2.58}$$

$$\hat{h}_A^{\mathrm{FC}} = -\frac{8\pi\alpha^2}{3} \sum_i \delta(\mathbf{r}_{iA})\mathbf{m}_A \tag{2.59}$$

Finally, taking the mixed second derivative with respect to the external magnetic field and the nuclear magnetic moments yields the diamagnetic shielding (DS) operator $\hat{h}_A^{\mathrm{DS}}$ as

$$\hat{h}_A^{\mathrm{DS}} = \frac{\alpha^2}{2} \sum_i \frac{(\mathbf{r}_{i0} \cdot \mathbf{r}_{iA})\mathbf{1} - \mathbf{r}_{iA}\mathbf{r}_{i0}^{\mathrm{T}}}{r_{iA}^3} \,. \tag{2.60}$$

The individual terms in eq. (2.55) can then be assigned to physical observables by mapping them onto a corresponding phenomenological Hamiltonian according to the order of the perturbation. In the case of EPR, the phenomenological EPR Hamiltonian $\hat{\mathcal{H}}^{\mathrm{EPR}}$ is given by [83]

$$\hat{\mathcal{H}}^{\mathrm{EPR}} = \mu_B \mathbf{B}^{\mathrm{T}} \mathbf{g} \hat{\mathbf{S}} + \sum_A \hat{\mathbf{S}}^{\mathrm{T}} \mathbf{A}_A \mathbf{m}_A \,, \tag{2.61}$$

where μ_B is the Bohr magneton, $\hat{\mathbf{S}}$ is the total spin operator, $\mathbf{g}$ is the g-tensor and $\mathbf{A}_A$ is the hyperfine coupling tensor of nucleus A. In the case of NMR, the phenomenological NMR Hamiltonian $\hat{\mathcal{H}}^{\mathrm{NMR}}$ given as [77, 83]

$$\hat{\mathcal{H}}^{\mathrm{NMR}} = -\sum_A \mathbf{m}_A \cdot (\mathbf{1} - \boldsymbol{\sigma})\mathbf{B} + \frac{1}{2} \sum_{A \neq B} \mathbf{m}_A \cdot (\mathbf{D}_{AB} + \mathbf{K}_{AB})\mathbf{m}_B \,, \tag{2.62}$$

where $\boldsymbol{\sigma}$ is the chemical shielding tensor, $\mathbf{K}_{AB}$ is the indirect nuclear spin-spin coupling tensor, and $\mathbf{D}_{AB}$ is the dipolar interaction tensor between nuclei A and B.

2.3.3. Hyperfine Coupling Constants

Based on the expression for the phenomenological EPR Hamiltonian in eq. (2.61), the hyperfine coupling tensor $\mathbf{A}_A$ of a nucleus A can be obtained as the term linear in the nuclear magnetic moment $\mathbf{m}_A$. Comparing this to the Taylor series expansion of the energy in the presence of magnetic fields in eq. (2.55) reveals the spin-dipole and the

Fermi contact interaction to be the origin of the hyperfine coupling.[4] Given by eq. (2.59), the FC interaction requires a finite probability of the electron to reside at the position of the nucleus, which is only fulfilled for s electrons, for which the orbital has no node at the nucleus. Consequently, since the s orbitals are spherically symmetric, the FC contribution to the hyperfine coupling is entirely isotropic. In contrast, since the SD interaction between the magnetic moment of the electron and the nuclear spin involves an averaging over the spatial distribution of the electron's spin in the respective orbitals, the SD interaction is anisotropic.

Due to the described difference of physical origin, the total hyperfine coupling tensor $\mathbf{A}_A$ can be separated into an isotropic part $A_{\mathrm{iso},A}$ and the purely anisotropic contribution $\mathbf{T}_A$ as [84]

$$\mathbf{A}_A = A_{\mathrm{iso},A}\mathbf{1} + \mathbf{T}_A \,. \tag{2.63}$$

For practical applications, the isotropic hyperfine coupling in a single-particle AO basis is given by

$$A_{\mathrm{iso},A} = \frac{\mu_0}{3} g_e g_{N_A} \mu_B \mu_N \langle S_z \rangle^{-1} \sum_{\mu\nu} P^{\alpha-\beta}_{\mu\nu} \langle \chi_\mu(\mathbf{r}) | \delta(\mathbf{r} - \mathbf{R}_A) | \chi_\nu(\mathbf{r}) \rangle \,, \tag{2.64}$$

where μ_0 is the vacuum permeability, g_e is the electronic and g_{N_A} the nuclear g-factor of nucleus A, μ_N is the nuclear magneton, and $\langle S_z \rangle$ is the mean of the spin angular momentum S_z. Furthermore, $\mathbf{P}^{\alpha-\beta}$ is the electron spin density, which multiplies the so-called Fermi contact integral obtained as the representation of the FC operator from eq. (2.59) in the AO basis. Therefore, from eq. (2.64) it is easily verifiable that the FC term will only contribute for a finite electron spin density at the position of the nucleus.

In **Publication II** the low-scaling formulation of MP2 gradients by Vogler *et al.* [35, 36] is used as a starting point for the derivation of the analytic MP2 gradient with respect to the nuclear magnetic moment for the computation of isotropic hyperfine coupling constants. For this purpose the spin density in the FC term is evaluated at the MP2 level of theory using the derivative approach of Section 2.3.1. The efficiency of the method is significantly increased by the application of the tensor hypercontraction approximation (*cf.* Section 2.4) for electron repulsion integrals, resulting in speedups on the order of 500× over existing implementations.

2.3.4. Nuclear Magnetic Resonance Shieldings

Comparing the expression for the phenomenological NMR Hamiltonian in eq. (2.62) with the Taylor expansion in eq. (2.55), reveals that the chemical shielding tensor

---

[4] The paramagnetic spin-orbit coupling operator also arises from the Hamiltonian in eq. (2.54). However, since it describes the coupling of a particle's spin with its motion inside a potential, it is considered a relativistic effect. Therefore it only contributes a lesser correction except for heavy atoms and is neglected here.

$\boldsymbol{\sigma}$ can be obtained as the mixed second derivative of the energy with respect to the external magnetic field $\mathbf{B}$ and the nuclear magnetic moment $\mathbf{m}_A$ [76, 83, 85]. Based on the discussion in Section 2.3.2, the shielding arises from the diamagnetic shielding operator $\hat{h}_A^{\mathrm{DS}}$ in eq. (2.60). Furthermore, to ensure gauge-origin independence in practical applications gauge-including atomic orbitals (GIAOs) [86–88] given by

$$\chi_\mu(\mathbf{r},\mathbf{B}) = \chi_\mu(\mathbf{r},\mathbf{B}=\mathbf{0})\,\exp\Big(-\frac{\mathrm{i}}{2}[\mathbf{B}\times(\mathbf{R}_\mu-\mathbf{R}_0)]\,\mathbf{r}\Big) \tag{2.65}$$

are employed. Here, $\chi_\mu(\mathbf{r},\mathbf{B}=\mathbf{0})$ denotes the field-independent AO basis function centered at $\mathbf{R}_\mu$, and $\mathbf{R}_0$ is the gauge origin. As a consequence of the field-dependence of the AOs, additional contributions to the shielding tensor arise [77] in the form of the paramagnetic spin-orbit operator $\hat{h}^{\mathrm{PSO}}$ and the orbital-Zeeman operator $\hat{h}^{\mathrm{OZ}}$.[5]

Physically, the interaction mechanisms given in eqs. (2.56), (2.57), and (2.60) describe the system's response to an applied external magnetic field. Since – according to the Biot–Savart law [89] – this generates an electronic current, the effective magnetic field $\mathbf{B}_{\mathrm{eff}}$ felt by the nuclear magnetic moments is thereby given as the sum of the external $\mathbf{B}$ and the induced field $\mathbf{B}_{\mathrm{ind}}$ as [76, 83, 90]

$$\mathbf{B}_{\mathrm{eff}} = \mathbf{B} + \mathbf{B}_{\mathrm{ind}}\,. \tag{2.66}$$

Here, the shielding tensor $\boldsymbol{\sigma}$ describes the proportionality between the applied and the induced field as

$$\mathbf{B}_{\mathrm{ind}} = -\boldsymbol{\sigma}\mathbf{B}\,. \tag{2.67}$$

In liquid phase NMR experiments the shielding tensor itself is generally not measurable due to orientational averaging, only the isotropic chemical shift δ_{iso} is accessible. The isotropic chemical shift δ_{iso} is given by

$$\delta_{\mathrm{iso}} = \sigma_{\mathrm{iso,ref}} - \sigma_{\mathrm{iso}}\,, \tag{2.68}$$

with the isotropic shielding σ_{iso} defined as

$$\sigma_{\mathrm{iso}} = \frac{1}{3}\mathrm{Tr}\,\boldsymbol{\sigma}\,. \tag{2.69}$$

---

[5] All operators in eqs. (2.57)–(2.59) arise from the differentiation with respect to the nuclear magnetic moment $\mathbf{m}_A$. However, since only the PSO operator produces a singlet contribution when applied to a closed-shell wave function, the field dependence – upon further differentiation with respect to the magnetic field $\mathbf{B}$ – of the FC and SD operators vanishes for closed-shell wave functions, since these operators only produce triplet contributions for closed-shell wave functions [77]. Therefore, only the PSO operator contributes to the shielding tensor.

In **Publication III** an analytic expression for the NMR chemical shielding tensor on the dRPA level of theory as a post-KS method based on the ACFDT is developed. **Publication III** builds on promising results for chemical shieldings based on dRPA from the work of Glasbrenner *et al.* [37], which employed numerical second differentiation. In contrast to numerical differentiation, the analytical second derivative expression presented in **Publication III** provides access to theoretical chemical shifts of molecules beyond those accessible by numerical differentiation and represents an ideal stepping stone for efficient low-scaling implementations in future work. The derivation highlights the similarities between the expressions for the second derivative of the AO-MP2 and the dRPA energy, also discussed in Appendix A.3. Furthermore, **Publication III** reports for the first time an analytic expression for a second-order property based on the dRPA as a post-KS method.

2.4. Tensor Hypercontraction

2.4.1. Introduction

Higher-order tensors are ubiquitous in quantum chemistry ranging from the fourth-order electron repulsion integral (ERI) tensor, to the amplitude tensors in CC theory (*cf.* Section 2.2.3), and higher-order integral tensors occurring, e.g., in F12 methods [91]. From an implementation point of view, these tensors represent multi-way arrays [92]. Consequently, their contraction with other tensors as well as the necessity to store them in memory or on disk is often the bottleneck of modern correlation methods. To obtain a low-dimensional and – ideally – low-rank representation of the ERI tensor, two basic approaches can be used, either tensor decomposition or tensor construction [92, 93]. In the tensor decomposition approach the tensor is subjected to a reduction, in which a higher-order tensor is represented as a sum of simpler, lower-dimensional tensors. In principle, a tensor decomposition method is therefore any scheme for expressing a tensor as a sequence of elementary operations acting on other, often simpler tensors. Computational advantage is achieved if 1) the memory requirements in the compressed format are lower than that of the original tensor and/or 2) if the tensor contractions can be performed with the lower-dimensional constituting tensors instead. However, tensor decomposition entails an overhead since the (full) higher-order tensor has to be computed at least once to construct the approximating lower-order tensors. In contrast, tensor construction allows to build up a higher-order tensor if an underlying equation for its elements or potential lower-order approximating tensors exist. This allows to completely avoid calculating and storing the computationally demanding higher-order tensor and to instead build the factorization from the bottom up.

In this context, the so-called resolution-of-the-identity (RI) approximation [21–25] is an example of a tensor construction method for the ERI tensor and is implemented in many quantum chemistry program packages.[6] By ansatz, the RI approximation is achieved by an insertion of the identity

$$\hat{1} = \sum_{\alpha} |\alpha)(\alpha| \,, \tag{2.70}$$

where the complete set of functions $\{\alpha\}$ spans the so-called auxiliary space. Inserting the above identity into eq. (2.5) once yields

---

[6] There are many more examples of tensor approximation techniques in the context of quantum chemistry like the matrix product state (MPS) [94], or tensor train (TT) ansatz in density matrix renormalization group (DMRG) [95], tensor decomposition techniques such as higher-order singular value decomposition (HOSVD) [96] or canonical polyadic (CP) [97] decomposition as well as hierarchical tensor representations such as the continuous fast multipole method (CFMM) [98] or the $\mathcal{H}^2$-ERI representation [99], which make use of the block low-rank structure of the ERI tensor. For an exhaustive discussion of tensor methods in the context of quantum chemistry see Ref. [93]. Here the discussion is restricted to the historically most commonly used methods for approximating the conventional ERI tensor.

$$(\mu\nu|\lambda\sigma) = \sum_{\alpha} (\mu\nu\alpha)(\alpha|\lambda\sigma)\,, \tag{2.71}$$

which is known as single RI [23]. Instead inserting the identity from eq. (2.70) twice, before and after the Coulomb operator, results in

$$(\mu\nu|\lambda\sigma) = \sum_{\alpha\beta} (\mu\nu\alpha)(\alpha|\beta)(\beta\lambda\sigma)\,, \tag{2.72}$$

which is referred to as double RI. Assuming real basis functions, the three-center Coulomb integrals $(\mu\nu|\alpha)$, the three-center overlap integrals $(\mu\nu\alpha)$ and the two-center Coulomb integrals $(\alpha|\beta)$ are given by

$$(\mu\nu|\alpha) = \iint_{\mathbb{R}^6} d\mathbf{r}_1 d\mathbf{r}_2\, \chi_\mu(\mathbf{r}_1)\chi_\nu(\mathbf{r}_1)\, \hat{g}(\mathbf{r}_1,\mathbf{r}_2)\, \chi_\alpha(\mathbf{r}_2)\,, \tag{2.73}$$

$$(\mu\nu\alpha) = \int_{\mathbb{R}^3} d\mathbf{r}\, \chi_\mu(\mathbf{r})\chi_\nu(\mathbf{r})\chi_\alpha(\mathbf{r})\,, \tag{2.74}$$

$$(\alpha|\beta) = \iint_{\mathbb{R}^6} d\mathbf{r}_1 d\mathbf{r}_2\, \chi_\alpha(\mathbf{r}_1)\, \hat{g}(\mathbf{r}_1,\mathbf{r}_2)\, \chi_\beta(\mathbf{r}_2)\,. \tag{2.75}$$

For practical applications eq. (2.70) has to be approximated since the relation only holds for a complete auxiliary basis, which – for most applications – is unachievable. Since an ERI can be viewed as the Coulomb interaction between two charge densities, as outlined in Appendix A.1.5, the pair-products $|\mu\nu)$ of the AO basis functions can be fitted with the coefficients $C_\alpha^{\mu\nu}$ according to

$$\frac{\partial}{\partial C_\alpha^{\mu\nu}} (\mu\nu - \widetilde{\mu\nu}|\hat{g}|\mu\nu - \widetilde{\mu\nu}) \overset{!}{=} 0 \qquad \text{with} \qquad |\widetilde{\mu\nu}) = \sum_{\alpha} C_\alpha^{\mu\nu} |\chi_\alpha)\,, \tag{2.76}$$

which is known as density fitting (DF) [100]. Related is the Cholesky decomposition (CD) [101–106] approach, in which the full ERI tensor is Cholesky-decomposed or the factorized form is built from the ground up by specialized integral kernels. Either way, the same reduction from the fourth-order ERI tensor to at most third-order RI/CD tensors for each charge density is achieved. Visually, the RI approximated ERI tensor can be represented by the tensor network diagrams shown in Fig. 2.2 (a-c).

Conceptual reiteration of the process of approximating the highest-order occurring tensor, decomposition of the third-order RI tensor representing the bra pair-products $(\mu\nu|$ results in the so-called pseudospectral (PS) [108–110] method, which is shown as a tensor network diagram in Fig. 2.2 (d).[7] The PS factorization is achieved by using the RI ansatz of

---

[7] Closely related to RI is also the interpolative separable density fitting (ISDF) [111–119] method, which allows for further unpinning of the AO indices in the fitted AO pair products. ISDF will be discussed in Section 2.4.2.

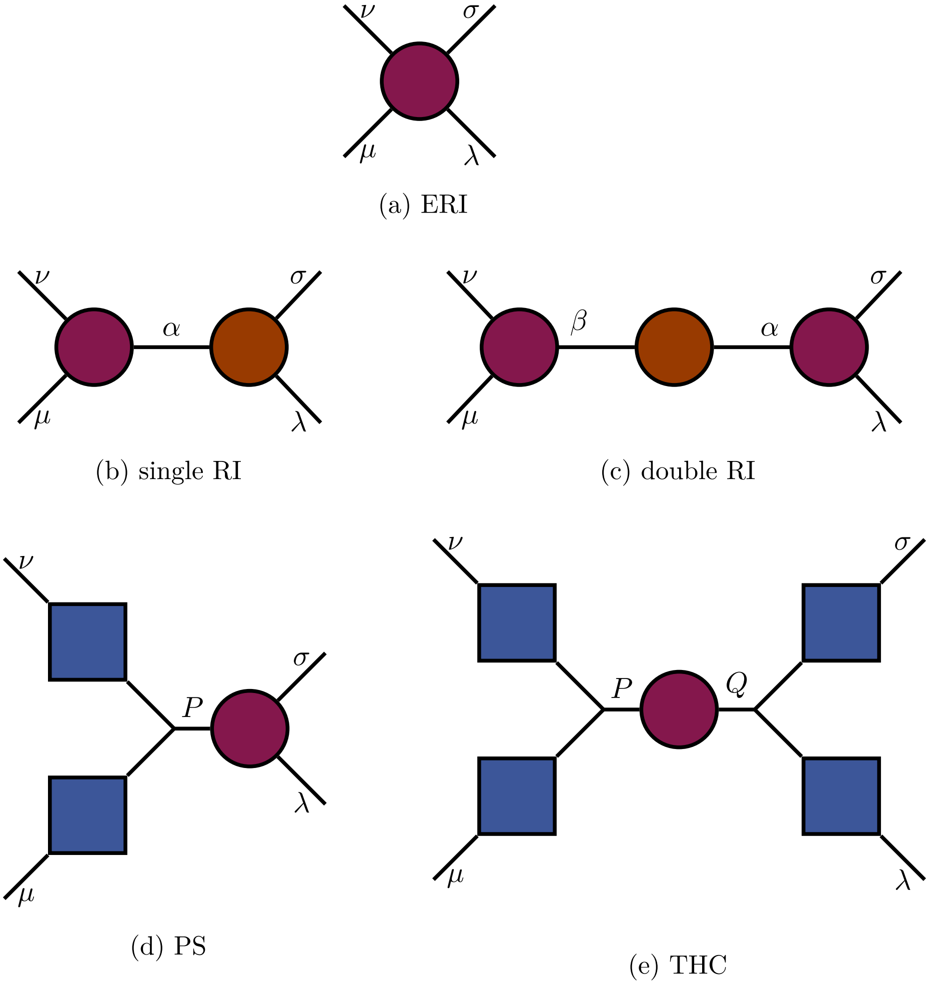

(a) ERI

(b) single RI

(c) double RI

(d) PS

(e) THC

Figure 2.2.: Tensor network diagrams for (a) the full ERI tensor as well as (b) the single RI and (c) double RI, (d) for the PS and (e) for the THC representation. For an introduction of tensor network diagrams see Ref. [107]. Additionally, here 🟣 and 🟠 are used to denote tensors involving analytical integration of basis functions, whereas 🟦 is used to denote tensors that involve numerical quadrature.

inserting the identity from eq. (2.70) into the ERIs once and taking the auxiliary functions to be delta functions $\delta(\mathbf{r}-\mathbf{r}_P)$ in physical space. Here and throughout, indices P, Q, R, S are used for auxiliary functions in physical space (grid space) and α, β for auxiliary functions in spectral space (basis function space). The PS approximation is then obtained as

$$\begin{aligned}(\mu\nu|\lambda\sigma) &\overset{\mathrm{RI}}{=} \sum_P (\mu\nu P)(P|\lambda\sigma) \qquad \text{with} \qquad \chi_P(\mathbf{r}) = \delta(\mathbf{r}-\mathbf{r}_P) \\ &= \sum_P w_P \chi_\mu(\mathbf{r}_P)\chi_\nu(\mathbf{r}_P) \int_{\mathbb{R}^3} d\mathbf{r} \frac{\chi_\lambda(\mathbf{r})\chi_\sigma(\mathbf{r})}{|\mathbf{r}-\mathbf{r}_P|} \\ &= \sum_P X_\mu^P X_\nu^P A_{\lambda\sigma}^P \,, \end{aligned} \tag{2.77}$$

where the collocation tensor $\mathbf{X}$ is given by evaluation of the basis functions at the grid nodes multiplied by the square root grid weights w_P. Furthermore, the third-order three-center one-electron integral tensor $\mathbf{A}$ is the representation of the $|\lambda\sigma)$ charge density in physical space. In this regard, the PS approximation is closely related to the chain of spheres for exchange (COSX) algorithm by Neese and coworkers [120] as well as to seminumerical linear-scaling exact exchange (sn-LinK) method by Laqua *et al.* [121, 122], which both achieve the same tensor decomposition of the ERI tensor.

Since the PS approximation is obtained by insertion of a delta function into single RI approximated ERIs, the same should be possible for double RI approximated ERIs, as in eq. (2.72). Consequently not only a decomposition of the three-center two-electron RI integral tensor representing the bra charge density should be achieved, but also an identical decomposition for the ket. Following the derivation for the PS representation of the ERI tensor in eq. (2.77), the same approach can be used based on eq. (2.72) to yield

$$\begin{aligned}(\mu\nu|\lambda\sigma) &\overset{\mathrm{RI}}{=} \sum_{PQ} (\mu\nu P)(P|Q)(Q\lambda\sigma) \qquad \text{with} \qquad \chi_P(\mathbf{r}) = \delta(\mathbf{r}-\mathbf{r}_P) \\ &= \sum_{PQ} w_P w_Q \, \chi_\mu(\mathbf{r}_P)\chi_\nu(\mathbf{r}_P) \, \frac{1}{|\mathbf{r}_P-\mathbf{r}_Q|} \, \chi_\lambda(\mathbf{r}_Q)\chi_\sigma(\mathbf{r}_Q) \\ &= \sum_{PQ} X_\mu^P X_\nu^P \frac{1}{r_{PQ}} X_\lambda^Q X_\sigma^Q \,. \end{aligned} \tag{2.78}$$

On the one hand, this achieves further reduction of the dimensionality of the highest-order representing tensor – here only second-order tensors are necessary to approximate the full ERI tensor. On the other hand, this approach is fundamentally flawed since for any finite size quadrature grid the $1/r_{PQ}$ term introduces a singularity when $\mathbf{r}_P = \mathbf{r}_Q$ [28]. To remedy this issue while preserving the underlying tensor structure presented in Fig. 2.2 (e), the tensor hypercontraction approximation was derived by Martínez and coworkers [27–30].

2.4.2. Variants

Conceptually, tensor hypercontraction (THC) aims to factorize the ERI tensor according to the tensor network diagram shown in Fig. 2.2 (e). Consequently, the goal is to find a representation of the formally fourth-order ERI tensor entirely in second-order tensors. Since the introduction of the notion of THC in the seminal work by Hohenstein, Parrish and Martínez [27] in 2012 a variety of algorithms to obtain the THC-factorized form of the ERI tensor have been proposed.

In their introductory work Martínez and coworkers used a variant of the double RI-factorized form of the ERI tensor in eq. (2.72) as a starting point. The central two-center auxiliary integral tensor is already of second-order and only the three-center overlap integrals need to be further decomposed. Inspired by successes in other areas of science, the canonical polyadic/parallel factors decomposition (CANDECOMP/PARAFAC or CPD) [97] can be applied. Given an N^{th}-order tensor $\mathcal{T} \in \mathbb{R}^{d_1 \times \cdots \times d_N}$, the CPD is defined as

$$\mathcal{T} = \sum_{r=1}^{R} \bigotimes_{n=1}^{N} \mathbf{a}_r^{(n)} = \bigotimes_{n=1}^{N} \mathbf{A}^{(n)} \tag{2.79}$$

where $\mathbf{a}_r^{(n)} \in \mathbb{R}^{d_n}$ and $1 \leq n \leq N$. CPD therefore allows to represent any tensor as a linear combination of R outer products of N first-order tensors, which optionally can be collected in the second-order tensors $\mathbf{A}^{(n)}$. Applied to the three-center overlap integrals, which are represented by a third-order tensor, the CPD factorization can be visualized as in Fig. 2.3.

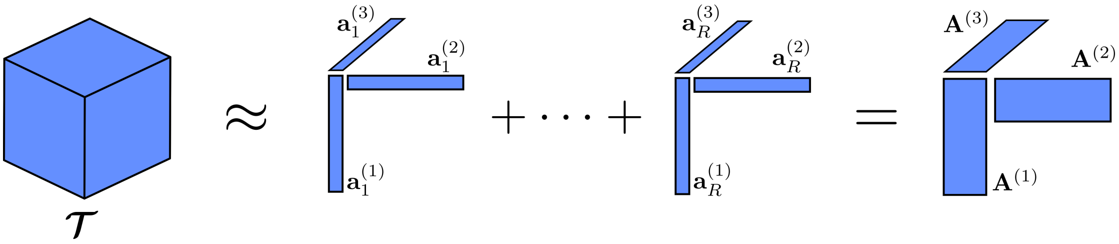

Figure 2.3.: Visualization of the CPD for a third-order tensor $\mathcal{T}$ given by eq. (2.79) following Ref. [92].

In order to obtain the CPD-factorized RI integrals, an alternating least squares (ALS) approach [123, 124] can be applied to yield

$$(\mu\nu\alpha) \overset{\text{CPD}}{=} \sum_{P} X_\mu^P X_\nu^P Y_\alpha^P \,, \tag{2.80}$$

with the additional constraint that $\mathbf{A}^{(1)}$ and $\mathbf{A}^{(2)}$ need to be identical ($\mathbf{X}$) to preserve the permutational symmetry of the AO indices. Overall, this results in a factorization of the ERI tensor as[8]

$$(\mu\nu|\lambda\sigma) = \sum_{PQ} X_\mu^P X_\nu^P Z^{PQ} X_\lambda^Q X_\sigma^Q \,, \tag{2.81}$$

$$Z^{PQ} = \sum_{\alpha\beta\gamma\delta} Y_\alpha^P [\mathbf{S}^{-1}]_{\alpha\beta} (\beta|\gamma) [\mathbf{S}^{-1}]_{\gamma\delta} Y_\delta^Q \,. \tag{2.82}$$

Evidently, eq. (2.81) fits the tensor network diagram shown in Fig. 2.2 e) for the THC format, without depending on real space quadrature and thus avoiding the Coulomb singularity of eq. (2.78). Due to relying on CPD, this way of achieving the THC factorization was later coined PF-THC or direct THC [28]. Naturally, the CPD also permits a half-factorized form of the ERI tensor in the spirit of the PS approximation. Applying the CPD only to one of the three-center integral tensors in eq. (2.72) yields a PS-like factorization without relying on real space quadrature. This so-called partial THC (P-THC) can be combined with the fully THC-factorized form of the ERI tensor according to the tensor network diagram shown in Fig. 2.4.

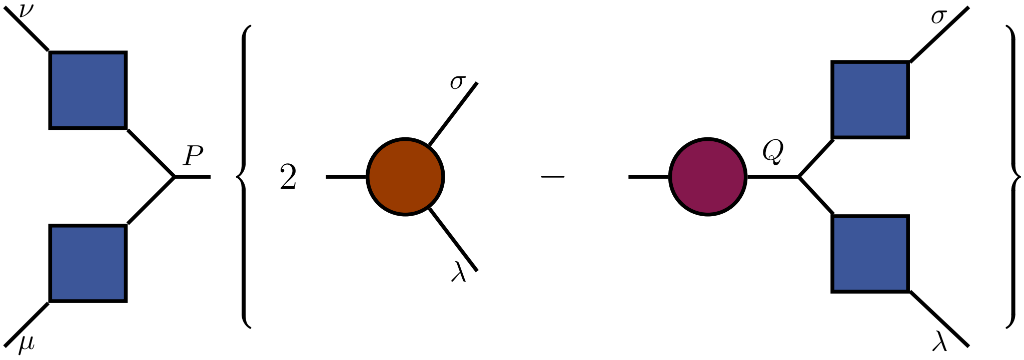

Figure 2.4.: Tensor network diagram of the robust THC factorization of the ERI tensor.

For this so-called robust THC (R-THC) factorization the leading error term is canceled, when comparing the elements of the R-THC approximated with the original RI integral tensor [126, 127]. The increased accuracy of R-THC, however, comes with the cost of having to store and contract the third-order tensor resulting from the P-THC factorization.

By design, THC aims at unpinning the orbital indices also for the ket codensities. Revisiting the idea of inserting delta functions in place of the auxiliary functions in the RI-factorized form of the ERI tensor in eq. (2.78) allows to achieve a separable form of the third-order RI tensors. The central idea is that the orbital pair products are of low

---

[8] In contrast to eq. (2.72), here the fact that the auxiliary functions are taken to be Gaussian-type functions, which are usually non-orthogonal, is taken into account. This is addressed by means of Löwdin orthogonalization [125] resulting in $(\mu\nu|\lambda\sigma) = \sum_{\alpha\beta\gamma\delta} (\mu\nu\alpha)[\mathbf{S}^{-1}]_{\alpha\beta}(\beta|\gamma)[\mathbf{S}^{-1}]_{\gamma\delta}(\delta\lambda\sigma)$, sometimes also referred to as the RI-SVS factorization.

rank in real space allowing a separation of the DF coefficient to $C_\alpha^{\mu\nu} \rightarrow \chi_\mu(\mathbf{r}_P)\chi_\nu(\mathbf{r}_P)$, which results in

$$\begin{aligned}
|\widetilde{\mu\nu}) &= \chi_\mu(\mathbf{r})\chi_\nu(\mathbf{r}) \\
&\overset{\mathrm{RI}}{=} \sum_\alpha C_\alpha^{\mu\nu}\chi_\alpha(\mathbf{r}) \\
&\overset{\mathrm{ISDF}}{=} \sum_P \xi_P(\mathbf{r})\chi_\mu(\mathbf{r}_P)\chi_\nu(\mathbf{r}_P)\,, \qquad (2.83)
\end{aligned}$$

which is known as separable RI (RI-RS) [128, 129] or interpolative separable DF (ISDF) [111–119]. Here, like for the PS approximation, $\{\mathbf{r}_i\}_{i=1}^{N_\mathrm{grid}}$ is a set of real space points, which the basis functions are evaluated on. What remains to be determined are actual interpolation points (IPs) $\{\mathbf{r}_P\}_{P=1}^{N_\mathrm{IP}}$, which form a subset of $\{\mathbf{r}_i\}_{i=1}^{N_\mathrm{grid}}$ and the so-called interpolation vectors (IVs) $\xi_P(\mathbf{r})$. The former can be obtained by QR factorization with column pivoting (QRCP) [113] of the discretized orbital pair products or by centroidal Voronoi tessellation (CVT) using Lloyd's algorithm [114], while the IVs can be computed from a least-squares fit of eq. (2.83). Closely related to ISDF is least-squares THC (LS-THC), in the sense that here also real space quadrature in combination with least-squares fitting is applied to achieve the characteristic separable form of the ERI tensor.

2.4.3. Least-squares Tensor Hypercontraction

2.4.3.1. Introduction

Due to the Coulomb singularity at $\mathbf{r}_P = \mathbf{r}_Q$ in eq. (2.78), two-sided quadrature cannot be invoked to obtain a THC-factorized form of the ERI tensor. Instead seeking a discretized version of the $1/r_{12}$ Coulomb operator which is optimal in the least-squares sense given the L2-norm estimator [28]

$$O = \frac{1}{2}\left\| (\mu\nu|\lambda\sigma) - X_\mu^P X_\nu^P Z^{PQ} X_\lambda^Q X_\sigma^Q \right\|_2^2 , \qquad (2.84)$$

results in the renormalized Z representation of the singular $1/r$ operator. Recasting the above expression into a general least-squares problem yields

$$O = \frac{1}{2}\left\| \mathbf{B} - \mathbf{A}\mathbf{Y}\mathbf{A}^\mathrm{T} \right\|_2^2 , \qquad (2.85)$$

where $\mathbf{B} \in \mathbb{R}^{N_\mathrm{bf}^2 \times N_\mathrm{bf}^2}$, $\mathbf{A} \in \mathbb{R}^{N_\mathrm{bf}^2 \times N_\mathrm{grid}}$ and $\mathbf{Y} \in \mathbb{R}^{N_\mathrm{grid} \times N_\mathrm{grid}}$, when rearranging the ERI tensor $\boldsymbol{\mathcal{I}}$ into a $N_\mathrm{bf}^2 \times N_\mathrm{bf}^2$ supermatrix. The solution (supplementary information of **Publication II**) of the least-squares problem in eq. (2.85) through the associated normal equations is known to be

$$\mathbf{Y} = (\mathbf{A}^{\mathrm{T}}\mathbf{A})^{-1}\mathbf{A}^{\mathrm{T}}\mathbf{B}\mathbf{A}(\mathbf{A}^{\mathrm{T}}\mathbf{A})^{-1}\,. \tag{2.86}$$

Applied to the LS-THC estimator in eq. (2.84), the analytical expression for the central **Z** tensor [28] is given by

$$\begin{aligned}\mathbf{Z} &= (\mathbf{R}^{\mathrm{T}}\mathbf{R})^{-1}\mathbf{R}^{\mathrm{T}}\boldsymbol{\mathcal{I}}\mathbf{R}(\mathbf{R}^{\mathrm{T}}\mathbf{R})^{-1}\,,\\ &= \mathbf{S}^{-1}\mathbf{E}\mathbf{S}^{-1}\,,\end{aligned}$$

with $\mathbf{R} \coloneqq \mathbf{X} \otimes_c \mathbf{X}$. Here, $\mathbf{S} \coloneqq \mathbf{R}^{\mathrm{T}}\mathbf{R}$ is the THC grid metric tensor and $\mathbf{E} \coloneqq \mathbf{R}^{\mathrm{T}}\boldsymbol{\mathcal{I}}\mathbf{R}$ is the real space representation of the ERI tensor. As long as the number of real space points is at least $N_{\mathrm{bf}}(N_{\mathrm{bf}}+1)/2$ the obtained THC factorization is exact [29, 130]. In practice, however, the aim is to reduce the number of grid points to $N_{\mathrm{grid}} \ll N_{\mathrm{bf}}(N_{\mathrm{bf}}+1)/2$ to achieve computational speedup compared to the canonical formulation.

LS-THC has distinct advantages over PF-THC, which is the other currently most prevalently employed variant of THC. PF-THC offers a relatively simple way of achieving the THC format in terms of the underlying CPD and without the necessity of resorting to real space quadrature [27]. However, a feasible implementation of CPD for large systems is currently not known, partially also due to the known convergence problems [92, 130]. In contrast, in LS-THC the limiting factor is the formation of the grid-projected ERI tensor **E**, which requires an expensive ($\mathcal{O}(N^5)$) and memory intensive ($\mathcal{O}(N^4)$) transformation of the ERI tensor from spectral to real space [28]. To overcome this limitation a low-scaling implementation is presented in **Publication I**, which relies on pre-approximating the ERI tensor using attenuated Coulomb RI [31, 32] and performing the involved tensor contractions using integral screening [33] and sparse linear algebra, as explained in Section 2.5. The developed LS-THC algorithm is applied to MP2 energies in **Publication I** and extended to MP2 hyperfine coupling constants (HFCCs) in **Publication II** to achieve significant speedups compared to previously implemented MP2 methods. Furthermore, an integral-direct and density-based version of LS-THC is presented in **Publication IV**, which is applied to ground and excited state calculations using the (LR-)CC2 (*cf.* Section 2.2.3.2) and ADC(2) (*cf.* Section 2.2.4) methods. The LS-THC algorithm developed in **Publication IV** only relies on three key ingredients: 1) the ability to evaluate basis functions on a density function theory (DFT)-like grid, 2) the ability to perform Coulomb builds, and 3) BLAS level 3 linear algebra. All of these requirements are met by any quantum chemistry program, which implements basic KS-DFT and the newly proposed algorithm therefore simplifies the process of adopting LS-THC in other program packages.

2.4.3.2. Grids

Key to achieving computational benefits from applying LS-THC, instead of using the canonical ERI tensor or, e.g., the RI approximation, is that the quadrature grid defining the real space must be as compact as possible. In the original work, Parrish *et al.*

[28] employed Becke-type grids [131], which were superseded by specifically optimized molecular grids [132]. The optimized grids originate from common DFT in the sense that for the atom-centered grids Lebedev-Laikov integration [133] is carried out for the spherical part and the radial integration is performed using optimized Handy grids [134]. The final molecular grid is then constructed by fuzzy Voronoi partitioning [135] to form the atomic weights. The position of the radial nodes in the Handy scheme are then optimized on an objective function assessing the accuracy of THC-MP2 compared to canonical MP2. Overall, this allows to achieve accuracies on the order of 0.1 kcal/mol using $N_{\text{grid}} \approx 3N_{\text{aux}}$ grid points for a common double-ζ basis set [28].

Roughly 100 grid points per atom – assuming a double-ζ basis set – is certainly close to being as compact as possible without compromising significantly on accuracy. However, the hand-optimized grids are only available for the cc-pVXZ (X $\in$ {D,T}) basis sets and therein only for the first two rows of the periodic table [132]. Leveraging the connection of LS-THC to ISDF, Lee *et al.* [118] proposed a variation of the IP selection process through CVT, which selects a subset $\{\mathbf{r}_P\}_{P=1}^{N_{\text{IP}}}$ of quadrature nodes from a larger molecular parent grid $\{\mathbf{r}_i\}_{i=1}^{N_{\text{grid}}}$. This way, a real space grid can be constructed on-the-fly in a systematically improvable fashion through the choice of the number of IPs. As stated in Section 2.4.2, IPs can also be selected by applying a QRCP decomposition of the supermatrix formed by evaluating orbital pair products $|\mu\nu)$ on a larger real space grid. It can be shown that this procedure is related to a pivoted Cholesky decomposition (PCD) of the THC grid metric tensor $\mathbf{S}$ and selection of the interpolation points via the pivoting contained in the permutation matrix [130]. On a side note, this is also related to the almost error-free RI method by Schurkus *et al.* [136], in which contributing auxiliary functions are selected through singular value decomposition from a larger parent auxiliary basis.

In **Publications I** and **II** the hand-optimized grids developed by Martínez and coworkers are employed as they yield satisfactory accuracy for both energies and HFCCs. In **Publication IV** the PCD approach by Matthews [130] is adopted, pruning from the optimized cc-pVTZ based LS-THC grid. The latter was chosen as a trade-off between accuracy and feasibility. On the one hand, the developed THC-CC2 and THC-ADC(2) methods require THC fitting of less compact (vv|vo)-type integrals – compared to the (ov|ov)-type integrals in MP2 theory – and therefore more quadrature points for the same kind of accuracy. On the other hand, performing a PCD on the $N_{\text{grid}} \times N_{\text{grid}}$ grid metric tensor $\mathbf{S}$ is hardly computationally feasible if larger systems beyond 10000 basis functions are investigated, when not already using a compact parent grid.

2.5. Reduced-scaling Techniques

Without application of further mathematical transformations or sensibly designed algorithms the electron correlation methods presented in Section 2.2 exhibit prohibitive scaling with the system and basis set size. On the one hand, a sufficiently large basis set is crucial for the accurate description of electron correlation. On the other hand, the strive to tackle increasingly large systems of thousands of atoms is propelled by experimental basic research on – and material design of – systems with ever increasing complexity. The applicability of the quantum chemical methods in Section 2.2 to these problems is governed by the scaling of the computational cost – in terms of both computation time and memory requirements – with increasing system size. All canonical formulations of the correlation methods presented in Section 2.2 exhibit prohibitive polynomial $\mathcal{O}(N^{\geq 5})$ scaling. In order to be able to treat systems beyond a handful of atoms, the scaling exponent has to be reduced, while keeping the prefactor as low as possible. In this regard, some of the mathematical techniques in the realm of tensor numerical methods, like the RI or the THC approximation, have already been discussed in Section 2.4. It should however be noted that these methods, exemplarily applied to MP2 (*cf.* Section 2.2.2), do not necessarily decrease the scaling exponent but in some cases only lower the prefactor. On the one hand, for RI-MP2 this is the case because the orbital indices in the energy denominator in eq. (2.23) remain pinned, requiring to rebuild the canonical ERI tensor from the RI integrals. On the other hand, for the fitting procedure in LS-THC-MP2 this is the case because the ERI tensor has to be projected onto the real space grid. Since as outlined in Section 2.4, the manipulation and storage of the integral tensors is usually the limiting factor in terms of computation time and memory requirements, further optimizations have to be performed to make these methods applicable to larger systems.

2.5.1. Sparse Linear Algebra

It is well known that the density matrix decays exponentially with spatial orbital separation with the decay rate being the energy gap between the highest occupied (HOMO) and the lowest unoccupied molecular orbital (LUMO) [137]. Therefore, for any system with a significant HOMO-LUMO gap, for which the density matrix is expressed in a localized basis such as the AOs, the density matrix is expected to be sparse, as exemplarily shown in Fig. 2.5 (a). Likewise, an integral tensor over local orbitals, such as the AOs, will also exhibit significant sparsity as demonstrated for the three-center RI integral tensor using the regular $1/r_{12}$ operator ($\boldsymbol{\mathcal{B}}$) in Fig 2.5 (b) or the short-ranged $\mathrm{erfc}(\omega r_{12})/r_{12}$ metric ($\boldsymbol{\mathcal{B}}_\omega$) in Fig 2.5 (c).

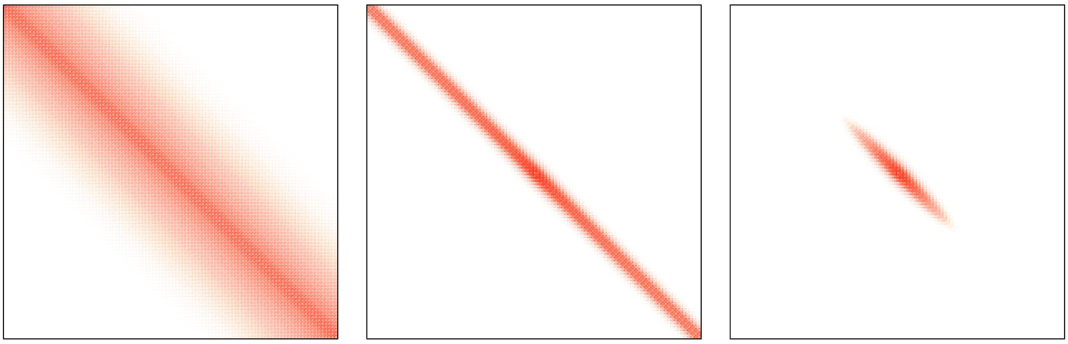

(a) $\mathbf{P}_{\mathrm{occ}}$ (b) $\boldsymbol{\mathcal{B}}[:,:,N_{\mathrm{aux}}/2]$ (c) $\boldsymbol{\mathcal{B}}_{\omega}[:,:,N_{\mathrm{aux}}/2]$

Figure 2.5.: Sparsity patterns for the occupied density matrix $\mathbf{P}_{\mathrm{occ}}$ (a) and a slice of the three-center RI integral tensor for a fixed auxiliary function using the regular Coulomb operator ($\boldsymbol{\mathcal{B}}$, b) as well as an attenuated Coulomb metric [31, 32] ($\boldsymbol{\mathcal{B}}_{\omega}$, c) with an attenuation strength of $\omega = 0.1$. All patterns are obtained for the linear alkane $C_{100}H_{202}$ using the cc-pVDZ/cc-pVDZ-RI basis set combination.

The inherent sparsity of central quantities such as the density matrix or the integral tensors thus opens up the possibility to leverage said sparsity using sparse linear algebra [138]. The key idea here is to save only non-zero tensor elements above a predefined sparsity threshold to achieve a compression in a vectorized storage format [139, 140]. An example of such a storage scheme frequently used in quantum chemistry packages is the block compressed sparse row (BCSR) format, which is depicted in Fig. 2.6 on the left.

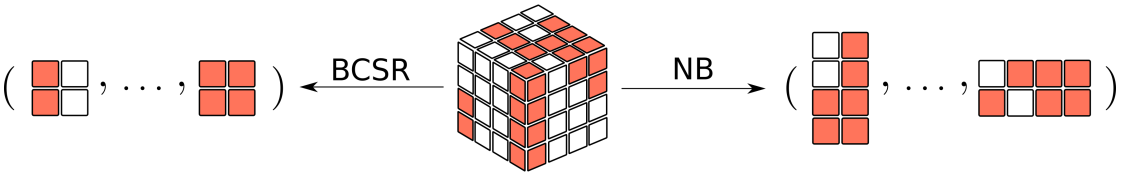

Figure 2.6.: Visualization of the BCSR and the NB tensor compression schemes. Significant elements (blocks) are depicted in red, while zero elements (blocks) are shown in white.

Converting a tensor to BCSR format requires dividing the tensor into submatrices (blocks) of predefined, cache-friendly sizes ($\sim 48 \times 48$) and allocating memory for a block if and only if its norm is above the sparsity threshold. Furthermore, in two additional auxiliary vectors the offsets of the blocks in the uncompressed tensor are stored. While this entails an overhead compared to the dense format, savings can be achieved if a certain minimum sparsity is present in the uncompressed tensor. Not only does this save memory, but also floating point operations (FLOPS) when performing common linear algebra routines. On the example of matrix-matrix multiplications, the advantage lies in the fact that the product of two allocated blocks is computed only if the product of their norms is above a given threshold.

Instead of discarding insignificant blocks, natural blocking (NB), shown in Fig. 2.6 on the right, relies on removing whole rows or columns of tensor slices if none of the elements are considered significant. Like for the BCSR format this requires bookkeeping of the offsets of the retained rows and columns in so-called significance lists. This, however, allows to apply set theoretical considerations to screen out unnecessary operations when performing tensor contractions in the NB format, as explained in more detail in **Publication II**. The benefit of the NB over the BCSR format is that by discarding whole subvectors, the resulting slices are large and dense allowing to leverage large matrix optimizations like the Strassen algorithm [141] as implement in the Intel Math Kernel Library (MKL) [142]. Upon inspection of the sparsity patterns in Fig. 2.5 it is evident, that NB only recovers the sparsity in tensors with a locally dense substructure, as exemplarily shown for the ω-RI integral tensor $\boldsymbol{\mathcal{B}}_\omega$. In case of a predominantly band-diagonal pattern, like for the occupied density matrix $\mathbf{P}_{\text{occ}}$ or the RI integral tensor $\boldsymbol{\mathcal{B}}$, each row/column will possess non-zero elements, which prevents screening out whole subvectors. In other words, when applied to the compression of integrals, BCSR is favorable for long-ranged operators like the $1/r_{12}$ operator, while NB can be advantageous for short-ranged ones, like the $\text{erfc}(\omega r_{12})/r_{12}$ operator. **Publications I** and **II** make use of the NB format to achieve low-scaling implementations of the linear algebra required for MP2 energies and first derivatives, while the BCSR scheme is applied in **Publication IV** for efficient implementations of CC2, LR-CC2, and ADC(2).

2.5.2. Local Molecular Orbitals

As outlined in the previous section, integrals over localized orbitals, like the AOs, exhibit favorable sparsity which can be used by sparse linear algebra routines. Unfortunately, this does not hold for delocalized bases, such as for the MOs. To reintroduce sparsity in these canonically non-sparse integral tensors, a number of orbital localization schemes, such as the Foster–Boys [143, 144], Edmiston–Ruedenberg [145], or Pipek–Mezey [146] approach as well as modern renditions such as pair natural orbitals (PNOs) [147] or orbital specific virtuals (OSVs) [148] have been developed. These localization schemes are driven by the observation that many molecular properties are local in character, in turn motivating the assumption that only the atoms in close vicinity to a specific site contribute to the property under investigation [106]. Orbital localization relies on the fact that the one-particle density matrix is invariant under orbital rotations causing an infinite number of representations for the MOs to be possible. To achieve a favorable local representation all mentioned localization schemes optimize a localization functional with respect to these rotations in an iterative fashion. In contrast, the localization scheme by Aquilante *et al.* [106, 149] provides a fast, numerically stable and non-iterative way to obtain localized orbitals directly from the one-particle density matrix. Since the occupied density matrix $\mathbf{P}_{\text{occ}}$ is positive semidefinite with rank equal to the number of occupied orbitals N_{occ}, it permits a factorization by pivoted Cholesky decomposition (PCD). Unlike many of the aforementioned localization schemes, this also holds for the virtual density matrix $\mathbf{P}_{\text{virt}}$. The resulting set of therefore named Cholesky MOs is orthonormal and the individual orbitals are localized, resulting in considerable sparsity for Cholesky-MO-transformed integrals. In **Publications I** and **II** Cholesky MOs are used to reduce the scaling of transforming the three-center RI integrals to the MO basis before the grid projection for the THC fitting. Furthermore, PCD is also leveraged for the final energy/property calculation in a so-called Cholesky pseudo-MO basis obtained by a PCD of the pseudodensities (*cf.* Appendix A.3.1, eqs. (A.37) and (A.38)) obtained by the application of the Laplace transformation to the MP2 energy denominator.

2.5.3. Integral Screening

Examination of the underlying physical structure of the formally $\mathcal{O}(N^4)$ scaling ERI tensor reveals that the number of significant elements reduces to $\mathcal{O}(N^2)$ for large systems [150]. Since the comprising basis functions are Gaussians, the therefrom derived charge distributions quickly become negligible with spatial separation of the basis functions as already outlined in Section 2.4.1. Therefore, only a linear scaling number of orbital pairs $|\mu\nu)$ and $|\lambda\sigma)$ have to be taken into account. Furthermore, the significance of an element of the ERI tensor can be estimated from the Cauchy–Schwarz inequality [21]

$$|(\mu\nu|\lambda\sigma)| \leq |(\mu\nu|\mu\nu)|^{\frac{1}{2}} |(\lambda\sigma|\lambda\sigma)|^{\frac{1}{2}} = Q_{\mu\nu} Q_{\lambda\sigma}\,, \tag{2.87}$$

which provides a rigorous upper bound. To further capture the $1/r_{12}$ dependence of the bra-ket separation, the QQR integral estimates [151, 152] given by

$$|(\mu\nu|\lambda\sigma)| \approx \frac{Q_{\mu\nu} Q_{\lambda\sigma}}{R - \text{ext}_{\mu\nu} - \text{ext}_{\lambda\sigma}}\,, \tag{2.88}$$

can be used, which are based on the previously developed multipole-based integral estimates (MBIE) [153]. Here, $\text{ext}_{\mu\nu}$ denotes the spatial extents of the $|\mu\nu)$ charge distribution. In QQR, however, the expressions for the extents are non-rigorous, which led to the development of the integral partition bounds (IPBs) [33]. The IPBs provide analytic expressions for the extents through partitioning of the integration space in eq. (2.5) into balls centered around the $|\mu\nu)$ charge distributions and their complements. Not only do the mentioned integral estimates allow for the calculation of only significant elements of the ERI tensor, they can further be leveraged to provide the foundation for the significance lists in NB. Therefore, the rigorous IPBs were employed in **Publications I** and **II** for the integral evaluation in the THC fitting procedure and the subsequent tensor contractions in conjunction with NB. In total, this yields an asymptotically linear scaling algorithm for the grid projection in the THC fitting and additionally permits an $\mathcal{O}(N)$ scaling approach for exchange-like contractions in MP2.

3. Publications

3.1. Publication I: Low-Scaling Tensor Hypercontraction in the Cholesky Molecular Orbital Basis Applied to Second-Order Møller–Plesset Perturbation Theory

F. H. Bangerter, M. Glasbrenner, C. Ochsenfeld

J. Chem. Theory Comput. **17**, 211-221 (2021).

Abstract

We employ various reduced scaling techniques to accelerate the recently developed least-squares tensor hypercontraction (LS-THC) approximation [Parrish, R. M., Hohenstein, E. G., Martínez, T. J., Sherrill, C. D. *J. Chem. Phys.* *137*, 224106 (**2012**)] for electron repulsion integrals (ERIs) and apply it to second-order Møller–Plesset perturbation theory (MP2). The grid-projected ERI tensors are efficiently constructed using a localized Cholesky molecular orbital basis from density-fitted integrals with an attenuated Coulomb metric. Additionally, rigorous integral screening and the natural blocking matrix format are applied to reduce the complexity of this step. By recasting the equations to form the quantized representation of the $1/r$ operator $\mathbf{Z}$ into the form of a system of linear equations, the bottleneck of inverting the grid metric via pseudoinversion is removed. This leads to a reduced scaling THC algorithm and application to MP2 yields the (sub-)quadratically scaling THC-ω-RI-CDD-SOS-MP2 method. The efficiency of this method is assessed for various systems including DNA fragments with over 8000 basis functions and the subquadratic scaling is illustrated.

Reprinted with permission from:

F. H. Bangerter, M. Glasbrenner, C. Ochsenfeld
"Low-Scaling Tensor Hypercontraction in the Cholesky Molecular Orbital Basis Applied to Second-Order Møller–Plesset Perturbation Theory"
J. Chem. Theory Comput. **17**, 211-221 (2021).

`https://pubs.acs.org/doi/10.1021/acs.jctc.0c00934`

JCTC Journal of Chemical Theory and Computation

pubs.acs.org/JCTC Article

Low-Scaling Tensor Hypercontraction in the Cholesky Molecular Orbital Basis Applied to Second-Order Møller–Plesset Perturbation Theory

Felix H. Bangerter, Michael Glasbrenner, and Christian Ochsenfeld*

Cite This: *J. Chem. Theory Comput.* 2021, 17, 211–221 Read Online

ACCESS | Metrics & More | Article Recommendations | Supporting Information

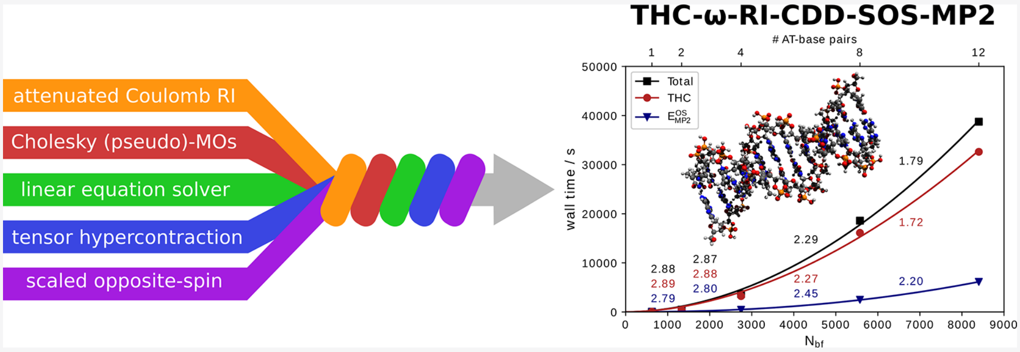

ABSTRACT: We employ various reduced scaling techniques to accelerate the recently developed least-squares tensor hypercontraction (LS-THC) approximation [Parrish, R. M., Hohenstein, E. G., Martínez, T. J., Sherrill, C. D. *J. Chem. Phys. 137*, 224106 (**2012**)] for electron repulsion integrals (ERIs) and apply it to second-order Møller–Plesset perturbation theory (MP2). The grid-projected ERI tensors are efficiently constructed using a localized Cholesky molecular orbital basis from density-fitted integrals with an attenuated Coulomb metric. Additionally, rigorous integral screening and the natural blocking matrix format are applied to reduce the complexity of this step. By recasting the equations to form the quantized representation of the $1/r$ operator **Z** into the form of a system of linear equations, the bottleneck of inverting the grid metric via pseudoinversion is removed. This leads to a reduced scaling THC algorithm and application to MP2 yields the (sub-)quadratically scaling THC-ω-RI-CDD-SOS-MP2 method. The efficiency of this method is assessed for various systems including DNA fragments with over 8000 basis functions and the subquadratic scaling is illustrated.

1. INTRODUCTION

One of the simplest quantum chemical methods to recapture the electron correlation neglected by Hartree–Fock (HF) theory is second-order Møller–Plesset perturbation theory (MP2),[1] which has been extensively studied in the past decades.[2] Today, it remains popular as a post-HF method with affordable cost and also as part of double-hybrid density functionals (DHDF).[3,4] It has further proven to provide accurate results for molecular properties such as NMR chemical shifts.[5] The computational cost of conventional MP2 is governed by the transformation of the electron repulsion integrals (ERI) from atomic orbital (AO) to molecular orbital (MO) basis, which scales as $O(N^5)$ with the number of basis functions N. The formal fifth power scaling of the computational cost and the $O(N^4)$ storage requirements severely restrict the size of computationally accessible molecules. Naturally, considerable effort has been put into reducing the computational cost of MP2 calculations. Methods aiming at reducing the scaling behavior of MP2 can be grouped into two different categories: first, methods aiming at exploiting the sparsity of the MP2 problem, either of intrinsic nature such as in the AO-MP2 formulation[6−8] or created by ansatz as in local MP2 methods[9−18] and, second, methods based on tensor decompositions of the ERIs involved.[19−27]

The pioneering work of Pulay and Sæbø[9−11] on the local treatment of correlation in the 1980s served as a stepping stone for the development of the family of local correlation (LC) methods by Werner, Schütz, and others.[12−18] In the LC methods developed by Werner and Schütz,[12−15,17] the occupied space is spanned by localized molecular orbitals (LMOs), which are obtained from the canonical orbitals by localization

Received: September 8, 2020
Published: December 29, 2020

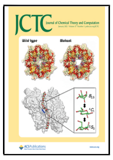

https://dx.doi.org/10.1021/acs.jctc.0c00934

techniques, such as Foster−Boys[28] or Pipek−Mezey,[29] while the virtual space is spanned by nonorthogonal projected AOs (PAOs), which are obtained from the AO basis by projecting out the occupied orbitals. Using the locality created by a standard localization procedure for the occupied MOs and the inherent locality of the PAOs, low- and linear-scaling algorithms can be devised. The latter has been demonstrated for MP2,[13,17] the singles and doubles coupled cluster method (CCSD),[12,14] and even for additional perturbative triple excitations (CCSD(T)).[15,30] In order to overcome the sometimes large PAO domains needed to converge the correlation energy, Neese *et al.*[31] proposed a compression of the virtual space by means of pair natural orbitals (PNOs). In combination with careful prescreening and a multipole expansion for distant orbital pairs, Werner *et al.*[32] developed the PNO-LMP2 method that scales as $\mathcal{O}(M)$ with respect to the molecule size M and has good parallel efficiency. Conceptually similar is the domain-based local PNO (DLPNO) implementation of local MP2 by Pinski *et al.*,[33] which was extended to a linear scaling implementation of the DLPNO-CCSD(T) method.[34−36] An alternative approach to this is the divide-expand-consolidate (DEC) group of methods,[34−36] which achieve massive parallelization[37] and therefore allow the computation of very large molecules by partitioning of the orbital space.

In spite of their favorable scaling and efficiency, local correlation methods suffer from distinct drawbacks. One of the most severe disadvantages is that the domains may change as a function of the molecular geometry, which can reduce the accuracy and may even lead to discontinuities in the potential energy surface.[38,39] Thus, instead of localizing the orbital space, a second approach to reduce the scaling of the MP2 algorithm is to recast the MP2 equations into the AO basis. Making use of the Laplace transformation for the orbital energy denominator occurring in the canonical MP2 formulation introduced by Almlöf and Häser,[6,40,41] in combination with efficient integral screening, our group developed an asymptotically linear scaling AO-MP2 method.[8] To overcome the large prefactor associated with the AO-based formulation, the RI-CDD-MP2 method[42] was introduced, which uses a pivoted Cholesky decomposition of the pseudo-density matrices (CDD) to obtain a localized Cholesky pseudo-MO basis. RI-CDD-MP2 significantly reduces the prefactor of the MP2 calculation while scaling asymptotically cubic if no further approximations are applied.[42]

In contrast to the above, methods aiming at decomposing the tensors involved in the calculations usually do not lower the scaling exponent of the method they are applied to, but rather lower the prefactor of the respective method. The most established approach in the family of tensor decomposition methods is the density fitting or resolution-of-the-identity ansatz,[19,43−45] which approximates a generalized charge density $\rho_{\mu\nu}(\mathbf{r}_1) = \chi_\mu(\mathbf{r}_1)\chi_\nu(\mathbf{r}_1)$ with an auxiliary basis $\{\chi_\alpha(\mathbf{r}_1)\}$. Closely related is the Cholesky decomposition (CD) approach[20−22,46−50] of the ERIs, in which the auxiliary basis is constructed on-the-fly as an orthogonalized subset of the basis function space $\{\chi_\mu\}$. Both RI and CD achieve a factorization of the fourth-order ERI tensor into two third-order tensors. Today, RI is routinely applied to Møller−Plesset perturbation theory,[51−53] density functional theory (DFT),[54,55] the random phase approximation (RPA),[56,57] or coupled cluster (CC)[58] theory. Further decomposition of the ERIs into two second-order and one third-order tensor is possible within the pseudospectral approach,[23−25] in which the integral over one electronic coordinate is solved analytically and the other by numerical quadrature. Conceptually related are the chain-of-spheres approach (COSX)[59] and the seminumerical exact-exchange formalism (sn-LinK)[60] that make use of the same kind of decomposition. Taking this approach one step further and attempting a two-sided decomposition of the ERI, one arrives at the recently developed tensor hypercontraction (THC)[27,61−63] factorization. Within the THC framework, it is possible to approximate the fourth-order ERI tensor as a product of just five factor matrices, reducing the highest order tensor necessary to represent the full ERI to only two. While different flavors of THC have been proposed, like parallel factors THC (PF-THC),[26] which achieves the factorization by canonical polyadic decomposition (CPD) of the three-center overlap integrals within the overlap metric RI formalism, we focus our discussion on the more accurate least-squares THC (LS-THC)[27] approach. In passing, we note that the atomic-batched tensor decomposition by Schmitz *et al.*[64,65] can also be viewed as a THC-like factorization starting from RI-approximated ERIs with further decomposition by singular value decomposition of the third-order subtensors belonging to atom pairs. THC attempts a quantization of the spatial coordinates via $\mathbf{r}_1 \rightarrow \{\mathbf{r}_P\}$ and $\mathbf{r}_2 \rightarrow \{\mathbf{r}_Q\}$ and replacing the singular grid operator $r_{12}^{-1} \rightarrow \{r_{PQ}^{-1}\}$ with a renormalized operator Z^{PQ}. Together with the RI approximation, LS-THC has proven to be a flexible and efficient framework and has been successfully applied to exact exchange,[66] MP2,[26,27,62,63,66−69] MP3,[26,66] CCSD,[70] second-order approximated CC (CC2),[71] as well as equation-of-motion CC2 (EOM-CC2),[72] RPA,[73] and second-order complete active space perturbation theory (CASPT2).[74]

In this work, we aim to combine different linear scaling techniques to obtain an efficient and low-scaling THC algorithm. In particular, we extend the RI-LS-THC formalism developed by Martínez and co-workers[27,61−63] using an attenuated Coulomb metric[75] for the THC fitting procedure. Together with a localized Cholesky-MO basis, we seek to efficiently exploit the sparsity in the three-center integrals for the subsequent contractions. In our integral code, we make use of efficient integral screening based on the recently developed integral partition bounds (IPB).[76] Furthermore, we employ the natural blocking scheme originally developed by Jung *et al.*[77] for the transformation to the Cholesky-MO basis and subsequent projection onto the quadrature grid. In addition to thereby lowering the scaling of the formally most expensive step, i.e., the formation of the grid-projected ERI tensor, we present ways to circumvent the computational bottleneck of forming the pseudoinverse of the grid metric necessary for building the quantized and renormalized grid-projected potential operator. We do this by decomposition of the grid metric matrix followed by a forward and a backward substitution step. This is in contrast to the local-THC approximation by Song *et al.*[63] in which the molecule is partitioned into fragments to reduce the complexity of the inversion. After contraction of one-half of the projected potential operator, obtained by the linear solve step, with its transpose and the two-center RI integrals, the familiar $\mathbf{Z}$ tensor is obtained. Finally, we apply our efficient THC algorithm to MP2, for which the energy evaluation is performed in a localized Cholesky pseudo-MO basis using block-sparse linear algebra to efficiently exploit sparsity and reduce the scaling of this step. Together with the scaled opposite-spin (SOS)[78] approximation, we present the (sub-)quadratically scaling THC-ω-RI-CDD-SOS-MP2 method.

2. THEORY

2.1. Notation. We briefly summarize the relevant indices below:

- $\mu, \nu, \lambda, \sigma$: atomic orbital indices belonging to the AO basis $\{\chi_\mu\}$ of size N_{bf}.
- $\alpha, \beta, \gamma, \delta$: auxiliary basis indices belonging to the density fitting basis $\{\chi_\alpha\}$ of size N_{aux} (usually $N_{\mathrm{aux}} \approx 3 \cdot N_{\mathrm{bf}}$).
- P, Q, R, S: grid point indices belonging to the LS-THC grid of size N_{grid} (usually $N_{\mathrm{grid}} \approx 3 \cdot N_{\mathrm{aux}}$).
- i, j, k: occupied molecular orbital indices belonging to the MO basis $\{\phi_i\}$ of size N_{occ}.
- a, b, c: virtual molecular orbital indices belonging to the MO basis $\{\phi_a\}$ of size N_{virt} ($N_{\mathrm{virt}} \gg N_{\mathrm{occ}}$).
- κ: index of the Laplace quadrature points for the MP2 energy denominator (usually integration with 5−8 points is sufficiently accurate).

2.2. Review of Tensor Hypercontraction. The LS-THC estimator[27] for approximating the ERIs in the occupied-virtual (OV) subspace of the MO integrals using a physical-space quadrature is defined as

$$\arg\min_{Z} \sum_{ijab} \frac{1}{2} \|\Delta_{iajb}\|^2 \tag{1}$$

where the deviation Δ_{iajb} of the THC factorization from the exact ERI tensor is given by

$$\Delta_{iajb} = (ia|jb) - \sum_{PQ} X_i^P X_a^P Z^{PQ} X_j^Q X_b^Q \tag{2}$$

Note that we perform the THC fitting not in the AO space, but instead in the OV subspace of the MO space, since this is the only block of the MO integrals needed for evaluating the MP2 equation. Additionally, since the fitting space is smaller, grids with fewer grid points can be used, or, if the same grids are applied, more accurate results can be expected.[27,62,66] In contrast to the AO-based local-THC approximation by Song *et al.*,[63] we make use of a global description of the THC factorization, i.e., using a single global **Z** tensor, that is not prone to discontinuities of the potential energy surface. The latter is demonstrated in the Supporting Information for the rotation around the 4C−5C bond in vitamin K$_2$ as a representative example.

As is already evident from eqs 1 and 2, THC provides a more flexible tensor decomposition than all methods discussed above as it effectively unpins all four MO indices. A direct consequence of this is that fewer indices need to be carried over during tensor contractions, providing means for the formulation of lower-scaling algorithms. As shown by Parrish *et al.*,[27] differentiating eq 1 with respect to **Z** and subsequently solving the stationary condition for **Z** gives the analytic solution

$$Z^{PQ} = \sum_{P'Q'} [\mathbf{S}^{-1}]^{PP'} E^{P'Q'} [\mathbf{S}^{-1}]^{QQ'} \tag{3}$$

where the grid metric **S** is defined as

$$S^{PP'} = \sum_{i'a'} X_{i'}^P X_{i'}^{P'} X_{a'}^P X_{a'}^{P'} \tag{4}$$

and the grid-projected ERI tensor **E** is defined as

$$E^{P'Q'} = \sum_{ijab} X_i^{P'} X_a^{P'} (ia|jb) X_j^{Q'} X_b^{Q'} \tag{5}$$

Within the LS-THC framework,[27] the **X** tensors are chosen to be collocation matrices, i.e., results of evaluating the basis functions $\{\chi_\mu\}$ at the real-space grid $\{\mathbf{r}_P\}$ given by

$$X'^P_\mu = \sqrt[4]{w_P}\, \chi_\mu(\mathbf{r}_P) \tag{6}$$

where w_P are the associated grid weights. For reasons of numerical stability, we found it useful to additionally balance the collocation matrices **X** according to

$$X_\mu^P = v_P X'^P_\mu \quad \text{with} \quad v_P = \frac{1}{\sqrt{\sum_\mu X'^P_\mu X'^P_\mu}} \tag{7}$$

as proposed by Parrish *et al.*[61] After rebalancing, the collocation matrices are transformed into Cholesky-MO space[79] according to

$$X_i^P = \sum_\mu L_{\mu i} X_\mu^P \tag{8}$$

$$X_a^P = \sum_\nu L_{\nu a} X_\nu^P \tag{9}$$

where $L_{\mu i}$ and $L_{\nu a}$ are the local Cholesky factors obtained from the occupied density matrix **P** and the virtual density matrix **Q**, respectively. We note that here and throughout CDD refers to the Cholesky decomposition of the ground state densities as well as the pseudo-densities in the energy evaluation (eq 30). Since **P** and **Q** are both invariant under orbital rotations, an infinite number of MO coefficient representations of the density matrix exists.[79] The Cholesky factors thus represent one possible set of MO coefficients with the advantage that the Cholesky-MOs are local and the coefficients sparse, which can be exploited during subsequent contractions.

2.3. Construction of the Grid-Projected ERI Tensor E. Inserting the RI factorization of the ERI tensor into eq 5 allows one to reduce the formal scaling of the construction of the **E** tensor to only quartic or $O(N_{\mathrm{occ}} N_{\mathrm{virt}} N_{\mathrm{aux}} N_{\mathrm{grid}})$ to be more precise.[27] Thus, since all other operations in obtaining the THC factorization scale at most cubic, the formation of **E** will still be the rate-determining step in the asymptotic limit. To circumvent this issue in the THC algorithm, we substitute the ERI tensor by a double density-fitted RI approximation with a complementary error function (erfc-) attenuated Coulomb metric[75]

$$(\mu\nu|\lambda\sigma) = \sum_{\alpha\beta\gamma\delta} (\mu\nu:\alpha) [\mathbf{V}^{-1}]_{\alpha\gamma} [\mathbf{J}]_{\gamma\delta} [\mathbf{V}^{-1}]_{\delta\beta} (\beta:\lambda\sigma) \tag{10}$$

where the two- and three-center integrals with the erfc-attenuated Coulomb operator are given by

$$(\mu\nu:\alpha) = \iint_{\mathbb{R}^3} \mathrm{d}\mathbf{r}_1\, \mathrm{d}\mathbf{r}_2\, \chi_\mu(\mathbf{r}_1) \chi_\nu(\mathbf{r}_1) \frac{\mathrm{erfc}(\omega r_{12})}{r_{12}} \chi_\alpha(\mathbf{r}_2) \tag{11}$$

$$V_{\alpha\gamma} = \iint_{\mathbb{R}^3} \mathrm{d}\mathbf{r}_1\, \mathrm{d}\mathbf{r}_2\, \chi_\alpha(\mathbf{r}_1) \frac{\mathrm{erfc}(\omega r_{12})}{r_{12}} \chi_\gamma(\mathbf{r}_2) \tag{12}$$

and $[\mathbf{J}]_{\gamma\delta}$ is the usual two-center Coulomb integral of the auxiliary functions. In the limits of $\lim_{\omega \to 0}$ and $\lim_{\omega \to \infty}$, the attenuated Coulomb operator reduces to the Coulomb metric $1/r_{12}$ or the overlap metric $\delta(r_{12})$, respectively. Tuning the attenuation parameter ω thus provides a way to interpolate between the more accurate Coulomb metric and the overlap metric, which provides greater sparsity in the corresponding

https://dx.doi.org/10.1021/acs.jctc.0c00934
J. Chem. Theory Comput. 2021, 17, 211−221

integrals. An attenuation strength of $\omega = 0.1$ was shown to yield acceptable accuracy while providing sparsity comparable to the overlap metric.[56] Due to the locality of the erfc-attenuated three-center integrals, their computation can be reduced to linear scaling by applying screening based on the recently developed rigorous integral partition bounds (IPB).[76] For the THC fitting in the Cholesky-MO basis, the three-center AO integrals have first to be transformed to the OV subspace according to

$$(ia\,\vdots\,\alpha) = \sum_{\mu\nu} L_{\mu i} L_{\nu a} (\mu\nu\,\vdots\,\alpha) \tag{13}$$

where $L_{\mu i}$ and $L_{\nu a}$ are again the local Cholesky factors obtained from the occupied density matrix $\mathbf{P}$ and the virtual density matrix $\mathbf{Q}$, respectively. The contraction is carried out stepwise and to reduce the computational complexity of these two steps we make use of the natural blocking matrix format initially proposed by Jung *et al.*,[77] as recently reported in our work on reduced-scaling ω-RI-CDD-MP2.[80] In short, third-order tensors are usually internally stored as arrays of matrices, so-called tensor slices, which can in turn be stored in any sparse matrix format. Within the natural blocking approach,[77] entire rows and columns of these slices are removed if all their values fall below a certain threshold, the so-called natural blocking threshold ε_{NB}. For the natural blocking format to be efficient, only a constant number of rows and columns of a given slice should be significant. The latter is given using an attenuated Coulomb operator causing coupling over only short distances between the bra and ket and by transformation into the localized Cholesky-MO basis, which reintroduces coupling between the bra indices. To keep track of the significant rows and columns, natural blocking relies on bookkeeping in terms of significance lists. Adopting the notation introduced in our work on ω-RI-CDD-MP2,[80] an example would be the list $\{\mu\}_\alpha$, which is defined as

$$\{\mu\}_\alpha \equiv \{\mu | \max_\nu |(\mu\nu\,\vdots\,\alpha)| > \varepsilon_{\text{NB}}\} \tag{14}$$

and stores all significant AO indices μ for a given auxiliary function α. A second type of lists, which goes beyond the original natural blocking approach introduced by Jung *et al.*,[77] is based on integral screening prior to the AO-to-MO transformation.[80] For this, two matrices $\mathbf{M}$ and $\mathbf{N}$, defined as

$$M_{\mu\nu} = \max_\alpha |(\mu\nu\,\vdots\,\alpha)| \tag{15}$$

$$N_{\nu\alpha} = \max_\mu |(\mu\nu\,\vdots\,\alpha)| \tag{16}$$

are constructed in the three-center integral kernel. With these screening matrices, upper bounds for the transformed integrals can be constructed. A detailed algorithm for the transformation of the three-center integrals to the Cholesky-MO basis is provided in the Supporting Information. Here, we rather focus on the construction of intermediate $\mathbf{Y}$, defined as

$$Y_\alpha^{P'} = \sum_{ia} X_i^{P'} X_a^{P'} (ia\,\vdots\,\alpha) \tag{17}$$

obtained by inserting the ω-RI ansatz from eq 10 into the definition of the $\mathbf{E}$ tensor from eq 5. One advantage of performing the THC fitting in the Cholesky-MO space is that the prefactor of the contraction above will be reduced compared to a formulation in AOs as one occupied index is present. The projection of the RI integrals onto the THC grids then follows the same general procedure as their transformation into Cholesky-MO space. The significance list $[P]_i$, meaning the grid points significant for a given occupied orbital can readily be obtained from the Cholesky-MO-transformed collocation matrix according to

$$[P]_i \equiv \{P | |X_i^P| > \varepsilon_{\text{NB}}\} \tag{18}$$

Due to the local nature of the Cholesky-MOs, for systems with significant bandgaps, the number of significant grid points can be expected to be small and constant for large enough molecules. Using the lists $\{a\}_i$ and $\{\alpha\}_i$, obtained during the integral transformation analogously to eq 14 and the upper bound list $[P]_i$, all tensors from eq 17 will have reduced sizes. Due to the coupling between all integral indices and the locality of the grid-projected Cholesky-MOs, the algorithm shown below for the evaluation of $Y_\alpha^{P'}$ can be expected to be asymptotically linear scaling.

Algorithm 1 ω-RI algorithm for $Y_\alpha^{P'}$

```
procedure BUILD_Y
    $\mathbf{Y} \leftarrow \mathbf{0}_{N_{\text{grid}},N_{\text{aux}}}$
    for all $i$ do
        for all $\alpha \in \{\alpha\}_i$ and $P' \in [P]_i$ do
            $(iP'\,\vdots\,\alpha) \leftarrow \sum_{a\in\{a\}_i} X_a^{P'} (ia\,\vdots\,\alpha)$
            $Y_\alpha^{P'} \mathrel{+}= X_i^{P'} (iP'\,\vdots\,\alpha)$
        end for
    end for
    return $\mathbf{Y}$
end procedure
```

Here we note, that the grid-projected integral tensor $\mathbf{E}$ can be obtained from $\mathbf{Y}$ according to

$$E^{P'Q'} = \sum_{\alpha\beta} Y_\alpha^{P'} \tilde{C}_{\alpha\beta} Y_\beta^{Q'} \tag{19}$$

where $\tilde{C}_{\alpha\beta}$ is the contraction of all two-center RI integrals in eq 10. However, retaining this factorization allows for a more efficient reformulation of obtaining the $\mathbf{Z}$ tensor, as will be discussed below.

2.4. Removing the Pseudoinversion Bottleneck.

Despite the formal quartic scaling computation of the $\mathbf{E}$ tensor, Martínez and co-workers[27,62,63] reported the inversion of the grid metric $\mathbf{S}$ to be the bottleneck of the THC procedure. Since the metric tensor is generally ill-conditioned and singular, pseudoinversion with a cutoff ε_{SVD} between 10^{-10} to 10^{-12} is applied to remove the near-linear dependencies.[27,66] Due to the large prefactor of the underlying singular value decomposition (SVD), forming the inverse $\mathbf{S}^{-1}$ is usually the most time-consuming step. Using a local ansatz of the THC factorization[63] based on partitioning of the molecular system was presented as one way of avoiding this.

Here, we present an alternative for which we make use of our factorization of the $\mathbf{E}$ tensor and rewrite eq 3:

$$Z^{PQ} = \sum_{P'Q'} \sum_{\alpha\beta} [\mathbf{S}^{-1}]^{PP'} Y_\alpha^{P'} \tilde{C}_{\alpha\beta} Y_\beta^{Q'} [\mathbf{S}^{-1}]^{QQ'} \tag{20}$$

Taking only the tensors for the P' grid index of eq 20, we define a new intermediate $\mathbf{\Lambda}$, given by

$$\Lambda_\alpha^P \equiv \sum_{P'} [\mathbf{S}^{-1}]^{PP'} Y_\alpha^{P'} \Leftrightarrow Y_\alpha^{P'} = \sum_P S^{PP'} \Lambda_\alpha^P \tag{21}$$

As becomes evident from the right side of eq 21, instead of solving for $\mathbf{\Lambda}$ by inversion of the metric, the equation can also be treated as a system of linear equations with multiple right-hand sides, i.e., $\mathbf{B} = \mathbf{AX}$. Standard procedures to solving linear systems can then be applied, which typically involve a factorization of the coefficient matrix, here $\mathbf{S}$, followed by forward and backward substitution. Since the grid metric is generally singular and thus not symmetric positive definite, Cholesky decomposition cannot be applied for the factorization. However, other matrix decompositions like the modified blocked LDL factorization with diagonal pivoting or LU decomposition with partial pivoting are applicable. Inserting, for example, the pivoted LU decomposition $\mathbf{S} = \mathbf{\Pi LU}$ into eq 21 gives the following triangular systems of linear equations

$$\mathbf{\Pi}^{\mathrm{T}}\mathbf{Y} = \mathbf{LW} \triangleright \text{ solve for } \mathbf{W} \tag{22}$$

$$\mathbf{W} = \mathbf{U\Lambda} \triangleright \text{ solve for } \mathbf{\Lambda} \tag{23}$$

which can be solved efficiently by forward and backward substitution, respectively. We note that this procedure was recently also suggested by Matthews,[69] although in a slightly different context, i.e., for the automatic grid generation in LS-THC using a pivoted Cholesky decomposition of the grid metric constructed from a larger parent grid.

The asymptotic scaling of finding the grid metric inverse remains $O(N^3)$, albeit with a significantly lower prefactor, which makes this step irrelevant for the overall scaling for all but the largest molecules. It should be emphasized that applying linear solvers instead of pseudoinversion removes the bias of choosing a cutoff parameter $\varepsilon_{\mathrm{SVD}}$ while also providing numerical stability comparable to pseudoinversion. For large enough molecules with a significant HOMO−LUMO gap, the metric $\mathbf{S}$ will become sparse and diagonally dominant with appropriate reordering, which allows for the use of specialized algorithms for banded matrices. The latter allows us to reduce the scaling of this step to quadratic, as will be discussed in Section 3.

Having computed one side of the projected potential operator $\mathbf{\Lambda}$, the familiar $\mathbf{Z}$ tensor is obtained by contraction with its transpose and the two-center RI integrals $\tilde{\mathbf{C}}$ according to

$$Z^{PQ} = \sum_{\alpha\beta} \Lambda_\alpha^P \tilde{C}_{\alpha\beta} \Lambda_\beta^Q \tag{24}$$

After the construction of the $\mathbf{X}$ and $\mathbf{Z}$ tensors, they can be used to approximate ERIs in various correlation methods.

2.5. Evaluation of the THC-CDD-MP2 Energy. The THC-CDD-MP2 equations[26] are based on the AO formulation of the MP2 energy, as originally proposed by Almlöf and Häser,[6,40,41] which makes use of the Laplace transformation for the energy denominator

$$E_{\mathrm{MP2}}^{\mathrm{AO}} = -\sum_\kappa \sum_{\mu\nu\lambda\sigma} \sum_{\mu'\nu'\lambda'\sigma'} \underline{P}_{\mu\mu'} \overline{P}_{\nu\nu'} \underline{P}_{\lambda\lambda'} \overline{P}_{\sigma\sigma'} (\mu\nu|\lambda\sigma) \cdot [2(\mu'\nu'|\lambda'\sigma') - (\mu'\sigma'|\lambda'\nu')] \tag{25}$$

where $\underline{\mathbf{P}}$ and $\overline{\mathbf{P}}$ are the occupied and virtual pseudo-density matrices, respectively. It should be noted that the Laplace transformation is especially important for the THC format as it allows to unpin all four orbital indices and thus to make full use of the THC factorization. The pseudo-densities, defined as

$$\underline{P}_{\mu\mu'} = (\omega^{(\kappa)})^{1/4} \sum_i C_{\mu i}\, \mathrm{e}^{\varepsilon_i t^{(\kappa)}} C_{\mu' i} \tag{26}$$

$$\overline{P}_{\nu\nu'} = (\omega^{(\kappa)})^{1/4} \sum_a C_{\nu a}\, \mathrm{e}^{-\varepsilon_a t^{(\kappa)}} C_{\nu' a} \tag{27}$$

are contractions of the MO coefficients and the orbital energies at a given Laplace point κ. Inserting the THC factorization of the ERIs into eq 25 and Cholesky decomposing the pseudo-densities, as is done in CDD-MP2,[42] i.e.,

$$\underline{P}_{\mu\mu'} = \sum_i \underline{L}_{\mu i} \underline{L}_{\mu' i} \tag{28}$$

$$\overline{P}_{\nu\nu'} = \sum_a \overline{L}_{\nu a} \overline{L}_{\nu' a} \tag{29}$$

the THC-CDD-MP2 energy equation is obtained

$$E_{\mathrm{MP2}}^{\mathrm{THC\text{-}CDD}} = -\sum_\kappa \sum_{PQRS} \sum_{ijab} \underline{X}_i^P \overline{X}_a^P Z^{PQ} \underline{X}_j^Q \overline{X}_b^Q \cdot [2\underline{X}_i^R \overline{X}_a^R Z^{RS} \underline{X}_j^S \overline{X}_b^S - \underline{X}_i^R \overline{X}_b^R Z^{RS} \underline{X}_j^S \overline{X}_a^S] \tag{30}$$

Since the Cholesky pseudo-MOs span the same space as the canonical and the Cholesky-MOs, the THC fitting can be performed once in the Cholesky-MO basis and does not have to be repeated for every Laplace point. $\underline{\mathbf{X}}$ and $\overline{\mathbf{X}}$ are the collocation matrices transformed into the Cholesky pseudo-MO basis given by

$$\underline{X}_i^P = \sum_\mu \underline{L}_{\mu i} X_\mu^P \tag{31}$$

$$\overline{X}_a^P = \sum_\nu \overline{L}_{\nu a} X_\nu^P \tag{32}$$

The benefit of evaluating the THC-MP2 energy in the Cholesky pseudo-MO basis is that the collocation matrices are expected to be sparse and contractions involving them can efficiently be done using sparse linear algebra. Since the $\mathbf{Z}$ tensor is the grid representation of the long-ranged $1/r_{12}$ operator, it is generally not sparse. For this reason, the Coulomb- and exchange-like parts of the MP2 energy are evaluated by first contracting all possible collocation matrices, only including the $\mathbf{Z}$ tensors in the last step, to carry the sparsity in $\mathbf{X}$ through most of the computation. By doing this, we obtain an algorithm with reduced scaling compared to the formal quartic scaling of this step. Detailed algorithms for the evaluation of the Coulomb- and exchange-like contributions to the MP2 energy are provided in the Supporting Information. It should also be noted that the computation times of the evaluation of the Coulomb-like energy are nearly independent of the choice of MOs because the time-determining step involves the contraction of the THC $\mathbf{Z}$ matrix with an intermediate that is invariant under orbital rotation. A more detailed discussion of this matter is included as a separate section in the Supporting Information. For our timings in Section 3, we make use of the SOS approximation[78] of the MP2 energy, considering only the Coulomb-like term

$$E_{\mathrm{SOS\text{-}MP2}}^{\mathrm{THC\text{-}CDD}} = -c_{\mathrm{OS}} \sum_\kappa \sum_{PQRS} \sum_{ijab} \underline{X}_i^P \overline{X}_a^P Z^{PQ} \underline{X}_j^Q \overline{X}_b^Q \cdot \underline{X}_i^R \overline{X}_a^R Z^{RS} \underline{X}_j^S \overline{X}_b^S \tag{33}$$

where c_{OS} is the opposite-spin scaling factor, for which we use 1.3 as reported by Jung *et al.*[78] The SOS approximation reduces the formal scaling of the energy evaluation to cubic once the **X** and **Z** tensors are obtained. The actual scaling will, however, have a reduced scaling exponent due to the aforementioned use of sparse linear algebra, see Section 3.2. For a formal comparison of THC-RI-SOS-MP2 against different SOS-MP2 methods, see the corresponding section in the Supporting Information.

3. RESULTS AND DISCUSSION

We implemented the above-described THC algorithm together with the THC-RI-CDD-MP2 method within our quantum chemistry package FermiONs++.[81−83] The cc-pVDZ and cc-pVTZ basis sets[84] are used in combination with the corresponding auxiliary basis sets for all RI calculations and the corresponding optimized THC grids.[67] For the phosphorus atoms occurring in the calculations on DNA, the fluorine grids were used. We demonstrate in the Supporting Information that this does not lead to an additional error by benchmarking against a small set of selected phosphorus species. DIIS acceleration[85] is used for the preceding SCF calculations, for which the SCF energy is converged to 10^{-12} and the commutator $\mathbf{FPS} - \mathbf{SPF}$ to 5×10^{-9} for the S22 test set[86] and the L7 test set,[87] together with 10 Laplace points for the integration of the orbital energy denominator. For the assessment of the scaling, the thresholds 10^{-7} and 10^{-6} were used, respectively, in combination with seven Laplace points, which is expected to provide sufficient accuracy in the submilli-Hartree regime. Fermi shifting is applied to the formation of the pseudo-density matrices as proposed by Ayala and Scuseria.[7] For the evaluation of the energy equations, we employ a block-sparse matrix format with a block threshold of 10^{-7} for the Frobenius norm of a block. All timings are done on an Intel Xeon E5-2667 v4 (3.20 GHz) CPU node with 256 GB RAM and three 960 GB SSD drives.

3.1. Accuracy of the THC-ω-RI-CDD-SOS-MP2 Method.

We begin with the analysis of the accuracy of the linear solver algorithm for the solution of eq 21 compared to the pseudoinversion ($\varepsilon_{\mathrm{SVD}} = 10^{-12}$) suggested by Martínez and co-workers.[27,61−63] For this, benchmark calculations on the S22 test set were performed with our implementation of the THC-RI-CDD-SOS-MP2 method using the cc-pVDZ and cc-pVTZ basis sets. The modified Cholesky decomposition (LDL) was chosen as the linear solver routine, but we found that the solution based on LU decomposition provides virtually identical results. Table 1 summarizes the deviations of the absolute energies for the S22 monomers and dimers as well as the deviations of the relative energies for the complexes.

Table 1. Deviation of the Linear Solver Algorithm Compared to Pseudoinversion for the S22 Test Set

	ΔE_{abs}[a]		ΔE_{rel}[b]	
S22	MAD	MAX	MAD	MAX
cc-pVDZ	0.4	3.8	<0.001	0.002
cc-pVTZ	2.0	7.8	0.003	0.011

[a] Deviations in μH. [b] Deviations in kcal/mol.

It can be seen that the mean absolute deviations (MAD) of the absolute energies and the maximum error (MAX) are on the order of 10^{-6} H. As a consequence, the relative energies are also accurately reproduced. It should be emphasized that these deviations are not with respect to a reference method, like, e.g., RI-SOS-MP2, but to the pseudoinversion variant of THC, meaning that the errors are more likely due to cutoff errors based on the SVD threshold. The latter will be illustrated by comparing the results against RI-SOS-MP2 in the following.

After having established that implicitly forming the inverse of the grid metric matrix can be accurately done by the linear solution of eq 21, we now assess the accuracy of our THC-RI-CDD-SOS-MP2 method against the reference RI-SOS-MP2 method. For this, we compare two different variants of the THC algorithm against the reference with the cc-pVDZ and cc-pVTZ basis sets. The first variant uses the regular Coulomb metric and a tight natural blocking threshold of 10^{-10}, henceforth termed THC-RI-CDD-SOS-MP2 and the second variant uses the attenuated Coulomb metric from eq 10 with an attenuation strength ω of 0.1 and a looser natural blocking threshold of 10^{-6}, from here on referred to as THC-ω-RI-CDD-SOS-MP2. In Table 2, the absolute and relative errors are compared to the reference RI-SOS-MP2 method for the S22 and the larger L7 test sets.

Table 2. Error of THC-RI-CDD-SOS-MP2 and THC-ω-RI-CDD-SOS-MP2 Compared to Canonical RI-SOS-MP2 for the S22 and L7 Test Set Using the cc-pVXZ/cc-pVXZ-RI ($X \in \{D,T\}$) Basis Sets

			ΔE_{abs}[a]		ΔE_{rel}[b]	
test set	basis	THC variant	MAD	MAX	MAD	MAX
S22	cc-pVDZ	RI	8.8	38.9	0.003	0.013
		ω-RI	13.9	57.9	0.008	0.030
	cc-pVTZ	RI	2.0	14.0	0.001	0.010
		ω-RI	7.8	26.0	0.005	0.015
L7	cc-pVDZ	RI	72.8	284.8	0.027	0.067
		ω-RI	50.3	183.3	0.045	0.129
	cc-pVTZ	RI	50.6	187.3	0.010	0.030
		ω-RI	45.4	137.0	0.022	0.049

[a] Deviations in μH. [b] Deviations in kcal/mol.

Table 2 shows that for the S22 test set both THC variants provide good accuracies for the absolute energies with a MAD on the order of 10^{-6} H, which shows that the THC factorization only introduces an insignificant error compared to the well-established RI error.[27] Furthermore, the use of an attenuated Coulomb metric does not worsen the mean error significantly. The maximum errors are larger but still on the order of 10^{-5} H and in all cases correspond to aromatic molecules, like the nucleobases uracil or thymine, in the test set. The latter can be attributed to the fact that delocalized electronic structures are more difficult to fit with small grids in the LS-THC procedure, which has previously been reported by Parrish *et al.*[27] for acenes. Since the mean errors for the absolute energies are small, the relative energies are also accurately reproduced. For the L7 test set, comprised of larger molecules, the errors are worse compared to the results for the S22 test set and are roughly an order of magnitude larger. This is somewhat expected since the L7 test set represents a collection of worst case molecules, in a sense that all complexes involve large, strongly delocalized electronic structures. Remarkably, for this case, the errors for the cc-pVTZ basis set are smaller than for the cc-pVDZ basis set. This can be rationalized by the fact that for the triple-ζ basis set larger integration grids are used, which allow for better fitting of the delocalized orbitals. Furthermore, for the absolute energies, the errors decrease when using the attenuated Coulomb metric and integral screening, most likely due to favorable error cancellation. For the interaction energies, the same trend of

https://dx.doi.org/10.1021/acs.jctc.0c00934
J. Chem. Theory Comput. 2021, 17, 211−221

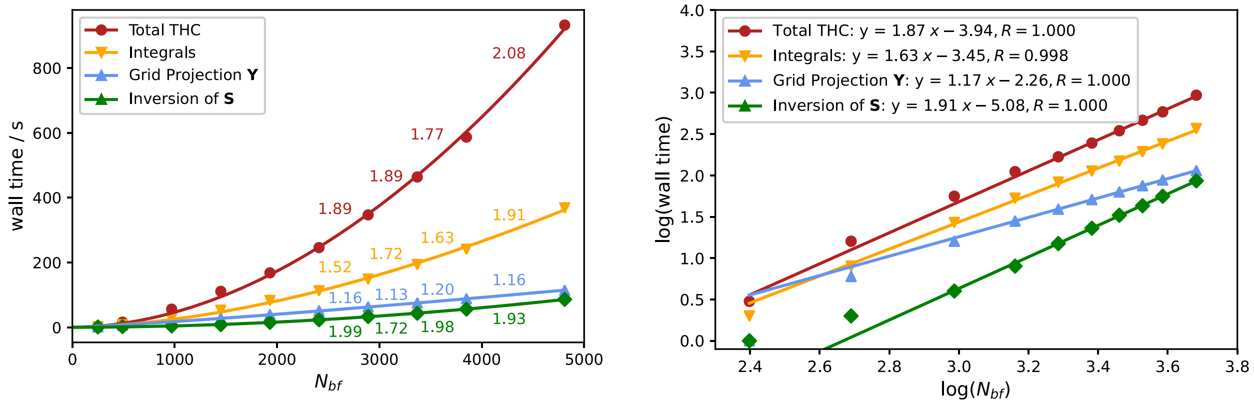

Figure 1. Total execution time of the THC algorithm (red) and individual contributions from the most expensive constituting steps, i.e., the formation of the RI integrals (orange), the construction of intermediate **Y** (blue), and the inversion of the grid metric **S** (green) for linear alkanes C_nH_{2n+2} using the cc-pVDZ basis set (left) and the corresponding double logarithmic plot (right). The colored numbers correspond to the scaling exponent with respect to the preceding fragment, and the scaling for the largest molecules was determined by linear regression starting from $C_{60}H_{122}$ ($N_{bf} = 1450$) up to $C_{200}H_{402}$ ($N_{bf} = 4810$).

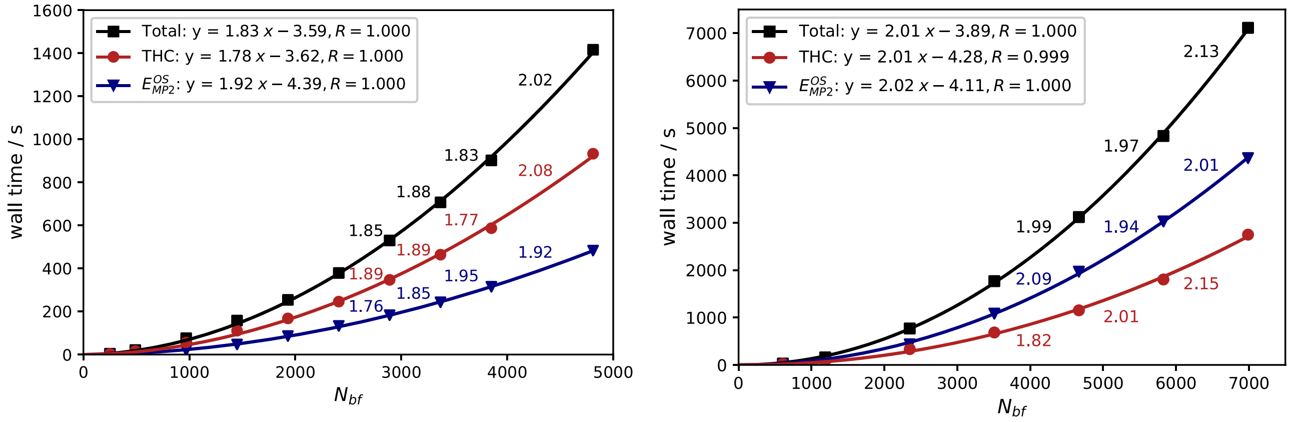

(a) cc-pVDZ (b) cc-pVTZ

Figure 2. Plots of the total execution times for the THC-ω-RI-CDD-SOS-MP2 method (black) for linear alkanes C_nH_{2n+2} as well as the individual contributions from the THC fitting (red) and the computation of the MP2 energy (blue) for the cc-pVDZ (left) and cc-pVTZ basis sets (right). The scaling exponent for the longest chains, starting from $C_{60}H_{122}$, was determined by linear regression in the double logarithmic plot, and the colored numbers correspond to the scaling with respect to the preceding fragment.

increasing errors as compared to the S22 test set is observed. Nonetheless, the deviations are significantly lower than 1 kcal/mol, which can be considered to be chemical accuracy. To conclude, the THC-ω-RI-CDD-SOS-MP2 method introduces no significant errors compared to the THC-RI-CDD-SOS-MP2 implementation and provides good accuracy for the variety of compounds present in the test sets under investigation. We also note that our THC algorithm is not only able to accurately reproduce final MP2 energies but also provides good accuracy for important intermediate quantities such as MP2 amplitudes, which is demonstrated in the Supporting Information.

3.2. Performance Analysis. In the following, the performance of the here developed THC-ω-RI-CDD-SOS-MP2 method is assessed in terms of computational complexity and asymptotic scaling behavior. First, we focus on the THC routine itself, i.e., without the computation of the MP2 energy to investigate the most expensive steps of forming the THC factorized integrals. For this, we consider the construction of the RI integrals in the Cholesky-MO basis, the formation of the grid-projected RI integrals **Y** (eq 17), which is the formally highest scaling step and the inversion—or rather the linear solution to find the implicit inverse—of the grid metric **S** (eq 21). In Figure 1, this analysis is exemplarily carried out for linear alkanes up to $C_{200}H_{402}$ using the cc-pVDZ basis set. On the left, the computation times of the total THC procedure (red) and the individual steps are plotted against the number of basis functions.

It can be seen that the construction and contraction of the RI integrals dominate the scaling behavior. Initially, subquadratic scaling is observed for the RI integrals, which increases with bigger molecule sizes. This is caused by the fact that, for the largest chains, the inversion of the two-center integrals in eq 10 becomes computationally significant and starts to dominate the overall scaling of the construction of the RI integrals. We note that, for chemically relevant molecules, with a less sparse structure, this crossover is expected to be for larger molecule sizes. As the inversion is asymptotically cubic scaling, this worsens the overall scaling of this step, while the formation of the three-center integrals becomes close to linear scaling with the screening outlined in Section 2.3. As the same screening in combination with the natural blocking approach for the tensor contractions is applied to the construction of the **Y** tensor, this step also becomes close to linear scaling. For the linear solution of eq 21, a specialized band matrix version of the LU decomposition (LAPACK: xgbsv) was used. For this, reverse Cuthill−McKee[88] reordering of the atoms is performed in order to minimize the bandwidth of the resulting grid-projected overlap matrix. The bandwidth can then be determined numerically by the algorithm presented in the Supporting Information and converted to the LAPACK band storage format. We found that, after a certain chain length, here $C_{40}H_{82}$, the bandwidth is constant and the number of elements in **S** only increases linearly, which results in an overall quadratic scaling of this step. Even if no specialized linear solvers are applied, the prefactor of this step is small, such that it only makes up a small fraction of the total computation time. In total, using an attenuated Coulomb metric in the RI integrals and natural blocking for the corresponding contractions in combination with a localized Cholesky basis and specialized algorithms for the inversion of **S**, the overall scaling of obtaining the THC factorization becomes quadratic. It should, however, be noted that, for even larger molecule sizes, the scaling will eventually be dominated by asymptotically cubic scaling steps, such as the inversion of the two-center integrals or the formation of **Z** (eq 24), which involves only dense matrices.

Next, we focus the discussion on the overall scaling of the evaluation of the SOS-MP2 energy equation with the THC algorithm presented above. We first again consider linear alkanes as a model system to determine the asymptotic scaling behavior. Figure 2 shows the corresponding plots of the computation times against the number of basis functions for the cc-pVDZ (left) and cc-pVTZ basis sets (right). For this, the total wall times for the evaluation of the THC-ω-RI-CDD-SOS-MP2 equations are shown (black) as well as the contributions from obtaining the THC factorization (red) and the calculation of the SOS-MP2 energy (blue).

For both basis sets, roughly quadratic scaling is observed for the THC-ω-RI-CDD-SOS-MP2 method. Through the use of sparse matrix algebra, the evaluation of the SOS-MP2 energy can efficiently be performed since all quantities are sparse—except for the **Z** tensor—due to the transformation into the Cholesky pseudo-MO basis. It can be seen that for the smaller double-ζ basis set, obtaining the THC factorization is the rate-determining step and the energy evaluation only makes up 1/3 of the total computation time. This highlights an advantage of using a global THC formulation as, for the local-THC approximation, the evaluation of the SOS-MP2 energy seems to be dominating.[63] The latter is especially problematic when using more expensive correlation methods than MP2. For the larger triple-ζ basis set, however, the evaluation of the energy equations also becomes rate-determining for our global THC algorithm. Here, larger grids are employed and the basis set includes more diffuse functions, resulting in less sparse intermediates in the energy evaluation. Overall, for linear alkanes, as a sparse model, both the THC factorization and the energy evaluation are quadratic scaling with a low prefactor for the considered molecule sizes.

Even though linear alkanes provide a valuable model for assessing the efficiency of screening algorithms and the scaling of a method, we now focus on a class of molecules that is more representative for practical applications in the form of adenine−thymine base pair stacks $(AT)_n$ ($n \in \{1,2,4,8,12\}$). The same calculations as in Figure 2 with the cc-pVDZ basis set were performed for the DNA fragments, and the results are shown in Figure 3.

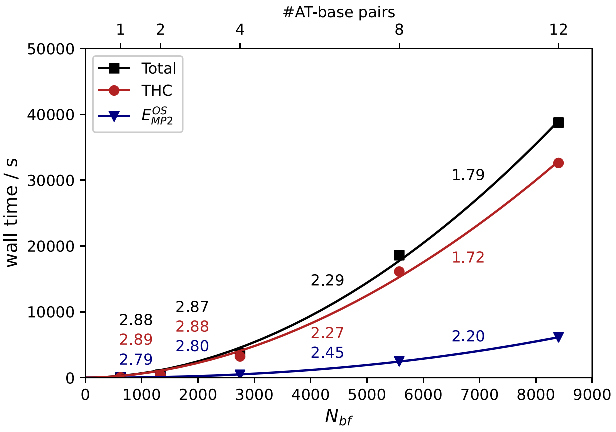

Figure 3. Total execution time of the THC-ω-RI-CDD-SOS-MP2 method (black) for $(AT)_n$ base pair stacks as well as the individual contributions from the THC fitting (red) and the computation of the MP2 energy (blue) for the cc-pVDZ basis set. The colored numbers correspond to the scaling with respect to the preceding fragment.

Here, all observations discussed before for linear alkanes still hold. The evaluation of the SOS-MP2 energy equations approaches quadratic scaling for the largest DNA fragment while obtaining the THC factorization reaches subquadratic scaling. The latter is due to the fact that, for the less sparse DNA systems, as compared to linear alkanes, the cubic scaling steps cease to be significant and the scaling is dominated by the linear scaling integral contractions. Thus, the whole THC-ω-RI-CDD-SOS-MP2 method also becomes subquadratically scaling. The more globular structure of DNA, however, causes a later onset of subquadratic scaling (linear alkanes: $N_{bf} \approx 1000$, DNA: $N_{bf} \approx 6000$) because only for the largest fragments the sparsity in the tensors involved becomes sufficiently large to be exploited by screening and sparse matrix algebra. It can be expected, that for even larger fragments the scaling behavior of the energy evaluation will reduce and approach the scaling observed for linear alkanes. For the largest fragment, i.e., $(AT)_{12}$, detailed wall times for the individual steps of the THC-ω-RI-CDD-SOS-MP2 method are presented in Table 3.

Table 3. Detailed Computation Times for the Individual Steps of the THC-ω-RI-CDD-SOS-MP2 Method for an $(AT)_{12}$ DNA Fragment (cc-pVDZ)

step	wall time (s)	%
integrals (eqs 11−13)	17,768	45.9
X (eqs 6−9)	208	0.5
Y (eq 17)	11,970	30.9
S (eq 4)	410	1.1
$\mathbf{S}^{-1}$ (eq 21)	960	2.5
Z (eq 24)	683	1.8
$E_{SOS\text{-}MP2}$ (eq 33)	6132	15.8
total	38,745	

As can be seen from Table 3, the operations involving the RI integrals, i.e., their construction and transformation into the MO basis as well as the grid projection to obtain intermediate **Y**, make up roughly 75% of the total computation time. However, we were able to show that these steps have been made linear scaling through the use of an attenuated Coulomb metric and the local Cholesky-MO basis in combination with integral screening (see Figure 1), with the exception of the inversion of the two-center integrals. Furthermore, the previously reported bottleneck of the THC procedure, i.e., the inversion of the grid metric **S**, was removed by the use of linear solvers, such that now this step only contributes 2.5% of the total computation time for the largest DNA fragment under consideration. Additionally, here the other cubic scaling steps, i.e., obtaining the **Z** tensor and inverting the two-center integrals, only contribute a small percentage of the total wall time and are not rate-determining. Finally, the evaluation of the SOS-MP2 energy equation only requires roughly 15% of the total wall time.

4. CONCLUSIONS

In the present work, we showed that, through a combination of different reduced-scaling methods, the computational complexity of the LS-THC formalism can significantly be reduced: By combining the locality of Cholesky orbitals with an erfc-attenuated Coulomb metric and appropriate integral screening for the RI integrals, all contractions involving these integrals can be performed in linear time complexity. This especially allowed us to perform the formally highest scaling step, i.e., the projection of the RI integrals onto the THC grids to form intermediate **Y**, in a linear scaling fashion. Additionally, the prefactor of the usually most expensive step, i.e., forming the inverse of the grid metric **S**, can be significantly reduced by reformulation of the underlying equations and application of linear equation solvers. All of this leads to a subquadratically scaling formulation of the LS-THC procedure for chemically relevant molecules. We note that this still involves cubic scaling steps, like the inversion of the two-center integrals or the final contraction to form the **Z** tensor; however, these steps have small enough prefactors to only show up for very large molecule sizes. Applying our THC method to SOS-MP2 leads to an overall subquadratically scaling MP2 method, which we term THC-ω-RI-CDD-SOS-MP2.

■ ASSOCIATED CONTENT

Supporting Information

The Supporting Information is available free of charge at https://pubs.acs.org/doi/10.1021/acs.jctc.0c00934.

> A more detailed description of the algorithm for the transformation of the RI integrals to the Cholesky-MO basis using the natural blocking formalism and the computation of the THC-CDD-MP2 energy; a comparison between using canonical and Cholesky (pseudo)-MOs and a comparison of THC-RI-SOS-MP2 against different SOS-MP2 methods; and details regarding the accuracy of final MP2 energies and MP2 amplitudes (PDF)

■ AUTHOR INFORMATION

Corresponding Author

Christian Ochsenfeld − *Chair of Theoretical Chemistry, Department of Chemistry, University of Munich (LMU), D-81377 Munich, Germany*; orcid.org/0000-0002-4189-6558; Email: christian.ochsenfeld@cup.uni-muenchen.de

Authors

Felix H. Bangerter − *Chair of Theoretical Chemistry, Department of Chemistry, University of Munich (LMU), D-81377 Munich, Germany*

Michael Glasbrenner − *Chair of Theoretical Chemistry, Department of Chemistry, University of Munich (LMU), D-81377 Munich, Germany*

Complete contact information is available at: https://pubs.acs.org/10.1021/acs.jctc.0c00934

Notes

The authors declare no competing financial interest.

■ ACKNOWLEDGMENTS

The authors acknowledge financial support by the "Deutsche Forschungsgemeinschaft" (DFG) via the SFB 1309-32587107 and the cluster of excellence (EXC2111-390814868) "Munich Center for Quantum Science and Technology" (MCQST). F.H.B. thanks the "Fonds der Chemischen Industrie" (FCI) for a graduate fellowship. M.G. thanks the "Studienstiftung des Deutschen Volkes" for a graduate fellowship. C.O. acknowledges additional financial support as a Max-Planck-Fellow at MPI-FKF Stuttgart.

■ REFERENCES

(1) Møller, C.; Plesset, M. S. Note on an approximation treatment for many-electron systems. *Phys. Rev.* **1934**, *46*, 618−622.

(2) Cremer, D. Møller-Plesset perturbation theory: from small molecule methods to methods for thousands of atoms. *WIREs Comput. Mol. Sci.* **2011**, *1*, 509−530.

(3) Grimme, S. Semiempirical hybrid density functional with perturbative second-order correlation. *J. Chem. Phys.* **2006**, *124*, No. 034108.

(4) Schwabe, T.; Grimme, S. Double-hybrid density functionals with long-range dispersion corrections: Higher accuracy and extended applicability. *Phys. Chem. Chem. Phys.* **2007**, *9*, 3397−3406.

(5) Flaig, D.; Maurer, M.; Hanni, M.; Braunger, K.; Kick, L.; Thubauville, M.; Ochsenfeld, C. Benchmarking Hydrogen and Carbon NMR Chemical Shifts at HF, DFT, and MP2 Levels. *J. Chem. Theory Comput.* **2014**, *10*, 572−578.

(6) Häser, M.; Almlöf, J. Laplace transform techniques in Møller-Plesset perturbation theory. *J. Chem. Phys.* **1992**, *96*, 489.

(7) Ayala, P. Y.; Scuseria, G. E. Linear scaling second-order Møller-Plesset theory in the atomic orbital basis for large molecular systems. *J. Chem. Phys.* **1999**, *110*, 3660.

(8) Doser, B.; Lambrecht, D. S.; Kussmann, J.; Ochsenfeld, C. Linear-scaling atomic orbital-based second-order Møller-Plesset perturbation theory by rigorous integral screening criteria. *J. Chem. Phys.* **2009**, *130*, No. 064107.

(9) Sæbø, S.; Pulay, P. Local configuration interaction: An efficient approach for larger molecules. *Chem. Phys. Lett.* **1985**, *113*, 13−18.

(10) Sæbø, S.; Pulay, P. Fourth-order Møller-Plessett perturbation theory in the local correlation treatment. I. Method. *J. Chem. Phys.* **1987**, *86*, 914.

(11) Sæbø, S.; Pulay, P. Local treatment of electron correlation. *Annu. Rev. Phys. Chem.* **1993**, *44*, 213−236.

(12) Hampel, C.; Werner, H. J. Local treatment of electron correlation in coupled cluster theory. *J. Chem. Phys.* **1996**, *104*, 6286.

(13) Schütz, M.; Hetzer, G.; Werner, H. J. Low-order scaling local electron correlation methods. I. Linear scaling local MP2. *J. Chem. Phys.* **1999**, *111*, 5691.

(14) Schütz, M.; Werner, H. J. Low-order scaling local electron correlation methods. IV. Linear scaling local coupled-cluster (LCCSD). *J. Chem. Phys* **2001**, *114*, 661.

(15) Schütz, M. A new, fast, semi-direct implementation of linear scaling local coupled cluster theory. *Phys. Chem. Chem. Phys.* **2002**, *4*, 3941−3947.

(16) Lee, M. S.; Maslen, P. E.; Head-Gordon, M. Closely approximating second-order Møller-Plesset perturbation theory with a local triatomics in molecules model. *J. Chem. Phys.* **2000**, *112*, 3592.

(17) Werner, H. J.; Manby, F. R.; Knowles, P. J. Fast linear scaling second-order Møller-Plesset perturbation theory (MP2) using local and density fitting approximations. *J. Chem. Phys.* **2003**, *118*, 8149.

(18) Maslen, P. E.; Head-Gordon, M. Noniterative local second order Møller-Plesset theory: Convergence with local correlation space. *J. Chem. Phys.* **1998**, *109*, 7093.

(19) Dunlap, B. I.; Connolly, J. W. D.; Sabin, J. R. On some approximations in applications of Xα theory. *J. Chem. Phys.* **1979**, *71*, 3396.

(20) Beebe, N. H. F.; Linderberg, J. Simplifications in the Generation and Transformation of Two-Electron Integrals in Molecular Calculations. *Int. J. Quantum Chem.* **1977**, *12*, 683−705.

(21) Røeggen, I.; Wisløff-Nilssen, E. On the Beebe-Linderberg two-electron integral approximation. *Chem. Phys. Lett.* **1986**, *132*, 154−160.

(22) Weigend, F.; Kattannek, M.; Ahlrichs, R. Approximated electron repulsion integrals: Cholesky decomposition versus resolution of the identity methods. *J. Chem. Phys.* **2009**, *130*, 164106.

(23) Ringnalda, M. N.; Belhadj, M.; Friesner, R. A. Pseudospectral Hartree-Fock theory: Applications and algorithmic improvements. *J. Chem. Phys.* **1990**, *93*, 3397−3407.

(24) Martínez, T. J.; Mehta, A.; Carter, E. A. Pseudospectral full configuration interaction. *J. Chem. Phys.* **1992**, *97*, 1876.

(25) Murphy, R. B.; Beachy, M. D.; Friesner, R. A.; Ringnalda, M. N. Pseudospectral localized Møller-Plesset methods: Theory and calculation of conformational energies. *J. Chem. Phys.* **1995**, *103*, 1481−1490.

(26) Hohenstein, E. G.; Parrish, R. M.; Martínez, T. J. Tensor hypercontraction density fitting I. Quartic scaling second- and third-order Møller-Plesset perturbation theory. *J. Chem. Phys.* **2012**, *137*, No. 044103.

(27) Parrish, R. M.; Hohenstein, E. G.; Martínez, T. J.; Sherrill, C. D. Tensor hypercontraction II. Least-squares renormalization. *J. Chem. Phys.* **2012**, *137*, 224106.

(28) Foster, J. M.; Boys, S. F. Canonical Configurational Interaction Procedure. *Rev. Mod. Phys.* **1960**, *32*, 300−302.

(29) Pipek, J.; Mezey, P. G. A fast intrinsic localization procedure applicable for ab initio and semiempirical linear combination of atomic orbital wave functions. *J. Chem. Phys.* **1989**, *90*, 4916.

(30) Riplinger, C.; Pinski, P.; Becker, U.; Valeev, E. F.; Neese, F. Sparse maps - A systematic infrastructure for reduced-scaling electronic structure methods. II. Linear scaling domain based pair natural orbital coupled cluster theory. *J. Chem. Phys.* **2016**, *144*, No. 024109.

(31) Neese, F.; Wennmohs, F.; Hansen, A. Efficient and accurate local approximations to coupled-electron pair approaches: An attempt to revive the pair natural orbital method. *J. Chem. Phys.* **2009**, *130*, 114108.

(32) Werner, H. J.; Knizia, G.; Krause, C.; Schwilk, M.; Dornbach, M. Scalable electron correlation methods I.: PNO-LMP2 with linear scaling in the molecular size and near-inverse-linear scaling in the number of processors. *J. Chem. Theory Comput.* **2015**, *11*, 484−507.

(33) Pinski, P.; Riplinger, C.; Valeev, E. F.; Neese, F. Sparse maps - A systematic infrastructure for reduced-scaling electronic structure methods. I. An efficient and simple linear scaling local MP2 method that uses an intermediate basis of pair natural orbitals. *J. Chem. Phys.* **2015**, *143*, No. 034108.

(34) Høyvik, I. M.; Kristensen, K.; Jansik, B.; Jørgensen, P. The divide-expand-consolidate family of coupled cluster methods: Numerical illustrations using second order Møller-Plesset perturbation theory. *J. Chem. Phys.* **2012**, *136*, No. 014105.

(35) Baudin, P.; Ettenhuber, P.; Reine, S.; Kristensen, K.; Kjærgaard, T. Efficient linear-scaling second-order Møller-Plesset perturbation theory: The divide-expand-consolidate RI-MP2 model. *J. Chem. Phys.* **2016**, *144*, No. 054102.

(36) Ettenhuber, P.; Baudin, P.; Kjærgaard, T.; Jørgensen, P.; Kristensen, K. Orbital spaces in the divide-expand-consolidate coupled cluster method. *J. Chem. Phys.* **2016**, *144*, 164116.

(37) Kristensen, K.; Kjærgaard, T.; Høyvik, I. M.; Ettenhuber, P.; Jørgensen, P.; Jansik, B.; Reine, S.; Jakowski, J. The divide-expand-consolidate MP2 scheme goes massively parallel. *Mol. Phys.* **2013**, *111*, 1196−1210.

(38) Russ, N. J.; Crawford, T. D. Potential energy surface discontinuities in local correlation methods. *J. Chem. Phys.* **2004**, *121*, 691.

(39) Mata, R. A.; Werner, H. J. Calculation of smooth potential energy surfaces using local electron correlation methods. *J. Chem. Phys.* **2006**, *125*, 184110.

(40) Almlöf, J. Elimination of energy denominators in Møller-Plesset perturbation theory by a Laplace transform approach. *Chem. Phys. Lett.* **1991**, *181*, 319.

(41) Häser, M. Møller-Plesset (MP2) perturbation theory for large molecules. *Theor. Chim. Acta* **1993**, *87*, 147−173.

(42) Maurer, S. A.; Clin, L.; Ochsenfeld, C. Cholesky-decomposed density MP2 with density fitting: Accurate MP2 and double-hybrid DFT energies for large systems. *J. Chem. Phys.* **2014**, *140*, 224112.

(43) Whitten, J. L. Coulombic potential energy integrals and approximations. *J. Chem. Phys.* **1973**, *58*, 4496.

(44) Vahtras, O.; Almlöf, J.; Feyereisen, M. W. Integral approximations for LCAO-SCF calculations. *Chem. Phys. Lett.* **1993**, *213*, 514−518.

(45) Weigend, F.; Häser, M.; Patzelt, H.; Ahlrichs, R. RI-MP2: Optimized auxiliary basis sets and demonstration of efficiency. *Chem. Phys. Lett.* **1998**, *294*, 143−152.

(46) Røeggen, I.; Johansen, T. Cholesky decomposition of the two-electron integral matrix in electronic structure calculations. *J. Chem. Phys.* **2008**, *128*, 194107.

(47) Boström, J.; Aquilante, F.; Pedersen, T. B.; Lindh, R. Ab initio density fitting: Accuracy assessment of auxiliary basis sets from cholesky decompositions. *J. Chem. Theory Comput.* **2009**, *5*, 1545−1553.

(48) Aquilante, F.; Gagliardi, L.; Pedersen, T. B.; Lindh, R. Atomic Cholesky decompositions: A route to unbiased auxiliary basis sets for density fitting approximation with tunable accuracy and efficiency. *J. Chem. Phys.* **2009**, *130*, 154107.

(49) Aquilante, F.; Delcey, M. G.; Pedersen, T. B.; Galván, I. F.; Lindh, R. Inner projection techniques for the low-cost handling of two-electron integrals in quantumchemistry. *Mol. Phys.* **2017**, *115*, 2052−2064.

(50) Folkestad, S. D.; Kjønstad, E. F.; Koch, H. An efficient algorithm for Cholesky decomposition of electron repulsion integrals. *J. Chem. Phys.* **2019**, *150*, 194112.

(51) Feyereisen, M.; Fitzgerald, G.; Komornicki, A. Use of approximate integrals in ab initio theory. An application in MP2 energy calculations. *Chem. Phys. Lett.* **1993**, *208*, 359−363.

(52) Bernholdt, D. E.; Harrison, R. J. Largescale correlated electronic structure calculations: The RI-MP2 method on parallel computers. *Chem. Phys. Lett.* **1996**, *250*, 477−484.

(53) Weigend, F.; Häser, M. RI-MP2: First derivatives and global consistency. *Theor. Chem. Acc.* **1997**, *97*, 331−340.

(54) Černý, J.; Jurečka, P.; Hobza, P.; Valdés, H. Resolution of identity density functional theory augmented with an empirical dispersion term (RI-DFT-D): A promising tool for studying isolated small peptides. *J. Phys. Chem. A* **2007**, *111*, 1146−1154.

(55) Grimme, S.; Neese, F. Double-hybrid density functional theory for excited electronic states of molecules. *J. Chem. Phys.* **2007**, *127*, 154116.

(56) Luenser, A.; Schurkus, H. F.; Ochsenfeld, C. Vanishing-Overhead Linear-Scaling Random Phase Approximation by Cholesky Decomposition and an Attenuated Coulomb-Metric. *J. Chem. Theory Comput.* **2017**, *13*, 1647−1655.

(57) Graf, D.; Beuerle, M.; Ochsenfeld, C. Low-Scaling Self-Consistent Minimization of a Density Matrix Based Random Phase Approximation Method in the Atomic Orbital Space. *J. Chem. Theory Comput.* **2019**, *15*, 4468−4477.

(58) Epifanovsky, E.; Zuev, D.; Feng, X.; Khistyaev, K.; Shao, Y.; Krylov, A. I. General implementation of the resolution-of-the-identity and Cholesky representations of electron repulsion integrals within coupled-cluster and equation-of-motion methods: Theory and benchmarks. *J. Chem. Phys.* **2013**, *139*, 134105.

(59) Neese, F.; Wennmohs, F.; Hansen, A.; Becker, U. Efficient, approximate and parallel Hartree-Fock and hybrid DFT calculations. A

'chain-of-spheres' algorithm for the Hartree-Fock exchange. *Chem. Phys.* **2009**, *356*, 98−109.

(60) Laqua, H.; Thompson, T. H.; Kussmann, J.; Ochsenfeld, C. Highly Efficient, Linear-Scaling Seminumerical ExactExchange Method for Graphic Processing Units. *J. Chem. Theory Comput.* **2020**, *16*, 1456−1468.

(61) Parrish, R. M.; Hohenstein, E. G.; Martínez, T. J.; Sherrill, C. D. Discrete variable representation in electronic structure theory: Quadrature grids for least-squares tensor hypercontraction. *J. Chem. Phys.* **2013**, *138*, 194107.

(62) Song, C.; Martínez, T. J. Atomic orbital-based SOS-MP2 with tensor hypercontraction. I. GPU-based tensor construction and exploiting sparsity. *J. Chem. Phys.* **2016**, *144*, 174111.

(63) Song, C.; Martínez, T. J. Atomic orbital-based SOS-MP2 with tensor hypercontraction. II. Local tensor hypercontraction. *J. Chem. Phys.* **2017**, *146*, No. 034104.

(64) Schmitz, G.; Madsen, N. K.; Christiansen, O. Atomic-batched tensor decomposed two-electron repulsion integrals. *J. Chem. Phys.* **2017**, *146*, 134112.

(65) Schmitz, G.; Christiansen, O. Assessment of the overlap metric in the context of RI-MP2 and atomic batched tensor decomposed MP2. *Chem. Phys. Lett.* **2018**, *701*, 7−14.

(66) Lee, J.; Lin, L.; Head-Gordon, M. Systematically Improvable Tensor Hypercontraction: Interpolative Separable Density Fitting for Molecules Applied to Exact Exchange, Second- and Third-Order Møller-Plesset Perturbation Theory. *J. Chem. Theory Comput.* **2019**, *16*, 243−263.

(67) Kokkila Schumacher, S. I. L.; Hohenstein, E. G.; Parrish, R. M.; Wang, L.-P.; Martínez, T. J. Tensor Hypercontraction Second-Order Møller-Plesset Perturbation Theory: Grid Optimization and Reaction Energies. *J. Chem. Theory Comput.* **2015**, *11*, 3042−3052.

(68) Song, C.; Martínez, T. J. Analytical gradients for tensor hypercontracted MP2 and SOS-MP2 on graphical processing units. *J. Chem. Phys.* **2017**, *147*, 161723.

(69) Matthews, D. A. Improved Grid Optimization and Fitting in Least Squares Tensor Hypercontraction. *J. Chem. Theory Comput.* **2020**, *16*, 1382−1385.

(70) Parrish, R. M.; David Sherrill, C.; Hohenstein, E. G.; Kokkila, S. I. L.; Martínez, T. J. Communication: Acceleration of coupled cluster singles and doubles via orbital-weighted least-squares tensor hypercontraction. *J. Chem. Phys.* **2014**, *140*, 181102.

(71) Hohenstein, E. G.; Kokkila, S. I. L.; Parrish, R. M.; Martínez, T. J. Quartic scaling second-order approximate coupled cluster singles and doubles via tensor hypercontraction: THC-CC2. *J. Chem. Phys.* **2013**, *138*, 124111.

(72) Hohenstein, E. G.; Kokkila, S. I. L.; Parrish, R. M.; Martínez, T. J. Tensor hypercontraction equation-of-motion second-order approximate coupled cluster: Electronic excitation energies in O(N4) time. *J. Phys. Chem. B* **2013**, *117*, 12972−12978.

(73) Schutski, R.; Zhao, J.; Henderson, T. M.; Scuseria, G. E. Tensor-structured coupled cluster theory. *J. Chem. Phys.* **2017**, *147*, 184113.

(74) Song, C.; Martínez, T. J. Reduced scaling CASPT2 using supporting subspaces and tensor hyper-contraction. *J. Chem. Phys.* **2018**, *149*, No. 044108.

(75) Reine, S.; Tellgren, E.; Krapp, A.; Kjærgaard, T.; Helgaker, T.; Jansik, B.; Høst, S.; Salek, P. Variational and robust density fitting of four-center two-electron integrals in local metrics. *J. Chem. Phys.* **2008**, *129*, 104101.

(76) Thompson, T. H.; Ochsenfeld, C. Integral partition bounds for fast and effective screening of general one-, two-, and manyelectron integrals. *J. Chem. Phys.* **2019**, *150*, No. 044101.

(77) Jung, Y.; Shao, Y.; Head-Gordon, M. Fast Evaluation of Scaled Opposite Spin Second-Order Møller-Plesset Correlation Energies Using Auxiliary Basis Expansions and Exploiting Sparsity. *J. Comput. Chem.* **2007**, *28*, 1953−1964.

(78) Jung, Y.; Lochan, R. C.; Dutoi, A. D.; Head-Gordon, M. Scaled opposite-spin second order Møller-Plesset correlation energy: An economical electronic structure method. *J. Chem. Phys.* **2004**, *121*, 9793.

(79) Aquilante, F.; Bondo Pedersen, T.; Sánchez De Merás, A.; Koch, H. Fast noniterative orbital localization for large molecules. *J. Chem. Phys.* **2006**, *125*, 174101.

(80) Glasbrenner, M.; Graf, D.; Ochsenfeld, C. Efficient reduced-scaling second-order Møller-Plesset perturbation theory with Cholesky-decomposed densities and an attenuated Coulomb metric. *J. Chem. Theory Comput.* **2020**, *16*, 6856−6868.

(81) Kussmann, J.; Ochsenfeld, C. Preselective screening for matrix elements in linear-scaling exact exchange calculations. *J. Chem. Phys.* **2013**, *138*, 134114.

(82) Kussmann, J.; Ochsenfeld, C. Preselective screening for linear-scaling exact exchange-gradient calculations for graphics processing units and general strong-scaling massively parallel calculations. *J. Chem. Theory Comput.* **2015**, *11*, 918−922.

(83) Kussmann, J.; Ochsenfeld, C. Hybrid CPU/GPU Integral Engine for Strong-Scaling Ab Initio Methods. *J. Chem. Theory Comput.* **2017**, *13*, 3153−3159.

(84) Dunning, T. H. Gaussian basis sets for use in correlated molecular calculations. I. The atoms boron through neon and hydrogen. *J. Chem. Phys.* **1989**, *90*, 1007.

(85) Pulay, P. Convergence acceleration of iterative sequences. the case of SCF iteration. *Chem. Phys Lett.* **1980**, *73*, 393−398.

(86) Jurečka, P.; Šponer, J.; Černý, J.; Hobza, P. Benchmark database of accurate (MP2 and CCSD(T) complete basis set limit) interaction energies of small model complexes, DNA base pairs, and amino acid pairs. *Phys. Chem. Chem. Phys.* **2006**, *8*, 1985−1993.

(87) Sedlak, R.; Janowski, T.; Pitoňák, M.; Řezáč, J.; Pulay, P.; Hobza, P. Accuracy of quantum chemical methods for large noncovalent complexes. *J. Chem. Theory Comput.* **2013**, *9*, 3364−3374.

(88) Cuthill, E.; McKee, J. Reducing the bandwidth of sparse symmetric matrices. *Proceedings of the 1969 24th national conference*; ACM *1969*, 157−172.

Supporting Information: Low-scaling Tensor Hypercontraction in the Cholesky Molecular Orbital Basis Applied to Second-Order Møller-Plesset Perturbation Theory

Felix H. Bangerter, Michael Glasbrenner, and Christian Ochsenfeld*

Chair of Theoretical Chemistry, Department of Chemistry, University of Munich (LMU), Butenandtstrasse 5-13, D-81377 Munich, Germany

E-mail: christian.ochsenfeld@cup.uni-muenchen.de

Contents

1 Transformation of the Three-center Integrals

Following up on our work on ω-RI-CDD-MP2,[S1] we employ the natural blocking matrix format[S2] in combination with screening based on integral partition bounds (IPB)[S3] for the transformation of the three-center RI integrals into Cholesky-MO basis. In short, in the three-center AO integral kernel the matrices **M** and **N**,

$$M_{\mu\nu} = \max_{\alpha} |(\mu\nu \vdots \alpha)|, \tag{1}$$

$$N_{\mu\alpha} = \max_{\nu} |(\mu\nu \vdots \alpha)|, \tag{2}$$

are constructed. The screening matrices **M** and **N** can then be turned into upper bounds for the transformation into Cholesky-MO basis by contraction with the absolute Cholesky factors $L_{\mu i}$ and $L_{\mu a}$ according to

$$|(i\nu \vdots \alpha)| \leq N_{i\alpha} = \sum_{\mu} |L_{\mu i}| N_{\mu\alpha}, \tag{3}$$

$$|(a\nu \vdots \alpha)| \leq N_{a\alpha} = \sum_{\mu} |L_{\mu a}| N_{\mu\alpha}. \tag{4}$$

The elements of $N_{i\alpha}$ and $N_{a\alpha}$ can then be used to construct significance lists

$$[i]_{\alpha} \equiv \{i | N_{i\alpha} > \epsilon_{\mathrm{NB}}\}, \tag{5}$$

$$[a]_{\alpha} \equiv \{a | N_{a\alpha} > \epsilon_{\mathrm{NB}}\}. \tag{6}$$

With these significance lists the Cholesky-MO transformation can be carried out in linear-scaling fashion using the algorithm presented below.

Algorithm 1 Transform the three-center RI integrals into Cholesky-MO basis.

```
procedure TRANSFORMRI
    for all $\alpha$ do
        for all $i \in [i]_\alpha$ and $\nu \in \{\nu\}_\alpha$ do
            $(\alpha \vdots i\nu) = \sum_{\mu \in \{\mu\}_\alpha} L_{\mu i}(\alpha \vdots \mu\nu)$
        end for
        build $\{i\}_\alpha$ list
    end for
    for all $\alpha$ do
        for all $i \in \{i\}_\alpha$ and $a \in [a]_\alpha$ do
            $(\alpha \vdots ia) = \sum_{\nu \in \{\nu\}_\alpha} L_{\nu a}(\alpha \vdots i\nu)$
        end for
        build $\{a\}_\alpha$ list
    end for
    reorder: $(\alpha \vdots ia) \rightarrow (ia \vdots \alpha)$
    build $\{a\}_i$ list
    return $(ia \vdots \alpha)$
end procedure
```

2 Band Matrix Solver for Y

Here we present the pseudocode for determining the numerical bandwidth of a symmetric matrix **A** of size $n \times n$ and converting it into the band matrix storage format of LAPACK. Following the notation of the LAPACK documentation, kl is the number of significant subdiagonals and ku the number of superdiagonals. Since **A** is expected to be symmetric $kl = ku$ and the total bandwidth is given by $2kl + 1$. The algorithm determines the bandwidth by iterating over all subdiagonals and accumulating the elements of a given subdiagonal in the variable `sum`. Once the sum is less than the number of elements in this subdiagonals times a given truncation threshold `thresh`, the subdiagonal is considered to be insignificant.

Algorithm 2 Determine the numerical band width of a symmetric matrix **A**.

```
procedure DETERMINE_NUMERICAL_BANDWIDTH(A)
    kl ← 0
    for sub ← 1 to sub < n do                      ▷ iterate over all subdiagonals
        sum ← 0.0
        for k ← 0 to k < n - sub do                ▷ iterate over all elements in a subdiagonal
            sum ← sum + A(k + sub, k)
        end for
        if sum < ((n - sub) × thresh) then
            break
        end if
        kl ← kl + 1
    end for
    return kl
end procedure
```

Algorithm 3 Convert matrix **A** to LAPACK band matrix storage format.

```
procedure CONVERT_TO_BAND_STORAGE(A)
    kl, ku ← DETERMINE_NUMERICAL_BANDWIDTH(A)
    B ← 0(kl+ku+1, n)
    for j ← 0 to j < n do
        for i ← max(0, j-ku) to i < min(n, j + kl) do
            B(ku + i - j, j) ← A(i, j)
        end for
    end for
    return B
end procedure
```

Finally, we note that for the `xgbsv` routine the resulting matrix **B** has to be copied to a zero-padded matrix with dimensions (2`kl`+`ku`+1)×`n`.

3 Evaluation of the MP2 Energy Equations using THC

Here the pseudocode for the algorithms to compute the THC-CDD-MP2 energy is presented. The algorithms for the Coulomb-like and exchange-like energy contribution are shown separately, but both make use of first contracting all possible MO indices after transformation of the collocation matrices into pseudo-MO basis. Here, we present the algorithm to compute the Coulomb-like contribution $E_{\text{MP2-J}}^{\text{THC-CDD}}$ to the MP2 energy with $\mathcal{O}(N^3)$ scaling. We note, that not all contractions are considered explicitly as some of the intermediates are equivalent.

Algorithm 4 Compute the Coulomb-like MP2 energy $E_{\text{MP2-J}}^{\text{THC-CDD}}$

```
procedure $E_{\text{MP2-J}}^{\text{THC-CDD}} \leftarrow -2 \sum_{\kappa} \sum_{PQRS} \sum_{ijab} \underline{X}_i^P \overline{X}_a^P Z^{PQ} \underline{X}_j^Q \overline{X}_b^Q \cdot \underline{X}_i^R \overline{X}_a^R Z^{RS} \underline{X}_j^S \overline{X}_b^S$
    $E_{\text{MP2-J}} \leftarrow 0.0$
    for $\kappa \leftarrow 1$ to $N_\kappa$ do                                ▷ Laplace quadrature
        $\underline{X}_i^P \leftarrow \sum_{\mu} \underline{L}_{\mu i} X_\mu^P$                       ▷ $\mathcal{O}(N_{\text{grid}} N_{\text{bf}} N_{\text{occ}})$
        $\overline{X}_a^P \leftarrow \sum_{\nu} \overline{L}_{\nu a} X_\nu^P$                       ▷ $\mathcal{O}(N_{\text{grid}} N_{\text{bf}} N_{\text{virt}})$
        $A_{(\kappa)}^{PR} \leftarrow \sum_i \underline{X}_i^P \underline{X}_i^R$                     ▷ $\mathcal{O}(N_{\text{grid}}^2 N_{\text{occ}})$
        $B_{(\kappa)}^{PR} \leftarrow \sum_a \overline{X}_a^P \overline{X}_a^R$                     ▷ $\mathcal{O}(N_{\text{grid}}^2 N_{\text{virt}})$
        $C_{(\kappa)}^{PR} \leftarrow A_{(\kappa)}^{PR} \circ B_{(\kappa)}^{PR}$                      ▷ $\mathcal{O}(N_{\text{grid}}^2)$
        $D_{(\kappa)}^{PS} \leftarrow \sum_R C_{(\kappa)}^{PR} Z^{RS}$                      ▷ $\mathcal{O}(N_{\text{grid}}^3)$
        $E_{\text{MP2-J}}$ += $-2 \sum_{PS} D_{(\kappa)}^{PS} D_{(\kappa)}^{SP}$                ▷ $\mathcal{O}(N_{\text{grid}}^2)$
    end for
end procedure
```

Next, the algorithm to compute the exchange-like contribution $E_{\text{MP2-K}}^{\text{THC-CDD}}$ to the MP2 energy with $\mathcal{O}(N^4)$ scaling is presented. To circumvent memory issues, the accumulation of the final $E_{\text{MP2-K}}^{\text{THC-CDD}}$ energy contribution is batched over the occupied index i which avoids the necessity of storing higher than second-order tensors. Again, we note that not all contractions are considered explicitly as some of the intermediates are equivalent. Here, this is especially relevant for intermediates $A_{(\kappa)}^{PR}$ and $A_{(\kappa)}^{QS}$.

Algorithm 5 Compute the exchange-like MP2 energy $E^{\text{THC-CDD}}_{\text{MP2-K}}$

```
procedure $E^{\text{THC-CDD}}_{\text{MP2-K}} \leftarrow \sum_{\kappa}\sum_{PQRS}\sum_{ijab} \underline{X}_i^P \overline{X}_a^P Z^{PQ} \underline{X}_j^Q \overline{X}_b^Q \cdot \underline{X}_i^R \overline{X}_b^R Z^{RS} \underline{X}_j^S \overline{X}_a^S$
    $E_{\text{MP2-K}} \leftarrow 0.0$
    for $\kappa \leftarrow 1$ to $N_\kappa$ do                              ▷ Laplace quadrature
        $\underline{X}_i^P \leftarrow \sum_\mu \underline{L}_{\mu i} X_\mu^P$                      ▷ $\mathcal{O}(N_{\text{grid}} N_{\text{bf}} N_{\text{occ}})$
        $\overline{X}_a^P \leftarrow \sum_\nu \overline{L}_{\nu a} X_\nu^P$                      ▷ $\mathcal{O}(N_{\text{grid}} N_{\text{bf}} N_{\text{virt}})$
        $A^{PR}_{(\kappa)} \leftarrow \sum_i \underline{X}_i^P \underline{X}_i^R$                  ▷ $\mathcal{O}(N^2_{\text{grid}} N_{\text{occ}})$
        $B^{PS}_{(\kappa)} \leftarrow \sum_a \overline{X}_a^P \overline{X}_a^S$                  ▷ $\mathcal{O}(N^2_{\text{grid}} N_{\text{virt}})$
        $e^{(\kappa)}_{\text{MP2-K}} \leftarrow 0.0$
        for $i \leftarrow 1$ to $i \leq \text{rk}(\underline{\mathbf{P}})$ do          ▷ Batching over occupied index $i$
            $C^{PS}_{(\kappa)} \leftarrow B^{PS}_{(\kappa)} \underline{X}_i^P(i,:)$              ▷ $\mathcal{O}(N^2_{\text{grid}} N_{\text{occ}})$
            $D^{QS}_{(\kappa)} \leftarrow \sum_P Z^{PQ} C^{PS}_{(\kappa)}$                ▷ $\mathcal{O}(N^3_{\text{grid}} N_{\text{occ}})$
            $e^{(\kappa)}_{\text{MP2-K}}$ += $\sum_{QS} A^{QS}_{(\kappa)} D^{QS}_{(\kappa)} D^{SQ}_{(\kappa)}$     ▷ $\mathcal{O}(N^2_{\text{grid}} N_{\text{occ}})$
        end for
        $E_{\text{MP2-K}}$ += $e^{(\kappa)}_{\text{MP2-K}}$
    end for
end procedure
```

4 Comparison of Different SOS-MP2 Methods

To put our THC-RI-SOS-MP2 method into context with different SOS-MP2 methods we compare it to LT-RI-SOS-MP2 based on work by Jung *et al.*[S4] and to CD-SOS-MP2 based on work by Aquilante *et al.*[S5] The LT-RI-SOS-MP2 method makes use of the Laplace transformation of the orbital energy denominator of the MP2 energy, which in combination with density-fitted integrals achieves a decoupling of the bra- and ket-indices. As noted in the original publication,[S4] the most expensive step of the method is the contraction of two third-order **B**-tensors to form the final intermediate for the energy evaluation, i.e., **Z**. Asymptotically this step scales as $\mathcal{O}(N_{\text{occ}} N_{\text{virt}} N^2_{\text{aux}})$ and has to be performed for every Laplace point. The CD-SOS-MP2 method on the other hand is based on a Cholesky decomposition of the MP2 amplitudes while the remaining ERI can either be approximated by RI or also be Cholesky-decomposed. This – similar to LT-RI-SOS-MP2 – achieves a factorization into at most third-order tensors. For CD-SOS-MP2, however, the time-determining steps have to be performed only once as a preprocessing step before the actual energy calculation. Asymptotically both methods are quartic scaling with the relative performance mainly governed by the ratio of these steps. THC-RI-SOS-MP2 is another quartic scaling SOS-MP2 method which like LT-RI-SOS-MP2 uses a Laplace transformation of the orbital energy denominator and a preprocessing step in the form of factorizing the ERIs into THC format. The quartic scaling step in THC-RI-SOS-MP2 is the contraction of the collocation matrices $\mathbf{X}$ with the third-order RI tensors. The actual energy calculation requires at most $\mathcal{O}(N_{\text{grid}}^3)$ scaling steps and therefore offers an advantage over LT-RI-SOS-MP2 and CD-SOS-MP2. The energy expressions of the three methods together with the scaling behavior of the most expensive steps are presented below.

LT-RI-SOS-MP2

$$
\begin{aligned}
E_\text{OS-MP2} &= -2\sum_\kappa\sum_{ijab}(\underline{i}\overline{a}|\underline{j}\overline{b})(\underline{i}\overline{a}|\underline{j}\overline{b}) \\
&= -2\sum_\kappa\sum_{\alpha\beta}\sum_{ia}B^\alpha_{\underline{i}\overline{a}}B^\beta_{\underline{i}\overline{a}}\sum_{jb}B^\alpha_{\underline{j}\overline{b}}B^\beta_{\underline{j}\overline{b}} \\
&= -2\sum_\kappa\sum_{\alpha\beta}Z_{\alpha\beta}Z_{\alpha\beta}
\end{aligned}
$$

B^α_{ia}	$\mathcal{O}(N_\text{bf}^2N_\text{occ}N_\text{aux})+\mathcal{O}(N_\text{bf}N_\text{occ}N_\text{virt}N_\text{aux})$
$B^\alpha_{\underline{i}\overline{a}}$	$\mathcal{O}(N_\text{occ}N_\text{virt}N_\text{aux})$
$\mathbf{Z}$	$\mathcal{O}(N_\text{occ}N_\text{virt}N_\text{aux}^2)$
E	$\mathcal{O}(N_\text{aux}^2)$
memory	$\mathcal{O}(N_\text{bf}^2N_\text{aux})^{\text{a)}}$ or $\mathcal{O}(N_\text{occ}N_\text{virt}N_\text{aux})$

CD-SOS-MP2

$$
\begin{aligned}
E_\text{OS-MP2} &= -2\sum_{ijab}t_{ij}^{ab}(ia|jb) \\
&= -2\sum_K\sum_J\sum_{ia}R_{ia}^KL_{ia}^J\sum_{jb}R_{jb}^KL_{jb}^J \\
&= -2\sum_K\sum_J Z^{KJ}Z^{KJ}
\end{aligned}
$$

t_{ij}^{ab}	$\mathcal{O}(N_\text{occ}N_\text{virt}N_\text{aux}N_\text{chol})+\mathcal{O}(N_\text{occ}N_\text{virt}N_\text{chol}^2/2)$
$\mathbf{Z}$	$\mathcal{O}(N_\text{occ}N_\text{virt}N_\text{aux}N_\text{chol})$
E	$\mathcal{O}(N_\text{aux}N_\text{chol})$
memory	$\mathcal{O}(N_\text{occ}^2N_\text{virt}^2)^{\text{b)}}$ or $\mathcal{O}(N_\text{occ}N_\text{virt}N_\text{chol})$

THC-RI-SOS-MP2

$$
\begin{aligned}
E_\text{OS-MP2} &= -2\sum_\kappa\sum_{PQRS}\sum_{ijab}\underline{X}_i^P\overline{X}_a^PZ^{PQ}\underline{X}_j^Q\overline{X}_b^Q\cdot \\
&\qquad \underline{X}_i^R\overline{X}_a^RZ^{RS}\underline{X}_j^S\overline{X}_b^S \\
&= -2\sum_\kappa\sum_{PQRS}A^{PR}_{(\kappa)}B^{PR}_{(\kappa)}Z^{PQ}Z^{RS}A^{QS}_{(\kappa)}B^{QS}_{(\kappa)} \\
&= -2\sum_\kappa\sum_{PQRS}C^{PR}_{(\kappa)}Z^{PQ}Z^{RS}C^{QS}_{(\kappa)} \\
&= -2\sum_\kappa\sum_{PS}D^{PS}_{(\kappa)}D^{PS}_{(\kappa)}
\end{aligned}
$$

$\mathbf{Y}$	$\mathcal{O}(N_\text{occ}N_\text{virt}N_\text{aux}N_\text{grid})+\mathcal{O}(N_\text{occ}N_\text{aux}N_\text{grid})$
$\mathbf{Z}$	$\mathcal{O}(N_\text{aux}N_\text{grid}^2)$
$\mathbf{A},\mathbf{B}$	$\mathcal{O}(N_\text{occ}N_\text{grid}^2)$, $\mathcal{O}(N_\text{virt}N_\text{grid}^2)$
$\mathbf{D}$	$\mathcal{O}(N_\text{grid}^3)$
E	$\mathcal{O}(N_\text{grid}^2)$
memory	$\mathcal{O}(N_\text{bf}^2N_\text{aux})^{\text{a)}}$ or $\mathcal{O}(N_\text{occ}N_\text{virt}N_\text{aux})^{\text{a)}}$ or $\mathcal{O}(N_\text{grid}^2)$

a) if not implemented with on-the-fly integral calculation/contraction

b) if t_{ij}^{ab} is not computed on-the-fly and Cholesky decomposition of the t_{ij}^{ab} supermatrix is performed

All methods are formally quartic scaling and their relative performance can be assessed by comparing the time-determining steps of CD-SOS-MP2 and THC-RI-SOS-MP2 against LT-RI-SOS-MP2. For LT-RI-SOS-MP2 we assume an operation count proportional to $N_\text{occ}N_\text{virt}N_\text{aux}^2$, for CD-SOS-MP2 an operation count of $2N_\text{occ}N_\text{virt}N_\text{aux}N_\text{chol}+N_\text{occ}N_\text{virt}N_\text{chol}^2/2$ and for THC-RI-SOS-MP2 an operation count of $N_\text{occ}N_\text{virt}N_\text{aux}N_\text{grid}$. As explained by

Aquilante *et al.*[S5] the relative performance of CD-SOS-MP2 against LT-RI-SOS-MP2 is governed by the ratio of $\sigma = 2\,N_{\text{chol}}/N_{\text{aux}} + \left(N_{\text{chol}}/N_{\text{aux}}\right)^2/2$ to the number of Laplace points N_κ. For reasonable accuracy the ratio $N_{\text{chol}}/N_{\text{aux}}$ should be greater or equal to one and assuming $N_{\text{chol}}/N_{\text{aux}} = 1$ simplifies σ to $\sigma = 2.5$. Assuming that $N_{\text{chol}}/N_{\text{aux}} = 1$ results in µH accuracy of the final energies, for which in LT-RI-SOS-MP2 7–10 Laplace points would be needed, it can be argued that CD-SOS-MP2 requires roughly 2–4 times less operations. The quartic scaling step of the THC-RI-SOS-MP2 method has to be carried out only once, while in LT-RI-SOS-MP2 this step has to be performed for every Laplace point. Assuming that the number of THC grid points is three times greater than the number of auxiliary functions, this results in a ratio σ' of $\sigma' = 3/N_\kappa$. Assuming that again 7–10 Laplace points are used, THC-RI-SOS-MP2 offers an operation count advantage of roughly 2–3 times and is thus comparable to CD-SOS-MP2. Additionally, one of the strengths of THC-RI-SOS-MP2 is that – if all integral operations are performed on-the-fly – the storage requirements are an order of magnitude smaller than for the other two methods. Furthermore, once the THC factorization is obtained all subsequent steps of evaluating the SOS-MP2 energy are only cubic scaling.

5 Canonical MOs vs Cholesky MOs

The effect of using local Cholesky- and Cholesky pseudo-MOs for the formation of the THC factorized ERIs and the computation of the MP2 energy, respectively, is demonstrated. As outlined in the main part of the paper, our screening routines for both the transformation of the RI integrals into Cholesky-MO basis and the subsequent projection onto the THC grids by contraction with the collocation matrices $\mathbf{X}$ rely on the locality of the MOs used. Furthermore, the evaluation of the MP2 energy relies on sparse linear algebra and therefore also benefits from the locality of the Cholesky pseudo-MOs. To highlight this, the following figures compare computation times for our THC-ω-RI-CDD-SOS-MP2 method, split into contributions from obtaining the THC factorization and the evaluation of the SOS-MP2 energy, using canonical MOs (red) against using Cholesky (pseudo)-MOs (black).

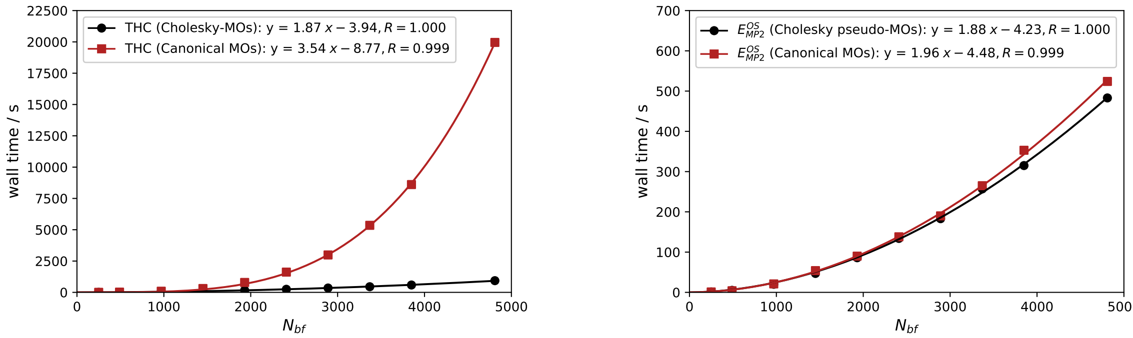

Figure S1: Total execution time of the THC algorithm (left) and the evaluation of the SOS-MP2 energy (right) using Cholesky (pseudo)-MOs (black) and canonical MOs (red) for linear alkanes C_nH_{2n+2} using the cc-pVDZ basis set. The scaling for the largest molecules was determined by linear regression starting from $C_{60}H_{122}$ ($N_{\text{bf}} = 1450$) up to $C_{200}H_{402}$ ($N_{\text{bf}} = 4810$).

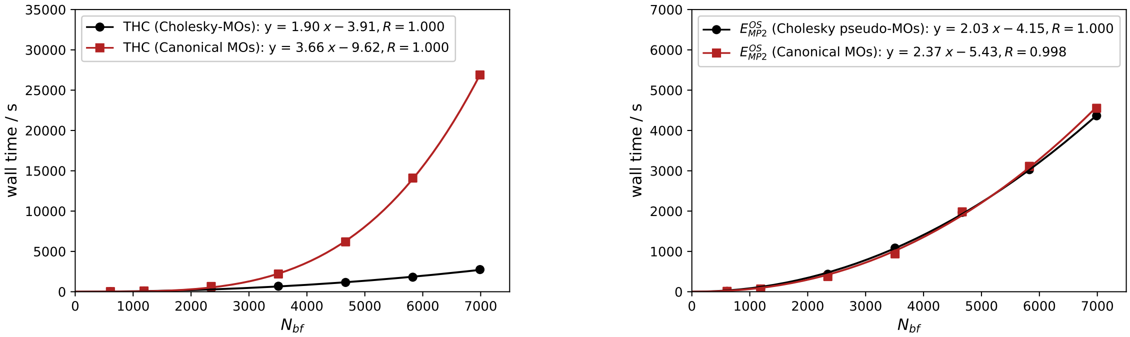

Figure S2: Total execution time of the THC algorithm (left) and the evaluation of the SOS-MP2 energy (right) using Cholesky (pseudo)-MOs (black) and canonical MOs (red) for linear alkanes C_nH_{2n+2} using the cc-pVTZ basis set. The scaling for the largest molecules was determined by linear regression starting from $C_{60}H_{122}$ ($N_{\text{bf}} = 3508$) up to $C_{120}H_{242}$ ($N_{\text{bf}} = 6988$).

The close to quartic scaling of obtaining the THC factorization when using canonical MOs is expected since the non-locality of the MOs causes the contraction of the collocation matrices $\mathbf{X}$ with the three-center RI integrals to approach its formal $\mathcal{O}(N^4)$ scaling. This clearly highlights the efficiency of our screening algorithms for the construction of the $\mathbf{Z}$ matrix. For the energy evaluation, Cholesky pseudo-MOs only provide a speedup for lines 6 and 7 of algorithm 4, i.e., for contractions of the type $\mathbf{X}\mathbf{X}^{\mathrm{T}}$. The product $\mathbf{A} = \underline{\mathbf{X}}\,\underline{\mathbf{X}}^{\mathrm{T}}$ is essentially a representation of the occupied density matrix in the THC grid basis. Analogously, $\mathbf{B} = \overline{\mathbf{X}}\overline{\mathbf{X}}^{\mathrm{T}}$ is a representation of the virtual density matrix. As such $\mathbf{A}$ and $\mathbf{B}$ possess a similar sparsity pattern as the regular density matrices and more importantly should be invariant under rotation of the MOs. The latter means, that $\mathbf{A}$ constructed as $\mathbf{A} = \sum_i \underline{X}_i^P \underline{X}_i^R$ using Cholesky pseudo-MOs and $\mathbf{A}'$ constructed from regular MOs as $\mathbf{A}' = \sum_i e^{\varepsilon_i t^{(\kappa)}} X_i^P X_i^R$ are identical. For this reason, the only step of the evaluation of the MP2 Coulomb-like energy that can be speeded up is the formation of intermediates $\mathbf{A}$ and $\mathbf{B}$, while all subsequent contractions are identical for both types of MOs. Since the contraction $\mathbf{D} = \mathbf{C}\mathbf{Z}$ from algorithm 4 is the time-determining step and $\mathbf{C}$ will have the same sparsity pattern irrespective of the choice of MOs, the overall computation times for the Coulomb-like MP2 energy are very similar (see right sides of figures S1 and S2).

6 Detailed Results for the S22 and L7 Test Set

6.1 Results for the S22 Test Set

Table S1: Absolute energies for the S22 test set monomers computed with our implementation of the RI-SOS-MP2 ($E^{\text{RI}}_{\text{SOS-MP2}}$) reference method as well as the THC-RI-CDD-SOS-MP2 ($E^{\text{THC-RI-CDD}}_{\text{SOS-MP2}}$) and the THC-$\omega$-RI-CDD-SOS-MP2 ($E^{\text{THC-}\omega\text{-RI-CDD}}_{\text{SOS-MP2}}$) method for the cc-pVDZ basis set. Additionally the deviations (ΔE) of the results from the THC methods to the RI-SOS-MP2 energies are shown.

molecule	$E^{\text{RI}}_{\text{SOS-MP2}}$ / H	$E^{\text{THC-RI-CDD}}_{\text{SOS-MP2}}$ / H	ΔE / µH	$E^{\text{THC-}\omega\text{-RI-CDD}}_{\text{SOS-MP2}}$ / H	ΔE / µH
2-aminopyridine	−302.703 924	−302.703 927	2.6	−302.703 906	18.5
2-pyridoxine	−322.546 423	−322.546 425	2.1	−322.546 406	16.9
adenine	−465.932 237	−465.932 233	3.1	−465.932 201	35.2
ammonia	−56.384 925	−56.384 925	<0.1	−56.384 928	3.0
benzene	−231.485 902	−231.485 910	8.1	−231.485 889	12.8
ethene	−78.323 148	−78.323 148	<0.1	−78.323 150	1.5
ethyne	−77.082 330	−77.082 330	<0.1	−77.082 333	3.3
formamide	−169.417 178	−169.417 178	0.1	−169.417 173	4.9
formicacid	−189.261 080	−189.261 079	0.4	−189.261 074	5.6
hydrocyanic acid	−93.163 064	−93.163 064	<0.1	−93.163 068	4.5
indole	−362.658 729	−362.658 743	14.4	−362.658 715	13.2
methane	−40.371 390	−40.371 390	<0.1	−40.371 397	6.1
phenol	−306.521 903	−306.521 911	7.5	−306.521 889	14.2
pyrazine	−263.507 029	−263.507 028	1.1	−263.507 005	24.2
thymine	−452.829 481	−452.829 469	12.7	−452.829 455	26.7
uracil	−413.641 115	−413.641 108	7.7	−413.641 090	24.8
water	−76.224 952	−76.224 952	<0.1	−76.224 952	0.4

Table S2: Absolute energies for the S22 test set dimers and complexes computed with our implementation of the RI-SOS-MP2 ($E^{\text{RI}}_{\text{SOS-MP2}}$) reference method as well as the THC-RI-CDD-SOS-MP2 ($E^{\text{THC-RI-CDD}}_{\text{SOS-MP2}}$) and the THC-$\omega$-RI-CDD-SOS-MP2 ($E^{\text{THC-}\omega\text{-RI-CDD}}_{\text{SOS-MP2}}$) method for the cc-pVDZ basis set. Additionally the deviations (ΔE) of the results from the THC methods to the RI-SOS-MP2 energies are shown.

molecule	$E^{\text{RI}}_{\text{SOS-MP2}}$ / H	$E^{\text{THC-RI-CDD}}_{\text{SOS-MP2}}$ / H	ΔE / µH	$E^{\text{THC-}\omega\text{-RI-CDD}}_{\text{SOS-MP2}}$ / H	ΔE / µH
2-pyridoxine + 2-aminopyridine	−625.277 430	−625.277 432	2.1	−625.277 395	35.0
adenine + thymine (stack)	−918.781 508	−918.781 497	11.6	−918.781 494	13.7
adenine + thymine (W.-C.)	−918.788 467	−918.788 458	8.8	−918.788 415	52.6
ammonia dimer	−112.776 724	−112.776 724	<0.1	−112.776 729	4.5
benzene + methane	−271.858 651	−271.858 660	8.6	−271.858 646	5.0
benzene + ammonia	−287.873 967	−287.873 978	10.9	−287.873 962	4.3
benzene dimer (‖)	−462.974 877	−462.974 902	24.8	−462.974 881	4.0
benzene dimer (⊥)	−462.975 643	−462.975 667	24.3	−462.975 635	8.4
benzene + hydrocyanic acid	−324.655 118	−324.655 128	9.9	−324.655 112	6.3
benzene + water	−307.715 837	−307.715 848	12.2	−307.715 830	6.5
ethene dimer	−156.647 632	−156.647 632	0.3	−156.647 630	1.9
ethene + ethyne	−155.407 786	−155.407 786	<0.1	−155.407 789	3.0
formamide dimer	−338.860 613	−338.860 611	2.1	−338.860 603	9.6
formic acid dimer	−378.552 763	−378.552 761	1.6	−378.552 751	12.0
indole + benzene (‖)	−594.150 675	−594.150 713	38.9	−594.150 696	21.2
indole + benzene (⊥)	−594.152 908	−594.152 942	34.5	−594.152 902	5.1
methane dimer	−80.743 019	−80.743 019	<0.1	−80.743 028	8.9
phenol dimer	−613.056 581	−613.056 617	36.4	−613.056 584	3.5
pyrazine dimer	−527.020 386	−527.020 372	13.8	−527.020 350	35.7
uracil dimer (H-bond)	−827.313 142	−827.313 116	25.9	−827.313 084	57.9
uracil dimer (stack)	−827.297 960	−827.297 941	18.3	−827.297 934	25.9
water dimer	−152.460 696	−152.460 696	<0.1	−152.460 695	1.0

Table S3: Absolute energies for the S22 test set monomers computed with our implementation of the RI-SOS-MP2 ($E_{\text{SOS-MP2}}^{\text{RI}}$) reference method as well as the THC-RI-CDD-SOS-MP2 ($E_{\text{SOS-MP2}}^{\text{THC-RI-CDD}}$) and the THC-$\omega$-RI-CDD-SOS-MP2 ($E_{\text{SOS-MP2}}^{\text{THC-}\omega\text{-RI-CDD}}$) method for the cc-pVTZ basis set. Additionally the deviations (ΔE) of the results from the THC methods to the RI-SOS-MP2 energies are shown.

molecule	$E_{\text{SOS-MP2}}^{\text{RI}}$ / H	$E_{\text{SOS-MP2}}^{\text{THC-RI-CDD}}$ / H	ΔE / µH	$E_{\text{SOS-MP2}}^{\text{THC-}\omega\text{-RI-CDD}}$ / H	ΔE / µH
2-aminopyridine	−303.110 460	−303.110 460	0.2	−303.110 465	5.2
2-pyridoxine	−322.966 088	−322.966 092	3.3	−322.966 094	6.0
adenine	−466.526 943	−466.526 939	3.9	−466.526 946	3.0
ammonia	−56.471 514	−56.471 515	<0.1	−56.471 516	1.4
benzene	−231.807 569	−231.807 569	0.7	−231.807 574	5.8
ethene	−78.441 379	−78.441 379	<0.1	−78.441 375	4.5
ethyne	−77.191 318	−77.191 318	<0.1	−77.191 326	7.7
formamide	−169.634 769	−169.634 768	0.8	−169.634 770	1.0
formicacid	−189.491 093	−189.491 093	0.5	−189.491 094	0.3
hydrocyanic acid	−93.276 293	−93.276 293	<0.1	−93.276 305	11.5
indole	−363.150 385	−363.150 381	4.1	−363.150 383	1.6
methane	−40.441 911	−40.441 911	<0.1	−40.441 911	<0.1
phenol	−306.931 762	−306.931 763	0.7	−306.931 766	4.0
pyrazine	−263.847 780	−263.847 780	0.2	−263.847 787	6.6
thymine	−453.403 928	−453.403 930	1.9	−453.403 930	2.8
uracil	−414.156 850	−414.156 843	6.7	−414.156 848	2.3
water	−76.328 144	−76.328 145	<0.1	−76.328 144	0.7

Table S4: Absolute energies for the S22 test set dimers and complexes computed with our implementation of the RI-SOS-MP2 ($E^{\text{RI}}_{\text{SOS-MP2}}$) reference method as well as the THC-RI-CDD-SOS-MP2 ($E^{\text{THC-RI-CDD}}_{\text{SOS-MP2}}$) and the THC-$\omega$-RI-CDD-SOS-MP2 ($E^{\text{THC-}\omega\text{-RI-CDD}}_{\text{SOS-MP2}}$) method for the cc-pVTZ basis set. Additionally the deviations (ΔE) of the results from the THC methods to the RI-SOS-MP2 energies are shown.

molecule	$E^{\text{RI}}_{\text{SOS-MP2}}$ / H	$E^{\text{THC-RI-CDD}}_{\text{SOS-MP2}}$ / H	ΔE / µH	$E^{\text{THC-}\omega\text{-RI-CDD}}_{\text{SOS-MP2}}$ / H	ΔE / µH
2-pyridoxine + 2-aminopyridine	−626.102 751	−626.102 756	3.6	−626.102 760	7.8
adenine + thymine (stack)	−919.953 279	−919.953 283	4.0	−919.953 305	26.0
adenine + thymine (W.-C.)	−919.956 369	−919.956 365	4.3	−919.956 365	3.9
ammonia dimer	−112.948 625	−112.948 625	<0.1	−112.948 624	1.1
benzene + methane	−272.251 679	−272.251 680	0.9	−272.251 685	6.5
benzene + ammonia	−288.282 957	−288.282 956	1.0	−288.282 970	12.5
benzene dimer (‖)	−463.620 183	−463.620 177	6.2	−463.620 192	9.4
benzene dimer (⊥)	−463.619 930	−463.619 927	3.9	−463.619 935	5.3
benzene + hydrocyanic acid	−325.091 880	−325.091 880	<0.1	−325.091 904	23.5
benzene + water	−308.141 724	−308.141 722	1.8	−308.141 728	3.6
ethene dimer	−156.884 286	−156.884 286	<0.1	−156.884 291	5.8
ethene + ethyne	−155.634 944	−155.634 945	1.0	−155.634 952	8.3
formamide dimer	−339.294 087	−339.294 085	2.3	−339.294 087	0.1
formic acid dimer	−379.010 826	−379.010 824	2.4	−379.010 851	24.6
indole + benzene (‖)	−594.967 113	−594.967 112	0.9	−594.967 130	16.6
indole + benzene (⊥)	−594.967 839	−594.967 834	4.7	−594.967 860	20.9
methane dimer	−80.884 303	−80.884 303	<0.1	−80.884 303	0.1
phenol dimer	−613.875 204	−613.875 205	1.2	−613.875 214	9.7
pyrazine dimer	−527.703 274	−527.703 273	1.2	−527.703 298	23.5
uracil dimer (H-bond)	−828.344 550	−828.344 536	14.0	−828.344 537	13.7
uracil dimer (stack)	−828.331 458	−828.331 460	2.1	−828.331 473	15.6
water dimer	−152.665 252	−152.665 252	<0.1	−152.665 250	1.7

6.2 Results for the L7 Test Set

Table S5: Absolute energies for the L7 test set monomers (2nd and 3rd row of each cell) and complexes (1st row of each cell) computed with our implementation of the RI-SOS-MP2 ($E^{\text{RI}}_{\text{SOS-MP2}}$) reference method as well as the THC-RI-CDD-SOS-MP2 ($E^{\text{THC-RI-CDD}}_{\text{SOS-MP2}}$) and the THC-$\omega$-RI-CDD-SOS-MP2 ($E^{\text{THC-}\omega\text{-RI-CDD}}_{\text{SOS-MP2}}$) method for the cc-pVDZ basis set. Additionally the deviations (ΔE) of the results from the THC methods to the RI-SOS-MP2 energies are shown.

molecule	$E^{\text{RI}}_{\text{SOS-MP2}}$ / H	$E^{\text{THC-RI-CDD}}_{\text{SOS-MP2}}$ / H	ΔE / µH	$E^{\text{THC-}\omega\text{-RI-CDD}}_{\text{SOS-MP2}}$ / H	ΔE / µH
circumcoronene	−2528.319 812	−2528.320 097	284.8	−2528.319 995	183.3
+	−465.934 047	−465.934 057	10.7	−465.934 025	21.3
adenine	−2062.358 644	−2062.358 811	167.1	−2062.358 643	1.4
circumcoronene	−2997.209 161	−2997.209 377	215.5	−2997.209 315	153.5
+	−934.805 872	−934.805 864	8.7	−934.805 814	58.6
GC	−2062.358 156	−2062.358 361	205.3	−2062.358 192	36.1
coronene	−1837.897 882	−1837.898 001	118.9	−1837.897 970	87.0
+	−918.932 012	−918.932 097	85.6	−918.932 029	17.4
coronone	−918.932 012	−918.932 097	85.6	−918.932 029	17.4
GC	−1869.612 341	−1869.612 225	115.2	−1869.612 216	124.0
+	−934.793 898	−934.793 872	25.5	−934.793 824	73.7
GC	−934.793 898	−934.793 872	25.5	−934.793 824	73.7
guanine	−1622.921 181	−1622.921 159	21.9	−1622.921 131	50.0
+	−540.978 004	−540.978 009	5.0	−540.977 979	24.9
2×guanine	−1081.938 478	−1081.938 454	24.5	−1081.938 429	49.4
octadecane	−1412.944 380	−1412.944 429	48.8	−1412.944 427	46.8
+	−706.468 122	−706.468 122	0.3	−706.468 123	1.3
octadecane	−706.468 122	−706.468 122	0.3	−706.468 123	1.3
phenylalanine	−2056.636 559	−2056.636 594	35.5	−2056.636 561	1.7
+	−685.518 803	−685.518 816	13.5	−685.518 802	1.0
2×phenylalanine	−1371.076 543	−1371.076 574	30.9	−1371.076 551	7.3

Table S6: Absolute energies for the L7 test set monomers (2nd and 3rd row of each cell) and complexes (1st row of each cell) computed with our implementation of the RI-SOS-MP2 ($E^{\text{RI}}_{\text{SOS-MP2}}$) reference method as well as the THC-RI-CDD-SOS-MP2 ($E^{\text{THC-RI-CDD}}_{\text{SOS-MP2}}$) and the THC-$\omega$-RI-CDD-SOS-MP2 ($E^{\text{THC-}\omega\text{-RI-CDD}}_{\text{SOS-MP2}}$) method for the cc-pVTZ basis set. Additionally the deviations (ΔE) of the results from the THC methods to the RI-SOS-MP2 energies are shown.

molecule	$E^{\text{RI}}_{\text{SOS-MP2}}$ / H	$E^{\text{THC-RI-CDD}}_{\text{SOS-MP2}}$ / H	ΔE / µH	$E^{\text{THC-}\omega\text{-RI-CDD}}_{\text{SOS-MP2}}$ / H	ΔE / µH
circumcoronene	−2531.676 601	−2531.676 470	131.4	−2531.676 470	131.4
+	−466.526 351	−466.526 346	5.7	−466.526 356	4.2
adenine	−2065.114 437	−2065.114 359	77.2	−2065.114 340	96.2
circumcoronene	−3001.162 208	−3001.162 191	17.5	−3001.162 191	17.5
+	−935.987 058	−935.987 033	25.6	−935.987 036	22.1
GC	−2065.114 682	−2065.114 673	9.6	−2065.114 659	23.8
coronene	−1840.399 230	−1840.399 043	187.3	−1840.399 093	137.0
+	−920.176 000	−920.175 898	101.9	−920.175 897	103.2
coronone	−920.176 000	−920.175 898	101.9	−920.175 897	103.2
GC	−1872.005 953	−1872.005 838	115.6	−1872.005 875	77.9
+	−935.988 309	−935.988 264	45.3	−935.988 265	43.9
GC	−935.988 309	−935.988 264	45.3	−935.988 265	43.9
guanine	−1624.970 678	−1624.970 622	55.0	−1624.970 653	24.1
+	−541.658 226	−541.658 214	11.8	−541.658 217	8.2
2×guanine	−1083.305 549	−1083.305 514	35.6	−1083.305 533	16.1
octadecane	−1415.073 527	−1415.073 509	18.1	−1415.073 463	63.9
+	−707.530 305	−707.530 297	8.3	−707.530 314	8.3
octadecane	−707.530 305	−707.530 297	8.3	−707.530 314	8.3
phenylalanine	−2059.357 071	−2059.357 044	27.3	−2059.357 062	8.6
+	−686.425 836	−686.425 827	8.6	−686.425 838	2.5
2×phenylalanine	−1372.890 709	−1372.890 692	17.3	−1372.890 706	3.5

7 Accuracy of THC-MP2 Amplitudes

As shown in the main part of this paper and section 6 of the SI, our THC-ω-RI-CDD-SOS-MP2 method is able to accurately reproduce RI-SOS-MP2 energies with average errors on the order of 10^{-6} H to 10^{-5} H for the investigated S22 and L7 test set. To show that our THC algorithm can also accurately reproduce important intermediate quantities and not only final energies, we compare RI-MP2 amplitudes, given as

$$t_{ij}^{ab}(\text{RI-MP2}) = \sum_{\alpha\beta} \frac{(ia|\alpha)\,[\mathbf{J}^{-1}]_{\alpha\beta}\,(\beta|jb)}{\varepsilon_i + \varepsilon_j - \varepsilon_a - \varepsilon_b}, \tag{7}$$

against the THC-ω-RI-MP2 amplitudes

$$t_{ij}^{ab}(\text{THC-}\omega\text{-RI-MP2}) = \sum_{PQ} \frac{X_i^P X_a^P Z^{PQ} X_j^Q X_b^Q}{\varepsilon_i + \varepsilon_j - \varepsilon_a - \varepsilon_b}, \tag{8}$$

as computed with our THC algorithm. The deviation of the THC-ω-RI-MP2 amplitudes from the RI-MP2 amplitudes is quantified by calculating the mean absolute deviation of the diagonal elements given by

$$\Delta t_{ii}^{aa} = \frac{1}{N_{\text{occ}} N_{\text{virt}}} \sum_{ia} |t_{ii}^{aa}(\text{RI-MP2}) - t_{ii}^{aa}(\text{THC-}\omega\text{-RI-MP2})| \tag{9}$$

for the molecules and complexes in the S22 test set using the cc-pVDZ and cc-pVTZ basis sets. The same thresholds and settings are used as in the main part of the paper.

Table S7: Deviations of the diagonal elements of the THC-ω-RI-MP2 amplitudes from the RI-MP2 amplitudes for the S22 test set monomers computed with the cc-pVDZ and cc-pVTZ basis sets.

molecule	Δt_{ii}^{aa} (cc-pVDZ) / 10^{-7}	Δt_{ii}^{aa} (cc-pVTZ) / 10^{-7}
2-aminopyridine	2.935	0.345
2-pyridoxine	3.053	0.455
adenine	3.139	0.464
ammonia	3.293	0.725
benzene	2.981	0.565
ethene	1.614	0.343
ethyne	2.742	0.691
formamide	1.571	0.614
formicacid	1.436	0.785
hydrocyanic acid	3.393	1.036
indole	3.194	0.669
methane	1.677	0.325
phenol	2.790	0.276
pyrazine	3.604	0.568
thymine	2.977	0.357
uracil	3.699	0.912
water	4.234	1.122
MAD	2.843	0.603
MAX	4.234	1.122

Table S8: Deviations of the diagonal elements of the THC-ω-RI-MP2 amplitudes from the RI-MP2 amplitudes for the S22 test set dimers and complexes computed with the cc-pVDZ and cc-pVTZ basis sets.

molecule	Δt_{ii}^{aa} (cc-pVDZ) / 10^{-7}	Δt_{ii}^{aa} (cc-pVTZ) / 10^{-7}
2-pyridoxine + 2-aminopyridine	1.529	0.177
adenine + thymine (stack)	1.872	0.180
adenine + thymine (W.-C.)	1.600	0.241
ammonia dimer	0.984	0.235
benzene + methane	2.018	0.366
benzene + ammonia	2.179	0.233
benzene dimer ($\|$)	2.327	0.145
benzene dimer ($\perp$)	1.610	0.343
benzene + hydrocyanic acid	2.027	0.260
benzene + water	2.352	0.237
ethene dimer	0.616	0.121
ethene + ethyne	0.761	0.195
formamide dimer	1.669	0.405
formic acid dimer	2.092	0.575
indole + benzene ($\|$)	2.677	0.133
indole + benzene ($\perp$)	1.898	0.261
methane dimer	0.651	0.936
phenol dimer	2.358	0.128
pyrazine dimer	2.235	0.271
uracil dimer (H-bond)	2.003	0.379
uracil dimer (stack)	2.253	0.214
water dimer	1.520	0.320
MAD	1.783	0.219
MAX	2.358	0.936

For the MP2 amplitude deviations similar effects as for the MP2 energies can be observed.

The THC factorization provides a quantitatively good approximation of the RI-MP2 amplitudes and deviations with the triple-ζ basis set are smaller due to larger THC grids being employed. Errors of the THC-ω-RI-MP2 amplitudes are on the order of 10^{-7} for the cc-pVDZ basis set and on the order of 10^{-8} for the cc-pVTZ basis set across the whole S22 test set. This was expected since the THC grids[S6] used were optimized to best fit density-fitted ERIs.

8 Validation of the Phosphorus Grids

The computation of DNA fragments requires THC grids for the atom types {H, C, N, O, P}. The grids provided by Martínez and coworkers[S6] were however only optimized for 1st- and 2nd-row elements. To still make computations of DNA fragments possible we chose to use the largest atom grids, i.e., the grids for fluorine, for the phosphorus atoms as well. To demonstrate that this does not result in an additional error beyond the regular THC error, we compare the Coulomb-like energies of the THC-RI-CDD-MP2 method against the RI-MP2 reference method for a selection of representative phosphorus species. This mini test set includes P_4, the trivalent PH_3 and the pentavalent H_3PO_4. H_3PO_4 is of special interest here because the DNA backbone contains structurally comparable phosphate moieties. The results are shown in the table below.

Table S9: Comparison of the Coulomb-like energies $E_{\text{MP2-J}}$ for the THC-RI-CDD-MP2 method against RI-MP2 for the validation of the phosphorus grids. All calculations were performed with the cc-pVDZ basis set and the cc-pVDZ-RI fitting basis set.

molecule	$E_{\text{MP2-J}}^{\text{RI}}$ / H	$E_{\text{MP2-J}}^{\text{THC-RI-CDD}}$ / H	ΔE / µH
P_4	-0.357244658	-0.357244828	0.17
PH_3	-0.115739227	-0.115739217	0.01
H_3PO_4	-0.637504139	-0.637504382	0.24

As can be seen from table S9, the errors are well below 1 µH and comparable to the regular THC error for the other atom types. This justifies the use of the fluorine grids for phosphorus atoms and shows that this does not lead to a significant error increase.

9 Demonstrating Continuousness of the Potential Energy Surface for a C−C Bond Rotation in Vitamin K_2

To demonstrate, that the THC-ω-RI-CDD-SOS-MP2 method is not prone to discontinuities in the potential energy surface, the rotation around a C−C bond in vitamin K_2 (menachinon-4), we computed the THC-ω-RI-CDD-SOS-MP2 energies for the rotation around the C−C bond between atoms 4 and 5 in steps of 10°. The same settings were used as in the main part of the paper, i.e., a natural blocking threshold of 10^{-6} and an attenuation strength $\omega = 0.1$. The corresponding energy diagram and additionally the structures at a rotation of -180° and 0° are shown in the figure below.

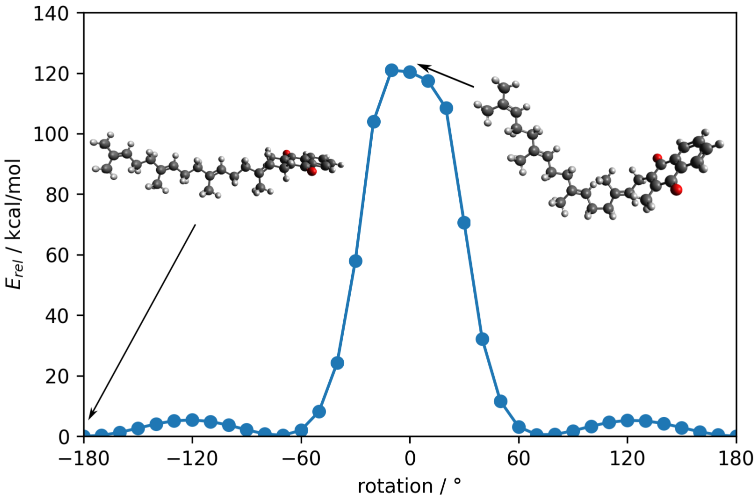

Figure S3: THC-ω-RI-CDD-SOS-MP2 energies relative to the geometry with a rotation angle of -180° of vitamin K_2. All calculations were performed with the cc-pVDZ basis set and the cc-pVDZ-RI fitting basis set.

The geometries of the Vitamin K_2 molecules are provided on our website.

References

(S1) Glasbrenner, M.; Graf, D.; Ochsenfeld, C. Efficient reduced-scaling second-order Møller-Plesset perturbation theory with Cholesky-decomposed densities and an attenuated Coulomb metric. *J. Chem. Theory Comput.* **2020**, *16*, 6856–6868.

(S2) Jung, Y.; Shao, Y.; Head-Gordon, M. Fast Evaluation of Scaled Opposite Spin Second-Order Møller-Plesset Correlation Energies Using Auxiliary Basis Expansions and Exploiting Sparsity. *J. Comput. Chem.* **2007**, *28*, 1953–1964.

(S3) Thompson, T. H.; Ochsenfeld, C. Integral partition bounds for fast and effective screening of general one-, two-, and many-electron integrals. *J. Chem. Phys.* **2019**, *150*, 044101.

(S4) Jung, Y.; Lochan, R. C.; Dutoi, A. D.; Head-Gordon, M. Scaled opposite-spin second order Møller-Plesset correlation energy: An economical electronic structure method. *J. Chem. Phys.* **2004**, *121*, 9793.

(S5) Aquilante, F.; Pedersen, T. B. Quartic scaling evaluation of canonical scaled opposite spin second-order Møller-Plesset correlation energy using Cholesky decompositions. *Chem. Phys. Lett.* **2007**, *449*, 354–357.

(S6) Kokkila Schumacher, S. I.; Hohenstein, E. G.; Parrish, R. M.; Wang, L. P.; Martínez, T. J. Tensor Hypercontraction Second-Order Møller-Plesset Perturbation Theory: Grid Optimization and Reaction Energies. *J. Chem. Theory Comput.* **2015**, *11*, 3042–3052.

3.2. Publication II: Tensor-Hypercontracted MP2 First Derivatives: Runtime and Memory Efficient Computation of Hyperfine Coupling Constants

F. H. Bangerter, M. Glasbrenner, C. Ochsenfeld

J. Chem. Theory Comput. **18**, 5233-5245 (2022).

Abstract

We employ our recently introduced tensor-hypercontracted (THC) second-order Møller–Plesset perturbation theory (MP2) method [Bangerter, F. H., Glasbrenner, M., Ochsenfeld, C. J. Chem. Theory Comput. **2021**, *17*, 211-221] for the computation of hyperfine coupling constants (HFCCs). The implementation leverages the tensor structure of the THC factorized electron repulsion integrals for an efficient formation of the integral-based intermediates. The computational complexity of the most expensive and formally quintic scaling exchange-like contribution is reduced to effectively subquadratic, by making use of the intrinsic, exponentially decaying coupling between tensor indices through screening based on natural blocking. Overall, this yields an effective subquadratic scaling with a low prefactor for the presented THC-based AO-MP2 method for the computation of isotropic HFCCs on DNA fragments with up to 500 atoms and 5000 basis functions. Furthermore, the implementation achieves considerable speedups with up to a factor of roughly 600–1000 compared to previous implementations [Vogler, S., Ludwig, M., Maurer, M., Ochsenfeld, C. J. Chem. Phys. **2017**, *147*, 024101] for medium-sized organic radicals, while also significantly reducing storage requirements.

Reprinted with permission from:

F. H. Bangerter, M. Glasbrenner, C. Ochsenfeld
“Tensor-Hypercontracted MP2 First Derivatives: Runtime and Memory Efficient Computation of Hyperfine Coupling Constants”
J. Chem. Theory Comput. **18**, 5233-5245 (2022).

`https://pubs.acs.org/doi/10.1021/acs.jctc.2c00118`

JCTC Journal of Chemical Theory and Computation

pubs.acs.org/JCTC Article

Tensor-Hypercontracted MP2 First Derivatives: Runtime and Memory Efficient Computation of Hyperfine Coupling Constants

Felix H. Bangerter, Michael Glasbrenner, and Christian Ochsenfeld*

Cite This: *J. Chem. Theory Comput.* 2022, 18, 5233−5245 Read Online

ACCESS | Metrics & More | Article Recommendations | Supporting Information

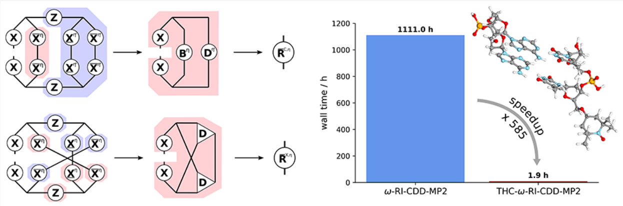

ABSTRACT: We employ our recently introduced tensor-hypercontracted (THC) second-order Møller−Plesset perturbation theory (MP2) method [Bangerter, F. H., Glasbrenner, M., Ochsenfeld, C. *J. Chem. Theory Comput.* **2021**, *17*, 211−221] for the computation of hyperfine coupling constants (HFCCs). The implementation leverages the tensor structure of the THC factorized electron repulsion integrals for an efficient formation of the integral-based intermediates. The computational complexity of the most expensive and formally quintic scaling exchange-like contribution is reduced to effectively subquadratic, by making use of the intrinsic, exponentially decaying coupling between tensor indices through screening based on natural blocking. Overall, this yields an effective subquadratic scaling with a low prefactor for the presented THC-based AO-MP2 method for the computation of isotropic HFCCs on DNA fragments with up to 500 atoms and 5000 basis functions. Furthermore, the implementation achieves considerable speedups with up to a factor of roughly 600−1000 compared to previous implementations [Vogler, S., Ludwig, M., Maurer, M., Ochsenfeld, C. *J. Chem. Phys.* **2017**, *147*, 024101] for medium-sized organic radicals, while also significantly reducing storage requirements.

1. INTRODUCTION

Ever since the advent of modern computers in the 1990s, Møller−Plesset perturbation theory (MP*n*)[1] has been a good compromise in the family of quantum chemical methods, being sufficiently accurate for many applications while still being computationally affordable.[2] As opposed to coupled cluster theory (CC), MP*n* lacks infinite-order corrections present in the cluster operator expansion of the CC models, which generally makes MP*n* less accurate.[2] However, when going from energies to gradients and molecular properties, MP*n*, especially second-order MP*n* (MP2), was shown to yield accurate hyperfine coupling constants (HFCCs)[3−7] and relative nuclear magnetic resonance (NMR) shifts.[8−12] However, MP2 is sensitive to spin-contamination in the Hartree−Fock wave function, which can be improved upon when used in its orbital-optimized variant[4] or as part of double-hybrid density functionals.[13]

Furthermore, when comparing MP*n* and CC at the same expansion orders, for example, MP2 and singles and doubles CC (CCSD), MP*n* comes with a scaling advantage, both in the prefactor and the scaling exponent. Nonetheless, canonical MP2, as well as the associated first and second derivative,[6,11] still scale with the fifth power of the molecule size, thereby severely restricting the accessible chemical space. To alleviate this limitation several formulations of the MP2 derivatives have been proposed.

Early work from Pulay and Sæbø[14,15] on local correlation was applied to the computation of MP2 gradients.[16,17] Following up on this, in recent years the domain-based local pair natural orbital (DLPNO) formulation of MP2 by Neese and co-workers[18−20] was extended to first and second derivatives. Conceptually related is the divide-expand-consolidate (DEC) formulation of MP2 by Jørgensen and co-workers,[21,22] which likewise was extended to the computation of molecular gradients in a linear-scaling and massively parallel manner.[23,24] Instead of exploiting locality in the correlation space, the equations of the MP2 first[6,25] and second derivative[11] can be reformulated entirely in terms of atomic orbitals (AOs). However, for an efficient implementation and the reduction of the scaling prefactor, an orbital localization by pivoted Cholesky decomposition (PCD) of the associated pseudodensities is essential.[6]

Besides ensuring low-scaling and efficiency, for derivative calculations of electron correlation methods in general, it is pivotal to efficiently manage the available memory and disk space. Compared to the energy equations, the associated gradients and higher derivatives often not only include electron repulsion integrals (ERIs), in either atomic or molecular orbital basis, but can also include partially transformed ERIs and derivatives thereof, for example, with respect to the magnetic field in NMR calculations. Since canonical ERIs are fourth-order tensors, their memory requirements prohibitively scale with the

Received: February 3, 2022
Published: August 9, 2022

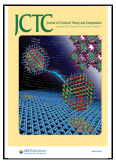

forth power of the number of basis functions and saving multiple such tensors quickly becomes unfeasible. To reduce the memory footprint of the ERIs, tensor decomposition methods, particularly the resolution-of-the-identity (RI) ansatz,[26−29] have been broadly applied in the context of MP2 derivatives.[5,6,12,30] However, with increasing molecule size, even the third-order RI tensors eventually exceed the available disk space of conventional high performance computing nodes. To overcome this storage limitation, further reduction of the dimensionality of the ERIs is desirable. This can be achieved by the recently introduced tensor hypercontraction (THC) factorization of Martínez and co-workers,[31−34] which in general terms approximates a fourth-order integral tensor $(\mu\nu|\hat{o}|\lambda\sigma)$, where $\hat{o}$ is a singular two electron interaction kernel, by five second-order tensors.[35] In the least-squares formulation of THC (LS-THC),[31] four of these tensors are simply obtained by evaluation of the basis functions at real-space grid nodes and the singular $\hat{o}$ operator is replaced by the LS-fitted $\mathbf{Z}$ matrix. If $\hat{o}$ is the Coulombic $1/r$ operator, a factorization of the regular ERIs is achieved, which has been employed in reduced scaling formulations of exact exchange,[36] different orders of MPn,[31,33−41] the random phase approximation (RPA),[42] complete active space perturbation theory (CASPT2),[43] and various flavors of CC theory,[44−46] as well as equation-of-motion CC (EOM-CC) theory.[47] Recently Matthews[35] thoroughly investigated amplitude factorizations within MP3, as a stepping stone toward CCSD, and noted that the LS-THC factorization of nonlocal integrals, such as the exchange integrals, incurs an additional error.

The applicability of THC for the computation of molecular gradients is largely unexplored. Song et al.[39] derived equations for the analytical gradient of THC-AO-MP2 with application to geometry optimizations and *ab initio* molecular dynamics (AIMD) simulations. As commonly the derivation of gradient equations of electron correlation methods is rather involved, Song et al.[48] also proposed an automatic differentiation scheme for the automated generation of working equations for gradients of THC-based correlation methods.

When it comes to applying tensor factorizations, be it RI or THC, two possible routes to molecular gradients can be taken: The first approach is to differentiate the RI- or THC-approximated energy equation, then the associated gradient describes the slope of an approximated potential energy surface (PES). The second approach is to take the gradient of the canonical energy and insert the approximation into the exact gradient; this way an approximate gradient is used to move along the exact PES.

The latter can lead to an unwanted buildup of errors during the course of a simulation, when used in molecular dynamics simulations. However, when used in conjunction with thermostats constant energy is traded for constant temperature, and depending on the extent of the gradient error, this approach can still be applicable but must be tested for the chosen gradient. The first approach was taken by Song et al.[39] for their THC-based MP2 molecular gradient, whereas in the present work, the gradient equations with respect to a perturbation, that the basis functions are independent of, are derived by inserting the THC factorization into the equations of the exact gradient. As will be discussed in section 2.4, the resulting equations are identical to the ones obtained by differentiating the THC-AO-MP2 energy equation. As a representative case of these kinds of perturbations, we apply our recently developed low-scaling LS-THC algorithm[41] to the AO-MP2 energy derivative with respect to the nuclear magnetic moment, for the computation of HFCCs on the MP2 level of theory.

We present ways to efficiently treat the Coulomb- and the exchange-like part of the most expensive intermediate of the derivative within the LS-THC approximation. We demonstrate the low-scaling behavior of our THC-ω-RI-CDD-MP2 derivative method for various chemically relevant systems. We also show that THC-ω-RI-CDD-MP2 significantly outperforms our previous implementation of ω-RI-CDD-MP2[6,30] for the computation of isotropic HFCCs.

2. THEORY

2.1. Notation. Throughout this publication we make use of the following indices:

- $\mu, \nu, \lambda, \sigma$: atomic orbital indices belonging to the AO basis $\{\chi_\mu\}$ of size N_{bf}.
- $\alpha, \beta, \gamma, \delta$: auxiliary basis indices belonging to the density fitting basis $\{\chi_\alpha\}$ of size N_{aux} (usually $N_{\mathrm{aux}} \approx 3 \cdot N_{\mathrm{bf}}$).
- P, Q, R, S: grid point indices belonging to the LS-THC grid of size N_{grid} (usually $N_{\mathrm{grid}} \approx 3 \cdot N_{\mathrm{aux}}$).
- i, j: occupied molecular orbital indices belonging to the MO basis $\{\phi_i\}$ of size N_{occ}.
- a, b: virtual molecular orbital indices belonging to the MO basis $\{\phi_a\}$ of size N_{virt} ($N_{\mathrm{virt}} \gg N_{\mathrm{occ}}$).
- η, η': spin indices, for either α- or β-electrons, with $\eta' \neq \eta$.
- κ: index of the Laplace quadrature points for the MP2 energy denominator with weights ω_κ (usually integration with 5−8 points is sufficiently accurate).
- k: index of the nucleus under consideration.

2.2. Review of the AO-MP2 Gradient. The unrestricted AO-MP2 energy with a Laplace transformation[49−51] for the energy denominator is given as

$$E_{AO-MP2} = -\frac{1}{2}\sum_{\kappa}\omega_\kappa \sum_{\eta\in\{\alpha,\beta\}} \mathcal{E}^{\eta}(\kappa) \tag{1}$$

with

$$\mathcal{E}^{\eta}(\kappa) = \sum_{\mu\nu\lambda\sigma} (\underline{\mu}\overline{\nu}|\underline{\lambda}\overline{\sigma})_{\eta\eta}(\mu\nu||\lambda\sigma) + \sum_{\mu\nu\lambda\sigma} (\underline{\mu}\overline{\nu}|\underline{\lambda}\overline{\sigma})_{\eta\eta'}(\mu\nu|\lambda\sigma) \tag{2}$$

for which the transformed ERIs are given by

$$(\underline{\mu}\overline{\nu}|\underline{\lambda}\overline{\sigma})_{\eta\eta'} = \sum_{\mu'\nu'\lambda'\sigma'} \underline{P}^{\eta}_{\mu'\mu}\overline{P}^{\eta}_{\nu'\nu}\underline{P}^{\eta'}_{\lambda'\lambda}\overline{P}^{\eta'}_{\sigma'\sigma}(\mu'\nu'|\lambda'\sigma') \tag{3}$$

and $\underline{\mathbf{P}}$ and $\overline{\mathbf{P}}$ are the usual pseudodensities, given by

$$\begin{aligned} \underline{P}^{\eta}_{\mu'\mu} &= \sum_{i} C^{\eta}_{\mu' i} e^{\varepsilon^{\eta}_{i} t^{(\kappa)}} C^{\eta}_{\mu i} \\ \overline{P}^{\eta}_{\nu'\nu} &= \sum_{a} C^{\eta}_{\nu' a} e^{-\varepsilon^{\eta}_{a} t^{(\kappa)}} C^{\eta}_{\nu a} \end{aligned} \tag{4}$$

To obtain the AO-MP2 gradient, eq 1 has to be differentiated with respect to a perturbation ξ. Since the focus of this work is on HFCCs, as an example for a property for which the basis functions are independent of the perturbation—here ξ'—the following derivation is restricted to this special case. An in-depth derivation of the AO-MP2 gradient equations, as well as a comparison to the MO-MP2 gradient, is available in refs 6 and 25.

In order to obtain the gradient of the AO-MP2 energy, eq 1 is differentiated with respect to ξ'

https://doi.org/10.1021/acs.jctc.2c00118
J. Chem. Theory Comput. 2022, 18, 5233−5245

$$\frac{\partial E_{\mathrm{AO-MP2}}}{\partial \xi'} = -\frac{1}{2}\sum_{\kappa} \omega_{\kappa} \sum_{\eta \in \{\alpha,\beta\}} \frac{\partial \mathcal{E}^{\eta}(\kappa)}{\partial \xi'} \tag{5}$$

with

$$\frac{\partial \mathcal{E}^{\eta}(\kappa)}{\partial \xi'} = 2\sum_{\mu'\mu} \overline{R}^{\eta}_{\mu'\mu}(\kappa)\frac{\partial \underline{P}^{\eta}_{\mu'\mu}}{\partial \xi'} + 2\sum_{\nu'\nu} \underline{R}^{\eta}_{\nu'\nu}(\kappa)\frac{\partial \overline{P}^{\eta}_{\nu'\nu}}{\partial \xi'} \tag{6}$$

and intermediates $\underline{\mathbf{R}}$ and $\overline{\mathbf{R}}$ given by

$$\begin{aligned}\overline{R}^{\eta}_{\mu'\mu}(\kappa) &= \sum_{\nu\lambda\sigma} (\mu'\overline{\nu}|\underline{\lambda}\overline{\sigma})_{\eta\eta}(\mu\nu||\lambda\sigma) + \sum_{\nu\lambda\sigma} (\mu'\overline{\nu}|\underline{\lambda}\overline{\sigma})_{\eta\eta'}(\mu\nu|\lambda\sigma)\\ \underline{R}^{\eta}_{\nu'\nu}(\kappa) &= \sum_{\mu\lambda\sigma} (\underline{\mu}\nu'|\underline{\lambda}\overline{\sigma})_{\eta\eta}(\mu\nu||\lambda\sigma) + \sum_{\mu\lambda\sigma} (\underline{\mu}\nu'|\underline{\lambda}\overline{\sigma})_{\eta\eta'}(\mu\nu|\lambda\sigma)\end{aligned} \tag{7}$$

The above **R** intermediates can be thought of as the contraction of all perturbation-independent parts of the gradient. Note that eq 5 only involves the derivative of the pseudodensities and no integral derivatives, as the basis functions are taken to be independent of ξ'. In order to avoid the evaluation of the derivatives of the perturbed occupied and virtual pseudodensities, these intermediates are expanded in terms of the regular occupied and virtual densities $\mathbf{P}_{\mathrm{occ}}$ and $\mathbf{P}_{\mathrm{virt}}$ as

$$\begin{aligned}\underline{P}^{\eta}_{\mu'\mu} &= (e^{\tau_{\kappa}\mathbf{P}^{\eta}_{\mathrm{occ}}\mathbf{F}^{\eta}}\mathbf{P}^{\eta}_{\mathrm{occ}})_{\mu'\mu}\\ \overline{P}^{\eta}_{\nu'\nu} &= (e^{-\tau_{\kappa}\mathbf{P}^{\eta}_{\mathrm{virt}}\mathbf{F}^{\eta}}\mathbf{P}^{\eta}_{\mathrm{virt}})_{\nu'\nu}\end{aligned} \tag{8}$$

Thus, the derivatives of eq 8 are given by

$$\begin{aligned}\frac{\partial \underline{\mathbf{P}}^{\eta}}{\partial \xi'} &= \frac{\partial e^{\tau_{\kappa}\mathbf{P}^{\eta}_{\mathrm{occ}}\mathbf{F}^{\eta}}}{\partial \xi'}\mathbf{P}^{\eta}_{\mathrm{occ}} + e^{\tau_{\kappa}\mathbf{P}^{\eta}_{\mathrm{occ}}\mathbf{F}^{\eta}}\frac{\partial \mathbf{P}^{\eta}_{\mathrm{occ}}}{\partial \xi'}\\ \frac{\partial \overline{\mathbf{P}}^{\eta}}{\partial \xi'} &= \frac{\partial e^{-\tau_{\kappa}\mathbf{P}^{\eta}_{\mathrm{virt}}\mathbf{F}^{\eta}}}{\partial \xi'}\mathbf{P}^{\eta}_{\mathrm{virt}} + e^{-\tau_{\kappa}\mathbf{P}^{\eta}_{\mathrm{virt}}\mathbf{F}^{\eta}}\frac{\partial \mathbf{P}^{\eta}_{\mathrm{virt}}}{\partial \xi'}\end{aligned} \tag{9}$$

By further making use of the identity

$$\mathbf{P}^{\eta}_{\mathrm{occ}}\mathbf{S} + \mathbf{P}^{\eta}_{\mathrm{virt}}\mathbf{S} = 1 \tag{10}$$

the perturbed virtual density can be related to the perturbed occupied density as

$$\frac{\partial \mathbf{P}^{\eta}_{\mathrm{virt}}}{\partial \xi'} = -\frac{\partial \mathbf{P}^{\eta}_{\mathrm{occ}}}{\partial \xi'} \tag{11}$$

Note again that eq 11 does not contain the derivative of the overlap matrix **S**, due to **S** being independent of ξ'. By making use of the above relations for the densities, eq 6 becomes

$$\begin{aligned}\frac{\partial \mathcal{E}^{\eta}(\kappa)}{\partial \xi'} &= 2\mathrm{tr}\left[\overline{\mathbf{R}}^{\eta}e^{\tau_{\kappa}\mathbf{P}^{\eta}_{\mathrm{occ}}\mathbf{F}^{\eta}}\frac{\partial \mathbf{P}^{\eta}_{\mathrm{occ}}}{\partial \xi'}\right] + 2\mathrm{tr}\left[\mathbf{P}^{\eta}_{\mathrm{occ}}\overline{\mathbf{R}}^{\eta}\frac{\partial e^{\tau_{\kappa}\mathbf{P}^{\eta}_{\mathrm{occ}}\mathbf{F}^{\eta}}}{\partial \xi'}\right]\\ &\quad - 2\mathrm{tr}\left[\underline{\mathbf{R}}^{\eta}e^{-\tau_{\kappa}\mathbf{P}^{\eta}_{\mathrm{virt}}\mathbf{F}^{\eta}}\frac{\partial \mathbf{P}^{\eta}_{\mathrm{occ}}}{\partial \xi'}\right]\\ &\quad + 2\mathrm{tr}\left[\mathbf{P}^{\eta}_{\mathrm{virt}}\underline{\mathbf{R}}^{\eta}\frac{\partial e^{-\tau_{\kappa}\mathbf{P}^{\eta}_{\mathrm{virt}}\mathbf{F}^{\eta}}}{\partial \xi'}\right]\end{aligned} \tag{12}$$

Cyclic permutation under the trace was applied above to obtain terms of the general form

$$\mathrm{tr}\left[\mathbf{B}\frac{\partial e^{\mathbf{A}}}{\partial \xi'}\right] = \mathrm{tr}\left[\mathbf{Y}\frac{\partial \mathbf{A}}{\partial \xi'}\right] \tag{13}$$

with

$$\mathbf{Y} = \sum_{k=1}^{\infty}\sum_{i=0}^{k-1}\frac{1}{k!}\mathbf{A}^{i}\mathbf{B}\mathbf{A}^{k-i-1} \tag{14}$$

which can be solved for **Y** by recursion, as detailed in refs 25 and 12. Let $\overline{\mathbf{Y}}^{\eta}$ be the solution of eq 13 with $\mathbf{A} \equiv \tau_{\kappa}\,\mathbf{P}^{\eta}_{\mathrm{occ}}\mathbf{F}^{\eta}$ and $\mathbf{B} \equiv \mathbf{P}^{\eta}_{\mathrm{occ}}\overline{\mathbf{R}}^{\eta}$, and let $\underline{\mathbf{Y}}^{\eta}$ be the solution with $\mathbf{A} \equiv -\,\tau_{\kappa}\,\mathbf{P}^{\eta}_{\mathrm{virt}}\mathbf{F}^{\eta}$ and $\mathbf{B} \equiv \mathbf{P}^{\eta}_{\mathrm{virt}}\underline{\mathbf{R}}^{\eta}$. Then, by making use of the other transformations outlined above, the derivative from eq 6 can be rewritten as

$$\frac{\partial \mathcal{E}^{\eta}(\kappa)}{\partial \xi'} = 2\mathrm{tr}\left[\mathcal{F}^{\eta}(\kappa)\frac{\partial \mathbf{h}}{\partial \xi'}\right] + 2\mathrm{tr}\left[\mathcal{P}^{\eta}(\kappa)\frac{\partial \mathbf{P}^{\eta}_{\mathrm{occ}}}{\partial \xi'}\right] \tag{15}$$

with

$$\begin{aligned}\mathcal{F}^{\eta}(\kappa) &= \tau_{\kappa}\overline{\mathbf{Y}}^{\eta}\mathbf{P}^{\eta}_{\mathrm{occ}} - \tau_{\kappa}\underline{\mathbf{Y}}^{\eta}\mathbf{P}^{\eta}_{\mathrm{virt}},\\ \mathcal{P}^{\eta}(\kappa) &= \tau_{\kappa}\mathbf{F}^{\eta}\overline{\mathbf{Y}}^{\eta} + \tau_{\kappa}\mathbf{F}^{\eta}\underline{\mathbf{Y}}^{\eta} + \mathbf{G}[\mathcal{F}^{\eta}(\kappa)] + \overline{\mathbf{R}}^{\eta}e^{\tau_{\kappa}\mathbf{P}^{\eta}_{\mathrm{occ}}\mathbf{F}^{\eta}}\\ &\quad - \underline{\mathbf{R}}^{\eta}e^{-\tau_{\kappa}\mathbf{P}^{\eta}_{\mathrm{virt}}\mathbf{F}^{\eta}}\end{aligned} \tag{16}$$

where intermediate $\mathbf{G}[\mathcal{F}^{\eta}(\kappa)]$ resembles the Fock matrix with $\mathcal{F}^{\eta}(\kappa)$ substituting for the density matrix; that is,

$$G_{\mu\nu}[\mathcal{F}^{\eta}(\kappa)] = \sum_{\lambda\sigma}\mathcal{F}^{\eta}_{\lambda\sigma}(\kappa)[2(\mu\nu|\lambda\sigma) - (\mu\sigma|\lambda\nu)] \tag{17}$$

Note that the first term in eq 15 only includes the derivative of the core Hamiltonian matrix as the integrals in the Fock matrix, from which this term originates from, are independent of ξ'.

Equation 15 permits an elegant solution for the perturbed density, avoiding the need to solve coupled-perturbed self-consistent field (CPSCF) equations for all perturbations ξ', by means of applying a AO-based *Z*-vector-like method[25] originally proposed by Handy and Schaefer.[52] The implicit first derivative of the occupied density can therefore be efficiently obtained by applying the density matrix-based Laplace-transform unrestricted CPSCF (DL-UCPSCF) method by Beer and Ochsenfeld.[53] The intricacies of this method are detailed in refs 53, 25, and 6.

To conclude, eqs 5 and 15 yield the first derivative of the AO-MP2 energy with respect to a perturbation ξ'. More specifically, if ξ' was an external electric field then eq 5 would yield permanent dipole moments, and if ξ' was equal to the nuclear magnetic moment M_k of a given nucleus k then the isotropic contribution to the HFCC of nucleus k in the absence of spin−orbit coupling would be obtained. The latter property will be used as a sample property for the newly developed THC-ω-RI-CDD-MP2 derivative method presented in section 2.4.

2.3. RI-CDD-MP2 HFCCs.

The computational bottleneck of obtaining the AO-MP2 gradient in eqs 5 and 15 are the integral contractions in the formation of the **R** matrix intermediates given by eq 7. Because forming the **R**-matrices involves the same contraction with the pseudodensities as the AO-MP2 energy, the computation of the gradient will *a priori* also have quintic scaling. As is common practice when dealing with these kinds of integral contractions, the RI approximation can be inserted into eq 7 to lower the computational cost as well as the memory requirements by avoiding the fourth-order ERI tensors. To further lower the prefactor of the integral transformations a PCD of the pseudodensities can be used, which is known as the Cholesky-decomposed pseudodensity (CDD) approach. The CDD method produces a set of so-called Cholesky pseudo-MO coefficient matrices $\underline{\mathbf{L}}$ and $\overline{\mathbf{L}}$ according to

$$\underline{P}^{\eta}_{\mu'\mu} = \sum_{i}^{\mathrm{rk}(\mathbf{P}_{\mathrm{occ}})} \underline{L}^{\eta}_{\mu' i}\underline{L}^{\eta}_{\mu i}$$

$$\overline{P}^{\eta}_{\nu'\nu} = \sum_{a}^{\mathrm{rk}(\mathbf{P}_{\mathrm{virt}})} \overline{L}^{\eta}_{\nu' a}\overline{L}^{\eta}_{\nu a} \tag{18}$$

which are used analogously to the regular MO coefficients. The combined RI-CDD approach leads to a reformulation of the integrals incorporated in the **R** intermediates as

$$(\underline{i}\overline{a}|\underline{j}\overline{b})_{\eta\eta'} = \sum_{\alpha} B^{\eta}_{\underline{i}\overline{a},\alpha}B^{\eta'}_{\underline{j}\overline{b},\alpha} \tag{19}$$

with

$$B^{\eta}_{\underline{i}\overline{a},\alpha} = \sum_{\beta}\sum_{\mu\nu}\underline{L}^{\eta}_{\mu i}\overline{L}^{\eta}_{\nu a}(\mu\nu|\beta)(\beta|\alpha)^{-1/2} \tag{20}$$

In combination with QQR-type integral screening the RI-CDD-MP2 gradient method was shown to yield cubic scaling for the computation of molecular gradients and HFCCs.[6] To further reduce the scaling, Vogler et al.[30] employed the attenuated Coulomb metric[54,55] in the RI approximation as well as the scaled-opposite spin (SOS)[56] approximation, which removes the same spin contribution entirely. Still, the expensive formation of the **R** intermediates has to be done for every Laplace point and thus constitutes the predominant part of the wall time for the evaluation of the MP2 gradient with respect to a perturbation ξ', even with the ω-RI-CDD-SOS-MP2 method.[6,30]

2.4. THC-CDD-MP2 HFCCs. ERIs are ubiquitous in electron correlation methods and their transformation and contraction usually represents the bottleneck of the calculation. This is especially the case when many different ERIs, that is, fully and partially transformed into the MO space or contracted with a perturbed density matrix, are needed, and their formation has to be carried out repeatedly, such as inside a Laplace expansion or during the iterative solution of amplitude equations. Since the scaling behavior of these operations is dependent on the dimensionality of the representation of the ERI tensor, a most compact representation is desirable. Of particular interest is thus the THC factorization, which in its AO formulation approximates an ERI as

$$(\mu\nu|\lambda\sigma) \approx \sum_{PQ} X^{P}_{\mu}X^{P}_{\nu}Z^{PQ}X^{Q}_{\lambda}X^{Q}_{\sigma} \tag{21}$$

and—in LS-THC—the **X**-matrices are simply obtained by evaluation of basis functions at the THC grid.[31] The analytical expression of the **Z**-matrix can be shown to be the solution to the normal equations associated with the least-squares equation of finding the THC factorization (see the Supporting Information). As has been shown previously,[33,34,36,39,41−43] the THC factorization can achieve major savings in computation time for intermediates involving ERI contractions, by reducing the representation of the ERIs to only second-order tensors. In this work, we make use of our recently reported low-scaling THC method[41] based on the ω-RI approximation for the ERIs contained in **Z** and natural blocking (NB).[57,58] However, in contrast to our work on THC-MP2 energies,[41] in the present work the AO ERIs are fitted, since the gradient for calculating the MP2 HFCCs is based on our RI-CDD approach to the computation of AO-MP2 energy gradients.[6] It is important to note here, that while the equations for the THC-based gradient method are derived by inserting the THC factorization into the equations of the RI-CDD-MP2 gradient with respect to ξ', there is no difference to directly differentiating the THC-AO-MP2 energy equations. This is the case, because neither **X** nor **Z** depend on the perturbation ξ' in the AO-THC formulation. This independence would not be given if either the MO-THC approach was used or for the more general derivative with respect to ξ, which would necessitate the derivatives of the THC tensors. In other words, by simply inserting the THC factorization into eq 7 the derivative of the THC-ω-RI-CDD-MP2 energy with respect to ξ' is obtained.

To reduce the computation time needed for forming the expensive **R**-matrices of the UMP2 gradient, the AO-THC factorization is inserted into eq 7 in its RI-CDD formulation to yield

$$\begin{aligned}
\overline{R}^{\eta}_{\mu'\mu}(\kappa) &= \textstyle\sum_j\sum_{ab}\sum_{PQRS} X^{P}_{\mu'}\overline{X}^{P,\eta}_{a}Z^{PQ}\underline{X}^{Q,\eta}_{j}\overline{X}^{Q,\eta}_{b}\cdot \\
&\quad [X^{R}_{\mu}\overline{X}^{R,\eta}_{a}Z^{RS}\underline{X}^{S,\eta}_{j}\overline{X}^{S,\eta}_{b} - X^{R}_{\mu}\overline{X}^{R,\eta}_{b}Z^{RS}\underline{X}^{S,\eta}_{j}\overline{X}^{S,\eta}_{a}] \\
&\quad + \textstyle\sum_j\sum_{ab}\sum_{PQRS} X^{P}_{\mu'}\overline{X}^{P,\eta}_{a}Z^{PQ}\underline{X}^{Q,\eta'}_{j}\overline{X}^{Q,\eta'}_{b}\cdot \\
&\quad X^{R}_{\mu}\overline{X}^{R,\eta}_{a}Z^{RS}\underline{X}^{S,\eta'}_{j}\overline{X}^{S,\eta'}_{b} \\
\underline{R}^{\eta}_{\nu'\nu}(\kappa) &= \textstyle\sum_{ij}\sum_{b}\sum_{PQRS} \underline{X}^{P,\eta}_{i}X^{P}_{\nu'}Z^{PQ}\underline{X}^{Q,\eta}_{j}\overline{X}^{Q,\eta}_{b}\cdot \\
&\quad [\underline{X}^{R,\eta}_{i}X^{R}_{\nu}Z^{RS}\underline{X}^{S,\eta}_{j}\overline{X}^{S,\eta}_{b} - \underline{X}^{R,\eta}_{i}\overline{X}^{R,\eta}_{b}Z^{RS}\underline{X}^{S,\eta}_{j}X^{S}_{\nu}] \\
&\quad + \textstyle\sum_{ij}\sum_{b}\sum_{PQRS} \underline{X}^{P,\eta}_{i}X^{P}_{\nu'}Z^{PQ}\underline{X}^{Q,\eta'}_{j}\overline{X}^{Q,\eta'}_{b}\cdot \\
&\quad \underline{X}^{R,\eta}_{i}X^{R}_{\nu}Z^{RS}\underline{X}^{S,\eta'}_{j}\overline{X}^{S,\eta'}_{b}
\end{aligned} \tag{22}$$

where $\underline{\mathbf{X}}$ and $\overline{\mathbf{X}}$ are the collocation matrices **X** transformed into the occupied and virtual Cholesky pseudo-MO basis, respectively. In MP2 it is often advisable to treat Coulomb- and exchange-like contributions separately,[58] thus the **R**-matrices are partitioned into $\mathbf{R}^{\mathrm{C}}$, the Coulomb-like contribution, and $\mathbf{R}^{\mathrm{X}}$, the exchange-like contribution.

*2.4.1. THC **R**-Matrices: Coulomb-like Contribution.* The Coulomb-like parts $\underline{\mathbf{R}}^{\mathrm{C}}$ and $\overline{\mathbf{R}}^{\mathrm{C}}$ are given by

$$\begin{aligned}
\overline{R}^{\eta,\mathrm{C}}_{\mu'\mu}(\kappa) &= \sum_{j}\sum_{ab}\sum_{PQRS} X^{P}_{\mu'}\overline{X}^{P,\eta}_{a}Z^{PQ}\underline{X}^{Q,\eta}_{j}\overline{X}^{Q,\eta}_{b}\cdot \\
&\quad X^{R}_{\mu}\overline{X}^{R,\eta}_{a}Z^{RS}\underline{X}^{S,\eta}_{j}\overline{X}^{S,\eta}_{b} \\
&\quad + \sum_{j}\sum_{ab}\sum_{PQRS} X^{P}_{\mu'}\overline{X}^{P,\eta}_{a}Z^{PQ}\underline{X}^{Q,\eta'}_{j}\overline{X}^{Q,\eta'}_{b}\cdot \\
&\quad X^{R}_{\mu}\overline{X}^{R,\eta}_{a}Z^{RS}\underline{X}^{S,\eta'}_{j}\overline{X}^{S,\eta'}_{b} \\
\underline{R}^{\eta,\mathrm{C}}_{\nu'\nu}(\kappa) &= \sum_{ij}\sum_{b}\sum_{PQRS} \underline{X}^{P,\eta}_{i}X^{P}_{\nu'}Z^{PQ}\underline{X}^{Q,\eta}_{j}\overline{X}^{Q,\eta}_{b}\cdot \\
&\quad \underline{X}^{R,\eta}_{i}X^{R}_{\nu}Z^{RS}\underline{X}^{S,\eta}_{j}\overline{X}^{S,\eta}_{b} \\
&\quad + \sum_{ij}\sum_{b}\sum_{PQRS} \underline{X}^{P,\eta}_{i}X^{P}_{\nu'}Z^{PQ}\underline{X}^{Q,\eta'}_{j}\overline{X}^{Q,\eta'}_{b}\cdot \\
&\quad \underline{X}^{R,\eta}_{i}X^{R}_{\nu}Z^{RS}\underline{X}^{S,\eta'}_{j}\overline{X}^{S,\eta'}_{b}
\end{aligned} \tag{23}$$

and can—in analogy to the THC-MP2 energy—be efficiently computed using sparse linear algebra.[41] In doing so, $\underline{\mathbf{R}}^{\mathrm{C}}$ and $\overline{\mathbf{R}}^{\mathrm{C}}$ are especially efficient to compute, as their formation only involves BLAS level 3 operations. For an efficient implementation it is important to realize, that for large enough molecules and appropriate ordering of the THC grid points, the collocation

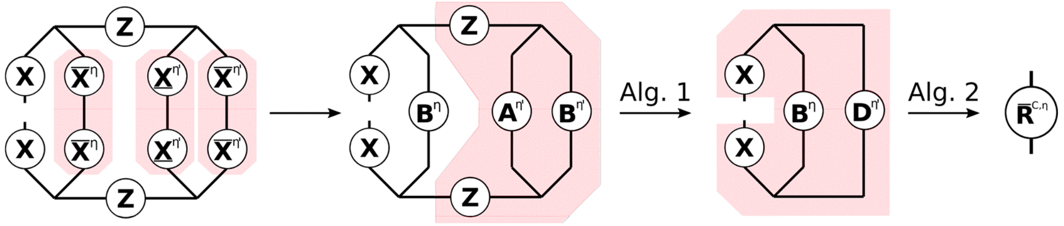

Figure 1. Tensor network representation of the contractions performed by Algorithms 1 and 2 for the formation of a Coulomb-like contribution $\overline{\mathbf{R}}^{\mathrm{C},\eta}$. By symmetry, $\underline{\mathbf{R}}^{\mathrm{C},\eta}$ can be formed analogously, but with intermediates **A** and **B** interchanged. Tensors contracted in ensuing steps are highlighted.

matrices **X** become sparse, while the **Z**-matrix, being the representation of the long-ranged $1/r$ operator, will always remain dense. By closer inspection of eq 23, it can be noticed, that the **X**-matrices corresponding to the MOs of the ket of the decomposed ERI and the **Z**-matrix are identical for all terms. Therefore, these matrices can be collected in an intermediate $\mathbf{D}^{\eta}$ given by Algorithm 1, where intermediates **A** and **B** are given by

$$A^{\mathrm{QS},\eta} = \sum_j \underline{X}_j^{Q,\eta} \underline{X}_j^{S,\eta},$$
$$B^{\mathrm{QS},\eta} = \sum_b \overline{X}_b^{Q,\eta} \overline{X}_b^{S,\eta}, \tag{24}$$

and represent the occupied and virtual pseudodensity in the grid basis, respectively. Additionally, the **Λ**-factorization of the **Z**-matrix, i.e., $\mathbf{Z} \equiv \mathbf{\Lambda}\mathbf{\Lambda}^{\mathrm{T}}$, is used to lower the prefactor of this step.[34,41]

Algorithm 1 Precontraction

```
procedure BUILD_D($\mathbf{A}^{\eta}, \mathbf{B}^{\eta}, \mathbf{\Lambda}$)
    $C^{QS,\eta} = A^{QS,\eta} B^{QS,\eta}$
    $D'^{\eta}_{\alpha\alpha'} = \sum_{QS} \Lambda^{Q}_{\alpha} C^{QS,\eta} \Lambda^{S}_{\alpha'}$
    $D^{PR,\eta} = \sum_{\alpha\alpha'} \Lambda^{P}_{\alpha} D'^{\eta}_{\alpha\alpha'} \Lambda^{R}_{\alpha'}$
    return $\mathbf{D}^{\eta}$
end procedure
```

As forming intermediate **D** requires a series of dense matrix–matrix-multiplications, this step will require the majority of the computation time for $\underline{\mathbf{R}}^{\mathrm{C}}$ and $\overline{\mathbf{R}}^{\mathrm{C}}$. However, Algorithm 1 has to be performed only once per Laplace point and electron spin. The final contribution to the **R**-matrices can then simply be obtained by a Schur product and two matrix–matrix-multiplications given by Algorithm 2.

Algorithm 2 Formation of a Coulomb-like contribution $\mathbf{R}^{\mathrm{C},\eta}$.

```
procedure BUILD_R^C($\mathbf{X}, \mathbf{C}^{\eta}, \mathbf{D}^{\eta'}$)
    $E^{PR,\eta} = C^{PR,\eta} D^{PR,\eta'}$
    $R^{\mathrm{C},\eta}_{\lambda'\lambda} = \sum_{PR} X^{P}_{\lambda'} E^{PR,\eta} X^{R}_{\lambda}$
    return $\mathbf{R}^{\mathrm{C},\eta}$
end procedure
```

The effects of Algorithms 1 and 2 can be best understood by visualizing the underlying tensor contractions in a tensor network diagram, as given in Figure 1. For an introduction of tensor network diagrams, also in the context of THC, refer to the work by Schutski et al.[46] Algorithms 1 and 2 are then pieced together with the algorithm for the exchange-like part, detailed in the next section, for the final Algorithm 4 in section 2.4.3.

*2.4.2. THC **R**-Matrices: Exchange-like Contribution.* Usually when higher than second-order tensors arise, the associated tensor contractions are either carried out with the tensors reshaped into matrices or batched over the dimensions exceeding matrix dimensionality in so-called tensor slices. For an efficient contraction when iterating over tensor slices it is advisable to make use of an underlying structure to reduce the dimensions of the slices, either by matrix decomposition of the slice or by neglecting noncontributing elements. If whole rows and columns are excluded based on some significance criterion, one arrives at the natural blocking (NB) formalism[57,58] for tensor contractions. NB relies on significance lists, which in general terms describe which pairs, of a general index pair i and j, contribute to a tensor contraction involving these indices. Mathematically speaking these lists are sets and thus can, in set-builder notation, be represented as

$$j_i \equiv \{j\}_i = \{j \mid |A_{ij}| > \varepsilon_{\mathrm{NB}}\} \tag{25}$$

where **A** is a screening matrix involving indices i and j, and $\varepsilon_{\mathrm{NB}}$ is the NB screening threshold. To avoid confusion, we use j_i as a shorthand notation for the set of all significant j for a particular index i and $\{j_i\}$ for the set of all j_i. If two elements in a set $\{j_i\}$ are identical, it technically becomes a multiset, as elements in sets are only allowed to have a multiplicity of 1. In set terminology, the set $\{i\}_j$ is the transpose of $\{j\}_i$ and can analogously determined from $\mathbf{A}^{\mathrm{T}}$ as

$$i_j \equiv \{i\}_j = \{i \mid |A_{ji}| > \varepsilon_{\mathrm{NB}}\} \tag{26}$$

or directly from $\{j_i\}$. Another important quantity is the number of significant pairs N_{ij}, which is defined as

$$N_{ij} = \sum_{i_j \in \{i_j\}} |i_j| \tag{27}$$

NB and THC work particularly well together for exchange-like contractions of ERIs, as within the THC formalism the necessary screening matrices can easily be constructed as outlined in the following. The following prototypical exchange-like ERI contraction from the THC-CDD-MP2 energy expression will serve as an example:

$$(\underline{i}\overline{a}|\underline{j}\overline{b})(\underline{i}\overline{b}|\underline{j}\overline{a}) \approx \sum_{PQRS} \underline{X}_i^P \overline{X}_a^P Z^{PQ} \underline{X}_j^Q \overline{X}_b^Q \cdot \underline{X}_i^R \overline{X}_b^R Z^{RS} \underline{X}_j^S \overline{X}_a^S \tag{28}$$

Two types of indices are present in the above equation, the orbital indices i and j (occupied space) as well as a and b (virtual space) and the THC auxiliary indices P, Q, R, and S. In the following discussion we use the LS formulation of THC, but the statements also hold for other THC variants. Thus, there are

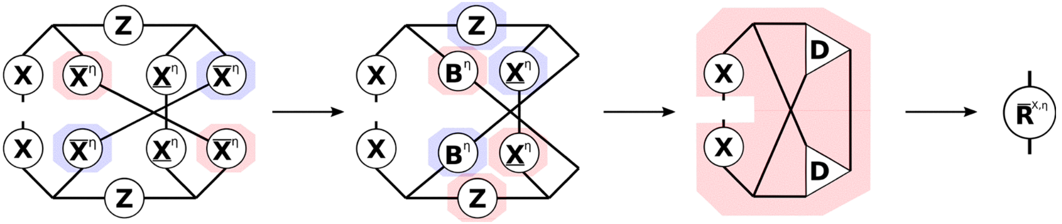

Figure 2. Tensor network representation of the contractions performed by Algorithm 3 for the formation of an exchange-like contribution $\overline{\mathbf{R}}^{X,\eta}$. By symmetry, $\underline{\mathbf{R}}^{X,\eta}$ can be formed analogously, however, in Algorithm 3 a different approach is used to reduce the prefactor. Tensors contracted in ensuing steps are highlighted.

three general types of index pairs: orbital−orbital, orbital−grid, and grid−grid index pairs. The set of significance lists for orbital-grid type pairs is especially easy to construct, since it can be directly derived from the collocation matrices **X**. For example, the set of all significant grid points *P* for a given occupied orbital *i* can be constructed as

$$P_i \equiv \{P\}_i = \{P|\, |\underline{X}_i^P| > \varepsilon_{\mathrm{NB}}\} \tag{29}$$

Significant orbital−orbital pairs are also easily obtained from the collocation matrices; for example, the set of significant virtual orbitals *a* for a given occupied orbital *i* can be built as

$$a_i \equiv \{a\}_i = \{a| \sum_P |\underline{X}_i^P||\overline{X}_a^P| > \varepsilon_{\mathrm{NB}}\} \tag{30}$$

The screening criterion from eq 30 can also be interpreted to yield only *ia* pairs, for which the orbitals have significant overlap and which produce non-negligible charge densities. For the development of low-scaling exchange-type contractions it is important to make use of the exponential coupling between all orbital indices. Orbital *i* couples to orbital *a* in an exponentially decaying fashion in the bra of the first ERI in eq 28. Likewise, orbital *j* also couples to orbital *a* in an exponentially decaying fashion in the ket of the second ERI. Thus, there is indirect exponential coupling between orbitals *i* and *j* via orbital *a* and the set of significant orbitals *i* for a given orbital *j* can be derived from the sets $\{a_j\}$, which is identical to $\{a_i\}$, and $\{a_i\}$:

$$i_j \equiv \{i\}_j = \{i|a_i \cap a_j \neq \varnothing\} \tag{31}$$

With the significance lists given by eqs 29, 30, and 31, an asymptotically linear scaling algorithm for the exchange-like energy contribution to MP2 can be devised. The algorithm is detailed in the Supporting Information and close to linear scaling is demonstrated. Here, however, the focus lies on the exchange-like parts of the **R**-matrices, which are conceptually similar, but different in that two AO indices remain uncontracted. The tensor contractions necessary for forming the $\mathbf{R}^X$ parts can again best be understood from the tensor network diagram in Figure 2.

While Figure 2 only shows the $\overline{\mathbf{R}}^X$ part, the $\underline{\mathbf{R}}^X$ contribution can be constructed analogously. First, intermediates **A** or **B** are formed from the collocation matrices $\underline{\mathbf{X}}$ or $\overline{\mathbf{X}}$, respectively. Second, the remaining collocation matrices, the **Z**-matrices and intermediates **A** or **B** are contracted to the third-order tensor intermediate **D**, where the symmetry of the tensors is used to reduce the operation count. The idea for an efficient implementation is then as follows: to avoid storing third-order tensors, the contraction is batched over the occupied orbital index common to both $\underline{\mathbf{R}}$ and $\overline{\mathbf{R}}$, and to reduce the cost of the `dgemm` operations within the loop NB is applied. In this way separate algorithms for $\underline{\mathbf{R}}^X$ and $\overline{\mathbf{R}}^X$ can be formulated, which are presented in the Supporting Information. By closer inspection, however, it can be seen, that both $\mathbf{R}^X$-matrices share the most expensive to compute intermediate, which incorporates the **Z**-matrix. Therefore, a joint computation as given by Algorithm 3 is preferred.

Algorithm 3 Formation of the exchange-like contributions $\underline{\mathbf{R}}^{X,\eta}$ and $\overline{\mathbf{R}}^{X,\eta}$.

```
 1: procedure BUILD_R^X($\mathbf{X}, \underline{\mathbf{X}}^\eta, \overline{\mathbf{X}}^\eta, \mathbf{A}^\eta, \mathbf{B}^\eta, \mathbf{Z}$)
 2:     build $\{S_j\}(\equiv \{Q_j\})$ from $|\underline{X}_j^{S,\eta}|$ (eq. 29)
 3:     build $\{b_R\}$ from $|\overline{X}_b^{R,\eta}|$ (eq. 29)
 4:     build $\{b_j\}$ from $\sum_Q |\underline{X}_j^{Q,\eta}||\overline{X}_b^{Q,\eta}|$ (eq. 30)
 5:     build $\{R_j\}(\equiv \{P_j\})$ from $\{b_R\}$ and $\{b_j\}$ (eq. 31)
 6:     $\mathbf{E}, \mathbf{F} = \mathbf{0}_{N_{\mathrm{grid}},N_{\mathrm{grid}}}$
 7:     for $j = 1$ to $j \leq \mathrm{rk}(\underline{\mathbf{P}}^\eta)$ do
 8:         for all $R \in \{R\}_j$ and $S \in \{S\}_j$ do
 9:             $C^{RS,\eta} = Z^{RS}\underline{X}_j^{S,\eta}$
10:         end for
11:         for all $P \in \{P\}_j$ and $R \in \{R\}_j$ do
12:             $D^{PR,\eta} = \sum_{Q\in\{Q\}_j} C^{PQ,\eta}B^{QR,\eta}$
13:         end for
14:         for all $P \in \{P\}_j$ and $R \in \{R\}_j$ do
15:             $E^{PR,\eta} \mathrel{+}= D^{PR,\eta}D^{RP,\eta}$
16:         end for
17:         for all $P \in \{P\}_j$ and $R \in \{R\}_j$ do
18:             $D^{PR,\eta} \times= A^{PR,\eta}$
19:         end for
20:         for all $P \in \{P\}_j$ and $S \in \{S\}_j$ do
21:             $F^{PS,\eta} \mathrel{+}= \sum_{R\in\{R\}_j} D^{PR,\eta}C^{RS,\eta}$
22:         end for
23:     end for
24:     $\overline{R}_{\mu'\mu}^{X,\eta} = \sum_{PR} X_{\mu'}^P E^{PR,\eta} X_\mu^R$
25:     $\underline{R}_{\nu'\nu}^{X,\eta} = \sum_{PS} X_{\nu'}^P F^{PS,\eta} X_\nu^S$
26:     return $\overline{\mathbf{R}}^{X,\eta}, \underline{\mathbf{R}}^{X,\eta}$
27: end procedure
```

First, according to eqs 29, 30, and 31 all necessary significance lists are computed and then the precursor intermediates to $\underline{\mathbf{R}}^X$ and $\overline{\mathbf{R}}^X$, that is, the matrices **E** and **F**, are accumulated in a loop over the common occupied orbital index *j*. Lines 12 and 21 represent the bottleneck of the algorithm as their evaluation formally scales as $O(N_{\text{grid}}^3 N_{\text{occ}})$. However, since all involved grid indices P, Q, and R are connected to j through the significance lists $\{S_j\}$ (identical to $\{Q_j\}$) and $\{R_j\}$ (identical to $\{P_j\}$), the size of the involved matrices in NB format is asymptotically constant. Therefore, as N_{occ} grows linearly with the molecule size, the formation of the $\mathbf{R}^{\text{X}}$-parts can be done in linear scaling time. For this, appropriate thresholds have to be chosen for the formation of the significance lists. Instead of using the same threshold for all pairs, we identify three different types of lists: (1) grid-occupied orbital index pairs, e.g., $\{S_j\}$, (2) grid-virtual orbital index pairs, e.g., $\{b_R\}$, where, in both cases, the orbital index is coupled to the grid index directly by a collocation matrix, and (3) virtual-occupied orbital index pairs, e.g., $\{b_j\}$, which are coupled in real-space over grid points. While the final algorithm only requires the $\{S_j\}$ and $\{R_j\}/\{P_j\}$ lists, the selection of index pairs included in $\{b_R\}$ and $\{b_j\}$ is still important, as the $\{R_j\}/\{P_j\}$ lists are built from these lists analogously to eq 31.

*2.4.3. THC **R**-Matrices: Final Algorithm.* Piecing together Algorithms 1 and 2 for the Coulomb-like part and Algorithm 3 for the exchange-like part, the final algorithm for the formation of the **R**-matrices is given by Algorithm 4.

Algorithm 4 Final algorithm for $\overline{\mathbf{R}}$ and $\underline{\mathbf{R}}$

```
procedure BUILD_R($\mathbf{X}, \underline{\mathbf{X}}^\eta, \overline{\mathbf{X}}^\eta, \mathbf{Z}, \mathbf{\Lambda}$)
    $\mathbf{A}^\alpha, \mathbf{A}^\beta, \mathbf{B}^\alpha, \mathbf{B}^\beta, \mathbf{D}^\alpha, \mathbf{D}^\beta = \mathbf{0}_{N_{\text{grid}},N_{\text{grid}}}$
    for $\eta \in \{\alpha, \beta\}$ do
        $\mathbf{A}^\eta = \underline{\mathbf{X}}^\eta(\underline{\mathbf{X}}^\eta)^{\text{T}}$
        $\mathbf{B}^\eta = \overline{\mathbf{X}}^\eta(\overline{\mathbf{X}}^\eta)^{\text{T}}$
        $\mathbf{D}^\eta = \text{BUILD\_D}(\mathbf{A}^\eta, \mathbf{B}^\eta, \mathbf{\Lambda})$
    end for
    $\overline{\mathbf{R}}^\alpha, \overline{\mathbf{R}}^\beta, \underline{\mathbf{R}}^\alpha, \underline{\mathbf{R}}^\beta = \mathbf{0}_{N_{\text{bf}},N_{\text{bf}}}$
    for $\eta \in \{\alpha, \beta\}$ do
        $\overline{\mathbf{R}}^\eta$ += BUILD_R$^{\text{C}}(\mathbf{X}, \mathbf{B}^\eta, \mathbf{D}^\eta)$
        $\overline{\mathbf{R}}^\eta$ += BUILD_R$^{\text{C}}(\mathbf{X}, \mathbf{B}^\eta, \mathbf{D}^{\eta'})$
        $\underline{\mathbf{R}}^\eta$ += BUILD_R$^{\text{C}}(\mathbf{X}, \mathbf{A}^\eta, \mathbf{D}^\eta)$
        $\underline{\mathbf{R}}^\eta$ += BUILD_R$^{\text{C}}(\mathbf{X}, \mathbf{A}^\eta, \mathbf{D}^{\eta'})$
        $\overline{\mathbf{R}}^\eta, \underline{\mathbf{R}}^\eta$ += BUILD_R$^{\text{X}}(\mathbf{X}, \underline{\mathbf{X}}^\eta, \overline{\mathbf{X}}^\eta,$
          $\mathbf{A}^\eta, \mathbf{B}^\eta, \mathbf{Z})$
    end for
    return $\overline{\mathbf{R}}^\alpha, \overline{\mathbf{R}}^\beta, \underline{\mathbf{R}}^\alpha, \underline{\mathbf{R}}^\beta$
end procedure
```

Overall, Algorithm 4 has to be executed once per Laplace point and is separated into a precontraction phase and the phase for the actual formation of the contributions to $\underline{\mathbf{R}}$ and $\overline{\mathbf{R}}$. In the precontraction phase intermediates $\mathbf{D}^\eta$ are formed, which represent the most expensive part for the Coulomb-like terms, as the subsequent calls to Algorithm 2 only contribute a Schur product and two `dgemm` operations. These `dgemm` calls contribute a negligible overhead compared with line 3 of Algorithm 1, as the dimensions of the matrices involved are reduced. In total, however, Algorithm 3 will dominate the runtime for forming the **R**-matrices due to its formal $O(N^4)$ scaling.

3. COMPUTATIONAL DETAILS

The above-described THC-ω-RI-CDD-MP2 HFCC code is implemented within our quantum chemistry package FERMIONS++.[59−61] For the THC-based HFCC calculations the hand-optimized grids by Martínez and co-workers[38] were used together with the Dunning cc-pVXZ (X ∈ {D, T}) basis sets[62] and the corresponding auxiliary basis sets. For the phosphorus atoms in the DNA backbone, the fluorine grids were used without loss of accuracy as reported in our work on THC-MP2 energies.[41] All calculations were carried out without the frozen-core approximation. All preceding SCF calculations were converged to an energy difference of 10^{-8} H and a **FPS−SPF** commutator difference of 10^{-7} using DIIS acceleration.[63] For the gradient calculations seven Laplace points were used in the expansion and the DL-UCPSCF algorithm was converged to an error of 10^{-4} for all molecules of the benchmark set in section 4. For all subsequent calculations on larger molecules, a threshold of 10^{-3} was used. These settings were shown to yield errors below 1 MHz.[6,30] For the assessment of the accuracy of the THC-ω-RI-CDD-MP2 HFCCs against other methods, the standard orientation was used. For the THC factorization of the ERIs an attenuation strength of 0.1 in the attenuated Coulomb metric was used[54,55] and the same general protocol for screening based on integral partition bounds (IPBs)[64] and NB, as in our work on THC-MP2 energies, was followed, although adjusted to fit ERIs in the AO basis.[41] All timings are done on an AMD EPYC 7302 (3.30 GHz) CPU node with 256 GB RAM and 1.7 TB of SSD disk space.

4. RESULTS AND DISCUSSION

First, the accuracy of the newly developed THC-ω-RI-CDD-MP2 method for the calculation of isotropic HFCCs is assessed against our reference ω-RI-CDD-MP2 implementation.[6,30] Next, the thresholds necessary for the screening in the expensive exchange-like contribution $\mathbf{R}^{\text{X}}$ are optimized on a set of medium-sized organic radicals. Finally, the scaling of the THC-ω-RI-CDD-MP2 method is analyzed and timings are compared to the ω-RI-CDD-MP2 reference for a set of representative radicals.

4.1. Accuracy of THC-ω-RI-CDD-MP2 HFCCs.

Throughout this publication, our ω-RI-CDD-MP2 implementation for the computation of HFCCs by Vogler et al.,[6,30] which was verified against the RI-MP2 implementation in the ORCA program package,[65] will serve as reference. The original implementation, however, made use of the SOS approximation and excluded the exchange-like terms. To enable a fair comparison, the exchange-like terms were added analogously to the earlier implemented RI-CDD-based AO-MP2 gradient,[6] albeit with the attenuated Coulomb metric for the RI integrals. For the comparison, first the accuracy of the presented THC-ω-RI-CDD-MP2 method for HFCCs is assessed. The THC-ω-RI-CDD-MP2 method is benchmarked using a set of 12 organic radicals from a recent study[7] on the effects of electron correlation, molecular dynamic contributions, and solvation effects on HFCCs. Mean absolute deviations (MAD), root-mean-square deviations (RMSD), and absolute maximum deviations (MAX) are given in Table 1. We note that we used all 12 radicals for the comparison, even though, as Vogler et al.[7] pointed out, some molecules are spin contaminated. While the latter certainly has an effect on the reliability of the results, when comparing to experiment, it should not influence the comparison of different methods.

https://doi.org/10.1021/acs.jctc.2c00118
J. Chem. Theory Comput. 2022, 18, 5233−5245

Table 1. Errors of the HFCCs Obtained with the THC-ω-RI-CDD-MP2 Method Compared to the ω-RI-CDD-MP2 Reference Implementation for the HFCC Benchmark Set from Vogler et al.[7] and the cc-pVXZ/cc-pVXZ-RI (X ∈{D, T}) Basis Sets

basis set	MAD[a]	RMSD[a]	MAX[a]
cc-pVDZ	0.304	0.478	1.822
cc-pVTZ	0.092	0.167	0.675

[a] Deviations in MHz.

Table 1 shows that the mean errors for the THC-ω-RI-CDD-MP2 method are below 1 MHz for both basis sets, while the MAX error corresponds to atoms with high spin density, that is, ^{19}F in the CF$_3$ radical for the double-ζ basis set and ^{11}B in the BH$_3$ radical for the triple-ζ basis set. While for these nuclei the absolute error is larger, the relative error is still below 1%, as due to their high spin density the HFCCs are large in magnitude. The origin of these errors is mainly based on the following two shortcomings: (1) Using the hand-optimized THC grids by Martínez and co-workers[38] for AO-THC incurs additional errors over MO-THC as these grids were optimized for fitting MO-based ERIs, for which the orbital space is much more compact compared to ERIs in the AO basis. This phenomenon was observed similarly in our recent work on THC-ω-RI-CDD-MP2 energies.[41] (2) Since grid-based THC uses DFT-like integration grids, THC-based properties are likewise prone to not being rotationally invariant. In DFT the problem is alleviated through larger grids, which THC cannot make use of without forfeiting the reduction in computational cost compared to the respective canonical method. However, we found that these rotational errors are on the order of 0.01−0.05 MHz, depending on the magnitude of the spin density on the respective nucleus. Overall, we consider a mean deviation of less than 1 MHz to be less than the method error of RI-MP2 and certainly accurate enough, when compared against experimental results, where, as shown by Vogler et al.,[7] other effects like dynamic contributions or solvation effects contribute significantly.

4.2. Threshold Optimization. After having established that the presented THC-ω-RI-CDD-MP2 method provides reliable HFCCs, the focus is now on optimizing the time complexity of the underlying algorithm while preserving the accuracy. An obvious point for optimization is the formation of the exchange-like parts $\mathbf{R}^X$, for which Algorithm 3 has quartic scaling if no screening is applied. However, as discussed in section 2.4.2, by applying NB with carefully chosen thresholds, the formation of $\mathbf{R}^X$ should be possible with linear time complexity. As outlined in section 2.4.2, different thresholds will be used in the screening process for the different types of significance lists. We associate the thresholds ε_{Sj}, ε_{bR}, and ε_{bj} with the significance lists $\{S_j\}$, $\{b_R\}$, and $\{b_j\}$, respectively. Since ε_{Sj} directly determines the pairs included in $\{S_j\}$, and $\varepsilon_{bR}/\varepsilon_{bj}$ only indirectly determine the pairs in $\{R_j\}$, the optimization of these thresholds is simplified by separately optimizing ε_{Sj} and $\varepsilon_{bR}/\varepsilon_{bj}$. The thresholds are first optimized for the smaller double-ζ basis set and later transferred to the triple-ζ basis. For this, we chose a set of six medium-sized radical molecules and supramolecular assemblies, which are large enough for the screening to have effect. For further information on this benchmark set see the Supporting Information. Table 2 summarizes the errors and the resulting average number of significant pairs $\bar{N}_{Sj}$ in $\{S_j\}$ for the optimization of ε_{Sj}.

Table 2. Threshold Optimization of ε_{Sj}: Errors of the HFCCs and Average Numbers of Significant Pairs ($\bar{N}_{Sj}$) from the Screening Benchmark Set, Obtained with the Chosen Threshold for ε_{Sj} (ε_{bR} = 0, ε_{bj} = 0, cc-pVDZ)

ε_{Sj}	$\bar{N}_{Sj}$[a]	MAD[b]	RMSD[b]	MAX[b]
10^{-6}	77.6	2.8×10^{-7}	8.7×10^{-7}	1.1×10^{-5}
10^{-5}	57.9	8.2×10^{-6}	2.0×10^{-5}	1.8×10^{-4}
10^{-4}	36.7	1.5×10^{-4}	3.5×10^{-4}	3.4×10^{-3}
10^{-3}	12.8	3.5×10^{-3}	1.1×10^{-2}	1.9×10^{-1}
10^{-2}	5.8	9.2×10^{-2}	3.6×10^{-1}	6.2×10^{0}

[a] Ratio in %. [b] Deviations in MHz.

While for threshold values of 10^{-6} through 10^{-4} the error remains negligible, the screening shows an effect in that $\bar{N}_{Sj}$ indicates that only roughly a third of the pairs in $\{S_j\}$ are necessary for this accuracy. The mean errors grow roughly linearly with loosening thresholds and remain sufficiently small for a range of threshold values. For $\varepsilon_{Sj} \geq 10^{-3}$ especially the MAX error deteriorates above 1 MHz, while the MAD remains below 0.1 MHz. For the optimization of ε_{bR} and ε_{bj}, combinations of thresholds have to be considered, since they determine, through eq 31, the significant pairs in $\{R_j\}$. The results of this optimization are shown in Figure 3 as a heatmap.

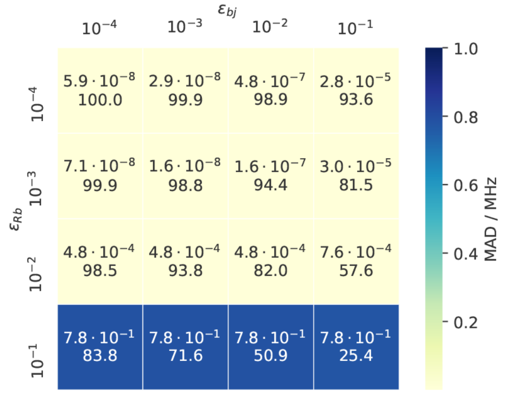

ε_{Rb} \ ε_{bj}	10^{-4}	10^{-3}	10^{-2}	10^{-1}
10^{-4}	$5.9 \cdot 10^{-8}$ 100.0	$2.9 \cdot 10^{-8}$ 99.9	$4.8 \cdot 10^{-7}$ 98.9	$2.8 \cdot 10^{-5}$ 93.6
10^{-3}	$7.1 \cdot 10^{-8}$ 99.9	$1.6 \cdot 10^{-8}$ 98.8	$1.6 \cdot 10^{-7}$ 94.4	$3.0 \cdot 10^{-5}$ 81.5
10^{-2}	$4.8 \cdot 10^{-4}$ 98.5	$4.8 \cdot 10^{-4}$ 93.8	$4.8 \cdot 10^{-4}$ 82.0	$7.6 \cdot 10^{-4}$ 57.6
10^{-1}	$7.8 \cdot 10^{-1}$ 83.8	$7.8 \cdot 10^{-1}$ 71.6	$7.8 \cdot 10^{-1}$ 50.9	$7.8 \cdot 10^{-1}$ 25.4

Figure 3. Threshold optimization of ε_{bR} and ε_{bj}: In each cell the MADs (in MHz) of the HFCCs (top value) and the average numbers of significant pairs ($\bar{N}_{Rj}$ in %, bottom value) are given as an average from the screening benchmark set (ε_{Sj} = 0, cc-pVDZ).

From Figure 3 it can be seen, that the MAD is stable through a wide range of threshold values, only significantly worsening when choosing $\varepsilon_{bR} > 10^{-2}$, irrespective of the value chosen for ε_{bj}. The observation that even for looser thresholds, for example, $\varepsilon_{bR} = \varepsilon_{bj} = 10^{-2}$, still roughly 80% of the pairs in $\{R_j\}$ are significant stems from the fact that indices R and j are coupled indirectly over a virtual orbital b. According to eq 31 a pair of indices R and j is only considered insignificant, if they do not share significant overlap with any virtual orbital b. Therefore, $\bar{N}_{Rj}$ will always be greater than $\bar{N}_{Sj}$ for any sensibly chosen combination of thresholds.

With the separate optimization of ε_{Sj} and $\varepsilon_{bR}/\varepsilon_{bj}$ as a starting point, different combinations of these three thresholds were tested. The best trade-off between accuracy and the number of significant pairs appeared to be for the thresholds $\varepsilon_{Sj} = 10^{-3}$, $\varepsilon_{bR} = 10^{-2}$, and $\varepsilon_{bj} = 10^{-2}$, for which the errors are summarized in Table 3.

The chosen combination of thresholds provides good accuracy for both basis sets, with the errors for the triple-ζ

Table 3. Errors of the HFCCs from the Screening Benchmark Set, Obtained with the Chosen Thresholds ($\varepsilon_{Sj} = 10^{-3}$, $\varepsilon_{bR} = 10^{-2}$, $\varepsilon_{bj} = 10^{-2}$) for the THC-$\omega$-RI-CDD-MP2 method referenced against the same method with disabled screening

basis set	MAD[a]	RMSD[a]	MAX[a]
cc-pVDZ	0.004	0.011	0.189
cc-pVTZ	0.023	0.077	0.941

[a] Deviations in MHz.

basis being somewhat larger. The latter could be improved through a separate optimization of the thresholds for the triple-ζ basis. However, in view of the fact that the mean errors are still below 0.1 MHz, the thresholds optimized for the double-ζ basis set seem to be suitable for the larger basis set as well.

4.3. Timings and Scaling. With the optimized screening thresholds at hand, the scaling behavior of the THC-ω-RI-CDD-MP2 method for the computation of HFCCs is analyzed and compared to the previous ω-RI-CDD-MP2 implementation.[6,30] For the assessment of the asymptotic scaling behavior, HFCCs for a series of linear alkyl radicals C_nH_{2n+1} are computed. In Figure 4 the timings are shown together with the underlying contributions from the most significant steps for both basis sets.

As is evident from Figure 4, the overall scaling behavior is governed by the contribution from the exchange-like parts of **R** (Algorithm 3), while the Coulomb-like terms (Algorithms 1 and 2) and the overhead from obtaining the THC factorization only contribute marginally. For both basis sets, the THC-ω-RI-CDD-MP2 method reaches subquadratic scaling, while the scaling is also partly influenced by the Fock matrix builds in the Z-vector step. The increased cost of the Z-vector step for larger fragment sizes in the case of the double-ζ basis set is also the reason for the overall scaling exponent slightly deteriorating beyond $C_{140}H_{281}$ to 1.62. To prevent this unfavorable scaling for the larger triple-ζ basis set, the recommendations by Laqua et al.,[66] which are default settings in FermiONs++, are followed, and the recently presented seminumerical exchange method (sn-LinK) is used for the exchange part of the Fock matrices. The latter makes the overall scaling for the cc-pVTZ basis set almost entirely be governed by Algorithm 3 (blue bars). Therefore, the scaling reduces to close to linear for the largest fragment size considered. The same is true for the cc-pVDZ basis set, for which Algorithm 3 reaches an apparent asymptotic scaling of 1.3.

To go toward more chemically relevant systems and beyond what was possible with our previous ω-RI-CDD-MP2 implementation, the scaling behavior for spin-labeled adenine−thymine base pair stacks $(AT)_n$ is assessed.

Figure 5 (left) shows the scaling behavior for spin-labeled DNA fragments up to seven repetition units or 5101 basis functions. As expected, the onset for subquadratic scaling is for greater fragment sizes compared to the alkyl radicals. Nonetheless, the scaling exponent decreases to 1.87 for $(AT)_6 \rightarrow (AT)_7$. Further reduction with increasing fragment size can be expected based on the growth rate of the number of significant pairs in $\{S_j\}$ and $\{R_j\}$. In Figure 5 (right) the logarithm of the total number of significant pairs is shown for all index pairs relevant for Algorithm 3. The runtime of Algorithm 3 is mainly governed by N_{Sj} and N_{Rj} and relies on only a constant number of grid points being significant for a given occupied orbital, see section 2.4.2. If only a constant number of grid points is significant for a given occupied orbital, then N_{Sj} and N_{Rj} will grow linearly with increasing molecule size. The latter is demonstrated for N_{Sj}, that is, the grid point-occupied orbital pair directly coupled by a collocation matrix. N_{Rj} is inherently greater than N_{Sj}, since $\{R_j\}$ is formed from eq 31 with coupling of R and j over a virtual orbital b. The latter is also the reason for the scaling exponent not quite reducing to 1.0 and there being an onset for the close to linear scaling. This also explains why Algorithm 3 reaches subquadratic scaling for the DNA system, but not quite linear scaling. Nonetheless, the THC-ω-RI-CDD-MP2 method also reaches subquadratic scaling for the spin-labeled DNA fragments under consideration and allows for the computation of HFCCs for almost 500 atoms and more than 5000 basis functions.

While the asymptotic scaling exponent of a quantum chemical method is certainly important for the treatment of large (bio)chemical systems, the prefactor oftentimes determines the applicability of a method for a certain problem. In other words, a method can be linear scaling, but have a prefactor so large, that calculations still remain unfeasible. Another aspect which determines feasibility are memory/storage requirements, oftentimes governed by the necessity to store ERIs or amplitude tensors present in electron correlation methods. These aspects are considered in the following for a comparison of the ω-RI-CDD-MP2 method in its all-nuclei variant[6,30] and the presented THC-ω-RI-CDD-MP2 method for a collection of organic radicals. An additional comparison against the selected-nuclei

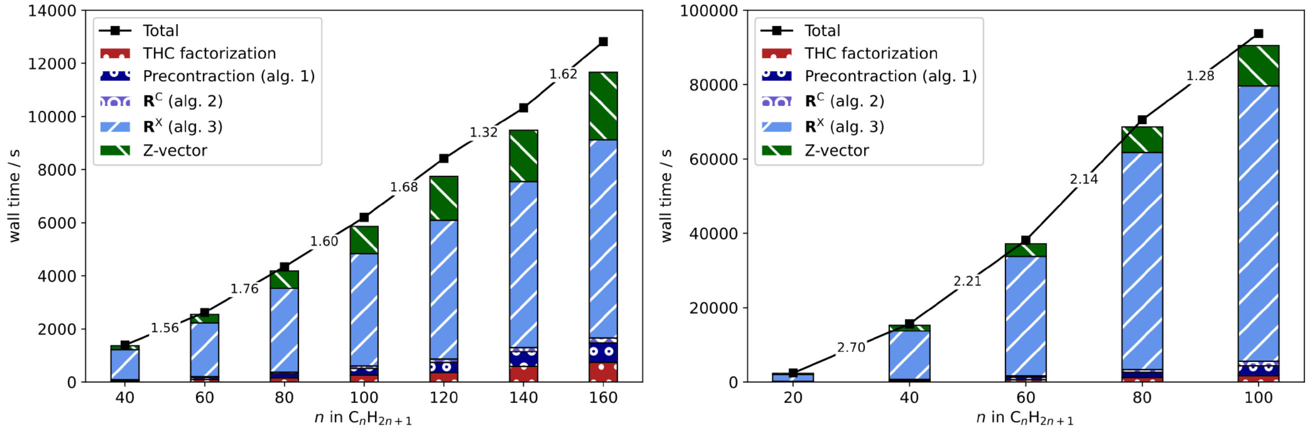

Figure 4. Detailed timings for the computation of HFCCs with the THC-ω-RI-CDD-MP2 method (black) for linear alkyl radicals C_nH_{2n+1} as well as significant contributions from underlying steps (colored bars) for the cc-pVDZ (left) and cc-pVTZ (right) basis sets. The numbers between fragments correspond to the scaling with respect to the preceding fragment.

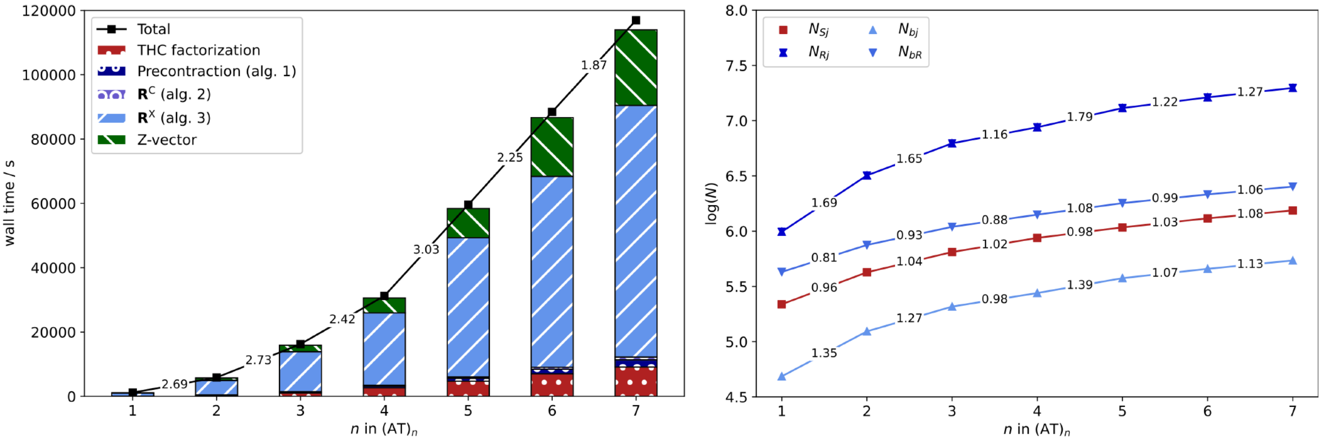

Figure 5. Detailed timings for the computation of HFCCs with the THC-ω-RI-CDD-MP2 method (black) for spin-labeled (AT)$_n$ radicals as well as significant contributions from underlying steps (colored bars) for the cc-pVDZ basis set. Scaling behavior of the number of significant index pairs $\{S_j\}$ (red) and $\{R_j\}$ (dark blue) for increasing fragment sizes (right). The numbers between fragments correspond to the scaling with respect to the preceding fragment.

variant of ω-RI-CDD-MP2,[30] which was proposed to alleviate some of the shortcomings of the ω-RI-CDD-MP2 method, is given in the Supporting Information. Here, the focus is on typical applications on medium-sized organic radicals. Table 4 summarizes the estimated storage requirements M_{est} and the wall times t for the radicals, as well as the speedups S relative to the ω-RI-CDD-MP2 implementation. More information on how the storage requirements are estimated is given in the Supporting Information.

Table 4. Comparison of the Memory Requirements M_{est}, Timings t, and Relative Speedups S of the THC-ω-RI-CDD-MP2 Method with the Previously Implemented ω-RI-CDD-MP2 Method

		ω-RI-CDD-MP2		THC-ω-RI-CDD-MP2		
system	N_{bf}	M_{est}/GB	t/h	M_{est}/GB	t/h	S
			cc-pVDZ			
$C_{60}H_{121}$	1445	201.0	101.8	11.7	0.7	145
TEMPO$_{H_2O}$	1444	208.5	345.9	11.7	1.5	230
(glu)$_4$	1074	90.0	380.2	5.9	0.7	540
PTMA$_3$	1102	93.8	620.9	6.5	1.2	517
(AT)$_2$	1566	286.0	1111.0	23.1	1.9	585
			cc-pVTZ			
$C_{20}H_{41}$	1174	66.1	363.3	8.7	0.6	606
TEMPO	582	8.2	160.1	2.1	0.2	891
Tyr	530	6.6	99.4	1.4	0.1	780
Thy	1260	86.6	1346.2[a]	8.7	1.1	1224
(AT)$_1$	1982	340.4	2727.8[a]	20.7	3.1	880

[a] Timings are estimated conservatively based on the time taken for the first Laplace point.

THC has a natural advantage over RI-based methods when it comes to storage requirements. In THC-based methods the largest tensors necessary to keep in memory or store on disk are second-order tensors of dimension $N_{\text{grid}} \times N_{\text{grid}}$. For RI-based methods the dimensionality of the factorized representation of the fourth-order ERI tensor increases to three with dimensions $N_{\text{occ}} \times N_{\text{virt}} \times N_{\text{aux}}$ in the MO basis. Therefore, THC-ω-RI-CDD-MP2 is superior with an order of magnitude less storage requirements, as can be seen from Table 4. Furthermore, the THC-based method considerably outperforms ω-RI-CDD-MP2 in terms of computation time with speedups up to roughly 600 for the double-ζ basis set and 800−1200 for the triple-ζ basis set. The relative speedups are somewhat reduced when comparing the methods for predominantly linear and very sparse systems like linear alkyl radicals, signifying that the ω-RI-CDD-MP2 uses the sparsity well in these model cases. For larger and more globular structures, the computational savings with the THC-ω-RI-CDD-MP2 method are significantly greater, indicating that Algorithm 4 utilizes the sparsity well, even in nonlinear systems. The latter, and the reduced memory requirements make the THC-ω-RI-CDD-MP2 method attractive for the computation of HFCCs of large, globular systems, as they are commonly encountered in proteins and enzymes. Furthermore, due to the greatly reduced computational cost, the method is applicable in double-hybrid functionals, where usually the MP2 part is the computational bottleneck, while also allowing for sampling of multiple points on the PES.

5. CONCLUSIONS AND OUTLOOK

In this work, we presented the THC-ω-RI-CDD-MP2 method for the efficient and accurate computation of isotropic HFCCs for large organic radicals. As usual for MP2 methods, the exchange-like terms, here $\mathbf{R}^X$, govern the scaling and runtime of the method. This issue was addressed through screening based on the THC collocation matrices $\mathbf{X}$ in combination with natural blocking for the tensor contractions. An asymptotically linear scaling recipe for the contraction of exchange-like terms in THC format is provided. This recipe is applied to the $\mathbf{R}^X$ terms, reducing the formal quartic scaling to effectively subquadratic, as shown for linear alkyl radicals and spin-labeled DNA strands. The THC-ω-RI-CDD-MP2 method furthermore highlights the attractiveness of THC-based methods for derivatives of electron correlation methods. Derivative calculations usually involve more types of ERIs, for example, half-transformed integrals, integrals with mixed spin in openshell calculations, or integrals contracted with perturbed densities. This generally increases storage requirements compared to single point calculations. Furthermore, the computational cost of the method is strongly increased due to additional ERI contractions. Both challenges are overcome by using THC-factorized ERIs, for which only second-order tensors have to be stored and integral transformations and contractions can be easily reduced to simple `dgemm` operations. The advantages of THC-based gradient methods are demonstrated for HFCC calculations on a range of medium-sized organic radicals and spin-labeled DNA strands with more than 5000 basis functions.

For future applications, the availability of THC grids has to be improved, as ideally EPR-specific basis sets,[67] and corresponding THC grids, should be used for the calculations presented. The grids used throughout this publications were hand optimized[38] and are only viable for the cc-pVXZ (X ∈{D,T}) basis sets. Furthermore, these grids were optimized based on MO-THC-MP2 and not for AO-THC, as used throughout this work. This incurs additional errors due to the larger fitting space. Different techniques for the on-the-fly generation of THC grids have been proposed, either based on PCD of the THC metric in a larger parent grid basis,[40] or based on centroidal Voronoi tesselation (CVT),[36] and could be applied for the calculation of THC-MP2 HFCCs in future work.

Finally, the developed THC-ω-RI-CDD-MP2 method can easily be used for the MP2 part of double-hybrid functionals and, once appropriate grids are available, enable accurate HFCC predictions for large molecules. Furthermore, due to the reduced computational complexity and memory requirements, THC-ω-RI-CDD-MP2, in conjunction with an appropriate double-hybrid functional, is an attractive candidate for QM/MM HFCC calculations.

■ ASSOCIATED CONTENT

Supporting Information

The Supporting Information is available free of charge at https://pubs.acs.org/doi/10.1021/acs.jctc.2c00118.

> Detailed algorithm for the asymptotically linear scaling formation of THC-MP2 exchange-like energy contribution as well as the individual formation of $\bar{\mathbf{R}}^X$ and $\underline{\mathbf{R}}^X$, detailed results for the benchmark calculations, details on the memory requirement estimation and comparison of selected-nuclei ω-RI-CDD-MP2 against THC-ω-RI-CDD-MP2 (PDF)
>
> Structures (ZIP)

■ AUTHOR INFORMATION

Corresponding Author

Christian Ochsenfeld − *Chair of Theoretical Chemistry, Department of Chemistry, University of Munich (LMU), D-81377 Munich, Germany; Max Planck Institute for Solid State Research, D-70569 Stuttgart, Germany;* orcid.org/0000-0002-4189-6558; Email: christian.ochsenfeld@cup.uni-muenchen.de

Authors

Felix H. Bangerter − *Chair of Theoretical Chemistry, Department of Chemistry, University of Munich (LMU), D-81377 Munich, Germany*

Michael Glasbrenner − *Chair of Theoretical Chemistry, Department of Chemistry, University of Munich (LMU), D-81377 Munich, Germany*

Complete contact information is available at: https://pubs.acs.org/10.1021/acs.jctc.2c00118

Funding

Open access funded by Max Planck Society.

Notes

The authors declare no competing financial interest.

■ ACKNOWLEDGMENTS

The authors acknowledge financial support by the "Deutsche Forschungsgemeinschaft" (DFG) via the SFB 1309-32587107 and the cluster of excellence (EXC2111-390814868) "Munich Center for Quantum Science and Technology" (MCQST). F.H.B. thanks the "Fonds der Chemischen Industrie" (FCI) for a graduate fellowship. M.G. thanks the "Studienstiftung des Deutschen Volkes" for a graduate fellowship. C.O. acknowledges additional financial support as a Max-Planck-Fellow at MPI-FKF Stuttgart. The authors thank J. Kussmann (LMU Munich) for providing a development version of the FermiONs++ program package.

■ REFERENCES

(1) Møller, C.; Plesset, M. S. Note on an approximation treatment for many-electron systems. *Phys. Rev.* **1934**, *46*, 618−622.

(2) Cremer, D. Møller-Plesset perturbation theory: From small molecule methods to methods for thousands of atoms. *Wiley Interdiscip. Rev. Comput. Mol. Sci.* **2011**, *1*, 509−530.

(3) Bent, G. D. Many-body perturbation theory electronic structure calculations for the methoxy radical. II. Hyperfine coupling coefficients. *J. Chem. Phys.* **1994**, *100*, 8219.

(4) Kossmann, S.; Neese, F. Correlated ab initio spin densities for larger molecules: Orbital-optimized spin-component-scaled MP2 method. *J. Phys. Chem. A* **2010**, *114*, 11768−11781.

(5) Sandhoefer, B.; Kossmann, S.; Neese, F. Derivation and assessment of relativistic hyperfine-coupling tensors on the basis of orbital-optimized second-order Møller-Plesset perturbation theory and the second-order Douglas-Kroll-Hess transformation. *J. Chem. Phys.* **2013**, *138*, 104102.

(6) Vogler, S.; Ludwig, M.; Maurer, M.; Ochsenfeld, C. Low-scaling first-order properties within second-order Møller-Plesset perturbation theory using Cholesky decomposed density matrices. *J. Chem. Phys.* **2017**, *147*, 024101.

(7) Vogler, S.; Dietschreit, J. C. B.; Peters, L. D. M.; Ochsenfeld, C. Important components for accurate hyperfine coupling constants: electron correlation, dynamic contributions, and solvation effects. *Mol. Phys.* **2020**, *118*, e1772515.

(8) Gauss, J. Calculation of NMR chemical shifts at second-order many-body perturbation theory using gauge-including atomic orbitals. *Chem. Phys. Lett.* **1992**, *191*, 614−620.

(9) Gauss, J. Effects of electron correlation in the calculation of nuclear magnetic resonance chemical shifts. *J. Chem. Phys.* **1993**, *99*, 3629−3643.

(10) Flaig, D.; Maurer, M.; Hanni, M.; Braunger, K.; Kick, L.; Thubauville, M.; Ochsenfeld, C. Benchmarking Hydrogen and Carbon NMR Chemical Shifts at HF, DFT, and MP2 Levels. *J. Chem. Theory Comput.* **2014**, *10*, 572−578.

(11) Maurer, M.; Ochsenfeld, C. A linear- and sublinear-scaling method for calculating NMR shieldings in atomic orbital-based second-order Møller-Plesset perturbation theory. *J. Chem. Phys.* **2013**, *138*, 174104.

(12) Glasbrenner, M.; Vogler, S.; Ochsenfeld, C. Efficient low-scaling computation of NMR shieldings at the second-order Møller-Plesset perturbation theory level with Cholesky-decomposed densities and an attenuated Coulomb metric. *J. Chem. Phys.* **2021**, *155*, 224107.

(13) Kossmann, S.; Kirchner, B.; Neese, F. Performance of modern density functional theory for the prediction of hyperfine structure: Meta-GGA and double hybrid functionals. *Mol. Phys.* **2007**, *105*, 2049−2071.

(14) Sæbø, S.; Pulay, P. Local configuration interaction: An efficient approach for larger molecules. *Chem. Phys. Lett.* **1985**, *113*, 13−18.

(15) Sæbø, S.; Pulay, P. Local treatment of electron correlation. *Annu. Rev. Phys. Chem.* **1993**, *44*, 213−236.

(16) El Azhary, A.; Rauhut, G.; Pulay, P.; Werner, H.-J. Analytical energy gradients for local second-order Møller-Plesset perturbation theory. *J. Chem. Phys.* **1998**, *108*, 5185.

(17) Schütz, M.; Werner, H. J.; Lindh, R.; Manby, F. R. Analytical energy gradients for local second-order Møller-Plesset perturbation theory using density fitting approximations. *J. Chem. Phys.* **2004**, *121*, 737.

(18) Pinski, P.; Neese, F. Communication: Exact analytical derivatives for the domain-based local pair natural orbital MP2 method (DLPNO-MP2). *J. Chem. Phys.* **2018**, *148*, 031101.

(19) Pinski, P.; Neese, F. Analytical gradient for the domain-based local pair natural orbital second order Møller-Plesset perturbation theory method (DLPNO-MP2). *J. Chem. Phys.* **2019**, *150*, 164102.

(20) Stoychev, G. L.; Auer, A. A.; Gauss, J.; Neese, F. DLPNO-MP2 second derivatives for the computation of polarizabilities and NMR shieldings. *J. Chem. Phys.* **2021**, *154*, 164110.

(21) Kristensen, K.; Høyvik, I. M.; Jansik, B.; Jørgensen, P.; Kjærgaard, T.; Reine, S.; Jakowski, J. MP2 energy and density for large molecular systems with internal error control using the Divide-Expand-Consolidate scheme. *Phys. Chem. Chem. Phys.* **2012**, *14*, 15706−15714.

(22) Baudin, P.; Ettenhuber, P.; Reine, S.; Kristensen, K.; Kjærgaard, T. Efficient linear-scaling second-order Møller-Plesset perturbation theory: The divide-expand-consolidate RI-MP2 model. *J. Chem. Phys.* **2016**, *144*, 054102.

(23) Kristensen, K.; Jorgensen, P.; Jansík, B.; Kjærgaard, T.; Reine, S. Molecular gradient for second-order Møller-Plesset perturbation theory using the divide-expand-consolidate (DEC) scheme. *J. Chem. Phys.* **2012**, *137*, 114102.

(24) Bykov, D.; Kristensen, K.; Kjærgaard, T. The molecular gradient using the divide-expand-consolidate resolution of the identity second-order Møller-Plesset perturbation theory: The DEC-RI-MP2 gradient. *J. Chem. Phys.* **2016**, *145*, 024106.

(25) Schweizer, S.; Doser, B.; Ochsenfeld, C. An atomic orbital-based reformulation of energy gradients in second-order Møller-Plesset perturbation theory. *J. Chem. Phys.* **2008**, *128*, 154101.

(26) Whitten, J. L. Coulombic potential energy integrals and approximations. *J. Chem. Phys.* **1973**, *58*, 4496.

(27) Dunlap, B. I.; Connolly, J. W.; Sabin, J. R. On some approximations in applications of Xα theory. *J. Chem. Phys.* **1979**, *71*, 3396.

(28) Vahtras, O.; Almlöf, J.; Feyereisen, M. W. Integral approximations for LCAO-SCF calculations. *Chem. Phys. Lett.* **1993**, *213*, 514−518.

(29) Weigend, F.; Häser, M.; Patzelt, H.; Ahlrichs, R. RI-MP2: Optimized auxiliary basis sets and demonstration of efficiency. *Chem. Phys. Lett.* **1998**, *294*, 143−152.

(30) Vogler, S.; Savasci, G.; Ludwig, M.; Ochsenfeld, C. Selected-Nuclei Method for the Computation of Hyperfine Coupling Constants within Second-Order Møller-Plesset Perturbation Theory. *J. Chem. Theory Comput.* **2018**, *14*, 3014−3024.

(31) Parrish, R. M.; Hohenstein, E. G.; Martínez, T. J.; Sherrill, C. D. Tensor hypercontraction. II. Least-squares renormalization. *J. Chem. Phys.* **2012**, *137*, 224106.

(32) Parrish, R. M.; Hohenstein, E. G.; Schunck, N. F.; Sherrill, C. D.; Martínez, T. J. Exact tensor hypercontraction: A universal technique for the resolution of matrix elements of local finite-range N-body potentials in many-body quantum problems. *Phys. Rev. Lett.* **2013**, *111*, 1−5.

(33) Song, C.; Martínez, T. J. Atomic orbital-based SOS-MP2 with tensor hypercontraction. I. GPU-based tensor construction and exploiting sparsity. *J. Chem. Phys.* **2016**, *144*, 174111.

(34) Song, C.; Martínez, T. J. Atomic orbital-based SOS-MP2 with tensor hypercontraction. II. Local tensor hypercontraction. *J. Chem. Phys.* **2017**, *146*, 034104.

(35) Matthews, D. A. A critical analysis of least-squares tensor hypercontraction applied to MP3. *J. Chem. Phys.* **2021**, *154*, 134102.

(36) Lee, J.; Lin, L.; Head-Gordon, M. Systematically Improvable Tensor Hypercontraction: Interpolative Separable Density-Fitting for Molecules Applied to Exact Exchange, Second- and Third-Order Møller-Plesset Perturbation Theory. *J. Chem. Theory Comput.* **2020**, *16*, 243−263.

(37) Hohenstein, E. G.; Parrish, R. M.; Martínez, T. J. Tensor hypercontraction density fitting. I. Quartic scaling second- and third-order Møller-Plesset perturbation theory. *J. Chem. Phys.* **2012**, *137*, 044103.

(38) Kokkila Schumacher, S. I.; Hohenstein, E. G.; Parrish, R. M.; Wang, L. P.; Martínez, T. J. Tensor Hypercontraction Second-Order Møller-Plesset Perturbation Theory: Grid Optimization and Reaction Energies. *J. Chem. Theory Comput.* **2015**, *11*, 3042−3052.

(39) Song, C.; Martínez, T. J. Analytical gradients for tensor hypercontracted MP2 and SOS-MP2 on graphical processing units. *J. Chem. Phys.* **2017**, *147*, 161723.

(40) Matthews, D. A. Improved Grid Optimization and Fitting in Least Squares Tensor Hypercontraction. *J. Chem. Theory Comput.* **2020**, *16*, 1382−1385.

(41) Bangerter, F. H.; Glasbrenner, M.; Ochsenfeld, C. Low-Scaling Tensor Hypercontraction in the Cholesky Molecular Orbital Basis Applied to Second-Order Møller-Plesset Perturbation Theory. *J. Chem. Theory Comput.* **2021**, *17*, 211−221.

(42) Shenvi, N.; Van Aggelen, H.; Yang, Y.; Yang, W. Tensor hypercontracted ppRPA: Reducing the cost of the particle-particle random phase approximation from O(r6) to O(r4). *J. Chem. Phys.* **2014**, *141*, 024119.

(43) Song, C.; Martínez, T. J. Reduced scaling CASPT2 using supporting subspaces and tensor hyper-contraction. *J. Chem. Phys.* **2018**, *149*, 044108.

(44) Hohenstein, E. G.; Kokkila, S. I.; Parrish, R. M.; Martínez, T. J. Quartic scaling second-order approximate coupled cluster singles and doubles via tensor hypercontraction: THC-CC2. *J. Chem. Phys.* **2013**, *138*, 124111.

(45) Parrish, R. M.; Sherrill, C. D.; Hohenstein, E. G.; Kokkila, S. I.; Martínez, T. J. Communication: Acceleration of coupled cluster singles and doubles via orbital-weighted least-squares tensor hypercontraction. *J. Chem. Phys.* **2014**, *140*, 181102.

(46) Schutski, R.; Zhao, J.; Henderson, T. M.; Scuseria, G. E. Tensor-structured coupled cluster theory. *J. Chem. Phys.* **2017**, *147*, 184113.

(47) Hohenstein, E. G.; Kokkila, S. I.; Parrish, R. M.; Martínez, T. J. Tensor hypercontraction equation-of-motion second-order approximate coupled cluster: Electronic excitation energies in O(N4) time. *J. Phys. Chem. B* **2013**, *117*, 12972−12978.

(48) Song, C.; Martínez, T. J.; Neaton, J. B. A diagrammatic approach for automatically deriving analytical gradients of tensor hypercontracted electronic structure methods. *J. Chem. Phys.* **2021**, *155*, 024108.

(49) Almlöf, J. Elimination of energy denominators in Møller-Plesset perturbation theory by a Laplace transform approach. *Chem. Phys. Lett.* **1991**, *181*, 319.

(50) Häser, M.; Almlöf, J. Laplace transform techniques in Møller-Plesset perturbation theory. *J. Chem. Phys.* **1992**, *96*, 489.

(51) Häser, M. Møller-Plesset (MP2) perturbation theory for large molecules. *Theor. Chim. Acta* **1993**, *87*, 147−173.

(52) Handy, N. C.; Schaefer, H. F. On the evaluation of analytic energy derivatives for correlated wave functions. *J. Chem. Phys.* **1984**, *81*, 5031−5033.

(53) Beer, M.; Ochsenfeld, C. Efficient linear-scaling calculation of response properties: Density matrix-based Laplace-transformed coupled-perturbed self-consistent field theory. *J. Chem. Phys.* **2008**, *128*, 221102.

(54) Reine, S.; Tellgren, E.; Krapp, A.; Kjærgaard, T.; Helgaker, T.; Jansik, B.; Høst, S.; Salek, P. Variational and robust density fitting of four-center two-electron integrals in local metrics. *J. Chem. Phys.* **2008**, *129*, 104101.

(55) Luenser, A.; Schurkus, H. F.; Ochsenfeld, C. Vanishing-Overhead Linear-Scaling Random Phase Approximation by Cholesky Decomposition and an Attenuated Coulomb-Metric. *J. Chem. Theory Comput.* **2017**, *13*, 1647−1655.

(56) Jung, Y.; Lochan, R. C.; Dutoi, A. D.; Head-Gordon, M. Scaled opposite-spin second order Møller-Plesset correlation energy: An economical electronic structure method. *J. Chem. Phys.* **2004**, *121*, 9793.

(57) Jung, Y.; Shao, Y.; Head-Gordon, M. Fast Evaluation of Scaled Opposite Spin Second-Order Møller-Plesset Correlation Energies

Using Auxiliary Basis Expansions and Exploiting Sparsity. *J. Comput. Chem.* **2007**, *28*, 1953−1964.

(58) Glasbrenner, M.; Graf, D.; Ochsenfeld, C. Efficient Reduced-Scaling Second-Order Møller-Plesset Perturbation Theory with Cholesky-Decomposed Densities and an Attenuated Coulomb Metric. *J. Chem. Theory Comput.* **2020**, *16*, 6856−6868.

(59) Kussmann, J.; Ochsenfeld, C. Pre-selective screening for matrix elements in linear-scaling exact exchange calculations. *J. Chem. Phys.* **2013**, *138*, 134114.

(60) Kussmann, J.; Ochsenfeld, C. Preselective screening for linear-scaling exact exchange-gradient calculations for graphics processing units and general strong-scaling massively parallel calculations. *J. Chem. Theory Comput.* **2015**, *11*, 918−922.

(61) Kussmann, J.; Ochsenfeld, C. Hybrid CPU/GPU Integral Engine for Strong-Scaling Ab Initio Methods. *J. Chem. Theory Comput.* **2017**, *13*, 3153−3159.

(62) Dunning, T. H. Gaussian basis sets for use in correlated molecular calculations. I. The atoms boron through neon and hydrogen. *J. Chem. Phys.* **1989**, *90*, 1007.

(63) Pulay, P. Convergence acceleration of iterative sequences. the case of scf iteration. *Chem. Phys. Lett.* **1980**, *73*, 393−398.

(64) Thompson, T. H.; Ochsenfeld, C. Integral partition bounds for fast and effective screening of general one-, two-, and many-electron integrals. *J. Chem. Phys.* **2019**, *150*, 044101.

(65) Neese, F. The ORCA program system. *Wiley Interdiscip. Rev. Comput. Mol. Sci.* **2012**, *2*, 73−78.

(66) Laqua, H.; Thompson, T. H.; Kussmann, J.; Ochsenfeld, C. Highly Efficient, Linear-Scaling Seminumerical Exact-Exchange Method for Graphic Processing Units. *J. Chem. Theory Comput.* **2020**, *16*, 1456−1468.

(67) Jakobsen, P.; Jensen, F. Probing basis set requirements for calculating hyperfine coupling constants. *J. Chem. Phys.* **2019**, *151*, 174107.

https://doi.org/10.1021/acs.jctc.2c00118
J. Chem. Theory Comput. 2022, 18, 5233−5245

Supporting Information: Tensor-hypercontracted MP2 First Derivatives: Runtime and Memory Efficient Computation of Hyperfine Coupling Constants

Felix H. Bangerter,† Michael Glasbrenner,† and Christian Ochsenfeld*,†,‡

†*Chair of Theoretical Chemistry, Department of Chemistry, University of Munich (LMU), D-81377 Munich, Germany*

‡*Max Planck Institute for Solid State Research, D-70569 Stuttgart, Germany*

E-mail: christian.ochsenfeld@cup.uni-muenchen.de

Contents

1 Alternative Derivation of the Analytical Expression for the THC Z-Matrix

The AO-THC least-squares objective function[S1] is given by

$$O = \frac{1}{2}\left\| (\mu\nu|\lambda\sigma) - \sum_{PQ} X_{\mu}^{P} X_{\nu}^{P} Z^{PQ} X_{\lambda}^{Q} X_{\sigma}^{Q} \right\|_{2}^{2}, \tag{1}$$

which is quartic in the collocation matrix $\mathbf{X}$ and linear in the grid representation of the $1/r$ operator, i.e., $\mathbf{Z}$. The LS problem can be generalized to

$$O = \frac{1}{2}\left\| \mathbf{B} - \mathbf{A}\mathbf{Y}\mathbf{A}^{\mathrm{T}} \right\|_{2}^{2}, \tag{2}$$

where $\mathbf{B} \in \mathbb{R}^{n\times n}$, $\mathbf{A} \in \mathbb{R}^{n\times m}$ and $\mathbf{Y} \in \mathbb{R}^{m\times m}$, with $n = N_{\mathrm{bf}}^{2}$ and $m = N_{\mathrm{grid}}$ in the case of LS-THC. The analytic expression for the THC $\mathbf{Z}$ matrix given by Martínez and coworkers[S1] is then simply the solution of the normal equations associated with eq 1. In general notation, the normal equations associated with the LS problem of eq 2 are simply given as

$$\mathbf{A}^{\mathrm{T}}\mathbf{A}\mathbf{Y}\mathbf{A}^{\mathrm{T}}\mathbf{A} = \mathbf{A}^{\mathrm{T}}\mathbf{B}\mathbf{A}. \tag{3}$$

To solve for $\mathbf{Y}$, the moment matrix $\mathbf{A}^{\mathrm{T}}\mathbf{A}$ has to be inverted and the solution is given by

$$\mathbf{Y} = (\mathbf{A}^{\mathrm{T}}\mathbf{A})^{-1}\mathbf{A}^{\mathrm{T}}\mathbf{B}\mathbf{A}(\mathbf{A}^{\mathrm{T}}\mathbf{A})^{-1}. \tag{4}$$

If the substitutions $\mathbf{A} = \mathbf{R}$, where $R_{\mu\nu}^{P} \equiv X_{\mu}^{P} X_{\nu}^{P}$, $\mathbf{B} = \boldsymbol{\mathcal{I}}$ and $\mathbf{Y} = \mathbf{Z}$ are made, the familiar analytic expression for the THC $\mathbf{Z}$-tensor is obtained

$$\begin{aligned} \mathbf{Z} &= (\mathbf{R}^{\mathrm{T}}\mathbf{R})^{-1}\mathbf{R}^{\mathrm{T}}\boldsymbol{\mathcal{I}}\mathbf{R}(\mathbf{R}^{\mathrm{T}}\mathbf{R})^{-1} \\ &= \mathbf{S}^{-1}\mathbf{E}\mathbf{S}^{-1}, \end{aligned} \tag{5}$$

where $\mathbf{S} \equiv \mathbf{R}^{\mathrm{T}}\mathbf{R}$ is the THC grid metric, $\boldsymbol{\mathcal{I}}$ is the matrix representation of the ERI tensor and $\mathbf{E} \equiv \mathbf{R}^{\mathrm{T}}\boldsymbol{\mathcal{I}}\mathbf{R}$ is the grid-projected ERI tensor.

2 THC-MP2 Exchange-like Contractions

The proposed algorithm for the computation of the exchange-like energy contribution for the THC-ω-RI-CDD-MP2 method follows the same ideas as the algorithm for the exchange-like contribution $\mathbf{R}^{\mathrm{X}}$ from the main part of this publication. Note, that this algorithm is applicable to all types of methods derived from THC-CDD-MP2, as the RI approximation is only used during the formation of the THC factorization.

Algorithm 1 Compute the exchange-like MP2 energy $E_{\text{MP2-K}}^{\text{THC-CDD}}$

```
procedure COMPUTE_THC_MP2_X($\mathbf{X}, \mathbf{Z}$)
    $E_{\text{MP2-K}} = 0.0$
    for $\kappa = 1$ to $N_\kappa$ do                                  ▷ Laplace quadrature
        $\underline{L}_{\mu i}, \overline{L}_{\nu a}$ = GET_CHOLESKY_FACTORS($\kappa$)
        $\underline{X}_i^P = \sum_\mu \underline{L}_{\mu i} X_\mu^P$
        $\overline{X}_a^P = \sum_\nu \overline{L}_{\nu a} X_\nu^P$
        $A^{PR} = \sum_i \underline{X}_i^P \underline{X}_i^R$
        $B^{PS} = \sum_a \overline{X}_a^P \overline{X}_a^S$
        build $\{S_j\}$ from $|\underline{X}_j^S|$
        build $\{a_P\}$ from $|\overline{X}_a^P|$
        build $\{a_j\}$ from $\sum_S |\underline{X}_j^S||\overline{X}_a^S|$
        build $\{P_j\}$ from $\{a_P\}$ and $\{a_j\}$                   ▷ identical to $\{R_j\}$
        $e_{\text{MP2-K}} = 0.0$
        for $j = 1$ to $j \leq \mathrm{rk}(\underline{\mathbf{P}})$ do        ▷ batching over occupied index $j$
            for all $P \in \{P\}_j$ and $S \in \{S\}_j$ do
                $C^{PS} = B^{PS} \underline{X}_j^S$
            end for
            for all $P \in \{P\}_j$ and $R \in \{R\}_j$ do
                $D^{PR} = \sum_{S \in \{S\}_j} Z^{RS} C^{PS}$
            end for
            $e_{\text{MP2-K}}$ += $\sum_{P \in \{P\}_j} \sum_{R \in \{R\}_j} A^{PR} D^{PR} D^{RP}$
        end for
        $E_{\text{MP2-K}}$ += $e_{\text{MP2-K}}$
    end for
    return $E_{\text{MP2-K}}$
end procedure
```

Asymptotic linear scaling of Algorithm 1 is exemplarily demonstrated for linear alkane chains up to $C_{120}H_{242}$ in Figure S1.

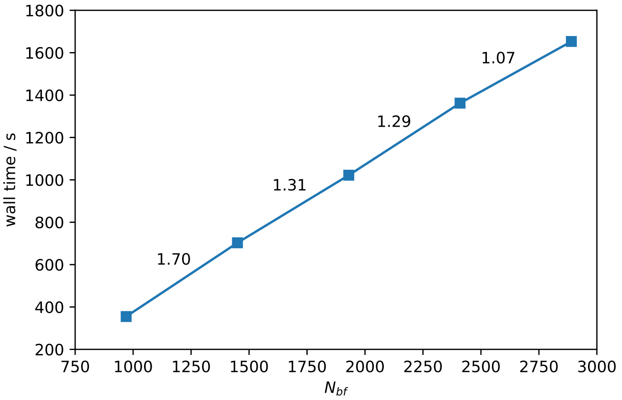

Figure S1: Wall times of Algorithm 1 for linear alkanes C_nH_{2n+2} (n ∈ {40, 60, 80, 100, 120}) and the cc-pVDZ basis set. Black numbers between fragments correspond to the scaling with respect to the preceding fragment.

3 Exchange Contribution to $\overline{R}_{\mu'\mu}$

The exchange-like contribution to $\overline{\mathbf{R}}$ for a single Laplace point is given by

$$\begin{aligned} \overline{R}^{\mathrm{X},\eta}_{\mu'\mu} &= \sum_{j}\sum_{ab}(\mu'\overline{a}|\underline{j}\overline{b})_{\eta\eta}(\mu\overline{b}|\underline{j}\overline{a})_{\eta\eta} \\ &\approx \sum_{j}\sum_{ab}\sum_{PQRS} X^{P}_{\mu'}\overline{X}^{P,\eta}_{a}Z^{PQ}\underline{X}^{Q,\eta}_{j}\overline{X}^{Q,\eta}_{b}\cdot X^{R}_{\mu}\overline{X}^{R,\eta}_{b}Z^{RS}\underline{X}^{S,\eta}_{j}\overline{X}^{S,\eta}_{a}, \end{aligned} \tag{6}$$

and can be efficiently obtained by the following algorithm:

Algorithm 2 Compute the exchange-like contribution to $\overline{R}_{\mu'\mu}$

```
procedure BUILD_RMUMUX($\mathbf{X}, \mathbf{Z}, \underline{\mathbf{X}}, \overline{\mathbf{X}}$)
    build $\{S_j\}$ from $|\underline{X}_j^{S,\eta}|$
    build $\{a_P\}$ from $|\overline{X}_a^{P,\eta}|$
    build $\{a_j\}$ from $\sum_S |\underline{X}_j^{S,\eta}||\overline{X}_a^{S,\eta}|$
    build $\{P_j\}$ from $\{a_P\}$ and $\{a_j\}$                ▷ identical to $\{R_j\}$
    $B^{PS,\eta} = \sum_a \overline{X}_a^{P,\eta} \overline{X}_a^{S,\eta}$
    $E^{PR,\eta} = \mathbf{0}_{N_\mathrm{grid}, N_\mathrm{grid}}$
    for $j = 1$ to $j \le \mathrm{rk}(\underline{\mathbf{P}}^\eta)$ do    ▷ batching over occupied index $j$
        for all $R \in \{R\}_j$ and $S \in \{S\}_j$ do
            $C^{RS,\eta} = Z^{RS} \underline{X}_j^{S,\eta}$
        end for
        for all $P \in \{P\}_j$ and $R \in \{R\}_j$ do
            $D^{PR,\eta} = \sum_{S \in \{S\}_j} C^{RS,\eta} B^{PS,\eta}$
        end for
        for all $P \in \{P\}_j$ and $R \in \{R\}_j$ do
            $E^{PR,\eta}$ += $D^{PR,\eta} D^{RP,\eta}$
        end for
    end for
    $\overline{R}_{\mu'\mu}^{\mathrm{X},\eta} = \sum_{PR} X_{\mu'}^P E^{PR,\eta} X_\mu^R$
    return $\overline{R}_{\mu'\mu}^{\mathrm{X},\eta}$
end procedure
```

4 Exchange Contribution to $\underline{R}_{\nu'\nu}$

The exchange-like contribution to $\underline{\mathbf{R}}$ for a single Laplace point is given by

$$\begin{aligned} \underline{R}_{\nu'\nu}^{\mathrm{X},\eta} &= \sum_{ij} \sum_{b} (\underline{i}\nu'|\underline{j}\overline{b})_{\eta\eta} (\underline{i}\overline{b}|\underline{j}\nu)_{\eta\eta} \\ &\approx \sum_{ij} \sum_{b} \sum_{PQRS} \underline{X}_i^{P,\eta} X_{\nu'}^P Z^{PQ} \underline{X}_j^{Q,\eta} \overline{X}_b^{Q,\eta} \cdot \underline{X}_i^{R,\eta} \overline{X}_b^{R,\eta} Z^{RS} \underline{X}_j^{S,\eta} X_\nu^S . \end{aligned} \tag{7}$$

By symmetry, the exchange contribution $\underline{R}_{\nu'\nu}^{\mathrm{X},\eta}$, given by equation 7, can be computed analogously to the exchange contribution $\overline{R}_{\mu'\mu}^{\mathrm{X},\eta}$, where the batching loop iterates over all virtual MOs b instead of all occupied MOs j. This, however, will increase the prefactor significantly as $N_\mathrm{virt} \approx N_\mathrm{bf} \gg N_\mathrm{occ}$. If instead the batching loop is kept over all occupied orbitals j, an additional Schur product and an additional matrix multiplication have to be performed, compared to the algorithm for $\overline{R}^{\mathrm{X},\eta}_{\mu'\mu}$. The number of floating point operations (FLOPs) for the batching over b is roughly $2N_{\mathrm{virt}}N_{\mathrm{grid}}^2 + N_{\mathrm{virt}}N_{\mathrm{grid}}^3$ (the scaling of $\mathbf{Z}$, a matrix multiplication and the accumulation in $\mathbf{E}$ for every b), whereas for the batching over j the FLOP count is $2N_{\mathrm{occ}}N_{\mathrm{grid}}^2 + 2N_{\mathrm{occ}}N_{\mathrm{grid}}^3$ (see Algorithm 3). It can easily be shown that the FLOP ratio is roughly $\frac{2N_{\mathrm{occ}}}{N_{\mathrm{virt}}}$ in favor of the batching over j. Therefore, the exchange-like contribution to $\overline{\mathbf{R}}$ for a single Laplace point can efficiently be computed with the following algorithm:

Algorithm 3 Compute the exchange-like contribution to $\underline{R}_{\nu'\nu}$

```
procedure Build_RnunuX($\mathbf{X}, \mathbf{Z}, \underline{\mathbf{X}}, \overline{\mathbf{X}}$)
    build $\{S_j\}$ from $|\underline{X}_j^{S,\eta}|$
    build $\{b_R\}$ from $|\overline{X}_b^{R,\eta}|$
    build $\{b_j\}$ from $\sum_Q |\underline{X}_j^{Q,\eta}||\overline{X}_b^{Q,\eta}|$
    build $\{R_j\}$ from $\{b_R\}$ and $\{b_j\}$                    ▷ identical to $\{P_j\}$
    $A^{PR,\eta} = \sum_i \underline{X}_i^{P,\eta}\underline{X}_i^{R,\eta}$
    $B^{QR,\eta} = \sum_b \overline{X}_b^{Q,\eta}\overline{X}_b^{R,\eta}$
    $E^{PS,\eta} = \mathbf{0}_{N_{\mathrm{grid}},N_{\mathrm{grid}}}$
    for $j = 1$ to $j \leq \mathrm{rk}(\underline{\mathbf{P}}^\eta)$ do        ▷ batching over occupied index $j$
        for all $R \in \{R\}_j$ and $S \in \{S\}_j$ do
            $C^{RS,\eta} = Z^{RS}\underline{X}_j^{S,\eta}$                    ▷ identical to $C^{PQ}$
        end for
        for all $P \in \{P\}_j$ and $R \in \{R\}_j$ do
            $D^{PR,\eta} = \sum_{Q\in\{Q\}_j} C^{PQ,\eta}B^{QR,\eta}$
        end for
        for all $P \in \{P\}_j$ and $R \in \{R\}_j$ do
            $D^{PR,\eta} \mathrel{\times}= A^{PR,\eta}$
        end for
        for all $P \in \{P\}_j$ and $S \in \{S\}_j$ do
            $E^{PS,\eta} \mathrel{+}= \sum_{R\in\{R\}_j} D^{PR,\eta}C^{RS,\eta}$
        end for
    end for
    $\underline{R}_{\nu'\nu}^{\mathrm{X},\eta} = \sum_{PS} X_{\nu'}^P E^{PS,\eta} X_\nu^S$
    return $\underline{R}_{\nu'\nu}^{\mathrm{X},\eta}$
end procedure
```

Finally, by closer inspection of algorithms 2 and 3 it can be seen that they share common intermediates, which makes a joined computation of $\overline{R}^{\mathrm{X},\eta}_{\mu'\mu}$ and $\underline{R}^{\mathrm{X},\eta}_{\nu'\nu}$ attractive, as explained in the main part of this publication.

5 Detailed Results for the Accuracy Benchmark

Table S1: Detailed comparison of THC-ω-RI-CDD-MP2 HFCCs against ω-RI-CDD-MP2 for the benchmark set by Vogler *et al.*[S2] and the cc-pVDZ/cc-pVDZ-RI basis set combination.

		ω-RI-CDD-MP2	THC-ω-RI-CDD-MP2		
radical	nucleus	A_{iso} / MHz	A_{iso} / MHz	ΔA_{iso} / MHz	ΔA_{iso} / %
1	^{14}N	67.454	67.422	0.032	0.05
	^{13}C	-36.580	-36.601	0.021	0.06
	^{1}H^{a}	94.085	94.150	0.065	0.07
	^{1}H^{b}	-3.286	-3.316	0.030	0.91
2	^{14}N	66.966	67.269	0.303	0.45
	^{13}C ($\underline{\mathrm{C}}$H)	-28.521	-28.999	0.478	1.68
	^{13}C^{a} ($\underline{\mathrm{C}}\mathrm{H}_3$)	59.983	60.232	0.249	0.42
	^{13}C^{b} ($\underline{\mathrm{C}}\mathrm{H}_3$)	10.989	11.186	0.197	1.79
	^{1}H (C$\underline{\mathrm{H}}$)	25.150	25.414	0.264	1.05
	^{1}H^{a} ($\mathrm{C}\underline{\mathrm{H}}_3$)	-0.186	-0.206	0.020	10.75
	^{1}H^{b} ($\mathrm{C}\underline{\mathrm{H}}_3$)	3.194	3.127	0.067	2.10
3	^{13}C	-17.038	-17.152	0.114	0.67
	^{1}H^{a}	346.221	346.092	0.129	0.04
	^{1}H^{b}	-19.814	-19.807	0.007	0.04
4	^{13}C ($\underline{\mathrm{C}}\mathrm{H}_3$)	-11.972	-11.991	0.019	0.16
	^{13}C ($\underline{\mathrm{C}}\mathrm{H}_2$)	43.314	43.340	0.026	0.06
	^{1}H ($\mathrm{C}\underline{\mathrm{H}}_2$)	-2.180	-2.141	0.039	1.79
	^{1}H^{a} ($\mathrm{C}\underline{\mathrm{H}}_3$)	12.536	12.557	0.021	0.17
	^{1}H^{b} ($\mathrm{C}\underline{\mathrm{H}}_3$)	150.898	151.181	0.283	0.19
5	^{14}N	-5.277	-4.714	0.563	10.67
	o-^{13}C	59.599	59.003	0.596	1.00
	m-^{13}C	2.734	2.951	0.217	7.94
	p-^{13}C	27.022	26.429	0.593	2.19
	o-^{1}H	-34.018	-33.485	0.533	1.57
	m-^{1}H	-5.813	-6.188	0.375	6.45
	p-^{1}H	-26.106	-25.747	0.359	1.38
6	^{14}N	145.403	146.474	1.071	0.74
	^{17}O	-78.435	-78.963	0.528	0.67

7	$^{13}\mathrm{C}$	160.828	160.825	0.003	0.00
	$^{1}\mathrm{H}$	-72.879	-72.873	0.006	0.01
8	$^{17}\mathrm{O}$	-121.219	-120.697	0.522	0.43
	$^{13}\mathrm{C}\ (\mathrm{H\underline{C}O})$	-92.061	-92.184	0.123	0.13
	$^{13}\mathrm{C}\ (\mathrm{\underline{C}H_3})$	55.048	55.202	0.154	0.28
	$^{1}\mathrm{H}\ (\mathrm{\underline{H}CO})$	296.678	297.826	1.148	0.39
	$^{1}\mathrm{H}\ (\mathrm{C\underline{H}_3})$	-7.866	-7.870	0.004	0.05
9	$^{13}\mathrm{C}$	665.612	666.734	1.122	0.17
	$^{19}\mathrm{F}$	432.589	434.411	1.822	0.42
10	$^{13}\mathrm{C}\ (\mathrm{\underline{C}H})$	300.933	300.431	0.502	0.17
	$^{13}\mathrm{C}\ (\mathrm{\underline{C}H_2})$	25.532	26.189	0.657	2.57
	$^{1}\mathrm{H}\ (\mathrm{C\underline{H}})$	57.738	57.880	0.142	0.25
	$^{1}\mathrm{H}\ (Z\text{-}\mathrm{C\underline{H}_2})$	109.551	109.340	0.211	0.19
	$^{1}\mathrm{H}\ (E\text{-}\mathrm{C\underline{H}_2})$	57.501	57.349	0.152	0.26
11	$^{13}\mathrm{C}$	-11.389	-11.089	0.300	2.63
	$^{14}\mathrm{N}$	35.343	35.348	0.005	0.01
	$^{1}\mathrm{H}$	158.759	158.818	0.059	0.04
12	$^{11}\mathrm{B}$	352.047	352.144	0.097	0.03
	$^{1}\mathrm{H}$	21.757	21.694	0.063	0.29

Table S2: Detailed comparison of THC-ω-RI-CDD-MP2 HFCCs against ω-RI-CDD-MP2 for the benchmark set by Vogler *et al.*[S2] and the cc-pVTZ/cc-pVTZ-RI basis set combination.

		ω-RI-CDD-MP2	THC-ω-RI-CDD-MP2		
radical	nucleus	A_{iso} / MHz	A_{iso} / MHz	ΔA_{iso} / MHz	ΔA_{iso} / %
1	^{14}N	19.036	18.984	0.052	0.27
	^{13}C	-32.174	-32.145	0.029	0.09
	^{1}H^{a}	98.541	98.156	0.385	0.39
	^{1}H^{b}	-3.236	-3.227	0.009	0.28
2	^{14}N	19.046	19.028	0.018	0.09
	^{13}C ($\underline{C}$H)	-24.324	-24.196	0.128	0.53
	^{13}C^{a} ($\underline{C}H_3$)	64.018	64.008	0.010	0.02
	^{13}C^{b} ($\underline{C}H_3$)	10.865	10.871	0.006	0.06
	^{1}H (C$\underline{H}$)	25.437	25.432	0.005	0.02
	^{1}H^{a} (C$\underline{H}_3$)	0.085	0.085	0.000	0.00
	^{1}H^{b} (C$\underline{H}_3$)	3.632	3.633	0.001	0.03
3	^{13}C	-44.461	-44.477	0.016	0.04
	^{1}H^{a}	374.836	374.851	0.015	0.00
	^{1}H^{b}	-19.968	-19.966	0.002	0.01
4	^{13}C ($\underline{C}H_3$)	-14.272	-14.278	0.006	0.04
	^{13}C ($\underline{C}H_2$)	-15.463	-15.498	0.035	0.23
	^{1}H (C$\underline{H}_2$)	0.306	0.323	0.017	5.56
	^{1}H^{a} (C$\underline{H}_3$)	14.002	14.001	0.001	0.01
	^{1}H^{b} (C$\underline{H}_3$)	162.255	162.255	0.000	0.00
5	^{14}N	4.593	4.485	0.108	2.35
	o-^{13}C	1.599	1.857	0.258	16.14
	m-^{13}C	-28.914	-29.369	0.545	1.88
	p-^{13}C	19.337	19.614	0.277	1.43
	o-^{1}H	-30.602	-30.675	0.073	0.24
	m-^{1}H	-3.842	-3.720	0.122	3.18
	p-^{1}H	-27.272	-27.391	0.119	0.44
6	^{14}N	129.520	129.454	0.066	0.05
	^{17}O	-53.697	-53.767	0.070	0.13
7	^{13}C	22.741	22.705	0.036	0.16

	$^{1}\mathrm{H}$	-68.648	-68.651	0.003	0.00
8	$^{17}\mathrm{O}$	-7.694	-8.519	0.175	2.27
	$^{13}\mathrm{C}\,(\mathrm{H\underline{C}O})$	-86.133	-86.369	0.236	0.27
	$^{13}\mathrm{C}\,(\mathrm{\underline{C}H_3})$	48.003	48.027	0.024	0.05
	$^{1}\mathrm{H}\,(\mathrm{\underline{H}CO})$	311.223	311.200	0.023	0.01
	$^{1}\mathrm{H}\,(\mathrm{C\underline{H}_3})$	-7.700	-7.746	0.046	0.60
9	$^{13}\mathrm{C}$	666.302	666.191	0.111	0.02
	$^{19}\mathrm{F}$	373.470	374.320	0.150	0.04
10	$^{13}\mathrm{C}\,(\mathrm{\underline{C}H})$	211.780	211.585	0.195	0.09
	$^{13}\mathrm{C}\,(\mathrm{\underline{C}H_2})$	49.607	49.648	0.041	0.08
	$^{1}\mathrm{H}\,(\mathrm{C\underline{H}})$	57.362	57.365	0.003	0.01
	$^{1}\mathrm{H}\,(Z\text{-}\mathrm{C\underline{H}_2})$	115.421	115.412	0.009	0.01
	$^{1}\mathrm{H}\,(E\text{-}\mathrm{C\underline{H}_2})$	71.645	71.667	0.022	0.03
11	$^{13}\mathrm{C}$	-8.745	-8.760	0.015	0.17
	$^{14}\mathrm{N}$	-10.393	-10.522	0.129	1.24
	$^{1}\mathrm{H}$	158.701	158.740	0.039	0.02
12	$^{11}\mathrm{B}$	326.791	327.116	0.675	0.21
	$^{1}\mathrm{H}$	23.902	23.886	0.016	0.07

Notes:

- the enumeration of radicals is identical to the enumeration used by Vogler *et al.*[S2]
- radicals **2** and **8**: the HFCCs for the ^{1}H nuclei belonging to the same methyl-group were averaged
- radicals **3** and **4**: due to symmetry there are a set of 4 and a set of 2 (close to) identical ^{1}H nuclei across both methyl-groups

For further notes on symmetry breaking due to Jahn-Teller effects in these molecules refer to the work by Vogler *et al.*[S2]

6 Estimation of Memory Requirements

When estimating the memory requirements for the ω-RI-CDD-MP2 method and its selected-nuclei variant by Vogler *et al.*,[S3] and the THC-ω-RI-CDD-MP2 method from the main part of this publication, only the highest-order tensors are considered. Without taking the integral screening into account, the memory footprint of the ω-RI-CDD-MP2 is governed by the **B**-intermediates, exemplarily given by

$$B^{\eta}_{\underline{i}\overline{a},\beta} = \sum_{\alpha} (\underline{i}\overline{a}|\alpha)_{\eta} (\alpha|\beta)^{-1/2}, \tag{8}$$

for fully MO-transformed three-center RI integrals. Besides the fully transformed $B_{\underline{i}\overline{a},\beta}$-intermediate and its permutation $B_{\overline{a}\underline{i},\beta}$ (needed for exchange-type contributions), also the half-transformed intermediates $B_{\mu\overline{a},\beta}$ and $B_{\underline{i}\nu,\beta}$ are needed. All four **B**-type intermediates are needed for the α and β electrons, amounting to a total of eight third-order tensors. Therefore, the memory requirements in GB, assuming double precision floating point arithmetic, can be estimated as

$$\begin{aligned} M_{\text{est},1} &= \underbrace{2}_{\alpha/\beta} \times \left(2 \times \underbrace{N_{\text{occ}} \times N_{\text{virt}} \times N_{\text{aux}}}_{B_{\underline{i}\overline{a},\beta}/B_{\overline{a}\underline{i},\beta}} + \underbrace{N_{\text{bf}} \times N_{\text{virt}} \times N_{\text{aux}}}_{B_{\mu\overline{a},\beta}} + \underbrace{N_{\text{occ}} \times N_{\text{bf}} \times N_{\text{aux}}}_{B_{\underline{i}\nu,\beta}} \right) \times \underbrace{\frac{8\,\text{B}}{1024^3\,\frac{\text{B}}{\text{GB}}}}_{\rightarrow\text{GB}} \\ &= 2\,N_{\text{aux}}\,(2N_{\text{occ}}N_{\text{virt}} + N_{\text{bf}}N_{\text{virt}} + N_{\text{occ}}N_{\text{bf}})\,\frac{8\,\text{B}}{1024^3\,\frac{\text{B}}{\text{GB}}} \\ &= 2\,N_{\text{aux}}\,\left(2N_{\text{occ}}N_{\text{virt}} + N_{\text{bf}}^2\right)\,\frac{8\,\text{B}}{1024^3\,\frac{\text{B}}{\text{GB}}}. \end{aligned} \tag{9}$$

The memory requirements for the selected-nuclei variant are similar, except that here additional **B**-intermediates half-transformed with the perturbed density matrix are required, which results in

$$
\begin{aligned}
M_{\text{est},2} &= \underbrace{2}_{\alpha/\beta} \times \left(2 \times \underbrace{N_{\text{occ}} \times N_{\text{virt}} \times N_{\text{aux}}}_{B_{\underline{i}\overline{a},\beta}/B_{\overline{a}\underline{i},\beta}} +2 \times \underbrace{N_{\text{bf}} \times N_{\text{virt}} \times N_{\text{aux}}}_{B_{\mu\overline{a},\beta}/B_{\mu^x\overline{a},\beta}} +2 \times \underbrace{N_{\text{occ}} \times N_{\text{bf}} \times N_{\text{aux}}}_{B_{\underline{i}\nu,\beta}/B_{\underline{i}\nu^x,\beta}} \right) \\
&\quad \times \underbrace{\frac{8\,\text{B}}{1024^3\,\frac{\text{B}}{\text{GB}}}}_{\to\text{GB}} \\
&= 4\,N_{\text{aux}}\left(N_{\text{occ}}N_{\text{virt}} + N_{\text{bf}}N_{\text{virt}} + N_{\text{occ}}N_{\text{bf}}\right)\frac{8\,\text{B}}{1024^3\,\frac{\text{B}}{\text{GB}}} \\
&= 4\,N_{\text{aux}}\left(N_{\text{occ}}N_{\text{virt}} + N_{\text{bf}}^2\right)\frac{8\,\text{B}}{1024^3\,\frac{\text{B}}{\text{GB}}}.
\end{aligned}
\tag{10}
$$

For the THC-ω-RI-CDD-MP2 method, assuming the three-center integrals are not kept in memory after obtaining the THC factorized ERIs, the most memory demanding intermediates are second-order tensors of dimension $N_{\text{grid}} \times N_{\text{grid}}$. Since the algorithm for the exchange-like contribution to the **R**-matrices requires more such intermediates and since the memory occupied by the algorithm for the Coulomb-like contribution can be reclaimed, the memory requirements are estimated based on the algorithm for the exchange-like contribution. The latter requires 9 $N_{\text{grid}} \times N_{\text{grid}}$ intermediates, namely the THC **Z**-tensor, intermediates **A** and **B** from the precontraction step for both spin cases, as well as four matrices for the accumulation of results. This results in a rough memory requirement estimate of

$$
\begin{aligned}
M_{\text{est},3} &= \underbrace{N_{\text{grid}}^2}_{\mathbf{Z}} + \underbrace{2}_{\alpha/\beta} \times \underbrace{2 \times N_{\text{grid}}^2}_{\mathbf{A}/\mathbf{B}} + \underbrace{4 \times N_{\text{grid}}^2}_{\text{helper intermediates}} \times \underbrace{\frac{8\,\text{B}}{1024^3\,\frac{\text{B}}{\text{GB}}}}_{\to\text{GB}} \\
&= 9\,N_{\text{grid}}^2 \frac{8\,\text{B}}{1024^3\,\frac{\text{B}}{\text{GB}}}.
\end{aligned}
\tag{11}
$$

We note, that the various transformed, half-transformed, and untransformed collocation matrices are neglected in this estimate. For a reasonably sized basis set the relations $N_{\text{grid}} \approx 10\,N_{\text{bf}}$ and $N_{\text{bf}} \approx N_{\text{virt}} \gg N_{\text{occ}}$ hold, and therefore even the most memory demanding collocation matrix, i.e., X_{μ}^{P} of size $N_{\text{grid}} \times N_{\text{bf}} \approx \frac{1}{10} N_{\text{grid}}^2$ is only a tenth of the size of the intermediates discussed above.

7 Comparison of (Selected-nuclei) ω-RI-CDD-MP2 and THC-ω-RI-CDD-MP2

7.1 Asymptotic Scaling Comparison

In the main part of this publication we demonstrated the superiority of THC-ω-RI-CDD-MP2 compared to ω-RI-CDD-MP2 in terms of runtime for a selection of application inspired organic radicals. Vogler et al.[S3] proposed a selected-nuclei variant of ω-RI-CDD-MP2 to reduce the long computation times of the ω-RI-CDD-MP2 by making use of the locality of the perturbation. Since both, the selected-nuclei variant of ω-RI-CDD-MP2 and THC-ω-RI-CDD-MP2, were proposed to overcome the shortcomings of ω-RI-CDD-MP2, here, the three methods are compared in terms of their asymptotic scaling behavior for linear alkyl radicals up to 4000 basis functions with the cc-pVDZ basis set.

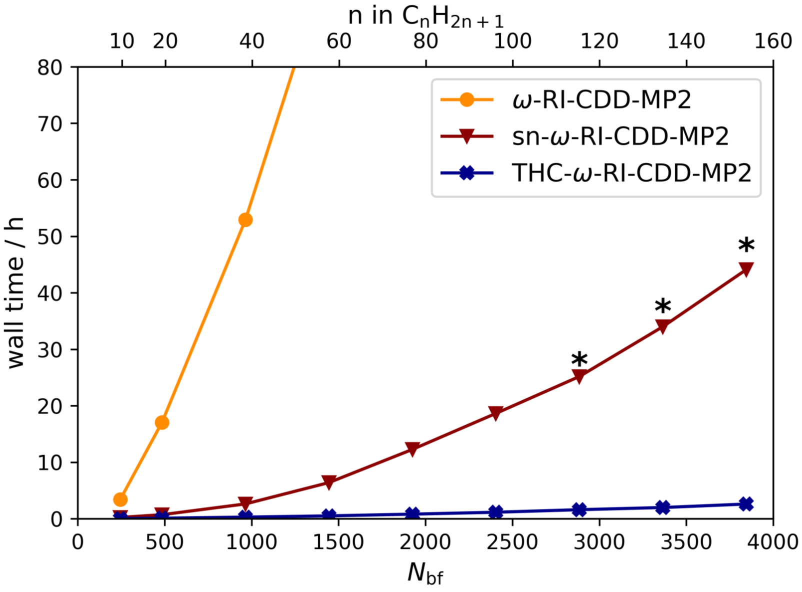

Figure S2: Comparison of the wall times and scaling of the ω-RI-CDD-MP2 (orange), the selected-nuclei ω-RI-CDD-MP2 (red), and the THC-ω-RI-CDD-MP2 method (blue) for linear alkyl radicals C_nH_{2n+1} ($n \in \{10, 20, 40, 60, 80, 100, 120, 140, 160\}$) using the cc-pVDZ basis set. Points marked with black asterisks were extrapolated conservatively.

As described in the literature,[S4] the RI-CDD-MP2 method is expected to scale quadratically due to the dominant runtime contribution of the formation of the **R**-matrices. Here, even subquadratic scaling is observed, which is because here – unlike in the original publication – an attenuated Coulomb metric in the RI integrals was used. The selected-nuclei variant of ω-RI-CDD-MP2 improves the runtimes considerably with similar subquadratic scaling. More drastic improvements are however obtained with the THC-ω-RI-CDD-MP2 method, which, as demonstrated in the main part of the publication, also has effective asymptotic subquadratic scaling. For the largest alkyl chain computed with the ω-RI-CDD-MP2 method, the selected-nuclei version provides a speedup of a factor of 15, while the THC method achieves a speedup of close to 200. It is apparent, that while all methods share an asymptotic subquadratic scaling, the drastically smaller prefactor – in addition to the reduced memory requirements – of the THC-ω-RI-CDD-MP2 make it vastly superior in terms of runtime. Furthermore, in contrast to the selected-nuclei ω-RI-CDD-MP2 method, the THC method is not limited to selected nuclei only but provides HFCCs for all nuclei simultaneously at reduced cost. In principle, THC-factorized ERIs can also be applied in the selected-nuclei approach, potentially leading to further speedups.

7.2 Timing Comparison With Selected-nuclei ω-RI-CDD-MP2

To compare the THC-ω-RI-CDD-MP2 method against the selected-nuclei variant of ω-RI-CDD-MP2 for more chemically relevant molecules, Table 4 of the main part of this publication is extended with timings obtained with the selected-nuclei ω-RI-CDD-MP2 method (see Table S3).

While the selected-nuclei method significantly improves upon the ω-RI-CDD-MP2 implementation in terms of computation time, with speedups up to 30–70, the THC-based method considerably outperforms both with speedups up to roughly 600–1000. The computational savings for the selected-nuclei method are greatest if the molecule under investigation is predominantly one-dimensional, like $(\mathrm{glu})_4$, whereas for globular systems, like the solvated TEMPO radical, speedups are reduced. The effect is also observed for the THC-ω-RI-CDD-

Table S3: Comparison of the memory requirements M_{est}, timings t, and relative speedups S of the THC-ω-RI-CDD-MP2 method with the ω-RI-CDD-MP2 method and its selected-nuclei variant. Speedups are determined relative to the timings obtained with the ω-RI-CDD-MP2 method.

			ω-RI-CDD-MP2		sel.-nuc. ω-RI-CDD-MP2			THC-ω-RI-CDD-MP2		
	molecule	N_{bf}	M_{est} / GB	t / h	M_{est} / GB	t / h	S	M_{est} / GB	t / h	S
cc-pVDZ	$C_{60}H_{121}$	1445	201.0	101.8	358.2	8.7	12	11.7	0.7	145
	TEMPO$_{H_2O}$	1444	208.5	345.9	366.0	51.1	7	11.7	1.5	230
	(glu)$_4$	1074	90.0	380.2	157.8	12.0	32	5.9	0.7	540
	PTMA$_3$	1102	93.8	620.9	165.8	18.1	34	6.5	1.2	517
	(AT)$_2$	1566	286.0	1111.0	500.3	53.1	21	23.1	1.9	585
cc-pVTZ	$C_{20}H_{41}$	1174	66.1	363.3	124.6	11.1	33	8.7	0.6	606
	TEMPO	582	8.2	160.1	15.5	3.4	47	2.1	0.2	891
	Tyr	530	6.6	99.4	12.3	2.2	45	1.4	0.1	780
	Thy	1260	86.6	1346.2$^{a)}$	161.5	18.4	73	8.7	1.1	1224
	(AT)$_1$	1982	340.4	2727.8$^{a)}$	634.0	38.1	72	20.7	3.1	880

$^{a)}$ timings are estimated conservatively based on the time taken for the first Laplace point

MP2 method, since the efficiency of both methods relies on the sparsity of the pseudo-density matrices. It is however less pronounced, indicating that the algorithm for the exchange-like part in the THC-ω-RI-CDD-MP2 utilizes the sparsity well even in nonlinear systems.

8 Structures

8.1 Benchmark Set of Small Organic Radicals

All structures were taken from the original publication by Vogler *et al.*[S2] and are available for download in a zip archive in the Supporting Information.

8.2 Benchmark Set of Medium-sized Organic Radicals

All structures used for optimizing the screening thresholds in the Coulomb- and exchange-like part of the **R**-matrices were optimized with the DL-FIND[S5] subprogram of FermiONs++[S6–S8] using the ωB97X functional and the def2-TZVP basis set. All structures are available for download in a zip archive in the Supporting Information. The benchmark set includes the following molecules and supramolecular assemblies:

- a linear alkyl radical: $C_{60}H_{121}$
- a spin-labeled adenine-thymine DNA fragment: $(AT)_2$
- a spin-labeled amylose chain: $(glu)_4$
- the poly(2,2,6,6-tetramethyl-piperidenyloxyl-4-yl methacrylate) (PTMA) trimer: $PTMA_3$
- a H_2O solvated (2,2,6,6-Tetramethylpiperidin-1-yl)oxyl (TEMPO) radical with 50 water molecules: $TEMPO_{H_2O}$
- a supramolecular assembly of the *tert*-butyl radical in a cucurbit[6]uril (CB[6]) host: *t*-butyl@CB[6]

8.3 Test Set for the Comparison Against ω-RI-CDD-MP2

All structures used for the comparison against ω-RI-CDD-MP2 were optimized with the DL-FIND[S5] subprogram of FermiONs++[S6–S8] using the ωB97X functional and the def2-TZVP basis set. All structures are available for download in a zip archive in the Supporting

Information.

The benchmark set includes the following molecules and supramolecular assemblies ...

- ... for the cc-pVDZ basis set:
  - a linear alkyl radical: $C_{60}H_{121}$
  - a H_2O solvated TEMPO radical with 50 water molecules: $\mathrm{TEMPO}_{\mathrm{H_2O}}$
  - a spin-labeled amylose chain: $(\mathrm{glu})_4$
  - the PTMA trimer: PTMA_3
  - a spin-labeled adenine-thymine DNA fragment: $(\mathrm{AT})_2$
- ... for the cc-pVTZ basis set:
  - a linear alkyl radical: $C_{20}H_{41}$
  - the TEMPO radical: TEMPO
  - the tyrosine radical: Tyr
  - a spin-labeled thymine molecule: Thy
  - a spin-labeled adenine-thymine DNA fragment: $(\mathrm{AT})_1$

References

(S1) Parrish, R. M.; Hohenstein, E. G.; Martínez, T. J.; Sherrill, C. D. Tensor hypercontraction. II. Least-squares renormalization. *J. Chem. Phys.* **2012**, *137*, 224106.

(S2) Vogler, S.; Dietschreit, J. C.; Peters, L. D.; Ochsenfeld, C. Important components for accurate hyperfine coupling constants: electron correlation, dynamic contributions, and solvation effects. *Mol. Phys.* **2020**, *118*.

(S3) Vogler, S.; Savasci, G.; Ludwig, M.; Ochsenfeld, C. Selected-Nuclei Method for the Computation of Hyperfine Coupling Constants within Second-Order Møller-Plesset Perturbation Theory. *J. Chem. Theory. Comput.* **2018**, *14*, 3014–3024.

(S4) Vogler, S.; Ludwig, M.; Maurer, M.; Ochsenfeld, C. Low-scaling first-order properties within second-order Møller-Plesset perturbation theory using Cholesky decomposed density matrices. *J. Chem. Phys.* **2017**, *147*, 024101.

(S5) Kästner, J.; Carr, J. M.; Keal, T. W.; Thiel, W.; Wander, A.; Sherwood, P. DL-FIND: An open-source geometry optimizer for atomistic simulations. *J. Chem. Phys. A* **2009**, *113*, 11856–11865.

(S6) Kussmann, J.; Ochsenfeld, C. Pre-selective screening for matrix elements in linear-scaling exact exchange calculations. *J. Chem. Phys.* **2013**, *138*, 134114.

(S7) Kussmann, J.; Ochsenfeld, C. Preselective screening for linear-scaling exact exchange-gradient calculations for graphics processing units and general strong-scaling massively parallel calculations. *J. Chem. Theory. Comput.* **2015**, *11*, 918–922.

(S8) Kussmann, J.; Ochsenfeld, C. Hybrid CPU/GPU Integral Engine for Strong-Scaling Ab Initio Methods. *J. Chem. Theory. Comput.* **2017**, *13*, 3153–3159.

3.3. Publication III: Analytical Second-Order Properties for the Random Phase Approximation: Nuclear Magnetic Resonance Shieldings

V. Drontschenko, F. H. Bangerter, C. Ochsenfeld

J. Chem. Theory Comput. **19**, 7542–7554 (2023)

Abstract

A method for the analytic computation of nuclear magnetic resonance (NMR) shieldings within the direct random phase approximation (RPA) is presented. As a starting point we use the RPA ground-state energy expression within the resolution-of-the-identity approximation in the atomic-orbital formalism. As has been shown in a recent benchmark study using numerical second derivatives [Glasbrenner, M. *et al.* *J. Chem. Theory Comput.* **2021**, *18*, 192], RPA based on a Hartree–Fock reference shows accuracies comparable to coupled cluster singles doubles (CCSD) for NMR chemical shieldings. Together with the much lower computational cost of RPA, it has emerged as an accurate method for the computation of NMR shieldings. Therefore, we aim to extend the applicability of RPA NMR to larger systems by introducing analytical second-order derivatives, making it a viable method for the accurate and efficient computation of NMR chemical shieldings.

Reprinted with permission from:

V. Drontschenko, F. H. Bangerter, C. Ochsenfeld
"Analytical Second-Order Properties for the Random Phase Approximation: Nuclear Magnetic Resonance Shieldings"
J. Chem. Theory Comput. **19**, 7542–7554 (2023)

`https://pubs.acs.org/doi/10.1021/acs.jctc.3c00542`

JCTC Journal of Chemical Theory and Computation

pubs.acs.org/JCTC Article

Analytical Second-Order Properties for the Random Phase Approximation: Nuclear Magnetic Resonance Shieldings

Viktoria Drontschenko,[§] Felix H. Bangerter,[§] and Christian Ochsenfeld*

Cite This: *J. Chem. Theory Comput.* 2023, 19, 7542−7554

Read Online

ACCESS | Metrics & More | Article Recommendations | Supporting Information

ABSTRACT: A method for the analytical computation of nuclear magnetic resonance (NMR) shieldings within the direct random phase approximation (RPA) is presented. As a starting point, we use the RPA ground-state energy expression within the resolution-of-the-identity approximation in the atomic-orbital formalism. As has been shown in a recent benchmark study using numerical second derivatives [Glasbrenner, M. et al. *J. Chem. Theory Comput.* **2022**, *18*, 192], RPA based on a Hartree−Fock reference shows accuracies comparable to coupled cluster singles and doubles (CCSD) for NMR chemical shieldings. Together with the much lower computational cost of RPA, it has emerged as an accurate method for the computation of NMR shieldings. Therefore, we aim to extend the applicability of RPA NMR to larger systems by introducing analytical second-order derivatives, making it a viable method for the accurate and efficient computation of NMR chemical shieldings.

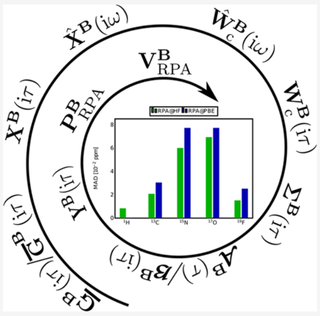

1. INTRODUCTION

Nuclear magnetic resonance (NMR) spectroscopy has emerged as an important tool for the structure determination of organic, inorganic, and macromolecular compounds in the field of chemistry and biochemistry.[1−4] However, the precise determination of molecular or solid state structures from experimental NMR spectra can be tedious due to the difficulty of assigning the signals.[2,5] In these cases, employing quantum chemical methods for the computation of NMR shielding tensors can aid in the interpretation of experimental spectra and, thus, help in the elucidation of structures.[2,6] Hence, a lot of effort has been put into the development of such methods, e.g., refs 2,7−10.

Methods for the computation of molecular NMR shifts range from Hartree−Fock (HF)[11−15] and density functional theory (DFT)[16−18] to wave function-based post-HF methods such as Møller−Plesset perturbation theory (MP2),[19,20] coupled cluster (CC) variants,[21−23] and multiconfigurational self-consistent field (MCSCF).[24] Among these methods, HF and DFT have the lowest computational cost, with comparably moderate accuracy. Nonetheless, the development of low-scaling implementations has made the computation of systems with over 1000 atoms possible.[25,26] MP2 has been shown to yield more accurate results than HF and DFT[20,27,28] while also being computationally more demanding. However, significant advancements have been made in the development of efficient methods for the computation of MP2 NMR shifts to alleviate this issue.[29−39] The most accurate methods for the computation of NMR shifts are coupled cluster singles and doubles (CCSD) as well as with additional perturbative triples (CCSD(T)).[40] However, the CC methods are accompanied by the highest computational cost among the above-mentioned methods and are, if no further approximations are applied, only feasible for very small systems.

A method that has proven to combine both high accuracy and low computational cost is the random phase approximation (RPA).[41] In a recent benchmark study,[41] it was shown that RPA provides comparable accuracy for NMR chemical shieldings as CCSD, albeit with reduced computational effort, also when compared to MP2.

RPA, originally introduced by Bohm and Pines in 1953,[42] is usually implemented as a post-Kohn−Sham (KS)[43] method. It stands on the fifth and highest rung of Jacob's ladder[44] and does not contain any empirical parameters. The expression for the RPA ground-state energy can be derived in the context of DFT[43,45] using the adiabatic-connection fluctuation−dissipation theorem (ACFDT).[46−48] However, the original formulation[46,48] has an $O(M^6)$ scaling with the system size M, making it only feasible for small systems. By introducing the resolution-of-the-identity (RI)[49−53] approximation, Furche and co-workers[54] lowered the formal scaling to $O(M^4)$, rendering RPA as one of the formally lowest scaling correlation methods. Further improvements for the computational efficiency of the RPA ground-state energies followed,[54−63] paving the way for the investigation of systems with more than 1000 atoms.[58−63]

Received: May 23, 2023
Published: October 20, 2023

For the investigation of many molecular properties, derivatives of the ground-state energy are necessary. In this regard, there are two routes to obtain higher-order derivatives, either numerically or analytically. Generally, analytical derivatives are superior to numerical schemes since they are significantly more efficient and avoid errors stemming from a finite step size.[8,64] It is worth noting here that mixed schemes, e.g., calculating the first derivative analytically and the second derivative numerically, are also conceivable and in fact often applied, e.g., for vibrational frequency calculations, as a trade-off between computational efficiency and development effort. While various methods have been developed for the analytical evaluation of first-order properties at the RPA level of theory,[65−71] to the best of our knowledge, no analytical second-order properties such as NMR shieldings with post-KS methods based on the ACFDT exist. A first step in this direction was taken by Glasbrenner et al.[41] by introducing a numerical implementation of RPA shielding tensors for benchmarking the performance of RPA and the closely related σ-functionals.[72] It has been found that RPA calculations based on a HF reference provide NMR shieldings comparable to the CCSD accuracy. Based on these promising results, we aim to extend the applicability of RPA NMR by deriving the expression for the RPA NMR shielding tensor as an analytical second derivative of the RPA energy. This enables the accurate prediction of NMR shieldings of large molecules with a low formal scaling behavior.

We want to note that refs 8,73−78, which describe RPA NMR, use RPA synonymously with coupled-perturbed HF as well as time-dependent HF. However, in our work, RPA stands for an ACFDT-based post-KS method and gives different results than coupled-perturbed HF and time-dependent HF. Therefore, the methods described in these references differ from the method introduced in this work.

This work is structured as follows: after establishing the notation used throughout this work in Section 2, we will derive the analytical mixed second derivative of the total RPA energy with respect to the nuclear magnetic moment and an external magnetic field to obtain the NMR shielding tensor in Section 3. To accomplish this, we will start by reviewing the expression for the RPA correlation energy within the atomic-orbital basis in Section 3.1 and subsequently derive its first derivative with respect to the nuclear magnetic moment in Section 3.2. In the main part of the theory in Section 3.3, we will derive the second derivative with respect to the magnetic field. Due to the close relation of RPA and MP2, we will make use of several methods used for the Laplace transformed atomic-orbital MP2 NMR method, as introduced by us earlier. Finally, after providing the computational details in Section 4, we will present the validation of our theory and implementation.

2. NOTATION

Throughout this work, we adopt the following notation:

- $\mu, \nu, \lambda, \sigma$: atomic-orbital indices; N: total number of AO-basis functions
- P, Q: auxiliary function indices; N_{aux}: total number of auxiliary functions

We use the Mulliken notation for two- and three-center integrals. Furthermore, Einstein's sum convention is employed.[79] For general intermediates containing both integrals and densities, the derivative with respect to a general perturbation ξ is denoted as O^{ξ}, while intermediate derivatives containing only the differentiated integrals are denoted as $O^{(\xi)}$. In all other cases, O^{ξ} is used as a short-hand notation for $\frac{\partial}{\partial \xi}O$.

3. THEORY

The elements of the NMR shielding tensor σ^A_{rs} of a nucleus A can be expressed as the mixed second derivative of the electronic energy E with respect to a coordinate of the nuclear magnetic moment m^A_s and the magnetic field B_r evaluated at zero according to

$$\sigma^A_{rs} = \frac{\partial^2}{\partial B_r \partial m^A_s} E \Bigg|_{\mathbf{m}^A=\mathbf{0},\mathbf{B}=\mathbf{0}} \qquad \forall\ r, s \in \{x, y, z\} \tag{1}$$

In this work, the focus is on NMR shieldings based on RPA, which are derived as the analytical second derivatives of the total RPA energy with respect to $\mathbf{B}$ and $\mathbf{m}$. To ensure gauge origin independence, we employ gauge-including atomic orbitals (GIAOs)[12,13,80−83] defined as

$$\chi_\mu(\mathbf{r}, \mathbf{B}) = \chi_\mu(\mathbf{r}, \mathbf{B} = \mathbf{0}) \exp\left(-\frac{\mathrm{i}}{2}[\mathbf{B} \times (\mathbf{R}_\mu - \mathbf{R}_0)]\mathbf{r}\right) \tag{2}$$

where i is the imaginary unit, $\chi_\mu(\mathbf{r}, \mathbf{B} = \mathbf{0})$ denotes the field-independent atomic-orbital basis function centered at $\mathbf{R}_\mu$, and $\mathbf{R}_0$ is the gauge origin. Through the utilization of GIAOs, we, therefore, formally introduce complex quantities.

The remainder of this section is structured as follows: we will first give a brief review of the RPA total energy in the atomic-orbital basis formulation and subsequently continue with the first derivative with respect to the nuclear magnetic moment $\mathbf{m}$. We derive both in terms of complex-valued orbitals without any assumptions on the symmetry of functions in the time and frequency domain. This general formulation of the RPA energy and first-order properties differs from the derivation presented by Beuerle and Ochsenfeld[68] for molecular gradients since it was carried out for real-valued orbitals only. Subsequently, the second derivative of the RPA energy with respect to the magnetic field $\mathbf{B}$ is derived and evaluated at $\mathbf{m} = \mathbf{0}$ and $\mathbf{B} = \mathbf{0}$. This leads to a simplification of the expressions, such that no complex-valued matrices enter the final equations. All matrices are either purely real and symmetric or purely imaginary and skew-symmetric. Further, all time- and frequency-dependent quantities are either odd or even functions in the time or frequency domain.

Please note that in the following sections, we will provide only a brief summary for RPA energies and gradients, which serve as a starting point for the second derivative. For a more detailed account, we refer the reader to previous publications on RPA energies[54−56,59−61] and gradients.[68,84]

3.1. AO-RPA Total Energies.

Within the adiabatic-connection formalism,[47] the total energy of the electronic ground state can be expressed as[46,48]

$$E^{\mathrm{total}}[\mathbf{P}] = E^{\mathrm{HF}}[\mathbf{P}] + E_{\mathrm{c}}[\mathbf{P}] \tag{3}$$

where the total electronic energy E^{total}, the Hartree−Fock energy E^{HF}, and the correlation energy E_{c} are evaluated with the density $\mathbf{P}$ obtained from a prior DFT or HF calculation. Please note that the following derivations will be carried out for the more general case of a KS-DFT reference calculation. However, we will note necessary changes for an HF reference calculation where needed. The correlation energy can be expressed within the zero-temperature fluctuation−dissipation theorem and the RPA[85] as well as the RI approximation[54−56] after analytical coupling-strength integration as

$$E_{\mathrm{c}}^{\mathrm{RPA}} = \frac{1}{4\pi}\int_{-\infty}^{+\infty} \mathrm{d}\omega \mathrm{Tr}[\ln(\mathbf{1} - \hat{\mathbf{X}}_0(\mathrm{i}\omega)\mathbb{V}) + \hat{\mathbf{X}}_0(\mathrm{i}\omega)\mathbb{V}] \tag{4}$$

Here, the electron−electron interaction operator in the auxiliary basis is given as

$$\mathbb{V}_{PQ} = (P|r_{12}^{-1}|Q)^{-1} \tag{5}$$

within the RI approximation with the r_{12}^{-1} Coulomb metric, where r_{12} is the interelectronic distance. For efficiency reasons, the noninteracting response function is computed in the imaginary time domain and transformed into the imaginary frequency domain using the Fourier transform

$$\hat{\mathbf{X}}_0(\mathrm{i}\omega) = \int_{-\infty}^{+\infty} \mathrm{d}\tau \exp(\mathrm{i}\omega\tau)\mathbf{X}_0(\mathrm{i}\tau) \tag{6}$$

The Fourier transform simplifies to a cosine transform[57,61] or, equivalently, to a double Laplace transform[59,60] if $\mathbf{X}_0(\mathrm{i}\tau)$ is an even function in the imaginary time domain. The response function in the imaginary time domain is given by[86]

$$\mathbf{X}_0(\mathrm{i}\tau) = \Theta(-\tau)\mathbf{X}_0^{-}(\mathrm{i}\tau) + \Theta(\tau)\mathbf{X}_0^{+}(\mathrm{i}\tau) \tag{7}$$

$$X_{0,\mathrm{PQ}}^{-}(\mathrm{i}\tau) = \underline{G}_{0,\lambda\nu}(-\mathrm{i}\tau)\mathbb{B}_{\mu\nu}^{P}\overline{G}_{0,\mu\sigma}(\mathrm{i}\tau)\mathbb{B}_{\lambda\sigma}^{Q} \tag{8}$$

$$X_{0,\mathrm{PQ}}^{+}(\mathrm{i}\tau) = \underline{G}_{0,\mu\sigma}(-\mathrm{i}\tau)\mathbb{B}_{\mu\nu}^{P}\overline{G}_{0,\lambda\nu}(\mathrm{i}\tau)\mathbb{B}_{\lambda\sigma}^{Q} \tag{9}$$

where the three-center RI integrals are defined as

$$\mathbb{B}_{\mu\nu}^{P} = (\mu\nu|r_{12}^{-1}|P) \tag{10}$$

and the noninteracting Green's functions are defined as

$$\mathbf{G}_0(\mathrm{i}\tau) = \Theta(-\tau)\underline{\mathbf{G}}_0(\mathrm{i}\tau) + \Theta(\tau)\overline{\mathbf{G}}_0(\mathrm{i}\tau) \tag{11}$$

$$\underline{\mathbf{G}}_0(\mathrm{i}\tau) = \mathbf{P}\exp(-\tau(\mathbf{H} - \epsilon_{\mathrm{F}}\mathbf{S})\mathbf{P}) \tag{12}$$

$$\overline{\mathbf{G}}_0(\mathrm{i}\tau) = -\mathbf{P}_{\mathrm{virt}}\exp(-\tau(\mathbf{H} - \epsilon_{\mathrm{F}}\mathbf{S})\mathbf{P}_{\mathrm{virt}}) \tag{13}$$

with the Fermi level ϵ_{F},[60,87] the Heaviside step function $\Theta(\tau)$, the occupied density $\mathbf{P}$, and the virtual density $\mathbf{P}_{\mathrm{virt}}$. Further, the Hamiltonian $\mathbf{H}$ is defined according to

$$\mathbf{H} = \mathbf{h} + \mathbf{G}[\mathbf{P}] \tag{14}$$

where $\mathbf{h}$ denotes the matrix representation of the one-electron Hamiltonian, and $\mathbf{G}[\mathbf{P}]$ is defined as

$$\mathbf{G}[\mathbf{P}] = \mathbf{J}[\mathbf{P}] + \mathbf{V}_{\mathrm{xc}}[\mathbf{P}] \tag{15}$$

with the matrix representation of the Coulomb potential $\mathbf{J}$ and the exchange-correlation potential $\mathbf{V}_{\mathrm{xc}}$. Please note that for a RPA calculation based on a Hartree−Fock reference, $\mathbf{V}_{\mathrm{xc}}$ is replaced by the Hartree−Fock exchange $\mathbf{K}$.

3.2. First Derivative with Respect to the Nuclear Magnetic Moment. The first derivative of the RPA total energy in eq 3 with respect to the nuclear magnetic moment $\mathbf{m}$ reads

$$\frac{\partial E^{\mathrm{total}}[\mathbf{P}]}{\partial \mathbf{m}} = \frac{\partial E^{\mathrm{HF}}[\mathbf{P}]}{\partial \mathbf{m}} + \frac{\partial E_{\mathrm{c}}^{\mathrm{RPA}}[\mathbf{P}]}{\partial \mathbf{m}} \tag{16}$$

In the following sections, we will first review the expression for $\frac{\partial E^{\mathrm{HF}}[\mathbf{P}]}{\partial \mathbf{m}}$ and subsequently derive an expression for the derivative of the RPA correlation energy $E_{\mathrm{c}}^{\mathrm{RPA}}$ with respect to $\mathbf{m}$.

3.2.1. First Derivative of the HF Functional with Respect to the Nuclear Magnetic Moment. The derivative of the HF energy with respect to the nuclear magnetic moment $\mathbf{m}$, given by the first term in eq 16, can be written as

$$\frac{\partial E^{\mathrm{HF}}[\mathbf{P}]}{\partial \mathbf{m}} = \mathrm{Tr}(\mathbf{P}\mathbf{h}^{\mathbf{m}}) + \mathrm{Tr}(\mathbf{H}_{\mathrm{HF}}\mathbf{P}^{\mathbf{m}}) \tag{17}$$

with

$$\mathrm{Tr}(\mathbf{H}_{\mathrm{HF}}\mathbf{P}^{\mathbf{m}}) = \mathrm{Tr}(\mathbf{P}^{\mathbf{m}}\mathbf{h} + \mathbf{P}^{\mathbf{m}}\mathbf{J}[\mathbf{P}] + \mathbf{P}^{\mathbf{m}}\mathbf{K}[\mathbf{P}]) \tag{18}$$

It is important to note that the HF energy is not stationary with respect to the KS density. Therefore, the density response, i.e., the last term in eq 17, has to be evaluated explicitly and cannot be avoided as in regular HF gradient calculations.[88] A most efficient alternative is to use the Z-vector method, as outlined later in this work.[84,89]

3.2.2. First Derivative of the RPA Correlation Energy with Respect to the Nuclear Magnetic Moment. The first derivative of the RPA correlation energy (eq 4) with respect to a general perturbation ξ is given by[68]

$$\begin{aligned}\frac{\partial E_{\mathrm{c}}^{\mathrm{RPA}}}{\partial \xi} &= \mathrm{Tr}\left(\frac{\partial E_{\mathrm{c}}^{\mathrm{RPA}}}{\partial \mathbb{V}}\frac{\partial \mathbb{V}}{\partial \xi}\right) + \mathrm{Tr}\left(\frac{\partial E_{\mathrm{c}}^{\mathrm{RPA}}}{\partial \mathbb{B}}\frac{\partial \mathbb{B}}{\partial \xi}\right)\\ &\quad + \mathrm{Tr}\left(\frac{\partial E_{\mathrm{c}}^{\mathrm{RPA}}}{\partial \mathbf{G}_0}\frac{\partial \mathbf{G}_0}{\partial \xi}\right)\end{aligned} \tag{19}$$

When considering the derivative with respect to the nuclear magnetic moment $\mathbf{m}$, the above equation reduces to

$$\frac{\partial E_{\mathrm{c}}^{\mathrm{RPA}}}{\partial \mathbf{m}} = \mathrm{Tr}\left(\int_{-\infty}^{+\infty} \mathrm{d}\omega \frac{\partial E_{\mathrm{c}}^{\mathrm{RPA}}(\mathrm{i}\omega)}{\partial \hat{\mathbf{X}}_0(\mathrm{i}\omega)}\frac{\partial \hat{\mathbf{X}}_0(\mathrm{i}\omega)}{\partial \mathbf{G}_0(\mathrm{i}\tau)}\frac{\partial \mathbf{G}_0(\mathrm{i}\tau)}{\partial \mathbf{m}}\right) \tag{20}$$

since both the electron−electron interaction operator in the auxiliary basis $\mathbb{V}$ and the three-center integral tensor $\mathbb{B}$ are independent of $\mathbf{m}$, and thus their derivative is zero.

For a given imaginary frequency, the first term in eq 20 evaluates to

$$\frac{\partial E_{\mathrm{c}}^{\mathrm{RPA}}(\mathrm{i}\omega)}{\partial \hat{\mathbf{X}}_0(\mathrm{i}\omega)} = -\frac{1}{4\pi}\hat{\mathbf{W}}_{\mathrm{c}}(\mathrm{i}\omega) \tag{21}$$

where the correlated screened Coulomb interaction, which is also one of the central quantities in the GW-approximation,[67,90,91] is defined as

$$\hat{\mathbf{W}}_{\mathrm{c}}(\mathrm{i}\omega) = \mathbb{V}[(\mathbf{1} - \hat{\mathbf{X}}_0(\mathrm{i}\omega)\mathbb{V})^{-1} - \mathbf{1}] \tag{22}$$

To evaluate the derivative of the RPA correlation energy with respect to $\mathbf{m}$ entirely in the imaginary time domain, eq 6 can be inserted into eq 20 to yield

$$\begin{aligned}\frac{\partial E_{\mathrm{c}}^{\mathrm{RPA}}}{\partial \mathbf{m}} = \mathrm{Tr}\Bigg(&-\frac{1}{4\pi}\int_{-\infty}^{+\infty} \mathrm{d}\omega \int_{-\infty}^{+\infty} \mathrm{d}\tau \hat{\mathbf{W}}_{\mathrm{c}}(\mathrm{i}\omega)\\ &\exp(\mathrm{i}\omega\tau)\frac{\partial \mathbf{X}_0(\mathrm{i}\tau)}{\partial \mathbf{G}_0(\mathrm{i}\tau)}\frac{\partial \mathbf{G}_0(\mathrm{i}\tau)}{\partial \mathbf{m}}\Bigg)\end{aligned} \tag{23}$$

Next, $\hat{\mathbf{W}}_c(\mathrm{i}\omega)$ has to be transformed into the imaginary time domain. Therefore, we consider the expression for its inverse Fourier transform

$$\mathbf{W}_c(\mathrm{i}\tau) = \frac{1}{2\pi}\int_{-\infty}^{+\infty} \mathrm{d}\omega \hat{\mathbf{W}}_c(\mathrm{i}\omega)\exp(-\mathrm{i}\omega\tau) \tag{24}$$

When comparing the right-hand side of eq 24 with eq 23, it becomes apparent that eq 23 cannot be rewritten directly in terms of $\mathbf{W}_c(\mathrm{i}\tau)$. However, $\mathbf{W}_c(\mathrm{i}\tau)$ can be expressed in terms of its even and odd part as $\mathbf{W}_c(\mathrm{i}\tau) = \mathbf{W}_c^{\mathrm{even}}(\mathrm{i}\tau) + \mathbf{W}_c^{\mathrm{odd}}(\mathrm{i}\tau)$, which allows us to rewrite the first two terms in eq 23 as

$$\begin{aligned}\tilde{\mathbf{W}}_c(\mathrm{i}\tau) &:= \frac{1}{2\pi}\int_{-\infty}^{+\infty} \mathrm{d}\omega \hat{\mathbf{W}}_c(\mathrm{i}\omega)\exp(\mathrm{i}\omega\tau)\\ &= \mathbf{W}_c^{\mathrm{even}}(\mathrm{i}\tau) - \mathbf{W}_c^{\mathrm{odd}}(\mathrm{i}\tau)\end{aligned} \tag{25}$$

with

$$\mathbf{W}_c^{\mathrm{even}}(\mathrm{i}\tau) = \frac{1}{\pi}\int_{0}^{+\infty} \mathrm{d}\omega\, \cos(\omega\tau)\hat{\mathbf{W}}_c(\mathrm{i}\omega) \tag{26}$$

$$\mathbf{W}_c^{\mathrm{odd}}(\mathrm{i}\tau) = -\frac{\mathrm{i}}{\pi}\int_{0}^{+\infty} \mathrm{d}\omega\, \sin(\omega\tau)\hat{\mathbf{W}}_c(\mathrm{i}\omega) \tag{27}$$

Inserting eq 25 into eq 23 finally yields

$$\frac{\partial E_c^{\mathrm{RPA}}}{\partial \mathbf{m}} = \frac{1}{2}\mathrm{Tr}\left(-\int_{-\infty}^{+\infty} \mathrm{d}\tau \tilde{\mathbf{W}}_c(\mathrm{i}\tau)\frac{\partial \mathbf{X}_0(\mathrm{i}\tau)}{\partial \mathbf{G}_0(\mathrm{i}\tau)}\frac{\partial \mathbf{G}_0(\mathrm{i}\tau)}{\partial \mathbf{m}}\right) \tag{28}$$

$$\begin{aligned}&= \frac{1}{2}\mathrm{Tr}\left(-\int_{0}^{+\infty} \mathrm{d}\tau \tilde{\mathbf{W}}_c(\mathrm{i}\tau)\frac{\partial \mathbf{X}_0(\mathrm{i}\tau)}{\partial \mathbf{G}_0(\mathrm{i}\tau)}\frac{\partial \mathbf{G}_0(\mathrm{i}\tau)}{\partial \mathbf{m}}\right)\\ &+\frac{1}{2}\mathrm{Tr}\left(-\int_{0}^{+\infty} \mathrm{d}\tau \tilde{\mathbf{W}}_c(-\mathrm{i}\tau)\frac{\partial \mathbf{X}_0(-\mathrm{i}\tau)}{\partial \mathbf{G}_0(-\mathrm{i}\tau)}\right.\\ &\left.\frac{\partial \mathbf{G}_0(-\mathrm{i}\tau)}{\partial \mathbf{m}}\right)\end{aligned} \tag{29}$$

After the evaluation of $\frac{\partial \mathbf{X}_0(\mathrm{i}\tau)}{\partial \mathbf{G}_0(\mathrm{i}\tau)}$, the following expression is obtained

$$\frac{\partial E_c^{\mathrm{RPA}}}{\partial \mathbf{m}} = \frac{1}{2}\mathrm{Tr}\left(\int_{0}^{+\infty} \mathrm{d}\tau \boldsymbol{\Sigma}(\mathrm{i}\tau)\underline{\mathbf{G}}_0^{\mathbf{m}}(-\mathrm{i}\tau) + \boldsymbol{\Sigma}(-\mathrm{i}\tau)\bar{\mathbf{G}}_0^{\mathbf{m}}(\mathrm{i}\tau)\right) \tag{30}$$

where the correlated self-energy $\boldsymbol{\Sigma}$ is introduced, which is another central quantity in the GW-approximation.[67] For positive and negative imaginary times, $\boldsymbol{\Sigma}(\mathrm{i}\tau)$ is defined as

$$\Sigma_{\nu\lambda}(\mathrm{i}\tau) = -\tilde{W}_{c,PQ}(-\mathrm{i}\tau)\mathbb{B}^{P}_{\mu\nu}G_{0,\mu\sigma}(\mathrm{i}\tau)\mathbb{B}^{Q}_{\lambda\sigma} \tag{31}$$

The last term that remains to be evaluated in eq 30 is the derivative of the Green's functions with respect to **m**. A detailed derivation can be found in ref 68. In the following, only the most important steps of the derivation are shown. Differentiating the Green's functions given in eqs 12 and 13 yields

$$\begin{aligned}\frac{\partial \underline{\mathbf{G}}_0(\mathrm{i}\tau)}{\partial \mathbf{m}} &= \mathbf{P}^{\mathbf{m}}\exp(-\tau(\mathbf{H} - \epsilon_F\mathbf{S})\mathbf{P})\\ &+ \mathbf{P}(\exp(-\tau(\mathbf{H} - \epsilon_F\mathbf{S})\mathbf{P}))^{\mathbf{m}}\end{aligned} \tag{32}$$

$$\begin{aligned}\frac{\partial \bar{\mathbf{G}}_0(\mathrm{i}\tau)}{\partial \mathbf{m}} &= -\mathbf{P}^{\mathbf{m}}_{\mathrm{virt}}\exp(-\tau(\mathbf{H} - \epsilon_F\mathbf{S})\mathbf{P}_{\mathrm{virt}})\\ &+ \mathbf{P}_{\mathrm{virt}}(\exp(-\tau(\mathbf{H} - \epsilon_F\mathbf{S})\mathbf{P}_{\mathrm{virt}}))^{\mathbf{m}}\end{aligned} \tag{33}$$

The occupied and virtual densities are related through the completeness relation

$$\mathbf{1} = \mathbf{PS} + \mathbf{P}_{\mathrm{virt}}\mathbf{S} \tag{34}$$

By differentiating the above identity with respect to the nuclear magnetic moment,[84] the following relation is obtained: $\mathbf{P}^{\mathbf{m}}_{\mathrm{virt}} = -\mathbf{P}^{\mathbf{m}}$, which only requires the evaluation of the occupied density. The derivative of the matrix exponentials can be evaluated by differentiating the corresponding series expansion.[84,87,92]

The final expression reads

$$\frac{\partial E_c^{\mathrm{RPA}}}{\partial \mathbf{m}} = \mathrm{Tr}\left(\frac{\partial E_c^{\mathrm{RPA}}}{\partial \mathbf{X}_0(\mathrm{i}\omega)}\frac{\partial \hat{\mathbf{X}}_0(\mathrm{i}\omega)}{\partial \mathbf{G}_0(\mathrm{i}\tau)}\frac{\partial \mathbf{G}_0(\mathrm{i}\tau)}{\partial \mathbf{m}}\right) \tag{35}$$

$$= \mathrm{Tr}(\mathbf{V}_{\mathrm{RPA}}\mathbf{P}^{\mathbf{m}} + \mathbf{P}_{\mathrm{RPA}}\mathbf{h}^{\mathbf{m}}) \tag{36}$$

where the following intermediates are introduced

$$\mathbf{V}_{\mathrm{RPA}} = \frac{1}{2}(\mathbf{M} + \mathbf{G}[\mathbf{P}_{\mathrm{RPA}}]) \tag{37}$$

$$\mathbf{P}_{\mathrm{RPA}} = \frac{1}{2}\int_{0}^{+\infty} \mathrm{d}\tau(\mathbf{P}\underline{\mathbf{Y}}(-\mathrm{i}\tau) - \mathbf{P}_{\mathrm{virt}}\bar{\mathbf{Y}}(\mathrm{i}\tau)) \tag{38}$$

as well as

$$\mathbf{M} = \bar{\mathbf{M}} + \underline{\mathbf{M}} \tag{39}$$

$$\begin{aligned}\bar{\mathbf{M}} = \int_{0}^{+\infty} \mathrm{d}\tau(&\bar{\mathbf{Y}}(\mathrm{i}\tau)(\mathbf{H} - \epsilon_F\mathbf{S})\\ &+ \exp(-\tau(\mathbf{H} - \epsilon_F\mathbf{S})\mathbf{P}_{\mathrm{virt}})\boldsymbol{\Sigma}(-\mathrm{i}\tau))\end{aligned} \tag{40}$$

$$\begin{aligned}\underline{\mathbf{M}} = \int_{0}^{+\infty} \mathrm{d}\tau(&\underline{\mathbf{Y}}(-\mathrm{i}\tau)(\mathbf{H} - \epsilon_F\mathbf{S})\\ &+ \exp(\tau(\mathbf{H} - \epsilon_F\mathbf{S})\mathbf{P})\boldsymbol{\Sigma}(\mathrm{i}\tau))\end{aligned} \tag{41}$$

and the matrices

$$\mathbf{Y}(\mathrm{i}\tau) = \Theta(-\tau)\underline{\mathbf{Y}}(\mathrm{i}\tau) + \Theta(\tau)\bar{\mathbf{Y}}(\mathrm{i}\tau) \tag{42}$$

$$\bar{\mathbf{Y}}(\mathrm{i}\tau) = \sum_{k=1}^{\infty}\sum_{l=0}^{k-1}\frac{1}{k!}\bar{\boldsymbol{\mathcal{A}}}^{k-l-1}(\tau)\bar{\boldsymbol{\mathcal{B}}}(\mathrm{i}\tau)\bar{\boldsymbol{\mathcal{A}}}^{l}(\tau) \tag{43}$$

$$\underline{\mathbf{Y}}(\mathrm{i}\tau) = \sum_{k=1}^{\infty}\sum_{l=0}^{k-1}\frac{1}{k!}\underline{\boldsymbol{\mathcal{A}}}^{k-l-1}(\tau)\underline{\boldsymbol{\mathcal{B}}}(\mathrm{i}\tau)\underline{\boldsymbol{\mathcal{A}}}^{l}(\tau) \tag{44}$$

with $\boldsymbol{\mathcal{A}}(\tau)$ defined as

$$\boldsymbol{\mathcal{A}}(\tau) = \Theta(-\tau)\underline{\boldsymbol{\mathcal{A}}}(\tau) + \Theta(\tau)\bar{\boldsymbol{\mathcal{A}}}(\tau) \tag{45}$$

$$\underline{\boldsymbol{\mathcal{A}}}(\tau) = -\tau(\mathbf{H} - \epsilon_F\mathbf{S})\mathbf{P} \tag{46}$$

$$\bar{\boldsymbol{\mathcal{A}}}(\tau) = -\tau(\mathbf{H} - \epsilon_F\mathbf{S})\mathbf{P}_{\mathrm{virt}} \tag{47}$$

and $\boldsymbol{\mathcal{B}}(\mathrm{i}\tau)$ as

$$\boldsymbol{\mathcal{B}}(\mathrm{i}\tau) = \Theta(-\tau)\underline{\boldsymbol{\mathcal{B}}}(\mathrm{i}\tau) + \Theta(\tau)\bar{\boldsymbol{\mathcal{B}}}(\mathrm{i}\tau) \tag{48}$$

$$\underline{\boldsymbol{\mathcal{B}}}(\mathrm{i}\tau) = -\tau\boldsymbol{\Sigma}(-\mathrm{i}\tau)\mathbf{P} \tag{49}$$

$$\overline{\mathcal{B}}(\mathrm{i}\tau) = -\tau \boldsymbol{\Sigma}(-\mathrm{i}\tau)\mathbf{P}_{\mathrm{virt}} \tag{50}$$

The **Y** matrices are most efficiently evaluated using a recursion scheme according to[34,84]

$$\mathbf{Y}(\mathrm{i}\tau) = \sum_{k=0}^{\infty} \mathbf{Y}_k(\mathrm{i}\tau) \tag{51}$$

$$\mathbf{Y}_k(\mathrm{i}\tau) = \begin{cases} 0 & k = 0 \\ \frac{1}{k}(\mathcal{A}(\tau)\mathbf{Y}_{k-1}(\mathrm{i}\tau) + \mathcal{B}(\mathrm{i}\tau)\mathcal{A}_{k-1}(\tau)) & k > 0 \end{cases} \tag{52}$$

with

$$\mathcal{A}_k(\tau) = \frac{1}{k!}\mathcal{A}^k(\tau) \tag{53}$$

3.3. Second Derivative with Respect to the Magnetic Field. The mixed second derivative of the total RPA energy with respect to **m** and **B** reads

$$\begin{aligned} \boldsymbol{\sigma} &= \left.\frac{\partial^2 E^{\mathrm{total}}[\mathbf{P}]}{\partial \mathbf{B} \partial \mathbf{m}}\right|_{\mathbf{m}=0,\mathbf{B}=0} \\ &= \left.\frac{\partial^2 E^{\mathrm{HF}}[\mathbf{P}]}{\partial \mathbf{B} \partial \mathbf{m}}\right|_{\mathbf{m}=0,\mathbf{B}=0} + \left.\frac{\partial^2 E_{\mathrm{c}}^{\mathrm{RPA}}[\mathbf{P}]}{\partial \mathbf{B} \partial \mathbf{m}}\right|_{\mathbf{m}=0,\mathbf{B}=0} \end{aligned} \tag{54}$$

In the following sections, the mixed second derivative of the HF energy, given by the first term in eq 54, is reviewed. Subsequently the second derivative of the RPA correlation energy, given by the second term in eq 54, is derived, and finally both components are combined to form the total shielding tensor.

3.3.1. Second Derivative of the HF Energy with Respect to the Magnetic Field. The second derivative of the HF energy with respect to **m** and **B** can be obtained by differentiating eq 17 with respect to **B** yielding

$$\begin{aligned} \left.\frac{\partial^2 E^{\mathrm{HF}}[\mathbf{P}]}{\partial \mathbf{B} \partial \mathbf{m}}\right|_{\mathbf{m}=0,\mathbf{B}=0} &= \mathrm{Tr}(\mathbf{P}^{\mathbf{B}}\mathbf{h}^{\mathbf{m}}) + \mathrm{Tr}(\mathbf{P}\mathbf{h}^{\mathbf{Bm}}) \\ &\quad + \mathrm{Tr}(\mathbf{H}_{\mathrm{HF}}^{\mathbf{B}}\mathbf{P}^{\mathbf{m}}) \\ &\quad + \mathrm{Tr}(\mathbf{H}_{\mathrm{HF}}\mathbf{P}^{\mathbf{Bm}}) \end{aligned} \tag{55}$$

$$\begin{aligned} &= \tilde{\boldsymbol{\sigma}}^{\mathrm{HF}} + \mathrm{Tr}(\mathbf{H}_{\mathrm{HF}}^{\mathbf{B}}\mathbf{P}^{\mathbf{m}}) \\ &\quad + \mathrm{Tr}(\mathbf{H}_{\mathrm{HF}}\mathbf{P}^{\mathbf{Bm}}) \end{aligned} \tag{56}$$

For simplicity in the following, the first two contributions from the HF functional are summarized in the intermediate $\tilde{\boldsymbol{\sigma}}^{\mathrm{HF}}$. We note here that the contributions from $\mathrm{Tr}(\mathbf{H}_{\mathrm{HF}}^{\mathbf{B}}\mathbf{P}^{\mathbf{m}})$ and $\mathrm{Tr}(\mathbf{H}_{\mathrm{HF}}\mathbf{P}^{\mathbf{Bm}})$ do not arise in the case of a HF reference, as explained in detail in Appendix A. The magnetic field derivative of the HF Hamiltonian $\mathbf{H}_{\mathrm{HF}}^{\mathbf{B}}$ is given by

$$\mathbf{H}_{\mathrm{HF}}^{\mathbf{B}} = \mathbf{h}^{\mathbf{B}} + \mathbf{J}^{\mathbf{B}}[\mathbf{P}] + \mathbf{K}^{\mathbf{B}}[\mathbf{P}] + \mathbf{K}[\mathbf{P}^{\mathbf{B}}] \tag{57}$$

where the term $\mathbf{J}[\mathbf{P}^{\mathbf{B}}]$ is zero, due to the skew symmetry of the purely imaginary **B**-field derivative of the density matrix.

3.3.2. Second Derivative of the RPA Correlation Energy with Respect to the Magnetic Field. The second derivative of the RPA correlation energy with respect to the magnetic field **B** can be obtained by differentiating eq 36

$$\begin{aligned} \left.\frac{\partial^2 E_{\mathrm{c}}^{\mathrm{RPA}}[\mathbf{P}]}{\partial \mathbf{B} \partial \mathbf{m}}\right|_{\mathbf{m}=0,\mathbf{B}=0} &= \mathrm{Tr}(\mathbf{V}_{\mathrm{RPA}}^{\mathbf{B}}\mathbf{P}^{\mathbf{m}}) + \mathrm{Tr}(\mathbf{V}_{\mathrm{RPA}}\mathbf{P}^{\mathbf{Bm}}) \\ &\quad + \mathrm{Tr}(\mathbf{P}_{\mathrm{RPA}}^{\mathbf{B}}\mathbf{h}^{\mathbf{m}}) + \mathrm{Tr}(\mathbf{P}_{\mathrm{RPA}}\mathbf{h}^{\mathbf{Bm}}) \end{aligned} \tag{58}$$

The derivative of the density with respect to the nuclear magnetic moment in the first term of eq 58 can, in principle, be evaluated by solving the coupled-perturbed KS (CPKS) equations for all perturbations of the nuclear magnetic moment. However, the response of the density can be obtained more efficiently using the Z-vector technique,[84,89] which requires the evaluation of only one CPKS equation. Within the AO-based formulation, the density matrix-based Laplace transformed CPKS method[93] developed by our group is employed.

In the next sections, the derivation of the **B**-field derivatives of the $\mathbf{P}_{\mathrm{RPA}}$ and the $\mathbf{V}_{\mathrm{RPA}}$ intermediates is explained in detail. Figure 1 provides a schematic overview of the necessary steps to derive an expression for the central intermediates $\mathbf{P}_{\mathrm{RPA}}^{\mathbf{B}}$ and $\mathbf{V}_{\mathrm{RPA}}^{\mathbf{B}}$. The next section starts with the evaluation of $\mathbf{P}_{\mathrm{RPA}}^{\mathbf{B}}$, which will lead to an expression for the magnetic field derivative of the correlated self-energy $\boldsymbol{\Sigma}^{\mathbf{B}}$. As can be seen in Figure 1, this requires the **B**-field differentiated correlated screened Coulomb interaction $\mathbf{W}_{\mathrm{c}}^{\mathbf{B}}$, which in turn contains the derivative of the noninteracting response function $\mathbf{X}_0^{\mathbf{B}}$. Subsequently, the evaluation of $\mathbf{V}_{\mathrm{RPA}}^{\mathbf{B}}$ will be detailed, and finally, the contributions from the HF functional and the RPA correlation energy are combined to formulate the final equation for the computation of the total RPA NMR shieldings.

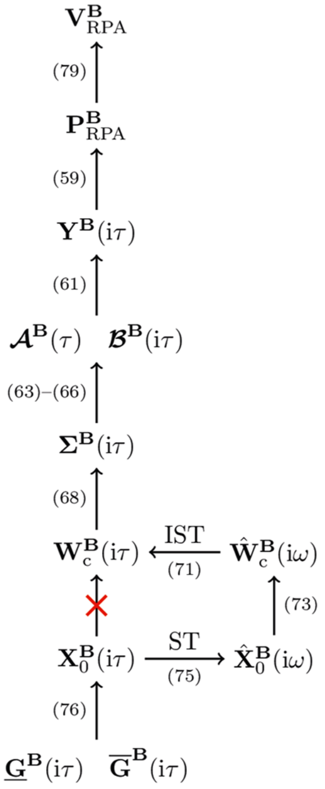

Figure 1. Schematic representation of the derivation of $\mathbf{V}_{\mathrm{RPA}}^{\mathbf{B}}$ and $\mathbf{P}_{\mathrm{RPA}}^{\mathbf{B}}$. ST denotes a sine transform and IST denotes an inverse sine transform. All arrows are labeled with the corresponding equations from the text.

3.3.3. *Derivative of P_{RPA} with Respect to the Magnetic Field.*

Differentiation of eq 38 with respect to the magnetic field yields

$$\mathbf{P}^{\mathbf{B}}_{\text{RPA}} = \frac{1}{2}\int_0^{+\infty} \mathrm{d}\tau(\mathbf{P}^{\mathbf{B}}\underline{\mathbf{Y}}(-\mathrm{i}\tau) + \mathbf{P}\underline{\mathbf{Y}}^{\mathbf{B}}(-\mathrm{i}\tau) - \mathbf{P}^{\mathbf{B}}_{\text{virt}}\overline{\mathbf{Y}}(\mathrm{i}\tau) - \mathbf{P}_{\text{virt}}\overline{\mathbf{Y}}^{\mathbf{B}}(\mathrm{i}\tau)) \tag{59}$$

The direct evaluation of $\mathbf{P}^{\mathbf{B}}_{\text{virt}}$ can again be avoided by differentiation of the completeness relation given in eq 34 with respect to the **B**-field

$$\mathbf{P}^{\mathbf{B}}_{\text{virt}} = \mathbf{P}^{\mathbf{B}} - \mathbf{S}^{-1}\mathbf{S}^{\mathbf{B}}\mathbf{S}^{-1} \tag{60}$$

Here, we note that at this stage the density response $\mathbf{P}^{\mathbf{B}}$ is evaluated directly by solving the CPKS equations for all **B**-field perturbations without utilizing the Z-vector technique. Since there are only three perturbations in total, this does not constitute a considerable overhead.

Apart from $\mathbf{P}^{\mathbf{B}}$, the evaluation of eq 59 requires the **B**-field derivative of the **Y** intermediates. Since the derivative of the **Y** matrices also arises in the evaluation of Laplace transformed atomic-orbital MP2 NMR shieldings,[33,34,38] the approach recently introduced by Glasbrenner et al.[34] is adopted for the evaluation of $\mathbf{Y}^{\mathbf{B}}(\mathrm{i}\tau)$. Differentiating the recursion formula for $\mathbf{Y}(\mathrm{i}\tau)$ given in eq 51 with respect to the **B**-field yields

$$\mathbf{Y}^{\mathbf{B}}(\mathrm{i}\tau) = \sum_{k=0}^{\infty} \mathbf{Y}^{\mathbf{B}}_k(\mathrm{i}\tau) \tag{61}$$

$$\mathbf{Y}^{\mathbf{B}}_k(\mathrm{i}\tau) = \frac{1}{k}(\mathcal{A}^{\mathbf{B}}(\tau)\mathbf{Y}_{k-1}(\mathrm{i}\tau) + \mathcal{A}(\tau)\mathbf{Y}^{\mathbf{B}}_{k-1}(\mathrm{i}\tau) + \mathcal{B}^{\mathbf{B}}(\mathrm{i}\tau)\mathcal{A}_{k-1}(\tau) + \mathcal{B}(\mathrm{i}\tau)\mathcal{A}^{\mathbf{B}}_{k-1}(\tau)) \quad \forall\, k > 0 \tag{62}$$

At this point the derivatives of $\mathcal{A}(\tau)$ and $\mathcal{B}(\mathrm{i}\tau)$ are required. Differentiation of the respective expressions given in eqs 46–50 results in

$$\underline{\mathcal{A}}^{\mathbf{B}}(\tau) = -\,\tau(\mathbf{H}^{\mathbf{B}} - \epsilon_{\mathrm{F}}\mathbf{S}^{\mathbf{B}})\mathbf{P} - \tau(\mathbf{H} - \epsilon_{\mathrm{F}}\mathbf{S})\mathbf{P}^{\mathbf{B}} \tag{63}$$

$$\overline{\mathcal{A}}^{\mathbf{B}}(\tau) = -\tau(\mathbf{H}^{\mathbf{B}} - \epsilon_{\mathrm{F}}\mathbf{S}^{\mathbf{B}})\mathbf{P}_{\text{virt}} - \tau(\mathbf{H} - \epsilon_{\mathrm{F}}\mathbf{S})\mathbf{P}^{\mathbf{B}}_{\text{virt}} \tag{64}$$

$$\underline{\mathcal{B}}^{\mathbf{B}}(i\tau) = -\,\tau\mathbf{\Sigma}^{\mathbf{B}}(-\mathrm{i}\tau)\mathbf{P} - \tau\mathbf{\Sigma}(-\mathrm{i}\tau)\mathbf{P}^{\mathbf{B}} \tag{65}$$

$$\overline{\mathcal{B}}^{\mathbf{B}}(\mathrm{i}\tau) = -\tau\mathbf{\Sigma}^{\mathbf{B}}(-\mathrm{i}\tau)\mathbf{P}_{\text{virt}} - \tau\mathbf{\Sigma}(-\mathrm{i}\tau)\mathbf{P}^{\mathbf{B}}_{\text{virt}} \tag{66}$$

where the **B**-field derivative of the Hamiltonian (eq 14) is given by

$$\mathbf{H}^{\mathbf{B}} = \mathbf{h}^{\mathbf{B}} + \mathbf{G}^{\mathbf{B}}[\mathbf{P}] + \mathbf{G}[\mathbf{P}^{\mathbf{B}}] \tag{67}$$

Up to this point, the only unknown quantity is the **B**-field derivative of the correlated self-energy, which is the focus of the next section.

3.3.4. *Derivative of the Correlated Self-Energy with Respect to the Magnetic Field.*

The derivative of the self-energy, i.e.,

$$\left.\frac{\partial\Sigma_{\nu\lambda}(\mathrm{i}\tau)}{\partial\mathbf{B}}\right|_{\mathbf{B}=\mathbf{0}} = \left.\frac{\partial}{\partial\mathbf{B}}(-\tilde{W}_{\mathrm{c,PQ}}(-\mathrm{i}\tau)\mathbb{B}^{P}_{\mu\nu}G_{0,\mu\sigma}(\mathrm{i}\tau)\mathbb{B}^{Q}_{\lambda\sigma})\right|_{\mathbf{B}=\mathbf{0}} \tag{68}$$

can be obtained by differentiating eq 31 using the product rule. Further simplifications can be made by considering the symmetries of all quantities when evaluating at $\mathbf{B} = \mathbf{0}$. Since the vector potential that describes the magnetic field is purely imaginary, any associated **B**-field differentiated Hermitian matrix will necessarily be purely imaginary and therefore skew-symmetric in the time domain. Furthermore, both the magnetic field derivative of the noninteracting response function $\mathbf{X}^{\mathbf{B}}_0(\mathrm{i}\tau)$ and the derivative of the correlated screened Coulomb interaction $\mathbf{W}^{\mathbf{B}}_{\mathrm{c}}(\mathrm{i}\tau)$ are odd functions in the imaginary time domain. All remaining, nondifferentiated quantities are purely real, symmetric, and even functions in the imaginary time domain. A detailed derivation is shown in Appendix B, while here only the resulting working equations are presented

$$\begin{aligned}\Sigma^{\mathbf{B}}_{\nu\lambda}(\mathrm{i}\tau) = &-\frac{\partial W_{\mathrm{c,PQ}}(\mathrm{i}\tau)}{\partial\mathbf{B}}\mathbb{B}^{P}_{\mu\nu}\overline{G}_{0,\mu\sigma}(\mathrm{i}\tau)\mathbb{B}^{Q}_{\lambda\sigma}\\ &- W_{\mathrm{c,PQ}}(\mathrm{i}\tau)\frac{\partial\mathbb{B}^{P}_{\mu\nu}}{\partial\mathbf{B}}\overline{G}_{0,\mu\sigma}(\mathrm{i}\tau)\mathbb{B}^{Q}_{\lambda\sigma}\\ &- W_{\mathrm{c,PQ}}(\mathrm{i}\tau)\mathbb{B}^{P}_{\mu\nu}\frac{\partial\overline{G}_{0,\mu\sigma}(\mathrm{i}\tau)}{\partial\mathbf{B}}\mathbb{B}^{Q}_{\lambda\sigma}\\ &- W_{\mathrm{c,PQ}}(\mathrm{i}\tau)\mathbb{B}^{P}_{\mu\nu}G_{0,\mu\sigma}(\mathrm{i}\tau)\frac{\partial\mathbb{B}^{Q}_{\lambda\sigma}}{\partial\mathbf{B}}\end{aligned} \tag{69}$$

$$\begin{aligned}\Sigma^{\mathbf{B}}_{\nu\lambda}(-\mathrm{i}\tau) = &+\frac{\partial W_{\mathrm{c,PQ}}(\mathrm{i}\tau)}{\partial\mathbf{B}}\mathbb{B}^{P}_{\mu\nu}\underline{G}_{0,\mu\sigma}(-\mathrm{i}\tau)\mathbb{B}^{Q}_{\lambda\sigma}\\ &- W_{\mathrm{c,PQ}}(\mathrm{i}\tau)\frac{\partial\mathbb{B}^{P}_{\mu\nu}}{\partial\mathbf{B}}\underline{G}_{0,\mu\sigma}(-\mathrm{i}\tau)\mathbb{B}^{Q}_{\lambda\sigma}\\ &- W_{\mathrm{c,PQ}}(\mathrm{i}\tau)\mathbb{B}^{P}_{\mu\nu}\frac{\partial\underline{G}_{0,\mu\sigma}(-\mathrm{i}\tau)}{\partial\mathbf{B}}\mathbb{B}^{Q}_{\lambda\sigma}\\ &- W_{\mathrm{c,PQ}}(\mathrm{i}\tau)\mathbb{B}^{P}_{\mu\nu}\underline{G}_{0,\mu\sigma}(-\mathrm{i}\tau)\frac{\partial\mathbb{B}^{Q}_{\lambda\sigma}}{\partial\mathbf{B}}\end{aligned} \tag{70}$$

If done stepwise, the computation of the self-energy and its **B**-field derivative formally scale as $O(N^2_{\text{aux}}N^2)$ and thus constitute the steepest scaling steps in the computation of RPA NMR shieldings.

In the following sections, first the **B**-field derivative of the correlated screened Coulomb interaction $\mathbf{W}_{\mathrm{c}}(\mathrm{i}\tau)$ is evaluated and subsequently the derivative of the Green's functions is evaluated.

Since no simple closed expression for the correlated screened Coulomb interaction in the imaginary time domain exists, the **B**-field derivative is evaluated in the imaginary frequency domain $\hat{\mathbf{W}}^{\mathbf{B}}_{\mathrm{c}}(\mathrm{i}\omega)$ and subsequently transformed back into the imaginary time domain using an inverse sine transform

$$\mathbf{W}^{\mathbf{B}}_{\mathrm{c}}(\mathrm{i}\tau) = 2\mathrm{i}\int_0^{+\infty}\mathrm{d}\omega\,\sin(\omega\tau)\hat{\mathbf{W}}^{\mathbf{B}}_{\mathrm{c}}(\mathrm{i}\omega) \tag{71}$$

$\hat{\mathbf{W}}^{\mathbf{B}}_{\mathrm{c}}(\mathrm{i}\omega)$ can be obtained by differentiating eq 22 with respect to the **B**-field yielding

$$\frac{\partial\hat{\mathbf{W}}_{\mathrm{c}}(\mathrm{i}\omega)}{\partial\mathbf{B}} = \frac{\partial}{\partial\mathbf{B}}(\mathbb{V}([\mathbf{1} - \hat{\mathbf{X}}_0(\mathrm{i}\omega)\mathbb{V}]^{-1} - \mathbf{1})) \tag{72}$$

$$= \mathbb{V}([\mathbf{1} - \hat{\mathbf{X}}_0(\mathrm{i}\omega)\mathbb{V}]^{-1}[\hat{\mathbf{X}}^{\mathbf{B}}_0(\mathrm{i}\omega)\mathbb{V}][\mathbf{1} - \hat{\mathbf{X}}_0(\mathrm{i}\omega)\mathbb{V}]^{-1}) \tag{73}$$

where the following identity for the derivative of matrix inverses of a general matrix $\mathcal{R}$ is used

$$\frac{\partial(\mathcal{R}^{-1})}{\partial\xi} = -\mathcal{R}^{-1}\frac{\partial\mathcal{R}}{\partial\xi}\mathcal{R}^{-1} \tag{74}$$

As can be seen from eq 73, for the computation of $\hat{\mathbf{W}}_c^{\mathbf{B}}(\mathrm{i}\omega)$, the **B**-field derivative of the response function in the imaginary frequency domain $\hat{\mathbf{X}}_0^{\mathbf{B}}(\mathrm{i}\omega)$ is needed. For efficiency reasons, the **B**-field derivative of the response function is computed in the imaginary time domain and transformed back into the imaginary frequency domain using the sine transform

$$\hat{\mathbf{X}}_0^{\mathbf{B}}(\mathrm{i}\omega) = 2\mathrm{i}\int_0^{+\infty} \mathrm{d}\tau\ \sin(\omega\tau)\mathbf{X}_0^{\mathbf{B}}(\mathrm{i}\tau) \tag{75}$$

By differentiating eq 9 using the product rule, an expression for $\mathbf{X}_0^{\mathbf{B}}(\mathrm{i}\tau)$ is obtained according to

$$\begin{aligned}\frac{\partial X^{+}_{0,\mathrm{PQ}}(\mathrm{i}\tau)}{\partial\mathbf{B}} = {}& \frac{\partial \underline{G}_{0,\mu\sigma}(-\mathrm{i}\tau)}{\partial\mathbf{B}}\mathbb{B}^{P}_{\mu\nu}\overline{G}_{0,\lambda\nu}(\mathrm{i}\tau)\mathbb{B}^{Q}_{\lambda\sigma}\\ &+ \underline{G}_{0,\mu\sigma}(-\mathrm{i}\tau)\frac{\partial\mathbb{B}^{P}_{\mu\nu}}{\partial\mathbf{B}}\overline{G}_{0,\lambda\nu}(\mathrm{i}\tau)\mathbb{B}^{Q}_{\lambda\sigma}\\ &+ \underline{G}_{0,\mu\sigma}(-\mathrm{i}\tau)\mathbb{B}^{P}_{\mu\nu}\frac{\partial\overline{G}_{0,\lambda\nu}(\mathrm{i}\tau)}{\partial\mathbf{B}}\mathbb{B}^{Q}_{\lambda\sigma}\\ &+ \underline{G}_{0,\mu\sigma}(-\mathrm{i}\tau)\mathbb{B}^{P}_{\mu\nu}\overline{G}_{0,\lambda\nu}(\mathrm{i}\tau)\frac{\partial\mathbb{B}^{Q}_{\lambda\sigma}}{\partial\mathbf{B}}\end{aligned} \tag{76}$$

Finally, to complete the evaluation of $\boldsymbol{\Sigma}(\mathrm{i}\tau)$, the **B**-field derivative of the Green's function is needed. Differentiating eqs 12 and 13 yields

$$\begin{aligned}\frac{\partial\underline{\mathbf{G}}_0(\mathrm{i}\tau)}{\partial\mathbf{B}} = {}& \mathbf{P}^{\mathbf{B}}\exp(-\tau(\mathbf{H}-\epsilon_{\mathrm{F}}\mathbf{S})\mathbf{P})\\ &+ \mathbf{P}(\exp(-\tau(\mathbf{H}-\epsilon_{\mathrm{F}}\mathbf{S})\mathbf{P}))^{\mathbf{B}}\end{aligned} \tag{77}$$

$$\begin{aligned}\frac{\partial\overline{\mathbf{G}}_0(\mathrm{i}\tau)}{\partial\mathbf{B}} = {}& -\mathbf{P}^{\mathbf{B}}_{\mathrm{virt}}\exp(-\tau(\mathbf{H}-\epsilon_{\mathrm{F}}\mathbf{S})\mathbf{P}_{\mathrm{virt}})\\ &- \mathbf{P}_{\mathrm{virt}}(\exp(-\tau(\mathbf{H}-\epsilon_{\mathrm{F}}\mathbf{S})\mathbf{P}_{\mathrm{virt}}))^{\mathbf{B}}\end{aligned} \tag{78}$$

The **B**-field derivative of the matrix exponentials in the above equations can be obtained, as explained in Section 3.2.[68]

3.3.5. Derivative of V_{RPA} with Respect to the Magnetic Field.

Field. Differentiating eq 37 yields

$$\mathbf{V}^{\mathbf{B}}_{\mathrm{RPA}} = \frac{1}{2}(\mathbf{M}^{\mathbf{B}} + \mathbf{G}^{\mathbf{B}}[\mathbf{P}_{\mathrm{RPA}}] + \mathbf{G}[\mathbf{P}^{\mathbf{B}}_{\mathrm{RPA}}]) \tag{79}$$

The evaluation of $\mathbf{P}^{\mathbf{B}}_{\mathrm{RPA}}$ was described in detail in the last section. An expression for $\mathbf{M}^{\mathbf{B}} = \overline{\mathbf{M}}^{\mathbf{B}} + \underline{\mathbf{M}}^{\mathbf{B}}$ can be obtained by differentiating eqs 40 and 41 using the product rule yielding

$$\begin{aligned}\overline{\mathbf{M}}^{\mathbf{B}} = \int_0^{+\infty} & \mathrm{d}\tau(\overline{\mathbf{Y}}^{\mathbf{B}}(\mathrm{i}\tau)(\mathbf{H}-\epsilon_{\mathrm{F}}\mathbf{S})\\ &+ \overline{\mathbf{Y}}(\mathrm{i}\tau)(\mathbf{H}^{\mathbf{B}}-\epsilon_{\mathrm{F}}\mathbf{S}^{\mathbf{B}}) + [\exp(-\tau(\mathbf{H}-\epsilon_{\mathrm{F}}\mathbf{S})\mathbf{P}_{\mathrm{virt}})]^{\mathbf{B}}\boldsymbol{\Sigma}\\ &(-\mathrm{i}\tau) + \exp(-\tau(\mathbf{H}-\epsilon_{\mathrm{F}}\mathbf{S})\mathbf{P}_{\mathrm{virt}})\boldsymbol{\Sigma}^{\mathbf{B}}(-\mathrm{i}\tau))\end{aligned} \tag{80}$$

$$\begin{aligned}\underline{\mathbf{M}}^{\mathbf{B}} = \int_0^{+\infty} & \mathrm{d}\tau(\underline{\mathbf{Y}}^{\mathbf{B}}(-\mathrm{i}\tau)(\mathbf{H}-\epsilon_{\mathrm{F}}\mathbf{S})\\ &+ \underline{\mathbf{Y}}(-\mathrm{i}\tau)(\mathbf{H}^{\mathbf{B}}-\epsilon_{\mathrm{F}}\mathbf{S}^{\mathbf{B}})\\ &+ [\exp(\tau(\mathbf{H}-\epsilon_{\mathrm{F}}\mathbf{S})\mathbf{P})]^{\mathbf{B}}\boldsymbol{\Sigma}(\mathrm{i}\tau)\\ &+ \exp(\tau(\mathbf{H}-\epsilon_{\mathrm{F}}\mathbf{S})\mathbf{P})\boldsymbol{\Sigma}^{\mathbf{B}}(\mathrm{i}\tau))\end{aligned} \tag{81}$$

The evaluation of all **B**-field derivatives in the above expression has been described in the previous section.

3.3.6. Second Derivative of the Total RPA Energy.

By combining eqs 56 and 58, an expression for the total RPA energy can be obtained according to

$$\begin{aligned}\left.\frac{\partial^2 E^{\mathrm{total}}[\mathbf{P}]}{\partial\mathbf{B}\partial\mathbf{m}}\right|_{\mathbf{m}=0,\mathbf{B}=0} = {}& \mathrm{Tr}([\mathbf{V}^{\mathbf{B}}_{\mathrm{RPA}} + \mathbf{H}^{\mathbf{B}}_{\mathrm{HF}}]\mathbf{P}^{\mathbf{m}})\\ &+ \mathrm{Tr}([\mathbf{V}_{\mathrm{RPA}} + \mathbf{H}_{\mathrm{HF}}]\mathbf{P}^{\mathbf{Bm}})\\ &+ \mathrm{Tr}(\mathbf{P}^{\mathbf{B}}_{\mathrm{RPA}}\mathbf{h}^{\mathbf{m}}) + \mathrm{Tr}(\mathbf{P}_{\mathrm{RPA}}\mathbf{h}^{\mathbf{Bm}}) + \tilde{\boldsymbol{\sigma}}^{\mathrm{HF}}\end{aligned} \tag{82}$$

For simplicity, the contribution $\tilde{\boldsymbol{\sigma}}^{\mathrm{HF}}$ is treated separately with the usual techniques used for the computation of HF and DFT shifts. The contribution of the remaining terms will be described in detail in the next section.

3.3.7. Final Equation for RPA NMR Shieldings: Nested Z-Vector Approach for Avoiding P^{Bm}.

The nested Z-vector approach provides an efficient way to evaluate $\mathbf{P}^{\mathbf{Bm}}$ with a reduced number of CPKS equations. It was first introduced by Maurer and Ochsenfeld[33] for AO-MP2 NMR shieldings and recently improved by Glasbrenner et al.[34] Here, we want to stress that Gauss had already introduced the respective MO-based Z-vector equations in the framework of MO-MP2 in 1992.[19]

In the following, the basic idea for the nested Z-vector method is reviewed, and subsequently the final equations are presented. A detailed derivation can be found in ref 34.

The objective is to evaluate $\mathrm{Tr}([\mathbf{V}_{\mathrm{RPA}} + \mathbf{H}_{\mathrm{HF}}]\mathbf{P}^{\mathbf{Bm}})$, i.e., the second term in eq 82. For this, we first consider the CPKS equation for the **B**-field derivative of the density

$$\mathbf{A}\mathbf{P}^{\mathbf{B}} = \mathbf{b}^{\mathbf{B}} \tag{83}$$

where **A** is the KS Hessian matrix and $\mathbf{b}^{\mathbf{B}}$ is the right-hand side of the CPKS equation. Next, eq 83 is differentiated with respect to **m** and rearranged to obtain an expression for $\mathbf{P}^{\mathbf{Bm}}$ according to

$$\mathbf{P}^{\mathbf{Bm}} = \mathbf{A}^{-1}(\mathbf{b}^{\mathbf{Bm}} - \mathbf{A}^{\mathbf{m}}[\mathbf{P}^{\mathbf{B}}]) \tag{84}$$

Using eq 84 together with the Z-vector ansatz allows to rewrite $\mathrm{Tr}([\mathbf{V}_{\mathrm{RPA}} + \mathbf{H}_{\mathrm{HF}}]\mathbf{P}^{\mathbf{Bm}})$ as

$$\mathrm{Tr}([\mathbf{V}_{\mathrm{RPA}} + \mathbf{H}_{\mathrm{HF}}]\mathbf{P}^{\mathbf{Bm}}) = \mathrm{Tr}(\mathbf{Z}(\mathbf{b}^{\mathbf{Bm}} - \mathbf{A}^{\mathbf{m}}[\mathbf{P}^{\mathbf{B}}])) \tag{85}$$

where **Z** is computed by solving one CPKS equation $\mathbf{AZ} = \mathbf{V}_{\mathrm{RPA}} + \mathbf{H}_{\mathrm{HF}}$. Next, all terms in $\mathrm{Tr}(\mathbf{Z}(\mathbf{b}^{\mathbf{Bm}} - \mathbf{A}^{\mathbf{m}}[\mathbf{P}^{\mathbf{B}}]))$ need to be reordered, such that only terms of the form $\mathrm{Tr}[\cdots\mathbf{P}^{\mathbf{m}}]$ result, which renders the expression amenable to another Z-vector step. The reordering is performed analogously to eqs D12–D28 in ref 34. It was shown that this, in combination with the terms $\mathrm{Tr}[\mathbf{V}^{\mathbf{B}}_{\mathrm{RPA}}\mathbf{P}^{\mathbf{m}}]$ from eq 58 and $\mathrm{Tr}[\mathbf{H}^{\mathbf{B}}_{\mathrm{HF}}\mathbf{P}^{\mathbf{m}}]$ from eq 56, leads to

$$\begin{aligned}&\mathrm{Tr}(\mathbf{Z}(\mathbf{b}^{\mathbf{Bm}} - \mathbf{A}^{\mathbf{m}}[\mathbf{P}^{\mathbf{B}}])) + \mathrm{Tr}([\mathbf{V}^{\mathbf{B}}_{\mathrm{RPA}} + \mathbf{H}^{\mathbf{B}}_{\mathrm{HF}}]\mathbf{P}^{\mathbf{m}})\\ &\quad = \mathrm{Tr}(\mathbf{O}_{\mathbf{F}^{\mathbf{m}}}\mathbf{h}^{\mathbf{m}}) + \mathrm{Tr}(\mathbf{O}_{\mathbf{Y}^{\mathbf{m}}}\mathbf{h}^{\mathbf{m}}) + \mathrm{Tr}(\mathbf{O}\mathbf{P}^{\mathbf{m}})\end{aligned} \tag{86}$$

Applying eqs 85 and 86 to eq 82 and rearranging terms, yields the final expression for the RPA NMR shieldings as

$$\begin{aligned}\boldsymbol{\sigma} = {}& \mathrm{Tr}([\mathbf{P}_{\mathrm{RPA}} + \mathbf{O}_{\mathbf{Y}^{\mathbf{m}}}]\mathbf{h}^{\mathbf{Bm}}) + \mathrm{Tr}([\mathbf{P}^{\mathbf{B}}_{\mathrm{RPA}} + \mathbf{O}_{\mathbf{F}^{\mathbf{m}}}]\mathbf{h}^{\mathbf{m}})\\ &+ \mathrm{Tr}(\mathbf{Z}_{\mathbf{O}}\mathbf{b}^{\mathbf{m}}) + \tilde{\boldsymbol{\sigma}}^{\mathrm{HF}}\end{aligned} \tag{87}$$

The introduced quantities $\mathbf{O}_{\mathbf{Y}^{\mathbf{m}}}$, $\mathbf{O}_{\mathbf{F}^{\mathbf{m}}}$, **O**, and $\mathbf{Z}_{\mathbf{O}}$ are defined in ref 34. Here, we note that following the notation of ref 34 in the context of the AO-MP2 NMR shieldings, the intermediates $\mathbf{P}_{\mathrm{RPA}}$ and $(\mathbf{V}_{\mathrm{RPA}} + \mathbf{H}_{\mathrm{HF}})$ correspond to the intermediates $\mathcal{F}$ and $\mathcal{P}$, respectively, and likewise for the differentiated intermediates. In essence, for an efficient treatment of the

https://doi.org/10.1021/acs.jctc.3c00542
J. Chem. Theory Comput. 2023, 19, 7542−7554

contributions from the HF Hamiltonian, i.e., Tr($\mathbf{H}_{\text{HF}}\ \mathbf{P}^{\mathbf{Bm}}$) and Tr($\mathbf{H}_{\text{HF}}^{\mathbf{B}}\ \mathbf{P}^{\mathbf{m}}$) from eq 56, $\mathbf{H}_{\text{HF}}$ needs to be added to the $\mathbf{V}_{\text{RPA}}$ intermediate, and likewise for the **B**-field differentiated quantities, to avoid the solution of two nested Z-vector equations. Finally, an overview of all necessary steps to compute NMR chemical shieldings at the RPA level of theory is provided in the Supporting Information.

4. COMPUTATIONAL DETAILS

Analytical NMR shifts at the RPA level of theory were implemented within our quantum chemistry package FermiONs++.[94−96] As a starting point for the RPA calculations, DFT with the generalized gradient approximation of Perdew−Burke−Ernzerhof (PBE),[97] as provided by the Libxc library version 5.1.1,[98] as well as the Hartree−Fock method, are employed. For all PBE reference calculations, an uncoupled DFT scheme is used.[99,100] The frozen core approximation is not utilized. Further, dense matrix algebra routines from the Intel Math Kernel Library (version 2022.0.0) are employed. Dunning's correlation-consistent basis sets with core weighted functions (cc-pwCVDZ, cc-pwCVTZ)[101] are used in combination with the corresponding RI basis sets.[102] For the time and frequency integration[57,61] as well as the cosine[57,61] and sine transformation[90] to switch between two domains, optimized minimax grids[57] are employed. For this, we use 15 grid points, which is proven to be sufficiently accurate, as shown in Section 5.2. The derivatives of numerical integration roots and weights used for the numerical imaginary time and frequency quadratures are neglected. This is justified by earlier work on RPA gradients,[67,68] which employ the same integration grids and for which it was found that this approximation yields sufficiently accurate results. Further, the validity of the gauge origin independence was confirmed by carrying out calculations after shifting each coordinate of the gauge origin by 5 Å. The isotropic shieldings showed deviations that did not exceed 0.05 ppm. Detailed results are provided in the Supporting Information. As commonly done in implementations of NMR shieldings, the explicit use of complex-valued matrices is avoided by treating purely imaginary matrices using skew-symmetric, real-valued matrices.

To validate our implementation, we further computed numerical RPA NMR shifts that were recently presented by our group.[41] In this context, the RPA correlation energy is computed within the RI approximation using the method of Furche and co-workers.[54] For the numerical frequency integration, we employ the Clenshaw−Curtis scheme[54,103] with 120 grid points, which was confirmed to provide accurate results in ref 41.

5. RESULTS AND DISCUSSION

5.1. Validation of the Implementation.

For the validation of our implementation of analytical RPA NMR shifts, the shifts are compared against the results obtained with the numerical RPA NMR reference implementation.[41] Therefore, analytical and numerical RPA NMR shifts based on a preceding PBE reference calculation (RPA@PBE) and based on a HF reference (RPA@HF) were computed for the molecules in the test set assembled by Gauss and co-workers[104] as well as the test set of Flaig et al.[27] For the Gauss benchmark set, the molecules SO_2 and O_3 are excluded, as in ref 104, as well as PN, which is a difficult case for theoretical computations in general.[105]

The results for the Gauss benchmark set are shown in Figure 2 and in more detail in Table 1, where the mean absolute deviations (MADs) of the analytical istropic NMR shifts with respect to the numerical results are shown for the most common nuclei in the test set, i.e., ^{1}H, ^{13}C, ^{15}N, ^{17}O, and ^{19}F, at the RPA@HF and RPA@PBE levels of theory using the cc-pwCVTZ basis set with the corresponding RI basis set. As can be seen, the MADs for the different nuclei at the RPA@HF and RPA@PBE levels of theory are all on the order of 10^{-2} ppm, which is well within the error of numerical differentiation.

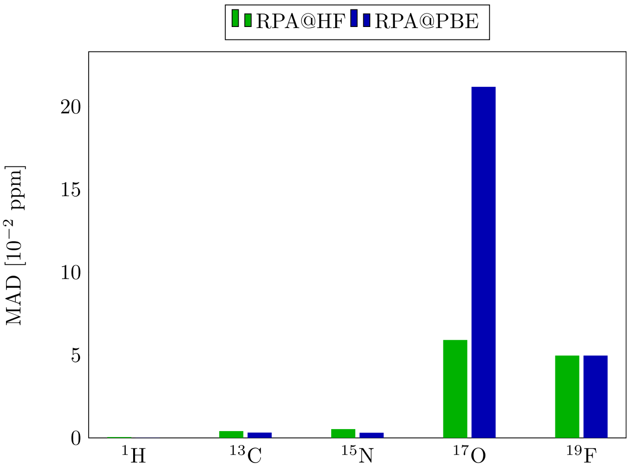

Figure 2. MADs in 10^{-2} ppm of analytical to numerical isotropic NMR shifts for the ^{1}H, ^{13}C, ^{15}N, ^{17}O, and ^{19}F nuclei at the RPA@HF and RPA@PBE levels of theory for the molecules in the Gauss[104] benchmark set. All calculations were carried out using the cc-pwCVTZ basis set with the corresponding RI basis set.

Table 1. Comparison of MADs in 10^{-2} ppm of Analytical to Numerical Isotropic NMR Shifts for the ^{1}H, ^{13}C, ^{15}N, ^{17}O, and ^{19}F Nuclei at the RPA@HF and RPA@PBE Levels of Theory[a]

benchmark	reference	^{1}H	^{13}C	^{15}N	^{17}O	^{19}F
Gauss	HF	0.05	0.41	0.53	5.91	4.97
	PBE	0.01	0.32	0.31	21.19	6.44
Flaig	HF	0.84	2.08	6.01	6.94	1.52
	PBE	0.04	3.05	7.73	7.73	2.52

[a] All Calculations were carried out with the cc-pwCVTZ basis set for the Gauss benchmark set and with the cc-pwCVDZ basis set for the Flaig benchmark set.

The corresponding results for the Flaig benchmark set are provided in Figure 3 and in more detail in Table 1 for the nuclei ^{1}H, ^{13}C, ^{15}N, ^{17}O, and ^{19}F. All calculations were carried out using the cc-pwCVDZ basis set with the corresponding RI basis set. Evidently, for this benchmark set, all MADs are also on the order of 10^{-2} ppm and comparable with the results obtained for the Gauss benchmark set. Since the errors are well within the error of numerical differentiation, it is safe to conclude that the presented theory and the implementation thereof are correct.

5.2. Accuracy: Convergence of the Minimax Grid.

To motivate the choice for the number of numerical integration points for the minimax grids in the previous section, NMR shift calculations on the benchmark set by Gauss and co-workers[104] are performed at the RPA@HF level of theory

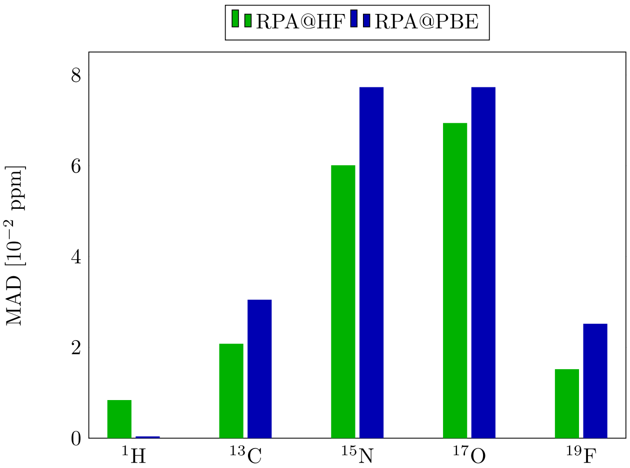

Figure 3. MADs in 10^{-2} ppm of analytical to numerical isotropic NMR shifts for the ^{1}H, ^{13}C, ^{15}N, ^{17}O, and ^{19}F nuclei at the RPA@HF and RPA@PBE levels of theory for the molecules in the Flaig[27] benchmark set. All calculations were carried out using the cc-pwCVDZ basis set with the corresponding RI basis set.

using the cc-pwCVTZ basis set for a varying number of integration points. The MADs with respect to the results obtained with the largest available integration grid are presented in Table 2 for the most represented nuclei in this benchmark set, i.e., ^{1}H, ^{13}C, ^{15}N, ^{17}O, and ^{19}F.

Table 2. Analysis of the RPA NMR Shift Convergence for the ^{1}H, ^{13}C, ^{15}N, ^{17}O, and ^{19}F Nuclei with the Number of Minimax Grid Points N_g[a]

N_g	^{1}H	^{13}C	^{15}N	^{17}O	^{19}F
10	0.01	0.62	1.75	3.20	0.97
11	0.01	0.50	1.40	2.57	0.77
12	0.01	0.41	1.14	2.07	0.61
13	0.01	0.36	0.91	1.73	0.49
14	0.00	0.26	0.70	1.31	0.42
15	0.00	0.24	0.54	1.07	0.31
16	0.00	0.15	0.39	0.75	0.23
17	0.00	0.13	0.26	0.53	0.39
18	0.00	0.09	0.14	0.32	0.34
19	0.00	0.04	0.07	0.15	0.08
20	-	-	-	-	-

[a] All values are given as MADs in 10^{-2} ppm with respect to the results obtained for $N_g = 20$ at the RPA@HF level of theory. All calculations were carried out using the cc-pwCVTZ basis set with the corresponding RI basis set.

The results in Table 2 show that the numerical integration grids allow to smoothly converge the obtained chemical shifts. For lighter elements, such as ^{1}H, the errors are almost independent of the grid size and smaller than 10^{-3} ppm. For heavier elements, such as ^{17}O, a grid size of 15 integration points allows one to obtain an accuracy on the order of 10^{-2} ppm, compared to the converged result obtained with 20 integration points. In conclusion, based on the obtained results, the choice of 15 integration points provides a good compromise between accuracy and computational cost, which is why this number of grid points was employed in all presented calculations.

6. CONCLUSIONS

An analytical expression for NMR chemical shieldings at the direct RPA level of theory as a post-KS method based on ACFDT is presented for the first time. By taking the mixed second derivative of the RPA ground-state energy expression with respect to the nuclear magnetic moment and an external magnetic field, the NMR shielding tensor is obtained. For this, a rigorous derivation for the analytical expression is presented, with which the evaluation of the shielding tensor is possible with formal $O(N^4)$ time complexity, in contrast to the higher-scaling of other correlation methods such as MP2 or CC. The derived expressions and the implementation are sensibly verified by comparing the obtained chemical shifts against the numerical implementation by Glasbrenner et al.[41] For this, calculations on established NMR benchmark sets were carried out with both HF and a commonly used representative for DFT functionals, i.e., PBE, as reference. While the employed implementation is only preliminarily optimized in terms of computational efficiency and not yet optimized in terms of memory requirements, the presented equations represent an ideal stepping stone toward a low-scaling and efficient implementation of NMR shieldings at the RPA level of theory in future work. Similar to the AO-RPA gradients, the evaluation of the noninteracting response function and the correlated self-energy in the imaginary time domain represent the formally highest scaling steps, and the necessity to compute their magnetic field derivatives adds additional $O(N^4)$ scaling steps. However, efficient techniques, such as the attenuated Coulomb RI approximation[60] and Cholesky molecular orbitals, to treat the involved integral contractions can be leveraged for a low-scaling implementation at reduced cost in future work. The application of these low-scaling techniques therefore provides a valuable route toward NMR shift calculations on large molecules with good accuracy and affordable cost.

Furthermore, the derived expression for the analytical second derivative of the RPA energy can easily be extended to the related σ-functionals[72] to profit from the reduced errors not only for atomization, reaction, and noncovalent interaction energies but possibly also for NMR shifts.

APPENDICES

A. Derivation of the Hartree–Fock Energy Functional Shielding Contribution

The Hartree–Fock energy functional is given as

$$E^{\mathrm{HF}}[\mathbf{P}] = \mathrm{Tr}\left(\mathbf{Ph} + \frac{1}{2}\mathbf{PG}[\mathbf{P}]\right) \tag{88}$$

To compute the HF contribution to the total NMR shielding tensor, this expression is first differentiated with respect to the nuclear magnetic moment $\mathbf{m}$ given by

$$\frac{\partial E^{\mathrm{HF}}[\mathbf{P}]}{\partial \mathbf{m}} = \mathrm{Tr}(\mathbf{P}^{\mathbf{m}}\mathbf{h} + \mathbf{P}\mathbf{h}^{\mathbf{m}} + \mathbf{P}^{\mathbf{m}}\mathbf{G}[\mathbf{P}]) \tag{89}$$

As the basis functions are independent of $\mathbf{m}$, the contribution from the differentiated integrals, i.e., $\mathbf{G}^{\mathbf{m}}[\mathbf{P}]$ is zero. The terms contracted with the response of the density matrix $\mathbf{P}^{\mathbf{m}}$ can be collected in the HF Hamiltonian $\mathbf{H}_{\mathrm{HF}}$ to yield

$$\frac{\partial E^{\mathrm{HF}}[\mathbf{P}]}{\partial \mathbf{m}} = \mathrm{Tr}(\mathbf{P}\mathbf{h}^{\mathbf{m}} + \mathbf{P}^{\mathbf{m}}\mathbf{H}_{\mathrm{HF}}) \tag{90}$$

Since the occupied−occupied part of $\mathbf{P}^{\mathbf{m}}$ is given by $\mathbf{P}^{\mathbf{m}}_{\mathrm{oo}} = -\mathbf{PSP}^{\mathbf{m}}\mathbf{P} = \mathbf{0}$ and the virtual−virtual part is necessarily zero, the density response is given by the nonzero occupied−virtual and virtual−occupied blocks as

$$\mathbf{P}^{\mathbf{m}} = \mathbf{PSP}^{\mathbf{m}}(\mathbf{1} - \mathbf{SP}) + (\mathbf{1} - \mathbf{PS})\mathbf{P}^{\mathbf{m}}\mathbf{SP} \tag{91}$$

$$= \mathbf{P}^{\mathbf{m}}_{\mathrm{ov}} + \mathbf{P}^{\mathbf{m}}_{\mathrm{vo}} \tag{92}$$

At the same time the occupied−virtual and virtual−occupied parts of the HF Hamiltonian, given by the following subspace projections,

$$\mathbf{SPH}_{\mathrm{HF}}(\mathbf{1} - \mathbf{PS}) = (\mathbf{1} - \mathbf{SP})\mathbf{H}_{\mathrm{HF}}\mathbf{PS} = \mathbf{0} \tag{93}$$

$$\mathbf{H}_{\mathrm{HF,ov}} = \mathbf{H}_{\mathrm{HF,vo}} = \mathbf{0} \tag{94}$$

vanish for a matching converged HF density. Therefore, the trace of $\mathbf{P}^{\mathbf{m}}\mathbf{H}_{\mathrm{HF}}$ is zero and the HF contribution to the total shielding tensor, after second differentiation with respect to $\mathbf{B}$, is given by

$$\frac{\partial^2 E^{\mathrm{HF}}[\mathbf{P}]}{\partial \mathbf{B}\partial \mathbf{m}} = \mathrm{Tr}(\mathbf{P}^{\mathbf{B}}\mathbf{h}^{\mathbf{m}}) + \mathrm{Tr}(\mathbf{P}\mathbf{h}^{\mathbf{Bm}}) \tag{95}$$

However, in the case of a KS reference density, the HF energy functional is nonstationary with respect to the density and thus the occupied−virtual and virtual−occupied parts of the HF Hamiltonian are nonzero. Therefore, in this case, the HF contribution to the total shielding tensor is given by

$$\frac{\partial^2 E^{\mathrm{HF}}[\mathbf{P}]}{\partial \mathbf{B}\partial \mathbf{m}} = \mathrm{Tr}(\mathbf{P}^{\mathbf{B}}\mathbf{h}^{\mathbf{m}}) + \mathrm{Tr}(\mathbf{P}\mathbf{h}^{\mathbf{Bm}}) + \mathrm{Tr}(\mathbf{H}^{\mathbf{B}}_{\mathrm{HF}}\mathbf{P}^{\mathbf{m}}) + \mathrm{Tr}(\mathbf{H}_{\mathrm{HF}}\mathbf{P}^{\mathbf{Bm}}) \tag{96}$$

B. Derivative of the Self-Energy with Respect to the Magnetic Field

Carrying out the differentiation in eq 68 for the self-energy $\boldsymbol{\Sigma}(-\mathrm{i}\tau)$ in the negative imaginary time domain yields

$$\begin{aligned}\left.\frac{\partial \Sigma_{\nu\lambda}(-\mathrm{i}\tau)}{\partial \mathbf{B}}\right|_{\mathbf{B}=\mathbf{0}} = &-\frac{\partial \tilde{W}_{\mathrm{c,PQ}}(+\mathrm{i}\tau)}{\partial \mathbf{B}}\mathbb{B}^{P}_{\mu\nu}\underline{G}_{0,\mu\sigma}(-\mathrm{i}\tau)\mathbb{B}^{Q}_{\lambda\sigma}\\ &- \tilde{W}_{\mathrm{c,PQ}}(+\mathrm{i}\tau)\frac{\partial \mathbb{B}^{P}_{\mu\nu}}{\partial \mathbf{B}}\underline{G}_{0,\mu\sigma}(-\mathrm{i}\tau)\mathbb{B}^{Q}_{\lambda\sigma}\\ &- \tilde{W}_{\mathrm{c,PQ}}(+\mathrm{i}\tau)\mathbb{B}^{P}_{\mu\nu}\frac{\partial \underline{G}_{0,\mu\sigma}(-\mathrm{i}\tau)}{\partial \mathbf{B}}\mathbb{B}^{Q}_{\lambda\sigma}\\ &- \tilde{W}_{\mathrm{c,PQ}}(+\mathrm{i}\tau)\mathbb{B}^{P}_{\mu\nu}\underline{G}_{0,\mu\sigma}(-\mathrm{i}\tau)\frac{\partial \mathbb{B}^{Q}_{\lambda\sigma}}{\partial \mathbf{B}}\end{aligned} \tag{97}$$

When evaluating the above expression at $\mathbf{B} = \mathbf{0}$, all quantities that are not $\mathbf{B}$-field derivatives evaluate to real-valued matrices (symmetric) and even functions in the imaginary time domain. All $\mathbf{B}$-field derivatives are purely imaginary quantities (skew-symmetric) and odd functions in the imaginary time domain. With this in mind, $\frac{\partial \tilde{W}_{\mathrm{c,PQ}}(+\mathrm{i}\tau)}{\partial \mathbf{B}}$ can further be simplified by using the definition in eq 25 and the fact that it is an odd function in the imaginary time domain:

$$\frac{\partial \tilde{W}_{\mathrm{c,PQ}}(+\mathrm{i}\tau)}{\partial \mathbf{B}} = \frac{\partial \mathbf{W}^{\mathrm{even}}_{\mathrm{c}}(\mathrm{i}\tau)}{\partial \mathbf{B}} - \frac{\partial \mathbf{W}^{\mathrm{odd}}_{\mathrm{c}}(\mathrm{i}\tau)}{\partial \mathbf{B}} \tag{98}$$

$$= -\frac{\partial \mathbf{W}^{\mathrm{odd}}_{\mathrm{c}}(\mathrm{i}\tau)}{\partial \mathbf{B}} = -\frac{\partial \mathbf{W}_{\mathrm{c}}(\mathrm{i}\tau)}{\partial \mathbf{B}} \tag{99}$$

Inserting the above expression into eq 97 yields the final expression given in eq 70.

By analogy, the self-energy in the positive time domain can be written according to

$$\begin{aligned}\left.\frac{\partial \Sigma_{\nu\lambda}(+\mathrm{i}\tau)}{\partial \mathbf{B}}\right|_{\mathbf{B}=\mathbf{0}} = &-\frac{\partial \tilde{W}_{\mathrm{c,PQ}}(-\mathrm{i}\tau)}{\partial \mathbf{B}}\mathbb{B}^{P}_{\mu\nu}\overline{G}_{0,\mu\sigma}(\mathrm{i}\tau)\mathbb{B}^{Q}_{\lambda\sigma}\\ &- \tilde{W}_{\mathrm{c,PQ}}(-\mathrm{i}\tau)\frac{\partial \mathbb{B}^{P}_{\mu\nu}}{\partial \mathbf{B}}\overline{G}_{0,\mu\sigma}(\mathrm{i}\tau)\mathbb{B}^{Q}_{\lambda\sigma}\\ &- \tilde{W}_{\mathrm{c,PQ}}(-\mathrm{i}\tau)\mathbb{B}^{P}_{\mu\nu}\frac{\partial \overline{G}_{0,\mu\sigma}(\mathrm{i}\tau)}{\partial \mathbf{B}}\mathbb{B}^{Q}_{\lambda\sigma}\\ &- \tilde{W}_{\mathrm{c,PQ}}(-\mathrm{i}\tau)\mathbb{B}^{P}_{\mu\nu}\overline{G}_{0,\mu\sigma}(\mathrm{i}\tau)\frac{\partial \mathbb{B}^{Q}_{\lambda\sigma}}{\partial \mathbf{B}}\end{aligned} \tag{100}$$

Again, rewriting $\frac{\partial \tilde{W}_{\mathrm{c,PQ}}(-\mathrm{i}\tau)}{\partial \mathbf{B}}$ using eq 25 and considering that it is an odd function in the imaginary time domain yields

$$\frac{\partial \tilde{W}_{\mathrm{c,PQ}}(-\mathrm{i}\tau)}{\partial \mathbf{B}} = \frac{\partial \mathbf{W}^{\mathrm{even}}_{\mathrm{c}}(-\mathrm{i}\tau)}{\partial \mathbf{B}} - \frac{\partial \mathbf{W}^{\mathrm{odd}}_{\mathrm{c}}(-\mathrm{i}\tau)}{\partial \mathbf{B}} \tag{101}$$

$$= +\frac{\partial \mathbf{W}^{\mathrm{odd}}_{\mathrm{c}}(\mathrm{i}\tau)}{\partial \mathbf{B}} = +\frac{\partial \mathbf{W}_{\mathrm{c}}(\mathrm{i}\tau)}{\partial \mathbf{B}} \tag{102}$$

Finally, inserting the above equation into eq 100 yields eq 69.

■ ASSOCIATED CONTENT

Supporting Information

The Supporting Information is available free of charge at https://pubs.acs.org/doi/10.1021/acs.jctc.3c00542.

Algorithm for the presented RPA NMR method, detailed results for the demonstration of the validity of the gauge origin independence, and detailed results for the Gauss[104] and Flaig[27] benchmark set as well as for the minimax convergence analysis (PDF)

■ AUTHOR INFORMATION

Corresponding Author

Christian Ochsenfeld − *Chair of Theoretical Chemistry, Department of Chemistry, University of Munich (LMU), D-81377 Munich, Germany; Max Planck Institute for Solid State Research, D-70569 Stuttgart, Germany;* orcid.org/0000-0002-4189-6558; Email: christian.ochsenfeld@cup.uni-muenchen.de

Authors

Viktoria Drontschenko − *Chair of Theoretical Chemistry, Department of Chemistry, University of Munich (LMU), D-81377 Munich, Germany*

Felix H. Bangerter − *Chair of Theoretical Chemistry, Department of Chemistry, University of Munich (LMU), D-81377 Munich, Germany;* orcid.org/0000-0001-5649-1599

Complete contact information is available at:
https://pubs.acs.org/10.1021/acs.jctc.3c00542

Author Contributions

§V.D. and F.H.B. contributed equally to this work.

Notes

The authors declare no competing financial interest.

■ ACKNOWLEDGMENTS

The authors acknowledge the financial support by the "Deutsche Forschungsgemeinschaft" (DFG) under Grant TRR325 "Assembly Controlled Chemical Photocatalysis" (Grant No. 444632635) and the cluster of excellence (EXC2111-390814868) "Munich Center for Quantum Science and Technology" (MCQST). C.O. acknowledges the additional support as Max-Planck-Fellow at the MPI-FKF Stuttgart. F.H.B. thanks the "Fonds der Chemischen Industrie" (FCI) for a graduate fellowship. The authors thank Y. Lemke (LMU Munich) for helpful discussions and Dr. J. Kussmann (LMU Munich) for providing a development version of the FermiONs++ program package.

■ REFERENCES

(1) Schmidt-Rohr, K.; Spiess, H. W. *Multidimensional Solid-State NMR and Polymers*; Academic Press, 1994.

(2) Bühl, M.; van Mourik, T. NMR spectroscopy: quantum-chemical calculations. *Wiley Interdiscip. Rev.: Comput. Mol. Sci.* **2011**, *1*, 634−647.

(3) James, T. *Nuclear Magnetic Resonance in Biochemistry*; Elsevier, 2012.

(4) Hodgkinson, P. *Nuclear Magnetic Resonance Vol. 47*; Nuclear Magnetic Resonance; Royal Society of Chemistry, 2021.

(5) Hodgkinson, P. *Nuclear Magnetic Resonance Vol. 46*; SPR Nuclear Magnetic Resonance; Royal Society of Chemistry, 2020.

(6) Harris, R.; Wasylishen, R.; Duer, M. *NMR Crystallography*; eMagRes Books; Wiley, 2009.

(7) Gauss, J. Effects of electron correlation in the calculation of nuclear magnetic resonance chemical shifts. *J. Chem. Phys.* **1993**, *99*, 3629−3643.

(8) Helgaker, T.; Jaszunski, M.; Ruud, K. Ab initio methods for the calculation of NMR shielding and indirect spin-spin coupling constants. *Chem. Rev.* **1999**, *99*, 293−352.

(9) Casabianca, L. B.; De Dios, A. C. Ab initio calculations of NMR chemical shifts. *J. Chem. Phys.* **2008**, *128*, No. 052201.

(10) Lodewyk, M. W.; Siebert, M. R.; Tantillo, D. J. Computational prediction of 1H and 13C chemical shifts: a useful tool for natural product, mechanistic, and synthetic organic chemistry. *Chem. Rev.* **2012**, *112*, 1839−1862.

(11) Stevens, R. M.; Pitzer, R.; Lipscomb, W. Perturbed Hartree−Fock Calculations. I. Magnetic Susceptibility and Shielding in the LiH Molecule. *J. Chem. Phys.* **1963**, *38*, 550−560.

(12) Ditchfield, R. Self-consistent perturbation theory of diamagnetism: I. A gauge-invariant LCAO method for NMR chemical shifts. *Mol. Phys.* **1974**, *27*, 789−807.

(13) Wolinski, K.; Hinton, J. F.; Pulay, P. Efficient implementation of the gauge-independent atomic orbital method for NMR chemical shift calculations. *J. Am. Chem. Soc.* **1990**, *112*, 8251−8260.

(14) Häser, M.; Ahlrichs, R.; Baron, H.; Weis, P.; Horn, H. Direct computation of second-order SCF properties of large molecules on workstation computers with an application to large carbon clusters. *Theor. Chim. Acta* **1992**, *83*, 455−470.

(15) Larsen, H.; Helgaker, T.; Olsen, J.; Jørgensen, P. Geometrical derivatives and magnetic properties in atomic-orbital density-based Hartree−Fock theory. *J. Chem. Phys.* **2001**, *115*, 10344−10352.

(16) Schreckenbach, G.; Ziegler, T. Calculation of NMR shielding tensors using gauge-including atomic orbitals and modern density functional theory. *J. Phys. Chem. A* **1995**, *99*, 606−611.

(17) Cheeseman, J. R.; Trucks, G. W.; Keith, T. A.; Frisch, M. J. A comparison of models for calculating nuclear magnetic resonance shielding tensors. *J. Chem. Phys.* **1996**, *104*, 5497−5509.

(18) Rauhut, G.; Puyear, S.; Wolinski, K.; Pulay, P. Comparison of NMR shieldings calculated from Hartree- Fock and density functional wave functions using gauge-including atomic orbitals. *J. Phys. Chem. A* **1996**, *100*, 6310−6316.

(19) Gauss, J. Calculation of NMR chemical shifts at second-order many-body perturbation theory using gauge-including atomic orbitals. *Chem. Phys. Lett.* **1992**, *191*, 614−620.

(20) Gauss, J.; Stanton, J. F. Electron-correlated approaches for the calculation of NMR chemical shifts. *Adv. Chem. Phys.* **2002**, *123*, 355−422.

(21) Gauss, J.; Stanton, J. F. Gauge-invariant calculation of nuclear magnetic shielding constants at the coupled−cluster singles and doubles level. *J. Chem. Phys.* **1995**, *102*, 251−253.

(22) Gauss, J.; Stanton, J. F. Perturbative treatment of triple excitations in coupled-cluster calculations of nuclear magnetic shielding constants. *J. Chem. Phys.* **1996**, *104*, 2574−2583.

(23) Kállay, M.; Gauss, J. Analytic second derivatives for general coupled-cluster and configuration-interaction models. *J. Chem. Phys.* **2004**, *120*, 6841−6848.

(24) Ruud, K.; Helgaker, T.; Kobayashi, R.; Jørgensen, P.; Bak, K. L.; Jensen, H. J. A. Multiconfigurational self-consistent field calculations of nuclear shieldings using London atomic orbitals. *J. Chem. Phys.* **1994**, *100*, 8178−8185.

(25) Ochsenfeld, C.; Kussmann, J.; Koziol, F. Ab initio NMR spectra for molecular systems with a thousand and more atoms: a linear-scaling method. *Angew. Chem.* **2004**, *116*, 4585−4589.

(26) Kussmann, J.; Ochsenfeld, C. Linear-scaling method for calculating nuclear magnetic resonance chemical shifts using gauge-including atomic orbitals within Hartree-Fock and density-functional theory. *J. Chem. Phys.* **2007**, *127*, No. 054103.

(27) Flaig, D.; Maurer, M.; Hanni, M.; Braunger, K.; Kick, L.; Thubauville, M.; Ochsenfeld, C. Benchmarking hydrogen and carbon NMR chemical shifts at HF, DFT, and MP2 levels. *J. Chem. Theory Comput.* **2014**, *10*, 572−578.

(28) Stoychev, G. L.; Auer, A. A.; Neese, F. Efficient and accurate prediction of nuclear magnetic resonance shielding tensors with double-hybrid density functional theory. *J. Chem. Theory Comput.* **2018**, *14*, 4756−4771.

(29) Kollwitz, M.; Gauss, J. A direct implementation of the GIAO-MBPT (2) method for calculating NMR chemical shifts. Application to the naphthalenium and anthracenium ions. *Chem. Phys. Lett.* **1996**, *260*, 639−646.

(30) Kollwitz, M.; Häser, M.; Gauss, J. Non-Abelian point group symmetry in direct second-order many-body perturbation theory calculations of NMR chemical shifts. *J. Chem. Phys.* **1998**, *108*, 8295−8301.

(31) Gauss, J.; Werner, H.-J. NMR chemical shift calculations within local correlation methods: the GIAO-LMP2 approach. *Phys. Chem. Chem. Phys.* **2000**, *2*, 2083−2090.

(32) Loibl, S.; Schütz, M. NMR shielding tensors for density fitted local second-order Møller-Plesset perturbation theory using gauge including atomic orbitals. *J. Chem. Phys.* **2012**, *137*, No. 084107.

(33) Maurer, M.; Ochsenfeld, C. A linear-and sublinear-scaling method for calculating NMR shieldings in atomic orbital-based second-order Møller-Plesset perturbation theory. *J. Chem. Phys.* **2013**, *138*, No. 174104.

(34) Glasbrenner, M.; Vogler, S.; Ochsenfeld, C. Efficient low-scaling computation of NMR shieldings at the second-order Møller−Plesset perturbation theory level with Cholesky-decomposed densities and an attenuated Coulomb metric. *J. Chem. Phys.* **2021**, *155*, No. 224107.

(35) Burger, S.; Lipparini, F.; Gauss, J.; Stopkowicz, S. NMR chemical shift computations at second-order Møller−Plesset

perturbation theory using gauge-including atomic orbitals and Cholesky-decomposed two-electron integrals. *J. Chem. Phys.* **2021**, *155*, No. 074105.

(36) Stoychev, G. L.; Auer, A. A.; Gauss, J.; Neese, F. DLPNO-MP2 second derivatives for the computation of polarizabilities and NMR shieldings. *J. Chem. Phys.* **2021**, *154*, No. 164110.

(37) Grimme, S. Improved second-order Møller−Plesset perturbation theory by separate scaling of parallel-and antiparallel-spin pair correlation energies. *J. Chem. Phys.* **2003**, *118*, 9095−9102.

(38) Maurer, M.; Ochsenfeld, C. Spin Component-Scaled Second-Order Møller−Plesset Perturbation Theory for Calculating NMR Shieldings. *J. Chem. Theory Comput.* **2015**, *11*, 37−44.

(39) Jung, Y.; Lochan, R. C.; Dutoi, A. D.; Head-Gordon, M. Scaled opposite-spin second order Møller−Plesset correlation energy: An economical electronic structure method. *J. Chem. Phys.* **2004**, *121*, 9793−9802.

(40) Gauss, J.; Stanton, J. F. Analytic CCSD(T) second derivatives. *Chem. Phys. Lett.* **1997**, *276*, 70−77.

(41) Glasbrenner, M.; Graf, D.; Ochsenfeld, C. Benchmarking the Accuracy of the Direct Random Phase Approximation and σ-Functionals for NMR Shieldings. *J. Chem. Theory Comput.* **2022**, *18*, 192−205.

(42) Bohm, D.; Pines, D. A collective description of electron interactions: III. Coulomb interactions in a degenerate electron gas. *Phys. Rev.* **1953**, *92*, 609.

(43) Kohn, W.; Sham, L. J. Self-consistent equations including exchange and correlation effects. *Phys. Rev.* **1965**, *140*, A1133.

(44) Perdew, J. P.; Schmidt, K. Jacob's ladder of density functional approximations for the exchange-correlation energy. *AIP Conf. Proc.* **2001**, *577*, 1−20.

(45) Hohenberg, P.; Kohn, W. Inhomogeneous electron gas. *Phys. Rev.* **1964**, *136*, B864.

(46) Langreth, D. C.; Perdew, J. P. The exchange-correlation energy of a metallic surface. *Solid State Commun.* **1975**, *17*, 1425−1429.

(47) Gunnarsson, O.; Lundqvist, B. I. Exchange and correlation in atoms, molecules, and solids by the spin-density-functional formalism. *Phys. Rev. B* **1976**, *13*, 4274.

(48) Langreth, D. C.; Perdew, J. P. Exchange-correlation energy of a metallic surface: Wave-vector analysis. *Phys. Rev. B* **1977**, *15*, 2884.

(49) Whitten, J. L. Coulombic potential energy integrals and approximations. *J. Chem. Phys.* **1973**, *58*, 4496.

(50) Dunlap, B. I.; Connolly, J. W. D.; Sabin, J. R. On some approximations in applications of Xα theory. *J. Chem. Phys.* **1979**, *71*, 3396.

(51) Feyereisen, M.; Fitzgerald, G.; Komornicki, A. Use of approximate integrals in ab initio theory. An application in MP2 energy calculations. *Chem. Phys. Lett.* **1993**, *208*, 359−363.

(52) Eichkorn, K.; Treutler, O.; Öhm, H.; Häser, M.; Ahlrichs, R. Auxiliary basis sets to approximate Coulomb potentials. *Chem. Phys. Lett.* **1995**, *240*, 283−290.

(53) Eichkorn, K.; Weigend, F.; Treutler, O.; Ahlrichs, R. Auxiliary basis sets for main row atoms and transition metals and their use to approximate Coulomb potentials. *Theor. Chem. Acc.* **1997**, *97*, 119−124.

(54) Eshuis, H.; Yarkony, J.; Furche, F. Fast computation of molecular random phase approximation correlation energies using resolution of the identity and imaginary frequency integration. *J. Chem. Phys.* **2010**, *132*, No. 234114.

(55) Furche, F. Developing the random phase approximation into a practical post-Kohn-Sham correlation model. *J. Chem. Phys.* **2008**, *129*, No. 114105.

(56) Eshuis, H.; Furche, F. Basis set convergence of molecular correlation energy differences within the random phase approximation. *J. Chem. Phys.* **2012**, *136*, No. 084105.

(57) Kaltak, M.; Klimes, J.; Kresse, G. Low scaling algorithms for the random phase approximation: Imaginary time and Laplace transformations. *J. Chem. Theory Comput.* **2014**, *10*, No. 2498.

(58) Kállay, M. Linear-scaling implementation of the direct random-phase approximation. *J. Chem. Phys.* **2015**, *142*, No. 204105.

(59) Schurkus, H. F.; Ochsenfeld, C. Communication: An effective linear-scaling atomic-orbital reformulation of the random-phase approximation using a contracted double-Laplace transformation. *J. Chem. Phys.* **2016**, *144*, No. 031101.

(60) Luenser, A.; Schurkus, H. F.; Ochsenfeld, C. Vanishing-overhead linear-scaling random phase approximation by Cholesky decomposition and an attenuated Coulomb-metric. *J. Chem. Theory Comput.* **2017**, *13*, 1647.

(61) Graf, D.; Beuerle, M.; Schurkus, H. F.; Luenser, A.; Savasci, G.; Ochsenfeld, C. Accurate and Efficient Parallel Implementation of an Effective Linear-Scaling Direct Random Phase Approximation Method. *J. Chem. Theory Comput.* **2018**, *14*, 2505.

(62) Drontschenko, V.; Graf, D.; Laqua, H.; Ochsenfeld, C. Lagrangian-based minimal-overhead batching scheme for the efficient integral-direct evaluation of the RPA correlation energy. *J. Chem. Theory and Comput.* **2021**, *17*, 5623−5634.

(63) Wilhelm, J.; Seewald, P.; Del Ben, M.; Hutter, J. Large-scale cubic-scaling random phase approximation correlation energy calculations using a Gaussian basis. *J. Chem. Theory Comput.* **2016**, *12*, 5851−5859.

(64) Gauss, J. Molecular properties. *Modern Methods and Algorithms of Quantum Chemistry* **2000**, *3*, 541−592.

(65) Rekkedal, J.; Coriani, S.; Iozzi, M. F.; Teale, A. M.; Helgaker, T.; Pedersen, T. B. Communication: Analytic gradients in the random-phase approximation. *J. Chem. Phys.* **2013**, *139*, No. 081101.

(66) Burow, A. M.; Bates, J. E.; Furche, F.; Eshuis, H. Analytical first-order molecular properties and forces within the adiabatic connection random phase approximation. *J. Chem. Theory Comput.* **2014**, *10*, 180−194.

(67) Ramberger, B.; Schäfer, T.; Kresse, G. Analytic interatomic forces in the random phase approximation. *Phys. Rev. Lett.* **2017**, *118*, 106403.

(68) Beuerle, M.; Ochsenfeld, C. Low-scaling analytical gradients for the direct random phase approximation using an atomic orbital formalism. *J. Chem. Phys.* **2018**, *149*, No. 244111.

(69) Thierbach, A.; Görling, A. Analytic energy gradients for the exact exchange Kohn−Sham method. *J. Chem. Phys.* **2020**, *152*, No. 114113.

(70) Tahir, M. N.; Zhu, T.; Shang, H.; Li, J.; Blum, V.; Ren, X. Localized resolution of identity approach to the analytical gradients of random-phase approximation ground-state energy: algorithm and benchmarks. *J. Chem. Theory Comput.* **2022**, *18*, 5297−5311.

(71) Drontschenko, V.; Graf, D.; Laqua, H.; Ochsenfeld, C. Efficient Method for the Computation of Frozen-Core Nuclear Gradients within the Random Phase Approximation. *J. Chem. Theory Comput.* **2022**, *18*, 7359−7372.

(72) Trushin, E.; Thierbach, A.; Görling, A. Toward chemical accuracy at low computational cost: Density-functional theory with σ-functionals for the correlation energy. *J. Chem. Phys.* **2021**, *154*, No. 014104.

(73) Hansen, A. E.; Bouman, T. D. Localized orbital/local origin method for calculation and analysis of NMR shieldings. Applications to 13C shielding tensors. *J. Chem. Phys.* **1985**, *82*, 5035−5047.

(74) Tossell, J. A.; Lazzeretti, P. Ab initio calculation of 77Se NMR shielding constants in H2Se and SeF6 and other second-order properties of H2Se. *J. Magn. Reson. (1969)* **1988**, *80*, 39−44.

(75) Tossell, J. A. Calculation of the 29 Si NMR shielding tensor in forsterite. *Phys. Chem. Miner.* **1992**, *19*, 338−342.

(76) Sauer, S. P.; Špirko, V.; Paidarová, I.; Kraemer, W. P. The vibrational dependence of the hydrogen and oxygen nuclear magnetic shielding constants in OH- and OH-· H2O. *Chem. Phys.* **1997**, *214*, 91−101.

(77) Visscher, L.; Enevoldsen, T.; Saue, T.; Jensen, H. J. A.; Oddershede, J. Full four-component relativistic calculations of NMR shielding and indirect spin-spin coupling tensors in hydrogen halides. *J. Comput. Chem.* **1999**, *20*, 1262−1273.

(78) Gimenez, C. A.; Kozioł, K.; Aucar, G. A. Quantum electrodynamics effects on NMR magnetic shielding constants of

He-like and Be-like atomic systems. *Phys. Rev. A* **2016**, *93*, No. 032504.

(79) Einstein, A. The foundation of the general theory of relativity. *Ann. Phys.* **1916**, *354*, 769.

(80) Hameka, H. F. Theory of Magnetic Properties of Molecules with Particular Emphasis on the Hydrogen Molecule. *Rev. Mod. Phys.* **1962**, *34*, 87−101.

(81) Zeroka, D.; Hameka, H. F. Calculation of Magnetic Shielding Constants of Diatomic Molecules. I. General Theory and Application to HF Molecule. *J. Chem. Phys.* **1966**, *45*, 300−311.

(82) London, F. Théorie quantique des courants interatomiques dans les combinaisons aromatiques. *J. Phys. Radium* **1937**, *8*, 397−409.

(83) Helgaker, T.; Jørgensen, P. An electronic Hamiltonian for origin independent calculations of magnetic properties. *J. Chem. Phys.* **1991**, *95*, 2595−2601.

(84) Schweizer, S.; Doser, B.; Ochsenfeld, C. An atomic orbital-based reformulation of energy gradients in second-order Møller−Plesset perturbation theory. *J. Chem. Phys.* **2008**, *128*, No. 154101.

(85) Furche, F.; Van Voorhis, T. Fluctuation-dissipation theorem density-functional theory. *J. Chem. Phys.* **2005**, *122*, No. 164106.

(86) Hedin, L. New method for calculating the one-particle Green's function with application to the electron-gas problem. *Phys. Rev.* **1965**, *139*, A796.

(87) Ayala, P. Y.; Scuseria, G. E. Linear scaling second-order M?ller−Plesset theory in the atomic orbital basis for large molecular systems. *J. Chem. Phys.* **1999**, *110*, 3660−3671.

(88) Pulay, P. Ab initio calculation of force constants and equilibrium geometries in polyatomic molecules: I. Theory. *Mol. Phys.* **1969**, *17*, 197−204.

(89) Handy, N. C.; Schaefer, H. F., III On the evaluation of analytic energy derivatives for correlated wave functions. *J. Chem. Phys.* **1984**, *81*, 5031−5033.

(90) Liu, P.; Kaltak, M.; Klimeš, J.; Kresse, G. Cubic scaling G W: Towards fast quasiparticle calculations. *Phys. Rev. B* **2016**, *94*, 165109.

(91) Wilhelm, J.; Golze, D.; Talirz, L.; Hutter, J.; Pignedoli, C. A. Toward GW calculations on thousands of atoms. *J. Phys. Chem. Lett.* **2018**, *9*, 306−312.

(92) Surján, P. R. The MP2 energy as a functional of the Hartree−Fock density matrix. *Chem. Phys. Lett.* **2005**, *406*, 318−320.

(93) Beer, M.; Ochsenfeld, C. Efficient linear-scaling calculation of response properties: Density matrix-based Laplace-transformed coupled-perturbed self-consistent field theory. *J. Chem. Phys.* **2008**, *128*, No. 221102.

(94) Kussmann, J.; Ochsenfeld, C. Pre-selective screening for matrix elements in linear-scaling exact exchange calculations. *J. Chem. Phys.* **2013**, *138*, No. 134114.

(95) Kussmann, J.; Ochsenfeld, C. Preselective screening for linear-scaling exact exchange-gradient calculations for graphics processing units and general strong-scaling massively parallel calculations. *J. Chem. Theory Comput.* **2015**, *11*, 918−922.

(96) Kussmann, J.; Ochsenfeld, C. Hybrid CPU/GPU Integral Engine for Strong-Scaling Ab Initio Methods. *J. Chem. Theory Comput.* **2017**, *13*, 3153−3159.

(97) Perdew, J. P.; Burke, K.; Ernzerhof, M. Generalized gradient approximation made simple. *Phys. Rev. Lett.* **1996**, *77*, 3865.

(98) Marques, M. A.; Oliveira, M. J.; Burnus, T. Libxc: A library of exchange and correlation functionals for density functional theory. *Comput. Phys. Commun.* **2012**, *183*, 2272−2281.

(99) Malkin, V. G.; Malkina, O. L.; Salahub, D. R. Calculations of NMR Shielding Constants by Uncoupled Density Functional Theory. *Chem. Phys. Lett.* **1993**, *204*, 80−86.

(100) Beer, M.; Kussmann, J.; Ochsenfeld, C. Nuclei-selected NMR shielding calculations: A sublinear-scaling quantum-chemical method. *J. Chem. Phys.* **2011**, *134*, No. 074102.

(101) Peterson, K. A.; Dunning, T. H., Jr Accurate correlation consistent basis sets for molecular core-valence correlation effects: The second row atoms Al−Ar, and the first row atoms B−Ne revisited. *J. Chem. Phys.* **2002**, *117*, 10548−10560.

(102) Hättig, C. Optimization of auxiliary basis sets for RI-MP2 and RI-CC2 calculations: Core-valence and quintuple-ζ basis sets for H to Ar and QZVPP basis sets for Li to Kr. *Phys. Chem. Chem. Phys.* **2005**, *7*, 59−66.

(103) Boyd, J. P. Exponentially convergent Fourier-Chebshev quadrature schemes on bounded and infinite intervals. *J. Sci. Comput.* **1987**, *2*, 99−109.

(104) Teale, A. M.; Lutnæs, O. B.; Helgaker, T.; Tozer, D. J.; Gauss, J. Benchmarking density-functional theory calculations of NMR shielding constants and spin-rotation constants using accurate coupled-cluster calculations. *J. Chem. Phys.* **2013**, *138*, No. 024111.

(105) Kupka, T.; Leszczyńska, M.; Ejsmont, K.; Mnich, A.; Broda, M.; Thangavel, K.; Kaminsky̌, J. Phosphorus mononitride: A difficult case for theory. *Int. J. Quantum Chem.* **2019**, *119*, No. e26032.

Supporting Information: Analytical Second-Order Properties for the Random Phase Approximation: Nuclear Magnetic Resonance Shieldings

Viktoria Drontschenko,[†] Felix H. Bangerter,[†] and Christian Ochsenfeld[*,†,‡]

†*Chair of Theoretical Chemistry, Department of Chemistry, University of Munich (LMU), D-81377 Munich, Germany*

‡*Max Planck Institute for Solid State Research, D-70569 Stuttgart, Germany*

E-mail: christian.ochsenfeld@cup.uni-muenchen.de

Contents

1 Implementation

The following algorithm summarizes the necessary steps for computing NMR chemical shieldings at the RPA level of theory.

Algorithm 1 Compute RPA NMR chemical shieldings.

```
compute $\mathbf{H}$, $\mathbf{S}$, $\mathbf{P}$, $\mathbf{P}_{\mathrm{virt}}$, $\mathbb{V}$, and $\mathbb{B}$        ▷ SCF intermediates
compute $\mathbf{h}^{\mathbf{m}}$, $\mathbf{h}^{\mathbf{Bm}}$, $\mathbf{S}^{\mathbf{B}}$, $\mathbf{H}^{(\mathbf{B})}$, and $\mathbb{B}^{\mathbf{B}}$
solve CPSCF for $\mathbf{P}^{\mathbf{B}}$
compute $\mathbf{P}^{\mathbf{B}}_{\mathrm{virt}}$
compute $\mathbf{H}^{\mathbf{B}}$
if not Hartree–Fock reference then
    compute $\mathbf{H}_{\mathrm{HF}}$ and $\mathbf{H}^{\mathbf{B}}_{\mathrm{HF}}$
end if
compute $\mathbf{G}_0(\mathrm{i}\tau)$        ▷ first derivative intermediates
compute $\mathbf{X}_0(\mathrm{i}\tau)$
cosine transform of $\mathbf{X}_0(\mathrm{i}\tau)$ to $\hat{\mathbf{X}}_0(\mathrm{i}\omega)$
compute $\hat{\mathbf{W}}_{\mathrm{c}}(\mathrm{i}\omega)$
inverse cosine transform of $\hat{\mathbf{W}}_{\mathrm{c}}(\mathrm{i}\omega)$ to $\mathbf{W}_{\mathrm{c}}(\mathrm{i}\tau)$
compute $\mathbf{\Sigma}(\mathrm{i}\tau)$
compute $\mathbf{Y}(\mathrm{i}\tau)$ by recursion with $\boldsymbol{\mathcal{A}}(\tau)$ and $\boldsymbol{\mathcal{B}}(\mathrm{i}\tau)$
integrate $\mathbf{Y}(\mathrm{i}\tau)$ to form $\mathbf{P}_{\mathrm{RPA}}$
integrate $\mathbf{Y}(\mathrm{i}\tau)$ and $\mathbf{\Sigma}(\mathrm{i}\tau)$ to form $\mathbf{M}$
compute $\mathbf{V}_{\mathrm{RPA}}$
for every $\mathbf{B}$-field component do        ▷ second derivative intermediates
    compute $\mathbf{G}^{\mathbf{B}}_0(\mathrm{i}\tau)$
    compute $\mathbf{X}^{\mathbf{B}}_0(\mathrm{i}\tau)$
    sine transform of $\mathbf{X}^{\mathbf{B}}_0(\mathrm{i}\tau)$ to $\hat{\mathbf{X}}^{\mathbf{B}}_0(\mathrm{i}\omega)$
    compute $\hat{\mathbf{W}}^{\mathbf{B}}_{\mathrm{c}}(\mathrm{i}\omega)$
    inverse sine transform of $\hat{\mathbf{W}}^{\mathbf{B}}_{\mathrm{c}}(\mathrm{i}\omega)$ to $\mathbf{W}^{\mathbf{B}}_{\mathrm{c}}(\mathrm{i}\tau)$
    compute $\mathbf{\Sigma}^{\mathbf{B}}(\mathrm{i}\tau)$
    compute $\mathbf{Y}^{\mathbf{B}}(\mathrm{i}\tau)$ by recursion with $\boldsymbol{\mathcal{A}}^{\mathbf{B}}(\tau)$ and $\boldsymbol{\mathcal{B}}^{\mathbf{B}}(\mathrm{i}\tau)$
    integrate $\mathbf{Y}(\mathrm{i}\tau)$ and $\mathbf{Y}^{\mathbf{B}}(\mathrm{i}\tau)$ to form $\mathbf{P}^{\mathbf{B}}_{\mathrm{RPA}}$
    integrate $\mathbf{Y}(\mathrm{i}\tau)$, $\mathbf{Y}^{\mathbf{B}}(\mathrm{i}\tau)$, $\mathbf{\Sigma}(\mathrm{i}\tau)$, and $\mathbf{\Sigma}^{\mathbf{B}}(\mathrm{i}\tau)$ to form $\mathbf{M}^{\mathbf{B}}$
    compute $\mathbf{V}^{\mathbf{B}}_{\mathrm{RPA}}$
end for
solve Z-vector equation $\mathbf{Z}_{\mathbf{V}_{\mathrm{RPA}}} = \mathbf{A}^{-1}(\mathbf{V}_{\mathrm{RPA}} + \mathbf{H}_{\mathrm{HF}})$        ▷ nested Z-vector/final shieldings
compute $\mathbf{O}$, $\mathbf{O}_{\mathbf{F}^{\mathbf{m}}}$, and $\mathbf{O}_{\mathbf{Y}^{\mathbf{m}}}$
solve Z-vector equation $\mathbf{Z}_{\mathbf{O}} = \mathbf{A}^{-1}\mathbf{O}$
compute $\boldsymbol{\sigma} = \mathrm{Tr}([\mathbf{P}_{\mathrm{RPA}} + \mathbf{O}_{\mathbf{Y}^{\mathbf{m}}}]\mathbf{h}^{\mathbf{Bm}}) + \mathrm{Tr}([\mathbf{P}^{\mathbf{B}}_{\mathrm{RPA}} + \mathbf{O}_{\mathbf{F}^{\mathbf{m}}}]\mathbf{h}^{\mathbf{m}}) + \mathrm{Tr}(\mathbf{Z}_{\mathbf{O}}\mathbf{b}^{\mathbf{m}}) + \tilde{\boldsymbol{\sigma}}^{\mathrm{HF}}$
```

The algorithm can roughly be grouped into four stages. First, the computation of all intermediates also present in HF NMR shieldings, i.e., the densities, the Hamiltonian, the integrals, etc., as well as their derivatives. Second, the formation of all intermediates also occurring in the first derivative of the RPA equations, which are independent of the magnetic field. Third, **B**-field derivatives of the intermediates of the first derivative, and lastly the nested Z-vector step to obtain the final intermediates for the NMR shieldings.

The most involved steps in terms of computational effort are the computation of the response function $\mathbf{X}_0(\mathrm{i}\tau)$ and the self-energy $\mathbf{\Sigma}(\mathrm{i}\tau)$ in the imaginary time domain, as well as their **B**-field derivatives. Here, $\mathbf{X}_0(\mathrm{i}\tau)$ is most efficiently computed according to, e.g., Ref. S1 by premultiplying the Green's functions with the three-center integrals and then using a matrix multiplication to multiply both third-order tensors. The same approach can be used for the **B**-field derivative of the response function. The self-energy is computed as explained in Ref. S2 and its SI. For the **B**-field derivative of the self-energy we use the same approach. Here, we want to note that for the matrix multiplications we use the high parallel performance of the MKL library for dense matrix algebra routines.

2 Gauge Invariance

Table S1: Testing the gauge origin independence at the RPA@HF level of theory using the def2-SVP and cc-pwCVTZ basis sets with the corresponding RI basis sets for the molecules in the Gauss benchmark set. For each basis set the NMR shifts are given in ppm for the initial geometry (reference) and after each atom has been translated by 5 Å(transl.) as well as the resulting absolute deviation (abs. err.).

		def2-SVP [ppm]			cc-pwCVTZ [ppm]		
molecule	element	transl.	reference	abs. err.	transl.	reference	abs. err.
AlF							
	Al	-4.1606	-4.1605	0.0001	-4.8933	-4.8936	0.0002
	F	3.7843	3.7823	0.0020	-2.5863	-2.5871	0.0008
C_2H_4							
	C	13.5843	13.5850	0.0007	8.0167	8.0169	0.0003
	C	13.5843	13.5850	0.0007	8.0172	8.0169	0.0003
	H	0.3400	0.3400	0.0000	0.1530	0.1499	0.0031
	H	0.3400	0.3400	0.0000	0.1466	0.1499	0.0033
	H	0.3400	0.3400	0.0000	0.1531	0.1499	0.0032
	H	0.3400	0.3400	0.0000	0.1468	0.1499	0.0031
C_3H_4							
	C	-0.8958	-0.8959	0.0001	-2.3976	-2.3762	0.0213
	C	16.5324	16.5323	0.0001	10.5089	10.5229	0.0140
	C	16.5324	16.5323	0.0001	10.5468	10.5229	0.0239
	H	0.7695	0.7695	0.0000	0.5412	0.5476	0.0064
	H	0.7695	0.7695	0.0000	0.5391	0.5476	0.0085
	H	0.1390	0.1390	0.0000	0.0055	0.0054	0.0000
	H	0.1390	0.1390	0.0000	0.0001	0.0054	0.0053
CH_2O							
	O	120.5025	120.5017	0.0008	82.7901	82.7902	0.0000
	C	21.1176	21.1176	0.0000	12.2381	12.2387	0.0006
	H	0.3273	0.3273	0.0000	0.1245	0.1186	0.0058
	H	0.3273	0.3273	0.0000	0.1126	0.1186	0.0060
CH_3F							
	C	0.6198	0.6197	0.0001	-1.3122	-1.3128	0.0007
	F	-9.1903	-9.1894	0.0009	-7.9269	-7.9254	0.0016
	H	0.0139	0.0139	0.0000	-0.1095	-0.1076	0.0019
	H	0.0139	0.0139	0.0000	-0.1051	-0.1076	0.0025
	H	0.0139	0.0139	0.0000	-0.1083	-0.1076	0.0007
CH_4							
	C	1.1768	1.1747	0.0021	1.3187	1.3182	0.0005
	H	0.0179	0.0180	0.0001	-0.0461	-0.0460	0.0001
	H	0.0180	0.0180	0.0000	-0.0460	-0.0460	0.0000
	H	0.0180	0.0180	0.0000	-0.0460	-0.0460	0.0000

	H	0.0180	0.0180	0.0001	-0.0459	-0.0460	0.0001
CO							
	C	34.8474	34.8478	0.0004	24.6474	24.6476	0.0002
	O	49.7149	49.7178	0.0028	33.9522	33.9530	0.0008
FCCH							
	C	4.5935	4.5934	0.0001	2.0948	2.0918	0.0030
	C	2.7262	2.7263	0.0001	-0.2682	-0.2672	0.0010
	H	0.3649	0.3649	0.0000	0.2173	0.2173	0.0000
	F	-0.1199	-0.1190	0.0009	-3.9647	-3.9823	0.0176
FCN							
	F	7.1241	7.1225	0.0016	-0.2682	-0.2703	0.0021
	C	8.2799	8.2794	0.0005	5.3903	5.3900	0.0003
	N	30.1391	30.1381	0.0010	20.9845	20.9848	0.0003
H_2C_2O							
	C	4.3011	4.3010	0.0001	2.2121	2.2113	0.0009
	C	15.1969	15.1970	0.0001	8.7411	8.7352	0.0059
	O	42.7184	42.7181	0.0003	26.3746	26.3681	0.0064
	H	0.4432	0.4432	0.0000	0.1693	0.1673	0.0021
	H	0.4432	0.4432	0.0000	0.1646	0.1673	0.0026
H_2O							
	O	6.1048	6.1066	0.0018	5.8646	5.8657	0.0011
	H	0.5146	0.5146	0.0000	0.4335	0.4339	0.0004
	H	0.5146	0.5146	0.0000	0.4333	0.4339	0.0006
H_2S							
	S	8.2477	8.2485	0.0009	8.7821	8.7865	0.0044
	H	0.5157	0.5157	0.0000	0.2848	0.2857	0.0009
	H	0.5157	0.5157	0.0000	0.2845	0.2857	0.0012
H_4C_2O							
	O	-11.4164	-11.4150	0.0014	-14.9307	-14.8794	0.0513
	C	0.2379	0.2380	0.0001	-1.7721	-1.7721	0.0000
	C	0.2381	0.2380	0.0000	-1.7677	-1.7721	0.0045
	H	-0.0084	-0.0084	0.0000	-0.1355	-0.1444	0.0088
	H	-0.0084	-0.0084	0.0000	-0.1488	-0.1444	0.0044
	H	-0.0084	-0.0084	0.0000	-0.1346	-0.1444	0.0098
	H	-0.0084	-0.0084	0.0000	-0.1479	-0.1444	0.0035
HCN							
	H	0.1919	0.1919	0.0000	0.0776	0.0776	0.0000
	C	15.7958	15.7957	0.0001	11.5072	11.5071	0.0000
	N	43.4703	43.4703	0.0000	32.1927	32.1927	0.0000
HCP							
	H	-0.0709	-0.0709	0.0000	-0.1727	-0.1727	0.0000
	C	26.8904	26.8920	0.0015	18.0367	18.0369	0.0002
	P	48.7256	48.7297	0.0041	32.5252	32.5260	0.0008

HF							
	H	0.8963	0.8964	0.0001	0.8973	0.8972	0.0001
	F	3.4654	3.4627	0.0027	3.0933	3.0962	0.0029
HFCO							
	O	59.6156	59.6138	0.0017	37.5707	37.5889	0.0182
	C	11.8853	11.8851	0.0002	6.0880	6.0736	0.0144
	F	2.8728	2.8736	0.0008	-7.2110	-7.2375	0.0266
	H	0.0653	0.0653	0.0000	-0.1022	-0.0882	0.0140
HOF							
	O	94.8495	94.8534	0.0039	73.5406	73.5422	0.0017
	H	1.9550	1.9549	0.0001	1.5882	1.5875	0.0007
	F	-66.9284	-66.9253	0.0031	-76.2030	-76.2082	0.0052
LiF							
	Li	-0.8679	-0.8679	0.0000	-0.8239	-0.8239	0.0000
	F	-12.5098	-12.5098	0.0001	-1.8842	-1.8845	0.0004
LiH							
	H	0.4265	0.4265	0.0000	0.3036	0.3036	0.0000
	Li	0.3786	0.3786	0.0000	-0.1106	-0.1107	0.0001
N_2							
	N	60.9736	60.9742	0.0005	46.4441	46.4434	0.0007
	N	60.9736	60.9742	0.0005	46.4441	46.4434	0.0007
N_2O							
	N	47.6472	47.6460	0.0011	37.0936	37.0939	0.0003
	N	47.6002	47.5990	0.0011	37.8976	37.8977	0.0001
	O	34.7642	34.7621	0.0021	22.7467	22.7465	0.0003
NH_3							
	N	3.8785	3.8787	0.0002	4.0256	4.0258	0.0002
	H	0.2181	0.2181	0.0000	0.1343	0.1341	0.0002
	H	0.2181	0.2181	0.0000	0.1344	0.1341	0.0003
	H	0.2180	0.2181	0.0000	0.1345	0.1341	0.0004
OCS							
	O	32.8266	32.8281	0.0015	19.9120	19.9142	0.0022
	C	25.1191	25.1194	0.0002	17.9478	17.9482	0.0004
	S	24.1941	24.1940	0.0001	9.8036	9.8036	0.0000
OF_2							
	O	68.5144	68.5128	0.0016	34.5995	34.6088	0.0093
	F	3.3360	3.3362	0.0002	-18.4908	-18.4840	0.0068
	F	3.3412	3.3362	0.0049	-18.5005	-18.4840	0.0165

3 Detailed Validation Results

In the following section detailed results for the Gauss[S3] and the Flaig[S4] benchmark set are presented. The order of the nuclei corresponds to the order given in the geometry files of the respective molecules obtained from the SI in the case of the Gauss[S3] benchmark set and from the download section of the Ochsenfeld group website[S5] in the case of the Flaig[S4] benchmark set. Shifts of nuclei which are not chemically equivalent are labeled appropriately for an unambiguous assignment. For smaller molecules the respective functional group, and if necessary the orientation, is given and for aromatics numbering according to the IUPAC nomenclature is chosen.

3.1 Detailed Validation Results: Gauss Benchmark Set

Table S2: Detailed results of the RPA NMR shifts for all molecules in the Gauss benchmark set[S3] at the RPA@HF/cc-pwCVTZ level of theory for the numerical reference implementation (reference) as well as the analytical implementation (result). All shifts and the resulting deviations are given in ppm.

molecule	element	result	reference	abs. err.
AlF				
	Al	-4.8936	-4.8950	0.0015
	F	-2.5871	-2.4875	0.0995
C_2H_4				
	C	8.0169	8.0204	0.0035
	C	8.0169	8.0204	0.0035
	H	0.1499	0.1503	0.0004
	H	0.1499	0.1503	0.0004
	H	0.1499	0.1503	0.0004
	H	0.1499	0.1503	0.0004
C_3H_4				
	C	-2.3762	-2.3758	0.0005
	C	10.5229	10.5281	0.0051
	C	10.5229	10.5281	0.0051
	H	0.5476	0.5463	0.0013
	H	0.5476	0.5463	0.0012
	H	0.0054	0.0058	0.0004
	H	0.0054	0.0058	0.0004
CH_2O				

	O	82.7902	82.6459	0.1443
	C	12.2387	12.2425	0.0038
	H	0.1186	0.1195	0.0009
	H	0.1186	0.1195	0.0008
CH_3F				
	C	-1.3128	-1.3089	0.0039
	F	-7.9254	-7.9222	0.0032
	H	-0.1076	-0.1071	0.0005
	H	-0.1076	-0.1071	0.0005
	H	-0.1076	-0.1071	0.0005
CH_4				
	C	1.3182	1.3200	0.0019
	H	-0.0460	-0.0460	0.0000
	H	-0.0460	-0.0460	0.0000
	H	-0.0460	-0.0460	0.0000
	H	-0.0460	-0.0460	0.0000
CO				
	C	24.6476	24.6488	0.0011
	O	33.9530	33.9399	0.0131
FCCH				
	C	2.0918	2.0954	0.0036
	C	-0.2672	-0.2641	0.0031
	H	0.2173	0.2161	0.0012
	F	-3.9823	-3.9386	0.0437
FCN				
	F	-0.2703	-0.2593	0.0110
	C	5.3900	5.3935	0.0034
	N	20.9848	20.9702	0.0146
H_2C_2O				
	C	2.2113	2.2086	0.0026
	C	8.7352	8.7477	0.0125
	O	26.3681	26.3467	0.0215
	H	0.1673	0.1676	0.0003
	H	0.1673	0.1675	0.0002
H_2O				
	O	5.8657	5.8665	0.0008
	H	0.4339	0.4339	0.0000
	H	0.4339	0.4339	0.0000
H_2S				
	S	8.7865	8.7782	0.0083
	H	0.2857	0.2858	0.0001
	H	0.2857	0.2858	0.0001
H_4C_2O				

	O	-14.8794	-14.8979	0.0185
	C	-1.7721	-1.7677	0.0044
	C	-1.7721	-1.7677	0.0044
	H	-0.1444	-0.1437	0.0006
	H	-0.1444	-0.1437	0.0006
	H	-0.1444	-0.1437	0.0006
	H	-0.1444	-0.1437	0.0006
HCN				
	H	0.0776	0.0761	0.0015
	C	11.5071	11.5120	0.0048
	N	32.1927	32.1900	0.0027
HCP				
	H	-0.1727	-0.1741	0.0014
	C	18.0369	18.0328	0.0041
	P	32.5260	32.4875	0.0385
HF				
	H	0.8972	0.8971	0.0001
	F	3.0962	3.0949	0.0013
HFCO				
	O	37.5889	37.5400	0.0489
	C	6.0736	6.0813	0.0077
	F	-7.2375	-7.2411	0.0036
	H	-0.0882	-0.0875	0.0007
HOF				
	O	73.5422	73.4006	0.1416
	H	1.5875	1.5873	0.0002
	F	-76.2082	-76.0488	0.1594
LiF				
	Li	-0.8239	-0.8231	0.0008
	F	-1.8845	-1.8240	0.0605
LiH				
	H	0.3036	0.3036	0.0000
	Li	-0.1107	-0.1096	0.0011
N_2				
	N	46.4434	46.4436	0.0002
	N	46.4434	46.4437	0.0003
N_2O				
	N	37.0939	37.0826	0.0113
	N	37.8977	37.8925	0.0052
	O	22.7465	22.7367	0.0097
NH_3				
	N	4.0258	4.0283	0.0025
	H	0.1341	0.1341	0.0000

	H	0.1341	0.1341	0.0000
	H	0.1341	0.1341	0.0000
OCS				
	O	19.9142	19.9108	0.0034
	C	17.9482	17.9512	0.0031
	S	9.8036	9.7461	0.0575
OF_2				
	O	34.6088	34.4193	0.1895
	F	-18.4840	-18.4269	0.0571
	F	-18.4840	-18.4266	0.0574

Table S3: Detailed results of the RPA NMR shifts for all molecules in the Gauss benchmark set[S3] at the RPA@PBE/cc-pwCVTZ level of theory for the numerical reference implementation (reference) as well as the analytical implementation (result). All shifts and the resulting deviations are given in ppm.

molecule	element	result	reference	abs. err.
AlF				
	Al	-12.5395	-12.5407	0.0012
	F	-25.8208	-25.8211	0.0003
C_2H_4				
	C	20.7298	20.7377	0.0079
	C	20.7298	20.7377	0.0079
	H	0.3384	0.3386	0.0002
	H	0.3384	0.3386	0.0002
	H	0.3384	0.3386	0.0002
	H	0.3384	0.3386	0.0002
C_3H_4				
	C	-2.9284	-2.9238	0.0046
	C	21.3029	21.3117	0.0088
	C	21.3029	21.3117	0.0088
	H	0.9359	0.9361	0.0002
	H	0.9359	0.9361	0.0002
	H	-0.1389	-0.1389	0.0000
	H	-0.1389	-0.1389	0.0000
CH_2O				
	O	220.4304	219.8347	0.5958
	C	31.8927	31.8966	0.0039
	H	0.0714	0.0715	0.0001
	H	0.0714	0.0715	0.0001
CH_3F				
	C	-1.9967	-1.9966	0.0001
	F	-20.7658	-20.7645	0.0013
	H	-0.4794	-0.4794	0.0000
	H	-0.4794	-0.4794	0.0000
	H	-0.4794	-0.4794	0.0000
CH_4				
	C	1.8436	1.8456	0.0020
	H	-0.0590	-0.0590	0.0000
	H	-0.0590	-0.0590	0.0000
	H	-0.0590	-0.0590	0.0000
	H	-0.0590	-0.0590	0.0000
CO				
	C	52.3831	52.3850	0.0019
	O	71.6005	71.5951	0.0055

FCCH				
	C	8.9862	8.9872	0.0010
	C	5.0325	5.0352	0.0027
	H	0.4341	0.4343	0.0002
	F	-5.5674	-5.5578	0.0096
FCN				
	F	-9.4155	-9.4147	0.0008
	C	18.3118	18.3125	0.0006
	N	50.2996	50.2937	0.0058
H_2C_2O				
	C	3.7803	3.7816	0.0013
	C	26.7004	26.7042	0.0038
	O	61.5271	61.4990	0.0281
	H	0.2732	0.2732	0.0001
	H	0.2732	0.2732	0.0001
H_2O				
	O	4.0511	4.0525	0.0014
	H	0.8537	0.8537	0.0000
	H	0.8537	0.8537	0.0000
H_2S				
	S	10.5790	10.5488	0.0301
	H	0.4957	0.4957	0.0000
	H	0.4957	0.4957	0.0000
H_4C_2O				
	O	-19.6393	-19.6391	0.0002
	C	-2.9245	-2.9235	0.0009
	C	-2.9245	-2.9236	0.0009
	H	-0.5762	-0.5762	0.0000
	H	-0.5762	-0.5762	0.0000
	H	-0.5762	-0.5762	0.0000
	H	-0.5762	-0.5762	0.0000
HCN				
	H	-0.1525	-0.1526	0.0000
	C	27.2219	27.2264	0.0045
	N	65.8816	65.8822	0.0006
HCP				
	H	-0.4788	-0.4788	0.0000
	C	43.6045	43.6065	0.0019
	P	100.7949	100.7578	0.0372
HF				
	H	1.7421	1.7421	0.0000
	F	0.5872	0.5846	0.0026
HFCO				

	O	100.6239	100.5588	0.0651
	C	19.8154	19.8164	0.0010
	F	-29.0573	-29.0556	0.0017
	H	-0.3361	-0.3361	0.0000
HOF				
	O	121.8165	121.2863	0.5303
	H	2.2540	2.2541	0.0001
	F	-71.9220	-72.1018	0.1798
LiF				
	Li	-2.0030	-2.0031	0.0000
	F	-15.1874	-15.1811	0.0063
LiH				
	H	-0.0427	-0.0428	0.0000
	Li	1.3533	1.3550	0.0018
N_2				
	N	80.3644	80.3690	0.0046
	N	80.3644	80.3690	0.0046
N_2O				
	N	59.5667	59.5670	0.0003
	N	66.8380	66.8419	0.0038
	O	38.3326	38.3284	0.0042
NH_3				
	N	3.6714	3.6733	0.0019
	H	0.2822	0.2822	0.0000
	H	0.2822	0.2822	0.0000
	H	0.2822	0.2822	0.0000
OCS				
	O	38.5240	38.5158	0.0082
	C	41.5165	41.5165	0.0000
	S	13.8466	13.8308	0.0158
OF_2				
	O	55.7934	54.9134	0.8800
	F	-28.0742	-28.2949	0.2206
	F	-28.0742	-28.2949	0.2206

3.2 Detailed Validation Results: Flaig Benchmark Set

Table S4: Detailed results of the RPA NMR shifts for all molecules in the Flaig benchmark set[S4] at the RPA@HF/cc-pwCVDZ level of theory for the numerical reference implementation (reference) as well as the analytical implementation (result). All shifts and the resulting deviations are given in ppm.

molecule	element	result	reference	abs. err.
Acetylene (C_2H_2)				
	H	0.0861	0.0859	0.0002
	C	8.4582	8.4780	0.0198
	C	8.4582	8.4781	0.0198
	H	0.0861	0.0859	0.0002
Ethylene (C_2H_4)				
	H	0.3076	0.3084	0.0009
	H	0.3076	0.3084	0.0009
	C	13.4627	13.4998	0.0371
	H	0.3076	0.3084	0.0009
	C	13.4626	13.4998	0.0372
	H	0.3076	0.3084	0.0009
Ethane (C_2H_6)				
	H	-0.0524	-0.0522	0.0001
	H	-0.0524	-0.0522	0.0001
	H	-0.0524	-0.0522	0.0001
	C	1.4695	1.4784	0.0089
	H	-0.0524	-0.0522	0.0001
	H	-0.0524	-0.0523	0.0001
	C	1.4694	1.4784	0.0090
	H	-0.0524	-0.0523	0.0001
Benzene (C_6H_6)				
	H	0.2580	0.2591	0.0011
	H	0.2580	0.2591	0.0011
	C	11.9683	12.0091	0.0409
	H	0.2580	0.2591	0.0011
	C	11.9683	12.0092	0.0410
	H	0.2580	0.2591	0.0011
	C	11.9683	12.0092	0.0410
	H	0.2580	0.2591	0.0011
	C	11.9683	12.0092	0.0410
	C	11.9683	12.0092	0.0410
	C	11.9683	12.0091	0.0409
	H	0.2580	0.2591	0.0011
Tetrachloromethane (CCl_4)				
	C	-0.9163	-0.9147	0.0016
	Cl	-10.1405	-10.1198	0.0207

	Cl	-10.1405	-10.1198	0.0207
	Cl	-10.1405	-10.1198	0.0207
	Cl	-10.1405	-10.1198	0.0207
Tetrafluoromethane (CF_4)				
	F	1.3975	1.4164	0.0188
	F	1.3975	1.4166	0.0191
	F	1.3975	1.4166	0.0191
	C	-5.6193	-5.6128	0.0064
	F	1.3975	1.4165	0.0189
Propadiene (CH_2CCH_2)				
	H	0.1796	0.1802	0.0006
	H	0.1796	0.1802	0.0006
	$\underline{C}\mathrm{H}_2$	6.2350	6.2590	0.0239
	$\mathrm{C}{=}\underline{C}{=}\mathrm{C}$	20.6112	20.6644	0.0532
	H	0.1796	0.1802	0.0006
	$\underline{C}\mathrm{H}_2$	6.2351	6.2589	0.0239
	H	0.1796	0.1802	0.0006
Acetaldehyde (CH_3CHO)				
	O	77.9944	78.1373	0.1429
	$\mathrm{C}\underline{H}\mathrm{O}$	0.1444	0.1452	0.0008
	$\underline{C}\mathrm{HO}$	20.9302	20.9626	0.0324
	$\mathrm{C}\underline{H}_3$, out of CCO plane	0.0217	0.0219	0.0002
	$\mathrm{C}\underline{H}_3$, out of CCO plane	0.0217	0.0219	0.0002
	$\underline{C}\mathrm{H}_3$	2.4229	2.4315	0.0086
	$\mathrm{C}\underline{H}_3$, in CCO plane	0.2397	0.2399	0.0002
Chloroform (CH_3Cl)				
	C	2.9458	2.9462	0.0003
	Cl	-21.6412	-21.6328	0.0084
	H	0.1091	0.1091	0.0000
	H	0.1091	0.1091	0.0000
	H	0.1091	0.1091	0.0000
Acetonitrile (CH_3CN)				
	N	42.4969	42.5614	0.0645
	$\underline{C}\mathrm{N}$	14.4076	14.4328	0.0252
	H	0.0640	0.0641	0.0001
	H	0.0655	0.0655	0.0001
	$\underline{C}\mathrm{H}_3$	0.9050	0.9119	0.0069
	H	0.0653	0.0654	0.0001
Acetone (CH_3COCH_3)				
	H, in CCC plane	0.2100	0.2101	0.0002
	H, out of CCC plane	-0.0359	-0.0357	0.0002
	H, out of CCC plane	-0.0359	-0.0354	0.0005
	$\underline{C}\mathrm{H}_3$	2.2390	2.2466	0.0075
	O	59.2885	59.4418	0.1533

	$\underline{C}$O	21.0772	21.1097	0.0325
	H, out of CCC plane	-0.0359	0.2102	0.2461
	H, out of CCC plane	-0.0359	-0.0357	0.0002
	$\underline{C}H_3$	2.2390	2.2468	0.0078
	H, in CCC plane	0.2100	-0.0360	0.2460
Fluoromethane (CH_3F)				
	F	-9.8763	-9.8764	0.0001
	H	-0.0009	-0.0009	0.0001
	H	-0.0009	-0.0009	0.0001
	C	1.0363	1.0428	0.0065
	H	-0.0009	-0.0008	0.0001
Methylamine (CH_3NH_2)				
	N$\underline{H}_2$	0.0521	0.0521	0.0001
	N$\underline{H}_2$	0.0521	0.0521	0.0001
	N	2.1892	2.2004	0.0112
	C$\underline{H}_3$, antiperiplanar to lone pair	-0.1745	-0.0625	0.1120
	C$\underline{H}_3$, gauche to lone pair	-0.0626	-0.0625	0.0001
	C	0.7933	0.8019	0.0086
	C$\underline{H}_3$, gauche to lone pair	-0.0626	-0.1744	0.1118
Dimethyl ether (CH_3OCH_3)				
	H, in COC plane	-0.0900	-0.0898	0.0001
	H, out of COC plane	-0.1058	-0.1057	0.0001
	H, out of COC plane	-0.1058	-0.1057	0.0001
	C	0.2035	0.2118	0.0083
	O	-6.7843	-6.7804	0.0039
	H, out of COC plane	-0.1058	-0.1057	0.0001
	H, out of COC plane	-0.1058	-0.1057	0.0001
	C	0.2035	0.2118	0.0082
	H, in COC plane	-0.0900	-0.0898	0.0001
Methanol (CH_3OH)				
	O$\underline{H}$	0.3536	0.3535	0.0001
	O	-0.8619	-0.8536	0.0082
	C$\underline{H}_3$, gauche to OH	-0.1264	-0.0263	0.1001
	C$\underline{H}_3$, gauche to OH	-0.1264	-0.1263	0.0001
	C	0.4881	0.4958	0.0077
	C$\underline{H}_3$, antiperiplanar to OH	-0.0264	-0.1263	0.0999
Methylphosphine (CH_3PH_2)				
	C	1.6790	1.6800	0.0011
	P	6.7592	6.7706	0.0114
	P$\underline{H}_2$	0.1609	0.1609	0.0001
	P$\underline{H}_2$	0.1609	0.1609	0.0001
	C$\underline{H}_3$, gauche to lone pair	-0.0006	-0.0006	0.0000
	C$\underline{H}_3$, gauche to lone pair	-0.0006	-0.0006	0.0000
	C$\underline{H}_3$, antiperiplanar to lone pair	-0.0018	-0.0017	0.0000

Methanethiol (CH_3SH)				
	C	1.3876	1.3884	0.0008
	S	4.3638	4.3698	0.0060
	S$\underline{H}$	0.3022	0.3022	0.0000
	C$\underline{H}_3$, antiperiplanar to SH	0.0278	0.0278	0.0000
	C$\underline{H}_3$, gauche to SH	0.0002	0.0003	0.0000
	C$\underline{H}_3$, gauche to SH	0.0002	0.0003	0.0000
Methane (CH_4)				
	H	0.0182	0.0184	0.0002
	H	0.0182	0.0184	0.0002
	H	0.0182	0.0184	0.0002
	C	1.9054	1.9133	0.0079
	H	0.0182	0.0184	0.0002
Carbon dioxide (CO_2)				
	O	19.3097	19.3454	0.0357
	C	13.4738	13.4891	0.0152
	O	19.3097	19.3453	0.0356
Carbon monoxide (CO)				
	O	47.7924	47.8807	0.0883
	C	35.0061	35.0445	0.0384
Furan (C_4H_4O)				
	3-H	0.2051	0.2057	0.0005
	2-H	0.2082	0.2087	0.0005
	3C	9.5302	9.5488	0.0185
	4-H	0.2051	0.2057	0.0005
	2C	12.4641	12.4850	0.0209
	4C	9.5302	9.5488	0.0186
	1O	10.3533	10.4096	0.0562
	5C	12.4642	12.4851	0.0209
	5-H	0.2082	0.2087	0.0005
Glycine (NH_2CH_2COOH)				
	N$\underline{H}_2$	0.0221	0.0222	0.0001
	N$\underline{H}_2$	0.0592	0.0593	0.0001
	N	1.5762	1.5853	0.0091
	C$\underline{H}_2$	0.0746	0.0747	0.0001
	C$\underline{H}_2$	0.0224	0.0224	0.0000
	$\underline{C}$H$_2$	1.2177	1.2256	0.0079
	C=$\underline{O}$	37.2847	37.3778	0.0931
	$\underline{C}$OOH	14.9177	14.9401	0.0224
	$\underline{O}$H	9.7918	9.8330	0.0412
	O$\underline{H}$	0.3915	0.3921	0.0006
Formaldehyde (H_2CO)				
	O	111.0888	111.1752	0.0864
	H	0.2826	0.2836	0.0009

	C	21.1961	21.2295	0.0333
	H	0.2826	0.2836	0.0010
Hydrogen cyanide (HCN)				
	H	0.0601	0.0598	0.0003
	C	16.3948	16.4221	0.0273
	N	42.1806	42.2535	0.0729
Formamide ($HCONH_2$)				
	$\mathrm{N}\underline{H}_2$	0.3538	0.3543	0.0005
	$\mathrm{N}\underline{H}_2$	0.3662	0.3667	0.0005
	N	7.2581	7.2796	0.0215
	$\mathrm{C}\underline{H}\mathrm{O}$	0.0740	0.0743	0.0003
	C	16.7315	16.7528	0.0213
	O	34.4261	34.5238	0.0976
Formic acid (HCOOH)				
	$\mathrm{O}\underline{H}$	0.5611	0.5616	0.0005
	$\underline{O}\mathrm{H}$	9.1381	9.1754	0.0373
	$\mathrm{C}\underline{H}$	0.1191	0.1194	0.0003
	C	14.8579	14.8790	0.0211
	$\mathrm{C}{=}\underline{O}$	41.7052	41.7970	0.0918
Imidazole ($C_3H_4N_2$)				
	3-H	0.1194	0.1202	0.0008
	2-H	0.4273	0.4280	0.0007
	3N	10.7744	10.8151	0.0406
	4-H	0.3158	0.3165	0.0007
	2C	17.1388	17.1675	0.0287
	4C	10.9611	10.9867	0.0256
	1N	35.5496	35.6308	0.0813
	5C	12.2712	12.2994	0.0282
	5-H	0.3522	0.3530	0.0008
Pyridine (C_5H_5N)				
	2-H	0.3683	0.3695	0.0012
	1N	42.2988	42.4102	0.1114
	6-H	0.3683	0.3695	0.0012
	2C	15.5825	15.6170	0.0345
	3-H	0.1291	0.1297	0.0006
	6C	15.5825	15.6170	0.0345
	5-H	0.1291	0.1297	0.0006
	3C	7.3790	7.4037	0.0248
	5C	7.3790	7.4037	0.0248
	4C	15.7400	15.7658	0.0259
	4-H	0.3905	0.3912	0.0007
Pyrimidine ($C_4H_4N_2$)				
	6-H	0.3878	0.3888	0.0010
	1N	24.1426	24.2371	0.0944

	2-H	0.2580	0.2592	0.0012
	6C	18.0969	18.1322	0.0353
	5-H	0.0596	0.0604	0.0008
	1C	16.0559	16.0916	0.0357
	5C	4.4116	4.4397	0.0281
	3N	24.1424	24.2367	0.0943
	4C	18.0960	18.1311	0.0351
	4-H	0.3875	0.3885	0.0010
Tetramethylsilane (Si(CH_3)$_4$)				
	H	-0.0658	-0.0658	0.0000
	H	-0.0658	-0.0658	0.0000
	H	-0.0658	-0.0658	0.0000
	H	-0.0658	-0.0658	0.0000
	H	-0.0658	-0.0658	0.0000
	H	-0.0658	-0.0658	0.0000
	H	-0.0658	-0.0658	0.0000
	H	-0.0658	-0.0658	0.0000
	H	-0.0658	-0.0658	0.0000
	C	2.0029	2.0043	0.0014
	C	2.0029	2.0043	0.0014
	C	2.0029	2.0043	0.0014
	Si	-11.3421	-11.3278	0.0144
	H	-0.0658	-0.0658	0.0000
	H	-0.0658	-0.0658	0.0000
	C	2.0029	2.0043	0.0014
	H	-0.0658	-0.0658	0.0000

Table S5: Detailed results of the RPA NMR shifts for all molecules in the Flaig benchmark set[S4] at the RPA@PBE/cc-pwCVDZ level of theory for the numerical reference implementation (reference) as well as the analytical implementation (result). All shifts and the resulting deviations are given in ppm.

molecule	element	result	reference	abs. err.
Acetylene (C_2H_2)				
	H	0.0787	0.0784	0.0003
	C	19.1544	19.1837	0.0292
	C	19.1544	19.1837	0.0292
	H	0.0787	0.0784	0.0003
Ethylene (C_2H_4)				
	H	0.5381	0.5391	0.0010
	H	0.5381	0.5391	0.0010
	C	27.1906	27.2432	0.0526
	H	0.5451	0.5461	0.0010
	C	27.2817	27.3347	0.0530
	H	0.5451	0.5461	0.0010
Ethane (C_2H_6)				
	H	-0.1615	-0.1614	0.0001
	H	-0.1615	-0.1614	0.0001
	H	-0.1615	-0.1614	0.0001
	C	1.6414	1.6559	0.0145
	H	-0.1618	-0.1616	0.0001
	H	-0.1618	-0.1616	0.0001
	C	1.6159	1.6304	0.0146
	H	-0.1618	-0.1616	0.0001
Benzene (C_6H_6)				
	H	0.4910	0.4922	0.0012
	H	0.4910	0.4922	0.0013
	C	24.1266	24.1809	0.0542
	H	0.4910	0.4922	0.0013
	C	24.1267	24.1809	0.0543
	H	0.4910	0.4922	0.0013
	C	24.1267	24.1809	0.0543
	H	0.4910	0.4922	0.0013
	C	24.1267	24.1809	0.0543
	C	24.1267	24.1809	0.0543
	C	24.1266	24.1809	0.0542
	H	0.4910	0.4922	0.0013
Tetrachloromethane (CCl_4)				
	C	7.7902	7.7945	0.0043
	Cl	-36.5447	-36.5615	0.0168
	Cl	-36.5447	-36.5615	0.0168
	Cl	-36.5447	-36.5615	0.0168

	Cl	-36.5447	-36.5615	0.0168
Tetrafluoromethane (CF_4)				
	F	-6.0114	-5.9824	0.0290
	F	-6.0116	-5.9817	0.0299
	F	-6.0116	-5.9817	0.0299
	C	-4.0609	-4.0475	0.0134
	F	-6.0117	-5.9821	0.0296
Propadiene (CH_2CCH_2)				
	H	0.2550	0.2557	0.0007
	H	0.2765	0.2772	0.0007
	$\underline{C}\mathrm{H}_2$	14.4060	14.4407	0.0347
	$\mathrm{C}{=}\underline{C}{=}\mathrm{C}$	41.5436	41.6158	0.0722
	H	0.2658	0.2664	0.0007
	$\underline{C}\mathrm{H}_2$	14.4060	14.4399	0.0339
	H	0.2658	0.2664	0.0007
Acetaldehyde (CH_3CHO)				
	O	205.4081	205.4133	0.0052
	$\mathrm{C}\underline{H}\mathrm{O}$	0.0321	0.0334	0.0013
	$\underline{C}\mathrm{HO}$	41.5548	41.6041	0.0494
	$\mathrm{C}\underline{H}_3$, out of CCO plane	-0.0362	-0.0359	0.0003
	$\mathrm{C}\underline{H}_3$, out of CCO plane	-0.0362	-0.0359	0.0003
	$\underline{C}\mathrm{H}_3$	4.5204	4.5366	0.0162
	$\mathrm{C}\underline{H}_3$, in CCO plane	0.4048	0.4052	0.0003
Chloroform (CH_3Cl)				
	C	4.2965	4.2981	0.0016
	Cl	-41.3884	-41.3727	0.0157
	H	-0.0046	-0.0045	0.0000
	H	-0.0046	-0.0045	0.0000
	H	-0.0046	-0.0045	0.0000
Acetonitrile (CH_3CN)				
	N	71.8026	71.8871	0.0845
	$\underline{C}\mathrm{N}$	30.2404	30.2746	0.0342
	H	-0.0142	-0.0141	0.0001
	H	-0.0118	-0.0117	0.0001
	$\underline{C}\mathrm{H}_3$	0.5402	0.5514	0.0112
	H	-0.0120	-0.0119	0.0001
Acetone (CH_3COCH_3)				
	H, in CCC plane	0.3530	0.3532	0.0002
	H, out of CCC plane	-0.2379	-0.2377	0.0003
	H, out of CCC plane	-0.2379	-0.2377	0.0003
	$\underline{C}\mathrm{H}_3$	4.5256	4.5392	0.0136
	O	174.4594	174.5093	0.0499
	$\underline{C}\mathrm{O}$	41.1737	41.2223	0.0486
	H, out of CCC plane	-0.2479	-0.2476	0.0004

	H, out of CCC plane	-0.2479	-0.2476	0.0004
	$\underline{C}H_3$	4.4580	4.4728	0.0148
	H, in CCC plane	0.3383	0.3386	0.0003
Fluoromethane (CH_3F)				
	F	-26.8766	-26.8692	0.0074
	H	-0.3595	-0.3594	0.0001
	H	-0.3595	-0.3594	0.0001
	C	0.9788	0.9902	0.0114
	H	-0.3595	-0.3594	0.0001
Methylamine (CH_3NH_2)				
	$N\underline{H}_2$	-0.0521	-0.0521	0.0000
	$N\underline{H}_2$	-0.0521	-0.0521	0.0000
	N	0.4456	0.4641	0.0186
	$C\underline{H}_3$, antiperiplanar to lone pair	-0.7037	-0.7036	0.0001
	$C\underline{H}_3$, gauche to lone pair	-0.2410	-0.2408	0.0001
	C	0.6955	0.7109	0.0154
	$C\underline{H}_3$, gauche to lone pair	-0.2410	-0.2408	0.0001
Dimethyl ether (CH_3OCH_3)				
	H, in COC plane	-0.3361	-0.3360	0.0002
	H, out of COC plane	-0.4440	-0.4439	0.0001
	H, out of COC plane	-0.4440	-0.4439	0.0001
	C	0.6376	0.6523	0.0147
	O	-14.9422	-14.9251	0.0171
	H, out of COC plane	-0.4440	-0.4439	0.0001
	H, out of COC plane	-0.4440	-0.4439	0.0001
	C	0.6373	0.6523	0.0149
	H, in COC plane	-0.3361	-0.3360	0.0002
Methanol (CH_3OH)				
	$O\underline{H}$	0.3781	0.3777	0.0003
	O	-7.8372	-7.8206	0.0165
	$C\underline{H}_3$, gauche to OH	-0.6123	-0.6121	0.0001
	$C\underline{H}_3$, gauche to OH	-0.6123	-0.6121	0.0001
	C	0.1934	0.2073	0.0139
	$C\underline{H}_3$, antiperiplanar to OH	-0.2089	-0.2088	0.0001
Methylphosphine (CH_3PH_2)				
	C	1.0495	1.0519	0.0024
	P	14.2332	14.2472	0.0140
	$P\underline{H}_2$	0.0468	0.0468	0.0001
	$P\underline{H}_2$	0.0468	0.0468	0.0001
	$C\underline{H}_3$, gauche to lone pair	-0.1364	-0.1363	0.0000
	$C\underline{H}_3$, gauche to lone pair	-0.1364	-0.1363	0.0000
	$C\underline{H}_3$, antiperiplanar to lone pair	-0.1528	-0.1528	0.0001
Methanethiol (CH_3SH)				
	C	0.9706	0.9728	0.0022

	S	4.3320	4.3284	0.0036
	S$\underline{H}$	0.3438	0.3439	0.0001
	C$\underline{H}_3$, antiperiplanar to SH	-0.0761	-0.0761	0.0000
	C$\underline{H}_3$, gauche to SH	-0.1995	-0.1995	0.0000
	C$\underline{H}_3$, gauche to SH	-0.1995	-0.1995	0.0000
Methane (CH_4)				
	H	0.0014	0.0016	0.0002
	H	0.0014	0.0016	0.0002
	H	0.0014	0.0016	0.0002
	C	2.2800	2.2920	0.0120
	H	0.0014	0.0016	0.0002
Carbon dioxide (CO_2)				
	O	29.8121	29.8546	0.0425
	C	27.1710	27.1911	0.0201
	O	29.8121	29.8546	0.0425
Carbon monoxide (CO)				
	O	87.4544	87.5640	0.1096
	C	63.0853	63.1363	0.0509
Furan (C_4H_4O)				
	3-H	0.4369	0.4375	0.0006
	2-H	0.4133	0.4139	0.0006
	3C	20.4635	20.4898	0.0263
	4-H	0.4369	0.4375	0.0006
	2C	25.2926	25.3221	0.0296
	4C	20.4633	20.4898	0.0265
	1O	41.2453	41.3227	0.0774
	5C	25.2923	25.3221	0.0299
	5-H	0.4133	0.4139	0.0006
Glycine (NH_2CH_2COOH)				
	N$\underline{H}_2$	-0.3357	-0.3356	0.0001
	N$\underline{H}_2$	-0.1692	-0.1691	0.0001
	N	-2.9521	-2.9364	0.0158
	C$\underline{H}_2$	-0.1440	-0.1439	0.0001
	C$\underline{H}_2$	-0.1341	-0.1341	0.0000
	$\underline{C}$H$_2$	3.1432	3.1575	0.0143
	C=$\underline{O}$	107.4834	107.5693	0.0859
	$\underline{C}$OOH	32.4836	32.5163	0.0328
	$\underline{O}$H	13.1910	13.2577	0.0666
	O$\underline{H}$	0.3283	0.3291	0.0008
Formaldehyde (H_2CO)				
	O	270.1876	269.8305	0.3571
	H	0.4016	0.4033	0.0017
	C	43.2373	43.2921	0.0548
	H	0.4018	0.4035	0.0017

Hydrogen cyanide (HCN)				
	H	-0.1398	-0.1402	0.0004
	C	32.4556	32.4908	0.0352
	N	77.7749	77.8627	0.0878
Formamide ($HCONH_2$)				
	$\mathrm{N}\underline{H}_2$	0.5833	0.5839	0.0006
	$\mathrm{N}\underline{H}_2$	0.4932	0.4939	0.0006
	N	13.5060	13.5393	0.0334
	$\mathrm{C}\underline{H}\mathrm{O}$	0.0313	0.0317	0.0005
	C	37.0433	37.0737	0.0304
	O	106.7358	106.8051	0.0692
Formic acid (HCOOH)				
	$\mathrm{O}\underline{H}$	0.7453	0.7460	0.0007
	$\underline{O}\mathrm{H}$	8.1066	8.1726	0.0660
	$\mathrm{C}\underline{H}$	0.1891	0.1895	0.0004
	C	34.6067	34.6384	0.0317
	$\mathrm{C}{=}\underline{O}$	112.0754	112.1526	0.0772
Imidazole ($C_3H_4N_2$)				
	3-H	0.4304	0.4314	0.0010
	2-H	0.6165	0.6173	0.0008
	3N	29.9086	29.9642	0.0556
	4-H	0.4904	0.4912	0.0008
	2C	28.2279	28.2661	0.0382
	4C	23.6096	23.6444	0.0349
	1N	73.2228	73.3188	0.0960
	5C	24.7178	24.7582	0.0404
	5-H	0.6076	0.6085	0.0010
Pyridine (C_5H_5N)				
	2-H	0.4742	0.4757	0.0015
	1N	85.5818	85.7092	0.1273
	6-H	0.4742	0.4757	0.0015
	2C	27.1182	27.1686	0.0504
	3-H	0.4988	0.4998	0.0010
	6C	27.1182	27.1687	0.0505
	5-H	0.4988	0.4998	0.0010
	3C	20.3647	20.4059	0.0412
	5C	20.3647	20.4059	0.0412
	4C	26.3408	26.3839	0.0431
	4-H	0.5778	0.5787	0.0010
Pyrimidine ($C_4H_4N_2$)				
	6-H	0.5046	0.5060	0.0014
	1N	70.4828	70.6091	0.1263
	2-H	0.2864	0.2881	0.0017
	6C	29.3256	29.3789	0.0533
	5-H	0.5507	0.5516	0.0009

	1C	27.3475	27.4033	0.0558
	5C	17.7443	17.7867	0.0424
	3N	70.4820	70.6095	0.1275
	4C	29.3232	29.3762	0.0530
	4-H	0.5041	0.5055	0.0013
Tetramethylsilane ($Si(CH_3)_4$)				
	H	-0.2583	-0.2582	0.0001
	H	-0.2583	-0.2582	0.0000
	H	-0.2583	-0.2582	0.0000
	H	-0.2583	-0.2582	0.0000
	H	-0.2583	-0.2582	0.0001
	H	-0.2583	-0.2582	0.0000
	H	-0.2582	-0.2582	0.0000
	H	-0.2582	-0.2582	0.0000
	H	-0.2582	-0.2582	0.0000
	C	1.6427	1.6451	0.0024
	C	1.6426	1.6452	0.0026
	C	1.6420	1.6452	0.0032
	Si	-13.0176	-12.9900	0.0275
	H	-0.2583	-0.2582	0.0000
	H	-0.2583	-0.2582	0.0001
	C	1.6426	1.6452	0.0026
	H	-0.2583	-0.2582	0.0001

3.3 Detailed Validation Results: Summary For All Nuclei

Table S6: Comparison of MADs in ppm of the analytical to the numerical isotropic NMR shifts for all nuclei in the Gauss benchmark set[S3] at the RPA@HF/cc-pwCVTZ and RPA@PBE/cc-pwCVTZ level of theory. Additionally, the number of occurrences $N_{\text{nuc}}^{\text{test}}$ of a given element within the benchmark set is given.

reference	^{1}H	^{7}Li	^{13}C	^{15}N	^{17}O	^{19}F	^{27}Al	^{31}P	^{33}S
$N_{\text{nuc}}^{\text{test}}$	37	2	20	8	15	10	1	2	3
HF	0.0005	0.0009	0.0041	0.0053	0.0591	0.0497	0.0015	0.0385	0.0329
PBE	0.0001	0.0009	0.0032	0.0031	0.2119	0.0644	0.0012	0.0372	0.0230

Table S7: Comparison of MADs in ppm of the analytical to the numerical isotropic NMR shifts for all nuclei in the Flaig benchmark set[S4] at the RPA@HF/cc-pwCVDZ and RPA@PBE/cc-pwCVDZ level of theory. Additionally, the number of occurrences $N_{\text{nuc}}^{\text{test}}$ of a given element within the benchmark set is given.

reference	^{1}H	^{13}C	^{15}N	^{17}O	^{19}F	^{29}Si	^{31}P	^{33}S	^{35}Cl
$N_{\text{nuc}}^{\text{test}}$	111	61	10	14	5	1	1	1	5
HF	0.0084	0.0208	0.0601	0.0694	0.0152	0.0144	0.0114	0.0060	0.0183
PBE	0.0004	0.0305	0.0773	0.0773	0.0252	0.0275	0.0140	0.0036	0.0166

4 Detailed Results for the Convergence of the Minimax Grid

Table S8: Detailed results of the RPA NMR shift convergence for all nuclei in the Gauss benchmark set[S3] with the number of minimax integration points N_g. All values are given as MADs in ppm in comparison to the results obtained with $N_g = 20$ at the RPA@HF level of theory using the cc-pwCVTZ/cc-pwCVTZ-RI basis sets.

N_g	^{1}H	^{7}Li	^{13}C	^{15}N	^{17}O	^{19}F	^{27}Al	^{31}P	^{33}S
10	0.0001	0.0003	0.0062	0.0175	0.0320	0.0097	0.0108	0.0366	0.0166
11	0.0001	0.0002	0.0050	0.0140	0.0257	0.0077	0.0075	0.0297	0.0130
12	0.0001	0.0002	0.0041	0.0114	0.0207	0.0061	0.0059	0.0244	0.0103
13	0.0001	0.0001	0.0036	0.0091	0.0173	0.0049	0.0049	0.0190	0.0084
14	0.0000	0.0001	0.0026	0.0070	0.0131	0.0042	0.0040	0.0156	0.0066
15	0.0000	0.0000	0.0024	0.0054	0.0107	0.0031	0.0029	0.0114	0.0053
16	0.0000	0.0000	0.0015	0.0039	0.0075	0.0023	0.0021	0.0088	0.0039
17	0.0000	0.0000	0.0013	0.0026	0.0053	0.0039	0.0015	0.0058	0.0027
18	0.0000	0.0000	0.0009	0.0014	0.0032	0.0034	0.0010	0.0039	0.0015
19	0.0000	0.0000	0.0004	0.0007	0.0015	0.0008	0.0005	0.0022	0.0006
20	–	–	–	–	–	–	–	–	–

References

(S1) Graf, D.; Beuerle, M.; Schurkus, H. F.; Luenser, A.; Savasci, G.; Ochsenfeld, C. Accurate and Efficient Parallel Implementation of an Effective Linear-Scaling Direct Random Phase Approximation Method. *J. Chem. Theory Comput.* **2018**, *14*, 2505–2515.

(S2) Beuerle, M.; Ochsenfeld, C. Low-scaling analytical gradients for the direct random phase approximation using an atomic orbital formalism. *J. Chem. Phys.* **2018**, *149*, 244111.

(S3) Teale, A. M.; Lutnæs, O. B.; Helgaker, T.; Tozer, D. J.; Gauss, J. Benchmarking density-functional theory calculations of NMR shielding constants and spin–rotation constants using accurate coupled-cluster calculations. *J. Chem. Phys.* **2013**, *138*, 024111.

(S4) Flaig, D.; Maurer, M.; Hanni, M.; Braunger, K.; Kick, L.; Thubauville, M.; Ochsenfeld, C. Benchmarking hydrogen and carbon NMR chemical shifts at HF, DFT, and MP2 levels. *J. Chem. Theory Comp.* **2014**, *10*, 572–578.

(S5) `https://www.cup.uni-muenchen.de/pc/ochsenfeld/download/`.

3.4. Publication IV: Efficient Low-scaling Calculation of THC-SOS-LR-CC2 and THC-SOS-ADC(2) Excitation Energies Through Density-based Integral-direct Tensor Hypercontraction

F. Sacchetta, F. H. Bangerter, H. Laqua, C. Ochsenfeld

J. Chem. Theory Comput., *in preparation*

Abstract

In recent years, rapid improvements in computer hardware, as well as theoretical and algorithmic advances have enabled the calculation of ever larger systems in computational chemistry. In this avenue, we present efficient implementations of the scaled opposite-spin (SOS) second-order approximate coupled cluster (CC2) method and the closely related second-order algebraic diagrammatic construction (ADC(2)) method. The implementations leverage the least-squares tensor hypercontraction (THC) approximation, for which a new density-based integral-direct reformulation of the grid-projection of the electron integral tensor is presented. Together with screening based on local Cholesky orbitals stemming from the decomposition of the one-particle densities (CDD) in the Laplace integration and optimized block-sparse linear algebra, effectively $\mathcal{O}(N^2)$ scaling variants of linear-response (LR) SOS-CC2 and SOS-ADC(2) are obtained. The derived CDD-THC-SOS-LR-CC2/ADC(2) methods are shown to be capable of targeting excitation energies of systems up to ∼1000 atoms and ∼10000 basis functions on a single compute node.

Efficient Low-scaling Calculation of THC-SOS-LR-CC2 and THC-SOS-ADC(2) Excitation Energies Through Density-based Integral-direct Tensor Hypercontraction

Filippo Sacchetta,[†,¶] Felix H. Bangerter,[†,¶] Henryk Laqua,[†] and Christian Ochsenfeld[*,†,‡]

[†] *Chair of Theoretical Chemistry, Department of Chemistry, University of Munich (LMU), D-81377 Munich, Germany*

[‡] *Max Planck Institute for Solid State Research, D-70569 Stuttgart, Germany*

[¶] *These authors contributed equally to this work.*

E-mail: christian.ochsenfeld@cup.uni-muenchen.de

Abstract

In recent years, rapid improvements in computer hardware, as well as theoretical and algorithmic advances have enabled the calculation of ever larger systems in computational chemistry. In this avenue, we present efficient implementations of the scaled opposite-spin (SOS) second-order approximate coupled cluster (CC2) method and the closely related second-order algebraic diagrammatic construction (ADC(2)) method. The implementations leverage the least-squares tensor hypercontraction (THC) approximation, for which a new density-based integral-direct reformulation of the grid-projection of the electron integral tensor is presented. Together with screening based on local Cholesky orbitals stemming from the decomposition of the one-particle densities (CDD) in the Laplace integration and optimized block-sparse linear algebra, effectively $\mathcal{O}(N^2)$ scaling variants of linear-response (LR) SOS-CC2 and SOS-ADC(2) are obtained. The derived CDD-THC-SOS-LR-CC2/ADC(2) methods are shown to be capable of targeting excitation energies of systems up to ∼1000 atoms and ∼10000 basis functions on a single compute node.

1 Introduction

An accurate description of electronic excited states of chemical systems is crucial for the useful interplay of theory and experiment,[1] where spectroscopy measures transitions between different quantum states, covering electronic, vibrational, or rotational excitations. Amongst the spectroscopic methods probing transitions between the ground and electronically excited states, UV-vis spectroscopy, which involves the absorption and emission of photons in the ultraviolet (UV) and visible (vis) regions, and X-ray absorption spectroscopy (XAS), which involves the excitation of core electrons, are two of the most widely used methods.[2–4] Thus, in order to relate the experimentally observed absorption/emission bands to electronic transitions, accurate methods to compute vertical excitation energies are required.

While exact excitation energies can – in the limit of the Born–Oppenheimer approximation and a finite basis set – be obtained through the full configuration interaction (FCI) method,[5,6] its exponentially scaling cost renders it inapplicable for all but the smallest systems. Therefore, considerable effort has been put into the formulation of approximate methods, also in combination with reduced scaling techniques to reach ever larger system sizes, preferably without sacrificing accuracy. Here, considerable theoretical as well as algorithmic advances have been made in the past decades.[6–8] The former include reformulations of many of the commonly encountered methods in quantum chemistry under the paradigm of response theory, i.e., the quasidegenerate second-order perturbation corrected configuration interaction singles (CIS(D_∞)),[9] time-dependent density functional theory (TDDFT),[10–12] the family of complete active space self-consistent field (CASSCF)[13–15] methods, algebraic diagrammatic construction (ADC)[7,16–19] methods, as well as linear-response coupled cluster (LR-CC)[20–24] theory. Here also approximate CC models were introduced, such as the commonly used approximate CC singles and doubles (CC2).[25] Without further approximations, CC2 and the closely related second-order ADC (ADC(2)) method exhibit quintic scaling, which necessitates additional algorithmic improvements in order for the methods to be applicable to larger systems. While conceptually simple, the scaled opposite-spin (SOS)[26–28] approximation by Jung *et al.* achieves a significant reduction of the scaling prefactor by complete neglect of the expensive same-spin terms, while at the same time largely retaining the accuracy.[29,30] Due to the required transformation of the electron repulsion integral (ERI) tensor into the molecular orbital (MO) basis, the scaling remains as $\mathcal{O}(N^5)$. However, a reduction of the scaling exponent can be achieved by using a factorized form of the ERI tensor, such as the resolution-of-the-identity (RI)[29,31–34] approximation or the Cholesky decomposition[35] in conjunction with the Laplace transformation[29,36,37] to obtain a separable form of the orbital energy denominator. Recently, Ochsenfeld, Dreuw, and coworkers[38,39] put forth atomic orbital (AO) based formulations of SOS-CC2 and SOS-ADC(2), which achieve sub-quadratic to linear scaling through a combination of the RI approximation with an attenuated Coulomb metric (ω-RI)[40] and Cholesky decomposed densities (CDD).[40–42,42–45] To achieve even further reduction of both the memory requirements and the number of required floating point operations (FLOP), tensor hypercontraction (THC) by Martínez and coworkers[46–49] can be applied, which entirely circumvents the necessity to store and contract third- (or higher-) order tensors. THC variants of CC methods have previously been reported for CC2,[50] CCSD,[51–53] and CCSD(T)[54] ground state energies as well as for excitation energies based on equation-of-motion (EOM) CC2.[55]

In this work, we propose a density-matrix-based and integral-direct approach for obtaining the THC-factorized ERI tensor, which adds only a small overhead when applied to an electron correlation method. In this regard, SOS-LR-CC2 and SOS-ADC(2) are ideal methods for the application of THC, since they 1) require the AO-ERI tensor to be repeatedly transformed into different MO subspaces, which can efficiently be done by matrix-matrix multiplications, and 2) only include opposite-spin (OS) contributions, for which THC allows to reformulate the expressions to only use matrix linear algebra without the occurrence of any tensors higher than second order. By combining THC with local Cholesky pseudo-MOs from the CDD approach in the Laplace integration and block-sparse linear algebra, effectively $\mathcal{O}(N^2)$ scaling formulations of SOS-LR-CC2 and SOS-ADC(2) are obtained. The proposed excited state methods are benchmarked using a set of medium- to large-size systems to assess the scaling of the error with respect to the system size. The accuracy of the ground state energies is analyzed by considering an additional set previously used by DiStasio *et al.*[56] for relative energies. Finally, the efficiency of the proposed methods is demonstrated for nucleic acid double helices up to ∼1000 atoms and ∼12000 basis functions, which reveals overall $\mathcal{O}(N^2)$ scaling.

2 Theory

2.1 Notation

Throughout this work, we employ the following notation:

- $\mu, \nu, \lambda, \sigma$: atomic orbital indices belonging to the AO basis $\{\chi_\mu\}$ of size N_{bf}.
- $\alpha, \beta, \gamma, \delta$: auxiliary function basis indices belonging to the density fitting basis $\{\chi_\alpha\}$ of size N_{aux} (usually $N_{\text{aux}} \approx 3 \cdot N_{\text{bf}}$).
- P, Q, R, S: auxiliary function basis indices belonging to the THC basis; in LS-THC these are equivalent to grid points belonging to the LS-THC grid of size N_{grid} (usually $N_{\text{grid}} \approx 3 \cdot N_{\text{aux}}$).
- i, j, k: occupied molecular orbital indices belonging to the MO basis $\{\phi_i\}$ of size N_{occ}.

- a, b, c: virtual molecular orbital indices belonging to the MO basis $\{\phi_a\}$ of size N_{virt} ($N_{\text{virt}} \gg N_{\text{occ}}$).
- $\underline{i}, \underline{k}, \underline{j}$: occupied local Cholesky orbitals basis $\{\phi_{\underline{i}}\}$ of size N_{occ}; obtained via pivoted Cholesky decomposition of the occupied one-electron density.
- p, q, r, s: general orbital indices.
- τ: root of the Laplace quadrature with N_τ integration points (usually $5 \leq N_\tau \leq 10$ is sufficiently accurate).

2.2 Integral-direct Tensor Hypercontraction

2.2.1 Basics of Tensor Hypercontraction

In its most general form, tensor hypercontraction (THC) is a low-dimensional representation of a multi-dimensional tensor, which – in the context of quantum mechanics – represents the interactions between particles in a system. For a two-body potential $\hat{V} = 1/r_{12}$, said representation of the electron-electron interactions in a real one-particle basis is the integral tensor, the elements of which are given by

$$(pq|rs) = \iint d\mathbf{r}_1 d\mathbf{r}_2 \, \varphi_p(\mathbf{r}_1)\varphi_q(\mathbf{r}_1)\frac{1}{r_{12}}\varphi_r(\mathbf{r}_2)\varphi_s(\mathbf{r}_2) \tag{1}$$

However, in practical quantum chemistry calculations, the manipulation and storage of such a high-dimensional tensor quickly becomes computationally intractable as the system or the basis set size grows. To alleviate this issue, THC provides the means to formally compress the fourth-order integral tensor into five second-order tensors as

$$(pq|rs) = \sum_{PQ} X_p^P X_q^P Z^{PQ} X_r^Q X_s^Q \tag{2}$$

The factorization is exact if the number of THC auxiliary functions is at least $N_{\text{bf}}(N_{\text{bf}}+1)/2$,[57] but only reduces computational demands and storage requirements if it is significantly smaller. If sufficient accuracy is reached with significantly less than N_{bf}^2 THC auxiliary functions, the THC factorization enables efficient storage and manipulation of the ERI tensor, making complex calculations feasible for larger systems.

In the least-squares variant of THC (LS-THC),[47] the THC auxiliary indices are taken to be grid points of a molecular grid similar to the ones commonly used in density function theory. For LS-THC the time-determining step of factorizing the ERI tensor into the THC format is the quintic scaling grid-projection of the ERI tensor, which in the AO basis is given by

$$E^{PQ} = \sum_{\mu\nu\lambda\sigma} X_\mu^P X_\nu^P (\mu\nu|\lambda\sigma) X_\lambda^Q X_\sigma^Q \tag{3}$$

where the so-called collocation matrices $\mathbf{X}$ are simply the AO basis functions χ_μ evaluated at the THC grid nodes scaled by the node's weight w_P, given as

$$X_\mu^P = \sqrt[4]{w_P}\,\chi_\mu(\mathbf{r}_P) \tag{4}$$

In the general MO formulation, the above equation becomes

$$E^{PQ} = \sum_{pqrs} X_p^P X_q^P (pq|rs) X_r^Q X_s^Q \tag{5}$$

which requires a transformation of the AO ERI tensor into the MO basis. From $\mathbf{E}$, the final

Z tensor in eq. 2 is obtained as

$$Z^{PQ} = \sum_{P'Q'} [\mathbf{S}^{-1}]^{PP'} E^{P'Q'} [\mathbf{S}^{-1}]^{QQ'} \tag{6}$$

where $\mathbf{S}^{-1}$ is the inverse of the THC grid metric, i.e., the inverse of

$$S^{PP'} = \sum_{pq} X_p^P X_p^{P'} X_q^P X_q^{P'} \tag{7}$$

Note, that eq. 6 can be solved either by direct inversion of the grid metric,[47] which generally requires pseudoinversion due to its rank-deficiency, or by solving the associated system of linear equations.[58,59]

2.2.2 Density-based Integral-direct Tensor Hypercontraction

By undoing the AO-to-MO transformations in eq. 5, i.e.,

$$E^{PQ} = \sum_{pqrs} \sum_{\mu\nu\lambda\sigma} \sum_{\mu'\nu'\lambda'\sigma'} X_\mu^P C_{\mu p} \cdot X_\nu^P C_{\nu q} \cdot C_{\mu' p} C_{\nu' q} (\mu'\nu'|\lambda'\sigma') C_{\lambda' r} C_{\sigma' s} \cdot X_\lambda^Q C_{\lambda r} \cdot X_\sigma^Q C_{\sigma s} \tag{8}$$

and by summing up the MO indices first, the expression can be reformulated in terms of one-particle density matrices **P** as

$$E^{PQ} = \sum_{\mu\nu\lambda\sigma} \sum_{\mu'\nu'\lambda'\sigma'} X_\mu^P X_\nu^P P_{\mu\mu'} P_{\nu\nu'} (\mu'\nu'|\lambda'\sigma') P_{\lambda\lambda'} P_{\sigma\sigma'} X_\lambda^Q X_\sigma^Q \tag{9}$$

which – when contracting the densities with the THC **X** matrices – becomes

$$E^{PQ} = \sum_{\mu'\nu'\lambda'\sigma'} X_{\mu'}^P X_{\nu'}^P (\mu'\nu'|\lambda'\sigma') X_{\lambda'}^Q X_{\sigma'}^Q \tag{10}$$

To highlight the universality of this approach, we will use the intermediate $X^P_{\mu'}$ with the primed basis function index as a proxy for both the collocation matrix in the AO basis and when transformed with a general density matrix, i.e.,

$$X^P_{\mu'} = \sum_{\mu} X^P_{\mu} P_{\mu\mu'} \tag{11}$$

Therefore, the expressions for the AO-THC and the MO-THC variant only differ in an additional contraction of the THC **X** matrices with a density matrix. Consequently, the same routines can be used for the construction of intermediate **E** in both the AO and an arbitrary MO basis. The latter is particularly convenient since for many correlation methods different kinds of integrals, e.g., (oo|vo), (vo|vo), and (vv|vo) are required. Furthermore, the above expression permits an integral-direct formulation, as outlined in the following, which avoids the prohibitive storage requirements of the full ERI tensor before the transformation into the grid basis. The key idea is that the contraction of the ket side of the ERI tensor can be viewed as N_{grid} Coulomb matrix builds with slices of the joint collocation tensor **R**, defined as $R^Q_{\lambda\sigma} = X^Q_{\lambda} X^Q_{\sigma}$, acting as the density matrix. Intermediate **E** in the AO basis from eq. 3 can then exemplarily be formed according to algorithm 1.

Algorithm 1 Coulomb Matrix Build-based Integral-direct Formation of **E** in the AO Basis

```
$R^P_{\mu\nu} \leftarrow X^P_{\mu} X^P_{\nu}$
$R^Q_{\lambda\sigma} \leftarrow X^Q_{\lambda} X^Q_{\sigma}$
for all Q do
    $\mathbf{J} \leftarrow$ MakeJ($\mathbf{R}^{(Q)}$)        ▷ $R^{(Q)}_{\lambda\sigma}$ replaces $P_{\lambda\sigma}$ in the $\mathbf{J}$ build        ▷ $\mathcal{O}(N^5)$
    for all P do
        $E^{PQ} \leftarrow \sum_{\mu\nu} R^{(P)}_{\mu\nu} J_{\mu\nu}$                                                  ▷ $\mathcal{O}(N^4)$
    end for
end for
```

We note here, that for a memory efficient implementation the joint collocation tensor **R** should not be constructed explicitly. Instead, the required tensor slices $\mathbf{R}^{(Q)}$ can be constructed on-the-fly as a vector outer product of all elements of the **X** tensor belonging to the given grid point Q, i.e., $\mathbf{R}^{(Q)} = \mathbf{X}^Q_{:} \bigotimes (\mathbf{X}^Q_{:})^{\mathrm{T}}$.

Together with the idea to reformulate the MO-THC equations in a density-based manner, the Coulomb matrix-based approach permits an efficient and simultaneous formation of all intermediates required for the integrals occurring in CC2/ADC(2) (see Section 2.3.1) according to algorithm 2.

Algorithm 2 Coulomb Matrix Build-based Integral-direct Formation of $\mathbf{E}^{(\mathrm{oovo})}$, $\mathbf{E}^{(\mathrm{vovo})}$, and $\mathbf{E}^{(\mathrm{vvvo})}$

```
 1: $\mathbf{X}^{(\mathrm{o})} \leftarrow \mathbf{XP}$                         ▷ $\mathbf{P} \mathrel{\widehat{=}}$ occupied one-particle density matrix
 2: $\mathbf{X}^{(\mathrm{v})} \leftarrow \mathbf{XQ}$                         ▷ $\mathbf{Q} \mathrel{\widehat{=}}$ virtual one-particle density matrix
 3: $\mathbf{R}^{(\mathrm{oo})} \leftarrow \mathbf{X}^{(\mathrm{o})} \otimes_c \mathbf{X}^{(\mathrm{o})}$           ▷ $\otimes_c$ denotes the column-wise Kronecker product
 4: $\mathbf{R}^{(\mathrm{vo})} \leftarrow \mathbf{X}^{(\mathrm{v})} \otimes_c \mathbf{X}^{(\mathrm{o})}$
 5: $\mathbf{R}^{(\mathrm{vv})} \leftarrow \mathbf{X}^{(\mathrm{v})} \otimes_c \mathbf{X}^{(\mathrm{v})}$
 6: for all Q do
 7:     $\mathbf{P}^{(\mathrm{vo})} \leftarrow \mathbf{R}^{(Q),(\mathrm{vo})} + \big(\mathbf{R}^{(Q),(\mathrm{vo})}\big)^{\mathrm{T}}$
 8:     $\mathbf{J}^{(\mathrm{vo})} \leftarrow \frac{1}{2} \times \mathtt{MakeJ}(\mathbf{P}^{(\mathrm{vo})})$                        ▷ $\mathcal{O}(N^5)$
 9:     for all P do
10:         $E^{PQ,(\mathrm{oovo})} \leftarrow \sum_{\mu\nu} R^{(P),(\mathrm{oo})}_{\mu\nu} J^{(\mathrm{vo})}_{\mu\nu}$        ▷ $\mathcal{O}(N^4)$
11:         $E^{PQ,(\mathrm{vovo})} \leftarrow \sum_{\mu\nu} R^{(P),(\mathrm{vo})}_{\mu\nu} J^{(\mathrm{vo})}_{\mu\nu}$        ▷ $\mathcal{O}(N^4)$
12:         $E^{PQ,(\mathrm{vvvo})} \leftarrow \sum_{\mu\nu} R^{(P),(\mathrm{vv})}_{\mu\nu} J^{(\mathrm{vo})}_{\mu\nu}$        ▷ $\mathcal{O}(N^4)$
13:     end for
14: end for
```

The key ingredient for an efficient implementation is to perform the expensive formation of the **J** intermediate once in the ov space, since all integral types, i.e., (oo|vo), (vo|vo), and (vv|vo), share this as a common ket. We note here, that most routines for the construction of Coulomb-type matrices assume the density to be symmetric. This is not the case for slices of the joint collocation tensor $\mathbf{R}^{(\mathrm{vo})}$, which is why the transpose is added in line 7 and the resulting matrix is scaled by a factor of 1/2. Based on the resulting **J** intermediate, the final intermediates **E** for all integral types can be formed simultaneously without further integral evaluations. We also note, that the frozen-core approximation can easily be included in this formulation by simply using the frozen-core density matrix for the occupied space.

To lower the formal scaling behavior, the resolution-of-the-identity approximation (RI)[31–34] can be inserted into eq. 10, which allows to perform the grid-projection of the bra and the ket side of the ERI tensor separately at reduced scaling. Inserting the RI approximation into eq. 10 leads to

$$\begin{aligned}E^{PQ} &= \sum_{\alpha\beta\gamma} Y^P_\beta\,[\mathbf{V}^{-\frac{1}{2}}]_{\beta\alpha}[\mathbf{V}^{-\frac{1}{2}}]_{\alpha\gamma}\,Y^Q_\gamma \\ &= \sum_{\mu'\nu'\lambda'\sigma'}\sum_{\alpha\beta\gamma} X^P_{\mu'}X^P_{\nu'}(\mu'\nu'|\beta)[\mathbf{V}^{-\frac{1}{2}}]_{\beta\alpha}[\mathbf{V}^{-\frac{1}{2}}]_{\alpha\gamma}(\gamma|\lambda'\sigma')X^Q_{\lambda'}X^Q_{\sigma'}\end{aligned} \tag{12}$$

where $\mathbf{V}$ is the two-center RI integral tensor. Intermediate $\mathbf{Y}$ is given by

$$Y^P_\beta = \sum_{\mu'\nu'} X^P_{\mu'}X^P_{\nu'}(\mu'\nu'|\beta) \tag{13}$$

and represents one side of the grid-projected ERI tensor. Like for the $\mathbf{E}$ intermediate, the formally quartic scaling formation of the $\mathbf{Y}$ intermediate can be done in an integral-direct fashion. The final factorization then becomes

$$(pq|rs) = \sum_{PQ}\sum_{\alpha} X^P_p X^P_q \Gamma^P_\alpha \Gamma^Q_\alpha X^Q_r X^Q_s \tag{14}$$

with $\mathbf{\Gamma}$, representing one half of the $\mathbf{Z}$ tensor, defined as

$$\Gamma^P_\alpha = \sum_{P'}\sum_{\beta}[\mathbf{S}^{-1}]^{PP'}Y^{P'}_\beta\,[\mathbf{V}^{-\frac{1}{2}}]_{\beta\alpha} \tag{15}$$

Instead of employing routines for the construction of Coulomb matrices, for the $\mathbf{Y}$ intermediate existing routines for the contraction of density matrices with three-center RI integrals can be used. Amongst these routines, variants optimized for the contraction of multiple densities, such as the J-engine approach to SOS-RI-MP2 by Maurer *et al.*[60] or the RI-J implementation by Kussmann *et al.*[61] are employed since N_{grid} Coulomb matrix builds need to be performed for each $\mathbf{Y}$ intermediate. While these algorithms provide performance improvements over a naïve implementation, in which the Coulomb matrix kernel is simply invoked N_{grid} times, an optimized integral kernel for this kind of contraction is certainly favorable.

2.2.3 Efficient Integral-direct Algorithm for the Y Intermediate

Instead of relying on repetitive J-engine or RI-J based evaluations of the Coulomb potential for many density-like matrices, a more efficient algorithm is proposed inspired by our previous optimal-batching scheme[62] for evaluating correlation energies on the random phase approximation (RPA) level of theory. In the integral-direct variant shown in algorithm 3, the necessary 3-center-2-electron (3c2e) integrals $(\mu'\nu'|\alpha)$ and the vector outer products $\mathbf{R}$ are computed on-the-fly during the formation of the $\mathbf{Y}$ intermediate removing the unfavorable $\mathcal{O}(N^3)$ memory complexity associated with storing the full third-order tensors. The following discussion is exemplariliy carried out for the virtual-occupied subspace but is applicable to all required $\mathbf{\Gamma}$ intermediates.

The naïve application of the optimization scheme of Ref. 62 would predict minimal batch-sizes for the function-pair index $\mu'\nu'$ and the auxiliary basis function index α but maximal batch-sizes for the quadrature point index P, since the more points P are included per batch, the more often any computed given 3c2e integral $(\mu'\nu'|\alpha)$ can be reused for the computation of $\mathbf{Y}$. In practice, however, there are diminishing returns beyond 1000 P points per batch, so the batch size is rounded to the nearest power of 2, i.e., 1024 P points per batch. The batch sizes for α and $\mu'\nu'$ are chosen as 96, which is as small as possible, while still allowing for an efficient execution of the matrix-matrix multiplications within the formation of $\mathbf{Y}$ in line 17. In practice, the precise batch sizes of each batch slightly deviate from 96 to match a multiple of the number of functions/function-pairs for the respective l-quantum numbers of the shells/shell-pairs within a batch, because the 3c2e integral evaluation is most efficient if operating on full shell-triplets. This approach leads to batches with ∼10000 elements for $(\mu'\nu'|\alpha)$ and ∼100000 elements for $R^{P,(\mathrm{ov})}_{\mu'\nu'}$, making the algorithm cache-friendly, i.e., all necessary quantities can be stored in temporary static random access memory (SRAM) storage (cache) close to the processing units, even for large systems. Moreover, we always

Algorithm 3 Integral-direct Formation of $\mathbf{Y}$

```
Pre-process $\mathbf{X}^{(o)}$, $\mathbf{X}^{(v)}$ (Pure → Cartesian)    ▷ $\mathcal{O}(N^2)$
for all $P$-batches do    ▷ OpenMP parallel
    for all $\mu'\nu'$-batches do    ▷ only sign. function-pairs; OpenMP parallel
        for all $\mu'\nu'$ in batch do
            for all $P$ in batch do
                $R^{P,(\mathrm{vo})}_{\mu'\nu'} \leftarrow X^{P,(\mathrm{v})}_{\mu'} X^{P,(\mathrm{o})}_{\nu'}$ + transpose    ▷ $\mathcal{O}(N^3)$
            end for
        end for
        for all $\alpha$-batches do
            for all $\mu'\nu'$-shell-pairs in batch do
                for all $\alpha$-shells in batch do
                    Compute 3c2e integrals $(\mu'\nu'|\alpha)$    ▷ shell-triplet wise; $\mathcal{O}(N^3)$
                end for
            end for
            for all $\alpha$ in batch do
                for all $P$ in batch do
                    $Y^P_\alpha \mathrel{+}= \sum_{\mu'\nu'} R^{P,(\mathrm{vo})}_{\mu'\nu'} (\mu'\nu'|\alpha)$    ▷ BLAS-3; $\mathcal{O}(N^4)$
                end for
            end for
        end for
    end for
end for
Post-process $\mathbf{Y}$ (Cartesian → Pure, reordering, scale by $\frac{1}{2}$)    ▷ $\mathcal{O}(N^2)$
```

aim for multiples of 16 for the innermost loops and order each participating tensor such that the leading index matches the innermost loop. Both design decisions improve the efficiency of memory accesses (cache-lines) and are very favorable for single instruction multiple data (SIMD) vector execution.

In particular, the 3c2e integrals are stored with the auxiliary-shell index as the leading index, so that the 3c2e integral evaluation can make optimal use of SIMD vector routines parallelizing over shell-triplets, i.e., each SIMD-thread handles a separate shell-triplet. For the most efficient use of SIMD vector routines, the auxiliary basis set is considered fully uncontracted, since varying numbers of primitive Gaussian basis functions per shell would otherwise interfere with vectorization, which requires an identical workload for each thread to be efficient. In practice, this is of little concern, since the auxiliary basis sets used for RI-fitting of electron correlation energies (e.g., the Dunning RI basis sets[63–65] employed in Section 4) are usually completely – or at least mostly – uncontracted already. In addition, the transformation from Cartesian to pure (spherical harmonics) basis functions is not performed at the 3-center integral level, instead the whole $\mathbf{Y}$-build is carried out in the Cartesian basis so that only input and output need to be transformed, avoiding any transformations of third-order tensors.

The 3c2e integrals are evaluated using symbolically optimized Obara-Saika[66,67] recursion relations, similar to the integral kernels used for the 3-center-1-electron (3c1e) integrals within our seminumerical exchange method (sn-LinK),[68–70] but adjusted for 2-electron integrals, i.e., by including recurrence relations for both the AO shell-pair and the auxiliary shell. That is, for any given l-quantum number combination the recursion relations are fully expanded symbolically for each final primitive Cartesian integral within the shell-triplet until each integral is solely expressed in terms of primitive Boys integrals. Subsequently the entire set of equations is symbolically optimized by removing redundant sub-expressions within the shell-triplet using common-sub-expression-elimination (CSE) as provided by the SymPy[71] package.

Overall, algorithm 3 formally scales as $\mathcal{O}(N^4)$ and the matrix-matrix multiplication for the formation of $\mathbf{Y}$ in line 17 is by far the slowest step. This formal scaling is easily reduced to asymptotically $\mathcal{O}(N^3)$ by exploiting the sparsity of the function-pairs $\mu'\nu'$, i.e., only function-pairs belonging to significantly overlapping shell-pairs according to the Schwarz integral are considered. In addition, the batch-wise nature of the algorithm is also straightforward to OpenMP parallelize over multiple CPU cores using both the P-batch as well as the $\mu'\nu'$ batch index for parallelization. While P-batch execution is already embarrassingly parallel, parallelization over $\mu'\nu'$ requires special treatment of the race-condition associated with accumulation over that index. In practice, the workload is organized such that each thread accumulates as many $\mu'\nu'$-batches as possible in a thread-private buffer, so the serial (OpenMP critical section; mutually exclusive between threads) accumulation to the global $\mathbf{Y}$ needs to be performed as rarely as possible.

2.3 THC-CC2 and THC-ADC(2) for Ground and Excited States

2.3.1 Basics of CC2 and ADC(2)

The SOS-CC2 ground state energy in the THC approximation is defined as

$$\begin{aligned} E^{\text{SOS-CC2}} &= \langle \text{HF}|\hat{H} + c_{\text{os}}[\hat{H}, T_2^{\text{os}}]|\text{HF}\rangle \\ &= E_{\text{HF}} + c_{\text{os}} \sum_{aibj} t_{ai} t_{bj} \left[\sum_{\beta} \sum_{RS} X_a^{R,(\text{vo})} X_i^{R,(\text{vo})} \Gamma_\beta^{R,(\text{vo})} \Gamma_\beta^{S,(\text{vo})} X_b^{S,(\text{vo})} X_j^{S,(\text{vo})} \right] \\ &\quad - c_{\text{os}} \sum_{aibj} \hat{t}_{aibj}^{\text{os}} \left[\sum_{\beta} \sum_{RS} X_a^{R,(\text{vo})} X_i^{R,(\text{vo})} \Gamma_\beta^{R,(\text{vo})} \Gamma_\beta^{S,(\text{vo})} X_b^{S,(\text{vo})} X_j^{S,(\text{vo})} \right] \end{aligned} \tag{16}$$

where $\hat{H}$ is the similarity-transformed Hamiltonian and T_2^{os} is the two-electron excitation operator acting on two electrons with different spins.[27,29] The cluster amplitudes are determined by solving the CC equations, defined by

$$
\begin{aligned}
0 = \Omega_{\mu_1} &= \langle \mu_1 | \hat{H} + c_{\mathrm{os}}[\hat{H}, T_2^{\mathrm{os}}] | \mathrm{HF} \rangle = (\epsilon_a - \epsilon_i) t_{ai} + \Omega_{ai}^{\mathrm{G}} + \Omega_{ai}^{\mathrm{H}} + \Omega_{ai}^{\mathrm{I}} + \Omega_{ai}^{\mathrm{J}} \\
&= (\epsilon_a - \epsilon_i) t_{ai} + c_{\mathrm{os}} \sum_{cbj} \hat{t}_{cibj}^{\mathrm{os}} \left[\sum_{\beta} \sum_{RS} X_j^{R,(\mathrm{vo})} X_b^{R,(\mathrm{vo})} \Gamma_\beta^{R,(\mathrm{vo})} \Gamma_\beta^{S,(\mathrm{vv})} \hat{X}_a^{S,(\mathrm{vv})} X_c^{S,(\mathrm{vv})} \right] \\
&- c_{\mathrm{os}} \sum_{kbj} \hat{t}_{akbj}^{\mathrm{os}} \left[\sum_{\beta} \sum_{RS} X_j^{R,(\mathrm{vo})} X_b^{R,(\mathrm{vo})} \Gamma_\beta^{R,(\mathrm{vo})} \Gamma_\beta^{S,(\mathrm{oo})} X_k^{S,(\mathrm{oo})} \hat{X}_i^{S,(\mathrm{oo})} \right] + c_{\mathrm{os}} \sum_{bj} \hat{t}_{aibj}^{\mathrm{os}} \hat{F}_{jb} + \hat{F}_{ai}
\end{aligned}
\tag{17}
$$

$$
\begin{aligned}
0 = \Omega_{\mu_2} &= \langle \mu_2^{\mathrm{os}} | \hat{H} + [F, T_2^{\mathrm{os}}] | \mathrm{HF} \rangle = \Omega_{aibj}^{E} + \Omega_{aibj}^{F} \\
&= (\epsilon_a - \epsilon_i + \epsilon_b - \epsilon_j) \hat{t}_{aibj}^{\mathrm{os}} + \left[\sum_{\alpha} \sum_{PQ} \hat{X}_a^{P,(\mathrm{vo})} \hat{X}_i^{P,(\mathrm{vo})} \Gamma_\alpha^{P,(\mathrm{vo})} \Gamma_\alpha^{Q,(\mathrm{vo})} \hat{X}_b^{Q,(\mathrm{vo})} \hat{X}_j^{Q,(\mathrm{vo})} \right]
\end{aligned}
\tag{18}
$$

The Fock matrices $\hat{\mathbf{F}}$ are computed using the integral-direct RI-J[72] and sn-LinK[68–70] kernels to form the Coulomb and exchange terms with high efficiency. The explicit expressions are provided in the literature.[29,73] The OS scaling factor is set to $c_{\mathrm{os}} = 1.3$, as for SOS-MP2.[27,29] The solution of equations 16-18 scales as $\mathcal{O}(N^3)$ for the MO-based THC-SOS-CC2 formulation.[55] However, the MO energies in the denominator of the double amplitudes can be decoupled using Laplace integration

$$
\frac{1}{\epsilon_{aibj}} = \int_0^\infty e^{-\epsilon_{aibj}} dt = \sum_{\tau}^{n} w_\tau e^{-\epsilon_{aibj} t_\tau}
\tag{19}
$$

to rewrite eq. 18 as

$$
\begin{aligned}
\hat{t}_{aibj}^{\mathrm{os}} &= - \sum_{\tau} w_\tau \sum_{\alpha} \sum_{PQ} \hat{X}_a^{P,(\mathrm{vo})} \hat{X}_i^{P,(\mathrm{vo})} \Gamma_\alpha^{P,(\mathrm{vo})} \Gamma_\alpha^{Q,(\mathrm{vo})} \hat{X}_b^{Q,(\mathrm{vo})} \hat{X}_j^{Q,(\mathrm{vo})} e^{-\epsilon_{ai} t_\tau} e^{-\epsilon_{bj} t_\tau} \\
&= - \sum_{\tau} \sum_{\alpha} \sum_{PQ} \hat{X}_{a,\tau}^{P,(\mathrm{vo})} \hat{X}_{i,\tau}^{P,(\mathrm{vo})} \Gamma_\alpha^{P,(\mathrm{vo})} \Gamma_\alpha^{Q,(\mathrm{vo})} \hat{X}_{b,\tau}^{Q,(\mathrm{vo})} \hat{X}_{j,\tau}^{Q,(\mathrm{vo})}
\end{aligned}
\tag{20}
$$

The THC $\mathbf{X}$ matrices in eq. 16-20 are transformed using the transformation matrices

$$\Lambda^p_{\mu a} = C_{\mu a} - \sum_i C_{\mu i} t_{ai} \qquad\qquad \Lambda^h_{\mu i} = C_{\mu i} + \sum_a C_{\mu a} t_{ai} \tag{21}$$

according to

$$\hat{X}^P_{a,\tau} = w_\tau^{\frac{1}{4}} \hat{X}^P_a e^{-\epsilon_a t_\tau} \qquad\qquad \hat{X}^P_a = \sum_\mu \Lambda^p_{\mu a} X^P_\mu \tag{22}$$

$$\hat{X}^P_{i,\tau} = w_\tau^{\frac{1}{4}} \hat{X}^P_i e^{\epsilon_i t_\tau} \qquad\qquad \hat{X}^P_i = \sum_\nu \Lambda^h_{\nu i} X^P_\nu \tag{23}$$

The single amplitudes are obtained by inserting eq. 20 into eq. 17

$$-(\epsilon_a - \epsilon_i) t_{ai} = \Omega^{\mathrm{G}}_{ai} + \Omega^{\mathrm{H}}_{ai} + \Omega^{\mathrm{I}}_{ai} + \Omega^{\mathrm{J}}_{ai} \tag{24}$$

$$\Omega^{\mathrm{G}}_{ai} = -c_{\mathrm{os}} \sum_\tau \sum_{PS} \hat{X}^{P,(\mathrm{vo})}_{i,\tau} \hat{M}^{PS,(\mathrm{ovvv})}_\tau \hat{X}^{S,(\mathrm{vv})}_a \tag{25}$$

$$\Omega^{\mathrm{H}}_{ai} = c_{\mathrm{os}} \sum_\tau \sum_{PS} \hat{X}^{P,(\mathrm{vo})}_{a,\tau} \hat{N}^{PS,(\mathrm{vooo})}_\tau \hat{X}^{S,(\mathrm{oo})}_i \tag{26}$$

$$\Omega^{\mathrm{I}}_{ai} = -c_{\mathrm{os}} \sum_\tau \sum_{P} \hat{X}^{P,(\mathrm{vo})}_{a,\tau} \hat{X}^{P,(\mathrm{vo})}_{i,\tau} \hat{n}^{P,(\mathrm{vo})}_\tau \tag{27}$$

$$\Omega^{\mathrm{J}}_{ai} = \hat{F}_{ai} \tag{28}$$

The working equations of the intermediates in eq. 25-27 are provided in the SI. The evaluation of the MO-THC-SOS-CC2 correction to the ground state energy is then achieved with negligible computational cost as

$$E^{\text{SOS-CC2}} = c_{\mathrm{os}} \sum_{aibj} \sum_\beta \sum_{RS} t_{ai} t_{bj} X^{R,(\mathrm{vo})}_a X^{R,(\mathrm{vo})}_i \Gamma^{R,(\mathrm{vo})}_\beta \Gamma^{S,(\mathrm{vo})}_\beta X^{S,(\mathrm{vo})}_b X^{S,(\mathrm{vo})}_j - c_{\mathrm{os}} \sum_{\alpha\beta} \hat{D}^{\alpha\beta}_\tau \hat{D}^{\alpha\beta}_\tau \tag{29}$$

which can also be used to get the related MO-THC-SOS-MP2 energy correction by simply setting $\mathbf{t}_{\mu_1}$ to zero.

The SOS-LR-CC2 excitation energies are obtained as eigenvalues of the Jacobian matrix, which is defined as the derivative of the vector functions (eq. 17 and 18) with respect to the cluster amplitudes[25] and is given by

$$\mathbf{A}^{\text{SOS-CC2}} = \begin{pmatrix} A_{\mu_1\nu_1} & A_{\mu_1\nu_2} \\ A_{\mu_2\nu_1} & A_{\mu_2\nu_2} \end{pmatrix} = \begin{pmatrix} \langle\mu_1|[(\hat{H} + c_{\text{os}}[\hat{H}, T_2^{\text{os}}]), \tau_{\nu_1}]|HF\rangle & \langle\mu_1|c_{\text{os}}[\hat{H}, \tau_{\nu_2}^{\text{os}}]|HF\rangle \\ \langle\mu_2^{\text{os}}|[\hat{H}, \tau_{\nu_1}]|HF\rangle & \delta_{\mu_2\nu_2}\epsilon_{\mu_2} \end{pmatrix} \tag{30}$$

where the diagonal double-double block ($A_{\mu_2\nu_2}$) is equal to $\epsilon_{aibj} = \epsilon_a - \epsilon_i + \epsilon_b - \epsilon_j$. From eq. 30, secular matrices of simpler excited states methods are derived. The SOS-CIS(D$_\infty$) approach introduced by Head-Gordon *et al.*[9] can be derived from SOS-LR-CC2 theory by setting the singles part of the ground state cluster amplitudes $\mathbf{t}_1$ to zero, resulting in a vanishing contribution of the similarity transformated Hamiltonian. The SOS-CIS(D$_\infty$) Jacobian matrix is given by

$$\mathbf{A}^{\text{SOS-CIS(D}_\infty)} = \begin{pmatrix} \langle\mu_1|[(H + c_{\text{os}}[H, T_2^{\text{os}}]), \tau_{\nu_1}]|HF\rangle & \langle\mu_1|c_{\text{os}}[H, \tau_{\nu_2}^{\text{os}}]|HF\rangle \\ \langle\mu_2^{\text{os}}|[H, \tau_{\nu_1}]|HF\rangle & \delta_{\mu_2\nu_2}\epsilon_{\mu_2} \end{pmatrix} \tag{31}$$

where T_2^{os} denotes the MP2 double amplitudes. In addition, the secular matrix for the SOS-ADC(2) method is related to eq. 31 by the symmetrization[29,30,74]

$$\mathbf{A}^{\text{SOS-ADC(2)}} = \frac{1}{2}\left[\mathbf{A}^{\text{SOS-CIS(D}_\infty)} + (\mathbf{A}^{\text{SOS-CIS(D}_\infty)})^{\text{T}}\right] \tag{32}$$

As discussed by Krauter *et al.*,[30] it is important to derive the SOS-ADC(2) secular matrix from the SOS-CC2 Jabobian in order to reduce the dimension of the $A_{\mu_2\nu_2}$ block. In this work, the full CISD(D$_\infty$) matrix is not symmetrized but only the $A_{\mu_1\nu_1}$ block, i.e., the non-Hermiticity of the coupling blocks is retained and only the $A_{\mu_1\nu_2}$ block is scaled by the factor c_{os}.[29] Using the diagonal form of the double-double block, the doubles part of the excitation vector is obtained as

$$R^m_{\mu_2} = -\sum_{\nu_1} \frac{A_{\mu_2\nu_1} R_{\nu_1}}{\epsilon_{\gamma_2} - \bar{\omega}^m} \tag{33}$$

and the eigenvalue problem of SOS-LR-CC2 and SOS-ADC(2) is solved in the single excitations manifold[29,73] given by

$$\sum_{\nu_1} \left[A_{\mu_1\nu_1} - \sum_{\gamma_2} \frac{A_{\mu_1\gamma_2} A_{\gamma_2\nu_1}}{\epsilon_{\gamma_2} - \bar{\omega}} \right] R_{\nu_1} = \sum_{\nu_1} A^{\text{eff}}_{\mu_1\nu_1}(\bar{\omega}) R_{\nu_1} = \sigma_{\mu_1}(\bar{\omega}, R_{\nu_1}) = \bar{\omega} R_{\mu_1} \tag{34}$$

where the effective **A** matrix is Hermitian for ADC(2) and σ denotes the matrix-vector product.

In order to solve the nonlinear equation part of eq. 34, the excitation energies $\bar{\omega}$ and eigenvectors R_{μ_1} have to be found iteratively until self-consistency is reached. If the initial guess of the eigenvector and eigenvalue is close enough to the final results, a common choice for the solution of the nonlinear problem is an algorithm based on the direct inversion in the iterative subspace (DIIS) technique,[35,73,75] which was shown to be stable and rapidly convergent.[29,35] In addition, it has the advantage of being a single root algorithm, thus allowing to aim for high-lying excited states without converging all lower-lying states. On the contrary, if the initial guess is far from the converged CC2 or ADC(2) result, the eigenvalue and the eigenvector must be pre-optimized using an alternative algorithm. For this purpose, we use a modification of the Davidson algorithm,[73,76] leveraging the fact that a set of converged eigenvalues and -vectors will fulfill the linear generalized eigenproblem

$$\sum_{\mu_1\nu_1} R_{\mu_1} A^{\text{eff}}_{\mu_1\nu_1}(\bar{\omega}) R_{\nu_1} = \sum_{\mu_1} R_{\mu_1} \sigma_{\mu_1}(\bar{\omega}, R_{\nu_1}) = \sum_{\mu_1} \bar{\omega} R_{\mu_1} R_{\mu_1} \tag{35}$$

Both the DIIS and the Davidson procedure for CC2 and ADC(2) are described in literature[29,35,73,76] and will not be discussed here further. The time-determining step for the solution of the eigenvalue problem is the formation of the matrix-vector product:

$$\begin{aligned}\sigma_{ai}^{\text{SOS-CC2}} &= \sum_b \hat{F}_{ab} R_{bi} - \sum_j R_{aj} \hat{F}_{ji} + \bar{F}_{ai} - c_{\text{os}} \sum_b E_{ab} R_{bi} - c_{\text{os}} \sum_j R_{aj} E_{ji} \\ &+ \sigma_{ai}^{\text{G},(1)}(R_{\mu_2}) + \sigma_{ai}^{\text{H},(1)}(R_{\mu_2}) + \sigma_{ai}^{\text{I},(1)}(R_{\mu_2}) \end{aligned} \tag{36}$$

$$\begin{aligned}\sigma_{ai}^{\text{SOS-ADC(2)}} &= (\epsilon_a - \epsilon_i) R_{ai} + \bar{F}_{ai} - c_{\text{os}} \sum_b E'_{ab} R_{bi} - c_{\text{os}} \sum_j R_{aj} E'_{ji} \\ &+ \sigma_{ai}^{\text{G},(2)}(R_{\mu_2}) + \sigma_{ai}^{\text{H},(2)}(R_{\mu_2}) + \sigma_{ai}^{\text{I},(2)} \end{aligned} \tag{37}$$

Making use of the Laplace transformation of the energy denominator, the double part of the singlet excitation vector can be rewritten as

$$\begin{aligned} R_{ij}^{ab}(\bar{\omega}) = -\sum_\tau e^{\bar{\omega} t_\tau} \sum_{PQ} \sum_\alpha \Bigg\{ &\left[\bar{X}_{a,\tau}^{P,(\text{vo})} \hat{X}_{i,\tau}^{P,(\text{vo})} + \hat{X}_{a,\tau}^{P,(\text{vo})} \bar{X}_{i,\tau}^{P,(\text{vo})} \right] \Gamma_\alpha^{P,(\text{vo})} \Gamma_\alpha^{Q,(\text{vo})} \hat{X}_{b,\tau}^{Q,(\text{vo})} \hat{X}_{j,\tau}^{Q,(\text{vo})} \\ + &\left[\bar{X}_{b,\tau}^{P,(\text{vo})} \hat{X}_{j,\tau}^{P,(\text{vo})} + \hat{X}_{b,\tau}^{P,(\text{vo})} \bar{X}_{j,\tau}^{P,(\text{vo})} \right] \Gamma_\alpha^{P,(\text{vo})} \Gamma_\alpha^{Q,(\text{vo})} \hat{X}_{a,\tau}^{Q,(\text{vo})} \hat{X}_{i,\tau}^{Q,(\text{vo})} \Bigg\} \end{aligned} \tag{38}$$

for which the state-specific THC $\bar{\mathbf{X}}$ matrices using the transformation matrices $\bar{\boldsymbol{\Lambda}}$

$$\bar{\Lambda}_{\mu a}^p = \sum_i C_{\mu i} R_{ai} \qquad \bar{\Lambda}_{\mu i}^h = \sum_a C_{\mu a} R_{ai} \tag{39}$$

are given according to

$$\bar{X}_{a,\tau}^P = w_\tau^{\frac{1}{4}} \bar{X}_a^P e^{-\epsilon_a t_\tau} \qquad \bar{X}_a^P = \sum_\mu X_\mu^P \bar{\Lambda}_{\mu a}^p \tag{40}$$

$$\bar{X}_{i,\tau}^P = w_\tau^{\frac{1}{4}} \bar{X}_i^P e^{\epsilon_i t_\tau} \qquad \bar{X}_i^P = \sum_\mu X_\mu^P \bar{\Lambda}_{\mu i}^h \tag{41}$$

Inserting eq. 38 into 36, reduced scaling expressions for the most time-consuming contributions can be formulated as

$$\begin{aligned}
\sigma_{ai}^{\mathrm{G},(1)} &= +c_{\mathrm{os}} \sum_{jbc} R_{ij}^{cb}(\bar{\omega}) \left[\sum_{\beta} \sum_{RS} X_j^{R,(\mathrm{vo})} X_b^{R,(\mathrm{vo})} \Gamma_\beta^{R,(\mathrm{vo})} \Gamma_\beta^{S,(\mathrm{vv})} \hat{X}_a^{S,(\mathrm{vv})} X_c^{S,(\mathrm{vv})} \right] \\
&= -c_{\mathrm{os}} \sum_{\tau} e^{\bar{\omega} t_\tau} \sum_{PS} \left[\hat{X}_{i,\tau}^{P,(\mathrm{vo})} \bar{M}_\tau^{PS,(\mathrm{ovvv})} + \bar{X}_{i,\tau}^{P,(\mathrm{vo})} \hat{M}_\tau^{PS,(\mathrm{ovvv})} \right] \hat{X}_a^{S,(\mathrm{vv})} \\
&= \sum_S \bar{Y}_i^{S,(\mathrm{vv})} \hat{X}_a^{S,(\mathrm{vv})} \qquad (42)
\end{aligned}$$

$$\begin{aligned}
\sigma_{ai}^{\mathrm{H},(1)} &= -c_{\mathrm{os}} \sum_{jbk} R_{kj}^{ab}(\bar{\omega}) \left[\sum_{\beta} \sum_{RS} X_j^{R,(\mathrm{vo})} X_b^{R,(\mathrm{vo})} \Gamma_\beta^{R,(\mathrm{vo})} \Gamma_\beta^{S,(\mathrm{oo})} X_k^{S,(\mathrm{oo})} X_i^{S,(\mathrm{oo})} \right] \\
&= +c_{\mathrm{os}} \sum_{\tau} e^{\bar{\omega} t_\tau} \sum_{PS} \left[\bar{X}_{a,\tau}^{P,(\mathrm{vo})} \hat{N}_\tau^{PS,(\mathrm{vooo})} + \hat{X}_{a,\tau}^{P,(\mathrm{vo})} \bar{N}_\tau^{PS,(\mathrm{vooo})} \right] \hat{X}_i^{S,(\mathrm{oo})} \\
&= \sum_S \bar{Y}_a^{S,(\mathrm{oo})} \hat{X}_i^{S,(\mathrm{oo})} \qquad (43)
\end{aligned}$$

where the contained intermediates are given by

$$\begin{aligned}
\bar{M}_\tau^{PS,(\mathrm{ovvv})} &= \bar{M}_{\tau,(1)}^{PS,(\mathrm{ovvv})} + \bar{M}_{\tau,(2)}^{PS,(\mathrm{ovvv})} \\
&= \hat{B}_\tau^{PS,(\mathrm{ovvv})} \bar{D}_\tau^{PS,(\mathrm{ovvv})} + \bar{B}_\tau^{PS,(\mathrm{ovvv})} \hat{D}_\tau^{PS,(\mathrm{ovvv})} \qquad (44) \\
\bar{N}_\tau^{PS,(\mathrm{vooo})} &= \bar{N}_{\tau,(1)}^{PS,(\mathrm{vooo})} + \bar{N}_{\tau,(2)}^{PS,(\mathrm{vooo})} \\
&= \hat{A}_\tau^{PS,(\mathrm{vooo})} \bar{D}_\tau^{PS,(\mathrm{vooo})} + \bar{A}_\tau^{PS,(\mathrm{vooo})} \hat{D}_\tau^{PS,(\mathrm{vooo})} \qquad (45) \\
\bar{Y}_i^{S,(\mathrm{vv})} &= -c_{\mathrm{os}} \sum_{\tau} e^{\bar{\omega} t_\tau} \sum_{P} \left[\hat{X}_{i,\tau}^{P,(\mathrm{vo})} \bar{M}_\tau^{PS,(\mathrm{ovvv})} + \bar{X}_{i,\tau}^{P,(\mathrm{vo})} \hat{M}_\tau^{PS,(\mathrm{ovvv})} \right] \qquad (46) \\
\bar{Y}_a^{S,(\mathrm{oo})} &= +c_{\mathrm{os}} \sum_{\tau} e^{\bar{\omega} t_\tau} \sum_{P} \left[\bar{X}_{a,\tau}^{P,(\mathrm{vo})} \hat{N}_\tau^{PS,(\mathrm{vooo})} + \hat{X}_{a,\tau}^{P,(\mathrm{vo})} \bar{N}_\tau^{PS,(\mathrm{vooo})} \right] \qquad (47)
\end{aligned}$$

The contribution $\sigma^{\mathrm{I},(1)}$ is computed as:

$$\begin{aligned}
\sigma_{ai}^{\mathrm{I},(1)} &= +c_{\mathrm{os}} \sum_{bj} t_{aibj}^{\mathrm{os}} \bar{F}_{jb} + \sum_{bj} c_{\mathrm{os}} R_{ij}^{ab}(\bar{\omega}) \hat{F}_{jb} \\
&= -c_{\mathrm{os}} \sum_{\tau} e^{\bar{\omega} t_\tau} \sum_{P} \left[\bar{X}_{a,\tau}^{P,(\mathrm{vo})} \hat{X}_{i,\tau}^{P,(\mathrm{vo})} + \hat{X}_{a,\tau}^{P,(\mathrm{vo})} \bar{X}_{i,\tau}^{P,(\mathrm{vo})} \right] \hat{I}_{\tau}^{P,(\mathrm{vo})} - c_{\mathrm{os}} \sum_{\tau} \sum_{P} \hat{X}_{a,\tau}^{P,(\mathrm{vo})} \hat{X}_{i,\tau}^{P,(\mathrm{vo})} \bar{I}_{\tau,(1)}^{P,(\mathrm{vo})}
\end{aligned} \tag{48}$$

with

$$\bar{I}_{\tau,(1)}^{P,(\mathrm{vo})} = \sum_{bj} \hat{X}_{b,\tau}^{P,(\mathrm{vo})} \hat{X}_{j,\tau}^{P,(\mathrm{vo})} \bar{F}_{jb} \tag{49}$$

As for the ground state, the Fock-like terms

$$\bar{F}_{ai} = \sum_{ck} [2(ai\widehat{|}kc) - (ac\widehat{|}ki)] R_{ck} \qquad \bar{F}_{ld} = \sum_{ck} [2(ld\widehat{|}kc) - (lc\widehat{|}kd)] R_{ck} \tag{50}$$

are not reformulated using the THC factorization. Here it is noted that by applying the THC decomposition to eq. 37, a similar expression for the SOS-ADC(2) term is obtained. In fact, the contributions $\boldsymbol{\sigma}^{\mathrm{G},(2)}$ and $\boldsymbol{\sigma}^{\mathrm{H},(2)}$ are obtained from eq. 42 and 43, respectively, by simply setting $\mathbf{t}_{\mu_1}$ amplitudes to zero. The contribution $\boldsymbol{\sigma}^{\mathrm{I},(2)}$ is computed according to

$$\begin{aligned}
\sigma_{ai}^{\mathrm{I},(2)} &= +\frac{c_{\mathrm{os}}}{2} \sum_{bj} t_{aibj}^{\mathrm{os}} \bar{F}_{jb} + \frac{c_{\mathrm{os}}}{2} \sum_{bj} [2(ia\widehat{|}jb) - (ib\widehat{|}ja)] \Big[\sum_{ck} t_{ckbj}^{\mathrm{os}} R_{ck} \Big] \\
&= -\frac{c_{\mathrm{os}}}{2} \sum_{\tau} \sum_{P} X_{a,\tau}^{P,(\mathrm{vo})} X_{i,\tau}^{P,(\mathrm{vo})} \bar{I}_{\tau,(1)}^{P,(\mathrm{vo})} - \frac{c_{\mathrm{os}}}{2} \sum_{bj} [2(ia|jb) - (ib|ja)] \bar{I}_{bj}
\end{aligned} \tag{51}$$

where

$$\bar{I}_{bj} = \sum_{P} \sum_{\tau} X_{b,\tau}^{P,(\mathrm{vo})} X_{j,\tau}^{P,(\mathrm{vo})} \bar{I}_{\tau,(2)}^{P,(\mathrm{vo})} \tag{52}$$

$$\bar{I}_{\tau,(2)}^{P,(\mathrm{vo})} = \sum_{bj} X_{c,\tau}^{P,(\mathrm{vo})} X_{k,\tau}^{P,(\mathrm{vo})} R_{ck} \tag{53}$$

and $\bar{I}^{P,(\mathrm{vo})}_{\tau,(1)}$ is computed as in eq. 49 by setting $\hat{X}^P_a = X^P_a$ and $\hat{X}^P_i = X^P_i$. The explicit expressions for $\mathbf{E}$ and $\mathbf{E}' = \frac{1}{2}(\mathbf{E} + \mathbf{E}^\dagger)$ in eq. 36 and 37, as well as the working equations for the MO-based matrix-vector product are provided in the SI.

2.3.2 Reformulation of the Ground State Equations

As demonstrated in our previous work on RI-SOS-CC2,[38] the equations for the ground state energy can be reformulated in a local basis and hence the intermediates can be expressed in terms of the occupied and virtual one-electron densities

$$P_{\mu\nu} = \sum_i C_{\mu i} C_{\nu i} \qquad\qquad Q_{\mu\nu} = \sum_a C_{\mu a} C_{\nu a} \tag{54}$$

in order to benefit from the locality of the electronic structure. Despite decreasing the scaling with respect to the system size for the evaluation of most intermediates, the use of the AO basis increases the scaling with respect to the basis set size for a given system. To counteract this, the Cholesky decomposition of the occupied ground state density matrix with complete pivoting[77,78]

$$P_{\mu\nu} = \sum_{\underline{i}} L_{\mu\underline{i}} L_{\nu\underline{i}} \tag{55}$$

is applied. In addition, the idempotency relation of the occupied and virtual pseudo-density matrices $\mathbf{P}^\tau$ and $\mathbf{Q}^\tau$

$$P^\tau_{\mu\nu} = w_\tau^{\frac{1}{4}} \sum_i C_{\mu i} C_{\nu i} e^{\epsilon_i t_\tau} \tag{56}$$

$$Q^\tau_{\mu\nu} = w_\tau^{\frac{1}{4}} \sum_a C_{\mu a} C_{\nu a} e^{-\epsilon_a t_\tau} \tag{57}$$

$$P^\tau_{\mu\nu} = \sum_{\sigma\lambda} P^\tau_{\mu\sigma} S_{\sigma\lambda} P_{\lambda\nu} = \sum_{\sigma\lambda\underline{i}} P^\tau_{\mu\sigma} S_{\sigma\lambda} L_{\lambda\underline{i}} L_{\nu\underline{i}} \tag{58}$$

$$Q^\tau_{\mu\nu} = \sum_{\sigma\lambda} Q^\tau_{\mu\sigma} S_{\sigma\lambda} Q_{\lambda\nu} \tag{59}$$

is used.

For the solution of the SOS-CC2 equations, another set of asymmetric one-electron density matrices is generated from the T1-transformed coefficients:

$$\hat{Q}_{\mu\nu} = \sum_{d} C_{\mu d}\Lambda^{p}_{\nu d} = Q_{\mu\nu} - \sum_{\mu'\sigma\lambda\nu'} Q_{\mu\mu'}S_{\mu'\sigma}t_{\sigma\lambda}S_{\lambda\nu'}P_{\nu'\nu} \tag{60}$$

$$\hat{Q}^{\tau}_{\mu\nu} = \sum_{d} w_{\tau}^{\frac{1}{4}} C_{\mu d}e^{-\epsilon_d t_\tau}\Lambda^{p}_{\nu d} = Q^{\tau}_{\mu\nu} - \sum_{\mu'\sigma\lambda\nu'} Q^{\tau}_{\mu\mu'}S_{\mu'\sigma}t_{\sigma\lambda}S_{\lambda\nu'}P_{\nu'\nu} \tag{61}$$

$$\begin{aligned}\hat{P}_{\mu\nu} &= \sum_{l} \Lambda^{h}_{\mu l}C_{\nu l} = P_{\mu\nu} + \sum_{\mu'\sigma\lambda\nu'} Q_{\mu\mu'}S_{\mu'\sigma}t_{\sigma\lambda}S_{\lambda\nu'}P_{\nu'\nu} \\ &= \sum_{\underline{l}} \left(L_{\mu\underline{l}} + \sum_{\mu'\sigma\lambda\nu'} Q_{\mu\mu'}S_{\mu'\sigma}t_{\sigma\lambda}S_{\lambda\nu'}L_{\nu'\underline{l}} \right) L_{\nu\underline{l}} = \hat{P}_{\mu\underline{l}}L_{\nu\underline{l}}\end{aligned} \tag{62}$$

$$\begin{aligned}\hat{P}^{\tau}_{\mu\nu} &= \sum_{i} w_{\tau}^{\frac{1}{4}} \Lambda^{h}_{\mu i}e^{(\epsilon_i)t_\tau}C_{\nu i} \\ &= \sum_{\underline{i}} \left[\sum_{\sigma'\lambda'} \sum_{\underline{j}} \left(L_{\mu\underline{j}} + \sum_{\nu'\sigma\lambda\nu''} Q_{\mu\nu'}S_{\nu'\sigma}t_{\sigma\lambda}S_{\lambda\nu''}L_{\nu''\underline{j}} \right) L_{\sigma'\underline{j}}S_{\sigma'\lambda'}P^{\tau}_{\lambda'\underline{i}} \right] L_{\nu\underline{i}}\end{aligned} \tag{63}$$

To obtain an expression for the single amplitudes in the AO basis, eq. 17 in the MO basis is back-transformed to the AO basis according to

$$\Omega_{\mu\nu} = \sum_{ai} C_{\mu a}(\Omega^{\mathrm{G}}_{ai} + \Omega^{\mathrm{H}}_{ai} + \Omega^{\mathrm{I}}_{ai} + \Omega^{\mathrm{J}}_{ai})C_{\nu i} = \Omega^{\mathrm{G}}_{\mu\nu} + \Omega^{\mathrm{H}}_{\mu\nu} + \Omega^{\mathrm{I}}_{\mu\nu} + \Omega^{\mathrm{J}}_{\mu\nu} \tag{64}$$

for which the one-electron density matrices in eq. 54-63 permit to rewrite Ω_{μ_1} as

$$\begin{aligned}\Omega^{\mathrm{G}}_{\mu\nu} &= \sum_{\underline{i}} \Omega^{\mathrm{G}}_{\mu\underline{i}} L_{\nu\underline{i}} = \sum_{\underline{i}} \left[-c_{\mathrm{os}} \sum_{\tau} \sum_{PS} \sum_{\mu'} \hat{X}^{P,(\mathrm{vo})}_{\underline{i},\tau} \hat{M}^{PS,(\mathrm{ovvv})}_{\tau} X^{S,(\mathrm{vv})}_{\mu'} \hat{Q}_{\mu\mu'} \right] L_{\nu\underline{i}} \\ &= \sum_{\underline{i}} \left[-c_{\mathrm{os}} \sum_{S} \hat{Q}_{\mu\mu'} X^{S,(\mathrm{vv})}_{\mu'} \hat{Y}^{S,(\mathrm{vv})}_{\underline{i}} \right] L_{\nu\underline{i}} \end{aligned} \tag{65}$$

$$\begin{aligned}\Omega^{\mathrm{H}}_{\mu\nu} &= \sum_{\underline{i}} \Omega^{\mathrm{H}}_{\mu\underline{i}} L_{\nu\underline{i}} = \sum_{\underline{i}} \left[c_{\mathrm{os}} \sum_{\tau} \sum_{PS} \hat{X}^{P,(\mathrm{vo})}_{\mu,\tau} \hat{N}^{PS,(\mathrm{vooo})}_{\tau} \hat{X}^{S,(\mathrm{oo})}_{\underline{i}} \right] L_{\nu\underline{i}} \\ &= \sum_{\underline{i}} \left[c_{\mathrm{os}} \sum_{S} \hat{Y}^{Q,(\mathrm{oo})}_{\mu} \hat{X}^{S,(\mathrm{oo})}_{\underline{i}} \right] L_{\nu\underline{i}} \end{aligned} \tag{66}$$

$$\Omega^{\mathrm{I}}_{\mu\nu} = \sum_{\underline{i}} \Omega^{\mathrm{I}}_{\mu\underline{i}} L_{\nu\underline{i}} = \sum_{\underline{i}} \left[-c_{\mathrm{os}} \sum_{\tau} \sum_{P} \hat{X}^{P,(\mathrm{vo})}_{\mu,\tau} \hat{X}^{P,(\mathrm{vo})}_{\underline{i},\tau} \hat{n}^{P,(\mathrm{vo})}_{\tau} \right] L_{\nu\underline{i}} \tag{67}$$

$$\Omega^{\mathrm{J}}_{\mu\nu} = \sum_{\underline{i}} \Omega^{\mathrm{J}}_{\mu\underline{i}} L_{\nu\underline{i}} = \sum_{\underline{i}} \left[\hat{Q}_{\mu\mu'} \hat{F}_{\mu'\nu'} \hat{P}_{\nu'\underline{i}} \right] L_{\nu\underline{i}} \tag{68}$$

The $\mathbf{X}$ matrices are transformed with a computational effort scaling as $\mathcal{O}(N)$, by contraction with the T1-transformed one-electron densities as

$$\hat{X}^{P}_{\underline{i}} = \sum_{\mu'} X^{P}_{\mu'} \hat{P}_{\mu'\underline{i}} \tag{69}$$

$$\hat{X}^{P}_{\mu,\tau} = \sum_{\mu'} \hat{Q}^{\tau}_{\mu\mu'} X^{P}_{\mu'} \tag{70}$$

$$\hat{X}^{P}_{\underline{i},\tau} = \sum_{\mu'} X^{P}_{\mu'} \hat{P}^{\tau}_{\mu'\underline{i}} \tag{71}$$

The working equations in the Cholesky basis are provided in Table 1 together with the asymptotic computational scaling of each step.

The order of contractions follows the general ideas presented in Ref. 79. Naturally, to minimize the number of FLOP, common intermediates, such as $\hat{\mathbf{A}}$, $\hat{\mathbf{B}}$, and $\hat{\mathbf{D}}$ should be reused as much as possible. For this, first all possible $\mathbf{X}$ tensors are contracted over the orbital index. For the subsequent formation of the $\hat{\mathbf{D}}$ intermediates two possible routes have to be

Table 1: Working equations of the intermediates for the solution of the CDD-THC-SOS-CC2/MP2 equations. Throughout this table Einstein's summation convention is used.

	Intermediates	Asymptotic Scaling
(a)	$\hat{A}_{\tau}^{QR,(\mathrm{vovo})} = \hat{X}_{\underline{i},\tau}^{Q,(\mathrm{vo})} X_{\underline{i}}^{R,(\mathrm{vo})}$	$\mathcal{O}(N)$
(b)	$\hat{B}_{\tau}^{QR,(\mathrm{vovo})} = \hat{X}_{\mu,\tau}^{Q,(\mathrm{vo})} X_{\mu}^{R,(\mathrm{vo})}$	$\mathcal{O}(N)$
(c)	$\hat{C}_{\tau}^{QR,(\mathrm{vovo})} = \hat{A}_{\tau}^{QR,(\mathrm{vovo})} \hat{B}_{\tau}^{QR,(\mathrm{vovo})}$	$\mathcal{O}(N)$
(d)	$\hat{D}_{\tau}^{\alpha\beta} = \Gamma_{\alpha}^{Q,(\mathrm{vo})} \hat{C}_{\tau}^{QR,(\mathrm{vovo})} \Gamma_{\beta}^{R,(\mathrm{vo})}$	$\mathcal{O}(N^3)$
(e)	$\hat{D}_{\tau}^{PS,(\mathrm{ovvv})} = \Gamma_{\alpha}^{P,(\mathrm{vo})} \hat{D}_{\tau}^{\alpha\beta} \Gamma_{\beta}^{S,(\mathrm{vv})}$	$\mathcal{O}(N^3)$
(f)	$\hat{D}_{\tau}^{PS,(\mathrm{vooo})} = \Gamma_{\alpha}^{P,(\mathrm{vo})} \hat{D}_{\tau}^{\alpha\beta} \Gamma_{\beta}^{S,(\mathrm{oo})}$	$\mathcal{O}(N^3)$
(e')	$\hat{D}_{\tau}^{PS,(\mathrm{ovvv})} = Z^{PQ,(\mathrm{vovo})} \hat{C}_{\tau}^{QR,(\mathrm{vovo})} Z^{RS,(\mathrm{ovvv})}$	$\mathcal{O}(N^2)$
(f')	$\hat{D}_{\tau}^{PS,(\mathrm{vooo})} = Z^{PQ,(\mathrm{vovo})} \hat{C}_{\tau}^{QR,(\mathrm{vovo})} Z^{RS,(\mathrm{vooo})}$	$\mathcal{O}(N^2)$
(g)	$\hat{A}_{\tau}^{PS,(\mathrm{vooo})} = \hat{X}_{\underline{i},\tau}^{P,(\mathrm{vo})} X_{\underline{i}}^{S,(\mathrm{oo})}$	$\mathcal{O}(N)$
(h)	$\hat{B}_{\tau}^{PS,(\mathrm{ovvv})} = \hat{X}_{\mu,\tau}^{P,(\mathrm{vo})} X_{\mu}^{S,(\mathrm{vv})}$	$\mathcal{O}(N)$
(i)	$\hat{M}_{\tau}^{PS,(\mathrm{ovvv})} = \hat{D}_{\tau}^{PS,(\mathrm{ovvv})} \hat{B}_{\tau}^{PS,(\mathrm{ovvv})}$	$\mathcal{O}(N)$
(j)	$\hat{N}_{\tau}^{PS,(\mathrm{vooo})} = \hat{D}_{\tau}^{PS,(\mathrm{vooo})} \hat{A}_{\tau}^{PS,(\mathrm{vooo})}$	$\mathcal{O}(N)$
(k)	$\hat{Y}_{\mu}^{S,(\mathrm{oo})} = \hat{X}_{\mu,\tau}^{P,(\mathrm{vo})} \hat{N}_{\tau}^{PS,(\mathrm{vooo})}$	$\mathcal{O}(N)$
(l)	$\hat{Y}_{\underline{i}}^{S,(\mathrm{vv})} = \hat{X}_{\underline{i},\tau}^{P,(\mathrm{vo})} \hat{M}_{\tau}^{PS,(\mathrm{ovvv})}$	$\mathcal{O}(N)$
(m)	$\hat{I}_{\underline{j},\tau}^{P,(\mathrm{ov})} = \hat{X}_{\mu,\tau}^{P,(\mathrm{vo})} \hat{F}_{\underline{j}\mu}$	$\mathcal{O}(N^2)$
(n)	$\hat{n}_{\tau}^{P,(\mathrm{ov})} = \hat{X}_{\underline{j},\tau}^{P,(\mathrm{vo})} \hat{I}_{\underline{j},\tau}^{P,(\mathrm{ov})}$	$\mathcal{O}(N^2)$

considered. In order to minimize the number of FLOP, the $\mathbf{\Gamma}$-factorized form of the THC $\mathbf{Z}$ tensor should be used and contracted in a total of four matrix-matrix multiplications in steps (d)-(e). However, the fact that the one-electron density becomes sparse for sufficiently large systems with a significant HOMO-LUMO gap can be used here to perform the step in $\mathcal{O}(N^2)$ operations. The first contraction of $\mathbf{Z}$ with intermediate $\hat{\mathbf{C}}$ in steps (e')-(f') scales quadratically, since $\hat{\mathbf{C}}$ is sparse whereas $\mathbf{Z}$ is not. For the multiplication with the second $\mathbf{Z}$ matrix the fact that the resulting $\hat{\mathbf{D}}$ matrix is Schur multiplied with either the $\hat{\mathbf{A}}$ or the $\hat{\mathbf{B}}$ matrix in steps (i)-(j) can be leveraged. Since intermediate $\hat{\mathbf{A}}$ is sparse, the Schur product with intermediate $\hat{\mathbf{D}}$ will only contain elements which are significant in $\hat{\mathbf{A}}$. Therefore, only the elements in $\hat{\mathbf{D}}$, which are significant in $\hat{\mathbf{A}}$ need to be computed for step (j) and likewise for step (i) with intermediate $\hat{\mathbf{B}}$. In total, this enables the formation of the expensive $\hat{\mathbf{D}}$ intermediates in $\mathcal{O}(N^2)$ time. All final contractions in steps (k)-(n) are at most quadratically scaling, which results in overall quadratic scaling for the entire CDD-THC-SOS-CC2 method if $\mathbf{Z}$ is used. Notice that the same strategy can be leveraged when using $\mathbf{\Gamma}$ resulting in a further reduction of the computational effort. However, the formal computational complexity is not decreased because only the final matrix-matrix multiplication of steps (e) and (f) would scale quadratically. Therefore, the overall scaling behavior for the entire CDD-THC-SOS-CC2 method is cubic if $\mathbf{\Gamma}$ is used.

2.3.3 Reformulation of the Excited State Equations

The strategy outlined in the previous section can likewise be applied to the matrix-vector products of SOS-LR-CC2 and SOS-ADC(2). For simplicity, we will only discuss the reformulation of eq. 36 according to

$$\begin{aligned}\sigma_{\mu\nu}^{\text{SOS-CC2},(1)} &= \sum_{ai} C_{\mu a} C_{\nu i} \left(\sum_{b} \hat{F}_{ab} R_{bi} \right) - \sum_{ai} C_{\mu a} C_{\nu i} \left(\sum_{j} R_{aj} \hat{F}_{ji} \right) + \sum_{ai} C_{\mu a} C_{\nu i} \bar{F}_{ai} \\ &\quad - c_{\text{os}} \sum_{ai} C_{\mu a} C_{\nu i} \left(\sum_{b} E_{ab} R_{bi} \right) - c_{\text{os}} \sum_{ai} C_{\mu a} C_{\nu i} \left(\sum_{j} R_{aj} E_{ji} \right) \\ &\quad + \sum_{ai} C_{\mu a} C_{\nu i} \left(\sigma_{ai}^{\text{G},(1)} + \sigma_{ai}^{\text{H},(1)} + \sigma_{ai}^{\text{I},(1)} \right) \end{aligned} \tag{72}$$

The fourth and fifth term on the right-hand side are rewritten as

$$-c_{\text{os}} \sum_{ai} C_{\mu a} C_{\nu i} \left(\sum_{b} E_{ab} R_{bi} \right) = -c_{\text{os}} \sum_{\mu'\sigma\sigma'\nu'} \hat{E}'_{\mu'\nu'} Q_{\nu'\sigma'} \left[\sum_{\lambda'\lambda} S_{\sigma'\lambda'} R_{\lambda'\lambda} S_{\lambda\sigma} \right] P_{\sigma\nu} \tag{73}$$

$$-c_{\text{os}} \sum_{ai} C_{\mu a} C_{\nu i} \left(\sum_{j} R_{aj} E_{ji} \right) = -c_{\text{os}} \sum_{\mu'\sigma\sigma'\nu'} Q_{\mu\mu'} \left[\sum_{\lambda\lambda'} S_{\mu'\lambda'} R_{\lambda\lambda'} S_{\lambda\sigma} \right] P_{\sigma\sigma'} \hat{E}''_{\sigma'\nu'} \tag{74}$$

where the intermediates $\mathbf{E}$, given by

$$E'_{\mu\nu} = \sum_{S} \Big(\sum_{\tau} \sum_{P} \hat{X}_{\mu,\tau}^{P,(\text{vo})} \hat{N}_{\tau}^{PS,(\text{vovo})} \Big) X_{\nu}^{S,(\text{vo})} \tag{75}$$

$$E''_{\mu\nu} = \sum_{\underline{j}\underline{i}} L_{\mu\underline{j}} L_{\nu\underline{i}} \left[\sum_{S} \Big(\sum_{\tau} \sum_{P} \hat{X}_{\underline{i},\tau}^{P,(\text{vo})} \hat{M}_{\tau}^{PS,(\text{vovo})} \Big) X_{\underline{j}}^{S,(\text{vo})} \right] \tag{76}$$

depend only on ground state quantities and hence are computed once and stored on disk. The terms $\boldsymbol{\sigma}^{\mathrm{G},(1)}$, $\boldsymbol{\sigma}^{\mathrm{H},(1)}$ and $\boldsymbol{\sigma}^{\mathrm{I},(1)}$ are given as

$$\begin{aligned}
\sigma_{\mu\nu}^{\mathrm{G},(1)} &= -c_{\mathrm{os}} \sum_{\mu'\underline{i}} L_{\nu\underline{i}} \left\{ \sum_{\tau} e^{\bar{\omega} t_\tau} \sum_{PS} \left[\hat{X}_{\underline{i},\tau}^{P,(\mathrm{vo})} \bar{M}_{\tau}^{PS,(\mathrm{ovvv})} + \bar{X}_{\underline{i},\tau}^{P,(\mathrm{vo})} \hat{M}_{\tau}^{PS,(\mathrm{ovvv})} \right] X_{\mu'}^{S,(\mathrm{vv})} \right\} \hat{Q}_{\mu\mu'} \\
&= -c_{\mathrm{os}} \sum_{S} \sum_{\mu'\underline{i}} L_{\nu\underline{i}} \bar{Y}_{\underline{i}}^{S,(\mathrm{vv})} X_{\mu'}^{S,(\mathrm{vv})} \hat{Q}_{\mu\mu'} \qquad (77)
\end{aligned}$$

$$\begin{aligned}
\sigma_{\mu\nu}^{\mathrm{H},(1)} &= +c_{\mathrm{os}} \sum_{\underline{i}} L_{\nu\underline{i}} \left\{ \sum_{\tau} e^{\bar{\omega} t_\tau} \sum_{PS} \left[\bar{X}_{\mu,\tau}^{P,(\mathrm{vo})} \hat{N}_{\tau}^{PS,(\mathrm{vooo})} + \hat{X}_{\mu,\tau}^{P,(\mathrm{vo})} \bar{N}_{\tau}^{PS,(\mathrm{vooo})} \right] \hat{X}_{\underline{i}}^{S,(\mathrm{oo})} \right\} \\
&= +c_{\mathrm{os}} \sum_{S} \sum_{\underline{i}} \bar{Y}_{\mu}^{S,(\mathrm{oo})} \hat{X}_{\underline{i}}^{S,(\mathrm{oo})} L_{\nu\underline{i}} \qquad (78)
\end{aligned}$$

$$\begin{aligned}
\sigma_{\mu\nu}^{\mathrm{I},(1)} &= -c_{\mathrm{os}} \sum_{\underline{i}} L_{\nu\underline{i}} \left\{ \sum_{\tau} e^{\bar{\omega} t_\tau} \sum_{P} \left[\bar{X}_{\mu,\tau}^{P,(\mathrm{vo})} \hat{X}_{\underline{i},\tau}^{P,(\mathrm{vo})} + \hat{X}_{\mu,\tau}^{P,(\mathrm{vo})} \bar{X}_{\underline{i},\tau}^{P,(\mathrm{vo})} \right] \hat{I}_{\tau}^{P,(\mathrm{vo})} \right\} \\
&\quad - c_{\mathrm{os}} \sum_{\underline{i}} L_{\nu\underline{i}} \left\{ \sum_{\tau} \sum_{P} \hat{X}_{\mu,\tau}^{P,(\mathrm{vo})} \hat{X}_{\underline{i},\tau}^{P,(\mathrm{vo})} \bar{I}_{\tau,(1)}^{P,(\mathrm{vo})} \right\} \qquad (79)
\end{aligned}$$

with

$$\bar{I}_{\tau,(1)}^{P,(\mathrm{vo})} = \sum_{\mu\nu\underline{i}} \hat{X}_{\mu,\tau}^{P,(\mathrm{vo})} \hat{X}_{\underline{i},\tau}^{P,(\mathrm{vo})} \bar{F}_{\mu\nu} L_{\nu\underline{i}} \qquad (80)$$

The matrices $\bar{M}$ and $\bar{N}$, defined in eqs. 44 and45, are computed as shown in Table 2. The general approach for the order of contractions and the reduction of the scaling is similar to the ideas presented for Table 1. The state-specific THC $\bar{\mathbf{X}}$ matrices are given by

$$\bar{X}_{\mu,\tau}^{P,(\mathrm{vo})} = \sum_{\mu'} \bar{Q}_{\mu\mu'}^{\tau} X_{\mu'}^{P,(\mathrm{vo})} \qquad\qquad \bar{X}_{\underline{i},\tau}^{P,(\mathrm{vo})} = \sum_{\mu} \bar{P}_{\mu\underline{i}}^{\tau} X_{\mu}^{P,(\mathrm{vo})} \qquad (81)$$

where the densities $\bar{Q}$ and $\bar{P}$ are defined as

$$\bar{Q}^{\tau}_{\mu\nu} = \sum_{a} w_{\tau}^{\frac{1}{4}} C_{\mu a} e^{-\epsilon_a t_\tau} \bar{\Lambda}^{p}_{\nu a} = -\sum_{\mu'\nu'\underline{k}} Q^{\tau}_{\mu\mu'} \Big[\sum_{\sigma\lambda} S_{\mu'\sigma} R_{\sigma\lambda} S_{\lambda\nu'} \Big] L_{\nu'\underline{k}} L_{\underline{k}\nu} \tag{82}$$

$$\bar{P}^{\tau}_{\mu\nu} = \sum_{i} w_{\tau}^{\frac{1}{4}} \bar{\Lambda}^{h}_{\mu i} e^{\epsilon_i t_\tau} C_{\nu i} = \Bigg\{ \sum_{\mu'\nu'} \sum_{\underline{j}\sigma'\lambda'} Q_{\mu\mu'} \Big[S_{\mu'\lambda} R_{\lambda\sigma} S_{\sigma\nu'} \Big] L_{\nu'\underline{j}} L_{\sigma'\underline{j}} S_{\sigma'\lambda'} P^{\tau}_{\lambda'\underline{i}} \Bigg\} L_{\nu\underline{i}} \tag{83}$$

contain the information about the electronic transition. As discussed in Section 2.3.1, the SOS-ADC(2) matrix-vector product is easily obtained by setting the single amplitudes to zero and symmetrizing the intermediates in eqs. 75 and 76. Notice that, eq. 51 can be reformulated as

$$\begin{aligned} \sigma^{\mathrm{I},(2)}_{\mu\nu} &= -c_{\mathrm{os}} \sum_{\underline{i}} L_{\nu\underline{i}} \Bigg\{ \sum_{\tau} \sum_{P} X^{P,(\mathrm{vo})}_{\mu,\tau} X^{P,(\mathrm{vo})}_{\underline{i},\tau} \bar{I}^{P,(\mathrm{vo})}_{\tau,(1)} \Bigg\} \\ &\quad - c_{\mathrm{os}} \sum_{\mu'\nu'} \sum_{\underline{i}} Q_{\mu\nu'} \Bigg\{ \sum_{\sigma\lambda} [2(\mu'\nu'|\sigma\lambda) - (\mu'\lambda|\sigma\nu')] L_{\sigma\underline{k}} \bar{I}_{\lambda\underline{k}} \Bigg\} L_{\mu'\underline{i}} L_{\nu\underline{i}} \end{aligned} \tag{84}$$

$$\bar{I}_{\lambda\underline{i}} = \sum_{P} \sum_{\tau} X^{P,(\mathrm{vo})}_{\lambda,\tau} X^{P,(\mathrm{vo})}_{\underline{i},\tau} \bar{I}^{P,(\mathrm{vo})}_{\tau,(2)} \tag{85}$$

$$\bar{I}^{P,(\mathrm{vo})}_{\tau,(2)} = \sum_{\mu\underline{i}} X^{P,(\mathrm{vo})}_{\mu,\tau} X^{P,(\mathrm{vo})}_{\underline{i},\tau} \Bigg[\sum_{\nu\lambda\sigma\nu'} Q_{\mu\nu} S_{\nu\lambda} R_{\lambda\sigma} S_{\sigma\nu'} L_{\nu'\underline{i}} \Bigg] \tag{86}$$

In order to minimize the number of FLOP, common intermediates, such as $\bar{\mathbf{A}}$, $\bar{\mathbf{B}}$, $\bar{\mathbf{D}}$ should be reused as much as possible. For this, first all possible $\mathbf{X}$ tensors are contracted over the orbital index. The fact that the one-electron density and transition density become sparse can be used here to form the $\bar{\mathbf{D}}$ intermediates with $\mathcal{O}(N^2)$ scaling behavior. As discussed in Section 2.3.2, it is possible to carry out the computation of the $\bar{\mathbf{D}}$ intermediates using two possible routes. To obtain the theoretical quadratic scaling behavior in the asymptotic limit, the THC $\mathbf{Z}$ tensor can be used and contracted in a total of two matrix-matrix multiplications in steps (e')-(f') of Table 2. The first contraction of $\mathbf{Z}$ with intermediate $\bar{\mathbf{C}}$ in steps (e')-(f') scales quadratically, since $\bar{\mathbf{C}}$ is significantly sparse whereas $\mathbf{Z}$ is not. For the multiplication with the second $\mathbf{Z}$ matrix the fact that the resulting $\bar{\mathbf{D}}$ matrix is Schur multiplied with ei-

Table 2: Working equations for the evaluation of the σ^{G} and σ^{H} contributions to the CDD-THC-SOS-ADC(2)/LR-CC2 matrix-vector product. Throughout this table Einstein's summation convention is used. The ADC(2) equations are obtained by setting $\mathbf{t}_{\mu_1} = 0$.

	Intermediates	Asymptotic Scaling
(a)	$\bar{A}_{\tau}^{QR,(\mathrm{vovo})} = \bar{X}_{\underline{i},\tau}^{Q,(\mathrm{vo})} X_{\underline{i}}^{R,(\mathrm{vo})}$	$\mathcal{O}(N)$
(b)	$\bar{B}_{\tau}^{QR,(\mathrm{vovo})} = \bar{X}_{\mu,\tau}^{Q,(\mathrm{vo})} X_{\mu}^{R,(\mathrm{vo})}$	$\mathcal{O}(N)$
(c)	$\bar{C}_{\tau}^{QR,(\mathrm{vovo})} = \bar{A}^{QR,(\mathrm{vovo})} \hat{B}^{QR,(\mathrm{vovo})} + \hat{A}^{QR,(\mathrm{vovo})} \bar{B}^{QR,(\mathrm{vovo})}$	$\mathcal{O}(N)$
(d)	$\bar{D}_{\tau}^{P\beta,(\mathrm{vo})} = \Gamma_{\alpha}^{P,(\mathrm{vo})} (\Gamma_{\alpha}^{Q,(\mathrm{vo})} \bar{C}_{\tau}^{QR,(\mathrm{vovo})} \Gamma_{\beta}^{R,(\mathrm{vo})}) = \Gamma_{\alpha}^{P,(\mathrm{vo})} \bar{D}_{\tau}^{\alpha\beta}$	$\mathcal{O}(N^2)$
(e)	$\bar{D}_{\tau}^{PS,(\mathrm{ovvv})} = e^{\bar{\omega} t_{\tau}} \bar{D}_{\tau}^{P\beta,(\mathrm{vo})} \Gamma_{\beta}^{S,(\mathrm{vv})}$	$\mathcal{O}(N^2)$
(f)	$\bar{D}_{\tau}^{PS,(\mathrm{vooo})} = e^{\bar{\omega} t_{\tau}} \bar{D}_{\tau}^{P\beta,(\mathrm{vo})} \Gamma_{\beta}^{S,(\mathrm{oo})}$	$\mathcal{O}(N^2)$
(e')	$\bar{D}_{\tau}^{PS,(\mathrm{ovvv})} = e^{\bar{\omega} t_{\tau}} Z^{PQ,(\mathrm{vovo})} \bar{C}_{\tau}^{QR,(\mathrm{vovo})} Z^{RS,(\mathrm{ovvv})}$	$\mathcal{O}(N^2)$
(f')	$\bar{D}_{\tau}^{PS,(\mathrm{vooo})} = e^{\bar{\omega} t_{\tau}} Z^{PQ,(\mathrm{vovo})} \bar{C}_{\tau}^{QR,(\mathrm{vovo})} Z^{RS,(\mathrm{vooo})}$	$\mathcal{O}(N^2)$
(g)	$\bar{A}_{\tau}^{PS,(\mathrm{vooo})} = \bar{X}_{\underline{i},\tau}^{P,(\mathrm{vo})} X_{\underline{i}}^{S,(\mathrm{oo})}$	$\mathcal{O}(N)$
(h)	$\bar{B}_{\tau}^{PS,(\mathrm{ovvv})} = \bar{X}_{\mu,\tau}^{P,(\mathrm{vo})} X_{\mu}^{S,(\mathrm{vv})}$	$\mathcal{O}(N)$
(i)	$\bar{M}_{\tau}^{PS,(\mathrm{ovvv})} = \bar{M}_{\tau,(1)}^{PS,(\mathrm{ovvv})} + \bar{M}_{\tau,(2)}^{PS,(\mathrm{ovvv})}$	$\mathcal{O}(N)$
(j)	$\bar{M}_{\tau,(1)}^{PS,(\mathrm{ovvv})} = \hat{B}_{\tau}^{PS,(\mathrm{ovvv})} \bar{D}_{\tau}^{PS,(\mathrm{ovvv})}$	$\mathcal{O}(N)$
(k)	$\bar{M}_{\tau,(2)}^{PS,(\mathrm{ovvv})} = \bar{B}_{\tau}^{PS,(\mathrm{ovvv})} \hat{D}_{\tau}^{PS,(\mathrm{ovvv})}$	$\mathcal{O}(N)$
(l)	$\bar{N}_{\tau}^{PS,(\mathrm{vooo})} = \bar{N}_{\tau,(1)}^{PS,(\mathrm{vooo})} + \bar{N}_{\tau,(2)}^{PS,(\mathrm{vooo})}$	$\mathcal{O}(N)$
(m)	$\bar{N}_{\tau,(1)}^{PS,(\mathrm{vooo})} = \hat{A}_{\tau}^{PS,(\mathrm{vooo})} \bar{D}_{\tau}^{PS,(\mathrm{vooo})}$	$\mathcal{O}(N)$
(n)	$\bar{N}_{\tau,(2)}^{PS,(\mathrm{vooo})} = \bar{A}_{\tau}^{PS,(\mathrm{vooo})} \hat{D}_{\tau}^{PS,(\mathrm{vooo})}$	$\mathcal{O}(N)$
(o)	$\bar{Y}_{\mu}^{S,(\mathrm{oo})} = \bar{X}_{\mu,\tau}^{P,(\mathrm{vo})} \hat{N}_{\tau}^{PS,(\mathrm{vooo})} + \hat{X}_{\mu,\tau}^{P,(\mathrm{vo})} \bar{N}_{\tau}^{PS,(\mathrm{vooo})}$	$\mathcal{O}(N)$
(p)	$\bar{Y}_{\underline{i}}^{S,(\mathrm{vv})} = \hat{X}_{\underline{i},\tau}^{P,(\mathrm{vo})} \bar{M}_{\tau}^{PS,(\mathrm{ovvv})} + \bar{X}_{\underline{i},\tau}^{P,(\mathrm{vo})} \hat{M}_{\tau}^{PS,(\mathrm{ovvv})}$	$\mathcal{O}(N)$

ther the $\hat{\mathbf{A}}$ or the $\hat{\mathbf{B}}$ matrix in steps (i)-(j) can be leveraged. Since intermediate $\hat{\mathbf{A}}$ is sparse, the Schur product with intermediate $\hat{\mathbf{D}}$ will only contain elements that are significant in $\hat{\mathbf{A}}$. Therefore, only the elements in $\bar{\mathbf{D}}$, which are significant in $\hat{\mathbf{A}}$ need to be computed for step (j) and likewise for step (i) with intermediate $\hat{\mathbf{B}}$. In total, this enables the formation of the expensive $\bar{\mathbf{D}}$ intermediates in $\mathcal{O}(N^2)$ time. In order to minimize the number of FLOP, the $\mathbf{\Gamma}$-factorized form of the THC $\mathbf{Z}$ tensor should be used and contracted in a total of four matrix-matrix multiplications in steps (d)-(f) of Table 2. Leveraging the fact that the $\bar{\mathbf{C}}$, $\bar{\mathbf{A}}$, and $\bar{\mathbf{B}}$ intermediates are significantly sparse – for large systems and local electronic excitations – steps (d)-(f) in Table 2 effectively scale as $\mathcal{O}(N^2)$ in the asymptotic limit.

The ground state intermediates $\hat{\mathbf{D}}$ are recomputed as in Table 1 for each new matrix-vector product and used in steps (k) and (n) of Table 2. By leveraging the sparsity of $\bar{\mathbf{B}}$ in step (k) and $\bar{\mathbf{A}}$ in step (n), it is possible to compute $\hat{\mathbf{D}}$ with quadratic time complexity. All contractions in steps (i)-(p) are at most linear scaling, which results in overall asymptotic quadratic scaling for the entire CDD-THC-SOS-LR-CC2/ADC(2) methods.

3 Computational Details

The presented CDD-THC-SOS-LR-CC2 and CDD-THC-SOS-ADC(2) methods as well as the MO-based variants are implemented in the FERMIONS++[80–82] program. The program was compiled with the Intel C/C++ Compiler 2022.0.2 and linked against the Intel Math Kernel Library 2022.0.2 for the employed matrix algebra. All developed code was – as far as possible – parallelized with OpenMP.[83] The underlying Hartree–Fock calculations have been converged to a maximum element of the error matrix in the DIIS procedure below 10^{-7}. In the SCF, the Coulomb matrix is evaluated using the RI-J approach by Kussmann *et al.*[72] using the cc-pVDZ-JKfit or cc-pVTZ-JKfit[84] RI-J basis set, respectively. For the exchange matrix, the semi-numerical linear scaling exchange method by Laqua *et al.*[69,70] is used. For the solution of the least-squares equations in THC the pivoted Cholesky decomposition ansatz by Matthews[58] is used. The hand-optimized grid for the cc-pVTZ basis set by Kokkila Schumacher *et al.*[85] is used as a parent grid together with a pruning threshold of 10^{-10}, unless otherwise noted. As demonstrated in the SI, it is pivotal to reorder the grid points after the pruning, since the pivoting in the Cholesky decomposition significantly reduces the sparsity of intermediates based on the pruned collocation matrices. The computational performance of the CDD-THC-SOS-LR-CC2 and CDD-THC-SOS-ADC(2) methods is improved using sparse linear algebra. The current implementation leverages block-sparse (BS) matrices, which divide the matrices into smaller blocks of maximum size 96×96. Further information about the BS matrix implementation is provided in the SI of Ref. 38. The thresholds controlling the storage sparsity (ϑ_a) and the matrix-matrix multiply sparsity (ϑ_m) are set to 10^{-7} and 10^{-9}, respectively. The threshold controlling the storage sparsity of the transition density matrix is set to 10^{-4}. The single cluster amplitudes and ground state energy at the SOS-CC2 level are optimized via the DIIS procedure, which terminates when the L2-norm of the single vector function is lower than 10^{-5} and the variation in the energy is lower than 10^{-6}. For excited states calculations, the trial excitation vectors and energies are first optimized at the ADC(1)/CCS level via the Davidson procedure, until the L2-norm of residuals and the variation in the eigenvalues are below 10^{-3}. Then, SOS-LR-CC2 or SOS-ADC(2) excitation vectors and energies are optimized using the DIIS algorithm, which terminates when the L2-norm of the residuals are lower than 10^{-5} and the variations in the eigenvalues are lower than 10^{-6}. It is important to note that the ADC(1)/CCS trial vectors and eigenvalues can be pre-optimized via the Davidson procedure at the CC2 or ADC(2) level if the DIIS procedure fails to converge to the correct root. Optimized minimax grids with 7 quadrature points for the Laplace expansion are used for both ground and excited states calculations. Moreover, the frozen-core approximation is used in the THC fitting as well as in the ground state and excited states calculations. Throughout, the Dunning cc-pVXZ ($X \in \{D,T\}$) basis sets[63,64] are used together with their corresponding RI basis sets.[65] All calculations are performed using a compute node with two AMD EPYC 7452 32-Core 2.35 GHz CPUs (64 cores in total), 1 TB of RAM, and 24 TB of disk space. All runtimes are reported as wall times, not CPU times.

4 Results

4.1 Accuracy

The present work aims to increase the efficiency of the SOS-ADC(2) and SOS-LR-CC2 methods to extend their applicability to molecules with several hundreds of atoms while retaining accuracy as far as possible. To assess the accuracy of the ground state implementation, the errors produced by the MO-based as well as by the CDD-based THC-SOS-MP2/CC2 methods are investigated with respect to MO-RI-SOS-MP2/CC2. For this purpose, the THC error ΔE_{THC} is defined as $|E_{\text{MO-RI-SOS-MP2/CC2}} - E_{\text{MO-THC-SOS-MP2/CC2}}|$, i.e., measuring the error introduced by the THC approximation alone, whereas the CDD error ΔE_{CDD} is defined as $|E_{\text{MO-THC-SOS-MP2/CC2}} - E_{\text{CDD-THC-SOS-MP2/CC2}}|$, i.e., measuring the error introduced by CDD reformulation and the associated use of sparse matrix algebra. For the assessment of the accuracy for excitation energies, the definition of the ΔE_{THC} error and the ΔE_{CDD}

error is analogous.

4.1.1 THC Error

Table 3 summarizes the THC errors in terms of the mean absolute deviations (MAD), the maximum absolute errors (MAX), and the root mean square deviations (RMSD) for ground state calculations on three different benchmark sets: 1) the Thiel benchmark set,[86] 2) the benchmark set used by Hohenstein et al.[55] in their work on THC-EOM-CC2, and 3) a benchmark set comprised of 27 alanine tetrapeptide conformers.[56] For these sets of small and medium sized molecules, the CDD errors are negligible, *cf.* Section 5 of the SI containing detailed results for the three different benchmark sets.

Table 3: Mean absolute errors for the three different benchmark sets in Refs. 86, 55 and 56. Errors are reported as mean absolute deviations (MAD), maximum absolute errors (MAX), and root mean square deviations (RMSD) as obtained by the MO-THC-SOS-MP2/CC2 methods relative to the MO-RI-SOS-MP2/CC2 results. All calculations are performed with the cc-pVTZ/cc-pVTZ-RI basis set combination.

		ΔE_{THC} / eV	
		SOS-MP2	SOS-CC2
Thiel[86]			
[Abs. Energy]			
	MAD	< 0.001	0.006
	MAX	0.001	0.021
	RMSD	< 0.001	0.008
Hohenstein[55]			
[Abs. Energy]			
	MAD	0.002	0.024
	MAX	0.004	0.055
	RMSD	0.002	0.029
Alanine tetrapeptides[56]			
[Abs. Energy]			
	MAD	< 0.001	0.036
	MAX	0.001	0.039
	RMSD	< 0.001	0.036
[Rel. Energy]			
	MAD	< 0.001	0.004
	MAX	< 0.001	0.043
	RMSD	< 0.001	0.012

Regarding the accuracy of the THC approximation in MP2, MO-THC-SOS-MP2 shows only small deviations of the absolute energies on the order of $\sim 10^{-4} - 10^{-3}$ eV compared to the reference method MO-RI-SOS-MP2. For CC2, however, the use of THC in MO-THC-SOS-CC2 produces errors that are roughly one order of magnitude larger with a maximum error of 0.055 eV. These errors exhibit only modest error cancellation for relative energies, e.g., the RMSD for alanine tetrapeptides[56] reduces from 0.036 eV to 0.012 eV going from absolute to relative energies and the maximum error even slightly increases from 0.039 eV to 0.043 eV The larger THC errors in CC2 compared to MP2 are due to the inclusion of (ov|vv)-type integrals in the THC fitting as these are necessary for the iterative solution of the CC2 equations, whereas MP2 only requires (ov|ov)-type integrals. Fitting the much larger (ov|vv) subspace with the THC grids – originally optimized for MP2[85] – is substantially more challenging which explains the observed increase in the THC error going from MP2 to CC2. Note that these findings regarding larger THC errors for CC2 compared to MP2 are mostly in line with previous work,[50,51] albeit somewhat more pronounced due to our more comprehensive collection of benchmark sets and the use of the larger triple-zeta basis sets (cc-pVTZ/cc-pVTZ-RI) in contrast to the double-zeta basis sets used previously. Nevertheless, since the errors are below ∼0.1 eV ("chemical accuracy"), they are considered to be acceptable in most applications and are still substantially smaller than the method error of CC2 itself.

Going beyond ground state energies, the applicability of THC-SOS-CC2/ADC(2) for excitation energies is assessed by comparing MO-THC-SOS-LR-CC2/ADC(2) with the RI-based reference implementation. The absolute deviations are summarized in Table 4 for excitations to the three lowest-lying singlet (S) and triplet (T) states of the molecules in the Thiel benchmark set,[86] as well as in the benchmark set used by Hohenstein et al.[55] Analogous to the situation for ground state energies, the CDD errors here are also virtually zero, due to the small size of the molecules within the considered benchmark sets. Detailed data including the error for each individual molecule is provided in Section 5 of the SI.

Table 4: Errors for the excitation energies to the three lowest-lying singlet and triplet excited states of the molecules from the benchmark sets from Ref. 86 and Ref. 55. Errors are reported as mean absolute deviations (MAD), maximum absolute errors (MAX), and root mean square deviations (RMSD) from the reference energies obtained with MO-RI-SOS-LR-CC2/ADC(2). All calculations are performed with the cc-pVTZ/cc-pVTZ-RI basis set combination.

		ΔE_{THC} / eV	
		SOS-ADC(2)	SOS-LR-CC2
Thiel[86]			
[Singlet]			
	MAD	0.026	0.019
	MAX	0.190	0.055
	RMSD	0.046	0.023
[Triplet]			
	MAD	0.067	0.022
	MAX	0.320	0.200
	RMSD	0.130	0.034
Hohenstein[55]			
[Singlet]			
	MAD	0.026	0.017
	MAX	0.110	0.091
	RMSD	0.034	0.023
[Triplet]			
	MAD	0.075	0.012
	MAX	0.240	0.035
	RMSD	0.100	0.015

Compared to the results for ground state energies, the application of THC to SOS-ADC(2) and SOS-LR-CC2 produces errors that are significantly larger with mean absolute errors up to 0.075 eV and maximum errors up to 0.320 eV. In particular, triplet excitations are described less accurately compared to singlet excitations, with the largest observed deviation being 0.320 eV for THC-SOS-ADC(2) and 0.200 eV for THC-SOS-LR-CC2. However, these large errors are mostly exceptional, the vast majority (>95 %) of excitation energies are actually within 0.05 eV which we would consider acceptable for most applications. Again, these errors are mostly in line with previous work,[55] although the exceptional cases with errors in excess of 0.1 eV were not seen before and are probably a consequence of the more comprehensive data sets and the use of larger triple-zeta basis sets. Unfortunately, improving the accuracy of THC beyond the limitations imposed by the pre-defined THC grids is not trivial and beyond the scope of this work. Instead, we rather focus on the reduced-scaling local CDD-based reformulation and its advantages compared to the non-local MO-based RI reference algorithms, particularly in terms of accessible molecule sizes.

4.1.2 CDD Error

After having assessed the intrinsic errors associated with LS-THC, we now turn our attention toward the errors introduced by the local Cholesky-MOs and the sparse matrix algebra. Since the errors are only significant for larger molecules, the assessment provided in Tables 5 and 6 is carried out for a series of linear carboxylic acids (LCA_n) and adenine-thymine base pair stacks (AT_n) ranging from 62 atoms (AT_1) to 362 atoms (LCA_{120}).

For the LCA_n model systems, the CDD error increases linearly with the system size for ground state calculations using the CDD-THC-based versions of SOS-MP2 or SOS-CC2, as shown in Table 5. In passing, we note that the THC error also increases linearly with the system size, matching observations in previous work.[47] Moreover, the CDD error is almost identical between the CDD-THC-SOS-MP2 and the CDD-THC-SOS-CC2 method, whereas the THC error is increased going from SOS-MP2 to SOS-CC2, as discussed in the previous section. Overall, it is demonstrated that the CDD error is on the same order as the THC error only for SOS-MP2 energies of the LCA_n series, while in the remaining cases its contribution to the total CDD-THC error is negligible with a maximal error of 1.6 meV.

Regarding the accuracy for excitation energies, Table 6 demonstrates almost constant CDD errors as well as THC errors for the targeted excited states in the LCA_n series beyond LCA_{80}. This behavior is expected since the investigated electronic excitations are localized on the carboxylic acid group.

Table 5: Absolute ΔE_{THC} and ΔE_{CDD} errors for the ground state energies for a series of LCA$_n$ and AT$_n$ molecules. All calculations are performed with the (CDD-)THC-based reformulations of the SOS-MP2 and SOS-CC2 methods and employ the cc-pVTZ/cc-pVTZ-RI basis set combination.

	SOS-MP2		SOS-CC2	
	ΔE_{THC} / meV	ΔE_{CDD} / meV	ΔE_{THC} / meV	ΔE_{CDD} / meV
LCA$_{40}$	0.702	0.076	37.706	0.076
LCA$_{80}$	1.499	0.767	44.305	0.767
LCA$_{120}$	2.214	1.550	51.582	1.610
AT$_1$	2.511	0.007	48.738	0.002
AT$_2$	9.928	0.180	117.397	0.183
AT$_4$	21.910	0.117	233.018	0.167

For the more globular AT$_n$ series, the CDD errors are quite a bit larger with a maximum error of 9.4 meV, since the electronic structure is much less local compared to LCAs resulting in higher total errors from neglecting small (below the sparse algebra thresholds $\vartheta_a = 10^{-7}$ and $\vartheta_m = 10^{-9}$) contributions in the sparse-matrix algebra. Nonetheless, the CDD error are still smaller than the THC error and are not expected to pose significant challenges in practical applications. Moreover, the results can – in contrast to the THC error – always be converged to the desired accuracy using tighter thresholds.

Table 6: Absolute ΔE_{THC} and ΔE_{CDD} errors for the excitation energies to the lowest-lying singlet excited state for a series of LCA$_n$ and AT$_n$ molecules. All calculations are performed with the (CDD-)THC-based reformulations of the SOS-ADC(2) and SOS-LR-CC2 methods and employ the cc-pVTZ/cc-pVTZ-RI basis set combination.

	SOS-ADC(2)		SOS-LR-CC2	
	ΔE_{THC} / meV	ΔE_{CDD} / meV	ΔE_{THC} / meV	ΔE_{CDD} / meV
LCA$_{40}$	13.393	0.002	70.689	0.021
LCA$_{80}$	12.854	0.025	64.477	0.280
LCA$_{120}$	12.731	0.028	53.472	0.230
AT$_1$	21.919	0.002	12.183	0.177
AT$_2$	20.503	3.100	32.366	9.370

Considering the demonstrated influence of the application of the LS-THC approximation together with the CDD approach on the accuracy in Tables 5 and 6, the focus of the remainder of this work is on the computational improvements gained thereby in terms of runtime, asymptotic scaling behavior, and memory requirements.

4.2 Computational Efficiency

The sparsity of the ground state one-electron density is closely related to the energy gap between the highest occupied (HOMO) and the lowest unoccupied MO (LUMO). Given a significant HOMO-LUMO gap, asymptotically linear-scaling variants of many common quantum chemistry methods have been proposed.[87,88] In addition, for excited state calculations the transition density $\mathbf{R}$ with elements $R_{\mu\nu}$ in eqs. 82 and 83 must be considered, for which the sparsity is related to the locality of the excitation. In order to assess the computational complexity of the newly proposed density-based grid-projection algorithm for LS-THC and the resulting CDD-THC-SOS-LR-CC2 and CDD-THC-SOS-ADC(2) methods, a series of LCA_n molecules is selected as a best-case scenario. LCA_n are particularly suitable for the demonstration of the asymptotic time complexity, due to the strong locality of their electronic ground state and first singlet excited state (S_1), which is mostly localized on the carboxyl group. In addition, the time complexity of the presented methods is discussed for three-dimensional systems, here representatively DNA fragments in the AT_n series.

4.2.1 Integral-direct Tensor Hypercontraction

First, the efficiency of the proposed density-based, integral-direct algorithm for the grid-projection of the three-center RI integrals, i.e., for the formation of intermediates $\mathbf{Y}$ in eq. 13, is demonstrated. For this, a comparison between the previously published Cholesky MO-based natural blocking approach (*nat. block.*)[59] and density-based implementations based on the J-engine (*J-engine*),[60] RI-J (*RI-J*),[61] and the newly proposed method in Section 2.2.3 (*this work*) is drawn in Table 7.

For the natural blocking algorithm, the recommended settings from Ref. 59 are used, most notably, attenuated Coulomb RI[40] with an attenuation strength of $\omega = 0.1$. The latter is required to achieve sparsity in the three-center integrals, which makes this approach efficient. In contrast, all density-based approaches use the regular $1/r_{12}$ metric. As previously reported, the natural blocking-based formation of the $\mathbf{Y}$ intermediate approaches linear time

Table 7: Wall time in hours required for the formation of the $\mathbf{Y}^{(\mathrm{oo})}$, $\mathbf{Y}^{(\mathrm{vo})}$, and $\mathbf{Y}^{(\mathrm{vv})}$ intermediates based on the previously published natural blocking (*nat. block.*)[59] approach as well as density-based and integral-direct using the J-engine (*J-engine*),[60] the RI-J algorithm (*RI-J*),[61] and the proposed algorithm (*this work*) from Section 2.2.3. Since the natural blocking approach was optimized for the formation of $\mathbf{Y}$ in the virtual-occupied subspace, only timings for $\mathbf{Y}^{(\mathrm{vo})}$ are reported. Extrapolated values are marked with an asterisk (*).

		cc-pVDZ				cc-pVTZ			
		nat. block.	*J-engine*	*RI-J*	*this work*	*nat. block.*	*J-engine*	*RI-J*	*this work*
$\mathbf{Y}^{(\mathrm{oo})}$									
	LCA_{20}	–	<0.1	<0.1	<0.1	–	0.1	<0.1	<0.1
	LCA_{40}	–	0.1	<0.1	<0.1	–	0.5	0.1	<0.1
	LCA_{80}	–	1.2	0.1	<0.1	–	4.9	0.3	<0.1
	LCA_{160}	–	8.7	0.3	<0.1	–	52.8	1.2	0.4
$\mathbf{Y}^{(\mathrm{vo})}$									
	LCA_{20}	<0.1	0.1	<0.1	<0.1	<0.1	1.0	0.2	<0.1
	LCA_{40}	<0.1	0.7	0.1	<0.1	0.1	9.0	0.8	<0.1
	LCA_{80}	<0.1	9.1	0.5	<0.1	0.2	85.2	3.2	0.3
	LCA_{160}	0.1	69.8	1.9	0.2	0.7	924.0*	13.1	2.7
$\mathbf{Y}^{(\mathrm{vv})}$									
	LCA_{20}	–	0.1	0.1	<0.1	–	1.3	0.4	<0.1
	LCA_{40}	–	1.3	0.2	<0.1	–	11.8	1.5	0.1
	LCA_{80}	–	14.5	1.0	<0.1	–	113.8	5.8	0.4
	LCA_{160}	–	118.0	3.8	0.3	–	1235.4*	24.1	3.2

complexity for the largest molecule sizes and is the fastest among the approaches presented in Table 7, due to the efficiency of the screening in combination with the best-case sparsity of the LCA_n series. In contrast, the RI-J implementation exhibits quadratic scaling due to the considerable sparsity of the $\mathbf{R}^{(Q)}$ slices acting as the density matrix in the Coulomb matrix build, which is leveraged by density- and shell-pair-based screening in the RI-J implementation.[61] Both the J-engine implementation[60] as well as the algorithm proposed in Section 2.2.3 show cubic time complexity since shell-pair sparsity is leveraged while density-based screening is not employed. It is noteworthy, that, while both variants scale cubically with the system size, the J-engine based method has a significantly higher prefactor, which leads to it being slower than all other variants. In contrast, for the proposed – likewise cubically scaling – approach from Section 2.2.3 the prefactor is low enough to render the method competitive to the natural blocking approach even for very large and untypically sparse molecules like LCAs. In turn, the proposed algorithm is especially advantageous for more realistic, less sparse systems. In order to demonstrate the effectiveness of the algorithm, the time complexity for the formation of the $\mathbf{Y}^{(\mathrm{oo})}$, $\mathbf{Y}^{(\mathrm{vo})}$, and $\mathbf{Y}^{(\mathrm{vv})}$ intermediates for LCA$_n$ up to LCA$_{160}$ is shown in Figure 1 (left).

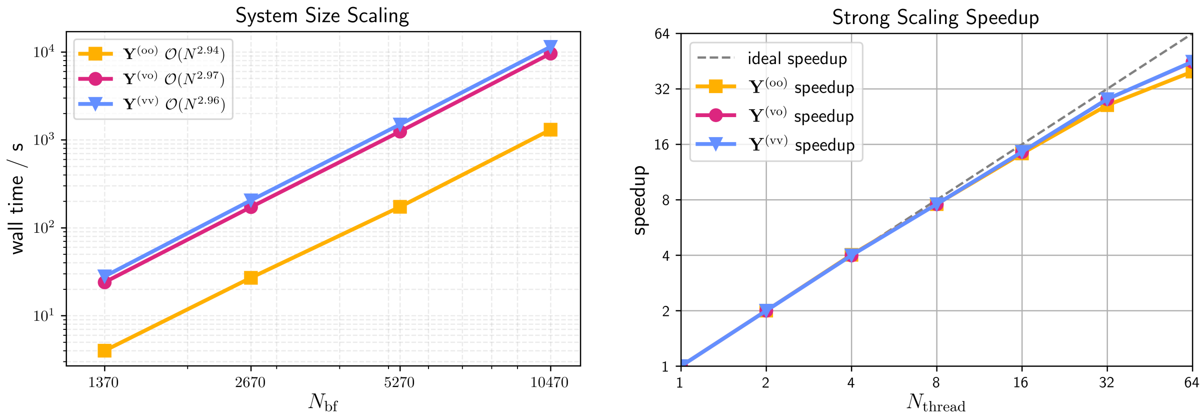

Figure 1: System size scaling (time complexity) presented as a log-log plot (left) and strong scaling speedup (right) of the proposed density-based integral-direct grid-projection algorithm for the cc-pVTZ/cc-pVTZ-RI basis set combination and linear carboxylic acids (LCA$_n$, $n \in \{20, 40, 80, 160\}$) of increasing size. The strong scaling analysis is performed using LCA$_{40}$ on a single dual-socket compute node comprised of 2×32 cores with core performance boost disabled and all cores operating at the base clock speed.

While the asymptotic time complexity is cubic as expected for all MO subspaces (oo, ov, vv), the grid-pruning technique from Matthews[58] reduces the prefactor for forming the $\mathbf{Y}^{(\mathrm{oo})}$ intermediate significantly due to the compactness of the occupied-occupied subspace. Additionally, the strong scaling, i.e., the time-to-solution behavior for the same molecule size but increasing numbers of threads, is assessed and shown in Figure 1 (right). Keeping the individual workload high enough on all processors is key to ideal strong scaling speedup. In this regard, good parallel efficiency and almost ideal strong scaling is observed for up to 32 threads, with only slightly diminishing returns beyond.

In summary, while the proposed grid-projection algorithm has asymptotic cubic time complexity with respect to the systems size, its prefactor is diminutive and it exhibits near-perfect strong scaling speedups. Furthermore, it is competitive to the previously published natural blocking approach while only relying on the shell-pair sparsity of the atomic orbitals, which makes it better suited for non-sparse three-dimensional systems.

4.2.2 THC-SOS-LR-CC2 and THC-SOS-ADC(2)

The computational complexity of the proposed CDD-THC-SOS-LR-CC2 and CDD-THC-SOS-ADC(2) implementations is investigated by taking into account the number of floating-point operations (FLOP) and wall times required to form the singles-manifold CC vector and the matrix-vector product for ground and excited state calculations, respectively. In particular, the number of FLOP and timings for the last iteration of the DIIS procedure is assessed. Note that the FLOP count and timings of LR-SOS-CC2 and SOS-ADC(2) are similar because the steps required to form the matrix-vector products are mostly identical. Figure 2 shows the time complexity measured by the number of FLOP (top) and wall times (bottom) for the ground (left) and the excited state calculations (right) for the MO-RI-SOS-LR-CC2/ADC(2) reference implementations (black) in comparison with the proposed MO/CDD-THC-SOS-LR-CC2/ADC(2) methods (colored) for the LCA$_n$ series.

The MO-based THC-SOS-LR-CC2 and THC-SOS-ADC(2) algorithms allow for a $\mathcal{O}(N^3)$ scaling evaluation of the ground state energy and excitation energies with an effort that is ~19 and ~33 times smaller than the respective $\mathcal{O}(N^4)$ scaling MO-RI reference variant for the largest molecule size considered. Reformulating the equations for the SOS-CC2 single amplitudes in the local Cholesky MO basis, as described in Section 2.3.2 and using sparse linear algebra to solve eq. 64 further decreases the computational effort to ~58-fold. Although the formal scaling behavior is cubic due to steps (e) and (f) in Table 1, a scaling exponent < 3 is observed for the ground state CDD-THC-SOS-CC2 method by leveraging the sparsity, as described in Section 2.3.2. For CDD-THC-SOS-LR-CC2 and CDD-THC-SOS-ADC(2) $\mathcal{O}(N^{2.3})$ scaling is obtained with a ~86-fold diminution of the effort to evaluate the matrix-vector product in eq. 72 for the largest LCA size considered. The observed scaling exponent is slightly larger than the theoretically predicted one reported in Table 2, due to the reduced sparsity of the density matrices within the larger triple-zeta basis. For the smaller

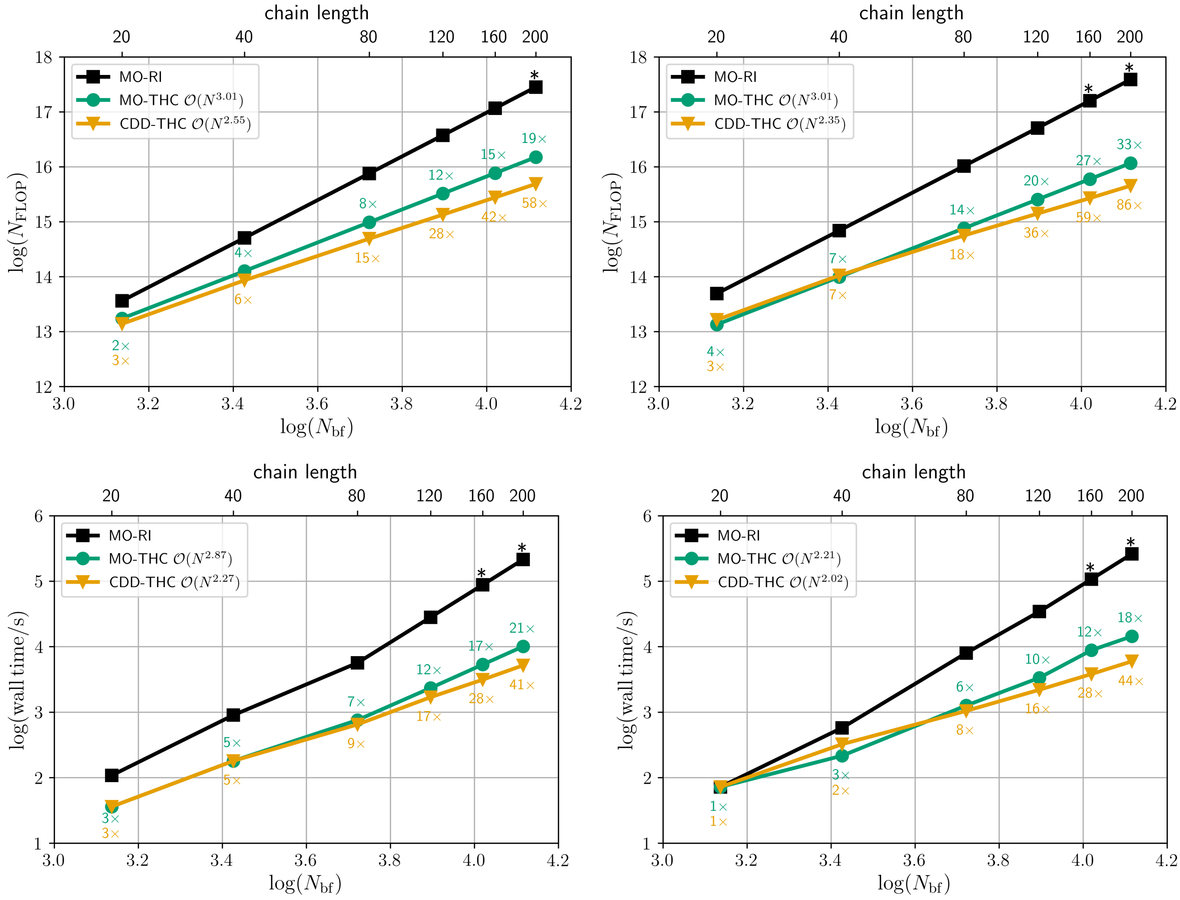

Figure 2: Number of FLOP and wall time required to evaluate the SOS-CC2 single amplitudes (left) and the SOS-LR-CC2/SOS-ADC(2) matrix-vector product (right) for a series of LCA$_n$ ($n \in \{20, 40, 80, 120, 160, 200\}$) molecules using the MO-THC (green) and the CDD-THC-based implementations (orange). Labels represent the FLOP reduction and time speedup compared to the MO-RI-SOS-LR-CC2/ADC(2) implementation (black) and all calculations are performed with the cc-pVTZ/cc-pVTZ-RI basis set combination. Extrapolated values are marked with an asterisk (*).

cc-pVDZ/cc-pVDZ-RI basis set combination, the observed scaling behavior is closer to the predicted quadratic scaling with an observed time complexity of $\mathcal{O}(N^{2.1})$, which is shown in Section 6.1 of the SI.

A significant reduction of the computational effort is likewise achieved for three-dimensional DNA fragments with up to 12 AT pairs. On the one hand, the cubically scaling MO-based THC-SOS-LR-CC2 and THC-SOS-ADC(2) methods grant ∼16-fold and ∼26-fold reduction of the effort for computing the contributions to the single amplitudes in eq. 24 and the matrix-vector product in eq. 37, respectively, as shown in Figure 3. On the other hand, the CDD-THC-SOS-LR-CC2 and CDD-THC-SOS-ADC(2) reformulations allow for the solution of the singles-manifold cluster equation in eq. 64 and the calculation of the matrix-vector product of eq. 72 with a computational effort in terms of FLOP that is ∼27 times smaller than their MO-RI variant in both cases. Consequently, the reduction of the number of FLOP translates to a decrease of the wall times up to 24 times for the ground state and up to 17 times for the excitation energy calculation. Despite the observed $\mathcal{O}(N^{2.5})$ behavior for the calculation of the excitation energies of the AT_n series, the scaling exponent is expected to decrease toward ∼2 in the asymptotic limit.

Overall, employing CDD-THC-SOS-ADC(2) makes it possible to compute the excitation energy to the two lowest-lying singlet excited states of AT_{12} for the cc-pVDZ/cc-pVDZ-RI basis set combination in ∼7.5 days, for which the most time-consuming steps are shown in Figure 4 with their individual contributions to the overall wall time. Most of the time is spent computing the ADC(2) excitation energies, which requires ∼72% of the total computation time, while only ∼18% of the total computation time is spent evaluating the THC $\mathbf{\Gamma}$ matrices. Note that the ADC(2) optimization procedure is converged with thresholds of 10^{-6} and 10^{-5} for the excitation vector and the energy, respectively. The guesses for the DIIS procedure are optimized at the ADC(1) level via Davidson optimization, which requires ∼10% of the total

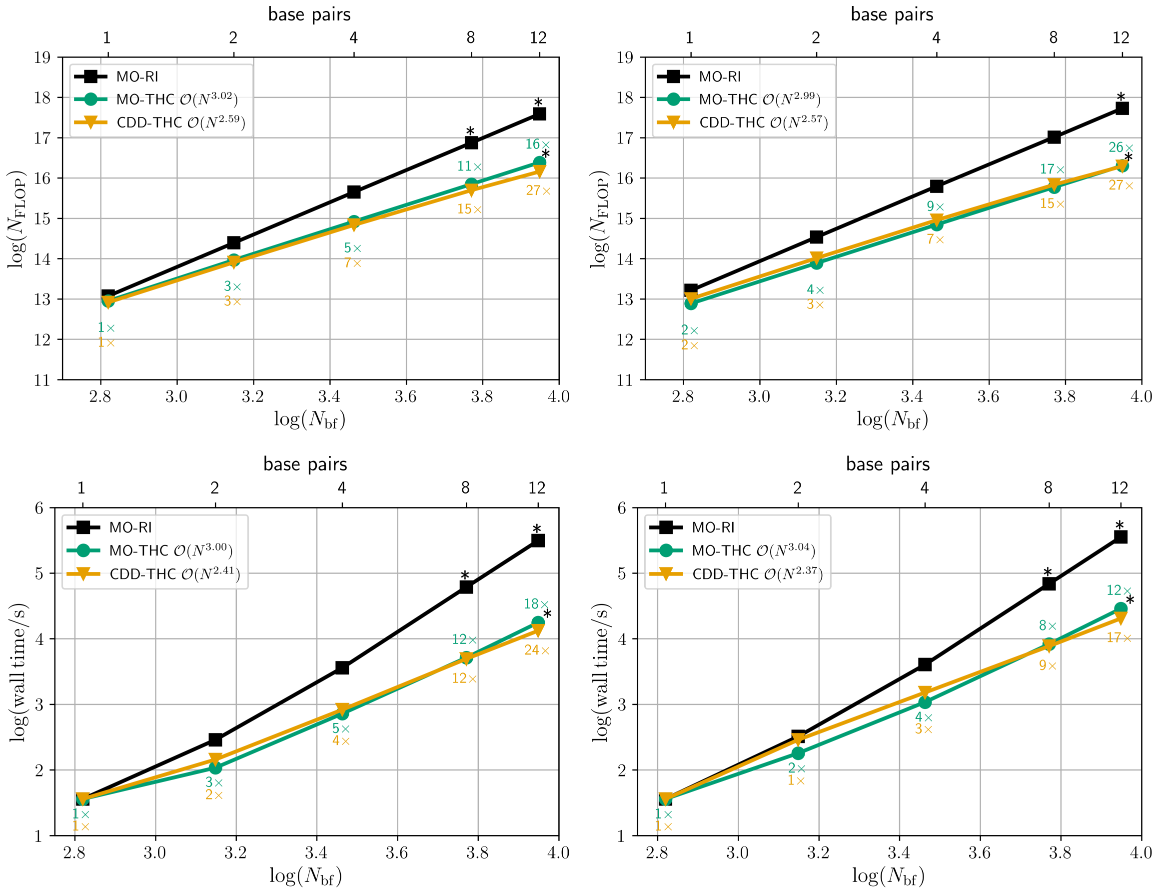

Figure 3: Number of FLOP and wall time required to evaluate the SOS-CC2 single amplitudes (left) and the SOS-LR-CC2/SOS-ADC(2) matrix-vector product (right) for a series of AT$_n$ ($n \in \{1, 2, 4, 8, 12\}$) molecules using the MO-THC (green) and the CDD-THC-based implementations (orange). Labels represent the FLOP reduction and time speedup compared to the MO-RI-SOS-LR-CC2/ADC(2) implementation (black) and all calculations are performed with the cc-pVDZ/cc-pVDZ-RI basis set combination. Extrapolated values are marked with an asterisk (*).

time. The SCF procedure, the calculation of the MP2 energy correction, and the evaluation of the ground state intermediates **E** from eq. 76 together requires ∼1% of the total time.

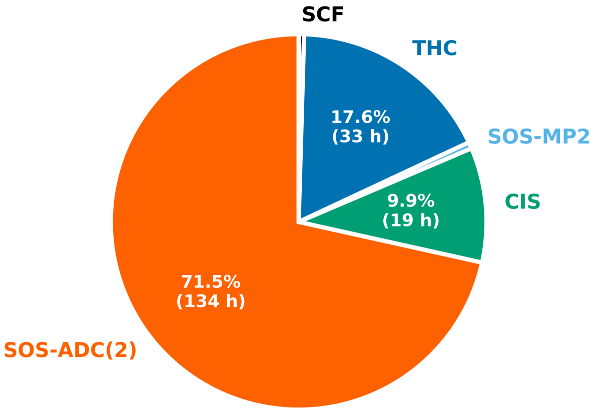

Figure 4: Distribution of the wall time for an illustrative CDD-THC-SOS-ADC(2) calculation of the excitation energies to the two lowest-lying singlet excited states of AT_{12} using the cc-pVDZ/cc-pVDZ-RI basis set combination.

Finally, the memory and storage savings of the THC-based algorithms should be considered which extends the applicability of SOS-ADC(2) and SOS-LR-CC2 to large basis sets and much larger systems, without the need of batching the workload until the ∼1000 atoms scale is reached. Indeed, in the THC-based reformulations only second-order tensors are stored and the space complexity is at most quadratic due to the integral-direct formation of the THC tensors. Moreover, within the CDD-THC-based approach, sparse linear algebra decreases the space complexity of most intermediates, further reducing the memory and storage requirements of the resulting methods. The space complexity is discussed in detail in Section 6.2 of the SI.

5 Conclusion

An efficient reformulation of SOS-CC2 for ground state and SOS-LR-CC2 as well as SOS-ADC(2) for excitation energies is presented. The implementation leverages the THC-factorized representation of the ERI tensor in conjunction with local Cholesky pseudo-MOs from the CDD approach together with block-sparse linear algebra for the resulting tensor contractions. For the expensive formation of the $\mathbf{Y}$ intermediates, which are the grid-projected three-center RI integrals, an efficient near-perfect strong-scaling integral-direct and density-based algorithm is proposed and implemented. The presented algorithm exhibits cubic time complexity with a very low prefactor, rendering it competitive to the previously published natural blocking approach. Further reduction to quadratic or even linear time complexity would require the use of a local metric, as in the natural blocking approach. In this way, an efficient way to obtain the THC tensors for any orbital space is provided, which is leveraged by THC-based reformulations of SOS-MP2, SOS-(LR-)CC2, and SOS-ADC(2) for both ground state and excitation energy calculations.

The derived methods show reasonable accuracy for both absolute and relative ground state energies. However, due to the larger fitting space of the (ov|vv)-type integrals required in SOS-CC2, the mean absolute errors are increased from $\sim 10^{-3}$ to 10^{-2} eV compared to SOS-MP2. The LS-THC errors are even more pronounced for SOS-ADC(2) and SOS-LR-CC2 excitation energies, especially for the triplet states, for which the maximum errors are as large as ~ 0.3 eV. Thus, more work regarding the accuracy of the THC approximation especially for (ov|vv)-type integrals is needed. One possible solution is the use of robust THC,[89] which however entails further computational complexity and is therefore not suitable for the target applications. In addition, a more comprehensive hierarchy of THC specific integration grids would enable finer grained control over the THC error so that more accurate results could be obtained for applications where this is necessary.

In contrast, the additional use of the CDD approach together with the application of sparse linear algebra, does not incur significant further errors, justifying the applicability of the presented methods. In particular, for small molecules the error introduced by the CDD approach sparse algebra is virtually zero as no sparsity can be exploited. For large systems the CDD algorithm proved to yield energies close to the MO-based one with error in the range of $\sim 10^{-5}$ to $\sim 10^{-3}$ eV, which can be rigorously controlled through the associated thresholds. Since both SOS-LR-CC2 and SOS-ADC(2) only involve Coulomb-type integral contractions, no higher than second-order tensors have to be formed and all FLOP-intensive contractions can be performed efficiently by matrix-matrix multiplications. Application of the THC approximation yields cubic scaling MO-based algorithms – contrary to the fourth-order scaling RI-based ones – and grants significant speedups for the evaluation of both ground and excitation energies. For ground state calculations, leveraging Cholesky-MOs and sparse algebra further reduces the computational effort and scaling, hence providing additional speedups. However, the scaling behavior of the time-determining steps and the overall scaling of CDD-THC-SOS-MP2 and CDD-THC-SOS-CC2 is reduced to $\mathcal{O}(N^2)$ only if the $\mathbf{Z}$ fitting tensor is used. Contrary to ground state calculations, the use of Cholesky-MOs and sparse algebra reduces the computational scaling of CDD-THC-SOS-ADC(2)/LR-CC2 to quadratic in the asymptotic limit while decreasing the computational effort up to ~25-fold for DNA fragments with approximately 800 atoms. The reformulation in the Cholesky-MOs basis and the use of sparse algebra within the LS-THC framework also allow for a significant reduction of the memory demand, which has at most quadratic space complexity. The overall demonstrated computational savings, in both FLOP and wall time required for the solution of the energy expressions, as well as the presented memory savings, render the implemented CDD-THC-based algorithms promising candidates for calculations on large molecular systems.

Acknowledgement

The authors acknowledge financial support by the cluster of excellence (EXC2111-390814868) “Munich Center for Quantum Science and Technology” (MCQST), the Deutsche Forschungsgemeinschaft (DFG) under Grant TRR325 “Assembly Controlled Chemical Photocatalysis” (grant no. 444632635), and the Marie Skłodowska-Curie European Training Network “COSINE - COmputational Spectroscopy In Natural sciences and Engineering” (grant no.

765739). C.O. acknowledges additional support as Max-Planck-Fellow at the MPI-FKF Stuttgart. F.H.B. thanks the "Fonds der Chemischen Industrie" (FCI) for a graduate fellowship. The authors thank Y. Lemke (LMU Munich) for helpful discussions and Dr. J. Kussmann (LMU Munich) for providing a development version of the FermiONs++ program package.

Supporting Information Available

Details about the sparsity-conserving grid pruning, explicit expressions for the THC-SOS-CC2 ground state energy and the THC-SOS-LR-CC2/ADC(2) triplet excited states, working equations for the MO-THC-SOS-LR-CC2 method, detailed results for the benchmark sets, and detailed results for the memory scaling of relevant intermediates.

References

(1) Serrano-Andrés, L.; Merchán, M. Quantum Chemistry of the Excited State: 2005 Overview. *J. Mol. Struct. Theochem* **2005**, *729*, 99–108.

(2) Hershenson, H. *Ultraviolet and visible absorption spectra*; Elsevier, 2012.

(3) Rodger, A.; Sanders, K. *Encyclopedia of spectroscopy and spectrometry*; Elsevier, 2017; pp 495–502.

(4) Agarwal, B. K. *X-ray spectroscopy: an introduction*; Springer, 2013; Vol. 15.

(5) Sherrill, C. D.; Schaefer III, H. F. *Advances in quantum chemistry*; Elsevier, 1999; Vol. 34; pp 143–269.

(6) Helgaker, T.; Jorgensen, P.; Olsen, J. *Molecular electronic-structure theory*; John Wiley & Sons, 2013.

(7) Dreuw, A.; Papapostolou, A.; Dempwolff, A. L. Algebraic Diagrammatic Construction Schemes Employing the Intermediate State Formalism: Theory, Capabilities, and Interpretation. *J. Phys. Chem. A* **2023**, *127*, 6635–6646.

(8) Crawford, T. D.; Kumar, A.; Bazanté, A. P.; Di Remigio, R. Reduced-scaling coupled cluster response theory: Challenges and opportunities. *Wiley Interdiscip. Rev. Comput. Mol. Sci.* **2019**, *9*, e1406.

(9) Head-Gordon, M.; Oumi, M.; Maurice, D. Quasidegenerate second-order perturbation corrections to single-excitation configuration interaction. *Mol. Phys.* **1999**, *96*, 593–602.

(10) Casida, M. E. *Recent Advances in Density Functional Methods*; 1999; Vol. 1.

(11) Casida, M. E.; Huix-Rotllant, M. Progress in time-dependent density-functional theory. *Annu. Rev. Phys. Chem.* **2012**, *63*, 287–323.

(12) Dreuw, A.; Head-Gordon, M. Single-reference ab initio methods for the calculation of excited states of large molecules. **2005**, *105*, 4009–4037.

(13) Roos, B. O.; Taylor, P. R.; Sigbahn, P. E. A complete active space SCF method (CASSCF) using a density matrix formulated super-CI approach. *Chem. Phys.* **1980**, *48*, 157–173.

(14) Roos, B. O.; Andersson, K.; Fulscher, M. P.; Malmqvist, P.-A.; Serrano-Andrés, L.; Pierloot, K.; Merchán, M. Multiconfigurational perturbation theory: Applications in electronic spectroscopy. *Adv Chem Phys.* **1996**, *93*, 219–331.

(15) Andersson, K.; Malmqvist, P. A.; Roos, B. O.; Sadlej, A. J.; Wolinski, K. Second-order perturbation theory with a CASSCF reference function. *J. Phys. Chem.* **1990**, *94*, 5483–5488.

(16) Schirmer, J. Beyond the random-phase approximation: A new approximation scheme for the polarization propagator. *Phys. Rev. A* **1982**, *26*, 2395.

(17) Dreuw, A.; Wormit, M. The algebraic diagrammatic construction scheme for the polarization propagator for the calculation of excited states. *Wiley Interdiscip. Rev. Comput. Mol. Sci* **2015**, *5*, 82–95.

(18) Mertins, F.; Schirmer, J. Algebraic propagator approaches and intermediate-state representations. I. The biorthogonal and unitary coupled-cluster methods. *Phys. Rev. A* **1996**, *53*, 2140.

(19) Harbach, P. H.; Wormit, M.; Dreuw, A. The third-order algebraic diagrammatic construction method (ADC (3)) for the polarization propagator for closed-shell molecules: Efficient implementation and benchmarking. *J. Phys. Chem.* **2014**, *141*, 064113.

(20) Sekino, H.; Bartlett, R. J. A linear response, coupled-cluster theory for excitation energy. *Int. J. Quantum Chem.* **1984**, *26*, 255–265.

(21) Koch, H.; Jørgensen, P. Coupled cluster response functions. *J. Phys. Chem.* **1990**, *93*, 3333.

(22) Pedersen, T. B.; Koch, H. Coupled cluster response functions revisited. *J. Phys. Chem.* **1997**, *106*, 8059–8072.

(23) Sneskov, K.; Christiansen, O. Excited state coupled cluster methods. *Wiley Interdiscip. Rev. Comput. Mol. Sci.* **2012**, *2*, 566–584.

(24) Christiansen, O.; Koch, H.; Jørgensen, P. Response functions in the CC3 iterative triple excitation model. *J. Phys. Chem.* **1995**, *103*, 7429–7441.

(25) Christiansen, O.; Koch, H.; Jørgensen, P. The second-order approximate coupled cluster singles and doubles model CC2. *Chem. Phys. Lett.* **1995**, *243*, 409–418.

(26) Grimme, S. Improved second-order Møller-Plesset perturbation theory by separate scaling of parallel-and antiparallel-spin pair correlation energies. *J. Phys. Chem.* **2003**, *118*, 9095–9102.

(27) Jung, Y.; Lochan, R. C.; Dutoi, A. D.; Head-Gordon, M. Scaled opposite-spin second order Møller-Plesset correlation energy: an economical electronic structure method. *J. Phys. Chem.* **2004**, *121*, 9793–9802.

(28) Jung, Y.; Shao, Y.; Head-Gordon, M. Fast evaluation of scaled opposite spin second-order Møller-Plesset correlation energies using auxiliary basis expansions and exploiting sparsity. *J. Comput. Chem.* **2007**, *28*, 1953–1964.

(29) Winter, N. O. C.; Hättig, C. Scaled Opposite-Spin CC2 for Ground and Excited States with Fourth Order Scaling Computational Costs. *J. Phys. Chem.* **2011**, *134*, 184101.

(30) Krauter, C. M.; Pernpointner, M.; Dreuw, A. Application of the scaled-opposite-spin approximation to algebraic diagrammatic construction schemes of second order. *J. Phys. Chem.* **2013**, *138*.

(31) Whitten, J. L. Coulombic Potential Energy Integrals and Approximations. *J. Phys. Chem.* **1973**, *58*, 4496.

(32) Dunlap, B. I.; Connolly, J. W.; Sabin, J. R. On Some Approximations in Applications of Xα Theory. *J. Chem. Phys.* **1979**, *71*, 3396.

(33) Feyereisen, M.; Fitzgerald, G.; Komornicki, A. Use of Approximate Integrals in Ab Initio Theory. An Application in MP2 Energy Calculations. *Chem. Phys. Lett.* **1993**, *208*, 359–363.

(34) Eichkorn, K.; Treutler, O.; Öhm, H.; Häser, M.; Ahlrichs, R. Auxiliary Basis Sets to Approximate Coulomb Potentials. *Chem. Phys. Lett.* **1995**, *240*, 283–290.

(35) Baudin, P.; Marín, J. S.; Cuesta, I. G.; Sánchez De Merás, A. M. J. Calculation of Excitation Energies from the CC2 Linear Response Theory Using Cholesky Decomposition. *J. Phys. Chem.* **2014**, *140*, 104111.

(36) Almlöf, J. Elimination of energy denominators in Møller—Plesset perturbation theory by a Laplace transform approach. *Chemical physics letters* **1991**, *181*, 319–320.

(37) Häser, M.; Almlöf, J. Laplace transform techniques in Møller–Plesset perturbation theory. *The Journal of chemical physics* **1992**, *96*, 489–494.

(38) Sacchetta, F.; Graf, D.; Laqua, H.; Ambroise, M. A.; Kussmann, J.; Dreuw, A.; Ochsenfeld, C. An Effective Sub-Quadratic Scaling Atomic-Orbital Reformulation of the Scaled Opposite-Spin RI-CC2 Ground-State Model Using Cholesky-decomposed Densities and an Attenuated Coulomb Metric. *J. Phys. Chem.* **2022**, *157*, 104104.

(39) Ambroise, M. A.; Sacchetta, F.; Graf, D.; Ochsenfeld, C.; Dreuw, A. Scaled Opposite-Spin Atomic-Orbital Based Algebraic Diagrammatic Construction Scheme for the Polarization Propagator with Asymptotic Linear-Scaling Effort: Theory and Implementation. *J. Phys. Chem.* **2023**, *158*, 124121.

(40) Luenser, A.; Schurkus, H. F.; Ochsenfeld, C. Vanishing-Overhead Linear-Scaling Random Phase Approximation by Cholesky Decomposition and an Attenuated Coulomb-Metric. *J. Chem. Theory Comput.* **2017**, *13*, 1647–1655.

(41) Maurer, S. A.; Clin, L.; Ochsenfeld, C. Cholesky-decomposed density MP2 with density fitting: Accurate MP2 and double-hybrid DFT energies for large systems. *J. Phys. Chem.* **2014**, *140*, 224112.

(42) Glasbrenner, M.; Graf, D.; Ochsenfeld, C. Efficient Reduced-Scaling Second-Order Møller-Plesset Perturbation Theory with Cholesky-Decomposed Densities and an Attenuated Coulomb Metric. *J. Chem. Theory Comput.* **2020**, *16*, 6856–6868.

(43) Beer, M.; Ochsenfeld, C. Efficient linear-scaling calculation of response properties: Density matrix-based Laplace-transformed coupled-perturbed self-consistent field theory. 2008.

(44) Beuerle, M.; Graf, D.; Schurkus, H. F.; Ochsenfeld, C. Efficient calculation of beyond RPA correlation energies in the dielectric matrix formalism. *J. Phys. Chem.* **2018**, *148*, 204104.

(45) Graf, D.; Beuerle, M.; Ochsenfeld, C. Low-scaling self-consistent minimization of a density matrix based random phase approximation method in the atomic orbital space. *J. Chem. Theory Comput.* **2019**, *15*, 4468–4477.

(46) Hohenstein, E. G.; Parrish, R. M.; Martínez, T. J. Tensor Hypercontraction Density Fitting. I. Quartic Scaling Second- and Third-Order Møller-Plesset Perturbation Theory. *J. Chem. Phys.* **2012**, *137*, 044103.

(47) Parrish, R. M.; Hohenstein, E. G.; Martínez, T. J.; Sherrill, C. D. Tensor Hypercontraction. II. Least-squares Renormalization. *J. Chem. Phys.* **2012**, *137*, 224106.

(48) Parrish, R. M.; Hohenstein, E. G.; Martínez, T. J.; Sherrill, C. D. Discrete Variable Representation in Electronic Structure Theory: Quadrature Grids for Least-Squares Tensor Hypercontraction. *J. Chem. Phys.* **2013**, *138*, 194107.

(49) Parrish, R. M.; Hohenstein, E. G.; Schunck, N. F.; Sherrill, C. D.; Martínez, T. J. Exact Tensor Hypercontraction: A Universal Technique for the Resolution of Matrix Elements of Local Finite-Range N-body Potentials in Many-Body Quantum Problems. *Phys. Rev. Lett.* **2013**, *111*, 1–5.

(50) Hohenstein, E. G.; Kokkila, S. I.; Parrish, R. M.; Martínez, T. J. Quartic Scaling Second-Order Approximate Coupled Cluster Singles and Doubles via Tensor Hypercontraction: THC-CC2. *J. Chem. Phys.* **2013**, *138*, 124111.

(51) Parrish, R. M.; Sherrill, C. D.; Hohenstein, E. G.; Kokkila, S. I.; Martínez, T. J. Communication: Acceleration of Coupled Cluster Singles and Doubles via Orbital-Weighted Least-Squares Tensor Hypercontraction. *J. Chem. Phys.* **2014**, *140*, 181102.

(52) Schutski, R.; Zhao, J.; Henderson, T. M.; Scuseria, G. E. Tensor-Structured Coupled Cluster Theory. *J. Chem. Phys.* **2017**, *147*, 184113.

(53) Hohenstein, E. G.; Fales, B. S.; Parrish, R. M.; Martínez, T. J. Rank-Reduced Coupled-Cluster. III. Tensor Hypercontraction of the Doubles Amplitudes. *J. Phys. Chem.* **2022**, *156*, 054102.

(54) Jiang, A.; Turney, J. M.; Schaefer, H. F. Tensor Hypercontraction Form of the Perturbative Triples Energy in Coupled-Cluster Theory. *J. Chem. Theory Comput.* **2023**, *19*, 1476–1486.

(55) Hohenstein, E. G.; Kokkila, S. I.; Parrish, R. M.; Martínez, T. J. Tensor Hypercontraction Equation-of-Motion Second-Order Approximate Coupled Cluster: Electronic Excitation Energies in O(N4) Time. *J. Phys. Chem. B* **2013**, *117*, 12972–12978.

(56) DiStasio, R. A.; Jung, Y.; Head-Gordon, M. A resolution-of-the-identity implementation of the local triatomics-in-molecules model for second-order Møller-Plesset perturbation theory with application to alanine tetrapeptide conformational energies. *J. Chem. Theory Comput.* **2005**, *1*, 862–876.

(57) Matthews, D. A. A Critical Analysis of Least-Squares Tensor Hypercontraction Applied to MP3. *J. Chem. Phys.* **2021**, *154*, 134102.

(58) Matthews, D. A. Improved Grid Optimization and Fitting in Least Squares Tensor Hypercontraction. *J. Chem. Theory Comput.* **2020**, *16*, 1382–1385.

(59) Bangerter, F. H.; Glasbrenner, M.; Ochsenfeld, C. Low-Scaling Tensor Hypercontraction in the Cholesky Molecular Orbital Basis Applied to Second-Order Møller-Plesset Perturbation Theory. *J. Chem. Theory Comput.* **2021**, *17*, 211–221.

(60) Maurer, S. A.; Kussmann, J.; Ochsenfeld, C. Communication: A Reduced Scaling J-

engine Based Reformulation of SOS-MP2 Using Graphics Processing Units. *J. Chem. Phys.* **2014**, *141*.

(61) Kussmann, J.; Laqua, H.; Ochsenfeld, C. Highly Efficient Resolution-of-Identity Density Functional Theory Calculations on Central and Graphics Processing Units. *J. Chem. Theory Comput.* **2021**, *17*, 1512–1521.

(62) Drontschenko, V.; Graf, D.; Laqua, H.; Ochsenfeld, C. Lagrangian-Based Minimal-Overhead Batching Scheme for the Efficient Integral-Direct Evaluation of the RPA Correlation Energy. *J. Chem. Theory Comput.* **2021**, *17*, 5623–5634.

(63) Dunning, T. H. Gaussian basis sets for use in correlated molecular calculations. I. The atoms boron through neon and hydrogen. *J. Chem. Phys.* **1989**, *90*, 1007–1023.

(64) Woon, D. E.; Dunning, T. H. Gaussian basis sets for use in correlated molecular calculations. III. The atoms aluminum through argon. *J. Chem. Phys.* **1993**, *98*, 1358–1371.

(65) Weigend, F.; Köhn, A.; Hättig, C. Efficient Use of the Correlation Consistent Basis Sets in Resolution of the Identity MP2 Calculations. *J. Chem. Phys.* **2002**, *116*, 3175–3183.

(66) Obara, S.; Saika, A. Efficient recursive computation of molecular integrals over Cartesian Gaussian functions. *J. Chem. Phys.* **1986**, *84*, 3963–3974.

(67) Obara, S.; Saika, A. General recurrence formulas for molecular integrals over Cartesian Gaussian functions. *J. Chem. Phys.* **1988**, *89*, 1540–1559.

(68) Laqua, H.; Kussmann, J.; Ochsenfeld, C. Efficient and Linear-Scaling Seminumerical Method for Local Hybrid Density Functionals. *J. Chem. Theory Comput.* **2018**, *14*, 3451–3458.

(69) Laqua, H.; Thompson, T. H.; Kussmann, J.; Ochsenfeld, C. Highly efficient, linear-scaling seminumerical exact-exchange method for graphic processing units. *J. Chem. Theory Comput.* **2020**, *16*, 1456–1468.

(70) Laqua, H.; Kussmann, J.; Ochsenfeld, C. Accelerating seminumerical Fock-exchange calculations using mixed single-and double-precision arithmethic. *J. Phys. Chem.* **2021**, *154*.

(71) Meurer, A.; Smith, C. P.; Paprocki, M.; Čertík, O.; Kirpichev, S. B.; Rocklin, M.; Kumar, A.; Ivanov, S.; Moore, J. K.; Singh, S.; Rathnayake, T.; Vig, S.; Granger, B. E.; Muller, R. P.; Bonazzi, F.; Gupta, H.; Vats, S.; Johansson, F.; Pedregosa, F.; Curry, M. J.; Terrel, A. R.; Roučka, v.; Saboo, A.; Fernando, I.; Kulal, S.; Cimrman, R.; Scopatz, A. SymPy: symbolic computing in Python. *PeerJ Computer Science* **2017**, *3*, e103.

(72) Kussmann, J.; Laqua, H.; Ochsenfeld, C. Highly efficient resolution-of-identity density functional theory calculations on central and graphics processing units. *J. Chem. Theory Comput.* **2021**, *17*, 1512–1521.

(73) Hättig, C.; Weigend, F. CC2 excitation energy calculations on large molecules using the resolution of the identity approximation. *J. Phys. Chem.* **2000**, *113*, 5154–5161.

(74) Hättig, C. Structure optimizations for excited states with correlated second-order methods: CC2 and ADC(2). *Adv. Quantum Chem.* **2005**, *50*, 37–60.

(75) Pulay, P. Improved SCF convergence acceleration. *J. Comput. Chem.* **1982**, *3*, 556–560.

(76) Kats, D.; Schütz, M. A multistate local coupled cluster CC2 response method based on the Laplace transform. *J. Phys. Chem.* **2009**, *131*.

(77) Higham, N. J. Cholesky factorization. *Wiley Interdiscip. Rev. Comput. Stat.* **2009**, *1*, 251–254.

(78) Harbrecht, H.; Peters, M.; Schneider, R. On the low-rank approximation by the pivoted Cholesky decomposition. *Appl. Numer. Math.* **2012**, *62*, 428–440.

(79) Bangerter, F. H.; Glasbrenner, M.; Ochsenfeld, C. Tensor-Hypercontracted MP2 First Derivatives: Runtime and Memory Efficient Computation of Hyperfine Coupling Constants. *J. Chem. Theory Comput.* **2022**, 5233–5245.

(80) Kussmann, J.; Ochsenfeld, C. Pre-selective screening for matrix elements in linear-scaling exact exchange calculations. *J. Chem. Phys.* **2013**, *138*, 134114.

(81) Kussmann, J.; Ochsenfeld, C. Preselective screening for linear-scaling exact exchange-gradient calculations for graphics processing units and general strong-scaling massively parallel calculations. *J. Chem. Theory Comput.* **2015**, *11*, 918–922.

(82) Kussmann, J.; Ochsenfeld, C. Hybrid CPU/GPU Integral Engine for Strong-Scaling Ab Initio Methods. *J. Chem. Theory Comput.* **2017**, *13*, 3153–3159.

(83) Dagum, L.; Menon, R. OpenMP: an industry standard API for shared-memory programming. *Computational Science & Engineering, IEEE* **1998**, *5*, 46–55.

(84) Weigend, F. A Fully Direct RI-HF Algorithm: Implementation, Optimised Auxiliary Basis Sets, Demonstration of Accuracy and Efficiency. *Phys. Chem. Chem. Phys.* **2002**, *4*, 4285–4291.

(85) Kokkila Schumacher, S. I.; Hohenstein, E. G.; Parrish, R. M.; Wang, L. P.; Martínez, T. J. Tensor Hypercontraction Second-Order Møller-Plesset Perturbation Theory: Grid Optimization and Reaction Energies. *J. Chem. Theory Comput.* **2015**, *11*, 3042–3052.

(86) Schreiber, M.; Silva-Junior, M. R.; Sauer, S.; Thiel, W. Benchmarks for electronically excited states: CASPT2, CC2, CCSD, and CC3. *J. Chem. Phys.* **2008**, *128*, 134110.

(87) Maslen, P. E.; Ochsenfeld, C.; White, C. A.; Lee, M. S.; Head-Gordon, M. Locality and sparsity of ab initio one-particle density matrices and localized orbitals. *J. Phys. Chem. A* **1998**, *102*, 2215–2222.

(88) Ochsenfeld, C.; Kussmann, J.; Lambrecht, D. S. Linear-scaling methods in quantum chemistry. *Rev. Comput. Chem.* **2007**, *23*, 1.

(89) Pierce, K.; Rishi, V.; Valeev, E. F. Robust Approximation of Tensor Networks: Application to Grid-Free Tensor Factorization of the Coulomb Interaction. *J. Chem. Theory Comput.* **2021**, *17*, 2217–2230.

TOC Graphic

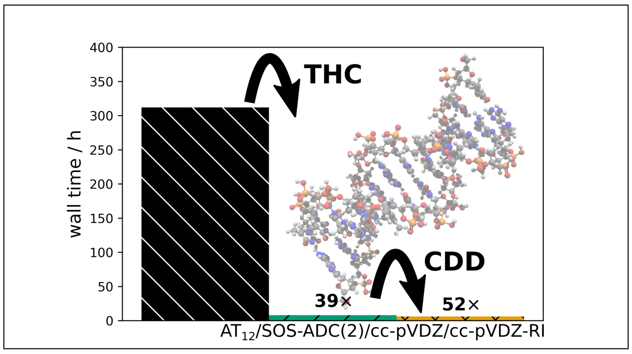

wall time / h
400
350
300
250
200
150
100
50
0
THC
CDD
39×
52×
AT$_{12}$/SOS-ADC(2)/cc-pVDZ/cc-pVDZ-RI

Supporting Information: Efficient Low-scaling Calculation of THC-SOS-LR-CC2 and THC-SOS-ADC(2) Excitation Energies Through Density-based Integral-direct Tensor Hypercontraction

Filippo Sacchetta,[†,¶] Felix H. Bangerter,[†,¶] Henryk Laqua,[†] and Christian Ochsenfeld[*,†,‡]

[†]*Chair of Theoretical Chemistry, Department of Chemistry, University of Munich (LMU), D-81377 Munich, Germany*

[‡]*Max Planck Institute for Solid State Research, D-70569 Stuttgart, Germany*

[¶]*These authors contributed equally to this work.*

E-mail: christian.ochsenfeld@cup.uni-muenchen.de

Contents

1 Sparsity-conserving Grid Pruning

Throughout this work the grid pruning technique by Matthews[S1] was used, which serves two purposes: 1) a removal of unnecessary linear combinations of grid points and 2) the solution of the system of linear equations required for forming the final $\mathbf{\Gamma}$ intermediates. Instead of defining novel parent grids from which to prune from, the hand-optimized grid for the cc-pVTZ basis set by Kokkila Schumacher *et al.*[S2] is used as a parent grid. In the following, the influence of the pruning threshold ε, i.e., the rank threshold in the underlying pivoted Cholesky decomposition (PCD), on the accuracy is assessed. Figure S1 shows the behavior of the error (solid lines) of THC-SOS-RI-MP2 compared to SOS-RI-MP2 as well as the growth of the numerical rank (dashed lines), i.e., the resulting number of grid points N_{grid} after pruning, for LCAs up to 160 carbon atoms.

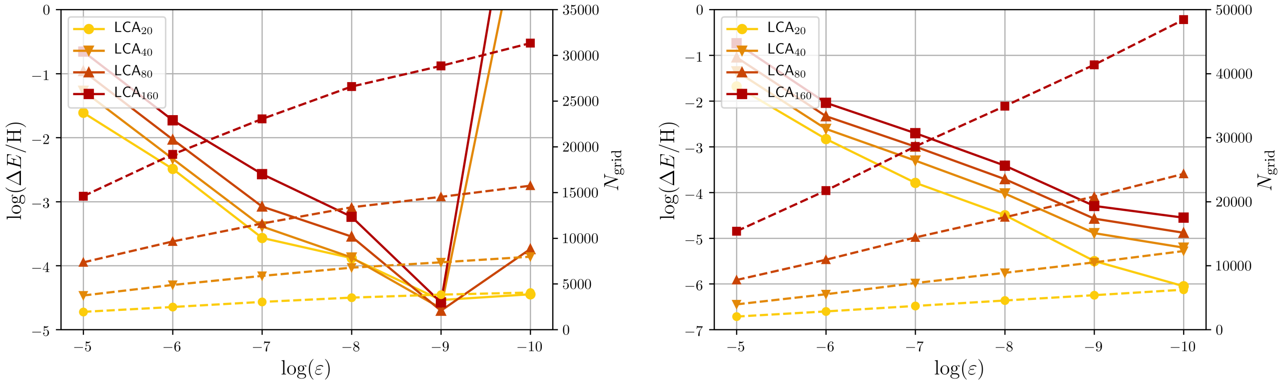

Figure S1: Behavior of the error (solid lines) of THC-SOS-RI-MP2 compared to SOS-RI-MP2 as well as the growth of the numerical rank (dashed lines) with an increasingly tight pruning threshold ε. All calculations were performed with the cc-pVDZ/cc-pVDZ-RI basis set combination and with the hand-optimized grids for the cc-pVDZ (left) and cc-pVTZ (right) basis set as parent grids.

In general a smooth linear reduction of the error and a linear growth of the number of resulting grid points is observed with increasingly tight pruning thresholds. Also, with the hand-optimized grid for the cc-pVDZ basis set serving as a parent grid, the accuracy deteriorates beyond a threshold of 10^{-9}. This has also been observed in previous work by Matthews[S1] and is most likely due to numerical instabilities in the pivoted Cholesky decomposition or the subsequent least-squares fitting. While with the tightest reasonable threshold an acceptable accuracy on the order of 10^{-5} H for absolute energies is achieved for both parent grids, the cc-pVTZ based parent grid was chosen for all calculations in the main part of this paper because of the more well-behaved error. Additionally note that by comparing the errors between the LCAs of different chain length, it is observed that the error grows linearly with the molecule size, as reported previously.[S1,S3]

One potential drawback of the PCD-based grid pruning is the pivoting, which changes the order of the grid points, or rather linear combinations thereof. To increase sparsity in the one-particle density matrix it is custom to reorder atoms according to the reverse Cuthill–McKee (RCM)[S4] algorithm in order to minimize the bandwidth of the resulting density matrix. Likewise, this reordering also reduces the bandwidth of grid-based intermediates like the grid metric **S**, for which the order of the grid points is predominately determined by the order of the atoms since the constituting grids are atom-centered. However, the pivoting in the PCD causes a reordering of the grid points, which results in unwanted fill-in. To preserve sparsity, all resulting grid points after pruning are assigned to their closest neighboring atom and then ordered according to their parent atom in the order determined by the RCM algorithm. Figure S2 demonstrates the described situation for the THC grid metric tensor **S** for LCA$_{80}$ and highlights the importance of the reordering of the grid points after pivoting.

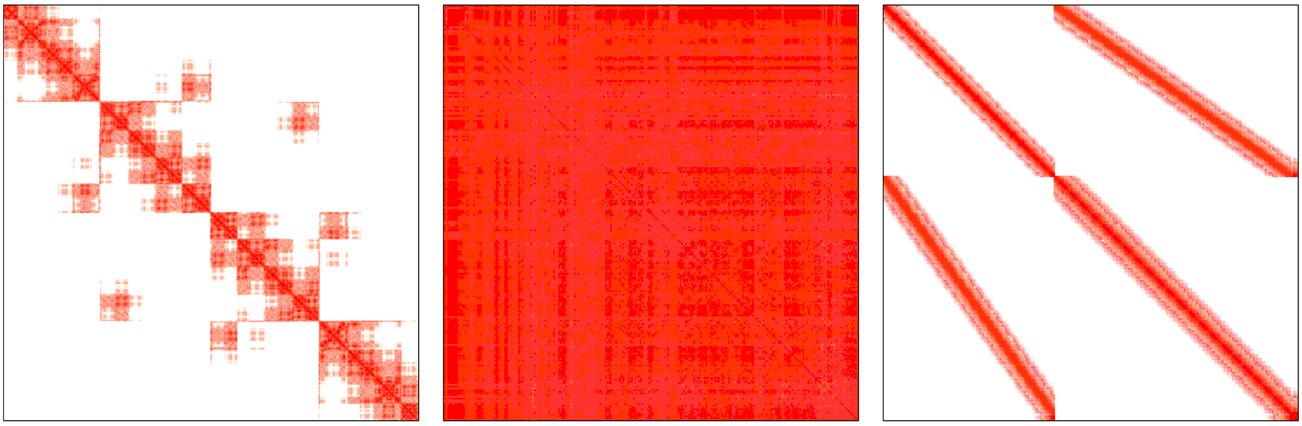

Figure S2: Block sparsity pattern of the THC grid metric **S** in the AO basis before (left) and after pruning (center), as well as after reordering of the grid points (right). Red pixels indicate significant blocks while white pixels represent blocks for which the norm is less than 10^{-10}. All sparsity patterns are obtained from LCA$_{80}$ using the cc-pVDZ basis set and pruning from the hand-optimized cc-pVTZ based grid for the occupied-virtual subspace. Note that the images for the **S** tensor after pruning are scaled up; before pruning **S** was of size 45411 × 45411 and after pruning of size 22906 × 22906.

2 Ground State Equations

In the following the working equations of the ground state expressions for the SOS-CC2 singles amplitudes and the SOS-CC2 energy in terms of the THC-based intermediates defined in the main part of this work are given.

$$\begin{aligned}
\Omega^{\mathrm{G}}_{ai} &= -c_{\mathrm{os}} \sum_{\tau} w_\tau \sum_{cbj} \sum_{\alpha\beta} \sum_{PQRS} \hat{X}^{P,(\mathrm{vo})}_{c} \hat{X}^{P,(\mathrm{vo})}_{i} \Gamma^{P,(\mathrm{vo})}_{\alpha} \Gamma^{Q,(\mathrm{vo})}_{\alpha} \hat{X}^{Q,(\mathrm{vo})}_{b} \hat{X}^{Q,(\mathrm{vo})}_{j} e^{-\epsilon_{ci} t_\tau} e^{-\epsilon_{bj} t_\tau} \\
&\cdot \left(X^{R,(\mathrm{vo})}_{j} X^{R,(\mathrm{vo})}_{b} \Gamma^{R,(\mathrm{vo})}_{\beta} \Gamma^{S,(\mathrm{vv})}_{\beta} \hat{X}^{S,(\mathrm{vv})}_{a} X^{S,(\mathrm{vv})}_{c} \right) \\
&= -c_{\mathrm{os}} \sum_{\tau} \sum_{PS} \hat{X}^{P,(\mathrm{vo})}_{i,\tau} \left[\sum_{\alpha\beta} \sum_{QR} \hat{B}^{PS,(\mathrm{ovvv})}_{\tau} \Gamma^{P,(\mathrm{vo})}_{\alpha} \Gamma^{Q,(\mathrm{vo})}_{\alpha} \hat{A}^{QR,(\mathrm{vovo})}_{\tau} \hat{B}^{QR,(\mathrm{vovo})}_{\tau} \Gamma^{R,(\mathrm{vo})}_{\beta} \Gamma^{S,(\mathrm{vv})}_{\beta} \right] \hat{X}^{S,(\mathrm{vv})}_{a} \\
&= -c_{\mathrm{os}} \sum_{\tau} \sum_{PS} \hat{X}^{P,(\mathrm{vo})}_{i,\tau} M^{PS,(\mathrm{ovvv})}_{\tau} \hat{X}^{S,(\mathrm{vv})}_{a} \qquad (1)
\end{aligned}$$

$$\begin{aligned}
\Omega^{\mathrm{H}}_{ai} &= c_{\mathrm{os}} \sum_{\tau} w_\tau \sum_{kbj} \sum_{\alpha\beta} \sum_{PQRS} \hat{X}^{P,(\mathrm{vo})}_{a} \hat{X}^{P,(\mathrm{vo})}_{k} \Gamma^{P,(\mathrm{vo})}_{\alpha} \Gamma^{Q,(\mathrm{vo})}_{\alpha} \hat{X}^{Q,(\mathrm{vo})}_{b} \hat{X}^{Q,(\mathrm{vo})}_{j} e^{-\epsilon_{ak} t_\tau} e^{-\epsilon_{bj} t_\tau} \\
&\cdot \left(X^{R,(\mathrm{vo})}_{j} X^{R,(\mathrm{vo})}_{b} \Gamma^{R,(\mathrm{vo})}_{\beta} \Gamma^{S,(\mathrm{oo})}_{\beta} X^{S,(\mathrm{oo})}_{k} \hat{X}^{S,(\mathrm{oo})}_{i} \right) \\
&= c_{\mathrm{os}} \sum_{\tau} \sum_{PS} \hat{X}^{P,(\mathrm{vo})}_{a,\tau} \left[\sum_{\alpha\beta} \sum_{QR} \hat{A}^{PS,(\mathrm{vooo})}_{\tau} \Gamma^{P,(\mathrm{vo})}_{\alpha} \Gamma^{Q,(\mathrm{vo})}_{\alpha} \hat{A}^{QR,(\mathrm{vovo})}_{\tau} \hat{B}^{QR,(\mathrm{vovo})}_{\tau} \Gamma^{R,(\mathrm{vo})}_{\beta} \Gamma^{S,(\mathrm{vv})}_{\beta} \right] \hat{X}^{S,(\mathrm{oo})}_{i} \\
&= c_{\mathrm{os}} \sum_{\tau} \sum_{PS} \hat{X}^{P,(\mathrm{vo})}_{a,\tau} N^{PS,(\mathrm{vooo})}_{\tau} \hat{X}^{S,(\mathrm{vv})}_{i} \qquad (2)
\end{aligned}$$

$$\begin{aligned}
E^{\text{SOS-CC2}} &= c_{\mathrm{os}} \sum_{aibj} \sum_{RS} \sum_{\alpha} t_{ai} t_{bj} X^{R,(\mathrm{vo})}_{a} X^{R,(\mathrm{vo})}_{i} \Gamma^{R,(\mathrm{vo})}_{\alpha} \Gamma^{S,(\mathrm{vo})}_{\alpha} X^{S,(\mathrm{vo})}_{b} X^{S,(\mathrm{vo})}_{j} \\
&- c_{\mathrm{os}} \sum_{\tau} w_\tau \sum_{aibj} \sum_{PQRS} \sum_{\alpha\beta} \hat{X}^{P,(\mathrm{vo})}_{a} \hat{X}^{P,(\mathrm{vo})}_{i} \Gamma^{P,(\mathrm{vo})}_{\alpha} \Gamma^{Q,(\mathrm{vo})}_{\alpha} \hat{X}^{Q,(\mathrm{vo})}_{b} \hat{X}^{Q,(\mathrm{vo})}_{j} e^{-\epsilon_{ai} t_\tau} e^{-\epsilon_{bj} t_\tau} \\
&\cdot \left(\hat{X}^{R,(\mathrm{vo})}_{a} \hat{X}^{R,(\mathrm{vo})}_{i} \Gamma^{R,(\mathrm{vo})}_{\beta} \Gamma^{S,(\mathrm{vo})}_{\beta} \hat{X}^{S,(\mathrm{vo})}_{b} \hat{X}^{S,(\mathrm{vo})}_{j} \right) \\
&= c_{\mathrm{os}} \sum_{aibj} \sum_{RS} \sum_{\alpha} t_{ai} t_{bj} X^{R,(\mathrm{vo})}_{a} X^{R,(\mathrm{vo})}_{i} \Gamma^{R,(\mathrm{vo})}_{\alpha} \Gamma^{S,(\mathrm{vo})}_{\alpha} X^{S,(\mathrm{vo})}_{b} X^{S,(\mathrm{vo})}_{j} \\
&- c_{\mathrm{os}} \sum_{\tau} w_\tau \sum_{\alpha\beta} \hat{C}^{\alpha\beta,(\mathrm{ovov})}_{\tau} \hat{C}^{\alpha\beta,(\mathrm{ovov})}_{\tau} \qquad (3)
\end{aligned}$$

3 Excited State Equations - Triplet States

The matrix-vector products for triplet (T) states are given by

$$\begin{aligned}
\sigma_{ai}^{\text{SOS-CC2,(T)}} &= \hat{F}_{ab}R_{bi} - R_{aj}\hat{F}_{ji} - \sum_{ck}(ac\hat{|}ki)R_{ck} - c_{\text{os}}\sum_{b}E_{ab}R_{bi} - c_{\text{os}}\sum_{j}R_{aj}E_{ji} \\
&+ \sigma_{ai}^{\text{G,(T)}} + \sigma_{ai}^{\text{H,(T)}} + \sigma_{ai}^{\text{I,(T)}} \\
\sigma_{ai}^{\text{SOS-ADC(2),(T)}} &= (\epsilon_a - \epsilon_i)R_{ai} - \sum_{ck}(ac|ki)R_{ck} - c_{\text{os}}\sum_{b}E_{ab}R_{bi} - c_{\text{os}}\sum_{j}R_{aj}E_{ji} \\
&+ \sigma_{ai}^{\text{G,(T)}} + \sigma_{ai}^{\text{H,(T)}} + \sigma_{ai}^{\text{I,(T)}} \qquad (4)
\end{aligned}$$

The derivation of the singlet equations is discussed in the main part of this work. In order to derive the equations for the triplet states it is necessary to consider the following spin-symmetry relationships for singlet

$$R_{a_\alpha i_\alpha} = R_{a_\beta i_\beta} \qquad (5)$$

and triplet states

$$R_{a_\alpha i_\alpha} = -R_{a_\beta i_\beta} \qquad (6)$$

where α, β here are the spin of the electrons. Accordingly, the intermediates of the matrix-vector product are given by

$$
\begin{aligned}
\bar{M}_{\tau}^{PS,(\mathrm{ovvv})} &= -\bar{M}_{\tau,(1)}^{PS,(\mathrm{ovvv})} + \bar{M}_{\tau,(2)}^{PS,(\mathrm{ovvv})} \\
&= -\hat{B}_{\tau}^{PS,(\mathrm{ovvv})}\bar{D}_{\tau}^{PS,(\mathrm{ovvv})} + \bar{B}_{\tau}^{PS,(\mathrm{ovvv})}\hat{D}_{\tau}^{PS,(\mathrm{ovvv})} \qquad (7)
\end{aligned}
$$

$$
\begin{aligned}
\bar{N}_{\tau}^{PS,(\mathrm{vooo})} &= -\bar{N}_{\tau,(1)}^{PS,(\mathrm{vooo})} + \bar{N}_{\tau,(2)}^{PS,(\mathrm{vooo})} \\
&= -\hat{A}_{\tau}^{PS,(\mathrm{vooo})}\bar{D}_{\tau}^{PS,(\mathrm{vooo})} + \bar{A}_{\tau}^{PS,(\mathrm{vooo})}\hat{D}_{\tau}^{PS,(\mathrm{vooo})} \qquad (8)
\end{aligned}
$$

$$
\begin{aligned}
\sigma_{ai}^{\mathrm{I,SOS\text{-}CC2,(T)}} &= +c_{\mathrm{os}}\sum_{bj} t_{aibj}^{\mathrm{os}}\bar{F}_{jb} + \sum_{bj} c_{\mathrm{os}} R_{ij}^{ab}(\bar{\omega})\hat{F}_{jb} \\
&= +c_{\mathrm{os}}\sum_{\tau}\sum_{P}\hat{X}_{a,\tau}^{P,(\mathrm{vo})}\hat{X}_{i,\tau}^{P,(\mathrm{vo})}\bar{I}_{\tau,(1)}^{P,(\mathrm{vo})} \\
&\quad - c_{\mathrm{os}}\sum_{\tau} e^{\bar{\omega}t_{\tau}}\sum_{P}\left[\bar{X}_{a,\tau}^{P,(\mathrm{vo})}\hat{X}_{i,\tau}^{P,(\mathrm{vo})} + \hat{X}_{a,\tau}^{P,(\mathrm{vo})}\bar{X}_{i,\tau}^{P,(\mathrm{vo})}\right]\hat{I}_{\tau}^{P,(\mathrm{vo})} \qquad (9)
\end{aligned}
$$

$$
\begin{aligned}
\sigma_{ai}^{\mathrm{I,SOS\text{-}ADC(2),(T)}} &= +\frac{c_{\mathrm{os}}}{2}\sum_{bj} t_{aibj}^{\mathrm{os}}\bar{F}_{jb} - \frac{c_{\mathrm{os}}}{2}\sum_{bj}(ib|ja)\Big[\sum_{ck} t_{ckbj}^{\mathrm{os}} R_{ck}\Big] \\
&= +\frac{c_{\mathrm{os}}}{2}\sum_{\tau}\sum_{P} X_{a,\tau}^{P,(\mathrm{vo})} X_{i,\tau}^{P,(\mathrm{vo})}\bar{I}_{\tau,(1)}^{P,(\mathrm{vo})} - \frac{c_{\mathrm{os}}}{2}\sum_{bj}(ib|ja)\bar{I}_{bj} \qquad (10)
\end{aligned}
$$

where for triplet states

$$
\bar{F}_{ib} = -(jc\hat{|}kb)R_{ck} \qquad (11)
$$

4 Working Equations for the MO-based algorithm

Table S1: Working equations of the intermediates for the solution of eq. 24 and 29 in the main part of this work. Notice that, for SOS-MP2 calculations, $t_{ai} = 0$ and only eq. (a)-(d) need to be solved.

	Intermediate	Formal Scaling
(a)	$\hat{A}_{\tau}^{QR,(\mathrm{vovo})} = \hat{X}_{i,\tau}^{Q,(\mathrm{vo})} X_{i}^{R,(\mathrm{vo})}$	$N_{\mathrm{occ}} N_{\text{grid-ov}}^{2}$
(b)	$\hat{B}_{\tau}^{QR,(\mathrm{vovo})} = \hat{X}_{a,\tau}^{Q,(\mathrm{vo})} X_{a}^{R,(\mathrm{vo})}$	$N_{\mathrm{virt}} N_{\text{grid-ov}}^{2}$
(c)	$\hat{A}_{\tau}^{PS,(\mathrm{vooo})} = \hat{X}_{i,\tau}^{P,(\mathrm{vo})} X_{i}^{S,(\mathrm{oo})}$	$N_{\mathrm{occ}} N_{\text{grid-ov}} N_{\text{grid-oo}}$
(d)	$\hat{B}_{\tau}^{PS,(\mathrm{ovvv})} = \hat{X}_{a,\tau}^{P,(\mathrm{vo})} X_{a}^{S,(\mathrm{vv})}$	$N_{\mathrm{virt}} N_{\text{grid-ov}} N_{\text{grid-vv}}$
(e)	$\hat{Y}_{a}^{S,(\mathrm{oo})} = \hat{X}_{a,\tau}^{P,(\mathrm{vo})} \hat{N}_{\tau}^{PS,(\mathrm{vooo})}$	$N_{\mathrm{virt}} N_{\text{grid-ov}} N_{\text{grid-oo}}$
(f)	$\hat{Y}_{i}^{S,(\mathrm{vv})} = \hat{X}_{i,\tau}^{P,(\mathrm{vo})} \hat{M}_{\tau}^{PS,(\mathrm{ovvv})}$	$N_{\mathrm{occ}} N_{\text{grid-ov}} N_{\text{grid-vv}}$
(g)	$\hat{I}_{j,\tau}^{P,(\mathrm{ov})} = \hat{X}_{b,\tau}^{P,(\mathrm{vo})} \hat{F}_{jb}$	$N_{\mathrm{virt}} N_{\mathrm{occ}} N_{\text{grid-ov}}$
(h)	$\hat{n}_{\tau}^{P,(\mathrm{ov})} = \hat{X}_{j,\tau}^{P,(\mathrm{vo})} \hat{I}_{j,\tau}^{P,(\mathrm{ov})}$	$N_{\mathrm{occ}} N_{\text{grid-ov}}$

Table S2: Working equations of the intermediates for the solution of the MO-THC-SOS-LR-CC2 excitation energy calculations.

	Intermediate	Formal Scaling
(a)	$\bar{A}_{\tau}^{QR,(\mathrm{vovo})} = \bar{X}_{i,\tau}^{Q,(\mathrm{vo})} X_{i}^{R,(\mathrm{vo})}$	$N_{\mathrm{occ}} N_{\text{grid-ov}}^{2}$
(b)	$\bar{B}_{\tau}^{QR,(\mathrm{vovo})} = \bar{X}_{a,\tau}^{Q,(\mathrm{vo})} X_{a}^{R,(\mathrm{vo})}$	$N_{\mathrm{virt}} N_{\text{grid-ov}}^{2}$
(c)	$\bar{A}_{\tau}^{PS,(\mathrm{vooo})} = \bar{X}_{i,\tau}^{P,(\mathrm{vo})} X_{i}^{S,(\mathrm{oo})}$	$N_{\mathrm{occ}} N_{\text{grid-ov}} N_{\text{grid-oo}}$
(d)	$\bar{B}_{\tau}^{PS,(\mathrm{ovvv})} = \bar{X}_{a,\tau}^{P,(\mathrm{vo})} X_{a}^{S,(\mathrm{vv})}$	$N_{\mathrm{virt}} N_{\text{grid-ov}} N_{\text{grid-vv}}$
(e)	$\bar{Y}_{a}^{S,(\mathrm{oo})} = \hat{X}_{a,\tau}^{P,(\mathrm{vo})} \hat{N}_{\tau}^{PS,(\mathrm{vooo})}$	$N_{\mathrm{virt}} N_{\text{grid-ov}} N_{\text{grid-oo}}$
(f)	$\bar{Y}_{i}^{S,(\mathrm{vv})} = \hat{X}_{i,\tau}^{P,(\mathrm{vo})} \hat{M}_{\tau}^{PS,(\mathrm{ovvv})}$	$N_{\mathrm{occ}} N_{\text{grid-ov}} N_{\text{grid-vv}}$

5 Detailed Results – Accuracy

In the following, detailed results for the accuracy of the proposed MO/CDD-THC-SOS variants of the MP2, CC2, LR-CC2, and ADC(2) methods are given. Section 5.1 summarizes the ground state energies of 27 tetraalanine conformers[S5] as obtained with the THC-SOS-MP2 and the THC-SOS-CC2 method in Tables S3 and S5, respectively. The resulting relative energies and the associated method errors are given in Tables S4 and S6. Additionally, the performance of the proposed methods is assessed for the Thiel benchmark set[S6] in Section 5.2 for both ground and excitation energies in Sections 5.2.1 and 5.2.2, respectively. The ground state energies relative to the MO-RI-SOS-based reference implementation are given in Table S7 for MP2 and in Table S8 for CC2. For the comparison of the excitation energies both the three lowest-lying singlet (S) and triplet states (T) are considered in Tables S9–S12 for ADC(2) and LR-CC2. Likewise, the same analysis is shown for the benchmark set used by Hohenstein et al.[S7] in their work on THC-EOM-CC2 in Tables S13–S18 in Section 5.3.

5.1 Tetraalanine Conformer Benchmark Set

Table S3: Detailed results for the ground state energies of the 27 conformers in the tetraalanine conformer benchmark set.[S5] Errors of the MO- and CDD-based THC-SOS-MP2 methods are reported as deviations from the RI-based reference implementation. All calculations are performed with the cc-pVTZ/cc-pVTZ-RI basis set combination.

conformer	E_{RI} / H	E_{THC} / H	ΔE_{THC} / H	$E_{\text{CDD-THC}}$ / H	$\Delta E_{\text{CDD-THC}}$ / H
1	$-3.667\,064$	$-3.667\,049$	$1.52{\times}10^{-5}$	$-3.667\,048$	1.5×10^{-5}
2	$-3.668\,537$	$-3.668\,520$	$1.71{\times}10^{-5}$	$-3.668\,520$	1.7×10^{-5}
3	$-3.674\,690$	$-3.674\,671$	$1.92{\times}10^{-5}$	$-3.674\,671$	1.9×10^{-5}
4	$-3.668\,832$	$-3.668\,819$	$1.38{\times}10^{-5}$	$-3.668\,818$	1.4×10^{-5}
5	$-3.668\,713$	$-3.668\,699$	$1.42{\times}10^{-5}$	$-3.668\,699$	1.4×10^{-5}
6	$-3.672\,337$	$-3.672\,329$	$7.37{\times}10^{-6}$	$-3.672\,329$	7.4×10^{-6}
7	$-3.674\,497$	$-3.674\,482$	$1.55{\times}10^{-5}$	$-3.674\,482$	1.6×10^{-5}
8	$-3.674\,896$	$-3.674\,873$	$2.25{\times}10^{-5}$	$-3.674\,873$	2.3×10^{-5}
9	$-3.674\,377$	$-3.674\,362$	$1.51{\times}10^{-5}$	$-3.674\,362$	1.5×10^{-5}
10	$-3.675\,256$	$-3.675\,246$	$1.05{\times}10^{-5}$	$-3.675\,246$	1.1×10^{-5}
11	$-3.675\,327$	$-3.675\,304$	$2.24{\times}10^{-5}$	$-3.675\,304$	2.2×10^{-5}
12	$-3.675\,834$	$-3.675\,814$	$1.99{\times}10^{-5}$	$-3.675\,814$	2.0×10^{-5}
13	$-3.670\,409$	$-3.670\,389$	$1.99{\times}10^{-5}$	$-3.670\,389$	2.0×10^{-5}
14	$-3.670\,941$	$-3.670\,924$	$1.70{\times}10^{-5}$	$-3.670\,924$	1.7×10^{-5}
15	$-3.676\,361$	$-3.676\,345$	$1.56{\times}10^{-5}$	$-3.676\,345$	1.6×10^{-5}
16	$-3.673\,609$	$-3.673\,596$	$1.29{\times}10^{-5}$	$-3.673\,596$	1.3×10^{-5}
17	$-3.675\,224$	$-3.675\,213$	$1.09{\times}10^{-5}$	$-3.675\,213$	1.1×10^{-5}
18	$-3.672\,219$	$-3.672\,201$	$1.81{\times}10^{-5}$	$-3.672\,201$	1.8×10^{-5}
19	$-3.672\,817$	$-3.672\,805$	$1.23{\times}10^{-5}$	$-3.672\,805$	1.2×10^{-5}
20	$-3.672\,345$	$-3.672\,322$	$2.34{\times}10^{-5}$	$-3.672\,322$	2.4×10^{-5}
21	$-3.673\,284$	$-3.673\,269$	$1.51{\times}10^{-5}$	$-3.673\,269$	1.5×10^{-5}
22	$-3.674\,540$	$-3.674\,531$	$9.07{\times}10^{-6}$	$-3.674\,530$	9.2×10^{-6}
23	$-3.674\,351$	$-3.674\,339$	$1.21{\times}10^{-5}$	$-3.674\,339$	1.2×10^{-5}
24	$-3.673\,938$	$-3.673\,932$	$6.20{\times}10^{-6}$	$-3.673\,932$	6.3×10^{-6}
25	$-3.672\,778$	$-3.672\,760$	$1.77{\times}10^{-5}$	$-3.672\,760$	1.8×10^{-5}
26	$-3.618\,773$	$-3.618\,761$	$1.15{\times}10^{-5}$	$-3.618\,761$	1.2×10^{-5}
27	$-3.673\,077$	$-3.673\,052$	$2.46{\times}10^{-5}$	$-3.673\,052$	2.5×10^{-5}

Table S4: Detailed results for the relative energies of the 27 conformers in the tetraalanine conformer benchmark set.[S5] Errors of the MO- and CDD-based THC-SOS-MP2 methods are reported as deviations from the RI-based reference implementation. All calculations are performed with the cc-pVTZ/cc-pVTZ-RI basis set combination.

conformer	E_{RI} / H	E_{THC} / H	ΔE_{THC} / H	$E_{\text{CDD-THC}}$ / H	$\Delta E_{\text{CDD-THC}}$ / H
1	0.001 473	0.001 471	1.9×10^{-6}	0.001 471	1.9×10^{-6}
2	0.006 153	0.006 151	2.2×10^{-6}	0.006 151	2.0×10^{-6}
3	−0.005 858	−0.005 852	5.4×10^{-6}	−0.005 853	5.2×10^{-6}
4	−0.000 119	−0.000 119	4.0×10^{-7}	−0.000 119	3.7×10^{-7}
5	0.003 623	0.003 630	6.9×10^{-6}	0.003 630	7.0×10^{-6}
6	0.002 160	0.002 152	8.2×10^{-6}	0.002 152	8.2×10^{-6}
7	0.000 399	0.000 392	7.0×10^{-6}	0.000 392	7.0×10^{-6}
8	−0.000 519	−0.000 511	7.4×10^{-6}	−0.000 511	7.4×10^{-6}
9	0.000 879	0.000 884	4.6×10^{-6}	0.000 884	4.5×10^{-6}
10	0.000 070	0.000 058	1.2×10^{-5}	0.000 059	1.2×10^{-5}
11	0.000 507	0.000 510	2.5×10^{-6}	0.000 510	2.5×10^{-6}
12	−0.005 425	−0.005 425	4.7×10^{-8}	−0.005 425	2.0×10^{-7}
13	0.000 532	0.000 535	2.9×10^{-6}	0.000 535	3.0×10^{-6}
14	0.005 420	0.005 421	1.4×10^{-6}	0.005 421	1.5×10^{-6}
15	−0.002 752	−0.002 749	2.7×10^{-6}	−0.002 749	2.7×10^{-6}
16	0.001 615	0.001 617	2.0×10^{-6}	0.001 617	2.0×10^{-6}
17	−0.003 005	−0.003 012	7.2×10^{-6}	−0.003 012	7.4×10^{-6}
18	0.000 598	0.000 603	5.8×10^{-6}	0.000 604	5.9×10^{-6}
19	−0.000 472	−0.000 483	1.1×10^{-5}	−0.000 483	1.1×10^{-5}
20	0.000 939	0.000 947	8.2×10^{-6}	0.000 947	8.4×10^{-6}
21	0.001 256	0.001 262	6.1×10^{-6}	0.001 262	6.0×10^{-6}
22	−0.000 188	−0.000 191	3.1×10^{-6}	−0.000 191	3.0×10^{-6}
23	−0.000 413	−0.000 407	5.9×10^{-6}	−0.000 407	5.9×10^{-6}
24	−0.001 161	−0.001 172	1.2×10^{-5}	−0.001 172	1.2×10^{-5}
25	−0.054 005	−0.053 999	6.2×10^{-6}	−0.053 999	6.1×10^{-6}
26	0.054 304	0.054 291	1.3×10^{-5}	0.054 291	1.3×10^{-5}
27	−0.006 013	−0.006 004	9.4×10^{-6}	−0.006 004	9.3×10^{-6}

Table S5: Detailed results for the ground state energies of the 27 conformers in the tetraalanine conformer benchmark set.[S5] Errors of the MO- and CDD-based THC-SOS-CC2 methods are reported as deviations from the RI-based reference implementation. All calculations are performed with the cc-pVTZ/cc-pVTZ-RI basis set combination.

conformer	E_{RI} / H	E_{THC} / H	ΔE_{THC} / H	$E_{\text{CDD-THC}}$ / H	$\Delta E_{\text{CDD-THC}}$ / H
1	$-3.704\,518$	$-3.703\,223$	1.3×10^{-3}	$-3.703\,222$	1.3×10^{-3}
2	$-3.706\,243$	$-3.704\,903$	1.3×10^{-3}	$-3.704\,903$	1.3×10^{-3}
3	$-3.713\,146$	$-3.711\,714$	1.4×10^{-3}	$-3.711\,714$	1.4×10^{-3}
4	$-3.706\,538$	$-3.705\,272$	1.3×10^{-3}	$-3.705\,272$	1.3×10^{-3}
5	$-3.706\,265$	$-3.704\,960$	1.3×10^{-3}	$-3.704\,960$	1.3×10^{-3}
6	$-3.710\,283$	$-3.708\,942$	1.3×10^{-3}	$-3.708\,942$	1.3×10^{-3}
7	$-3.712\,606$	$-3.711\,233$	1.4×10^{-3}	$-3.711\,233$	1.4×10^{-3}
8	$-3.713\,154$	$-3.711\,794$	1.4×10^{-3}	$-3.711\,794$	1.4×10^{-3}
9	$-3.712\,665$	$-3.711\,314$	1.4×10^{-3}	$-3.711\,314$	1.4×10^{-3}
10	$-3.713\,348$	$-3.712\,029$	1.3×10^{-3}	$-3.712\,029$	1.3×10^{-3}
11	$-3.713\,740$	$-3.712\,329$	1.4×10^{-3}	$-3.712\,329$	1.4×10^{-3}
12	$-3.714\,224$	$-3.712\,841$	1.4×10^{-3}	$-3.712\,841$	1.4×10^{-3}
13	$-3.708\,323$	$-3.706\,938$	1.4×10^{-3}	$-3.706\,937$	1.4×10^{-3}
14	$-3.708\,678$	$-3.707\,366$	1.3×10^{-3}	$-3.707\,366$	1.3×10^{-3}
15	$-3.714\,620$	$-3.713\,261$	1.4×10^{-3}	$-3.713\,261$	1.4×10^{-3}
16	$-3.711\,825$	$-3.710\,421$	1.4×10^{-3}	$-3.710\,421$	1.4×10^{-3}
17	$-3.713\,875$	$-3.712\,424$	1.5×10^{-3}	$-3.712\,424$	1.5×10^{-3}
18	$-3.710\,408$	$-3.709\,053$	1.4×10^{-3}	$-3.709\,053$	1.4×10^{-3}
19	$-3.711\,024$	$-3.709\,635$	1.4×10^{-3}	$-3.709\,635$	1.4×10^{-3}
20	$-3.710\,394$	$-3.709\,030$	1.4×10^{-3}	$-3.709\,030$	1.4×10^{-3}
21	$-3.711\,490$	$-3.710\,084$	1.4×10^{-3}	$-3.710\,084$	1.4×10^{-3}
22	$-3.712\,674$	$-3.711\,332$	1.3×10^{-3}	$-3.711\,332$	1.3×10^{-3}
23	$-3.712\,438$	$-3.711\,118$	1.3×10^{-3}	$-3.711\,118$	1.3×10^{-3}
24	$-3.711\,950$	$-3.710\,596$	1.4×10^{-3}	$-3.710\,596$	1.4×10^{-3}
25	$-3.710\,823$	$-3.709\,507$	1.3×10^{-3}	$-3.709\,507$	1.3×10^{-3}
26	$-3.665\,611$	$-3.665\,864$	2.5×10^{-4}	$-3.665\,864$	2.5×10^{-4}
27	$-3.711\,086$	$-3.709\,761$	1.3×10^{-3}	$-3.709\,760$	1.3×10^{-3}

Table S6: Detailed results for the relative energies of the 27 conformers in the tetraalanine conformer benchmark set.[S5] Errors of the MO- and CDD-based THC-SOS-CC2 methods are reported as deviations from the RI-based reference implementation. All calculations are performed with the cc-pVTZ/cc-pVTZ-RI basis set combination.

conformer	E_{RI} / H	E_{THC} / H	ΔE_{THC} / H	$E_{\text{CDD-THC}}$ / H	$\Delta E_{\text{CDD-THC}}$ / H
1	0.001 725	0.001 680	4.5×10^{-5}	0.001 680	4.5×10^{-5}
2	0.006 903	0.006 811	9.2×10^{-5}	0.006 811	9.2×10^{-5}
3	−0.006 608	−0.006 442	1.7×10^{-4}	−0.006 442	1.7×10^{-4}
4	−0.000 273	−0.000 312	3.9×10^{-5}	−0.000 312	3.9×10^{-5}
5	0.004 018	0.003 982	3.6×10^{-5}	0.003 982	3.6×10^{-5}
6	0.002 323	0.002 292	3.1×10^{-5}	0.002 292	3.1×10^{-5}
7	0.000 548	0.000 561	1.3×10^{-5}	0.000 561	1.3×10^{-5}
8	−0.000 489	−0.000 480	8.7×10^{-6}	−0.000 480	8.7×10^{-6}
9	0.000 683	0.000 715	3.2×10^{-5}	0.000 715	3.2×10^{-5}
10	0.000 392	0.000 299	9.3×10^{-5}	0.000 300	9.3×10^{-5}
11	0.000 484	0.000 513	2.9×10^{-5}	0.000 513	2.9×10^{-5}
12	−0.005 901	−0.005 904	2.9×10^{-6}	−0.005 904	3.1×10^{-6}
13	0.000 355	0.000 428	7.3×10^{-5}	0.000 428	7.3×10^{-5}
14	0.005 942	0.005 895	4.7×10^{-5}	0.005 895	4.7×10^{-5}
15	−0.002 795	−0.002 840	4.5×10^{-5}	−0.002 840	4.5×10^{-5}
16	0.002 049	0.002 004	4.6×10^{-5}	0.002 004	4.6×10^{-5}
17	−0.003 466	−0.003 372	9.5×10^{-5}	−0.003 372	9.5×10^{-5}
18	0.000 615	0.000 583	3.3×10^{-5}	0.000 583	3.3×10^{-5}
19	−0.000 630	−0.000 606	2.4×10^{-5}	−0.000 606	2.4×10^{-5}
20	0.001 097	0.001 054	4.3×10^{-5}	0.001 054	4.3×10^{-5}
21	0.001 184	0.001 248	6.5×10^{-5}	0.001 248	6.4×10^{-5}
22	−0.000 237	−0.000 214	2.2×10^{-5}	−0.000 214	2.2×10^{-5}
23	−0.000 488	−0.000 522	3.4×10^{-5}	−0.000 522	3.4×10^{-5}
24	−0.001 128	−0.001 090	3.8×10^{-5}	−0.001 090	3.8×10^{-5}
25	−0.045 211	−0.043 643	1.6×10^{-3}	−0.043 643	1.6×10^{-3}
26	0.045 474	0.043 896	1.6×10^{-3}	0.043 897	1.6×10^{-3}
27	−0.006 568	−0.006 538	3.0×10^{-5}	−0.006 538	3.0×10^{-5}

5.2 Thiel Benchmark Set

5.2.1 Ground State

Table S7: Detailed results for the ground state energies of the molecules in the benchmark set from Ref. S6. Errors of the MO- and CDD-based THC-SOS-MP2 methods are reported as deviations from the RI-based reference implementation. All calculations are performed with the cc-pVTZ/cc-pVTZ-RI basis set combination.

molecule	E_{RI} / H	E_{THC} / H	ΔE_{THC} / H	$E_{\text{CDD-THC}}$ / H	$\Delta E_{\text{CDD-THC}}$ / H
ethene	$-0.346\,126$	$-0.346\,126$	1.7×10^{-7}	$-0.346\,126$	1.7×10^{-7}
butadiene	$-0.658\,266$	$-0.658\,268$	1.3×10^{-6}	$-0.658\,268$	1.3×10^{-6}
hexatriene	$-0.971\,382$	$-0.971\,378$	4.0×10^{-6}	$-0.971\,378$	4.0×10^{-6}
octatetraene	$-1.284\,868$	$-1.284\,862$	5.5×10^{-6}	$-1.284\,862$	5.5×10^{-6}
cyclopropene	$-0.489\,211$	$-0.489\,212$	3.3×10^{-7}	$-0.489\,212$	3.3×10^{-7}
cyclopentadiene	$-0.801\,368$	$-0.801\,368$	4.8×10^{-7}	$-0.801\,368$	4.8×10^{-7}
norbornadiene	$-1.129\,467$	$-1.129\,454$	1.3×10^{-5}	$-1.129\,454$	1.3×10^{-5}
benzene	$-0.932\,969$	$-0.932\,963$	6.0×10^{-6}	$-0.932\,963$	6.0×10^{-6}
naphthalene	$-1.526\,318$	$-1.526\,281$	3.8×10^{-5}	$-1.526\,281$	3.8×10^{-5}
furan	$-0.849\,522$	$-0.849\,526$	4.6×10^{-6}	$-0.849\,526$	4.6×10^{-6}
pyrrole	$-0.830\,485$	$-0.830\,483$	1.8×10^{-6}	$-0.830\,483$	1.8×10^{-6}
imidazole	$-0.857\,685$	$-0.857\,677$	7.2×10^{-6}	$-0.857\,677$	7.2×10^{-6}
pyridine	$-0.960\,355$	$-0.960\,343$	1.2×10^{-5}	$-0.960\,343$	1.2×10^{-5}
pyrazine	$-0.990\,077$	$-0.990\,059$	1.9×10^{-5}	$-0.990\,059$	1.9×10^{-5}
pyrimidine	$-0.985\,217$	$-0.985\,200$	1.7×10^{-5}	$-0.985\,200$	1.7×10^{-5}
pyridazine	$-0.994\,744$	$-0.994\,716$	2.8×10^{-5}	$-0.994\,716$	2.8×10^{-5}
triazine	$-1.007\,924$	$-1.007\,900$	2.4×10^{-5}	$-1.007\,900$	2.4×10^{-5}
tetrazine	$-1.056\,582$	$-1.056\,545$	3.8×10^{-5}	$-1.056\,545$	3.8×10^{-5}
formaldehyde	$-0.394\,740$	$-0.394\,741$	6.3×10^{-7}	$-0.394\,741$	6.3×10^{-7}
acetone	$-0.742\,969$	$-0.742\,970$	1.1×10^{-6}	$-0.742\,970$	1.1×10^{-6}
benzoquinone	$-1.342\,556$	$-1.342\,550$	6.0×10^{-6}	$-1.342\,550$	6.0×10^{-6}
formamide	$-0.593\,511$	$-0.593\,510$	6.2×10^{-7}	$-0.593\,510$	6.2×10^{-7}
acetamide	$-0.767\,468$	$-0.767\,466$	1.7×10^{-6}	$-0.767\,466$	1.7×10^{-6}
propanamide	$-0.944\,016$	$-0.944\,017$	4.0×10^{-7}	$-0.944\,017$	4.0×10^{-7}
adenine	$-1.698\,357$	$-1.698\,320$	3.7×10^{-5}	$-1.698\,320$	3.7×10^{-5}
cytosine	$-1.404\,395$	$-1.404\,366$	2.9×10^{-5}	$-1.404\,366$	2.9×10^{-5}
thymine	$-1.602\,804$	$-1.602\,792$	1.2×10^{-5}	$-1.602\,792$	1.2×10^{-5}
uracil	$-1.424\,320$	$-1.424\,312$	8.1×10^{-6}	$-1.424\,312$	8.1×10^{-6}

Table S8: Detailed results for the ground state energies of the molecules in the benchmark set from Ref. S6. Errors of the MO- and CDD-based THC-SOS-CC2 methods are reported as deviations from the RI-based reference implementation. All calculations are performed with the cc-pVTZ/cc-pVTZ-RI basis set combination.

molecule	E_{RI} / H	E_{THC} / H	ΔE_{THC} / H	$E_{\text{CDD-THC}}$ / H	$\Delta E_{\text{CDD-THC}}$ / H
ethene	$-0.348\,739$	$-0.348\,686$	5.3×10^{-5}	$-0.348\,686$	5.3×10^{-5}
butadiene	$-0.663\,446$	$-0.663\,380$	6.6×10^{-5}	$-0.663\,380$	6.6×10^{-5}
hexatriene	$-0.979\,143$	$-0.979\,049$	9.4×10^{-5}	$-0.979\,049$	9.4×10^{-5}
octatetraene	$-1.295\,213$	$-1.295\,095$	1.2×10^{-4}	$-1.295\,095$	1.2×10^{-4}
cyclopropene	$-0.492\,823$	$-0.492\,790$	3.3×10^{-5}	$-0.492\,790$	3.3×10^{-5}
cyclopentadiene	$-0.807\,157$	$-0.807\,080$	7.7×10^{-5}	$-0.807\,080$	7.7×10^{-5}
norbornadiene	$-1.137\,341$	$-1.137\,264$	7.7×10^{-5}	$-1.137\,264$	7.7×10^{-5}
benzene	$-0.939\,401$	$-0.939\,347$	5.4×10^{-5}	$-0.939\,347$	5.4×10^{-5}
naphthalene	$-1.537\,366$	$-1.537\,288$	7.8×10^{-5}	$-1.537\,288$	7.8×10^{-5}
furan	$-0.857\,677$	$-0.857\,469$	2.1×10^{-4}	$-0.857\,469$	2.1×10^{-4}
pyrrole	$-0.836\,547$	$-0.836\,444$	1.0×10^{-4}	$-0.836\,444$	1.0×10^{-4}
imidazole	$-0.865\,179$	$-0.865\,023$	1.6×10^{-4}	$-0.865\,023$	1.6×10^{-4}
pyridine	$-0.968\,200$	$-0.968\,035$	1.7×10^{-4}	$-0.968\,035$	1.7×10^{-4}
pyrazine	$-0.998\,919$	$-0.998\,795$	1.2×10^{-4}	$-0.998\,795$	1.2×10^{-4}
pyrimidine	$-0.994\,847$	$-0.994\,602$	2.5×10^{-4}	$-0.994\,602$	2.5×10^{-4}
pyridazine	$-1.003\,959$	$-1.003\,804$	1.5×10^{-4}	$-1.003\,804$	1.5×10^{-4}
triazine	$-1.019\,467$	$-1.019\,106$	3.6×10^{-4}	$-1.019\,106$	3.6×10^{-4}
tetrazine	$-1.068\,661$	$-1.068\,384$	2.8×10^{-4}	$-1.068\,384$	2.8×10^{-4}
formaldehyde	$-0.400\,267$	$-0.400\,264$	3.6×10^{-6}	$-0.400\,264$	3.6×10^{-6}
acetone	$-0.750\,418$	$-0.750\,305$	1.1×10^{-4}	$-0.750\,305$	1.1×10^{-4}
benzoquinone	$-1.360\,323$	$-1.359\,716$	6.1×10^{-4}	$-1.359\,716$	6.1×10^{-4}
formamide	$-0.601\,044$	$-0.601\,090$	4.5×10^{-5}	$-0.601\,090$	4.5×10^{-5}
acetamide	$-0.775\,695$	$-0.775\,803$	1.1×10^{-4}	$-0.775\,803$	1.1×10^{-4}
propanamide	$-0.953\,435$	$-0.953\,162$	2.7×10^{-4}	$-0.953\,162$	2.7×10^{-4}
adenine	$-1.716\,516$	$-1.715\,858$	6.6×10^{-4}	$-1.715\,858$	6.6×10^{-4}
cytosine	$-1.422\,304$	$-1.421\,549$	7.5×10^{-4}	$-1.421\,549$	7.5×10^{-4}
thymine	$-1.623\,172$	$-1.622\,436$	7.4×10^{-4}	$-1.622\,436$	7.4×10^{-4}
uracil	$-1.444\,001$	$-1.443\,282$	7.2×10^{-4}	$-1.443\,282$	7.2×10^{-4}

5.2.2 Excited State

Table S9: Detailed results for the excitation energies to the first three singlet excited states for the molecules in the benchmark set from Ref. S6. Errors of the MO- and CDD-based THC-SOS-ADC(2) methods are reported as deviations from the RI-based reference implementation. All calculations are performed with the cc-pVTZ/cc-pVTZ-RI basis set combination.

molecule	state	E_{RI} / eV	E_{THC} / eV	ΔE_{THC} / eV	$E_{\mathrm{CDD\text{-}THC}}$ / eV	$\Delta E_{\mathrm{CDD\text{-}THC}}$ / eV
ethene	S1	8.357	8.351	0.005	8.351	0.005
	S2	8.732	8.736	0.003	8.736	0.003
	S3	8.930	8.932	0.003	8.932	0.003
butadiene	S1	6.549	6.557	0.008	6.557	0.008
	S2	8.011	8.019	0.008	8.019	0.008
	S3	8.098	8.103	0.005	8.103	0.005
hexatriene	S1	5.504	5.512	0.008	5.512	0.008
	S2	7.075	7.086	0.012	7.086	0.012
	S3	7.421	7.427	0.006	7.427	0.006
octatetraene	S1	4.835	4.842	0.007	4.842	0.007
	S2	6.308	6.320	0.012	6.320	0.012
	S3	6.836	7.002	0.166	7.002	0.166
cyclopropene	S1	7.090	7.098	0.008	7.098	0.008
	S2	7.232	7.237	0.004	7.237	0.004
	S3	8.245	8.246	0.002	8.246	0.002
cyclopentadiene	S1	5.699	5.708	0.008	5.708	0.008
	S2	7.360	7.372	0.012	7.372	0.012
	S3	8.253	8.264	0.011	8.264	0.011
norbornadiene	S1	5.826	5.837	0.011	5.837	0.011
	S2	6.817	6.856	0.039	6.856	0.039
	S3	7.608	7.623	0.015	7.623	0.015
benzene	S1	5.030	5.037	0.008	5.037	0.008
	S2	6.393	6.455	0.062	6.455	0.062
	S3	7.499	7.693	0.193	7.693	0.193
naphthalene	S1	4.302	4.308	0.006	4.308	0.006
	S2	4.918	4.930	0.012	4.930	0.012
	S3	6.348	6.504	0.155	6.504	0.155
furan	S1	6.713	6.729	0.016	6.729	0.016
	S2	6.850	6.955	0.105	6.955	0.105
	S3	7.810	7.824	0.014	7.824	0.014
pyrrole	S1	6.496	6.499	0.004	6.499	0.004
	S2	6.632	6.640	0.008	6.640	0.008
	S3	6.795	6.895	0.101	6.895	0.101
imidazole	S1	6.672	6.679	0.007	6.679	0.007
	S2	6.987	7.001	0.014	7.045	0.058
	S3	7.040	7.045	0.005	7.250	0.211
pyridine	S1	5.078	5.086	0.008	5.086	0.008
	S2	5.345	5.365	0.019	5.365	0.019
	S3	5.694	5.701	0.007	5.701	0.007
pyrazine	S1	4.507	4.514	0.008	4.514	0.008
	S2	4.924	4.962	0.038	4.962	0.038
	S3	5.351	5.360	0.009	5.360	0.009
pyrimidine	S1	4.751	4.759	0.008	4.759	0.008
	S2	5.093	5.103	0.010	5.103	0.010

	S3	5.253	5.269	0.016	5.269	0.016
pyridazine	S1	4.183	4.186	0.003	4.186	0.003
	S2	4.801	4.813	0.012	4.813	0.012
	S3	5.119	5.132	0.013	5.132	0.013
triazine	S1	4.864	4.871	0.007	4.871	0.007
	S2	5.034	5.047	0.013	5.047	0.013
	S3	5.117	5.133	0.016	5.133	0.016
tetrazine	S1	2.795	2.797	0.002	2.797	0.002
	S2	4.179	4.189	0.010	4.189	0.010
	S3	4.931	4.968	0.037	4.968	0.037
formaldehyde	S1	4.064	4.077	0.013	4.077	0.013
	S2	8.157	8.174	0.016	8.174	0.016
	S3	9.256	9.288	0.032	9.288	0.032
acetone	S1	4.448	4.462	0.013	4.462	0.013
	S2	7.642	7.643	0.002	7.643	0.002
	S3	9.068	9.135	0.067	9.135	0.067
benzoquinone	S1	3.132	3.153	0.021	3.153	0.021
	S2	3.215	3.237	0.022	3.237	0.022
	S3	5.031	5.111	0.079	5.111	0.079
formamide	S1	5.623	5.631	0.008	5.631	0.008
	S2	7.831	7.839	0.007	7.839	0.007
	S3	7.530	7.598	0.068	7.598	0.068
acetamide	S1	5.657	5.667	0.010	5.667	0.010
	S2	7.542	7.594	0.052	7.594	0.052
	S3	7.616	7.622	0.006	7.622	0.006
propanamide	S1	5.680	5.692	0.011	5.692	0.011
	S2	7.525	7.589	0.064	7.589	0.064
	S3	7.615	7.621	0.006	7.621	0.006
adenine	S1	5.169	5.182	0.013	5.182	0.013
	S2	5.444	5.518	0.074	5.518	0.074
	S3	5.523	5.532	0.009	5.532	0.009
cytosine	S1	4.822	4.831	0.010	4.831	0.010
	S2	5.415	5.427	0.012	5.427	0.012
	S3	5.870	5.938	0.067	5.938	0.067
thymine	S1	5.023	5.030	0.007	5.030	0.007
	S2	5.468	5.555	0.087	5.555	0.087
	S3	6.419	6.433	0.014	6.433	0.014
uracil	S1	5.000	5.011	0.012	5.011	0.012
	S2	5.544	5.631	0.087	5.631	0.087
	S3	6.350	6.362	0.011	6.362	0.011

Table S10: Detailed results for the excitation energies to the first three triplet excited states for the molecules in the benchmark set from Ref. S6. Errors of the MO- and CDD-based THC-SOS-ADC(2) methods are reported as deviations from the RI-based reference implementation. All calculations are performed with the cc-pVTZ/cc-pVTZ-RI basis set combination.

molecule	state	E_{RI} / eV	E_{THC} / eV	ΔE_{THC} / eV	$E_{\text{CDD-THC}}$ / eV	$\Delta E_{\text{CDD-THC}}$ / eV
ethene	T1	4.570	4.568	0.002	4.568	0.002
	T2	8.584	8.597	0.014	8.597	0.014
	T3	8.620	8.634	0.013	8.634	0.013
butadiene	T1	3.511	3.515	0.004	3.552	0.041
	T2	5.216	5.458	0.242	5.494	0.279
	T3	7.987	8.002	0.015	7.996	0.009
hexatriene	T1	2.960	2.964	0.004	2.964	0.004
	T2	4.424	4.667	0.243	4.667	0.243
	T3	5.457	5.684	0.227	5.684	0.227
octatetraene	T1	2.598	2.602	0.004	2.602	0.004
	T2	3.785	3.785	0.000	3.785	0.000
	T3	4.861	4.861	0.000	4.861	0.000
cyclopropene	T1	4.466	4.468	0.002	4.468	0.002
	T2	6.830	6.848	0.018	6.848	0.018
	T3	7.909	7.931	0.022	7.931	0.022
cyclopentadiene	T1	3.414	3.418	0.004	3.418	0.004
	T2	5.085	5.334	0.250	5.334	0.250
	T3	7.308	7.322	0.015	7.322	0.015
norbornadiene	T1	3.873	3.879	0.006	3.879	0.006
	T2	4.207	4.509	0.302	4.509	0.302
	T3	6.870	6.900	0.029	6.900	0.029
benzene	T1	4.298	4.303	0.006	4.303	0.006
	T2	4.991	5.076	0.085	5.076	0.085
	T3	6.010	6.039	0.029	6.039	0.029
naphthalene	T1	3.300	3.306	0.006	3.306	0.006
	T2	4.271	4.354	0.083	4.354	0.083
	T3	4.760	4.783	0.023	4.783	0.023
furan	T1	4.334	4.343	0.010	4.343	0.010
	T2	5.445	5.649	0.203	5.649	0.203
	T3	7.236	7.311	0.075	7.311	0.075
pyrrole	T1	4.639	4.642	0.003	4.642	0.003
	T2	6.603	6.614	0.011	6.614	0.011
	T3	7.057	7.200	0.144	7.200	0.144
imidazole	T1	4.845	4.848	0.003	4.848	0.003
	T2	5.821	5.982	0.161	5.982	0.161
	T3	6.765	6.838	0.073	6.838	0.073
pyridine	T1	4.449	4.454	0.005	4.454	0.005
	T2	4.924	5.003	0.079	5.003	0.079
	T3	5.145	5.292	0.148	5.292	0.148
pyrazine	T1	3.969	3.974	0.005	3.974	0.005
	T2	4.529	4.717	0.189	4.717	0.189
	T3	5.355	5.492	0.137	5.492	0.137
pyrimidine	T1	4.447	4.453	0.006	4.453	0.006
	T2	4.705	4.710	0.004	4.710	0.004
	T3	5.066	5.164	0.098	5.164	0.098
pyridazine	T1	3.562	3.563	0.001	3.563	0.001

	T2	4.419	4.679	0.260	4.679	0.260
	T3	4.877	4.994	0.117	4.994	0.117
triazine	T1	4.743	4.749	0.006	4.749	0.006
	T2	4.820	4.838	0.018	4.838	0.018
	T3	5.093	5.336	0.243	5.336	0.243
tetrazine	T1	2.240	2.240	0.000	2.240	0.000
	T2	3.956	3.976	0.020	3.976	0.020
	T3	4.486	4.580	0.094	4.580	0.094
formaldehyde	T1	3.678	3.688	0.011	3.688	0.011
	T2	5.917	6.290	0.373	6.290	0.373
	T3	7.842	7.868	0.025	7.868	0.025
acetone	T1	4.145	4.157	0.012	4.157	0.012
	T2	6.133	6.455	0.323	6.455	0.323
	T3	7.563	7.568	0.005	7.568	0.005
benzoquinone	T1	2.868	2.888	0.020	2.888	0.020
	T2	2.964	2.998	0.034	2.998	0.034
	T3	3.236	3.533	0.297	3.533	0.297
formamide	T1	5.386	5.394	0.008	5.394	0.008
	T2	5.923	6.151	0.227	6.151	0.227
	T3	7.506	7.521	0.015	7.521	0.015
acetamide	T1	5.443	5.453	0.010	5.453	0.010
	T2	6.057	6.272	0.215	6.272	0.215
	T3	7.309	7.328	0.019	7.328	0.019
propanamide	T1	5.470	5.481	0.010	5.481	0.010
	T2	6.075	6.290	0.214	6.290	0.214
	T3	7.308	7.323	0.014	7.323	0.014
adenine	T1	4.171	4.179	0.008	4.179	0.008
	T2	5.034	5.125	0.092	5.125	0.092
	T3	5.339	5.481	0.141	5.481	0.141
cytosine	T1	3.969	3.975	0.006	3.975	0.006
	T2	4.843	4.942	0.099	4.942	0.099
	T3	5.280	4.971	0.309	4.971	0.309
thymine	T1	3.872	3.878	0.006	3.878	0.006
	T2	4.857	4.875	0.019	4.875	0.019
	T3	5.606	5.781	0.176	5.781	0.176
uracil	T1	3.968	3.977	0.009	3.977	0.009
	T2	4.835	4.858	0.024	4.858	0.024
	T3	5.619	5.804	0.185	5.804	0.185

Table S11: Detailed results for the excitation energies to the first three singlet excited states for the molecules in the benchmark set from Ref. S6. Errors of the MO- and CDD-based THC-SOS-LR-CC2 methods are reported as deviations from the RI-based reference implementation. All calculations are performed with the cc-pVTZ/cc-pVTZ-RI basis set combination.

molecule	state	E_{RI} / eV	E_{THC} / eV	ΔE_{THC} / eV	$E_{\text{CDD-THC}}$ / eV	$\Delta E_{\text{CDD-THC}}$ / eV
ethene	S1	8.409	8.368	0.041	8.368	0.041
	S2	8.702	8.658	0.044	8.658	0.044
	S3	9.484	9.442	0.042	9.442	0.042
butadiene	S1	6.613	6.585	0.028	6.585	0.028
	S2	7.991	7.955	0.036	7.955	0.036
	S3	8.067	8.042	0.025	8.042	0.025
hexatriene	S1	5.567	5.556	0.012	5.556	0.012
	S2	7.059	7.034	0.026	7.034	0.026
	S3	7.384	7.376	0.007	7.376	0.007
octatetraene	S1	4.896	4.884	0.012	4.884	0.012
	S2	6.301	6.279	0.023	6.279	0.023
	S3	6.890	6.879	0.011	6.879	0.011
cyclopropene	S1	7.075	7.071	0.004	7.071	0.004
	S2	7.279	7.256	0.023	7.256	0.023
	S3	8.224	8.217	0.008	8.217	0.008
cyclopentadiene	S1	5.745	5.728	0.017	5.728	0.017
	S2	7.269	7.240	0.029	7.240	0.029
	S3	7.326	7.301	0.025	7.301	0.025
norbornadiene	S1	5.851	5.856	0.005	5.856	0.005
	S2	6.813	6.812	0.000	6.812	0.000
	S3	7.574	7.587	0.012	7.587	0.012
benzene	S1	5.018	5.000	0.018	5.000	0.018
	S2	6.429	6.420	0.009	6.420	0.009
	S3	7.511	7.499	0.013	7.499	0.013
naphthalene	S1	4.299	4.287	0.012	4.287	0.012
	S2	4.953	4.951	0.002	4.951	0.002
	S3	6.368	6.360	0.008	6.360	0.008
furan	S1	6.712	6.702	0.010	6.702	0.010
	S2	6.850	6.822	0.028	6.822	0.028
	S3	7.765	7.746	0.019	7.746	0.019
pyrrole	S1	6.493	6.459	0.034	6.459	0.034
	S2	6.558	6.558	0.000	6.558	0.000
	S3	6.797	6.790	0.006	6.790	0.006
imidazole	S1	6.676	6.648	0.029	6.648	0.029
	S2	6.979	6.956	0.023	6.956	0.023
	S3	7.018	7.005	0.013	7.005	0.013
pyridine	S1	5.070	5.016	0.054	5.016	0.054
	S2	5.345	5.335	0.010	5.335	0.010
	S3	5.703	5.687	0.016	5.687	0.016
pyrazine	S1	4.475	4.471	0.004	4.471	0.004
	S2	4.905	4.875	0.030	4.875	0.030
	S3	5.316	5.314	0.002	5.314	0.002
pyrimidine	S1	4.770	4.755	0.015	4.755	0.015
	S2	5.129	5.109	0.020	5.109	0.020
	S3	5.264	5.212	0.052	5.212	0.052
pyridazine	S1	4.163	4.161	0.001	4.161	0.001

	S2	4.772	4.777	0.005	4.777	0.005
	S3	5.111	5.068	0.043	5.068	0.043
triazine	S1	4.931	4.906	0.026	4.906	0.026
	S2	5.085	5.065	0.020	5.065	0.020
	S3	5.141	5.125	0.016	5.125	0.016
tetrazine	S1	2.748	2.739	0.009	2.739	0.009
	S2	4.123	4.117	0.006	4.117	0.006
	S3	4.931	4.876	0.055	4.876	0.055
formaldehyde	S1	4.218	4.197	0.021	4.197	0.021
	S2	8.243	8.213	0.030	8.213	0.030
	S3	9.409	9.411	0.002	9.411	0.002
acetone	S1	4.633	4.644	0.011	4.644	0.011
	S2	7.712	7.709	0.002	7.709	0.002
	S3	9.250	9.234	0.017	9.234	0.017
benzoquinone	S1	3.269	3.291	0.021	3.291	0.021
	S2	3.382	3.409	0.027	3.409	0.027
	S3	4.970	4.994	0.024	4.994	0.024
formamide	S1	5.853	5.844	0.010	5.844	0.010
	S2	7.673	7.650	0.022	7.650	0.022
	S3	7.808	7.777	0.031	7.777	0.031
acetamide	S1	5.888	5.879	0.009	5.879	0.009
	S2	7.594	7.570	0.024	7.570	0.024
	S3	7.653	7.642	0.011	7.642	0.011
propanamide	S1	5.912	5.937	0.025	5.937	0.025
	S2	7.594	7.574	0.021	7.574	0.021
	S3	7.653	7.663	0.010	7.663	0.010
adenine	S1	5.212	5.190	0.022	5.190	0.022
	S2	5.521	5.504	0.017	5.504	0.017
	S3	5.584	5.579	0.005	5.579	0.005
cytosine	S1	4.977	4.932	0.045	4.932	0.045
	S2	5.556	5.539	0.017	5.539	0.017
	S3	6.015	5.979	0.037	5.979	0.037
thymine	S1	5.264	5.253	0.011	5.253	0.011
	S2	5.552	5.546	0.006	5.546	0.006
	S3	6.660	6.639	0.021	6.639	0.021
uracil	S1	5.247	5.226	0.021	5.226	0.021
	S2	5.650	5.632	0.018	5.632	0.018
	S3	6.591	6.589	0.002	6.589	0.002

Table S12: Detailed results for the excitation energies to the first three triplet excited states for the molecules in the benchmark set from Ref. S6. Errors of the MO- and CDD-based THC-SOS-LR-CC2 methods are reported as deviations from the RI-based reference implementation. All calculations are performed with the cc-pVTZ/cc-pVTZ-RI basis set combination.

molecule	state	E_{RI} / eV	E_{THC} / eV	ΔE_{THC} / eV	$E_{\text{CDD-THC}}$ / eV	$\Delta E_{\text{CDD-THC}}$ / eV
ethene	T1	4.570	4.535	0.035	4.535	0.035
	T2	8.552	8.510	0.043	8.510	0.043
	T3	8.622	8.612	0.009	8.612	0.009
butadiene	T1	3.553	3.525	0.027	3.525	0.027
	T2	5.258	5.236	0.022	5.236	0.022
	T3	7.956	7.945	0.011	7.945	0.011
hexatriene	T1	2.967	2.955	0.012	2.955	0.012
	T2	4.432	4.418	0.013	4.418	0.013
	T3	5.464	5.455	0.009	5.455	0.009
octatetraene	T1	2.606	2.594	0.012	2.594	0.012
	T2	3.795	3.780	0.014	3.780	0.014
	T3	4.870	4.858	0.012	4.858	0.012
cyclopropene	T1	7.075	7.071	0.004	7.070	0.005
	T2	7.279	7.256	0.023	7.260	0.019
	T3	8.224	8.217	0.008	8.220	0.004
cyclopentadiene	T1	3.424	3.404	0.020	3.404	0.020
	T2	5.090	5.070	0.020	5.070	0.020
	T3	7.275	7.250	0.025	7.250	0.025
norbornadiene	T1	3.884	3.881	0.003	3.881	0.003
	T2	4.211	4.204	0.006	4.204	0.006
	T3	6.861	6.859	0.002	6.859	0.002
benzene	T1	4.296	4.280	0.016	4.280	0.016
	T2	4.999	4.983	0.016	4.983	0.016
	T3	6.042	6.034	0.008	6.034	0.008
naphthalene	T1	3.308	3.301	0.008	3.301	0.008
	T2	4.284	4.276	0.008	4.276	0.008
	T3	4.768	4.759	0.010	4.759	0.010
furan	T1	4.354	4.338	0.016	4.338	0.016
	T2	5.478	5.452	0.026	5.452	0.026
	T3	7.248	7.229	0.019	7.229	0.019
pyrrole	T1	4.650	4.637	0.013	4.637	0.013
	T2	6.531	6.530	0.001	6.530	0.001
	T3	7.046	7.027	0.019	7.027	0.019
imidazole	T1	4.863	4.842	0.021	4.842	0.021
	T2	5.835	5.810	0.025	5.810	0.025
	T3	6.621	6.759	0.138	6.759	0.138
pyridine	T1	4.447	4.419	0.028	4.419	0.028
	T2	4.935	4.895	0.040	4.895	0.040
	T3	5.157	5.119	0.038	5.119	0.038
pyrazine	T1	3.948	3.941	0.007	3.941	0.007
	T2	4.485	4.465	0.020	4.465	0.020
	T3	4.537	4.519	0.018	4.519	0.018
pyrimidine	T1	4.452	4.439	0.013	4.439	0.013
	T2	4.694	4.663	0.031	4.663	0.031
	T3	5.090	5.051	0.039	5.051	0.039
pyridazine	T1	3.553	3.546	0.007	3.546	0.007

	T2	4.423	4.398	0.024	4.398	0.024
	T3	4.891	4.864	0.027	4.864	0.027
triazine	T1	4.743	4.731	0.012	4.731	0.012
	T2	4.850	4.833	0.018	4.833	0.018
	T3	5.068	5.036	0.032	5.036	0.032
tetrazine	T1	2.204	2.192	0.011	2.192	0.011
	T2	3.909	3.901	0.008	3.901	0.008
	T3	4.492	4.458	0.034	4.458	0.034
formaldehyde	T1	3.806	3.785	0.021	3.785	0.021
	T2	5.982	5.930	0.052	5.930	0.052
	T3	7.911	7.882	0.029	7.882	0.029
acetone	T1	4.301	4.310	0.010	4.310	0.010
	T2	6.216	6.178	0.038	6.178	0.038
	T3	7.629	7.627	0.002	7.627	0.002
benzoquinone	T1	2.987	3.010	0.022	3.010	0.022
	T2	3.107	3.133	0.025	3.133	0.025
	T3	3.264	3.262	0.002	3.262	0.002
formamide	T1	5.586	5.578	0.008	5.578	0.008
	T2	5.992	5.958	0.034	5.958	0.034
	T3	7.473	7.444	0.029	7.444	0.029
acetamide	T1	5.644	5.635	0.009	5.635	0.009
	T2	6.136	6.103	0.033	6.103	0.033
	T3	7.279	7.257	0.023	7.257	0.023
propanamide	T1	5.672	5.693	0.021	5.693	0.021
	T2	6.155	6.134	0.021	6.134	0.021
	T3	7.280	7.261	0.019	7.261	0.019
adenine	T1	4.190	4.174	0.016	4.174	0.016
	T2	5.057	5.051	0.006	5.051	0.006
	T3	5.373	5.354	0.019	5.354	0.019
cytosine	T1	4.032	4.010	0.022	4.010	0.022
	T2	4.909	4.886	0.022	4.886	0.022
	T3	5.396	5.600	0.203	5.600	0.203
thymine	T1	3.915	3.909	0.006	3.909	0.006
	T2	5.071	5.062	0.010	5.062	0.010
	T3	5.669	5.658	0.012	5.658	0.012
uracil	T1	4.013	3.998	0.015	3.998	0.015
	T2	5.055	5.036	0.019	5.036	0.019
	T3	5.686	5.667	0.019	5.667	0.019

5.3 Martínez Benchmark Set

5.3.1 Ground State

Table S13: Detailed results for the ground state energies of the molecules in the benchmark set from Ref. S7. Errors of the MO- and CDD-based THC-SOS-MP2 methods are reported as deviations from the RI-based reference implementation. All calculations are performed with the cc-pVTZ/cc-pVTZ-RI basis set combination.

molecule	E_{RI} / H	E_{THC} / H	ΔE_{THC} / H	$E_{\text{CDD-THC}}$ / H	$\Delta E_{\text{CDD-THC}}$ / H
butadiene	$-0.658\,266$	$-0.658\,268$	1.3×10^{-6}	$-0.658\,268$	1.5×10^{-6}
hexatriene	$-0.971\,382$	$-0.971\,378$	4.0×10^{-6}	$-0.971\,378$	4.3×10^{-6}
malonaldehyde	$-0.928\,473$	$-0.928\,469$	4.3×10^{-6}	$-0.928\,469$	4.4×10^{-6}
methylsalicylate	$-1.910\,410$	$-1.910\,398$	1.2×10^{-5}	$-1.910\,398$	1.2×10^{-5}
HBT	$-2.543\,654$	$-2.543\,520$	1.3×10^{-4}	$-2.543\,520$	1.3×10^{-4}
stilbene	$-2.151\,922$	$-2.151\,908$	1.4×10^{-5}	$-2.151\,908$	1.4×10^{-5}
GFP	$-2.335\,196$	$-2.335\,177$	1.9×10^{-5}	$-2.335\,177$	1.9×10^{-5}
PYP	$-2.046\,621$	$-2.046\,610$	1.1×10^{-5}	$-2.046\,610$	1.1×10^{-5}
acridine red	$-2.913\,065$	$-2.912\,992$	7.4×10^{-5}	$-2.912\,992$	7.3×10^{-5}
anthanthrene	$-3.281\,459$	$-3.281\,362$	9.7×10^{-5}	$-3.281\,362$	9.7×10^{-5}
N-methyl-benzcarbaxole	$-2.783\,274$	$-2.783\,203$	7.0×10^{-5}	$-2.783\,203$	7.1×10^{-5}
coumarin 153	$-3.849\,149$	$-3.849\,068$	8.1×10^{-5}	$-3.849\,068$	8.1×10^{-5}
difluoro-indigo	$-3.626\,637$	$-3.626\,523$	1.1×10^{-4}	$-3.626\,523$	1.1×10^{-4}
nile red	$-3.927\,931$	$-3.927\,846$	8.5×10^{-5}	$-3.927\,846$	8.5×10^{-5}
oxazine 9	$-3.187\,605$	$-3.187\,530$	7.5×10^{-5}	$-3.187\,530$	7.5×10^{-5}
rubicene	$-3.878\,599$	$-3.878\,435$	1.6×10^{-4}	$-3.878\,435$	1.6×10^{-4}
ester	$-3.384\,816$	$-3.384\,736$	7.9×10^{-5}	$-3.384\,736$	8.0×10^{-5}

Table S14: Detailed results for the ground state energies of the molecules in the benchmark set from Ref. S7. Errors of the MO- and CDD-based THC-SOS-CC2 methods are reported as deviations from the RI-based reference implementation. All calculations are performed with the cc-pVTZ/cc-pVTZ-RI basis set combination.

molecule	E_{RI} / H	E_{THC} / H	ΔE_{THC} / H	$E_{\text{CDD-THC}}$ / H	$\Delta E_{\text{CDD-THC}}$ / H
butadiene	0.663 446	−0.663 380	6.6×10^{-5}	−0.663 380	6.6×10^{-5}
hexatriene	0.979 143	−0.979 049	9.4×10^{-5}	−0.979 049	9.4×10^{-5}
malonaldehyde	0.941 556	−0.940 910	6.5×10^{-4}	−0.940 910	6.5×10^{-4}
methylsalicylate	1.931 444	−1.930 642	8.0×10^{-4}	−1.930 642	8.0×10^{-4}
HBT	2.567 426	−2.566 600	8.3×10^{-4}	−2.566 600	8.3×10^{-4}
stilbene	2.167 465	−2.167 414	5.1×10^{-5}	−2.167 414	5.1×10^{-5}
GFP	2.360 494	−2.359 745	7.5×10^{-4}	−2.359 745	7.5×10^{-4}
PYP	2.068 245	−2.067 535	7.1×10^{-4}	−2.067 535	7.1×10^{-4}
acridine red	2.943 776	−2.941 744	2.0×10^{-3}	−2.941 744	2.0×10^{-3}
anthanthrene	3.307 075	−3.306 840	2.4×10^{-4}	−3.306 840	2.4×10^{-4}
N-methyl-benzcarbaxole	2.805 027	−2.804 581	4.5×10^{-4}	−2.804 581	4.5×10^{-4}
coumarin 153	3.887 952	−3.886 496	1.5×10^{-3}	−3.886 496	1.5×10^{-3}
difluoro-indigo	3.668 254	−3.667 169	1.1×10^{-3}	−3.667 169	1.1×10^{-3}
nile red	3.966 831	−3.965 170	1.7×10^{-3}	−3.965 170	1.7×10^{-3}
oxazine 9	3.221 792	−3.219 770	2.0×10^{-3}	−3.219 770	2.0×10^{-3}
rubicene	3.908 834	−3.908 510	3.2×10^{-4}	−3.908 510	3.2×10^{-4}
ester	3.426 647	−3.425 046	1.6×10^{-3}	−3.425 046	1.6×10^{-3}

5.3.2 Excited State

Table S15: Detailed results for the excitation energies to the first three singlet excited states for the molecules in the benchmark set from Ref. S7. Errors of the MO- and CDD-based THC-SOS-ADC(2) methods are reported as deviations from the RI-based reference implementation. All calculations are performed with the cc-pVTZ/cc-pVTZ-RI basis set combination.

molecule	state	E_{RI} / eV	E_{THC} / eV	ΔE_{THC} / eV	$E_{\text{CDD-THC}}$ / eV	$\Delta E_{\text{CDD-THC}}$ / eV
butadiene	S1	6.549	6.557	0.008	6.557	0.008
	S2	8.011	8.019	0.008	8.019	0.008
	S3	8.098	8.103	0.005	8.103	0.005
hexatriene	S1	5.504	5.512	0.008	5.512	0.008
	S2	7.075	7.086	0.012	7.086	0.012
	S3	7.421	7.427	0.006	7.427	0.006
malonaldehyde	S1	4.179	4.189	0.009	4.189	0.009
	S2	4.935	5.042	0.107	5.042	0.107
	S3	7.816	7.883	0.067	7.883	0.067
methylsalicylate	S1	4.289	4.301	0.012	4.301	0.012
	S2	5.517	5.530	0.014	5.530	0.014
	S3	5.565	5.605	0.040	5.605	0.040
HBT	S1	3.961	3.973	0.012	3.973	0.012
	S2	4.426	4.446	0.020	4.446	0.020
	S3	4.784	4.817	0.033	4.817	0.033
stilbene	S1	4.484	4.492	0.008	4.492	0.008
	S2	4.647	4.653	0.006	4.653	0.006
	S3	4.689	4.684	0.005	4.684	0.005
GFP	S1	3.919	3.934	0.015	3.934	0.015
	S2	4.195	4.211	0.016	4.211	0.016
	S3	4.494	4.500	0.006	4.500	0.006
PYP	S1	4.486	4.495	0.009	4.495	0.009
	S2	4.685	4.709	0.024	4.709	0.024
	S3	5.076	5.089	0.013	5.089	0.013
acridine red	S1	2.655	2.670	0.015	2.670	0.015
	S2	3.538	3.582	0.044	3.582	0.044
	S3	4.475	4.505	0.030	4.505	0.030
anthanthrene	S1	3.211	3.222	0.010	3.222	0.010
	S2	3.297	3.389	0.092	3.389	0.092
	S3	3.944	3.979	0.035	3.979	0.035
N-methyl-benzcarbaxole	S1	3.537	3.550	0.013	3.550	0.013
	S2	4.137	4.153	0.016	4.153	0.016
	S3	4.582	4.608	0.025	4.608	0.025
coumarin 153	S1	3.474	3.497	0.023	3.497	0.023
	S2	4.095	4.125	0.030	4.125	0.030
	S3	4.793	4.830	0.037	4.830	0.037
difluoro-indigo	S1	2.553	2.566	0.013	2.566	0.013
	S2	2.950	2.970	0.020	2.970	0.020
	S3	3.361	3.410	0.050	3.410	0.050
nile red	S1	2.905	2.921	0.017	2.921	0.017
	S2	3.402	3.411	0.009	3.411	0.009
	S3	3.820	3.861	0.041	3.861	0.041
oxazine 9	S1	2.349	2.360	0.010	2.360	0.011
	S2	3.239	3.278	0.039	3.280	0.041

	S3	3.971	3.987	0.016	3.990	0.019
rubicene	S1	2.838	2.857	0.019	2.860	0.022
	S2	3.209	3.268	0.059	3.270	0.061
	S3	3.412	3.449	0.038	3.450	0.038
ester	S1	4.025	4.047	0.022	4.047	0.022
	S2	4.702	4.753	0.050	4.753	0.050
	S3	5.098	5.165	0.067	5.165	0.067

Table S16: Detailed results for the excitation energies to the first three triplet excited states for the molecules in the benchmark set from Ref. S7. Errors of the MO- and CDD-based THC-SOS-ADC(2) methods are reported as deviations from the RI-based reference implementation. All calculations are performed with the cc-pVTZ/cc-pVTZ-RI basis set combination.

molecule	state	E_{RI} / eV	E_{THC} / eV	ΔE_{THC} / eV	$E_{\text{CDD-THC}}$ / eV	$\Delta E_{\text{CDD-THC}}$ / eV
butadiene	T1	3.548	3.552	0.004	3.552	0.004
	T2	5.253	5.494	0.242	5.494	0.242
	T3	7.979	7.996	0.017	7.996	0.017
hexatriene	T1	2.960	2.964	0.004	2.964	0.004
	T2	4.424	4.667	0.243	4.667	0.243
	T3	5.457	5.684	0.227	5.684	0.227
malonaldehyde	T1	3.673	3.682	0.009	3.682	0.009
	T2	3.987	4.009	0.023	4.009	0.023
	T3	6.325	6.548	0.223	6.548	0.223
methylsalicylate	T1	3.922	3.982	0.059	3.982	0.059
	T2	4.163	4.171	0.008	4.171	0.008
	T3	4.689	4.800	0.111	4.800	0.111
HBT	T1	3.359	3.370	0.011	3.370	0.011
	T2	4.149	4.117	0.032	4.117	0.032
	T3	4.389	4.306	0.083	4.306	0.083
stilbene	T1	2.966	2.970	0.004	2.970	0.004
	T2	4.100	4.284	0.185	4.284	0.185
	T3	4.578	4.666	0.088	4.666	0.088
GFP	T1	2.544	2.554	0.010	2.554	0.010
	T2	4.054	4.179	0.125	4.179	0.125
	T3	4.481	4.554	0.073	4.554	0.073
PYP	T1	3.181	3.187	0.006	3.187	0.006
	T2	4.572	4.568	0.004	4.568	0.004
	T3	4.823	4.736	0.088	4.736	0.088
acridine red	T1	2.303	2.316	0.013	2.316	0.013
	T2	3.302	3.368	0.066	3.368	0.066
	T3	3.613	3.728	0.115	3.728	0.115
anthanthrene	T1	1.969	1.983	0.014	1.983	0.014
	T2	3.158	3.290	0.132	3.290	0.132
	T3	3.364	3.422	0.057	3.422	0.057
N-methyl-benzcarbaxole	T1	2.863	2.873	0.011	2.873	0.011
	T2	3.624	3.677	0.054	3.677	0.054
	T3	3.899	3.940	0.040	3.940	0.040
coumarin 153	T1	2.779	2.796	0.018	2.796	0.018
	T2	3.942	4.030	0.087	4.030	0.087
	T3	4.281	4.385	0.104	4.385	0.104
difluoro-indigo	T1	2.304	2.364	0.060	2.364	0.060

	T2	3.039	3.160	0.122	3.160	0.122
	T3	3.550	3.649	0.100	3.649	0.100
nile red	T1	2.079	2.092	0.014	2.092	0.014
	T2	3.249	3.422	0.173	3.422	0.173
	T3	3.742	3.836	0.094	3.836	0.094
oxazine 9	T1	1.821	1.830	0.009	1.830	0.009
	T2	2.999	3.066	0.068	3.066	0.068
	T3	3.558	3.633	0.075	3.633	0.075
rubicene	T1	1.885	1.900	0.015	1.900	0.015
	T2	2.796	2.866	0.071	2.866	0.071
	T3	2.838	2.945	0.107	2.945	0.107
ester	T1	2.797	2.812	0.015	2.812	0.015
	T2	3.848	4.033	0.185	4.033	0.185
	T3	4.149	4.258	0.109	4.258	0.109

Table S17: Detailed results for the excitation energies to the first three singlet excited states for the molecules in the benchmark set from Ref. S7. Errors of the MO- and CDD-based THC-SOS-LR-CC2 methods are reported as deviations from the RI-based reference implementation. All calculations are performed with the cc-pVTZ/cc-pVTZ-RI basis set combination.

molecule	state	E_{RI} / eV	E_{THC} / eV	ΔE_{THC} / eV	$E_{\mathrm{CDD\text{-}THC}}$ / eV	$\Delta E_{\mathrm{CDD\text{-}THC}}$ / eV
butadiene	S1	6.613	6.585	0.028	6.585	0.028
	S2	7.991	7.955	0.036	7.955	0.036
	S3	8.067	8.042	0.025	8.042	0.025
hexatriene	S1	5.567	5.556	0.012	5.556	0.012
	S2	7.059	7.034	0.026	7.034	0.026
	S3	7.384	7.376	0.007	7.376	0.007
malonaldehyde	S1	4.397	4.390	0.007	4.390	0.007
	S2	5.103	5.064	0.039	5.064	0.039
	S3	7.865	7.846	0.020	7.846	0.020
methylsalicylate	S1	4.338	4.319	0.020	4.319	0.020
	S2	5.643	5.634	0.009	5.634	0.009
	S3	5.732	5.726	0.006	5.726	0.006
HBT	S1	4.010	3.997	0.012	3.997	0.012
	S2	4.454	4.440	0.014	4.440	0.014
	S3	4.850	4.837	0.013	4.837	0.013
stilbene	S1	4.502	4.491	0.010	4.491	0.010
	S2	4.640	4.623	0.017	4.623	0.017
	S3	4.697	4.683	0.014	4.683	0.014
GFP	S1	4.030	4.014	0.016	4.014	0.016
	S2	4.342	4.338	0.004	4.338	0.004
	S3	4.506	4.488	0.018	4.488	0.018
PYP	S1	4.517	4.498	0.019	4.498	0.019
	S2	4.769	4.749	0.019	4.749	0.019
	S3	5.314	5.295	0.019	5.295	0.019
acridine red	S1	2.861	2.794	0.067	2.790	0.071
	S2	3.683	3.652	0.031	3.650	0.033
	S3	4.580	4.556	0.024	4.560	0.020
anthanthrene	S1	3.208	3.201	0.007	3.201	0.007
	S2	3.330	3.331	0.000	3.331	0.000
	S3	3.949	3.964	0.015	3.964	0.015

N-methyl-benzcarbaxole	S1	3.556	3.553	0.004	3.550	0.006
	S2	4.147	4.149	0.001	4.150	0.003
	S3	4.605	4.597	0.008	4.600	0.005
coumarin 153	S1	3.577	3.580	0.003	3.580	0.003
	S2	4.147	4.157	0.011	4.160	0.013
	S3	4.850	4.864	0.014	4.864	0.014
difluoro-indigo	S1	2.629	2.639	0.010	2.639	0.010
	S2	3.051	3.067	0.015	3.067	0.015
	S3	3.397	3.396	0.001	3.396	0.001
nile red	S1	2.997	2.981	0.016	2.981	0.016
	S2	3.629	3.616	0.014	3.616	0.014
	S3	3.865	3.869	0.004	3.869	0.004
oxazine 9	S1	2.563	2.472	0.091	2.472	0.091
	S2	3.355	3.316	0.040	3.316	0.040
	S3	4.046	4.027	0.019	4.027	0.019
rubicene	S1	2.852	2.860	0.008	2.860	0.008
	S2	3.215	3.225	0.010	3.225	0.010
	S3	3.413	3.425	0.012	3.425	0.012
ester	S1	4.080	4.078	0.003	4.078	0.003
	S2	4.770	4.766	0.004	4.766	0.004
	S3	5.144	5.137	0.007	5.137	0.007

Table S18: Detailed results for the excitation energies to the first three triplet excited states for the molecules in the benchmark set from Ref. S7. Errors of the MO- and CDD-based THC-SOS-LR-CC2 methods are reported as deviations from the RI-based reference implementation. All calculations are performed with the cc-pVTZ/cc-pVTZ-RI basis set combination.

molecule	state	E_{RI} / eV	E_{THC} / eV	ΔE_{THC} / eV	$E_{\text{CDD-THC}}$ / eV	$\Delta E_{\text{CDD-THC}}$ / eV
butadiene	T1	3.553	3.525	0.027	3.525	0.027
	T2	5.258	5.236	0.022	5.236	0.022
	T3	7.956	7.945	0.011	7.945	0.011
hexatriene	T1	2.967	2.955	0.012	2.955	0.012
	T2	4.432	4.418	0.013	4.418	0.013
	T3	5.464	5.455	0.009	5.455	0.009
malonaldehyde	T1	3.738	3.711	0.027	3.711	0.027
	T2	4.173	4.169	0.004	4.169	0.004
	T3	6.436	6.401	0.035	6.401	0.035
methylsalicylate	T1	3.971	3.958	0.013	3.958	0.013
	T2	4.175	4.167	0.008	4.167	0.008
	T3	4.724	4.711	0.013	4.711	0.013
HBT	T1	3.392	3.387	0.005	3.387	0.005
	T2	4.154	4.147	0.007	4.147	0.007
	T3	4.419	4.413	0.006	4.413	0.006
stilbene	T1	2.973	2.962	0.010	2.962	0.010
	T2	4.102	4.092	0.010	4.092	0.010
	T3	4.593	4.583	0.010	4.583	0.010
GFP	T1	2.579	2.569	0.010	2.569	0.010
	T2	4.082	4.071	0.011	4.071	0.011
	T3	4.495	4.485	0.010	4.485	0.010
PYP	T1	3.214	3.198	0.016	3.198	0.016
	T2	4.589	4.576	0.013	4.576	0.013

	T3	4.846	4.833	0.013	4.833	0.013
acridine red	T1	2.381	2.361	0.020	2.361	0.020
	T2	3.411	3.389	0.022	3.389	0.022
	T3	3.712	3.678	0.033	3.678	0.033
anthanthrene	T1	1.968	1.969	0.001	1.969	0.001
	T2	3.168	3.165	0.003	3.165	0.003
	T3	3.706	3.711	0.005	3.711	0.005
N-methyl-benzcarbaxole	T1	2.867	2.866	0.001	2.866	0.001
	T2	3.638	3.633	0.004	3.633	0.004
	T3	3.919	3.916	0.003	3.916	0.003
coumarin 153	T1	2.831	2.837	0.006	2.837	0.006
	T2	4.003	4.008	0.004	4.008	0.004
	T3	4.362	4.342	0.019	4.342	0.019
difluoro-indigo	T1	2.369	2.364	0.005	2.364	0.005
	T2	3.061	3.058	0.003	3.058	0.003
	T3	3.590	3.586	0.003	3.586	0.003
nile red	T1	2.120	2.118	0.002	2.118	0.002
	T2	3.451	3.439	0.012	3.311	0.140
	T3	3.786	3.775	0.011	3.775	0.011
oxazine 9	T1	1.905	1.872	0.032	1.872	0.032
	T2	3.090	3.057	0.033	3.057	0.033
	T3	3.620	3.601	0.019	3.601	0.019
rubicene	T1	1.888	1.892	0.004	1.892	0.004
	T2	2.796	2.802	0.007	2.802	0.007
	T3	2.844	2.850	0.006	2.850	0.006
ester	T1	2.824	2.823	0.001	2.823	0.001
	T2	3.874	3.871	0.004	3.871	0.004
	T3	4.214	4.210	0.004	4.210	0.004

6 Detailed Results – Computational Efficiency

6.1 Time Complexity

In the following, supplementary results for the computational complexity of the proposed THC-based reformulations of the methods presented in the main part of this work are given.

The computational complexity of the MO/CDD-THC-SOS-MP2 methods is assessed by taking into account the number of FLOP required to evaluate the SOS-MP2 singles amplitude for the LCA$_n$ (Figure S3) and the AT$_n$ series (Figure S4).

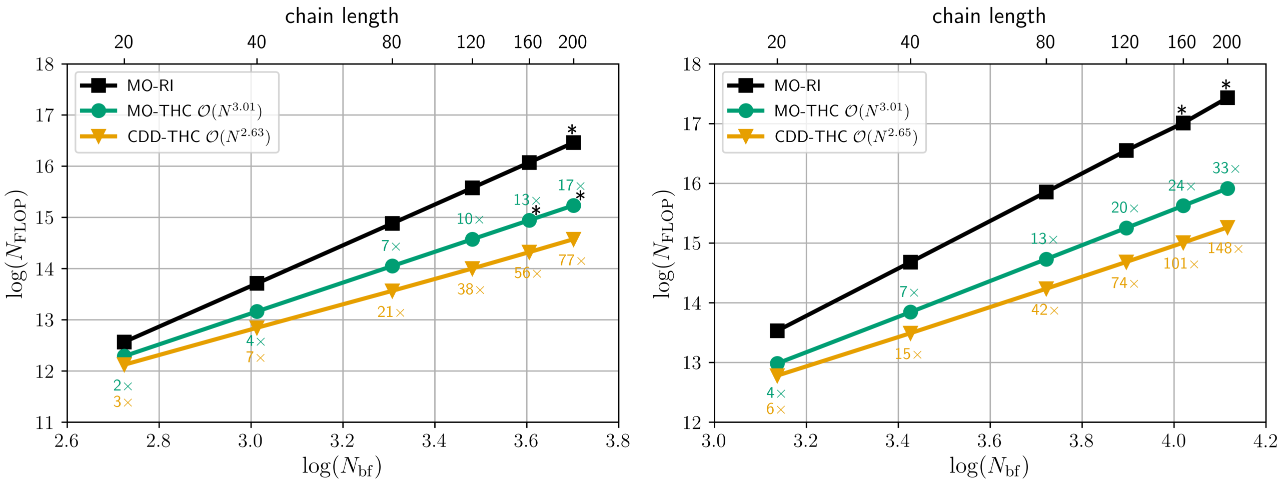

Figure S3: Number of FLOP required to evaluate the SOS-MP2 singles amplitudes for a series of LCA$_n$ ($n \in \{20, 40, 80, 120, 160, 200\}$) molecules. Labels represent the FLOP reduction compared to the MO-RI-SOS-MP2 implementation and all calculations are performed with the cc-pVDZ/cc-pVDZ-RI (left) or cc-pVTZ/cc-pVTZ-RI basis set combination (right). Extrapolated values are marked with an asterisk (*).

For the LCA$_n$ series, MO-THC-SOS-MP2 exhibits exactly cubic scaling with the system size for both basis set sizes considered. Overall, in comparison to the RI-based reference implementation, the application of MO-THC yields a 17-fold diminution of the effort for the double-ζ basis set and a 33-fold diminution of the effort for the larger triple-ζ basis set. Furthermore, a reformulation in the local Cholesky MO basis results in improvements of up to 148-fold for the largest LCA molecule considered, while reducing the apparent scaling exponent to $\sim$2.5. In the limit of the largest fragment sizes considered, the observed scaling behavior is similar for the less-sparse AT$_n$

series, as shown in Figure S4.

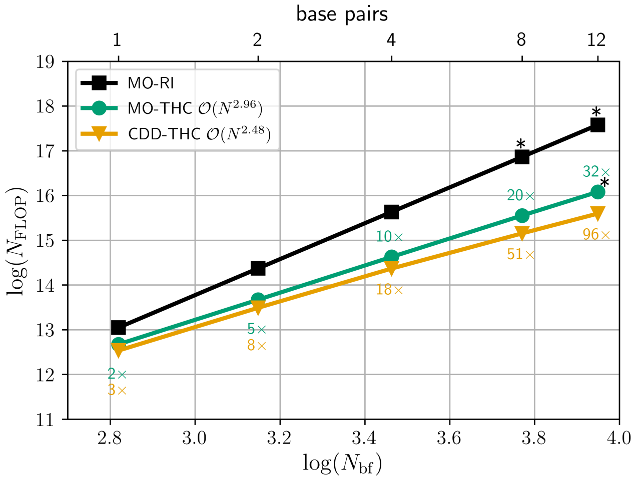

Figure S4: Number of FLOP required to evaluate the SOS-MP2 singles amplitudes for a series of AT$_n$ ($n \in \{1, 2, 4, 8, 12\}$) molecules. Labels represent the FLOP reduction compared to the MO-RI-SOS-MP2 implementation and all calculations are performed with the cc-pVDZ/cc-pVDZ-RI basis set combination. Extrapolated values are marked with an asterisk (*).

In addition to the results presented in the main part of this work for the larger triple-ζ basis set, Figure S5 shows the scaling behavior of the THC-SOS-LR-CC2/SOS-ADC(2) methods for the LCA$_n$ series using the cc-pVDZ/cc-pVDZ-RI basis set combination.

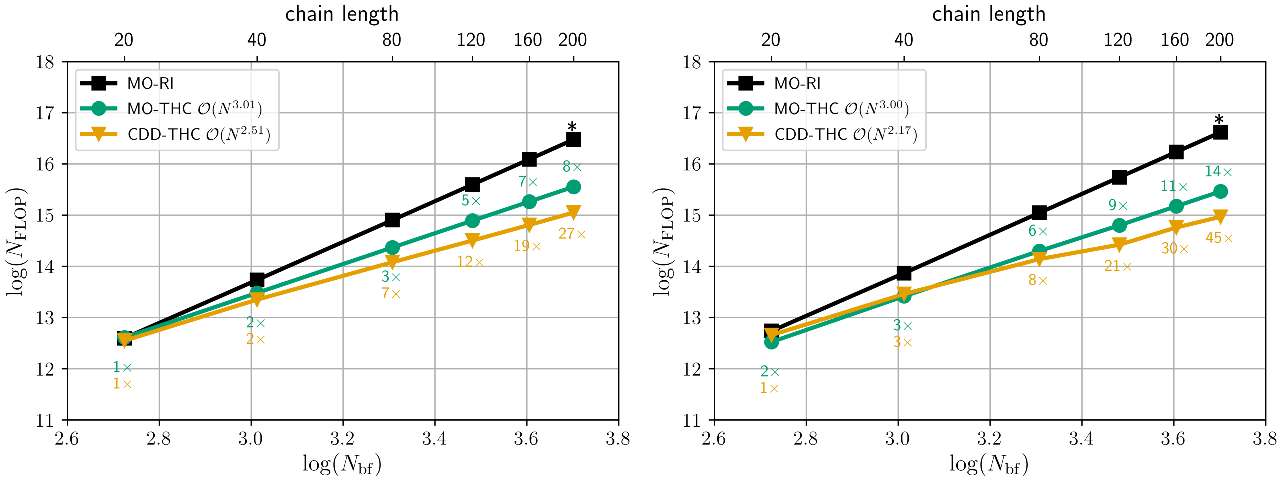

Figure S5: Number of FLOP required to evaluate the SOS-CC2 singles amplitudes (left) and the SOS-LR-CC2/SOS-ADC(2) matrix-vector product (right) for a series of LCA$_n$ ($n \in \{20, 40, 80, 120, 160, 200\}$) molecules. Labels represent the FLOP reduction compared to the MO-RI-SOS-LR-CC2/ADC(2) implementation and all calculations are performed with the cc-pVDZ/cc-pVDZ-RI basis set combination. Extrapolated values are marked with an asterisk (*).

6.1.1 THC Grid Comparison

Table S19: Average number of PFLOP (10^{15} FLOP) required per DIIS iteration to form the matrix-vector product in MO-THC-SOS-ADC(2) and CDD-THC-SOS-ADC(2). Additionally, the ×-fold reduction in the number of FLOP is shown with respect to MO-RI-SOS-ADC(2). All calculations are performed using the cc-pVDZ/cc-pVDZ-RI basis set combination and the grids generated from both the hand-optimized cc-pVDZ- (*grid 1*) and cc-pVTZ-based parent grids (*grid 2*) from Martínez and coworkers.[S2] Extrapolated values are marked with an asterisk (*).

			MO-RI	MO-THC			CDD-THC		
	System	N_{bf}	PFLOP	PFLOP	Scaling	Reduction	PFLOP	Scaling	Reduction
grid 1									
	AT_{04}	2904	6.2	0.3	—	20.3×	0.5	—	12.4×
	AT_{08}	5896	110.0*	2.6	3.0	41.0×	2.6	2.3	40.0×
	AT_{12}	5896	537.0*	8.8	3.0	61.0×	2.6	2.3	76.4×
	AT_{16}	11880	1800.0*	21.0	3.0	83.5×	15.0	2.5	119.3×
grid 2									
	AT_{04}	2904	6.2	0.7	—	8.9×	0.9	—	6.9×
	AT_{08}	5896	110.0*	5.9	3.0	17.8×	6.8	2.8	15.4×
	AT_{12}	5896	537.0*	20.0	3.0	41.0×	2.6	2.3	40.0×
	AT_{16}	11880	1800.0*	49.1*	3.0	35.7×	38.0*	2.5	46.1×

Table S20: Time required to perform one iteration of the excited state calculation. Scaling and speedups are reported for the THC-based methods relative to MO-RI-SOS-ADC(2) using the cc-pVDZ/cc-pVDZ-RI basis set combination together with the grids generated from both the hand-optimized cc-pVDZ- (*grid 1*) and cc-pVTZ-based parent grids (*grid 2*). Extrapolated values are marked with an asterisk (*).

			MO-RI	MO-THC		CDD-THC	
	System	N_{bf}	Time / h	Time / h	Speedup	Time / h	Speedup
grid 1							
	AT_{4}	2904	1.1	0.1	8.9×	0.3	4.1×
	AT_{8}	5896	19.0*	0.8	23.4×	1.0	18.8×
	AT_{12}	8888	98.7*				
	AT_{16}	11 880	312.2*	6.6*	47.0×	4.6	68.1×
grid 2							
	AT_{4}	2904	1.1	0.4	2.6×	0.5	2.2×
	AT_{8}	5896	19.0*	2.3	8.3×	2.5	7.7×
	AT_{12}	8888	98.7*	8.0*	8.3×	2.1	8.9×
	AT_{16}	11 880	312.2*	19.0*	16.4×	11.1*	28.1×

6.1.2 THC Z vs. Γ Tensor

In the following, the scaling of the computational effort required to evaluate the THC-SOS-LR-CC2/ADC(2) matrix-vector product using either a formulation of the intermediates in terms of the THC $\mathbf{Z}$ or the $\mathbf{\Gamma}$ tensor is exemplarily demonstrated for a series of LCA$_n$ molecules in Figure S6. Here, the label CDD-THC ($\mathbf{\Gamma}$) indicates the results obtained by using eqs. (d)–(f) in Table 2 in the main part of this work, whereas the CDD-THC ($\mathbf{Z}$) label indicates the results obtained using eqs. (e')–(f') in the same table.

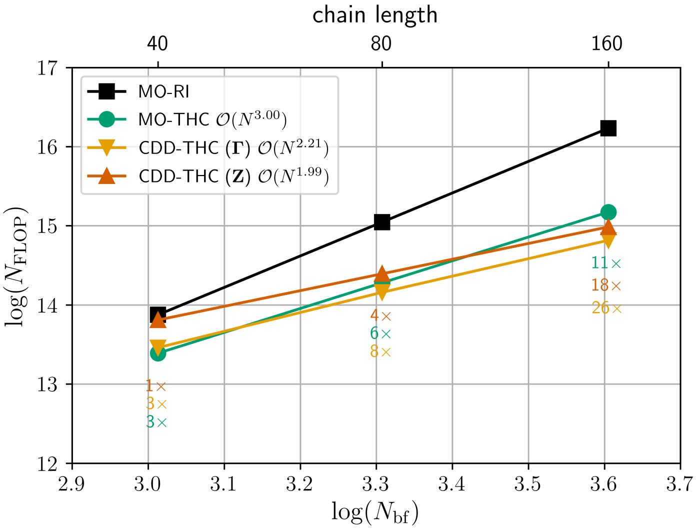

Figure S6: Number of FLOP required to evaluate the SOS-LR-CC2/SOS-ADC(2) matrix-vector product for a series of LCA$_n$ ($n \in \{40, 80, 160\}$) molecules. Labels represent the FLOP reduction compared to the MO-RI-SOS-LR-CC2/ADC(2) implementation. All calculations are performed with the cc-pVDZ/cc-pVDZ-RI basis set combination and the hand-optimized cc-pVDZ-based THC parent grid.

As expected, the MO-THC-based implementation exhibits cubic time complexity, whereas the use of the THC $\mathbf{\Gamma}$ or the THC $\mathbf{Z}$ tensor in conjunction with the CDD approach reduce the scaling exponent to ∼2.2 or ∼2.0, respectively. Despite the scaling advantage, the use of the THC $\mathbf{\Gamma}$ tensor is favorable in terms of the number of FLOP required to evaluate the CDD-THC-SOS-LR-CC2/ADC(2) matrix-vector due to the reduced dimension of the $\mathbf{\Gamma}$ vs. the $\mathbf{Z}$ tensor, i.e., $(N_{\mathrm{grid}} \times N_{\mathrm{aux}})$ vs. $(N_{\mathrm{grid}} \times N_{\mathrm{grid}})$.

6.2 Space Complexity

The memory demand of relevant intermediates in both ground and excited state calculations in the block sparse format is directly proportional to the number of significant and therefore allocated blocks within a given intermediate. The observed space complexity of the intermediates computed within the CDD-THC-SOS-CC2 and CDD-THC-SOS-LR-CC2/ADC(2) algorithms scale at most as $\mathcal{O}(N^{1.5})$ with the system size for both LCAs – Figures S7–S10 in the cc-pVTZ basis – and the AT pairs – Figures S11–S12 in the cc-pVDZ. Notice that the memory demands of the THC fitting matrices scale as $\mathcal{O}(N^2)$ since they are always dense. Thus, in the case of CDD-based reformulations and electronically sparse systems, the memory demands are dominated by either the $\mathbf{\Gamma}$ or $\mathbf{Z}$ THC fitting matrices and formally scale as $\mathcal{O}(N^2)$. Nonetheless, the reduction of the space complexity and the significant memory savings for the intermediates are crucial to extend the application of the proposed methods to systems with hundreds of atoms without the need to batch the work load.

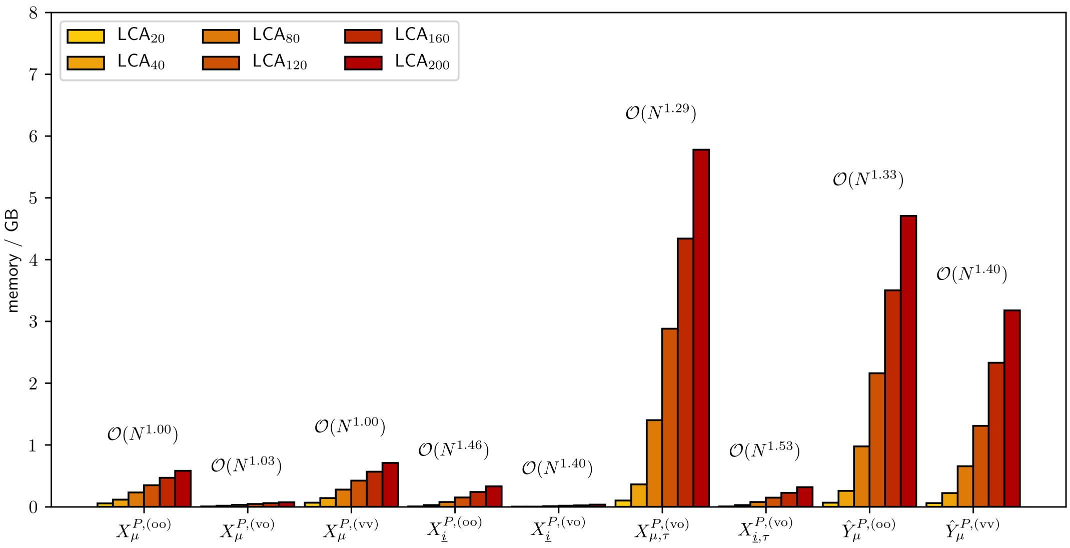

Figure S7: Scaling of the memory requirements of various intermediates of the CDD-THC-SOS-CC2 method. Here relevant intermediates of dimension $N_{\text{grid}} \times N_{\text{bf}}$ or $N_{\text{grid}} \times N_{\text{occ}}$ are included. For Laplace point-dependent intermediates the values are averaged over the number of quadrature points. All calculations are performed for a series of LCA$_n$ molecules with the cc-pVTZ/cc-pVTZ-RI basis set combination.

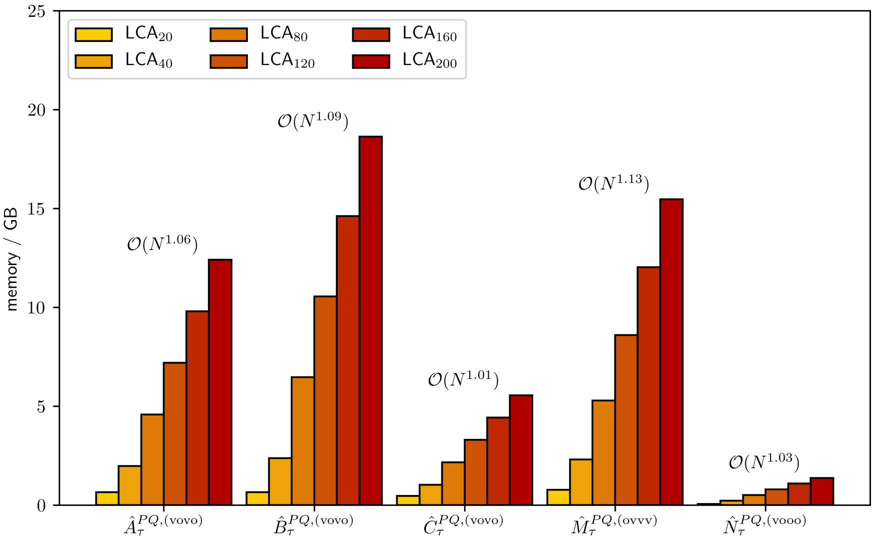

Figure S8: Scaling of the memory requirements of various intermediates of the CDD-THC-SOS-CC2 method. Here relevant intermediates of dimension $N_{\mathrm{grid}} \times N_{\mathrm{grid}}$ are included. For Laplace point-dependent intermediates the values are averaged over the number of quadrature points. All calculations are performed for a series of LCA$_n$ molecules with the cc-pVTZ/cc-pVTZ-RI basis set combination.

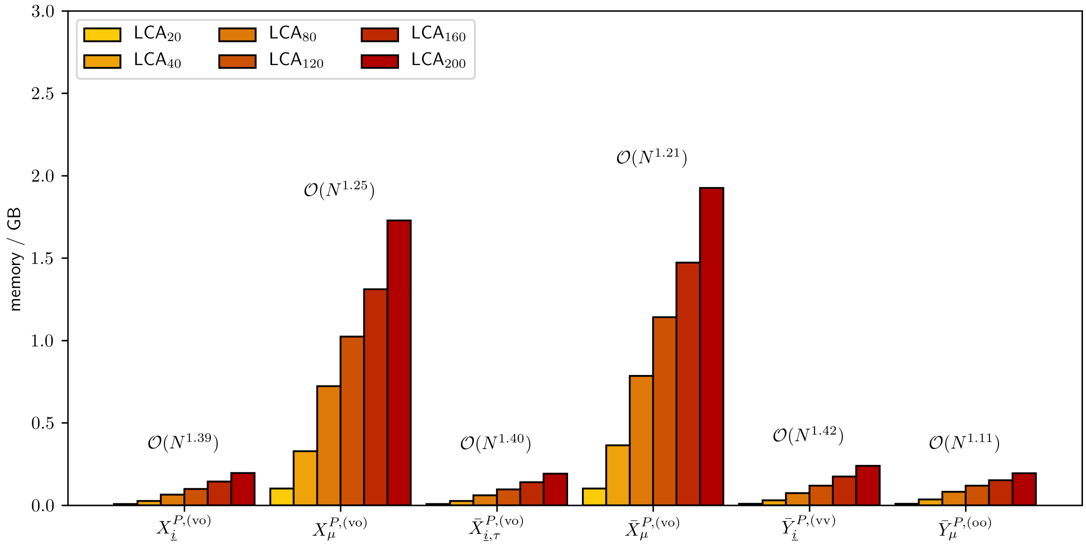

Figure S9: Scaling of the memory requirements of various intermediates of the CDD-THC-SOS-ADC(2) method. Here relevant intermediates of dimension $N_{\mathrm{grid}} \times N_{\mathrm{bf}}$ or $N_{\mathrm{grid}} \times N_{\mathrm{occ}}$ are included. For Laplace point-dependent intermediates the values are averaged over the number of quadrature points. All calculations are performed for a series of LCA$_n$ molecules with the cc-pVTZ/cc-pVTZ-RI basis set combination.

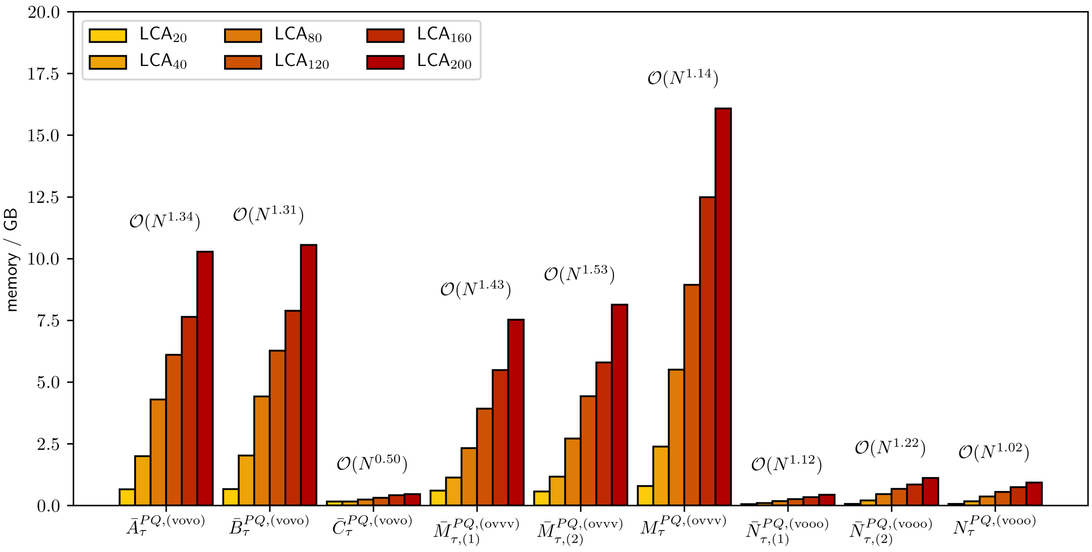

Figure S10: Scaling of the memory requirements of various intermediates of the CDD-THC-SOS-ADC(2) method. Here relevant intermediates of dimension $N_{\mathrm{grid}} \times N_{\mathrm{grid}}$ are included. For Laplace point-dependent intermediates the values are averaged over the number of quadrature points. All calculations are performed for a series of LCA$_n$ molecules with the cc-pVTZ/cc-pVTZ-RI basis set combination.

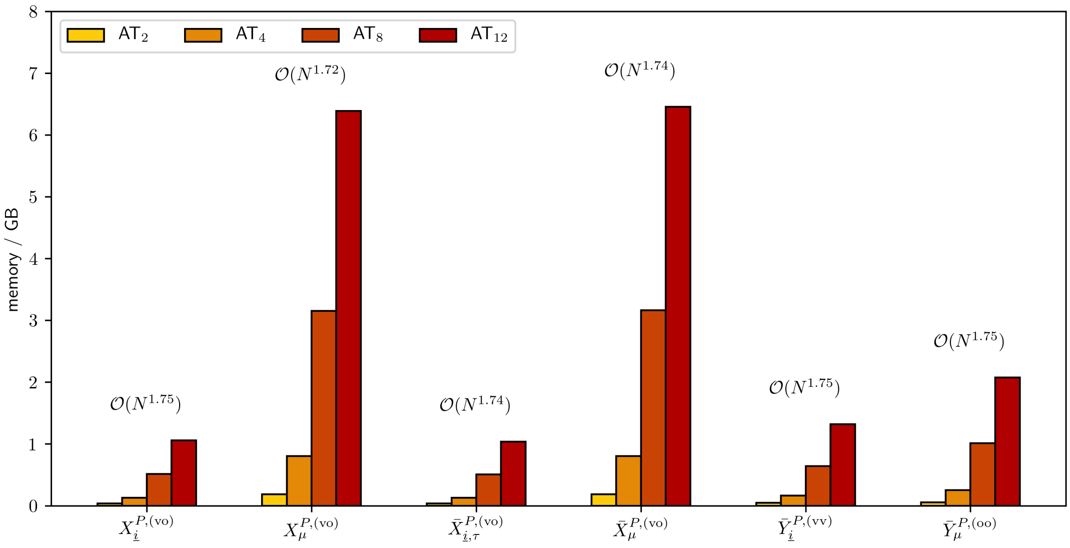

Figure S11: Scaling of the memory requirements of various intermediates of the CDD-THC-SOS-ADC(2) method. Here relevant intermediates of dimension $N_{\mathrm{grid}} \times N_{\mathrm{bf}}$ or $N_{\mathrm{grid}} \times N_{\mathrm{occ}}$ are included. For Laplace point-dependent intermediates the values are averaged over the number of quadrature points. All calculations are performed for a series of AT$_n$ molecules with the cc-pVDZ/cc-pVDZ-RI basis set combination.

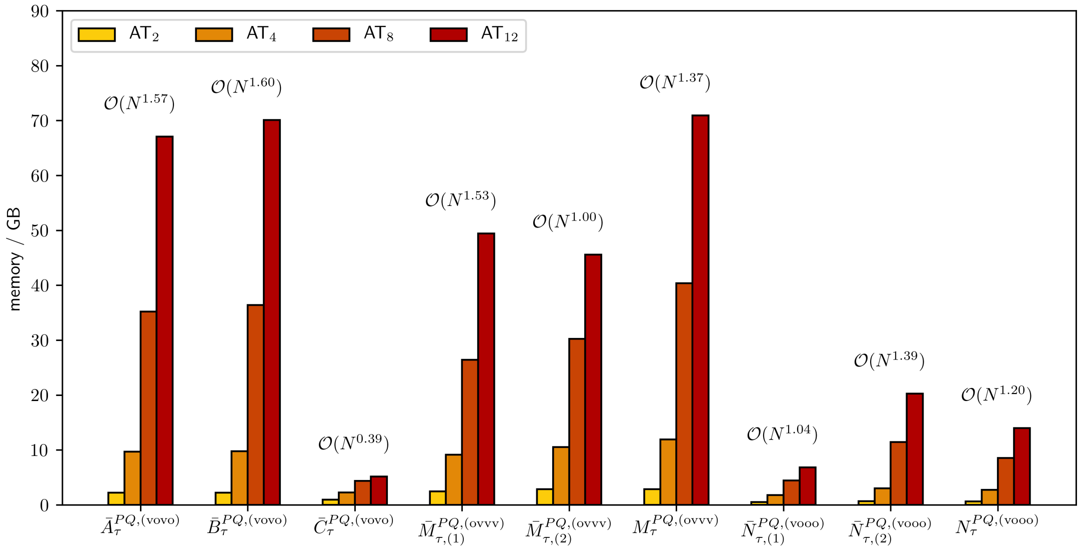

Figure S12: Scaling of the memory requirements of various intermediates of the CDD-THC-SOS-ADC(2) method. Here relevant intermediates of dimension $N_{\mathrm{grid}} \times N_{\mathrm{grid}}$ are included. For Laplace point-dependent intermediates the values are averaged over the number of quadrature points. All calculations are performed for a series of AT_n molecules with the cc-pVDZ/cc-pVDZ-RI basis set combination.

Taking AT_{12} as an illustrative example, one set of MO-based RI integrals using the cc-pVDZ/cc-pVDZ-RI basis set combination would require ∼6 TB of memory/disk space, with a $< 20\%$ saving if Cholesky pseudo-MOs and sparse algebra are put to use. Hence, considering that at least one other set of integrals must be stored in the CDD-RI-SOS-ADC(2) implementation, both the number of input/output (I/O) operations (IOP) as well as storage demands easily become a bottleneck for common high-performance compute nodes and would render batching – with its intrinsic overhead – mandatory. In contrast, for the same basis set the evaluation of the SOS-ADC(2) and SOS-LR-CC2 excitation energy of AT_{12} using THC only requires ∼500 GB of memory space. In addition, the presented implementations of MO- and CDD-THC-SOS-ADC(2)/CC2 only require disk I/O for the $\hat{\mathbf{D}}$ intermediates (∼72 GB for AT_{12}/cc-pVDZ/cc-pVDZ-RI) in the Laplace integration, while all other intermediates can be kept in memory.

References

(S1) Matthews, D. A. Improved Grid Optimization and Fitting in Least Squares Tensor Hypercontraction. *J. Chem. Theory Comput.* **2020**, *16*, 1382–1385.

(S2) Kokkila Schumacher, S. I.; Hohenstein, E. G.; Parrish, R. M.; Wang, L. P.; Martínez, T. J. Tensor Hypercontraction Second-Order Møller-Plesset Perturbation Theory: Grid Optimization and Reaction Energies. *J. Chem. Theory Comput.* **2015**, *11*, 3042–3052.

(S3) Parrish, R. M.; Hohenstein, E. G.; Martínez, T. J.; Sherrill, C. D. Tensor Hypercontraction. II. Least-squares Renormalization. *J. Chem. Phys.* **2012**, *137*, 224106.

(S4) Cuthill, E.; McKee, J. Reducing the Bandwidth of Sparse Symmetric Matrices. *Proceedings of the 1969 24th National Conference, ACM 1969* **1969**, 157–172.

(S5) DiStasio, R. A.; Jung, Y.; Head-Gordon, M. A resolution-of-the-identity implementation of the local triatomics-in-molecules model for second-order Møller- Plesset perturbation theory with application to alanine tetrapeptide conformational energies. *J. Chem. Theory Comput.* **2005**, *1*, 862–876.

(S6) Schreiber, M.; Silva-Junior, M. R.; Sauer, S.; Thiel, W. Benchmarks for electronically excited states: CASPT2, CC2, CCSD, and CC3. *J. Chem. Phys.* **2008**, *128*.

(S7) Hohenstein, E. G.; Kokkila, S. I.; Parrish, R. M.; Martínez, T. J. Tensor Hypercontraction Equation-of-Motion Second-Order Approximate Coupled Cluster: Electronic Excitation Energies in O(N4) Time. *J. Phys. Chem. B* **2013**, *117*, 12972–12978.

4. Conclusion

This thesis is mainly concerned with the development and extension of the LS-THC integral factorization method. LS-THC enables to decompose the fourth-order ERI tensor into second-order tensors and represents the next generation of integral factorizations, going beyond the capabilities of more established methods, like the PS or RI approximation. To extend the applicability of LS-THC, low-scaling and efficient algorithms to obtain the LS-THC tensor are developed. While the efficiency of the algorithm put forward in **Publication I** relies on integral screening and sparse linear algebra, in **Publication IV** an integral-direct density-based algorithm is proposed. The latter is particularly convenient for implementation, since it only requires the ability to evaluate basis functions on a DFT-like grid and to perform J-builds, which is readily available in all quantum chemistry packages which implement KS-DFT. With the presented algorithms to obtain the LS-THC tensors, the development of efficient reformulations of electron correlation methods is facilitated. This is demonstrated for MP2 and CC2 ground state energies, as well as for excitation energies at the LR-CC2 and ADC(2) levels of theory in **Publications I** and **IV**. Furthermore, the necessity to efficiently perform integral contractions is even more pronounced when going from energies to molecular properties through differentiation of the underlying energy functional. Here, many more types of integral tensor are present, due to the additional occurrence of differentiated integrals and density matrices. This is highlighted in **Publication II**, in which the MP2 equations for HFCCs are reformulated in terms of the LS-THC tensor. Compared to previous implementations, this approach enables the accelerated and low-scaling calculation of HFCCs with a low memory footprint at the MP2 level of theory. In general, the ability to theoretically predict molecular properties is crucial to bridge the gap between theory and experiment. Of particular note are spectroscopic methods that find widespread use in all fields of experimental chemistry, such as NMR. Inspired by the high accuracy of numerically calculated RPA NMR shifts, in **Publication III** an analytic expression is derived. It is noteworthy that this represents the first analytic derivation of a second-order property using RPA as a post-KS method based on the ACFDT. The developed theory represents a meaningful starting point for the development of an efficient method for accurate NMR shifts, due to the low formal quartic scaling of RI-RPA. In this regard, it would be beneficial to apply the developed LS-THC approach, as it was already demonstrated in **Publication II** that LS-THC leads to considerable savings in terms of computation time and memory requirements for the calculation of molecular properties. Since, as of yet, there is no analytic expression for the magnetic field derivatives of the LS-THC tensors, the development thereof is a natural extension of the presented research in future work.

A. Appendix

A.1. Second Quantization

A.1.1. Creation and Annihilation Operators

The Pauli exclusion principle [43] is one of the most fundamental axioms of quantum mechanics and states – in its stricter formulation – that the wave function for fermions must be antisymmetric. One way of ensuring the antisymmetry of the wave function upon interchange of the electronic coordinates of two identical particles, i.e., swapping the space and spin coordinates, is to encapsulate the information in the so-called Slater determinant wave function [3]. This ansatz is known as first quantization in quantum mechanics.

However, one is not restricted to encode the antisymmetry principle in the wave function, instead this requirement can also be met by transferring the antisymmetry property onto the algebraic properties of the operators, which is known as second quantization [44]. Since throughout this thesis second quantization will be used to concisely outline the fundamentals of the various correlation methods presented in Section 2.1, a brief explanation is given here.

Let $\hat{a}_p^\dagger$ be a *creation operator* defined by its action on a Slater determinant as

$$\hat{a}_p^\dagger|\varphi_q\cdots\varphi_s\rangle = |\varphi_p\varphi_q\cdots\varphi_s\rangle\,, \tag{A.1}$$

which creates an electron in the spin orbital φ_p. Likewise, let $\hat{a}_p$ be an *annihilation operator*, defined by its action as

$$\hat{a}_p|\varphi_p\varphi_q\cdots\varphi_s\rangle = |\varphi_q\cdots\varphi_s\rangle\,, \tag{A.2}$$

which annihilates an electron in spin orbital φ_p and is the adjoint of the creation operator $\hat{a}_p^\dagger$. Any Slater determinant may therefore be written in terms of the collective action of a chain of creation operators starting from the vacuum state $|\mathrm{VAC}\rangle$ as

$$|\varphi_p\varphi_q\cdots\varphi_s\rangle = \hat{a}_p^\dagger\hat{a}_q^\dagger\cdots\hat{a}_s^\dagger|\mathrm{VAC}\rangle\,. \tag{A.3}$$

Pairwise interchange of a set of creation or annihilation operators results in the following *anticommutation relations*

$$\{\hat{a}_p^\dagger, \hat{a}_q^\dagger\} = \hat{a}_p^\dagger \hat{a}_q^\dagger + \hat{a}_q^\dagger \hat{a}_p^\dagger = 0\,, \tag{A.4}$$

$$\{\hat{a}_p, \hat{a}_q\} = \hat{a}_p \hat{a}_q + \hat{a}_q \hat{a}_p = 0\,, \tag{A.5}$$

$$\{\hat{a}_p, \hat{a}_q^\dagger\} = \hat{a}_p \hat{a}_q^\dagger + \hat{a}_q^\dagger \hat{a}_p = \delta_{pq}\,, \tag{A.6}$$

which incorporate all properties of the Slater determinant. Using eq. (A.3) and the anticommutation relations from eqs. (A.4)–(A.6), any arbitrary Slater determinant can be formed. Furthermore, the one- and two-electron operators $\hat{O}_1$ and $\hat{O}_2$ can be expressed in second quantization as follows

$$\hat{O}_1 = \sum_{pq} \langle p|\hat{h}|q\rangle \hat{a}_p^\dagger \hat{a}_q\,, \tag{A.7}$$

$$\hat{O}_2 = \frac{1}{2} \sum_{pqrs} \langle pq|rs\rangle \hat{a}_p^\dagger \hat{a}_q^\dagger \hat{a}_s \hat{a}_r\,. \tag{A.8}$$

A.1.2. Field Operators

Alternative to the use of single-particle creation $\hat{a}_p^\dagger$ and annihilation operators $\hat{a}_p$, which create or destroy a particle in a specific state p, so-called field operators $\hat{\psi}^\dagger(\boldsymbol{\tau})$, $\hat{\psi}(\boldsymbol{\tau})$ can be applied to create and annihilate particles at different positions in space. A field operator can be expressed as the sum over all possible states in a single-particle basis and *vice versa* a creation/annihilation operator is obtained from a field operator by integration over the coordinate $\boldsymbol{\tau}$ as

$$\hat{\psi}(\boldsymbol{\tau}) = \sum_p \varphi_p(\boldsymbol{\tau})\, \hat{a}_p\,, \tag{A.9}$$

$$\hat{a}_p = \int d\boldsymbol{\tau}\, \varphi_p(\boldsymbol{\tau}) \hat{\psi}(\boldsymbol{\tau})\,. \tag{A.10}$$

Based on eqs. (A.4)–(A.6) the anticommutation relations for field operators are given by

$$\{\hat{\psi}^\dagger(\boldsymbol{\tau}_1), \hat{\psi}^\dagger(\boldsymbol{\tau}_2)\} = 0\,, \tag{A.11}$$

$$\{\hat{\psi}(\boldsymbol{\tau}_1), \hat{\psi}(\boldsymbol{\tau}_2)\} = 0\,, \tag{A.12}$$

$$\{\hat{\psi}^\dagger(\boldsymbol{\tau}_1), \hat{\psi}(\boldsymbol{\tau}_2)\} = \delta_{\boldsymbol{\tau}_1,\boldsymbol{\tau}_2}\,. \tag{A.13}$$

A.1.3. Normal Order

An arbitrary string of creation and annihilation operators $\hat{a}_p^\dagger \cdots \hat{a}_q$ is said to be in *normal order* if all creation operators are left to all annihilation operators. Let $\hat{A}$ be a string of creation and annihilation operators, then $\mathcal{N}(\hat{A})$ denotes the normal ordered form of $\hat{A}$.

Defining a normal order allows to directly evaluate the action of a string of creation and annihilation operators, e.g.,

$$\begin{aligned}
\mathcal{N}(\hat{A})|\mathrm{VAC}\rangle = 0 \quad &\rightarrow \quad \text{except when } \hat{A} \text{ contains only creation operators} \\
\langle\mathrm{VAC}|\mathcal{N}(\hat{A}) = 0 \quad &\rightarrow \quad \text{except when } \hat{A} \text{ contains only annihilation operators} \\
\langle\mathrm{VAC}|\mathcal{N}(\hat{A})|\mathrm{VAC}\rangle = 0 \quad &\rightarrow \quad \text{except when } \hat{A} \text{ contains no operators}
\end{aligned}$$

and avoids terms where annihilation operators act on the vacuum state, which would simply yield zero. To obtain normal ordered operators, Wick's theorem [45] can be applied, which states that an arbitrary string of creation and annihilation operators can be expressed as a linear combination of increasingly pairwise contracted normal ordered operator strings, i.e.,

$$\hat{a}\hat{b}\hat{c}\cdots\hat{x}\hat{y}\hat{z} = \mathcal{N}(\hat{a}\hat{b}\hat{c}\cdots\hat{x}\hat{y}\hat{z}) + \sum_{\text{singles}} \mathcal{N}(\wick{\c{\hat{a}}\c{\hat{b}}}\hat{c}\cdots\hat{x}\hat{y}\hat{z}) + \sum_{\text{doubles}} \mathcal{N}(\wick{\c1{\hat{a}}\c2{\hat{b}}\c1{\hat{c}}\cdots\c2{\hat{x}}}\hat{y}\hat{z}) + \cdots\,, \tag{A.14}$$

where "singles", "doubles", etc. symbolizes the sum over the given number of pairwise contractions. A *contraction* between two arbitrary creation and annihilation operators $\hat{a}$ and $\hat{b}$ is defined as

$$\wick{\c{\hat{a}}\c{\hat{b}}} = \hat{a}\hat{b} - \mathcal{N}(\hat{a}\hat{b}), \tag{A.15}$$

whereas the term *fully contracted* is used when all elementary operators in an operator string are pairwise contracted.

A.1.4. Particle-hole Formalism

Since the vacuum state $|\mathrm{VAC}\rangle$ is only of little interest for practical applications, it is more convenient to define the Hartree–Fock determinant $|0\rangle := |\Psi_{\mathrm{HF}}\rangle$ [3], also known as the Fermi vacuum, as the reference state. For this, the orbital space is partitioned into a hole (orbitals $i, j, k, \ldots$) and a particle space (orbitals $a, b, c, \ldots$), while operators creating or destroying particles or holes are referred to as *quasiparticle operators.* Based on the definition of the reference state, the operators $\hat{a}_a^\dagger$ and $\hat{a}_i$ are quasiparticle creation operators and $\hat{a}_a$ and $\hat{a}_i^\dagger$ are quasiparticle annihilation operators. The action of the quasiparticle creation operators $\hat{a}_a^\dagger$ and $\hat{a}_i$ is shown schematically in Fig. A.1.

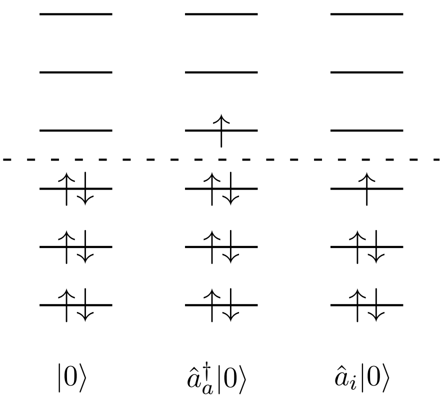

Figure A.1.: Schematic representation of the action of quasiparticle operators on the Fermi vacuum.

Changing the reference state to the Fermi vacuum requires to adjust the definition of the normal order. A string of quasiparticle operators is normal ordered with regard to the Fermi vacuum if all quasiparticle creation operators are left of all quasiparticle annihilation operators. As a consequence of the change of the definition of the normal order, the only non-zero contractions between quasiparticle operators are between quasiparticle annihilation operators that are left to quasiparticle creation operators, i.e.,

$$\overbracket{\hat{a}_i^\dagger\hat{a}_j} = \hat{a}_i^\dagger\hat{a}_j - \mathcal{N}(\hat{a}_i^\dagger\hat{a}_j) = \hat{a}_i^\dagger\hat{a}_j + \hat{a}_j\hat{a}_i^\dagger = \{\hat{a}_i^\dagger, \hat{a}_j\} = \delta_{ij}\,, \tag{A.16}$$

$$\overbracket{\hat{a}_a\hat{a}_b^\dagger} = \hat{a}_a\hat{a}_b^\dagger - \mathcal{N}(\hat{a}_a\hat{a}_b^\dagger) = \hat{a}_a\hat{a}_b^\dagger + \hat{a}_b^\dagger\hat{a}_a = \{\hat{a}_a, \hat{a}_b^\dagger\} = \delta_{ab}\,. \tag{A.17}$$

A.1.5. Electron-Electron Interaction Potential in Second Quantization

To describe pairwise interactions in systems with interacting particles, general two-particle operators $\hat{\mathcal{O}}_2$ are used. In this regard, every two-particle operator $\hat{\mathcal{O}}_2$ in second quantization can be expressed as

$$\hat{\mathcal{O}}_2 = \sum_{pqrs} \mathcal{O}_{pqrs}\hat{a}_p^\dagger\hat{a}_q^\dagger\hat{a}_s\hat{a}_r\,, \tag{A.18}$$

from the first quantized form, where $\mathcal{O}_{pqrs} = \langle pq|\hat{\mathcal{O}}_2|rs\rangle$. The two-particle electron-electron Coulomb interaction potential $\hat{V}_{\text{ee}} = \frac{1}{2}\sum_{i\neq j}\frac{1}{r_{ij}}$ is therefore given as

$$\hat{V}_{\text{ee}} = \frac{1}{2}\sum_{pqrs}\iint d\boldsymbol{\tau}_1 d\boldsymbol{\tau}_2 \varphi_p^*(\boldsymbol{\tau}_1)\varphi_q^*(\boldsymbol{\tau}_2)\frac{1}{r_{12}}\varphi_r(\boldsymbol{\tau}_1)\varphi_s(\boldsymbol{\tau}_2)\,\hat{a}_p^\dagger\hat{a}_q^\dagger\hat{a}_s\hat{a}_r\,, \tag{A.19}$$

which can be rewritten as

$$\hat{V}_{\text{ee}} = \frac{1}{2} \iint d\boldsymbol{\tau}_1 d\boldsymbol{\tau}_2 \, \hat{\psi}^\dagger(\boldsymbol{\tau}_1)\hat{\psi}^\dagger(\boldsymbol{\tau}_2)\frac{1}{r_{12}}\hat{\psi}(\boldsymbol{\tau}_2)\hat{\psi}(\boldsymbol{\tau}_1) \, , \tag{A.20}$$

using the field operators introduced in Section A.1.2. Applying the anticommutation relations given in eqs. (A.11)–(A.13) gives

$$\hat{\psi}^\dagger(\boldsymbol{\tau}_1)\hat{\psi}^\dagger(\boldsymbol{\tau}_2)\hat{\psi}(\boldsymbol{\tau}_2)\hat{\psi}(\boldsymbol{\tau}_1) = \hat{\psi}^\dagger(\boldsymbol{\tau}_1)\hat{\psi}(\boldsymbol{\tau}_1)\hat{\psi}^\dagger(\boldsymbol{\tau}_2)\hat{\psi}(\boldsymbol{\tau}_2) - \delta_{\boldsymbol{\tau}_1,\boldsymbol{\tau}_2}\hat{\psi}^\dagger(\boldsymbol{\tau}_1)\hat{\psi}(\boldsymbol{\tau}_1) \, . \tag{A.21}$$

Finally, defining the density operator as

$$\hat{n}(\mathbf{r}) = \int d\sigma \, \hat{\psi}^\dagger(\boldsymbol{\tau})\hat{\psi}(\boldsymbol{\tau}) \, , \tag{A.22}$$

allows to rewrite the electron-electron interaction as

$$\hat{V}_{\text{ee}} = \frac{1}{2} \iint d\mathbf{r}_1 d\mathbf{r}_2 \frac{1}{r_{12}} \left[\hat{n}(\mathbf{r}_1)\hat{n}(\mathbf{r}_2) - \delta_{\mathbf{r}_1,\mathbf{r}_2}\hat{n}(\mathbf{r}_1)\right] \, . \tag{A.23}$$

A.2. Many-body Green's Function

A.2.1. Mathematical Basics

In general, Green's functions are special solutions to inhomogeneous linear differential equations of the form

$$\hat{L}_x u(x) = f(x) \, , \tag{A.24}$$

where $\hat{L}_x$ is a linear differential operator and $f(x)$ is the inhomogeneity. The general solution to eq. (A.24) can be constructed from the homogeneous solution $u_0(x)$ of $\hat{L}_x u_0(x) = 0$ and the special solution. If for the special solution the inhomogeneity is taken to be a Dirac function, i.e.,

$$\hat{L}_x u_{\text{Green}}(x) = \delta(x - x') \, , \tag{A.25}$$

the solution $G(x) \coloneqq u_{\text{Green}}(x)$ is referred to as the fundamental solution or Green's function. From the Green's function the solution for eq. (A.24) for any inhomogeneity $f(x)$ can be obtained by convolution ($*$) with the Green's function, given as

$$u(x) = G(x) * f(x) = \int G(x - x')f(x')dx' \, . \tag{A.26}$$

A.2.2. Many-body Green's Functions in Quantum Chemistry

Like eq. (A.24), the time-dependent Schrödinger equation (TDSE) [38] represents a linear differential equation given by

$$\left(\mathrm{i}\frac{\partial}{\partial t} - \hat{\mathcal{H}}\right)|\Psi(\mathbf{r},t)\rangle = 0\,, \tag{A.27}$$

in atomic units, for which the wave function can be expressed as

$$\Psi(\mathbf{r},t) = \iint d\mathbf{r}'dt'G(\mathbf{r},t;\mathbf{r}',t')\Psi(\mathbf{r}',t')\,, \tag{A.28}$$

according to Section A.2.1. As implied by eq. (A.28), the Green's function acts as a propagator for the wave function and represents the probability amplitude that a particle gets from an event $(\mathbf{r},t)$ to an event $(\mathbf{r}',t')$. Depending on the number of interacting particles on a path, the Green's functions can be understood as single-, two-, ..., many-particle propagators. Fig. A.2 exemplarily shows diagrammatic representations of a single-particle electron propagator (left) used to describe ionization processes and a two-particle electron-hole propagator (right) used to describe excitations.

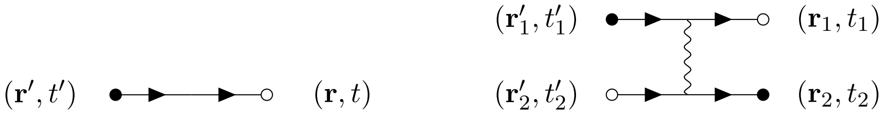

Figure A.2.: Diagrammatic representation of a single-particle electron propagator (left) and a two-particle electron-hole propagator (right). Electrons are represented by • and holes by ∘. The sine wave represents a photon interaction.

To demonstrate the action of a Green's function, consider the single-particle Green's function given by

$$G_{pq}(t,t') = -\mathrm{i}\Theta(t-t')\langle\Psi_0^N|\,\hat{T}\left(\hat{a}_p(t)\hat{a}_q^\dagger(t')\right)|\Psi_0^N\rangle\,, \tag{A.29}$$

where N for the wave function indicates the electron number. Furthermore, $\Theta(t)$ is the Heaviside function and $\hat{T}$ is the time-ordering operator defined as

$$\hat{T}\left(\hat{A}(t)\hat{B}(t')\right) = \begin{cases} \hat{A}(t)\hat{B}(t') & \text{for } t-t'>0 \\ -\hat{B}(t')\hat{A}(t) & \text{for } t-t'<0 \end{cases}\,. \tag{A.30}$$

In eq. (A.29) the Heisenberg operators $\hat{a}_p(t)$ and $\hat{a}_q^\dagger(t')$ create and destroy an electron in a single-particle state at the times t and t', respectively. Eq. (A.29) thereby describes the process of adding an electron in the single-particle state q at time t', which is added to the exact ground state. As a consequence of not being in an eigenstate of the Hamiltonian, the electron interacts with other electrons in the system and is then removed again at time t. The Green's function then describes the amplitude at the time of the removal. Furthermore, forming the Fourier transform of eq. (A.29) yields the spectral or Lehmann's representation [69] of the Green's function as

$$\begin{aligned} G_{pq}(\omega) = \sum_{n\neq 0} \Bigg(& \underbrace{\frac{\langle\Psi_0^N|\hat{a}_p|\Psi_n^{N+1}\rangle\langle\Psi_n^{N+1}|\hat{a}_q^\dagger|\Psi_0^N\rangle}{\omega - (E_n^{N+1} - E_0^N) + \mathrm{i}\eta}}_{G^+(t,t')} \\ & + \underbrace{\frac{\langle\Psi_0^N|\hat{a}_q^\dagger|\Psi_n^{N-1}\rangle\langle\Psi_n^{N-1}|\hat{a}_p|\Psi_0^N\rangle}{\omega + (E_0^N - E_n^{N-1}) - \mathrm{i}\eta}}_{G^-(t,t')} \Bigg), \end{aligned} \tag{A.31}$$

where $\eta = 0^+$ is the positive infinitesimal. Analyzing the poles of eq. (A.31) reveals that the first term $G^+(t,t')$ originating from the positive time domain of eq. (A.29) gives access to electron affinities (EA), while the second term $G^-(t,t')$ from the negative time domain of eq. (A.29) contains ionization potentials (IP):

$$\omega = (E_0^{N+1} - E_n^N) - \mathrm{i}\eta \qquad \Rightarrow \qquad \mathrm{EA} = E_0^N - E_n^{N+1} \tag{A.32}$$

$$\omega = (E_n^{N-1} - E_0^N) + \mathrm{i}\eta \qquad \Rightarrow \qquad \mathrm{IP} = E_n^{N-1} - E_0^N \tag{A.33}$$

The single-particle Green's function therefore contains spectral information about single-particle excitations which change the number of electrons in the system by one, with the poles corresponding to the excitation energies.

To obtain excitation energies for particle conserving processes the so-called polarization propagator can be formulated as

$$\begin{aligned} \Pi_{pqrs}(t,t') = & -\mathrm{i}\Theta(t-t')\langle\Psi_0^N|\,\hat{T}\left(\hat{a}_q^\dagger(t)\hat{a}_p(t)\hat{a}_r^\dagger(t')\hat{a}_s(t')\right)|\Psi_0^N\rangle \\ & + \mathrm{i}\langle\Psi_0^N|\,\hat{a}_q^\dagger\hat{a}_p|\Psi_0^N\rangle\langle\Psi_0^N|\,\hat{a}_r^\dagger\hat{a}_s|\Psi_0^N\rangle\,, \end{aligned} \tag{A.34}$$

in analogy to eq. (A.29). In the Heisenberg picture eq. (A.34) can also be rewritten in terms of the density fluctuation operator $\tilde{n}(\mathbf{r}) \coloneqq \hat{n}(\mathbf{r}) - n(\mathbf{r})$, with the density $n(\mathbf{r})$ obtained as the expectation value of the density operator $\hat{n}(\mathbf{r})$. Therefore, eq. (A.34) is also often referred to as the density-density response function, which is apparent by comparing against eq. (2.37) for the linear response function.[1] To obtain excitation energies from eq. (A.34), its Lehmann representation given by

---

[1] The nomenclature in the literature is ambiguous as to whether there is a difference between a response function and a propagator or not. Since both can be understood as two-particle correlation functions, the terms will be used interchangeably throughout.

$$
\begin{aligned}
\Pi_{pqrs}(\omega) = \sum_{n\neq 0} \Bigg(& \underbrace{\frac{\langle \Psi_0^N | \hat{a}_q^\dagger \hat{a}_p | \Psi_n^N \rangle \langle \Psi_n^N | \hat{a}_r^\dagger \hat{a}_s | \Psi_0^N \rangle}{\omega - (E_n^N - E_0^N) + \mathrm{i}\eta}}_{\Pi^+(t,t')} \\
& + \underbrace{\frac{\langle \Psi_0^N | \hat{a}_r^\dagger \hat{a}_s | \Psi_n^N \rangle \langle \Psi_n^N | \hat{a}_q^\dagger \hat{a}_p | \Psi_0^N \rangle}{\omega + (E_n^N - E_0^N) - \mathrm{i}\eta}}_{\Pi^-(t,t')} \Bigg) ,
\end{aligned}
\tag{A.35}
$$

can be analyzed for poles $\omega = E_n^N - E_0^N$, as for the single-particle Green's function.

A.3. Connection Between LT-AO-MP2 and AO-RI-dRPA

A.3.1. Correlation Energy

In matrix notation the Laplace-transform (LT-) AO-MP2 energy [154–156] equation is given by

$$
E^{\mathrm{c}}_{\mathrm{MP2}} = -\int_0^\infty d\tau \, \mathrm{Tr}\left[\left(\underline{\mathbf{P}}(\tau) \otimes \overline{\mathbf{P}}(\tau) \right) \boldsymbol{\mathcal{I}} \left(\underline{\mathbf{P}}(\tau) \otimes \overline{\mathbf{P}}(\tau) \right) (2\boldsymbol{\mathcal{I}} - \boldsymbol{\mathcal{I}}') \right] , \tag{A.36}
$$

where the analytic integral for the Laplace transformation is used instead of numerical integration. Here $\underline{\mathbf{P}}$ and $\overline{\mathbf{P}}$ are the usual pseudodensities, defined as

$$
\underline{\mathbf{P}}(\tau) = e^{\tau \mathbf{P}_{\mathrm{occ}} \mathbf{F}} \mathbf{P}_{\mathrm{occ}} \, , \tag{A.37}
$$

$$
\overline{\mathbf{P}}(\tau) = e^{-\tau \mathbf{P}_{\mathrm{virt}} \mathbf{F}} \mathbf{P}_{\mathrm{virt}} \, , \tag{A.38}
$$

while $\boldsymbol{\mathcal{I}}$ and $\boldsymbol{\mathcal{I}}'$ are the fourth-order ERI tensors associated with the integrals of type $(\mu\nu|\lambda\sigma)$ and $(\mu\sigma|\lambda\nu)$, respectively. Inserting the RI approximation from Section 2.4.1 into the ERI tensor $\boldsymbol{\mathcal{I}}$ results in

$$
\boldsymbol{\mathcal{I}} = \mathbf{B}\mathbf{V}\mathbf{B}^{\mathrm{T}} \, , \tag{A.39}
$$

where $\mathbf{B}$ is three-center and $\mathbf{V}$ is the two-center RI integral tensor. This results in the expression for the opposite-spin (OS) contribution to the LT-AO-MP2 energy given by

$$
\begin{aligned}
E^{\mathrm{c}}_{\text{OS-MP2}} &= -\int_0^\infty d\tau \, \mathrm{Tr}\left[\left(\underline{\mathbf{P}}(\tau) \otimes \overline{\mathbf{P}}(\tau) \right) \mathbf{B}\mathbf{V}\mathbf{B}^{\mathrm{T}} \left(\underline{\mathbf{P}}(\tau) \otimes \overline{\mathbf{P}}(\tau) \right) \mathbf{B}\mathbf{V}\mathbf{B}^{\mathrm{T}} \right] \\
&= -\int_0^\infty d\tau \, \mathrm{Tr}\left[\mathbf{B}^{\mathrm{T}} \left(\underline{\mathbf{P}}(\tau) \otimes \overline{\mathbf{P}}(\tau) \right) \mathbf{B}\mathbf{V}\mathbf{B}^{\mathrm{T}} \left(\underline{\mathbf{P}}(\tau) \otimes \overline{\mathbf{P}}(\tau) \right) \mathbf{B}\mathbf{V} \right] .
\end{aligned}
\tag{A.40}
$$

In the second rearrangement in eq. (A.40), cyclic permutation under the trace is used, which with the definition of an additional intermediate $\mathbf{Z}$ [157] given by

$$\mathbf{Z}(\tau) = \mathbf{B}^{\mathrm{T}} \left(\underline{\mathbf{P}}(\tau) \otimes \overline{\mathbf{P}}(\tau) \right) \mathbf{B} \,, \tag{A.41}$$

the OS contribution to the LT-AO-MP2 can be simplified to

$$E^{\mathrm{c}}_{\text{OS-MP2}} = -\int_0^\infty d\tau \, \mathrm{Tr}\left[\mathbf{Z}(\tau)\mathbf{V}\mathbf{Z}(\tau)\mathbf{V}\right] \,. \tag{A.42}$$

Furthermore, the AO-RI-dRPA energy expression [158, 159] is given by

$$E^{c}_{\text{dRPA}} = \int_0^\infty \frac{d\omega}{2\pi} \mathrm{Tr}\left[\ln\left(1 - \hat{\mathbf{X}}_0(\mathrm{i}\omega)\mathbf{V}\right) + \hat{\mathbf{X}}_0(\mathrm{i}\omega)\right] \,, \tag{A.43}$$

with the non-interacting density-density response function $\hat{\mathbf{X}}_0(\mathrm{i}\omega)$ in the imaginary frequency domain $\mathrm{i}\omega$ defined as the Fourier transform of the response function in the imaginary time domain $\mathrm{i}\tau$ given by

$$\hat{\mathbf{X}}_0(\mathrm{i}\omega) = \int_{-\infty}^\infty d\tau e^{\mathrm{i}\omega\tau} \mathbf{X}_0(\mathrm{i}\tau) \,, \tag{A.44}$$

$$\mathbf{X}_0(\mathrm{i}\tau) = \mathbf{B}^{\mathrm{T}} \left(\mathbf{G}_0(-\mathrm{i}\tau) \otimes \mathbf{G}_0(\mathrm{i}\tau)\right) \mathbf{B} \,. \tag{A.45}$$

Here, $\mathbf{G}_0(\mathrm{i}\tau)$ denotes the non-interacting Green's function in the imaginary time domain, see Section A.2, given by

$$\mathbf{G}_0(\mathrm{i}\tau) = \Theta(-\tau)\underline{\mathbf{G}}_0(\mathrm{i}\tau) + \Theta(\tau)\overline{\mathbf{G}}_0(\mathrm{i}\tau) \,, \tag{A.46}$$

$$\underline{\mathbf{G}}_0(\mathrm{i}\tau) = \mathbf{P}_{\mathrm{occ}} e^{-\tau(\mathbf{H}_{\mathrm{KS}} - \varepsilon_F \mathbf{S})\mathbf{P}_{\mathrm{occ}}} \,, \tag{A.47}$$

$$\overline{\mathbf{G}}_0(\mathrm{i}\tau) = -\mathbf{P}_{\mathrm{virt}} e^{-\tau(\mathbf{H}_{\mathrm{KS}} - \varepsilon_F \mathbf{S})\mathbf{P}_{\mathrm{virt}}} \,. \tag{A.48}$$

To compare the expressions for the LT-AO-MP2 energy in eq. (A.42) with the AO-RI-dRPA energy, the logarithm in eq. (A.43) can be expanded in a series as $\ln(1-x) = -\sum_n^\infty \frac{x^n}{n}$ yielding a corresponding series expansion for the energy. In this expansion the n^{th}-order term is given by

$$E^{(n)}_{\text{dRPA}} = -\frac{1}{4\pi}\frac{1}{n} \int_{-\infty}^\infty d\omega \, \mathrm{Tr}\left[\hat{\mathbf{X}}_0(\mathrm{i}\omega)\mathbf{V}\right]^n \qquad \forall n \geq 2 \,. \tag{A.49}$$

The lowest order contribution ($n = 2$) is therefore given by

$$E^{(2)}_{\text{dRPA}} = -\frac{1}{8\pi} \int_{-\infty}^\infty d\omega \, \mathrm{Tr}\left[\hat{\mathbf{X}}_0(\mathrm{i}\omega)\mathbf{V}\right]^2 \,, \tag{A.50}$$

and can be transformed to the imaginary time domain by inserting eq. (A.44) into eq. (A.50) and by using the identity $\int d\omega \, e^{\mathrm{i}\omega\tau} = 2\pi\delta(\tau)$, which yields

$$\begin{aligned} E^{(2)}_{\mathrm{dRPA}} &= -\frac{1}{4}\int_{-\infty}^{\infty} d\tau \,\mathrm{Tr}\left[\mathbf{X}_0(\mathrm{i}\tau)\mathbf{V}\right]^2 \,, \\ &= -\frac{1}{2}\int_{0}^{\infty} d\tau \,\mathrm{Tr}\left[\mathbf{X}_0(\mathrm{i}\tau)\mathbf{V}\mathbf{X}_0(\mathrm{i}\tau)\mathbf{V}\right] \,, \end{aligned} \tag{A.51}$$

where the symmetry of the response function is used to restrict the integral to the positive imaginary time domain.

Comparing eq. (A.42) for the LT-AO-MP2 energy, with the expression for the second-order contribution to the AO-RI-dRPA in eq. (A.51) reveals a close relation between the two expressions. Both expressions involve an integration over an (imaginary) time domain and the involved matrices closely resemble each other, as is evident by comparing eq. (A.41) for intermediate $\mathbf{Z}(\tau)$ with eq. (A.45) for the response function $\mathbf{X}_0(\mathrm{i}\tau)$.

A.3.2. Molecular Gradient of LT-AO-MP2

According to the chain rule of differentiation, the derivative with respect to a general perturbation ξ of the LT-AO-MP2 energy in eq. (A.36) can be obtained as

$$\begin{aligned} \frac{\partial E^{\mathrm{c}}_{\mathrm{MP2}}}{\partial \xi} &= \mathrm{Tr}\left\{\frac{\partial E^{\mathrm{c}}_{\mathrm{MP2}}}{\partial \boldsymbol{\mathcal{I}}}\frac{\partial \boldsymbol{\mathcal{I}}}{\partial \xi}\right\} + \mathrm{Tr}\left\{\frac{\partial E^{\mathrm{c}}_{\mathrm{MP2}}}{\partial \boldsymbol{\mathcal{I}}'}\frac{\partial \boldsymbol{\mathcal{I}}'}{\partial \xi}\right\} \\ &\quad + \mathrm{Tr}\left\{\frac{\partial E^{\mathrm{c}}_{\mathrm{MP2}}}{\partial \underline{\mathbf{P}}(\tau)}\frac{\partial \underline{\mathbf{P}}(\tau)}{\partial \xi}\right\} + \mathrm{Tr}\left\{\frac{\partial E^{\mathrm{c}}_{\mathrm{MP2}}}{\partial \overline{\mathbf{P}}(\tau)}\frac{\partial \overline{\mathbf{P}}(\tau)}{\partial \xi}\right\} . \end{aligned} \tag{A.52}$$

Here, the derivative of the MP2 correlation energy with respect to the ERI tensor $\boldsymbol{\mathcal{I}}$ is given by

$$\begin{aligned} \frac{\partial E^{\mathrm{c}}_{\mathrm{MP2}}}{\partial \boldsymbol{\mathcal{I}}} &= -\int_0^{\infty} d\tau \Big\{ \left(\underline{\mathbf{P}}(\tau)\otimes\overline{\mathbf{P}}(\tau)\right)\left(\underline{\mathbf{P}}(\tau)\otimes\overline{\mathbf{P}}(\tau)\right)\left(2\boldsymbol{\mathcal{I}}-\boldsymbol{\mathcal{I}}'\right) \\ &\quad + 2\left(\underline{\mathbf{P}}(\tau)\otimes\overline{\mathbf{P}}(\tau)\right)\boldsymbol{\mathcal{I}}\left(\underline{\mathbf{P}}(\tau)\otimes\overline{\mathbf{P}}(\tau)\right)\Big\} \\ &= -\int_0^{\infty} d\tau \Big\{ 4\left(\underline{\mathbf{P}}(\tau)\otimes\overline{\mathbf{P}}(\tau)\right)\boldsymbol{\mathcal{I}}\left(\underline{\mathbf{P}}(\tau)\otimes\overline{\mathbf{P}}(\tau)\right) \\ &\quad + \left(\underline{\mathbf{P}}(\tau)\otimes\overline{\mathbf{P}}(\tau)\right)\boldsymbol{\mathcal{I}}'\left(\underline{\mathbf{P}}(\tau)\otimes\overline{\mathbf{P}}(\tau)\right)\Big\} . \end{aligned} \tag{A.53}$$

Note that the permutation of terms is allowed here due to the surrounding trace in eq. (A.52). Likewise the derivative with respect to $\boldsymbol{\mathcal{I}}'$ is given by

$$\frac{\partial E^{\mathrm{c}}_{\mathrm{MP2}}}{\partial \boldsymbol{\mathcal{I}}'} = \int_0^{\infty} d\tau \left\{\left(\underline{\mathbf{P}}(\tau)\otimes\overline{\mathbf{P}}(\tau)\right)\boldsymbol{\mathcal{I}}\left(\underline{\mathbf{P}}(\tau)\otimes\overline{\mathbf{P}}(\tau)\right)\right\} . \tag{A.54}$$

The derivative of the MP2 correlation energy with respect to the occupied pseudodensity $\underline{\mathbf{P}}$ is given by

$$\begin{aligned}\frac{\partial E^{\mathrm{c}}_{\mathrm{MP2}}}{\partial \underline{\mathbf{P}}(\tau)} &= -\int_0^\infty d\tau \left\{ \overline{\mathbf{P}}(\tau)\boldsymbol{\mathcal{I}}\left(\underline{\mathbf{P}}(\tau)\otimes\overline{\mathbf{P}}(\tau)\right)(2\boldsymbol{\mathcal{I}}-\boldsymbol{\mathcal{I}}') + \left(\underline{\mathbf{P}}(\tau)\otimes\overline{\mathbf{P}}(\tau)\right)\boldsymbol{\mathcal{I}}\overline{\mathbf{P}}(\tau)(2\boldsymbol{\mathcal{I}}-\boldsymbol{\mathcal{I}}')\right\} \\ &= -\int_0^\infty d\tau \left\{ 2\overline{\mathbf{P}}(\tau)\boldsymbol{\mathcal{I}}\left(\underline{\mathbf{P}}(\tau)\otimes\overline{\mathbf{P}}(\tau)\right)(2\boldsymbol{\mathcal{I}}-\boldsymbol{\mathcal{I}}')\right\}\,, \qquad \text{(A.55)}\end{aligned}$$

and likewise the derivative with respect to the virtual pseudodensity $\overline{\mathbf{P}}$ is given by

$$\frac{\partial E^{\mathrm{c}}_{\mathrm{MP2}}}{\partial \overline{\mathbf{P}}(\tau)} = -\int_0^\infty d\tau \left\{ 2\underline{\mathbf{P}}(\tau)\boldsymbol{\mathcal{I}}\left(\underline{\mathbf{P}}(\tau)\otimes\overline{\mathbf{P}}(\tau)\right)(2\boldsymbol{\mathcal{I}}-\boldsymbol{\mathcal{I}}')\right\}\,. \qquad \text{(A.56)}$$

Combining all presented partial derivatives in eqs. (A.53)–(A.56), the final total derivative in eq. (A.52) becomes

$$\begin{aligned}\frac{\partial E^{\mathrm{c}}_{\mathrm{MP2}}}{\partial \xi} = -\int_0^\infty d\tau\,\mathrm{Tr}\Big\{ & 4\left(\underline{\mathbf{P}}(\tau)\otimes\overline{\mathbf{P}}(\tau)\right)\boldsymbol{\mathcal{I}}\left(\underline{\mathbf{P}}\otimes\overline{\mathbf{P}}(\tau)\right)\boldsymbol{\mathcal{I}}^{\xi} \\ & - \left(\underline{\mathbf{P}}(\tau)\otimes\overline{\mathbf{P}}(\tau)\right)\boldsymbol{\mathcal{I}}'\left(\underline{\mathbf{P}}(\tau)\otimes\overline{\mathbf{P}}(\tau)\right)\boldsymbol{\mathcal{I}}^{\xi} \\ & - \left(\underline{\mathbf{P}}(\tau)\otimes\overline{\mathbf{P}}(\tau)\right)\boldsymbol{\mathcal{I}}\left(\underline{\mathbf{P}}(\tau)\otimes\overline{\mathbf{P}}(\tau)\right)\boldsymbol{\mathcal{I}}'^{\xi} \\ & + 2\overline{\mathbf{P}}(\tau)\boldsymbol{\mathcal{I}}\left(\underline{\mathbf{P}}(\tau)\otimes\overline{\mathbf{P}}(\tau)\right)(2\boldsymbol{\mathcal{I}}-\boldsymbol{\mathcal{I}}')\underline{\mathbf{P}}(\tau)^{\xi} \\ & + 2\underline{\mathbf{P}}(\tau)\boldsymbol{\mathcal{I}}\left(\underline{\mathbf{P}}(\tau)\otimes\overline{\mathbf{P}}(\tau)\right)(2\boldsymbol{\mathcal{I}}-\boldsymbol{\mathcal{I}}')\overline{\mathbf{P}}(\tau)^{\xi}\Big\}\,. \qquad \text{(A.57)}\end{aligned}$$

In index notation it can easily be shown that the parts involving $\boldsymbol{\mathcal{I}}'$ are equivalent, i.e., $\sum_{\mu\nu\lambda\sigma}(\underline{\mu}\overline{\nu}|\underline{\lambda}\overline{\sigma})^{(\xi)}(\mu\sigma|\lambda\nu) = \sum_{\mu\nu\lambda\sigma}(\underline{\mu}\overline{\nu}|\underline{\lambda}\overline{\sigma})(\mu\sigma|\lambda\nu)^{\xi}$, where the short-hand notation (ξ) is used to denote that only the integrals are differentiated and not the pseudodensities. Therefore the derivative becomes

$$\begin{aligned}\frac{\partial E^{\mathrm{c}}_{\mathrm{MP2}}}{\partial \xi} = -\int_0^\infty d\tau\,,\mathrm{Tr}\Big\{ & 2\left(\underline{\mathbf{P}}(\tau)\otimes\overline{\mathbf{P}}(\tau)\right)\boldsymbol{\mathcal{I}}\left(\underline{\mathbf{P}}(\tau)\otimes\overline{\mathbf{P}}(\tau)\right)\left(2\boldsymbol{\mathcal{I}}^{\xi}-\boldsymbol{\mathcal{I}}'^{\xi}\right) \\ & + 2\overline{\mathbf{P}}(\tau)\boldsymbol{\mathcal{I}}\left(\underline{\mathbf{P}}(\tau)\otimes\overline{\mathbf{P}}(\tau)\right)(2\boldsymbol{\mathcal{I}}-\boldsymbol{\mathcal{I}}')\underline{\mathbf{P}}(\tau)^{\xi} \\ & + 2\underline{\mathbf{P}}(\tau)\boldsymbol{\mathcal{I}}\left(\underline{\mathbf{P}}(\tau)\otimes\overline{\mathbf{P}}(\tau)\right)(2\boldsymbol{\mathcal{I}}-\boldsymbol{\mathcal{I}}')\overline{\mathbf{P}}(\tau)^{\xi}\Big\}\,. \qquad \text{(A.58)}\end{aligned}$$

Defining the following intermediates

$$\begin{aligned} I(\tau) &\coloneqq \mathrm{Tr}\left\{\left(\underline{\mathbf{P}}(\tau)\otimes\overline{\mathbf{P}}(\tau)\right)\boldsymbol{\mathcal{I}}\left(\underline{\mathbf{P}}(\tau)\otimes\overline{\mathbf{P}}(\tau)\right)\left(2\boldsymbol{\mathcal{I}}^{\xi}-\boldsymbol{\mathcal{I}}'^{\xi}\right)\right\}\,, \qquad \text{(A.59)} \\ \overline{\mathbf{R}}(\tau) &\coloneqq \overline{\mathbf{P}}(\tau)\boldsymbol{\mathcal{I}}\left(\underline{\mathbf{P}}(\tau)\otimes\overline{\mathbf{P}}(\tau)\right)(2\boldsymbol{\mathcal{I}}-\boldsymbol{\mathcal{I}}')\,, \qquad \text{(A.60)} \\ \underline{\mathbf{R}}(\tau) &\coloneqq \underline{\mathbf{P}}(\tau)\boldsymbol{\mathcal{I}}\left(\underline{\mathbf{P}}(\tau)\otimes\overline{\mathbf{P}}(\tau)\right)(2\boldsymbol{\mathcal{I}}-\boldsymbol{\mathcal{I}}')\,, \qquad \text{(A.61)}\end{aligned}$$

where the perturbation independent parts of the integrals collected in the $\underline{\mathbf{R}}/\overline{\mathbf{R}}$ intermediates, the above expression becomes

$$\frac{\partial E^{\mathrm{c}}_{\mathrm{MP2}}}{\partial \xi} = -\int_0^\infty d\tau \left\{ 2I(\tau) + 2\mathrm{Tr}\left[\overline{\mathbf{R}}(\tau)\underline{\mathbf{P}}(\tau)^\xi\right] + 2\mathrm{Tr}\left[\underline{\mathbf{R}}(\tau)\overline{\mathbf{P}}(\tau)^\xi\right]\right\}, \tag{A.62}$$

which is consistent with the LT-AO-MP2 gradient equations given in Ref. [160]. In order to avoid the evaluation of the derivatives of $\underline{\mathbf{P}}(\tau)$ and $\overline{\mathbf{P}}(\tau)$, the pseudodensities are expanded in terms of the regular occupied and virtual densities $\mathbf{P}_{\mathrm{occ}}$ and $\mathbf{P}_{\mathrm{virt}}$ as

$$\underline{\mathbf{P}}(\tau) = e^{\tau \mathbf{P}_{\mathrm{occ}}\mathbf{F}}\mathbf{P}_{\mathrm{occ}}\,, \tag{A.63}$$

$$\overline{\mathbf{P}}(\tau) = e^{-\tau \mathbf{P}_{\mathrm{virt}}\mathbf{F}}\mathbf{P}_{\mathrm{virt}}\,. \tag{A.64}$$

Thus the derivatives of eqs. (A.63) and (A.64) are given by

$$\underline{\mathbf{P}}^\xi(\tau) = \frac{\partial e^{\tau \mathbf{P}_{\mathrm{occ}}\mathbf{F}}}{\partial \xi}\mathbf{P}_{\mathrm{occ}} + e^{\tau \mathbf{P}_{\mathrm{occ}}\mathbf{F}}\frac{\partial \mathbf{P}_{\mathrm{occ}}}{\partial \xi}\,, \tag{A.65}$$

$$\overline{\mathbf{P}}^\xi(\tau) = \frac{\partial e^{-\tau \mathbf{P}_{\mathrm{virt}}\mathbf{F}}}{\partial \xi}\mathbf{P}_{\mathrm{virt}} + e^{-\tau \mathbf{P}_{\mathrm{virt}}\mathbf{F}}\frac{\partial \mathbf{P}_{\mathrm{virt}}}{\partial \xi}\,. \tag{A.66}$$

By further making use of the identity

$$\mathbf{P}_{\mathrm{occ}}\mathbf{S} + \mathbf{P}_{\mathrm{virt}}\mathbf{S} = \mathbf{1}\,, \tag{A.67}$$

the perturbed virtual density can be related to the perturbed occupied density as

$$\mathbf{P}^\xi_{\mathrm{virt}} = -\mathbf{P}^\xi_{\mathrm{occ}} - \mathbf{S}^{-1}\mathbf{S}^\xi\mathbf{S}^{-1}\,. \tag{A.68}$$

With eqs. (A.63), (A.64), and (A.68), eq. (A.62) for the energy gradient becomes

$$\begin{aligned}
\frac{\partial E^{\mathrm{c}}_{\mathrm{MP2}}}{\partial \xi} &= -\int_0^\infty d\tau \left\{ 2I(\tau) + 2\mathrm{Tr}\left[\overline{\mathbf{R}}(\tau)\underline{\mathbf{P}}^\xi(\tau)\right] + 2\mathrm{Tr}\left[\underline{\mathbf{R}}(\tau)\overline{\mathbf{P}}^\xi(\tau)\right]\right\} \\
&= -2\int_0^\infty d\tau \Bigg\{ I(\tau) + \mathrm{Tr}\left[\overline{\mathbf{R}}(\tau)e^{\tau \mathbf{P}_{\mathrm{occ}}\mathbf{F}}\mathbf{P}^\xi_{\mathrm{occ}}\right] + \mathrm{Tr}\left[\mathbf{P}_{\mathrm{occ}}\overline{\mathbf{R}}(\tau)\frac{\partial e^{\tau \mathbf{P}_{\mathrm{occ}}\mathbf{F}}}{\partial \xi}\right] \\
&\quad - \mathrm{Tr}\left[\underline{\mathbf{R}}(\tau)e^{-\tau \mathbf{P}_{\mathrm{virt}}\mathbf{F}}(\mathbf{P}^\xi_{\mathrm{occ}} + \mathbf{S}^{-1}\mathbf{S}^\xi\mathbf{S}^{-1})\right] + \mathrm{Tr}\left[\mathbf{P}_{\mathrm{virt}}\underline{\mathbf{R}}(\tau)\frac{\partial e^{-\tau \mathbf{P}_{\mathrm{virt}}\mathbf{F}}}{\partial \xi}\right]\Bigg\}\,.
\end{aligned} \tag{A.69}$$

Here, cyclic permutation under the trace is applied to obtain terms with the general form of

$$\mathrm{tr}\left[\mathbf{B}\frac{\partial e^{\mathbf{A}}}{\partial \xi'}\right] = \mathrm{tr}\left[\mathbf{Y}\frac{\partial \mathbf{A}}{\partial \xi'}\right] , \tag{A.70}$$

with

$$\mathbf{Y} = \sum_{k=1}^{\infty}\sum_{i=0}^{k-1}\frac{1}{k!}\mathbf{A}^{i}\mathbf{B}\mathbf{A}^{k-i-1} , \tag{A.71}$$

which can be solved for $\mathbf{Y}$ by recursion, as detailed in Refs. [160] and [161]. Let $\overline{\mathbf{Y}}(\tau)$ be the solution of eq. (A.70) with $\mathbf{A} \equiv \tau\mathbf{P}_{\mathrm{occ}}\mathbf{F}$ and $\mathbf{B} \equiv \mathbf{P}_{\mathrm{occ}}\overline{\mathbf{R}}$, and let $\underline{\mathbf{Y}}(\tau)$ be the solution with $\mathbf{A} \equiv -\tau\mathbf{P}_{\mathrm{virt}}\mathbf{F}$ and $\mathbf{B} \equiv \mathbf{P}_{\mathrm{virt}}\underline{\mathbf{R}}$, then the intermediates $\underline{\mathbf{Y}}(\tau)$ and $\overline{\mathbf{Y}}(\tau)$ can be related to the intermediates $\underline{\mathbf{Y}}_1(\tau)$, $\underline{\mathbf{Y}}_2(\tau)$, $\overline{\mathbf{Y}}_1(\tau)$ and $\overline{\mathbf{Y}}_2(\tau)$ from the derivation by Schweizer *et al.* [160] by

$$\underline{\mathbf{Y}}_1(\tau) = -\tau\mathbf{F}\underline{\mathbf{Y}}(\tau) , \tag{A.72}$$

$$\underline{\mathbf{Y}}_2(\tau) = -\tau\underline{\mathbf{Y}}(\tau)\mathbf{P}_{\mathrm{virt}} , \tag{A.73}$$

$$\overline{\mathbf{Y}}_1(\tau) = \tau\mathbf{F}\overline{\mathbf{Y}}(\tau) , \tag{A.74}$$

$$\overline{\mathbf{Y}}_2(\tau) = \tau\overline{\mathbf{Y}}(\tau)\mathbf{P}_{\mathrm{occ}} . \tag{A.75}$$

The derivative from eq. (A.69) can then be rewritten as

$$\begin{aligned}\frac{\partial E^{\mathrm{c}}_{\mathrm{MP2}}}{\partial \xi} = -2\int_0^{\infty} d\tau \Big\{ & I(\tau) + \mathrm{Tr}\Big[\Big(\overline{\mathbf{Y}}_1(\tau) - \underline{\mathbf{Y}}_1(\tau) + \Big(\overline{\mathbf{Y}}_2(\tau) + \underline{\mathbf{Y}}_2(\tau)\Big)\left(2\boldsymbol{\mathcal{I}} - \boldsymbol{\mathcal{I}}'\right) \\ & + \overline{\mathbf{R}}(\tau)e^{\tau\mathbf{P}_{\mathrm{occ}}\mathbf{F}} - \underline{\mathbf{R}}(\tau)e^{-\tau\mathbf{P}_{\mathrm{virt}}\mathbf{F}}\Big)\mathbf{P}^{\xi}_{\mathrm{occ}}\Big] \\ & + \mathrm{Tr}\left[\Big(\overline{\mathbf{Y}}_2(\tau) + \underline{\mathbf{Y}}_2(\tau)\Big)\mathbf{F}^{(\xi)}\right] \\ & - \mathrm{Tr}\left[\Big(\underline{\mathbf{Y}}_1 + \underline{\mathbf{R}}(\tau)e^{-\tau\mathbf{P}_{\mathrm{virt}}\mathbf{F}}\Big)\mathbf{S}^{-1}\mathbf{S}^{\xi}\mathbf{S}^{-1}\right]\Big\} \\ = -2\int_0^{\infty} d\tau \Big\{ & I(\tau) + \mathrm{Tr}\left[\boldsymbol{\mathcal{P}}(\tau)\mathbf{P}^{\xi}_{\mathrm{occ}}\right] + \mathrm{Tr}\left[\boldsymbol{\mathcal{F}}(\tau)\mathbf{F}^{(\xi)}\right] - \mathrm{Tr}\left[\boldsymbol{\mathcal{S}}(\tau)\mathbf{S}^{-1}\mathbf{S}^{\xi}\mathbf{S}^{-1}\right]\Big\} ,\end{aligned} \tag{A.76}$$

with

$$\begin{aligned}\boldsymbol{\mathcal{P}}(\tau) &= \overline{\mathbf{Y}}_1(\tau) - \underline{\mathbf{Y}}_1(\tau) + (\overline{\mathbf{Y}}_2(\tau) + \underline{\mathbf{Y}}_2(\tau))(2\boldsymbol{\mathcal{I}} - \boldsymbol{\mathcal{I}}') \\ &\quad + \overline{\mathbf{R}}(\tau)e^{\tau\mathbf{P}_{\mathrm{occ}}\mathbf{F}} - \underline{\mathbf{R}}(\tau)e^{-\tau\mathbf{P}_{\mathrm{virt}}\mathbf{F}} ,\end{aligned} \tag{A.77}$$

$$\boldsymbol{\mathcal{F}}(\tau) = \overline{\mathbf{Y}}_2(\tau) + \underline{\mathbf{Y}}_2(\tau) , \tag{A.78}$$

$$\boldsymbol{\mathcal{S}}(\tau) = \underline{\mathbf{Y}}_1(\tau) + \underline{\mathbf{R}}(\tau)e^{-\tau\mathbf{P}_{\mathrm{virt}}\mathbf{F}} , \tag{A.79}$$

$$\mathbf{F}^{(\xi)} = \mathbf{h}^{\xi} + \mathbf{G}^{\xi}\left[\mathbf{P}_{\mathrm{occ}}\right] . \tag{A.80}$$

By realization that intermediate $\boldsymbol{\mathcal{F}}(\tau)$ also appears in the expression for $\boldsymbol{\mathcal{P}}(\tau)$, the latter can be reformulated to

$$\boldsymbol{\mathcal{P}}(\tau) = \overline{\mathbf{Y}}_1(\tau) - \underline{\mathbf{Y}}_1(\tau) + \mathbf{G}\left[\boldsymbol{\mathcal{F}}(\tau)\right] + \overline{\mathbf{R}}(\tau)e^{\tau\mathbf{P}_{\text{occ}}\mathbf{F}} - \underline{\mathbf{R}}(\tau)e^{-\tau\mathbf{P}_{\text{virt}}\mathbf{F}}\,, \tag{A.81}$$

where intermediate $\mathbf{G}\left[\boldsymbol{\mathcal{F}}(\tau)\right]$ resembles the two-electron part of the Fock matrix with $\boldsymbol{\mathcal{F}}(\tau)$ substituting the density matrix, i.e.,

$$G_{\mu\nu}\left[\boldsymbol{\mathcal{F}}(\tau)\right] = \sum_{\lambda\sigma} \mathcal{F}_{\lambda\sigma}(\tau)\left[2(\mu\nu|\lambda\sigma) - (\mu\sigma|\lambda\nu)\right]\,. \tag{A.82}$$

A.3.3. Nuclear Magnetic Moment Derivative of LT-AO-MP2

In the case of perturbations where the basis functions are independent of the perturbation, i.e., for the nuclear magnetic moment $\mathbf{m}$, eq. (A.76) for the LT-AO-MP2 gradient simplifies to

$$\frac{\partial E^{\text{c}}_{\text{MP2}}}{\partial \mathbf{m}} = -2\int_0^\infty d\tau\left(\text{Tr}\left[\boldsymbol{\mathcal{P}}(\tau)\mathbf{P}^{\mathbf{m}}_{\text{occ}}\right] + \text{Tr}\left[\boldsymbol{\mathcal{F}}(\tau)\mathbf{h}^{\mathbf{m}}\right]\right)\,, \tag{A.83}$$

where the functional independence of the basis functions from $\mathbf{m}$ causes the derivatives of the $I(\tau)$ and $\mathbf{S}^{\xi}$ intermediates to be zero. Furthermore, the partial Fock matrix derivative $\mathbf{F}^{(\xi)}$ simplifies to the derivative of the core Hamiltonian $\mathbf{h}$ only. Carrying out the integration for the $\boldsymbol{\mathcal{P}}(\tau)$ and $\boldsymbol{\mathcal{F}}(\tau)$ intermediates yields the final expression for the nuclear magnetic moment derivative as

$$\frac{\partial E^{\text{c}}_{\text{MP2}}}{\partial \mathbf{m}} = -2\left(\text{Tr}\left[\boldsymbol{\mathcal{P}}\mathbf{P}^{\mathbf{m}}_{\text{occ}}\right] + \text{Tr}\left[\boldsymbol{\mathcal{F}}\mathbf{h}^{\mathbf{m}}\right]\right)\,. \tag{A.84}$$

A.3.4. Comparison of the LT-AO-MP2 and AO-RI-dRPA Nuclear Magnetic Moment Derivatives

As derived in the previous section, the final expression for the AO-MP2 gradient with respect to the nuclear magnetic moment $\mathbf{m}$ is given by

$$\frac{\partial E^{\text{c}}_{\text{MP2}}}{\partial \mathbf{m}} = -2\text{Tr}\left[\boldsymbol{\mathcal{F}}\mathbf{h}^{\mathbf{m}} + \boldsymbol{\mathcal{P}}\mathbf{P}^{\mathbf{m}}_{\text{occ}}\right]\,. \tag{A.85}$$

Similarly, the AO-RI-dRPA gradient, as derived in **Publication III**, is given by

$$\frac{\partial E^{\text{c}}_{\text{RPA}}}{\partial \mathbf{m}} = \text{Tr}\left[\mathbf{P}_{\text{RPA}}\mathbf{h}^{\mathbf{m}} + \mathbf{V}_{\text{RPA}}\mathbf{P}^{\mathbf{m}}_{\text{occ}}\right]\,. \tag{A.86}$$

Evidently, the above equations for the LT-AO-MP2 and the AO-RI-dRPA gradient only differ by the definition of intermediates belonging to the $\mathbf{h^m}$-term and the $\mathbf{P}^{\mathbf{m}}_{\mathrm{occ}}$-term. Relabeling the MP2 intermediates as $\mathbf{P}_{\mathrm{MP2}}$ and $\mathbf{V}_{\mathrm{MP2}}$ allows to make a direct comparison between AO-RI-dRPA and LT-AO-MP2:

First, intermediates $\mathbf{P}_{\mathrm{MP2}}$ and $\mathbf{V}_{\mathrm{MP2}}$ are split up, to closer resemble the AO-RI-dRPA intermediates

$$\mathbf{P}_{\mathrm{MP2}} = \int_0^\infty d\tau \left(\overline{\mathbf{Y}}_2(\tau) + \underline{\mathbf{Y}}_2(\tau)\right) , \tag{A.87}$$

$$\mathbf{V}_{\mathrm{MP2}} = \int_0^\infty d\tau \left(\overline{\mathbf{Y}}_1(\tau) - \underline{\mathbf{Y}}_1(\tau) + \overline{\mathbf{R}}(\tau)e^{\tau\mathbf{P}_{\mathrm{occ}}\mathbf{F}} - \underline{\mathbf{R}}(\tau)e^{-\tau\mathbf{P}_{\mathrm{virt}}\mathbf{F}}\right) + \mathbf{G}\left[\mathbf{P}_{\mathrm{MP2}}\right] . \tag{A.88}$$

Next, intermediates $\underline{\mathbf{Y}}_1$, $\underline{\mathbf{Y}}_2$, $\overline{\mathbf{Y}}_1$ and $\overline{\mathbf{Y}}_2$ are substituted with their definitions in terms of $\underline{\mathbf{Y}}$ and $\overline{\mathbf{Y}}$ from eqs. (A.72)–(A.75) to yield

$$\mathbf{P}_{\mathrm{MP2}} = \int_0^\infty d\tau \left(\overline{\mathbf{Y}}(\tau)\mathbf{P}_{\mathrm{occ}} - \underline{\mathbf{Y}}(\tau)\mathbf{P}_{\mathrm{virt}}\right) , \tag{A.89}$$

$$\mathbf{V}_{\mathrm{MP2}} = \int_0^\infty d\tau \left(\mathbf{F}\overline{\mathbf{Y}}(\tau) + \mathbf{F}\underline{\mathbf{Y}}(\tau) + \overline{\mathbf{R}}(\tau)e^{\tau\mathbf{P}_{\mathrm{occ}}\mathbf{F}} - \underline{\mathbf{R}}(\tau)e^{-\tau\mathbf{P}_{\mathrm{virt}}\mathbf{F}}\right) + \mathbf{G}\left[\mathbf{P}_{\mathrm{MP2}}\right] . \tag{A.90}$$

With the definition of the additional intermediates $\underline{\mathbf{M}}$, $\overline{\mathbf{M}}$, and $\mathbf{M}_{\mathrm{MP2}}$ given by

$$\underline{\mathbf{M}} = \int_0^\infty d\tau \left[\mathbf{F}\underline{\mathbf{Y}}(\tau) + \overline{\mathbf{R}}(\tau)e^{\tau\mathbf{P}_{\mathrm{occ}}\mathbf{F}}\right] , \tag{A.91}$$

$$\overline{\mathbf{M}} = \int_0^\infty d\tau \left[\mathbf{F}\overline{\mathbf{Y}}(\tau) - \underline{\mathbf{R}}(\tau)e^{-\tau\mathbf{P}_{\mathrm{virt}}\mathbf{F}}\right] , \tag{A.92}$$

$$\mathbf{M}_{\mathrm{MP2}} = \underline{\mathbf{M}} + \overline{\mathbf{M}} , \tag{A.93}$$

intermediate $\mathbf{V}_{\mathrm{MP2}}$ becomes

$$\mathbf{V}_{\mathrm{MP2}} = \mathbf{M}_{\mathrm{MP2}} + \mathbf{G}\left[\mathbf{P}_{\mathrm{MP2}}\right] . \tag{A.94}$$

Furthermore, by expanding the two-electron integral contribution as $\mathbf{G}[\mathbf{P}_{\mathrm{MP2}}] = \mathbf{J}[\mathbf{P}_{\mathrm{MP2}}] + \mathbf{K}[\mathbf{P}_{\mathrm{MP2}}]$, intermediate $\mathbf{V}_{\mathrm{MP2}}$ becomes

$$\mathbf{V}_{\mathrm{MP2}} = \mathbf{M}_{\mathrm{MP2}} + \mathbf{J}[\mathbf{P}_{\mathrm{MP2}}] + \mathbf{K}[\mathbf{P}_{\mathrm{MP2}}] . \tag{A.95}$$

Finally, by comparing eqs. (A.89) and (A.95) to their counterparts in the AO-RI-dRPA gradient given in **Publication III** in eqs. 37 and 38 as

$$\mathbf{P}_{\text{RPA}} = \frac{1}{2}\int_0^{\infty} d\tau \left(\mathbf{P}_{\text{occ}}\underline{\mathbf{Y}}(-\text{i}\tau) - \mathbf{P}_{\text{virt}}\overline{\mathbf{Y}}(\text{i}\tau)\right) , \tag{A.96}$$

$$\mathbf{V}_{\text{RPA}} = \frac{1}{2}\left(\mathbf{M}_{\text{RPA}} + \mathbf{J}[\mathbf{P}_{\text{RPA}}] + \mathbf{V}_{\text{KS}}[\mathbf{P}_{\text{RPA}}]\right) , \tag{A.97}$$

it is evident that the LT-AO-MP2 and the AO-RI-RPA gradient only differ in three aspects:

1. The Fock matrix in MP2 theory is replaced with the level-shifted Kohn–Sham Hamiltonian in RPA theory:

$$\mathbf{F} \rightarrow \mathbf{H}_{\text{KS}} - \varepsilon_F \mathbf{S} \tag{A.98}$$

2. The exchange part of the two-electron integrals in MP2 theory is replaced with the Kohn–Sham potential:

$$\mathbf{G}[\mathbf{P}_{\text{MP2}}] = \mathbf{J}[\mathbf{P}_{\text{MP2}}] + \mathbf{K}[\mathbf{P}_{\text{MP2}}] \rightarrow \mathbf{G}[\mathbf{P}_{\text{RPA}}] = \mathbf{J}[\mathbf{P}_{\text{RPA}}] + \mathbf{V}_{\text{KS}}[\mathbf{P}_{\text{RPA}}] \tag{A.99}$$

3. The perturbation independent part of the two-electron interaction is given by the $\underline{\mathbf{R}}$ and $\overline{\mathbf{R}}$ intermediates in LT-AO-MP2 theory and by the correlated self-energy $\mathbf{\Sigma}$ in AO-RI-dRPA theory:

$$\underline{\mathbf{R}}/\overline{\mathbf{R}} \rightarrow \mathbf{\Sigma} \tag{A.100}$$

A.3.5. Comparison of the LT-AO-MP2 and AO-RI-dRPA NMR Second Derivatives

According to the approach presented in Section 2.3.4, eqs. (A.85) and (A.86) can be further differentiated with respect to an external magnetic field **B** to obtain analytic expressions for the calculation of the NMR shielding tensor. After establishing a close connection of the gradient expressions of both methods, it is evident that the NMR second derivatives also closely resemble each other. Following the derivation in **Publication III**, relevant intermediates – beyond those of the first derivative – are presented in Fig. A.3. Detailed expressions for the intermediates shown in Fig A.3 are given in Ref. [161] for LT-AO-MP2 and in **Publication III** for AO-RI-dRPA.

$$\begin{tikzcd}
\boldsymbol{\mathcal{P}}^{\mathbf{B}} \\
\boldsymbol{\mathcal{F}}^{\mathbf{B}} \arrow[u, "(32)"] \\
\underline{\mathbf{Y}}_1^{\mathbf{B}} \quad \overline{\mathbf{Y}}_1^{\mathbf{B}} \quad \underline{\mathbf{Y}}_2^{\mathbf{B}} \quad \overline{\mathbf{Y}}_2^{\mathbf{B}} \arrow[u, "(31)"] \\
\mathbf{A}^{\mathbf{B}} \quad \mathbf{B}^{\mathbf{B}} \arrow[u, "(\mathrm{B1})\text{–}(\mathrm{B5})"] \\
\underline{\mathbf{R}}^{\mathbf{B}} \quad \overline{\mathbf{R}}^{\mathbf{B}} \arrow[u] \\
\underline{\mathbf{P}}^{\mathbf{B}} \quad \overline{\mathbf{P}}^{\mathbf{B}} \arrow[u, "(38)\text{–}(39)"]
\end{tikzcd}$$

(a) LT-AO-MP2

$$\begin{tikzcd}
\mathbf{V}^{\mathbf{B}}_{\mathrm{RPA}} & \\
\mathbf{P}^{\mathbf{B}}_{\mathrm{RPA}} \arrow[u, "(79)"] & \\
\mathbf{Y}^{\mathbf{B}}(\mathrm{i}\tau) \arrow[u, "(59)"] & \\
\boldsymbol{\mathcal{A}}^{\mathbf{B}}(\tau) \quad \boldsymbol{\mathcal{B}}^{\mathbf{B}}(\mathrm{i}\tau) \arrow[u, "(61)"] & \\
\boldsymbol{\Sigma}^{\mathbf{B}}(\mathrm{i}\tau) \arrow[u, "(63)\text{–}(66)"] & \\
\mathbf{W}_{\mathrm{c}}^{\mathbf{B}}(\mathrm{i}\tau) \arrow[u, "(68)"] & \hat{\mathbf{W}}_{\mathrm{c}}^{\mathbf{B}}(\mathrm{i}\omega) \arrow[l, "\mathrm{IST}", "(71)"'] \\
\mathbf{X}_0^{\mathbf{B}}(\mathrm{i}\tau) \arrow[u, "\times" marking] \arrow[r, "\mathrm{ST}", "(75)"'] & \hat{\mathbf{X}}_0^{\mathbf{B}}(\mathrm{i}\omega) \arrow[u, "(73)"'] \\
\underline{\mathbf{G}}^{\mathbf{B}}(\mathrm{i}\tau) \quad \overline{\mathbf{G}}^{\mathbf{B}}(\mathrm{i}\tau) \arrow[u, "(76)"] &
\end{tikzcd}$$

(b) AO-RI-dRPA

Figure A.3.: Schematic representation of the derivation of the central intermediates for the calculation of the chemical shielding tensor in LT-AO-MP2 (left) and dRPA (right). The notation for the intermediates follows Ref. [161] for LT-AO-MP2 and **Publication III** for AO-RI-dRPA. All arrows are labeled with the corresponding equations from the respective publications. (b) Reprinted with permission from *J. Chem. Theory Comput.* **19**, 7542–7554 (2023). Copyright 2023 American Chemical Society.

Based on the derivation outlined in Fig. A.3, it is apparent that the NMR derivatives for LT-AO-MP2 and AO-RI-dRPA mainly differ in the intermediates containing the **B** field derivatives of the correlation terms $\underline{\mathbf{R}}^{\mathbf{B}}/\overline{\mathbf{R}}^{\mathbf{B}}$ and $\boldsymbol{\Sigma}^{\mathbf{B}}$, respectively. The ensuing steps are equivalent in both theories, which allows to treat LT-AO-MP2 and AO-RI-dRPA in an equal fashion. Their implementations can therefore be conjoined, even though at first glance the theories appear to be dissimilar.

Bibliography

[1] D. R. Hartree, *Math. Proc. Camb. Philos. Soc.* **1928**, *24*, 111–132.

[2] V. Fock, *Zeitschrift für Physik* **1930**, *61*, 126–148.

[3] J. C. Slater, *Phys. Rev.* **1929**, *34*, 1293–1322.

[4] C. Møller, M. S. Plesset, *Phys. Rev.* **1934**, *46*, 618–622.

[5] R. J. Bartlett, M. Musiał, *Rev. Mod. Phys.* **2007**, *79*, 291–352.

[6] G. D. Purvis, R. J. Bartlett, *J. Chem. Phys.* **1982**, *76*, 1910–1918.

[7] K. Raghavachari, G. W. Trucks, J. A. Pople, M. Head-Gordon, *Chem. Phys. Lett.* **1989**, *157*, 479–483.

[8] O. Christiansen, H. Koch, P. Jørgensen, *Chem. Phys. Lett.* **1995**, *243*, 409–418.

[9] H. Koch, O. Christiansen, P. Jørgensen, A. M. Sánchez De Merás, T. Helgaker, *J. Chem. Phys.* **1997**, *106*, 1808–1818.

[10] H. Sekino, R. J. Bartlett, *Int. J. Quantum Chem.* **1984**, *26*, 255–265.

[11] J. Schirmer, *Phys. Rev. A* **1982**, *26*, 2395–2416.

[12] W. Kohn, L. J. Sham, *Phys. Rev.* **1965**, *140*, A1133–A1138.

[13] P. Hohenberg, W. Kohn, *Phys. Rev.* **1964**, *136*, B864–B871.

[14] D. Langreth, J. Perdew, *Solid State Commun.* **1975**, *17*, 1425–1429.

[15] O. Gunnarsson, B. I. Lundqvist, *Phys. Rev. B* **1976**, *13*, 4274–4298.

[16] D. C. Langreth, J. P. Perdew, *Phys. Rev. B* **1977**, *15*, 2884–2901.

[17] F. Furche, *Phys. Rev. B* **2001**, *64*, 195120.

[18] F. Furche, *J. Chem. Phys.* **2008**, *129*, 114105.

[19] H. Eshuis, J. E. Bates, F. Furche, *Theor. Chem. Acc.* **2012**, *131*, 1084.

[20] G. P. Chen, V. K. Voora, M. M. Agee, S. G. Balasubramani, F. Furche, *Annu. Rev. Phys. Chem.* **2017**, *68*, 421–445.

[21] J. L. Whitten, *J. Chem. Phys.* **1973**, *58*, 4496–4501.

[22] B. I. Dunlap, J. W. Connolly, J. R. Sabin, *J. Chem. Phys.* **1979**, *71*, 3396.

[23] M. Feyereisen, G. Fitzgerald, A. Komornicki, *Chem. Phys. Lett.* **1993**, *208*, 359–363.

[24] K. Eichkorn, O. Treutler, H. Öhm, M. Häser, R. Ahlrichs, *Chem. Phys. Lett.* **1995**, *240*, 283–290.

[25] K. Eichkorn, F. Weigend, O. Treutler, R. Ahlrichs, *Theor. Chem. Acc.* **1997**, *97*, 119–124.

[26] H. Eshuis, J. Yarkony, F. Furche, *J. Chem. Phys.* **2010**, *132*, 234114.

[27] E. G. Hohenstein, R. M. Parrish, T. J. Martínez, *J. Chem. Phys.* **2012**, *137*, 044103.

[28] R. M. Parrish, E. G. Hohenstein, T. J. Martínez, C. D. Sherrill, *J. Chem. Phys.* **2012**, *137*, 224106.

[29] R. M. Parrish, E. G. Hohenstein, T. J. Martínez, C. D. Sherrill, *J. Chem. Phys.* **2013**, *138*, 194107.

[30] R. M. Parrish, E. G. Hohenstein, N. F. Schunck, C. D. Sherrill, T. J. Martínez, *Phys. Rev. Lett.* **2013**, *111*, 1–5.

[31] Y. Jung, A. Sodt, P. M. W. Gill, M. Head-Gordon, *Proc. Natl. Acad. Sci. U. S. A.* **2005**, *102*, 6692–6697.

[32] A. Luenser, H. F. Schurkus, C. Ochsenfeld, *J. Chem. Theory Comput.* **2017**, *13*, 1647–1655.

[33] T. H. Thompson, C. Ochsenfeld, *J. Chem. Phys.* **2019**, *150*, 044101.

[34] Y. Jung, R. C. Lochan, A. D. Dutoi, M. Head-Gordon, *J. Chem. Phys.* **2004**, *121*, 9793.

[35] S. Vogler, M. Ludwig, M. Maurer, C. Ochsenfeld, *J. Chem. Phys.* **2017**, *147*, 024101.

[36] S. Vogler, G. Savasci, M. Ludwig, C. Ochsenfeld, *J. Chem. Theory Comput.* **2018**, *14*, 3014–3024.

[37] M. Glasbrenner, D. Graf, C. Ochsenfeld, *J. Chem. Theory Comput.* **2022**, *18*, 192–205.

[38] E. Schrödinger, *Phys. Rev.* **1926**, *28*, 1049–1070.

[39] M. Born, R. Oppenheimer, *Ann. Phys.* **1927**, *389*, 457–484.

[40] P.-O. Löwdin, *Phys. Rev.* **1955**, *97*, 1509–1520.

[41] J. M. L. Martin, *Isr. J. Chem.* **2022**, *62*, e202100111.

[42] D. P. Tew, W. Klopper, T. Helgaker, *J. Comput. Chem.* **2007**, *28*, 1307–1320.

[43] W. Pauli, *Zeitschrift für Physik* **1925**, *31*, 765–783.

[44] T. Helgaker, P. Jørgensen, J. Olsen in *Molecular Electronic-Structure Theory*, John Wiley & Sons, Ltd, **2000**, Chapter 1, pp. 1–33.

[45] G. C. Wick, *Phys. Rev.* **1950**, *80*, 268–272.

[46] J. C. Slater, *Phys. Rev.* **1930**, *35*, 210–211.

[47] C. C. J. Roothaan, *Rev. Mod. Phys.* **1951**, *23*, 69–89.

[48] L. Brillouin, *J. Phys. Radium* **1932**, *3*, 373–389.

[49] E. Wigner, *Math. naturw. Anz. ungar.* **1935**, *53*, 475.

[50] I. Hubač, S. Wilson, *J. Phys. B: At. Mol. Opt. Phys.* **2000**, *33*, 365–374.

[51] E. Schrödinger, *Ann. Phys.* **1926**, *385*, 437–490.

[52] P.-O. Löwdin, *Phys. Rev.* **1955**, *97*, 1474–1489.

[53] L. Brillouin, *Actual. scientist. ind.* **1933**, *71*, 160.

[54] E. U. Condon, *Phys. Rev.* **1930**, *36*, 1121–1130.

[55] O. Christiansen, J. Olsen, P. Jørgensen, H. Koch, P.-A. Malmqvist, *Chem. Phys. Lett.* **1996**, *261*, 369–378.

[56] B. Datta, P. Sen, D. Mukherjee, *J. Phys. Chem.* **1995**, *99*, 6441–6451.

[57] O. Christiansen, H. Koch, P. Jørgensen, *J. Chem. Phys.* **1995**, *103*, 7429–7441.

[58] O. Christiansen, P. Jørgensen, C. Hättig, *Int. J. Quantum Chem.* **1998**, *68*, 1–52.

[59] E. Dalgaard, H. J. Monkhorst, *Phys. Rev. A* **1983**, *28*, 1217–1222.

[60] H. Koch, H. J. A. Jensen, P. Jørgensen, T. Helgaker, *J. Chem. Phys.* **1990**, *93*, 3345–3350.

[61] T. B. Pedersen, H. Koch, *J. Chem. Phys.* **1997**, *106*, 8059–8072.

[62] J. Schirmer, A. B. Trofimov, *J. Chem. Phys.* **2004**, *120*, 11449–11464.

[63] A. Dreuw, A. Papapostolou, A. L. Dempwolff, *J. Phys. Chem. A* **2023**, *127*, 6635–6646.

[64] A. Dreuw, M. Wormit, *WIREs Comput. Mol. Sci.* **2015**, *5*, 82–95.

[65] D. J. Rowe, *Nucl. Phys.* **1966**, *80*, 209–222.

[66] D. Bohm, D. Pines, *Phys. Rev.* **1953**, *92*, 609–625.

[67] X. Ren, P. Rinke, C. Joas, M. Scheffler, *J. Mater. Sci.* **2012**, *47*, 7447–7471.

[68] G. E. Scuseria, T. M. Henderson, D. C. Sorensen, *J. Chem. Phys.* **2008**, *129*, 231101.

[69] H. Lehmann, *Il Nuovo Cimento* **1954**, *11*, 342–357.

[70] E. K. U. Gross, W. Kohn, *Phys. Rev. Lett.* **1985**, *55*, 2850–2852.

[71] J. Gauss in *Modern Methods and Algorithms of Quantum Chemistry*, *Vol. 3*, John von Neumann Institute for Computing, **2000**, pp. 541–592.

[72] J. Almlöf, P. R. Taylor, *Int. J. Quantum Chem.* **1985**, *27*, 743–768.

[73] D. Craig, T. Thirunamachandran, *Molecular Quantum Electrodynamics: An Introduction to Radiation-Molecule Interactions*, Dover Publications, **1998**.

[74] J. Kussmann, C. Ochsenfeld, *J. Chem. Phys.* **2007**, *127*, 054103.

[75] T. Helgaker, P. Jørgensen, *J. Chem. Phys.* **1991**, *95*, 2595–2601.

[76] J. Gauss, J. F. Stanton in *Principles of Nuclear Magnetism*, **2002**, pp. 355–422.

[77] T. Helgaker, M. Jaszuński, K. Ruud, *Chem. Rev.* **1999**, *99*, 293–352.

[78] L. Cheng, S. Stopkowicz, J. Gauss, *Int. J. Quantum Chem.* **2014**, *114*, 1108–1127.

[79] P. Pulay in *Advances in Chemical Physics*, *Vol. 69*, Wiley, **1987**, pp. 241–286.

[80] T. Helgaker, P. Jørgensen in *Advances in Quantum Chemistry*, *Vol. 19*, Elsevier, **1988**, pp. 183–245.

[81] R. D. Amos, J. E. Rice, *Comput. Phys. Rep.* **1989**, *10*, 147–187.

[82] P. Pulay, *WIREs Comput. Mol. Sci.* **2014**, *4*, 169–181.

[83] P. Norman, K. Ruud, T. Saue, *Principles and Practices of Molecular Properties: Theory, Modeling and Simulations*, First edition, John Wiley & Sons, Hoboken, NJ, **2018**.

[84] J. A. Weil, J. R. Bolton, *Electron Paramagnetic Resonance: Elementary Theory and Practical Applications*, Wiley, **2006**.

[85] J. C. Facelli, *Concepts Magn. Reson. A* **2004**, *20A*, 42–69.

[86] R. Ditchfield, *J. Chem. Phys.* **1972**, *56*, 5688–5691.

[87] H. F. Hameka, *Rev. Mod. Phys.* **1962**, *34*, 87–101.

[88] F. London, *J. Phys. Radium* **1937**, *8*, 397–409.

[89] L. D. Landau, E. M. Lifschitz, *Band 2 Klassische Feldtheorie*, De Gruyter, Berlin, Boston, **1963**.

[90] D. Chesnut in Annual Reports on NMR Spectroscopy, Academic Press, **1994**, pp. 71–122.

[91] S. Ten-no, J. Noga, *Wiley Interdiscip. Rev. Comput. Mol. Sci.* **2012**, *2*, 114–125.

[92] T. G. Kolda, B. W. Bader, *SIAM Rev.* **2009**, *51*, 455–500.

[93] V. Khoromskaia, B. Khoromskij, *Tensor Numerical Methods in Quantum Chemistry*, De Gruyter, **2018**.

[94] U. Schollwöck, *Ann. Phys.* **2011**, *326*, 96–192.

[95] G. K.-L. Chan, S. Sharma, *Annu. Rev. Phys. Chem.* **2011**, *62*, 465–481.

[96] L. R. Tucker, *Psychometrika* **1966**, *31*, 279–311.

[97] R. A. Harshman, *Foundations of the PARAFAC Procedure: Models and Conditions for an "explanatory" Multi-model Factor Analysis*, **1970**, pp. 1–84.

[98] C. A. White, B. G. Johnson, P. M. W. Gill, M. Head-Gordon, *Chem. Phys. Lett.* **1994**, *230*, 8–16.

[99] X. Xing, H. Huang, E. Chow, *J. Chem. Phys.* **2020**, *153*, 084119.

[100] H. J. Werner, F. R. Manby, P. J. Knowles, *J. Chem. Phys.* **2003**, *118*, 8149.

[101] N. H. F. Beebe, J. Linderberg, *Int. J. Quantum Chem.* **1977**, *12*, 683–705.

[102] I. Røeggen, E. Wisløff-Nilssen, *Chem. Phys. Lett.* **1986**, *132*, 154–160.

[103] F. Aquilante, T. B. Pedersen, *Chem. Phys. Lett.* **2007**, *449*, 354–357.

[104] I. Røeggen, T. Johansen, *J. Chem. Phys.* **2008**, *128*, 194107.

[105] T. B. Pedersen, F. Aquilante, R. Lindh, *Theor. Chem. Acc.* **2009**, *124*, 1–10.

[106] F. Aquilante, L. Boman, J. Boström, H. Koch, R. Lindh, A. Sánchez De Merás, T. B. Pedersen in *Linear-Scaling Techniques in Computational Chemistry and Physics*, *Vol. 13*, Springer Netherlands, Dordrecht, **2011**, pp. 301–343.

[107] R. Schutski, J. Zhao, T. M. Henderson, G. E. Scuseria, *J. Chem. Phys.* **2017**, *147*, 184113.

[108] B. H. Greeley, T. V. Russo, D. T. Mainz, R. A. Friesner, J. M. Langlois, W. A. Goddard, R. E. Donnelly, M. N. Ringnalda, *J. Chem. Phys.* **1994**, *101*, 4028–4041.

[109] R. B. Murphy, M. D. Beachy, R. A. Friesner, M. N. Ringnalda, *J. Chem. Phys.* **1995**, *103*, 1481–1490.

[110] T. J. Martínez, E. A. Carter, *J. Chem. Phys.* **1995**, *102*, 7564–7572.

[111] J. Lu, L. Ying, *J. Comput. Phys.* **2015**, *302*, 329–335.

[112] J. Lu, L. Ying, *Ann. Math. Sci. Appl.* **2016**, *1*, 321–339.

[113] W. Hu, L. Lin, C. Yang, *J. Chem. Theory Comput.* **2017**, *13*, 5420–5431.

[114] K. Dong, W. Hu, L. Lin, *J. Chem. Theory Comput.* **2018**, *14*, 1311–1320.

[115] F. D. Malone, S. Zhang, M. A. Morales, *J. Chem. Theory Comput.* **2019**, *15*, 256–264.

[116] X. Qin, J. Liu, W. Hu, J. Yang, *J. Phys. Chem. A* **2020**, *124*, 5664–5674.

[117] W. Hu, J. Liu, Y. Li, Z. Ding, C. Yang, J. Yang, *J. Chem. Theory Comput.* **2020**, *16*, 964–973.

[118] J. Lee, L. Lin, M. Head-Gordon, *J. Chem. Theory Comput.* **2020**, *16*, 243–263.

[119] W. Gao, J. R. Chelikowsky, *J. Chem. Theory Comput.* **2020**, *16*, 2216–2223.

[120] B. Helmich-Paris, B. De Souza, F. Neese, R. Izsák, *J. Chem. Phys.* **2021**, *155*, 104109.

[121] H. Laqua, T. H. Thompson, J. Kussmann, C. Ochsenfeld, *J. Chem. Theory Comput.* **2020**, *16*, 1456–1468.

[122] H. Laqua, J. Kussmann, C. Ochsenfeld, *J. Chem. Phys.* **2021**, *154*, 214116.

[123] P. M. Kroonenberg, J. De Leeuw, *Psychometrika* **1980**, *45*, 69–97.

[124] G. Beylkin, M. J. Mohlenkamp, *Proc. Natl. Acad. Sci. U.S.A.* **2002**, *99*, 10246–10251.

[125] P.-O. Löwdin in *Advances in Quantum Chemistry*, *Vol. 5*, Elsevier, **1970**, pp. 185–199.

[126] K. Pierce, V. Rishi, E. F. Valeev, *J. Chem. Theory Comput.* **2021**, *17*, 2217–2230.

[127] A. Datar, D. A. Matthews, *J. Chem. Theory Comput.* **2024**, *20*, 708–720.

[128] I. Duchemin, X. Blase, *J. Chem. Phys.* **2019**, *150*, 174120.

[129] F. A. Delesma, M. Leucke, D. Golze, P. Rinke, *J. Chem. Phys.* **2024**, *160*, 024118.

[130] D. A. Matthews, *J. Chem. Phys.* **2021**, *154*, 134102.

[131] A. D. Becke, *J. Chem. Phys.* **1988**, *88*, 2547–2553.

[132] S. I. L. Kokkila Schumacher, E. G. Hohenstein, R. M. Parrish, L.-P. Wang, T. J. Martínez, *J. Chem. Theory Comput.* **2015**, *11*, 3042–3052.

[133] V. I. Lebedev, D. N. Laikov, *Dokl. Math.* **1999**, *59*, 477–481.

[134] C. W. Murray, N. C. Handy, G. J. Laming, *Mol. Phys.* **1993**, *78*, 997–1014.

[135] O. Treutler, R. Ahlrichs, *J. Chem. Phys.* **1995**, *102*, 346–354.

[136] H. F. Schurkus, A. Luenser, C. Ochsenfeld, *J. Chem. Phys.* **2017**, *146*, 211106.

[137] P. E. Maslen, C. Ochsenfeld, C. A. White, M. S. Lee, M. Head-Gordon, *J. Phys. Chem. A* **1998**, *102*, 2215–2222.

[138] J. R. Bunch, D. J. Rose, *Sparse Matrix Computations*, Academic Press, **2014**.

[139] G. H. Golub, C. F. Van Loan, *Matrix Computations*, Johns Hopkins University Press, **1996**.

[140] R. Barrett, M. Berry, T. F. Chan, J. Demmel, J. M. Donato, J. Dongarra, V. Eijkhout, R. Pozo, C. Romine, H. Van der Vorst, *Templates for the Solution of Linear Systems: Building Blocks for Iterative Methods*, Society for Industrial and Applied Mathematics, **1994**.

[141] V. Strassen, *Numer. Math.* **1969**, *13*, 354–356.

[142] Intel, oneAPI Math Kernel Library (oneMKL), **2024**, `https://www.intel.com/content/www/us/en/developer/tools/oneapi/onemkl.html` (visited on 01/24/2024).

[143] S. F. Boys, *Rev. Mod. Phys.* **1960**, *32*, 296–299.

[144] J. M. Foster, S. F. Boys, *Rev. Mod. Phys.* **1960**, *32*, 300–302.

[145] C. Edmiston, K. Ruedenberg, *Rev. Mod. Phys.* **1963**, *35*, 457–464.

[146] J. Pipek, P. G. Mezey, *J. Chem. Phys.* **1989**, *90*, 4916.

[147] F. Neese, F. Wennmohs, A. Hansen, *J. Chem. Phys.* **2009**, *130*, 114108.

[148] J. Yang, Y. Kurashige, F. R. Manby, G. K. L. Chan, *J. Chem. Phys.* **2011**, *134*, 044123.

[149] F. Aquilante, T. B. Pedersen, A. Sánchez De Merás, H. Koch, *J. Chem. Phys.* **2006**, *125*, 174101.

[150] C. Ochsenfeld, J. Kussmann, D. S. Lambrecht in *Reviews in Computational Chemistry, Vol. 23*, **2007**, pp. 1–82.

[151] S. A. Maurer, D. S. Lambrecht, D. Flaig, C. Ochsenfeld, *J. Chem. Phys.* **2012**, *136*, 144107.

[152] S. A. Maurer, D. S. Lambrecht, J. Kussmann, C. Ochsenfeld, *J. Chem. Phys.* **2013**, *138*, 014101.

[153] D. S. Lambrecht, C. Ochsenfeld, *J. Chem. Phys.* **2005**, *123*, 184101.

[154] J. Almlöf, *Chem. Phys. Lett.* **1991**, *181*, 319–320.

[155] M. Häser, J. Almlöf, *J. Chem. Phys.* **1992**, *96*, 489.

[156] M. Häser, *Theor. Chim. Acta* **1993**, *87*, 147–173.

[157] S. A. Maurer, J. Kussmann, C. Ochsenfeld, *J. Chem. Phys.* **2014**, *141*, 051106.

[158] H. F. Schurkus, C. Ochsenfeld, *J. Chem. Phys.* **2016**, *144*, 031101.

[159] D. Graf, M. Beuerle, H. F. Schurkus, A. Luenser, G. Savasci, C. Ochsenfeld, *J. Chem. Theory Comput.* **2018**, *14*, 2505–2515.

[160] S. Schweizer, B. Doser, C. Ochsenfeld, *J. Chem. Phys.* **2008**, *128*, 154101.

[161] M. Glasbrenner, S. Vogler, C. Ochsenfeld, *J. Chem. Phys.* **2021**, *155*, 224107.